



University
of Glasgow

Cascallana-Matias, Irene (2016) *Lightweight metal halide and hydride fast Li ion conductors*. PhD thesis.

<http://theses.gla.ac.uk/7609/>

Copyright and moral rights for this work are retained by the author

A copy can be downloaded for personal non-commercial research or study, without prior permission or charge

This work cannot be reproduced or quoted extensively from without first obtaining permission in writing from the author

The content must not be changed in any way or sold commercially in any format or medium without the formal permission of the author

When referring to this work, full bibliographic details including the author, title, awarding institution and date of the thesis must be given

Enlighten: Theses

<https://theses.gla.ac.uk/>
research-enlighten@glasgow.ac.uk

Lightweight Metal Halide and Hydride Fast
Li Ion Conductors



University
of Glasgow

Irene Cascallana Matías

Submitted in fulfilment of the requirements for the
Degree of Doctor of Philosophy

School of Chemistry
College of Science and Engineering

University of Glasgow

August 2016

Abstract

This work was motivated by the extensive research on lithium solid state materials, which have attracted increasing interest for potential applications in hydrogen storage and/or lithium ion batteries due to their extraordinary properties. In this thesis, LiBH_4 -derived materials, LiInBr_4 and complex phases based on lithium ammonia borane with potential use as solid state electrolytes were successfully synthesised and characterised.

Firstly, the hexagonal phase (HT) of LiBH_4 was stabilised and isolated at room temperature by anion substitution over a compositional range. Fast lithium ion conductivity is retained in these phases. The structural analysis performed at room temperature combining powder X-ray and neutron diffraction revealed a considerable disorder in both the position and orientation of the anions in this structure leading to highly anisotropic distribution of lithium scattering. BH_4^- anions were found to exhibit orientational disorder which can only be satisfactorily modelled using an inversion of the deuterium atoms. This implies substantial rotation of the BH_4^- units although not the free spherical rotation which has been observed in other complex anion fast ion conductors. Analysis of the Bragg scattering up to 573 K shows that the material retains the hexagonal structure, although the reduced intensity of the Bragg reflections does suggest increasing disorder (loss of long range order) in the material with heating.

Secondly, the synthesis and stabilisation of the high pressure (HP) phase of LiBH_4 is reported at room temperature and ambient pressure and achieves high ionic conductivity. In this chapter the results from the three different approaches used to stabilise the HP - LiBH_4 are discussed (**Methods 1, 2, and 3**). Firstly, by **Method 1**, mixed alkali borohydrides were studied using LiBH_4 and NaBH_4 . NaBH_4 was used because it has the same structure as the HP - LiBH_4 phase, a rock salt type structure. In **Method 2** the formation of mixed alkali metal - mixed anion borohydrides was suggested as an alternative route. Mixtures with different molar ratios of LiBH_4 and NaBr were studied. NaBr was used because it has the same structure as HP - LiBH_4 again, a rock salt type structure. In **Method 3** synthesis, structure, and phase diagram studies for the LiBH_4 - LiI - NaBH_4 system is discussed in detail. The ionic conductivity of some of these phases is discussed.

Thirdly, different complex phases based on lithium ammonia borane are proposed as electrolytes for the first time. Ammonia borane could be considered as part of a potential electrolyte structure because of its low molecular weight (30.7 g mol⁻¹), thermal stability and satisfactory air-stability. Ammonia borane is able to form different compounds with lithium-containing materials. So far, different lithium ammonia borane hydrides have been elucidated with pseudo-layered structures which could exhibit 1D, 2D or 3D lithium ion conductivity. Here in this work, we identified lithium ammonia borane hydrides, originally proposed for hydrogen storage, as candidates for electrolytes. Also we report two novel lithium iodide ammonia borane compounds which show high ionic conductivity. High quality powder X-ray diffraction data is reported for both new materials and their thermal stability has been determined.

Finally, LiInBr₄ is suggested as a candidate as a solid electrolyte for lithium ion batteries. In principle, this material has similarities with LiBH₄. It has been reported in the literature that its room temperature phase shows high ionic conductivity and that it undergoes a phase transition to a high temperature phase like LiBH₄. As for LiBH₄, we investigate the ionic conductivity of the bromide. Experiments were also performed using neutron powder diffraction and ⁷Li NMR measurements. Here we demonstrate that the room temperature structure was wrongly assigned in past reports. Data also suggest that a formal phase transition in this material does not occur. Instead, the redistribution of Li⁺ ions at elevated temperatures leads to two different routes for fast lithium ion motion in LiInBr₄.

List of Contents

Abstract	2
List of Contents	4
List of Tables.....	11
List of Figures	18
Acknowledgments	35
Abbreviations	37
Declaration	39
1. Introduction	40
1.1 Li ion batteries	41
1.1.1 Anodes, negative electrodes	44
1.1.2 Cathodes, positive electrodes.....	44
1.2 Electrolytes	47
1.2.1 Background.....	47
1.2.1.1 Small - scale lithium ion batteries.....	47
1.2.1.2 Large - scale lithium ion batteries.....	47
1.2.2 Drawbacks for large - scale lithium ion batteries	49
1.2.2.1 Organic liquid electrolytes.....	49
1.2.3 Safer electrolytes	52
1.2.3.1 Ionic liquids	53
1.2.3.2 Organic liquid - ionic liquid electrolytes.....	54
1.2.3.3 Solid - polymer electrolytes	54
1.2.3.4 Ionic liquid - Organic liquid - Solid polymer electrolytes	55
1.2.3.5 Solid state electrolytes.....	55
1.2.4 Solid state electrolytes.....	56
1.2.4.1 Crystalline inorganic Li ion conductors	56

1.2.4.2	Composite inorganic Li ion conductors.....	68
1.2.4.3	Amorphous inorganic Li ion conductors	68
1.2.5	Crystal defects, non-stoichiometry and solid solutions.....	69
1.2.6	Requirements for high ionic conductivity.....	72
1.3	Scope of this work.....	72
1.4	References	74
2.	Experimental.....	80
2.1	Preparative methods.....	80
2.1.1	Air sensitive handling techniques	80
2.2	Synthetic techniques.....	81
2.2.1	Ball milling	81
2.2.1.1	Background.....	81
2.2.1.2	Ball milling equipment	81
2.2.2	Thermal treatment.....	82
2.2.2.1	The Bridgman technique	82
2.3	Structural determination and characterisation techniques	84
2.3.1	Powder X-ray diffraction	84
2.3.1.1	Background.....	84
2.3.1.2	Sample preparation for X-ray diffraction.....	92
2.3.1.3	Data collection	92
2.3.1.4	Data analysis	93
2.3.2	I11 at Diamond.....	93
2.4	Powder neutron diffraction	95
2.4.1	Background	95
2.4.2	Time of flight Powder Neutron Diffraction	96
2.4.2.1	Data collection	98

2.4.2.2	Sample preparation	99
2.4.3	Constant Wavelength Powder Neutron Diffraction	99
2.4.3.1	Data collection	100
2.4.4	Data analysis: Rietveld refinement	100
2.5	Spectroscopy techniques	107
2.5.1	Vibrational spectroscopies: IR and Raman techniques	107
2.5.1.1	Raman spectroscopy	108
2.5.2	Raman spectroscopy of borohydride ions	110
2.6	Electron microscopy	111
2.6.1	Scanning electron microscopy	111
2.7	⁷ Li solid state nuclear magnetic resonance	113
2.8	Thermal analysis	113
2.9	Electrochemical impedance spectroscopy	114
2.9.1	Analysis data	119
2.9.2	Sample preparation	121
2.10	References	121
3.	Structural analysis of the fast ionic and high temperature phase of LiBH ₄ stabilised by anion substitution	123
3.1	Introduction	123
3.2	Experimental	127
3.2.1	Synthesis	127
3.2.2	Characterisation	128
3.3	Results and discussion	130
3.3.1	Ball milling	130
3.3.1.1	Powder X-ray diffraction	130
3.3.2	Ball milling and thermal treatment	132
3.3.3	Ball milling treatment only	133

3.3.4	Scanning electron microscopy	134
3.3.5	Phase diagram of the LiBH ₄ - LiBr system.....	135
3.3.6	Thermal stability	137
3.3.7	Electrochemical impedance spectroscopy	138
3.3.8	Powder neutron diffraction at room temperature	140
3.3.9	Powder neutron diffraction experiments at 393 - 573 K	143
3.3.10	Constant wavelength powder neutron diffraction experiments at low temperature.....	148
3.3.10.1	Results at room temperature.....	149
3.3.10.2	Results at low temperature (300 - 2 K)	152
3.3.10.3	Data on cooling from room temperature to 2 K	158
3.3.11	Discussion.....	160
3.4	Conclusions	165
3.5	References	165
4.	Stabilisation of the fast ionic and high pressure phase (HP) of LiBH ₄ stabilised by mixed cation - anion substitution	167
4.1	Introduction	167
4.2	Experimental.....	172
4.2.1	Synthesis of substituted HP - LiBH ₄ phases	172
4.2.1.1	Method 1 (LiBH ₄ - NaBH ₄)	173
4.2.1.2	Method 2 (LiBH ₄ - NaBr)	173
4.2.1.3	Method 3 (LiBH ₄ - LiX - NaBH ₄ , where X = Br ⁻ and I ⁻).....	173
4.2.2	Characterisation.....	174
4.3	Results and discussion	174
4.3.1	Mixed cation borohydride	174
4.3.1.1	Method 1 (LiBH ₄ - NaBH ₄ system)	174
4.3.2	Mixed cation - anion borohydrides.....	176

4.3.2.1	Method 2 (LiBH ₄ - NaBr system)	176
4.3.2.2	Method 3.....	178
4.3.3	Method 3: Characterisation of the HP - LiBH ₄ type phases.....	184
4.3.3.1	Raman spectroscopy	184
4.3.3.2	Electrochemical impedance spectroscopy.....	185
4.3.3.3	Powder X-ray diffraction experiments	190
4.3.3.4	Li ⁺ ion migration in HP - LiBH ₄ - type materials	192
4.4	Conclusions.....	196
4.5	References	198
5.	Lithium aminoboranes as candidates for solid state electrolytes.....	200
5.1	Introduction	200
5.2	Experimental.....	207
5.2.1	LiH - [NH ₃ BH ₃] system	207
5.2.1.1	Synthesis of LiNH ₂ BH ₃ (α - LiNH ₂ BH ₃ and β - LiNH ₂ BH ₃).....	207
5.2.1.2	Synthesis of LiNH ₂ BH ₃ ·NH ₃ BH ₃	208
5.2.1.3	Synthesis of Li[BH ₃ NH ₂ BH ₂ NH ₂ BH ₃].....	209
5.2.1.4	Synthesis of Li[BH ₃ NH ₂ BH ₂ NH ₂ BH ₂ NH ₂ BH ₃]	209
5.2.1.5	Synthesis of Li[BH ₄] _{1-x} [NH ₂ BH ₃] _x	210
5.2.1.6	Synthesis of Li ₂ [BH ₄][BH ₃ NH ₂ BH ₂ NH ₂ BH ₃].....	210
5.2.2	LiBH ₄ - [NH ₃ BH ₃] system	211
5.2.3	LiX' - [NH ₃ BH ₃] (X' = Br, I).....	211
5.3	Characterisation.....	212
5.4	Results and discussion	213
5.4.1	[LiH][NH ₃ BH ₃] system	213
5.4.1.1	Synthesis of LiNH ₂ BH ₃ (α - LiNH ₂ BH ₃ and β - LiNH ₂ BH ₃)	213
5.4.1.2	Synthesis of LiNH ₂ BH ₃ ·NH ₃ BH ₃	217

5.4.1.3	Synthesis of $\text{Li}[\text{BH}_3\text{NH}_2\text{BH}_2\text{NH}_2\text{BH}_3]$	217
5.4.1.4	Synthesis of $\text{Li}[\text{BH}_3\text{NH}_2\text{BH}_2\text{NH}_2\text{BH}_2\text{NH}_2\text{BH}_3]$	225
5.4.1.5	Synthesis of $\text{Li}_2[\text{BH}_4]_{1-x}[\text{NH}_2\text{BH}_3]_x$	226
5.4.1.6	Synthesis of $\text{Li}_2[\text{BH}_4][\text{BH}_3\text{NH}_2\text{BH}_2\text{NH}_2\text{BH}_3]$	228
5.4.2	$[\text{LiBH}_4][\text{NH}_3\text{BH}_3]$ system	229
5.4.2.1	Powder X-ray diffraction experiments	229
5.4.2.2	Raman spectroscopy	231
5.4.2.3	Thermal analysis	232
5.4.3	$\text{LiX}' - [\text{NH}_3\text{BH}_3]$	236
5.4.3.1	$\text{LiBr} - [\text{NH}_3\text{BH}_3]$ system	236
5.4.3.2	$\text{LiI} - [\text{NH}_3\text{BH}_3]$ system	237
5.4.3.3	Thermal analysis	240
5.4.3.4	Structural Analysis	246
5.4.3.5	High-resolution synchrotron diffraction at 292 K	255
5.4.3.6	Electrochemical impedance spectroscopy	264
5.5	Conclusions	270
5.6	References	271
6.	Structural analysis of LiInBr_4	273
6.1	Introduction	273
6.1.1	Experimental	277
6.1.1.1	Synthesis of LiInBr_4	277
6.1.1.2	Characterisation	277
6.2	Results and discussion	280
6.2.1	Synthesis	280
6.2.2	Raman spectroscopy	283
6.2.3	Thermal analysis	285

6.2.4	Electrochemical impedance spectroscopy	287
6.2.5	Powder neutron diffraction experiments	289
6.2.5.1	Powder neutron diffraction at room temperature	289
6.2.5.2	Powder neutron diffraction from room temperature to 353 K	293
6.2.5.3	Powder neutron diffraction at high temperature (353 K)	298
6.2.6	⁷ Li NMR.....	302
6.3	Conclusions.....	307
6.4	References	308
7.	Conclusions.....	310
8.	Appendices	314
8.1	Appendix A: Tables and Figures for Chapter 3.....	314
8.2	Appendix B: Tables and Figures for Chapter 4.....	317
8.3	Appendix C: Tables and Figures for Chapter 5.....	319

List of Tables

Table 1.1-1 Characteristics of cathode materials.	46
Table 1.2-1 Overview of the innovative and optimised electrolyte systems and their potential physicochemical properties, as well as a brief evaluation of their overall safety. ⁴⁴	53
Table 1.2-2 Structure of (X = Al, Ga and In) lithium halo complex salts and their conductivities, respectively.....	67
Table 2.3-1 Shape and symmetry representing the seven crystal systems. ..	88
Table 2.3-2 Volume of the unit cell.	89
Table 2.3-3 Relation of the lattice spacing d_{hkl} to cell parameters in the different crystal systems.	89
Table 2.3-4 Systematic absences due to lattice type	90
Table 2.4-1 Scattering length for a selection of elements. ²⁰	98
Table 3.1-1 Physical properties for alkali metal tetraborohydrides.	123
Table 3.2-1 Samples prepared by mechanochemical treatment (1 - 8).	127
Table 3.2-2 Sample composition and preparation technique (9 - 17).	128
Table 3.2-3 Summary of PND data collected from GEM at different temperatures (16a-16b) for sample 16.	129
Table 3.3-1 Sample $\text{Li}(\text{BH}_4)_{2/3}\text{Br}_{1/3}$ milled for different times (18 - 22).	133
Table 3.3-2 Structural results from PXRD (23 - 33).....	136
Table 3.3-3 Electrochemical Impedance measurements.	140
Table 3.3-4 Selected refinement parameters for ${}^7\text{Li}({}^{11}\text{BD}_4)_{2/3}\text{Br}_{1/3}$ (16) from neutron powder diffraction data.	145
Table 3.3-5 Atomic parameters for ${}^7\text{Li}({}^{11}\text{BD}_4)_{2/3}\text{Br}_{1/3}$ (16a) from neutron powder diffraction data at 293 K.	145
Table 3.3-6 Atomic parameters for ${}^7\text{Li}({}^{11}\text{BD}_4)_{2/3}\text{Br}_{1/3}$ (16b) from neutron powder diffraction data at 393 K.	146
Table 3.3-7 Selected bond angles for ${}^7\text{Li}({}^{11}\text{BD}_4)_{2/3}\text{Br}_{1/3}$ (16a) from neutron powder diffraction data at 293 K.	146
Table 3.3-8 Selected interatomic distances for ${}^7\text{Li}({}^{11}\text{BD}_4)_{2/3}\text{Br}_{1/3}$ (16a) from neutron powder diffraction data at 293 K.	147

Table 3.3-9 Selected bond angles for ${}^7\text{Li}({}^{11}\text{BD}_4)_{2/3}\text{Br}_{1/3}$ (16b) from neutron powder diffraction data at 393 K.	147
Table 3.3-10 Selected interatomic distances for ${}^7\text{Li}({}^{11}\text{BD}_4)_{2/3}\text{Br}_{1/3}$ (16b) from neutron powder diffraction data at 393 K.	148
Table 3.3-11 Selected refinement parameters for ${}^7\text{Li}({}^{11}\text{BD}_4)_{2/3}\text{Br}_{1/3}$ (17a-17e) from neutron powder diffraction D20 data from ILL.	149
Table 3.3-12 Atomic parameters for ${}^7\text{Li}({}^{11}\text{BD}_4)_{2/3}\text{Br}_{1/3}$ (17a) for neutron powder diffraction data at 300 K.	150
Table 3.3-13 Complete bond angles ${}^7\text{Li}({}^{11}\text{BD}_4)_{2/3}\text{Br}_{1/3}$ (17a) neutron powder diffraction data at 300 K.	150
Table 3.3-14 Complete bond lengths ${}^7\text{Li}({}^{11}\text{BD}_4)_{2/3}\text{Br}_{1/3}$ (17a) neutron powder diffraction data at 300 K.	150
Table 3.3-15 Atomic parameters for ${}^7\text{Li}({}^{11}\text{BD}_4)_{2/3}\text{Br}_{1/3}$ (17b) from neutron powder diffraction data at 150 K.	153
Table 3.3-16 Complete bond angles ${}^7\text{Li}({}^{11}\text{BD}_4)_{2/3}\text{Br}_{1/3}$ (17b) neutron powder diffraction data at 150 K.	153
Table 3.3-17 Complete bond lengths ${}^7\text{Li}({}^{11}\text{BD}_4)_{2/3}\text{Br}_{1/3}$ (17b) neutron powder diffraction data at 150 K.	154
Table 3.3-18 Atomic parameters for ${}^7\text{Li}({}^{11}\text{BD}_4)_{2/3}\text{Br}_{1/3}$ (17c) from neutron powder diffraction data at 50 K.	154
Table 3.3-19 Complete bond angles ${}^7\text{Li}({}^{11}\text{BD}_4)_{2/3}\text{Br}_{1/3}$ (17c) neutron powder diffraction data at 50 K.	155
Table 3.3-20 Complete bond lengths ${}^7\text{Li}({}^{11}\text{BD}_4)_{2/3}\text{Br}_{1/3}$ (17c) neutron powder diffraction data at 50 K.	155
Table 3.3-21 Atomic parameters for ${}^7\text{Li}({}^{11}\text{BD}_4)_{2/3}\text{Br}_{1/3}$ (17d) from neutron powder diffraction data at 10 K.	155
Table 3.3-22 Complete bond angles ${}^7\text{Li}({}^{11}\text{BD}_4)_{2/3}\text{Br}_{1/3}$ (17d) neutron powder diffraction data at 10 K.	155
Table 3.3-23 Complete bond lengths ${}^7\text{Li}({}^{11}\text{BD}_4)_{2/3}\text{Br}_{1/3}$ (17d) neutron powder diffraction data at 10 K.	156
Table 3.3-24 Atomic parameters for ${}^7\text{Li}({}^{11}\text{BD}_4)_{2/3}\text{Br}_{1/3}$ (17e) from neutron powder diffraction data at 2 K.	156

Table 3.3-25 Complete bond angles ${}^7\text{Li}({}^{11}\text{BD}_4)_{2/3}\text{Br}_{1/3}$ (17e) neutron powder diffraction data at 2 K.	156
Table 3.3-26 Complete bond lengths ${}^7\text{Li}({}^{11}\text{BD}_4)_{2/3}\text{Br}_{1/3}$ (17e) neutron powder diffraction data at 2 K.	156
Table 4.1-1 Tree different strategies used in this chapter.....	169
Table 4.1-2 Known phases of mixed cation light metal borohydrides and their crystallographic characteristics ^{25, 26}	170
Table 4.1-3 Known phases of mixed cation - anion light metal borohydrides and their crystallographic characteristics.	171
Table 4.3-1 Lattice parameters of samples from Method 1 (LiBH_4 - NaBH_4 mixtures, 34 - 37)	175
Table 4.3-2 Lattice parameters of samples from Method 2 (LiBH_4 - NaBr mixtures, 38 - 46)	177
Table 4.3-3 Composition of samples from Method 3-a (LiBH_4 - LiBr mixtures, 47a).....	179
Table 4.3-4 Lattice parameters of sample from Method 3-b (LiBH_4 - LiBr - NaBH_4 mixture, 47b - 47c).....	179
Table 4.3-5 Composition of samples from Method 3-a (LiBH_4 - LiI mixtures, 48 - 53)	182
Table 4.3-6 Lattice parameters of sample from Method 3-b (LiBH_4 - LiI - NaBH_4 mixture, 54 - 60)	182
Table 4.3-7 Ionic conductivities (σ) at 313 K and the activation energies (E_a) for conduction in $\text{Li}_{0.5}\text{Na}_{0.5}(\text{BH}_4)_{0.84}\text{Br}_{0.16}$ (47c, HP - LiBH_4), $\text{Li}_{0.5}\text{Na}_{0.5}(\text{BH}_4)_{0.84}\text{I}_{0.16}$ (57, HP - LiBH_4), LT - LiBH_4 , HP - LiBH_4 , LiI and NaBH_4	186
Table 4.3-8. Atom positions and isotropic temperature factors obtained from Rietveld refinement against PXD data of the $\text{Li}_{0.5}\text{Na}_{0.5}(\text{BH}_4)_{0.84}\text{Br}_{0.16}$ compounds at room temperature (47c).....	192
Table 4.3-9. Atom positions and isotropic temperature factors obtained from Rietveld refinement against PXD data of the $\text{Li}_{0.5}\text{Na}_{0.5}(\text{BH}_4)_{0.84}\text{I}_{0.16}$ compounds at room temperature (57).	192
Table 4.3-10 Indirect jump mechanism	195
Table 4.3-11 Migration energies of Li^+ ion through the two kinds of diffusion path in rock-salt type LiX ($X = \text{F}, \text{Cl}, \text{Br}$ and I). ⁵¹	196

Table 5.1-1 Reported lithium ammonia borane compounds.	201
Table 5.2-1 Summary of reactions (61 - 65), including experimental parameters used and powder X - ray products.	208
Table 5.2-2 Experimental conditions for synthesis of 66 including powder X - ray products.	208
Table 5.2-3 Experimental conditions for synthesis of 67 including powder X - ray products.	209
Table 5.2-4 Experimental conditions for synthesis of 67a including powder X - ray product.	209
Table 5.2-5 Experimental conditions for synthesis of 68 including powder X - ray product.	209
Table 5.2-6 Experimental conditions for synthesis of 68a including powder X - ray product.	210
Table 5.2-7 Summary of reactions (69 - 70), including experimental parameters used and powder X - ray product.	210
Table 5.2-8 Summary of reaction (71), including experimental parameters used and powder X - ray product.	210
Table 5.2-9 Summary of reactions (72 - 77), including experimental parameters used and powder X - ray product.	211
Table 5.2-10 Summary of reactions (78 - 82), including experimental parameters used and powder X - ray product.	212
Table 5.2-11 Summary of reactions (83 - 86), including experimental parameters used and powder X - ray product.	212
Table 5.4-1 Assignment of Raman spectra (wavenumber [cm^{-1}]) of $\text{Li}[\text{BH}_3\text{NH}_2\text{BH}_2\text{NH}_2\text{BH}_3]$ and LiNH_2BH_3 at room temperature. Absorption bands of fresh ammonia borane (AB) at RT are shown for comparison. (ν = stretching, δ = deformation: bending and torsional modes) (Abbreviations: sh, shoulder, s, strong; m, medium; w, weak). ⁹	220
Table 5.4-2 Decomposition pathway suggested in the literature for $\text{Li}[\text{BH}_3\text{NH}_2\text{BH}_2\text{NH}_2\text{BH}_3]$. ^{9, 27}	221
Table 5.4-3 Summary of thermal stability analysis including data from TGA/MS, XRD data and Raman analysis.	222

Table 5.4-4 Possible decomposition pathways for $\text{Li}[\text{BH}_3\text{NH}_2\text{BH}_2\text{NH}_3\text{BH}_3]$ (7a), according to this work. (b) and (c) are theoretical proposed reactions and calculated weight losses.	225
Table 5.4-5 Summary of thermal stability analysis including data from TGA/MS analysis.....	232
Table 5.4-6 Decomposition pathway suggested in the literature for $[\text{LiBH}_4]_2[\text{NH}_3\text{BH}_3]$. ^{9, 27}	234
Table 5.4-7 Summary of thermal stability analysis including data from TGA/MS analysis, XRD data and Raman spectroscopy.	240
Table 5.4-8 Possible decomposition pathways for NH_3BH_3	246
Table 5.4-9 Possible decomposition pathways for $[\text{Li}][\text{NH}_3\text{BH}_3]$ (84).....	246
Table 5.4-10 Possible decomposition pathways for $[\text{Li}][\text{NH}_3\text{BH}_3]_2$ (86).....	246
Table 5.4-11 Selected Rietveld refinement data from PXD data of the $[\text{Li}][\text{NH}_3\text{BH}_3]$ (84) compound at 292 K.	249
Table 5.4-12. Atom positions and isotropic temperature factors obtained from Rietveld refinement against PXD data of the $[\text{Li}][\text{NH}_3\text{BH}_3]$ compound at 292 K (84).	250
Table 5.4-13 Cell candidates for $[\text{Li}][\text{NH}_3\text{BH}_3]_2$ (86).	250
Table 5.4-14 Selected Rietveld refinement data from PXD data of the $[\text{Li}][\text{NH}_3\text{BH}_3]_2$ (86) compound at 292 K.	254
Table 5.4-15. Atom positions and isotropic temperature factors obtained from Rietveld refinement against PXD data for $[\text{Li}][\text{NH}_3\text{BH}_3]_2$ compound at 292 K (86).	255
Table 5.4-16 Selected Rietveld refinement data from synchrotron powder diffraction data of the compound $[\text{Li}][\text{NH}_3\text{BH}_3]$ at 292 K (84).....	258
Table 5.4-17. Atom positions and isotropic temperature factors obtained from Rietveld refinement against synchrotron powder diffraction data for the $[\text{Li}][\text{NH}_3\text{BH}_3]$ compound at 292 K (84).	259
Table 5.4-18 Selected bond lengths $[\text{Li}][\text{NH}_3\text{BH}_3]$ (84) from high-resolution synchrotron diffraction data at 292 K.	259
Table 5.4-19 Selected angles $[\text{Li}][\text{NH}_3\text{BH}_3]$ (84) from high-resolution synchrotron diffraction data at 292 K.	260
Table 5.4-20 Selected Rietveld refinement data from synchrotron powder diffraction data of $[\text{Li}][\text{NH}_3\text{BH}_3]_2$ (86) compound at 292 K.....	262

Table 5.4-21. Atom positions and isotropic temperature factors obtained from Rietveld refinement against synchrotron powder diffraction data of the [LiI][NH ₃ BH ₃] ₂ compound (86) at 292 K.	263
Table 5.4-22 Selected bond lengths [LiI][NH ₃ BH ₃] ₂ (86) from high-resolution synchrotron data at 292 K.	264
Table 5.4-23 Selected bond angles [LiI][NH ₃ BH ₃] ₂ (86) from high-resolution synchrotron data at 292 K.	264
Table 5.4-24 Ionic conductivities (σ) at 343 K and the activation energies (E_a) for conduction in Li[BH ₃ NH ₂ BH ₂ NH ₂ BH ₃] (67a), [LiBH ₄] ₂ [NH ₃ BH ₃] (73), [LiI][NH ₃ BH ₃] (), [LiI][NH ₃ BH ₃] ₂ (86), LiBH ₄ and LiI compared with some lithium complex hydrides.	268
Table 6.1-1 Summary of LiBr-InBr ₃ reactions (87 and 88). For experimental details, see text.	278
Table 6.1-2 Summary of PND data collected from GEM at different temperatures (87a-87d) for sample 87.	278
Table 6.2-1 Lattice parameters of LiInBr ₄ samples (LiBr-InBr ₃ mixtures, 87 and 88)	280
Table 6.2-2 Vibrational spectra of crystalline LiInBr ₄ (w: weak, m: medium, s: strong). ¹⁵	283
Table 6.2-3 Vibrational spectra of crystalline indium trichloride and tribromide. ¹⁵	284
Table 6.2-4 Selected Rietveld refinement data from powder neutron diffraction data of the LiInBr ₄ compound at room temperature (87).	290
Table 6.2-5. Atom positions and isotropic temperature factors obtained from Rietveld refinement against neutron diffraction data of the LiInBr ₄ compounds at room temperature (87).	291
Table 6.2-6 Interatomic distances in LiInBr ₄ (87) from powder neutron diffraction data at room temperature.	291
Table 6.2-7 Bond angles in LiInBr ₄ (87) from powder neutron diffraction data at room temperature.	291
Table 6.2-8 Selected Rietveld refinement data for LiInBr ₄ at 353 K (87d)..	300
Table 6.2-9. Atom positions and isotropic temperature factors obtained from Rietveld refinement against powder neutron diffraction data for LiInBr ₄ at 353 K (87d).	300

Table 6.2-10 Interatomic distances for LiInBr_4 at 353 K (87d).....	301
Table 6.2-11 Bond angles for LiInBr_4 at 353 K (87d).....	301
Table 8.2-1 Selected Rietveld refinement data from PXD data of the $\text{Li}_{0.5}\text{Na}_{0.5}(\text{BH}_4)_{0.84}\text{Br}_{0.16}$ (47c) compound at room temperature.	317
Table 8.2-2 Complete bond lengths $\text{Li}_{0.5}\text{Na}_{0.5}(\text{BH}_4)_{0.84}\text{Br}_{0.16}$ (47c) powder diffraction data at room temperature.	318
Table 8.2-3 Complete bond angles $\text{Li}_{0.5}\text{Na}_{0.5}(\text{BH}_4)_{0.84}\text{Br}_{0.16}$ (47c) powder diffraction data at room temperature.	318
Table 8.2-4 Selected Rietveld refinement data from PXD data of the $\text{Li}_{0.5}\text{Na}_{0.5}(\text{BH}_4)_{0.84}\text{I}_{0.16}$ (57) compound at room temperature	318
Table 8.2-5 Complete bond lengths $\text{Li}_{0.5}\text{Na}_{0.5}(\text{BH}_4)_{0.84}\text{I}_{0.16}$ (57) powder diffraction data at room temperature.	319
Table 8.2-6 Complete bond angles $\text{Li}_{0.5}\text{Na}_{0.5}(\text{BH}_4)_{0.84}\text{I}_{0.16}$ (57) powder diffraction data at room temperature.	319

List of Figures

Figure 1.1-1 Schematic of a (a) charge and (b) discharge battery process in a typical $\text{Li}_x\text{C}_6 / \text{Li}_{1-x}\text{CoO}_2$ Li ion battery. During discharge, lithium ions diffuse from a lithiated graphite (Li_xC_6) structure (the anode) into a delithiated $\text{Li}_{1-x}\text{CoO}_2$ structure (the cathode) with oxidation and reduction of the two electrodes, respectively. The reverse process occurs during charge. 41

Figure 1.1-2 Voltage versus capacity for positive- and negative-electrode materials presently used or under serious considerations for the next generation of rechargeable Li-based cells. The output voltage values for Li-ion cells or Li-metal cells are cathodes, positive electrodes represented. Note the huge difference in capacity between Li metal and the other negative electrodes, which is the reason why there is still great interest in solving the problem of dendrite growth.¹³ 44

Figure 1.2-1 Schematic overview of possible abuse conditions for LIBs, the resulting behaviour of the cell, and possible outcomes (Figure adapted from Kalhoff *et al.*).⁴⁴ 48

Figure 1.2-2 Schematic illustration of the combustion mechanism of conventional organic carbonate based electrolytes and the effect of FR additives.⁴⁴ 52

Figure 1.2-3 Ionic conductivity (represented as log) as a function of reciprocal temperature for lithium solid electrolytes, organic liquid electrolytes, polymer electrolytes, ionic liquids and gel electrolytes.⁷⁹⁻⁹⁰ 56

Figure 1.2-4 Crystal structure of $\text{Li}_{1.3}\text{Al}_{0.3}\text{Ti}_{1.7}(\text{PO}_4)_3$. Lithium, oxygen and phosphor are represented as red, light blue and light purple spheres. The octahedra formed by $(\text{Al}/\text{Ti})\text{O}_6$ is represented in light grey. The tetrahedra for PO_4 is represented in light purple. 57

Figure 1.2-5 Crystal structure of $\text{Li}_{14}\text{ZnGe}_4\text{O}_{16}$. Lithium, oxygen and titanium are represented as red, light blue and green spheres. The tetrahedra formed by GeO_4 is represented in light grey. The tetrahedra for $(\text{Li}/\text{Zn})\text{O}_4$ is represented in orange. 58

Figure 1.2-6 Total ionic conductivities of Li^+ solid state electrolytes with temperature a) LiBH_4 ,¹⁰¹ b) $\text{Li}(\text{BH}_4)_{0.75}\text{Cl}_{0.25}$,¹⁰² c) $\text{Li}(\text{BH}_4)_{0.75}\text{I}_{0.25}$,¹⁰² d) $\text{Li}_4(\text{BH}_4)(\text{NH}_2)_3$,¹⁰³

e) $\text{Li}_2(\text{BH}_4)(\text{NH}_2)$,¹⁰³ f) LiAlH_4 ,¹⁰⁴ g) Li_3AlH_6 ,¹⁰⁴ h) $\text{Li}(\text{NH}_2)_{0.67}\text{I}_{0.33}$,¹⁰⁵ i) LiNH_2 ,¹⁰⁶
 j) $\text{Li}_2\text{Mg}(\text{NH})_2$,¹⁰⁶ k) $\text{Li}_2\text{Ca}(\text{NH})_2$,¹⁰⁶ l) Li_2NH ,^{106, 107} m) $\text{Li}_{10}\text{GeP}_2\text{S}_{12}$,⁷⁹ n) $\text{Li}_7\text{P}_3\text{S}_{11}$
 (glass-ceramics),⁸² o) $\text{Li}_2\text{S}-\text{SiS}_2-\text{Li}_3\text{PO}_4$ (glass),^{108, 109} p)
 $\text{Li}_{3.25}\text{Ge}_{0.25}\text{P}_{0.75}\text{S}_4$ (thio-LISICON),⁸¹ q) Li- β -alumina,^{100, 110} r) $\text{Li}_{14}\text{Zn}(\text{GeO}_4)_4$ (LISICON),¹¹¹
 s) $\text{Li}_{0.34}\text{La}_{0.51}\text{TiO}_{2.94}$,^{80, 112} t) $\text{Li}_7\text{La}_3\text{Zr}_2\text{O}_{12}$,^{113, 114} and u) $\text{Li}_{1.3}\text{Al}_{0.3}\text{Ti}_{1.7}(\text{PO}_4)_3$ (LATP).⁹⁶ . 59

Figure 1.2-7 Crystal structure of (a) cubic (*Ia-3d*) and (b) tetragonal (*I4₁/acd*) $\text{Li}_7\text{La}_3\text{Zr}_2\text{O}_{12}$. Lithium, oxygen and lanthanum are represented as red, light blue and purple spheres. The ZrO_6 is represented in light grey. 61

Figure 1.2-8 (a) Structure of $\text{Li}_2\text{B}_{12}\text{H}_{12}$. (b) Relative geometry of the $\text{B}_{12}\text{H}_{12}^{2-}$ anion with boron and hydrogen atoms denoted by blue and grey spheres, respectively. $\text{Li}_2\text{B}_{12}\text{H}_{12}$ crystallises with a cubic structure (space group *Pa3*) with lattice parameters $a = 9.5771(2)$ Å.¹⁴⁵ 63

Figure 1.2-9 (a) Structure of $\text{Li}_2\text{B}_{10}\text{H}_{10}$. (b) Relative geometry of the $\text{B}_{10}\text{H}_{10}^{2-}$ anion with boron and hydrogen atoms denoted by blue and grey spheres, respectively. $\text{Li}_2\text{B}_{10}\text{H}_{10}$ crystallises with a hexagonal structure (space group *P6₄22*) with lattice parameters $a = 7.042(1)$ and $c = 14.931(2)$ Å.¹⁴⁸ 64

Figure 1.2-10 Relative geometry of the $\text{CB}_{11}\text{H}_{12}^-$ anion with boron, carbon, and hydrogen atoms denoted by blue, brown, and grey spheres, respectively. $\text{LiCB}_{11}\text{H}_{12}$ crystallises in a orthorhombic structure (space group *Pca2₁*) with lattice parameters $a = 9.6668(5)$, $b = 9.4892(5)$ and $c = 9.7273(5)$ Å.¹⁵⁰ 64

Figure 1.2-11 (a) Ionic conductivity measurements for $\text{LiNaB}_{12}\text{H}_{12}$, $\text{Na}_2\text{B}_{12}\text{H}_{12}$, and $\text{Li}_2\text{B}_{12}\text{H}_{12}$ and (b) for $\text{LiCB}_{11}\text{H}_{12}$ (blue)¹⁵⁰ and $\text{NaCB}_{11}\text{H}_{12}$ (red)¹⁵⁰ as a function of temperature (circles and squares denote the conductivities of the respective 1st and 2nd temperature cycles and closed and open symbols denote respective heating and cooling processes). The ionic conductivities are compared to other related materials: $\text{Na}_2\text{B}_{12}\text{H}_{12}$,¹⁴⁴ $\text{Na}_2\text{B}_{10}\text{H}_{10}$,¹⁴⁹ $\text{Na}_2\text{BH}_4\text{NH}_2$,¹⁴¹ NaBH_4 ¹⁴¹ and LiBH_4 ¹⁰¹ 65

Figure 1.2-12 Energy changes on introducing defects into a perfect crystal at a finite temperature. (Figure adapted from West).¹⁸³ 70

Figure 2.2-1. Classification of crystal growth techniques.³ 83

Figure 2.2-2. Horizontal Bridgman technique. 83

Figure 2.3-1 Schematic used for the derivation of Bragg's law for X-ray diffraction. A and B represent the incident X-ray beams striking with atoms with an angle θ . A' and B' are the scattered X-rays. The lattice spacing is denoted by d_{hkl} .

Bragg's law is satisfied when a constructive interference occurs (the angle of incidence has to be equal to the angle of scattering and the distance xyz must be equal to a whole number of wavelengths, $n\lambda$). 86

Figure 2.3-2 Representation of a 3D unit cell. 87

Figure 2.3-3 Interaction of X-ray beam (1 and 2) electrons in an atom. Beam 1' and 2' represent the scattered X-rays, Figure adapted from West.¹¹ 91

Figure 2.3-4 Form factors of Fe^{2+} , O, C and H.¹² 92

Figure 2.3-5 Schematic of Diamond Light Source in Oxfordshire¹⁶ showing the electron gun and the particle accelerators where the electrons are accelerated afterwards (Linac and Booster synchrotron) and then send into the storage ring where electrons circle until reach almost the speed of light generating a beamline which is directed into separate experimental stations (only shown one, I11). 94

Figure 2.3-6 Schematic representation of Beamline I11 showing the main components and their approximate distances from the IVU (X-ray source).¹⁷ 94

Figure 2.4-1 Rutherford Appleton Laboratory in Oxfordshire. (a) Production of H^- ions by a proton accelerator (b) Synchrotron ring where H^- ions are fired producing a H^+ beam (c) Generation of pulses of high energy H^+ which bombard the tungsten target, producing an extremely intense neutron pulse. The pulse is directed into separate experimental stations (Target Station 1 and 2). 95

Figure 2.4-2. Neutron scattering factors as a fraction of atomic number, Z .²⁰ 97

Figure 2.4-3. A schematic layout of the detector banks of the GEM detector array.²² 99

Figure 2.5-1. The vibrational modes of a linear molecule: Vibrations a) and b) are stretching modes. Bending mode c) occurs in the plane of the paper, while d) occurs in a plane perpendicular to that of the paper. The two modes require the same amount of energy and are therefore degenerate. 107

Figure 2.5-2 Mechanism of IR absorption and Raman scattering. In the IR technique, the frequency of the incident radiation is varied and the quantity of radiation absorbed or transmitted by the sample is obtained. In the Raman technique, the sample is illuminated with monochromatic light, usually generated by a laser. Two types of scattered light are produced by the sample. Rayleigh scatter emerges with exactly the same energy and wavelength as the incident light. Raman scatter

which is usually less intense than Rayleigh scatter, emerges at either longer or shorter wavelength than the incident light.	107
Figure 2.5-3. Energy level diagram illustrating energy changes of different types of Raman scattering.	108
Figure 2.5-4 The vibrational modes of a tetrahedral molecule. ^{29, 30}	110
Figure 2.6-1 Schematic of a typical SEM instrument.	112
Figure 2.9-1 Alternative current (AC) is a sinusoidal wave shape and has a frequency; therefore both potential (E_t) and current (I_t) oscillate shifted in phase, ϕ . ³³	115
Figure 2.9-2 (a) Nyquist or complex plane plot with the impedance vector indicated (b) Limiting cases for impedance.	118
Figure 3.1-1 Pressure-Temperature phase diagram of LiBH_4 . ⁷	124
Figure 3.1-2 Crystal structures of a) LT b) HT c) AT - LP and d) HP phases of LiBH_4 , respectively (Li^+ ions are shown in red and BH_4^- in blue tetrahedra).	125
Figure 3.1-3 a) Phase diagram of LiBH_4 depending on the temperature and pressure (dots represent where conductivity measurements were undertaken) and b) Conductivity of LiBH_4 phases. ¹⁵	126
Figure 3.3-1 Powder X-ray diffraction patterns of $\text{Li}(\text{BH}_4)_{1-x}\text{Br}_x$ mixtures after ball-milling. (From top to bottom in terms of LiBH_4 : LiBr ratio: 4:1 (1), 3:1 (2), 2:1 (3), 1:1 (4), 1:2 (5), 1:3 (6)).	130
Figure 3.3-2 Raman spectrum of HT - $\text{Li}(\text{BH}_4)_{1-x}\text{Br}_x$ ball milled for 4 h AT 500 rpm. LiBH_4 (ν = stretching, δ = deformation: bending and torsional modes).	131
Figure 3.3-3 Raman spectra of HT - $\text{Li}(\text{BH}_4)_{1-x}\text{Br}_x$ a) from 900 - 1500 cm^{-1} b) from 2100 - 2500 cm^{-1} (ν = stretching, δ = deformation: bending and torsional modes).	131
Figure 3.3-4 Powder X-ray diffraction patterns of $\text{Li}(\text{BH}_4)_{1-x}\text{Br}_x$ mixtures after ball-milling and thermal treatment. (From top to bottom in terms of LiBH_4 : LiBr ratio: 3:1 (9), 2.5:1 (10), 2:1 (11), 1.5:1 (12), 1:1 (13), 1:2 (14), 1:3 (15)).....	132
Figure 3.3-5 Raman spectrum of HT - $\text{Li}(\text{BH}_4)_{2/3}\text{Br}_{1/3}$ and a comparison with the corresponding spectrum of LT - LiBH_4 (ν = stretching, δ = deformation: bending and torsional modes).	133
Figure 3.3-6 Powder X-ray diffraction patterns of $\text{Li}(\text{BH}_4)_{2/3}\text{Br}_{1/3}$ mixture (LiBH_4 : LiBr , 2:1) after ball-milling for different periods of time. (From top to bottom in terms of ball milling time: 4 h (18), 8 h (19), 12 h (20), 16 h (21), 24 h (22))..	134

Figure 3.3-7 SEM images from $\text{Li}(\text{BH}_4)_{2/3}\text{Br}_{1/3}$ prepared by: a) milling and thermal treatment; b), c) and d) milling only.	135
Figure 3.3-8 Structure field map manifested as the respective unit cell volumes as a function of LiBr mole fraction in $\text{Li}(\text{BH}_4)_{1-x}\text{Br}_x$. I-V represent the distinct phase regions within compositional space. Black squares denote the LT orthorhombic LiBH_4 structure (top-left y axis); open circles denote the HT hexagonal LiBH_4 structure (bottom-left y axis); black triangles denote the cubic LiBr (NaCl-type) structure (right y axis).	137
Figure 3.3-9 TG-DTA profile of milled $\text{Li}(\text{BH}_4)_{2/3}\text{Br}_{1/3}$ on heating from room temperature to 573 K. The temperature is indicated by the dotted line.	138
Figure 3.3-10 Impedance data collected from $\text{Li}(\text{BH}_4)_{2/3}\text{Br}_{1/3}$ (MT/TT) (11) (a) at room temperature and (b) at 140 °C (right side). The data can be fitted using equivalent circuits as shown.	139
Figure 3.3-11 Impedance data collected from $\text{Li}(\text{BH}_4)_{2/3}\text{Br}_{1/3}$ (MT) (24) (a) at room temperature and (b) at 140 °C (right side). The data can be fitted using equivalent circuits as shown.	139
Figure 3.3-12 Plot of conductivity as a function of temperature for $\text{Li}(\text{BH}_4)_{(1-x)}\text{Br}_x$ on heating. Compound $x = 1/3$ was prepared by either mechanochemical and thermal treatment (MT/TT) or by MT.	139
Figure 3.3-13 Rietveld profile fits for (a) PXD data and high-resolution neutron powder diffraction data collected from (b) bank 4 ($50^\circ \leq 2\theta \leq 74^\circ$) and (c) bank 5 ($79^\circ \leq 2\theta \leq 106^\circ$) ²⁵ (of the GEM diffractometer for ${}^7\text{Li}({}^{11}\text{BD}_4)_{2/3}\text{Br}_{1/3}$ at 293 K (16a). Observed data are shown as dots, the calculated pattern as a solid line and the difference profile as a solid line at the bottom of the plot. Vertical bars represent the reflection positions for the phase.	142
Figure 3.3-14 Crystal structure models of ${}^7\text{Li}({}^{11}\text{BD}_4)_{2/3}\text{Br}_{1/3}$ (16a) with a polyhedral representation of the BD_4^- anion and showing: (a) a single Li site with displacement parameters refined anisotropically; (b) two partially occupied Li positions with isotropic displacement parameters;. (D atoms are omitted; Ellipsoids at 50 % probability level). Lithium, boron and bromine are represented as yellow, black and blue spheres. The BD_4 is represented in light blue.	143
Figure 3.3-15 Cell dimensions of ${}^7\text{Li}({}^{11}\text{BD}_4)_{2/3}\text{Br}_{1/3}$ as a function of temperature (16).	144

Figure 3.3-16 Rietveld profile fits for (a) GEM detector bank 4 and (b) GEM detector bank 5 for ${}^7\text{Li}({}^{11}\text{BD}_4)_{2/3}\text{Br}_{1/3}$ (16b) using high-resolution neutron powder diffraction data at 393 K. Measured data are shown as dots, the calculated profile is shown by a solid line through the measured data. The difference profile is shown along the bottom of the plot. Vertical bars represent the reflection positions for the phase. 144

Figure 3.3-17 Rietveld profile fits for (a) PXD data and high-resolution neutron powder diffraction data collected from (b) D20 from ${}^7\text{Li}({}^{11}\text{BD}_4)_{2/3}\text{Br}_{1/3}$ at 300 K (17a). Measured data are shown as dots, the calculated profile is shown by a solid line through the measured data. The difference profile is shown along the bottom of the plot. Vertical bars represent the reflection positions for the phase. 152

Figure 3.3-18 Rietveld profile fits for high-resolution neutron powder diffraction data collected from D20 from ${}^7\text{Li}({}^{11}\text{BD}_4)_{2/3}\text{Br}_{1/3}$ at 150 K (17b). Measured data are shown as dots, the calculated profile is shown by a solid line through the measured data. The difference profile is shown along the bottom of the plot. Vertical bars represent the reflection positions for the phase. 153

Figure 3.3-19 Variations of (a) atomic parameters from boron and bromide (boron and bromide represented with triangles and squares, respectively), (b) Li fraction occupancy, and (c) atomic parameter from Li on cooling from room temperature to 2 K in ${}^7\text{Li}({}^{11}\text{BD}_4)_{1-x}\text{Br}_x$ (17a - 17e). Error bars are represented in black. 157

Figure 3.3-20 Powder neutron diffraction patterns for ${}^7\text{Li}({}^{11}\text{BD}_4)_{1-x}\text{Br}_x$ on cooling from room temperature to 2 K as collected on D20 at ILL (17a - 17e) from $2\theta =$ (a) $33.2 - 68.9^\circ$ (b) $63.9 - 107.2^\circ$ and (c) $100.5 - 151.0^\circ$ 158

Figure 3.3-21 Variations of unit cell parameters on cooling from room temperature to 2 K in ${}^7\text{Li}({}^{11}\text{BD}_4)_{1-x}\text{Br}_x$ (17a - 17e). (a) a parameter, (b) c parameter and (c) cell volume. Error bars are represented in black. 159

Figure 4.1-1 Crystal structures of the LiBH_4 phases observed at 0-18 GPa at ambient temperature.⁷ Coordination environment of the BH_4 tetrahedra by Li atoms is highlighted. a) Tetrahedral coordination in the LT - phase. b) Square-planar coordination in the AT - LP phase. c) Octahedral coordination in the HP - phase. 167

Figure 4.1-2 Variation of the volume of the LiBH_4 formula unit in the three phases at ambient temperature. The circles represent experimental data. Vertical lines represent phase transitions. ⁷	168
Figure 4.1-3 Proposed mechanism for cation substitution in LiBH_4 using NaBH_4 (Method 1).....	170
Figure 4.1-4 Proposed mechanism for cation substitution in LiBH_4 using NaBr (Method 2).....	172
Figure 4.3-1 Na content in $\text{Li}_{1-x}\text{Na}_x\text{BH}_4$ (Method 1), where LT - LiBH_4 is represented with red squares and NaBH_4 with blue circles. Error bars are shown for each sample.	175
Figure 4.3-2 Phase diagram of LiBH_4 - NaBr system by mechanochemical treatment. Five different phases were identified: LT - LiBH_4 in red squares; HT - LiBH_4 in light blue squares; HP - LiBH_4 ($\text{Li}_{1-x}\text{Na}_x(\text{BH}_4)_{1-x}\text{Br}_x$) in green circles; NaBr in blue circles; and LiBr in orange circles. The left axes is for all the compounds apart from the HT - LiBH_4 that is represented in the right axes (Method 2). Error bars are shown for each sample.....	178
Figure 4.3-3 XRD pattern of sample 47a. Synthesis of the precursor (LiBH_4 : LiBr , 2:1) by mechanochemical treatment, for 24 h at 500 rpm (Method 3-a, HT phase). The peaks are indexed using the $P6_3mc$ space group of the high temperature polymorph of LiBH_4 structure.....	179
Figure 4.3-4 XRD pattern of sample 47b only by mechanochemical treatment for 10 h at 500 rpm (Method 3-b).	180
Figure 4.3-5 XRD pattern of sample 47c post mechanochemical (10 h at 500 rpm) and thermal treatment (5 K min^{-1} , 20 h at 598K, Method 3-b, HP phase). ...	181
Figure 4.3-6 XRD patterns of the precursors (LiBH_4 : LiI mixtures, HT phase, 48 - 53) (Method 3-a).	183
Figure 4.3-7 XRD pattern of [LiBH_4 : LiI] : NaBH_4 mixtures (54 - 60, Method 3-b) which could be identified as pure HP - LiBH_4 type phases.	183
Figure 4.3-8 Cell dimensions of 54 - 60 as a content of iodide. (Method 3-b, HP phase).	184
Figure 4.3-9 Raman spectra of 47c ($\text{Li}_{0.5}\text{Na}_{0.5}(\text{BH}_4)_{0.84}\text{Br}_{0.16}$) and 57 ($\text{Li}_{0.5}\text{Na}_{0.5}(\text{BH}_4)_{0.84}\text{I}_{0.16}$) and a comparison with the corresponding modes of HT - $\text{Li}(\text{BH}_4)_{0.67}\text{Br}_{0.33}$, HT - $\text{Li}(\text{BH}_4)_{0.67}\text{I}_{0.33}$, LT - LiBH_4 and NaBH_4	185

Figure 4.3-10 Nyquist plot of 47c and 57 at 313 K.....	186
Figure 4.3-11 Plot of conductivity as a function of temperature for LiBH_4 ²⁴ , NaBH_4 ²⁰ , and $\text{Li}_{(1-y)}\text{Na}_y(\text{BH}_4)_{(1-x+xy)}\text{X}'_{x(1-y)}$ or HP - LiBH_4 ($\text{X}' = \text{Br}^-$ (47c) and I^- (57) on heating.	187
Figure 4.3-12 Nyquist plots of 57 (frequency range 1MHz to 1Hz at 1mV). Measurements performed at a) 313 K and b) 413 K.	188
Figure 4.3-13 Conductivity measurements for (Li,Na) (BH_4 ,I) with low iodide content. Samples from bottom to top: 54, 55, 56 and 57.	189
Figure 4.3-14 Conductivity measurements for (Li,Na) (BH_4 ,I) with higher levels of iodide substitution. Samples from top to bottom: 57, 58 and 59.	189
Figure 4.3-15 Crystal structure of cubic $\text{Li}_{(1-y)}\text{Na}_y(\text{BH}_4)_{(1-x+xy)}\text{X}'_{x(1-y)}$ (HP - LiBH_4 - type). Borohydride anions are shown as B - centred polyhedra (blue) and halides are represented by purple spheres, whilst the cations are represented by spheres, Li^+ as red spheres and Na^+ as yellow spheres.	190
Figure 4.3-16 Profile plot from the Rietveld refinement against X-ray powder diffraction data for (a) $\text{Li}_{0.52(6)}\text{Na}_{0.48(6)}(\text{BH}_4)_{0.83(3)}\text{Br}_{0.17(3)}$ (47c) (b) $\text{Li}_{0.6(1)}\text{Na}_{0.4(1)}(\text{BH}_4)_{0.84(4)}\text{I}_{0.16(4)}$ (57) (Red crosses: experimental profile; green line: calculated profile; pink line: difference profile; tick marks: Bragg reflections for the NaCl-type borohydride halide phase).....	191
Figure 4.3-17 pathway for Li^+ migration in $\text{Li}_{0.5}\text{Na}_{0.5}(\text{BH}_4)_{(1-x+xy)}\text{X}'_{x(1-y)}$ (HP - LiBH_4 - type). Borohydride anions are shown as B(X') - centred polyhedra (blue), whilst the cations are represented by spheres, Li^+ as red spheres and Na^+ as yellow spheres. One corner Li^+ site is shown as “empty” (just as in NaCl, (Li, Na)(BH_4/X') would be expected to include a small number of intrinsic cation and anion vacancies) and a Li^+ ion from opposite corner moves to occupy it. The direct and indirect jump are represented as dotted line and curved arrow, respectively.	193
Figure 4.3-18 a) and c) represent the triangular channel of radius r' through which a moving Li^+ ion must pass in the borohydride compound. Blue circles 1, 2 and 3 are anions, either BH_4^- or X^- (where $\text{X} = \text{Br}$ or I). Yellow circles are cations (Li^+ or Na^+ , 50% probability). Note that this figure is adapted from West. ⁶⁰	193
Figure 5.1-1 Crystal structure of NH_3BH_3 . ³ Boron and nitrogen atoms are represented in black and green, respectively.....	200

Figure 5.1-2 The simplified mechanism of two competing reactions during the thermal decomposition of alkali metal amidoboranes: direct evolution of H₂ (top) and formation of M[BH₃NH₂BH₂NH₂BH₃] phases with the evolution of NH₃ (bottom).⁹ .. 203

Figure 5.1-3 a) PXD powder pattern of LiNH₂BH₃ presented by Z. Xiong *et al.* in 2008 (top).³ Signals representing Li[BH₃NH₂BH₂NH₂BH₃] are marked with grey stripes (top). For comparison PXD patterns of LiNH₂BH₃ and Li[BH₃NH₂BH₂NH₂BH₃] are shown (bottom). b) PXD powder pattern of LiNH₂BH₃ by C. Wu *et al.* in 2010 (top).^{12, 14} Signals representing Li[BH₃NH₂BH₂NH₂BH₃] are marked with grey stripes (top). For comparison PXD pattern of LiNH₂BH₃ and Li[BH₃NH₂BH₂NH₂BH₃] are shown (bottom).⁹ 203

Figure 5.1-4 Crystal structure of Li[BH₃NH₂BH₂NH₂BH₃]. 204

Figure 5.1-5 Crystal structures of a) [LiBH₄]₂[NH₃BH₃], b) Ca[BH₄]₂[NH₃BH₃] and c) Mg[BH₄]₂[NH₃BH₃]₂. 205

Figure 5.1-6. XRD patterns of the LiNH₂BH₃ (LiAB) - xLiBH₄ mixtures with (b) x = 0.1, (c) x = 0.2, (d) x = 0.25, (e) x = 0.33, (f) x = 0.5, (g) x = 1, (h) x = 2, (i) x = 10, respectively. XRD patterns of (a) as prepared LiNH₂BH₃ and (j) commercial LiBH₄ are shown for comparison.¹⁵ 206

Figure 5.1-7 Crystal structure of Li₂[BH₄][NH₂BH₃]. 206

Figure 5.4-1 PXD pattern of the reaction product (62) after ball milling LiH : NH₃BH₃ (1:1), ball milling for 16 h, 1 : 400. White squares represent α - LiNH₂BH₃ and grey circles represent Li[BH₃NH₂BH₂NH₂BH₃]. 214

Figure 5.4-2 PXD pattern of the reaction product (62) measured 2 days after being synthesised. White squares represent α - LiNH₂BH₃; grey squares represent LiNH₂BH₃·NH₃BH₃; and grey circles represent Li[BH₃NH₂BH₂NH₂BH₃]. 215

Figure 5.4-3 PXD pattern of the reaction product (63) after ball milling LiH : NH₃BH₃ (1:1), for 16 h (1 : 400, ball : powder ratio). White squares represent α - LiNH₂BH₃, grey squares represent LiNH₂BH₃·NH₃BH₃ and grey circles represent Li[BH₃NH₂BH₂NH₂BH₃]. 215

Figure 5.4-4 PXD pattern of the reaction products after ball milling LiH : NH₃BH₃ (1:1), for 5 h with ball : powder ratio of: (a) 1 : 80 (64) and (b) 1 : 400 (65). White squares represent α - LiNH₂BH₃, grey squares represent LiNH₂BH₃·NH₃BH₃, grey circles represent Li[BH₃NH₂BH₂NH₂BH₃] and white circles represent β - LiNH₂BH₃. 216

Figure 5.4-5 PXD pattern of the reaction product (66) after ball milling LiH : NH₃BH₃ (1:2), ball milling for 2 h (1 : 400 ball : powder ratio). Grey squares represent LiNH₂BH₃·NH₃BH₃, grey circles represent Li[BH₃NH₂BH₂NH₂BH₃] and black squares represent NH₃BH₃. 217

Figure 5.4-6 PXD pattern of the reaction product (67) post ball milling LiH : NH₃BH₃ (1:3), for 2 h, (1 : 400, ball : powder ratio). Grey squares represent LiNH₂BH₃·NH₃BH₃, grey circles represent Li[BH₃NH₂BH₂NH₂BH₃] and black squares represent NH₃BH₃. 218

Figure 5.4-7 PXD pattern of the reaction product (67a) of LiH : NH₃BH₃ (1:3) post ball milling and thermal treatment at 75 °C. Grey circles represent Li[BH₃NH₂BH₂NH₂BH₃]. 218

Figure 5.4-8 Raman spectra in the range 500 - 4000 cm⁻¹ using a 532 nm laser of commercial NH₃BH₃ and Li[BH₃NH₂BH₂NH₂BH₃] (sample 67a) (ν = stretching, δ = deformation: bending and torsional modes). 219

Figure 5.4-9 Typical TG-DTA plot of sample 67a. STA analysis was carried out in an Ar atmosphere, heating the sample at 5 °C min⁻¹ from ambient temperature to 200 °C. Black line represents TG curve and red line represents DTA curve. 221

Figure 5.4-10 Typical mass spectrum recorded of Li[BH₃NH₂BH₂NH₂BH₃] (67a) during thermal treatment. Gases monitored were: NH₃ (green); B₂H₆ (brown, blue and purple); B₃H₆N₃ (red); H₂ (black). 222

Figure 5.4-11 Post-TGA product after heating sample 7a under an Argon flow from room temperature to 200 °C at 5 °C min⁻¹. 223

Figure 5.4-12 Raman spectra in the range 2000 - 4000 cm⁻¹ using a 532 nm laser of (a) commercial LT - LiBH₄, (b) commercial NH₃BH₃, (c) Li[BH₃NH₂BH₂NH₂BH₃] (67a), and (d) post-TGA product after heating Li[BH₃NH₂BH₂NH₂BH₃] (67a) under an Argon flow from room temperature to 200 °C at 5 °C min⁻¹. 224

Figure 5.4-13 PXD pattern of the reaction product (68) of LiH : NH₃BH₃ (1:4) post ball milling. Grey circles represent Li[BH₃NH₂BH₂NH₂BH₃] and black squares represent NH₃BH₃. 226

Figure 5.4-14 PXD pattern of the reaction product (70) of LiBH₄ : LiNH₂BH₃ (1:2), ball milling 2 h. White triangles represent Li₂[BH₄][NH₂BH₃]. 227

Figure 5.4-15 PXD pattern of the reaction product (69) of $\text{LiBH}_4 : \text{LiNH}_2\text{BH}_3$ (1:1) after ball milling for 2 h. White triangles represent $\text{Li}_2[\text{BH}_4][\text{NH}_2\text{BH}_3]$; and black triangles represent LT - LiBH_4 228

Figure 5.4-16 PXD pattern of the reaction product (71) of $\text{Li}[\text{BH}_3\text{NH}_2\text{BH}_2\text{NH}_2\text{BH}_3] : \text{LiBH}_4$ (1:1), after ball milling for 2 h. Grey spheres represent $[\text{BH}_3\text{NH}_2\text{BH}_2\text{NH}_2\text{BH}_3]$ and black triangles represent LT - LiBH_4 229

Figure 5.4-17 PXD pattern of the reaction products of $\text{LiBH}_4 : \text{NH}_3\text{BH}_3$ mixtures (a) 3:1 (74) (b) 2:1 (73) (c) 1:1 (72). Arrows represent $\text{LiBH}_4 \cdot \text{NH}_3\text{BH}_3$; black squares represent NH_3BH_3 ; black diamonds represent $\text{Li}_2[\text{BH}_4]_2[\text{NH}_3\text{BH}_3]$; and black triangles represent LT - LiBH_4 230

Figure 5.4-18. PXD pattern of the reaction product (73) of $\text{LiBH}_4 : \text{NH}_3\text{BH}_3$ (2:1). Black diamonds represent $\text{Li}_2[\text{BH}_4]_2[\text{NH}_3\text{BH}_3]$ 230

Figure 5.4-19. Raman spectra in the range $500 - 4000 \text{ cm}^{-1}$ using a 532 nm laser of NH_3BH_3 , $[\text{LiBH}_4]_2\text{NH}_3\text{BH}_3$ (sample 73) and LiBH_4 , (ν = stretching, δ = deformation: bending and torsional modes). 231

Figure 5.4-20 Typical TG-DTA plot of sample 73. STA analysis was carried out in an Ar atmosphere, heating the sample at $5 \text{ }^\circ\text{C min}^{-1}$ from ambient temperature to $200 \text{ }^\circ\text{C}$. The black line represents the TG curve and the red line represents the DTA curve. 233

Figure 5.4-21 Post TG-DTA product after heating sample 73 under an Argon flow from room temperature to $200 \text{ }^\circ\text{C}$ at $5 \text{ }^\circ\text{C min}^{-1}$. Black triangles represent LT - LiBH_4 233

Figure 5.4-22 Typical mass spectra recorded of $[\text{LiBH}_4]_2[\text{NH}_3\text{BH}_3]$ (73) during thermal treatment. Gases monitored were: NH_3 (green); B_2H_6 (brown, blue and purple); $\text{B}_3\text{H}_6\text{N}_3$ (red); H_2 (black). 235

Figure 5.4-23 Raman spectra in the range of $3000 - 3600 \text{ cm}^{-1}$ and $2000 - 2800 \text{ cm}^{-1}$ (on the left and on the right, respectively) using a 532 nm laser of (a) NH_3BH_3 , (b) LiBH_4 , (c) $[\text{LiBH}_4]_2[\text{NH}_3\text{BH}_3]$ (sample 73), and (d) post-TGA product after heating sample 73 under an Argon flow from room temperature to $200 \text{ }^\circ\text{C}$ at $5 \text{ }^\circ\text{C min}^{-1}$. . 236

Figure 5.4-24 PXD patterns of the reaction products of $\text{LiBr} : \text{NH}_3\text{BH}_3$ mixtures of: (a) 2:1 (78); (b) 1:1 (79); (c) 1:2 (80); (d) 1:3 (81); and (e) 1:4 (82) ratios respectively. Black squares represent NH_3BH_3 and white circles represent LiBr . . 237

Figure 5.4-25 PXD patterns of the reaction products of Lil : NH ₃ BH ₃ mixtures: (a) 2:1 (83); (b) 1:1 (84); (c) 2:3 (85) and (d) 1:2 (86). Black circles represent Lil; black triangles represent “[Lil][NH ₃ BH ₃]’”; and white squares represent “[Lil][NH ₃ BH ₃] ₂ ”.....	238
Figure 5.4-26 Raman spectra of NH ₃ BH ₃ , [Lil][NH ₃ BH ₃] (sample 84) and [Lil][NH ₃ BH ₃] ₂ (sample 86) (ν = stretching, δ = deformation: bending and torsional modes).	239
Figure 5.4-27 Typical TG-DTA profiles of samples (a) 84 and (b) 86. STA analysis was carried out in an Ar atmosphere, heating the sample at 5 °C min ⁻¹ from ambient temperature to 200 °C. Straight lines represent STA curve and discontinuous lines represents TG curve.....	241
Figure 5.4-28 Post-TGA product after heating sample 84 under an Argon flow from room temperature to 200 °C at 5 °C min ⁻¹ . Black circles represent Lil.	242
Figure 5.4-29 Typical mass spectrum recorded for [Lil][NH ₃ BH ₃] (84) during thermal treatment. Gases monitored were: NH ₃ (green); B ₂ H ₆ (brown, blue and purple); B ₃ H ₆ N ₃ (red); H ₂ (black).	242
Figure 5.4-30 Raman spectra in the range of 3000 - 3600 cm ⁻¹ and 2000 - 2800 cm ⁻¹ (on the left and on the right, respectively) of (a) NH ₃ BH ₃ , (b) [Lil][NH ₃ BH ₃] (sample 84) and (c) post-TGA product after heating sample 84 under an Argon flow from room temperature to 200 °C at 5 °C min ⁻¹	243
Figure 5.4-31 Post-TGA product after heating sample 86 under an Argon flow from room temperature to 200 °C at 5 °C min ⁻¹ . Black circles represent Lil.	243
Figure 5.4-32 Typical mass spectra recorded of [Lil][NH ₃ BH ₃] ₂ (86) during thermal treatment. Gases monitored were: NH ₃ (green); B ₂ H ₆ (brown, blue and purple); B ₃ H ₆ N ₃ (red); H ₂ (black).	244
Figure 5.4-33 Raman spectra in the range of 3000 - 3600 cm ⁻¹ and 2000 - 2800 cm ⁻¹ (on the left and on the right, respectively) (a) NH ₃ BH ₃ , (b) [Lil][NH ₃ BH ₃] ₂ (sample 86) and (c) post-TGA product after heating sample 86 under an Argon flow from room temperature to 200 °C at 5 °C min ⁻¹	245
Figure 5.4-34 Profile plot from the Rietveld Refinement against X-ray powder diffraction data for (a) (black crosses: experimental profile; red line: calculated	

profile; blue line: difference profile; tick marks: Bragg reflections for the [LiI][NH ₃ BH ₃]).	247
Figure 5.4-35 Crystal structure of [LiI][NH ₃ BH ₃] (84). Lithium, iodide, nitrogen, boron and hydrogens are represented as red, purple, green, black and grey spheres, respectively.	248
Figure 5.4-36 Possible space groups for [LiI][NH ₃ BH ₃] ₂ a) <i>C2/m</i> , b) <i>Cm</i> and c) <i>C2</i> . ³²	251
Figure 5.4-37. <i>C2/m</i> , only half of the cell is represented with a mirror plane at (020), iodine atoms are shown in purple and residual electron density is in light blue.	251
Figure 5.4-38. Hypothetical <i>C2/m</i> symmetry model with the mirror plane represented in yellow. Lithium, iodide, nitrogen, boron and hydrogens are represented as green (large spheres), purple, dark green (small spheres), and light blue and white spheres, respectively.	252
Figure 5.4-39. Crystal structure of [LiI][NH ₃ BH ₃] ₂ (86) as refined in space group <i>C2</i> . Lithium, iodide, nitrogen, boron and hydrogens are represented as yellow, purple, green, black and grey spheres, respectively.	252
Figure 5.4-40 Profile plot from the Rietveld refinement against X-ray powder diffraction data for [LiI][NH ₃ BH ₃] ₂ (86) (black crosses: experimental profile; red line: calculated profile; blue line: difference profile; tick marks: Bragg reflections for the [LiI][NH ₃ BH ₃] ₂).	253
Figure 5.4-41 Crystal structure of [LiI][NH ₃ BH ₃] ₂ (86). Lithium, iodide, nitrogen, boron and hydrogens are represented as red, purple, green, black and grey spheres, respectively.	253
Figure 5.4-42 Plot for 24 from the Rietveld refinement against high-resolution synchrotron diffraction data (red dots: experimental profile; green line: calculated profile; pink line: difference profile; tick marks: Bragg reflections for the NH ₄ I (top), [LiI][NH ₃ BH ₃] ₂ (middle) and [LiI][NH ₃ BH ₃] (bottom).	256
Figure 5.4-43 Crystal structure of [LiI][NH ₃ BH ₃] (84). Lithium, iodide, nitrogen, boron and hydrogens are represented as red, purple, green, black and grey spheres, respectively.	257
Figure 5.4-44 Profile plot from the Rietveld refinement against high-resolution synchrotron diffraction data for 86 (red dots: experimental profile; green line:	

calculated profile; pink line: difference profile; tick marks: Bragg reflections for [LiI][NH ₃ BH ₃] ₂).	260
Figure 5.4-45 Crystal structure of [LiI][NH ₃ BH ₃] ₂ (86). Lithium, iodide, nitrogen, boron and hydrogens are represented as red, purple, green, black and grey spheres, respectively.	261
Figure 5.4-46 Nyquist plot for [LiBH ₄] ₂ [NH ₃ BH ₃] (73) and [LiI][NH ₃ BH ₃] ₂ (86) at 292 K represented in red and blue, respectively.	265
Figure 5.4-47 Nyquist plot for Li[BH ₃ NH ₂ BH ₂ NH ₂ BH ₃] (67a) (at 353 K) and [LiI][NH ₃ BH ₃] (84) (at 292 K) represented in purple and green, respectively.....	265
Figure 5.4-48 Plot of conductivity for Li[BH ₃ NH ₂ BH ₂ NH ₂ BH ₃] (67a), [LiBH ₄] ₂ [NH ₃ BH ₃] (73), [LiI][NH ₃ BH ₃] (84) and [LiI][NH ₃ BH ₃] ₂ (86) as a function of temperature on heating. LT - LiBH ₄ ³³ and LiI are plotted for comparison.	266
Figure 5.4-49 Comparison of the ionic conductivity between the four different lithium ammonia borane complexes synthesised (67a, 73, 84 and 86).	267
Figure 6.1-1 p block metals are represented in light orange; Metalloids are represented in green; Non-metals are represented in purple. Halogens are represented in light blue.	274
Figure 6.1-2 Proposed cubic spinel structure by Yamada et al. ¹ Lithium, indium and bromide ions are represented as red, purple, and green spheres, respectively.	275
Figure 6.1-3 Profile plot from the Rietveld Refinement against X-ray powder diffraction data for LiInBr ₄ conducted by Yamada <i>et al.</i> ¹ Black dots: experimental profile; black line: calculated profile lower; black line (apparently): difference profile; tick marks: Bragg reflections for the cubic LiInBr ₄ phase. Red arrows indicate missing reflections. ¹	275
Figure 6.1-4 Proposed monoclinic spinel structure by Yamada et al. ¹ Lithium, indium and bromide ions are represented as red, purple, and black spheres, respectively.	276
Figure 6.1-5 Plot of conductivity as a function of temperature for LiInBr ₄ and Li ₃ InBr ₆ on heating. ¹	276
Figure 6.1-6. LiInBr ₄ formation using CVT using a sealed silica tube.	277

Figure 6.2-1 PXD pattern of the reaction product after mechanochemical milling for 4 h (87). Miller indices for the rhombohedral LiInBr_4 phase are indicated.	280
Figure 6.2-2 PXD pattern of the reaction product after mechanochemical milling for 4 h and adapted Bridgman-Stockbarger methods for 12 h at 513 K (87). Miller indices for the rhombohedral LiInBr_4 phase are indicated.....	281
Figure 6.2-3 PXD pattern of the reaction product after quenching with liquid N_2 (88). Black squares represent RT LiInBr_4 phase.	282
Figure 6.2-4 PXD of the reaction product after (a) mechanochemical milling for 4 h and adapted Bridgman-Stockbarger methods for 12 h at 513 K (87) and (b) quenching with liquid N_2 (88). Black circles represent RT LiInBr_4 phase.	282
Figure 6.2-5 Variable temperature Raman spectra from 30 - 250 cm^{-1} for LiInBr_4 (87).	283
Figure 6.2-6 Normal modes of vibration of an octahedral ML_6 molecule belonging to the O_h point group. Stretching modes: (a), (b), and (c) and bending modes: (d), (e), and (f) are shown. Li/In cations are represented by red and purple spheres and Br anion by green spheres (Figure adapted from Reddy). ¹⁷	284
Figure 6.2-7 Typical TG-DTA plot of LiInBr_4 . STA analysis was carried out in an Ar atmosphere, heating the sample at 5 K min^{-1} from ambient temperature to 533 K. The black dotted line represents the TG curve and the solid black line represents the DTA curve.....	286
Figure 6.2-8 TG-DTA plot of LiInBr_4 on heating and cooling. STA analysis was carried out in an Ar atmosphere, heating the sample at 5 K min^{-1} from ambient temperature to 373 K, holding the temperature for 20 min (not shown) and cooled down to 305 K at 5 K min^{-1} . Red dotted line represents the TG curve and the solid red line represents the DTA curve, for heating. The black dotted line represents the TG curve and the black solid line represents the DTA curve, for cooling.	287
Figure 6.2-9 Nyquist plot of LiInBr_4 , 87, at room temperature (black open circles) and at 353 K (red open circles). Inset: Zoom the Nyquist plot of LiInBr_4 at 353 K.	288
Figure 6.2-10 Plot of log conductivity as a function of temperature for LiInBr_4 on heating.	288

Figure 6.2-11 Profile plot from the Rietveld refinement against (a) lab powder X-ray data and (b-d) GEM ToF powder neutron diffraction data; (b) bank 3, (c) bank 5, and (d) bank 6 at room temperature (red dots: experimental profile; green line: calculated profile; pink line: difference profile; tick marks: Bragg reflections for LiInBr_4 (87)).	289
Figure 6.2-12 Proposed crystal structure for the RT - LiInBr_4 . Bromide anions are represented as green spheres. Lithium and indium cations are represented as red/purple spheres, sharing the same site.	292
Figure 6.2-13 Variations of the unit cell parameters and the Br z coordinate on heating (87) from 292-353 K: (a) Cell Volume (b) a parameter (c) c parameter (d) bromide position. Error bars are represented in red.	294
Figure 6.2-14 Fourier-observed calculation at room temperature: (a) powder X-ray data combined with powder neutron diffraction data and (b) powder neutron diffraction data. (c) Crystal structure of LiInBr_4 at room temperature.	296
Figure 6.2-15 Fourier-observed calculation at 353 K for Model 1: (a) powder neutron diffraction data. (b) Model 1 of LiInBr_4 at 353 K.	297
Figure 6.2-16 Second model proposed for LiInBr_4 at 353 K. Lithium and indium ions are represented as red and purple spheres. Octahedra formed by (Li/In) and bromide are presented in light green.	298
Figure 6.2-17 Profile plot for sample 87 from the Rietveld refinement against GEM ToF powder neutron diffraction data from (a) detector bank 3, (b) detector bank 5, and (c) detector bank 6 (red dots: experimental profile; green line: calculated profile; pink line: difference profile; tick marks: Bragg reflections for the LiInBr_4).	299
Figure 6.2-18 Linewidth as a function of temperature.	302
Figure 6.2-19 Half-height linewidth as a function of temperature.	303
Figure 6.2-20 Fitting of the recovery curve with one and two components.	303
Figure 6.2-21 Two vs three component fit at 80 °C.	304
Figure 6.2-22 T1 (spin-lattice relaxation time) measurements, divided into three components ((a) T1(1), (b) T1(2) and (c) T1(3) which correspond to long, short and intermediate relaxing components) and (d) PWRA for these three components. Measurements taken at heating, cooling and at RT after the measurement was	

performed and are indicated in red, dark blue and cyan. Vertical lines show when there is a change in the tendency of the measurement.	305
Figure 6.2-23 Arrhenius plot for component $T_1(1)$ (slow relaxing) - heating.	307
Figure 8.1-1 Rietveld profile fits for high-resolution neutron powder diffraction data collected from D20 from ${}^7\text{Li}({}^{11}\text{BD}_4)_{2/3}\text{Br}_{1/3}$ at 50 K (17c). Measured data are shown as dots, the calculated profile is shown by a solid line through the measured data. The difference profile is shown along the bottom of the plot. Vertical bars represent the reflection positions for the phase.	314
Figure 8.1-2 Rietveld profile fits for high-resolution neutron powder diffraction data collected from D20 from ${}^7\text{Li}({}^{11}\text{BD}_4)_{2/3}\text{Br}_{1/3}$ at 10 K (17d). Measured data are shown as dots, the calculated profile is shown by a solid line through the measured data. The difference profile is shown along the bottom of the plot. Vertical bars represent the reflection positions for the phase.	314
Figure 8.1-3 Rietveld profile fits for high-resolution neutron powder diffraction data collected from D20 from ${}^7\text{Li}({}^{11}\text{BD}_4)_{2/3}\text{Br}_{1/3}$ at 2 K (17e). Measured data are shown as dots, the calculated profile is shown by a solid line through the measured data. The difference profile is shown along the bottom of the plot. Vertical bars represent the reflection positions for the phase.	315
Figure 8.1-4 Diffraction pattern on cooling from ${}^7\text{Li}({}^{11}\text{BD}_4)_{1-x}\text{Br}_x$ from room temperature to 2 K. Data collected at ILL (17).	315
Figure 8.1-5 Diffraction pattern on cooling from room temperature to 2 K. Data collected at ILL (17).	315
Figure 8.1-6 Thermal factors of deuterium, boron/bromide and lithium atoms represented with triangles, squares, and circles, respectively (17). Error bars are represented.	316
Figure 8.1-7 Fractional occupancy of the two tetrahedra units (BH_4^-) (17).	316
Figure 8.3-1 Nyquist plot of 55 at 313 K.	319
Figure 8.3-2 Nyquist plot of 54 (black), 56 (red), 58 (green), 59 (grey) and 60 (blue) at 298 K.	319

Acknowledgments

I would like to thank my supervisors, Prof Duncan H. Gregory and Dr Edmund J. Cussen, for offering me the possibility to work in their research group at University of Glasgow and University of Strathclyde and for their help, support and all the learning opportunities provided throughout my PhD.

I would like to acknowledge Dr David C. Apperley from Solid State NMR at Durham University, Prof David A. Keen from Rutherford Appleton Laboratory, Dr Annabelle Baker from Diamond Light Source and Dr Thomas Hansen from Institut Laue-Langevin for their patience while running my samples.

I would like to thank all of you for your support: Dr Tuan Hoang, Dr Sina Saremi, Dr Nuria Tapia-Ruiz, Dr Giulia Balducci, Dr Saleem Denholme, Dr Marc Segales, Dr Sebastian Schneider, Dr James Hanlon and Dr Iwona Malka. Mimmo, Davide, Simon, Joachim, Tina, Luis, Masha, Alex and Rurru: thanks guys for making the work area so friendly. Mharie Scott-Dickins, Naína Seolin and Yongzhi Yua, thanks to the three of you for helping me too, hope I was a nice supervisor.

Amaia, thanks for all the time that we have spent together during our PhD (coffees, lunches and so on). You made this experience less difficult. David and Susan Morrison both of you have made me feel like I had a second family in Scotland, many thanks.

A big big thanks goes to Stephen, being with you has made these years much easier. You made me laugh when I needed it the most, you supported me and never complained. Also thanks a lot for reading and checking my super long thesis. Love you!

And to my friends from Spain: Jose, Lauri, Debo, Albert, Sara, Cris, Maria, Lorena, Iris, Ascen y Xavi y también Elena, Sofi, Vila, Marta e Iván gracias chicos por darme todos esos buenos momentos, cada vez que volvía a casa, que tanto me ayudaban a cargar las pilas a tope.

Last but not least, I would like to thank my family, gracias papa y mama (Caski y Merche) por vuestro apoyo incondicional. Sin vosotros nunca hubiese podido acabar este proyecto. Male, siento no haber podido estar cuando más me has necesitado, pero espero que podamos recuperar todo este tiempo. Os quiero.

Me gustaría dedicar este proyecto a toda mi familia de León, Bilbao y Barcelona por siempre creer en mí, ayudarme a seguir adelante y animarme cada vez que los visitaba durante todo este periodo. A mis abuelos, en especial a esas tres mujeres de mi vida que me han servido de apoyo e inspiración. Gracias Mera, Irene y Sofía.

*“Caminante, son tus huellas
el camino y nada más;
Caminante, no hay camino,
se hace camino al andar.
Al andar se hace el camino,
y al volver la vista atrás
se ve la senda que nunca
se ha de volver a pisar.
Caminante no hay camino
sino estelas en la mar.”*

Antonio Machado (Joan Manuel Serrat)

Abbreviations

LIB	Li ion battery
EV	Electric vehicles
HEV	Hybrid electric vehicles
PHEV	Plug in hybrid electric vehicles
LTO	$\text{Li}_4\text{Ti}_5\text{O}_{12}$
LFT	LiFePO_4
LMP	LiMnPO_4
LMN	$\text{LiMn}_{1.5}\text{Ni}_{0.5}\text{O}_4$
LNMC	$\text{LiNi}_{1/3}\text{Mn}_{1/3}\text{Co}_{1/3}\text{O}_2$
LLZO	$\text{Li}_7\text{La}_3\text{Zr}_2\text{O}_{12}$
SEI	Solid - electrolyte interphase
EC	Ethylene carbonate
PC	Propylene carbonate
DMC	Dimethyl carbonate
ESW	Electrochemical stability window
DEC	Diethyl carbonate
FR	Flammable retardant
OLE	Organic liquid electrolytes
IL	Inorganic liquids

SPE	Solid-polymer electrolyte
GPE	Gel-polymer electrolyte
SE	Solid-state electrolyte
LIC	Lithium ion conductors
LLTO	Lithium lanthanum titanate
LATP	$\text{Li}_{1.3}\text{Al}_{0.3}\text{Ti}_{1.7}(\text{PO}_4)_3$
LGPS	$\text{Li}_{10}\text{GeP}_2\text{S}_{12}$
LATP	$\text{Li}_2\text{O}-\text{Al}_2\text{O}_3-\text{TiO}_2-\text{P}_2\text{O}_5$
LAGP	$\text{Li}_2\text{O}-\text{Al}_2\text{O}_3-\text{GeO}_2-\text{P}_2\text{O}_5$
CHs	Complex hydrides
LT	Low temperature phase
HT	High temperature phase
LP	Low pressure phase
HP	High pressure phase
PXD	Powder X-ray diffraction
PND	Powder neutron diffraction
SEM	Scanning electron microscopy
EIS	Electrochemical impedance spectroscopy

Declaration

The work presented in this thesis is the original work of the author except where specific reference is made to other sources. It has not been submitted, in whole or in part, for any other degree at this or any other institution.

Irene Cascallana Matías

Date: June 2016.

1. Introduction

Over the past century, human activities (burning fossil fuels to produce energy, industrial processes, and some agricultural practices) have released large amounts of CO₂ and other greenhouse gases (methane, nitrous oxide and chlorofluorocarbons (CFC)) into the atmosphere. These greenhouse gases act like a mirror and reflect back to the Earth some of the heat energy which would otherwise be lost to space. CFC form radicals with ultraviolet radiation from the Sun. These radicals react with the ozone layer in the stratosphere breaking down molecules of ozone. The depletion of ozone in the stratosphere results in reduced absorption of ultraviolet radiation. Consequently, unabsorbed and dangerous ultraviolet radiation is able to reach the Earth's surface at a higher intensity, causing the rising global temperatures.¹ The use of renewable energy resources, such as wind or solar power energy plants, is a simple sustainable solution at a reasonable cost that can be used for any task. However renewable energies are intermittent, and therefore require high efficiency storage systems. Electrochemical systems, such as batteries, could be the solution. Batteries efficiently store and deliver energy on demand in stand-alone power plants. These devices cover a range of applications independent from utility power ranging from portable consumer electronic devices to electric vehicles.

One of the sectors that are trying to decrease the emission of greenhouse gases and therefore decrease pollution and global warming is the automobile industry. According to studies from Wards Auto, in 2009 the global number of automobiles in use, was 980 million, however only one year later the number reached 1.015 billion. The OECD's International Transport Forum predicts for 2050 that the number of automobiles will increase up to 2.5 billion.²

From 2009 electric vehicles (EVs), hybrid electric vehicles (HEVs) and plug in hybrid vehicles (PHEV) were available.^{3, 4} These vehicles would help to reduce the emission of greenhouse gases and the dependence on oil resources.⁴ However the current limitation for electric vehicles is the storage battery. Compared with other batteries, Li ion batteries (LIBs) are the most suitable for electric vehicles because of their capacity for higher energy and power output per unit of battery mass.⁵⁻⁸ In fact, it is predicted that in 2020 more than half of the automobile sales will be EVs, HEVs and PHEVs. Nowadays nickel metal hydride (NiMH) batteries are the most used

in all hybrids on the market, but only within one decade it is expected that there will be a move from these batteries to LIBs in 70% HEVs, and 100% of PHEV and EVs.⁹

1.1 Li ion batteries

Li ion batteries play a significant role in portable devices due to their high gravimetric and volumetric energy density, high power density, long cycle life and low self-discharge property.¹⁰ LIBs are considered the most efficient energy storage materials for cellular phones, laptops and digital electronics. However if LIBs are applied to larger devices such as HEV, PHEV, and PEV, then the energy density needs to be increased.

A battery is a device which stores electrical energy by converting chemical energy. In a LIB, the anode (1.1) is the electronegative electrode and the cathode (1.2) is the electropositive electrode. The lithium ions move from the anode to the cathode during the discharge and from the cathode to the anode when charging, whereas the electrons flow in opposite directions (Figure 1.1-1). The anode is commonly graphite in current state of the art LIBs. The electrodes are separated by an electrolyte that transfers the ions inside the cell and forces the electrons outside the battery. The output on discharge is an external electronic current I at a voltage V for a time Δt . The chemical reaction must be reversible on the application of charging I and V .¹¹

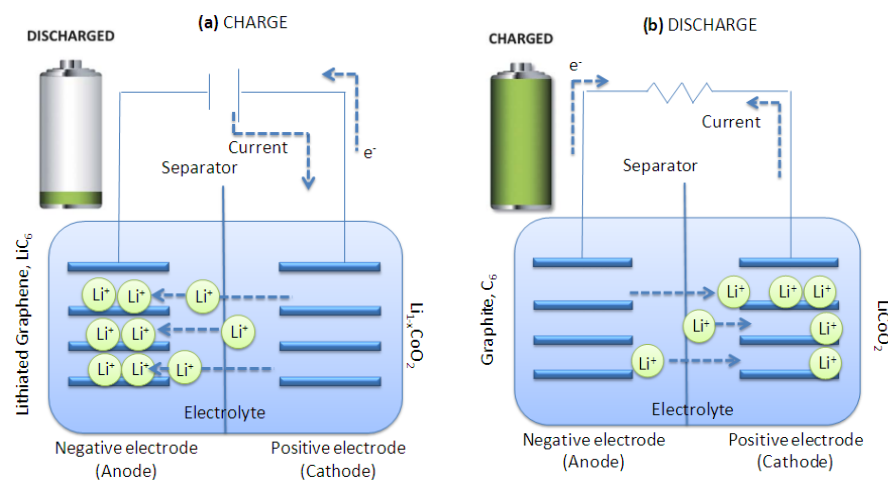
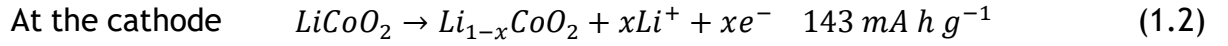
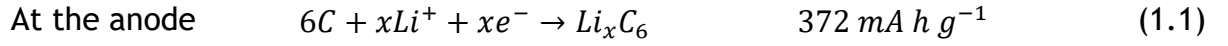


Figure 1.1-1 Schematic of a (a) charge and (b) discharge battery process in a typical $\text{Li}_x\text{C}_6 / \text{Li}_{1-x}\text{CoO}_2$ Li ion battery. During discharge, lithium ions diffuse from a lithiated graphite (Li_xC_6) structure (the anode) into a delithiated $\text{Li}_{1-x}\text{CoO}_2$ structure (the cathode) with oxidation and reduction of the two electrodes, respectively. The reverse process occurs during charge.



During discharge and charge, an internal battery resistance (R_b) to the ionic current $I_i = I$ reduces the output voltage V_{dis} from the open-circuit voltage V_{oc} by a polarization $\eta = I_{dis}R_b$ and increases the voltage V_{ch} required to reverse the chemical reaction on charge by an overvoltage $\eta = I_{ch}R_b$ ((1.3) and (1.4)):

$$V_{dis} = V_{oc} - \eta(q, I_{dis}) \quad (1.3)$$

$$V_{ch} = V_{oc} + \eta(q, I_{ch}) \quad (1.4)$$

where q represents state of the charge.

The open-circuit voltage of a cell is the difference between the electrochemical potentials μ_A and μ_C of the anode and cathode, respectively (1.5):

$$V_{oc} = (\mu_A - \mu_C)/e \quad (1.5)$$

The efficiency of a cell to store energy at a fixed I is as equation (1.6) shows:

$$\frac{\int_0^{Q_{dis}} V_{dis}(q) dq}{\int_0^{Q_{ch}} V_{ch}(q) dq} \times 100 \quad (1.6)$$

$$Q = \int_0^{\Delta t} I dt = \int_0^Q dq \quad (1.7)$$

where Q is the total charge per unit weight ($A \text{ h kg}^{-1}$) transferred by the current $I = dq/dt$ on discharge or charge (1.7). $Q(I)$ indicates the cell capacity for a given I ; The cell capacity depends on I because the rate of transfer of ions across electrode / electrolyte interfaces becomes diffusion-limited at high currents. A diffusion-limited loss of the Li inserted into an electrode particle at a high rate of charge or discharge represents reversible loss of capacity. However other phenomena that happen during charge / discharge cycling (changes in electrode volume, electrode-electrolyte chemical reactions, and/or electrode decomposition) can cause an irreversible loss of capacity. During the first cycling process, when the cell is discharged, an irreversible electrode-electrolyte reaction occurs which forms a passivating solid-electrolyte interface (SEI) layer on the surface of the electrode. This process is not

considered in the irreversible capacity loss during cycling. Therefore the Coulombic efficiency of a single cycle associated with the capacity loss is (1.8):

$$\frac{Q_{dis}}{Q_{ch}} \times 100 \quad (1.8)$$

The cycle life of a battery is defined as the number of the cycles until the capacity fades to 80% of its reversible value. The efficiency of the cell is also regulated by the cost, safety, density (specific and volumetric) of stored energy, output power ($P(q) = V(q)I_{dis}$ for a given discharge current) and calendar life. The energy stored in a fully charged cell depends on the discharge current I_{dis} ; the available energy stored in a fully charged cell (1.9) is obtained by measuring the time ($\Delta t(I_{dis})$) for its complete discharge at a constant $I_{dis} = dq / dt$:

$$energy = \int_0^{\Delta t} IV(t)dt = \int_0^Q V(q)dq \quad (1.9)$$

The gravimetric energy density ($W h kg^{-1}$) is dependent on I_{dis} through $Q(I_{dis})$. The volumetric energy density ($W h L^{-1}$) is of particular interest for portable batteries, especially those that power hand-held or laptop devices.¹¹

For instance, LIBs produce 3.7 V and demonstrate a capacity and power of 150 A h kg^{-1} and over 200 W h kg^{-1} , respectively. Nowadays rechargeable batteries have shown 30,000 charge / discharge cycles which could be equal to 10 year operational life.¹²

Lithium-ion cells, in their most common form, consist of a graphite anode, a lithium metal oxide cathode and an electrolyte of a lithium salt and an organic solvent (Figure 1.1-1 and Figure 1.1-2). Lithium is a good choice for an electrochemical cell due to its large standard electrode potential (-3.04 V) resulting in a high operating voltage, and the fact that it is the metal with the lowest density which reduces weight.

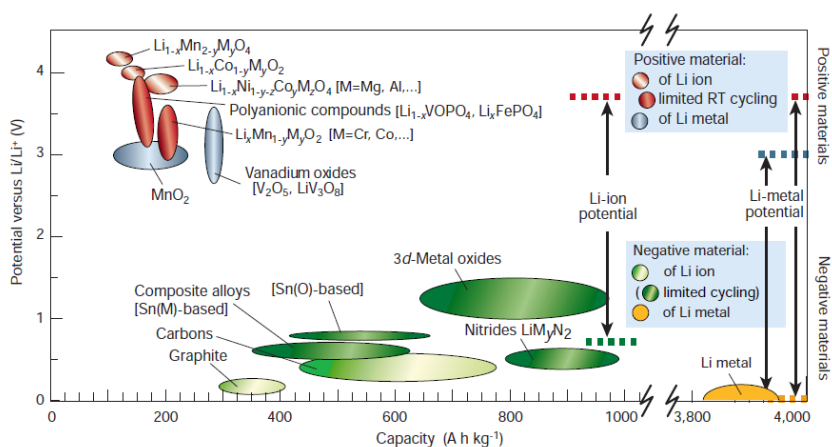


Figure 1.1-2 Voltage versus capacity for positive- and negative-electrode materials presently used or under serious considerations for the next generation of rechargeable Li-based cells. The output voltage values for Li-ion cells or Li-metal cells are cathodes, positive electrodes represented. Note the huge difference in capacity between Li metal and the other negative electrodes, which is the reason why there is still great interest in solving the problem of dendrite growth.¹³

1.1.1 Anodes, negative electrodes

The anode of the commercialised LIB with high power is composed of graphite due to its low potential with respect to Li^+/Li and high energy density with the formation of LiC_6 . However the graphite layers break and change shape when Li is incorporated because of the increase of the lattice volume which leads to the formation of the SEI passivation layer and hence the battery life decreases.¹² Therefore, efforts have been made to replace graphite with $\text{Li}_4\text{Ti}_5\text{O}_{12}$ (LTO). $\text{Li}_4\text{Ti}_5\text{O}_{12}$ has a spinel structure and an operating voltage of 1.5 V vs. Li^+/Li .¹⁴⁻¹⁷ Unlike graphite, $\text{Li}_4\text{Ti}_5\text{O}_{12}$ does not suffer a dilation of the lattice when Li^+ is incorporated in the structure and no stress is observed during cycling. The drawback of the $\text{Li}_4\text{Ti}_5\text{O}_{12}$ anode is that it has a low energy density which is important for fully EVs, but not for devices that demand more power than energy such as HEVs. Recent results obtained for LFP/LTO ($\text{LiFePO}_4/\text{Li}_4\text{Ti}_5\text{O}_{12}$) cells are making these electrode combinations really attractive because LIBs exhibit huge capacity.^{12, 18}

1.1.2 Cathodes, positive electrodes

LiCoO_2 is the most commonly used cathode because of its layered structure which permits the introduction of Li ions in to its framework. In 1990, the first LIB was commercialised by Sony Energytec¹⁹ which contained LiCoO_2 as a cathode material. These LIBs can be found in small devices, however they fail when employed

in to larger applications such as vehicles, mainly because of safety issues.^{20, 21} Therefore studies on other cathodes have been carried out to replace these materials. Mainly three different families of cathodes are known. Firstly, an extended family of lamellar compounds, based on LiCoO_2 , in which Co is partly substituted by other metals. In 2001, the first cathode of this family was reported which was $\text{LiNi}_{1/3}\text{Mn}_{1/3}\text{Co}_{1/3}\text{O}_2$ (LNMC).^{22, 23} Mn is added to order the Li position. $\text{LiNi}_{1/3}\text{Mn}_{1/3}\text{Co}_{1/3}\text{O}_2$ undergoes mixing of lithium in the lithium layer and nickel from the transition metal layers because of their similar cationic radii (Li^+) 0.76 Å, Ni^{2+} (0.69 Å). This cation disorder has been shown to be correlated to irreversible capacity, possibly because it impedes lithium diffusion. Therefore Mn is added to order the Li position, which prevents Ni to occupy the same site as Li. Ni is the electrochemically active element. Co is still needed to avoid the antisite defect, originated from Ni^{2+} on the Li^+ site,ⁱ because Li^+ and Ni^{2+} have similar ionic radii.²⁴ The antisite defect concentration cannot exceed more than 2% (Li/M %) otherwise the electrochemical performance of the battery is reduced.

The second family is the olivine compounds and the prototype of these materials is LiFePO_4 (LFP).²⁵ These cathodes show low intrinsic electronic conductivity and their use only became realistic when it was discovered that conductivity could be enhance sufficiently by coating the material with conductive carbon.²⁶ Since then, the material has been intensively studied. Different cathodes of the LiMPO_4 family have been reported (M = Mn, Co, Ni where the $\text{M}^{2+}/\text{M}^{3+}$ redox potential vs. Li^+/Li are 4.1, 4.8 and 5.1 V, respectively) however LiMPO_4 are not as competitive as LiFePO_4 (3.4 V vs Li^+/Li).²⁷ The most studied of the other olivines is LiMnPO_4 (LMP) as it shows a higher / theoretical energy density than LiFePO_4 (701 W h kg^{-1} and 586 W h kg^{-1} , respectively).²⁷ LMP's intrinsic electronic conductivity is lower than LiFePO_4 and coating with conductive carbon is necessary. However Fe is more reactive towards carbon than Mn^{28, 29} and the capacity remains lower than LiFePO_4 even when using high amounts of carbon. The carbon content must be high enough for full and homogeneous coating of the particles, thick coatings have a detrimental

ⁱ Antisite defect is defined as a substitutional defect which is caused when an atom A which should occupy an x site is occupying a y site where an atom B should be placed. This is neither a vacancy nor an interstitial, nor an impurity.

effect of the electrochemical performance, probably reflecting a kinetic hindrance to lithium ions penetration.³⁰ This issue leads to really low capacities compared to LiFePO_4 , even at high rates, which is required for high power supplies.

The third family is formed by spinel compounds, the prototype being LiMn_2O_4 . This material has been incorporated as a cathode in LIBs for EVs. However the manganese is soluble in the electrolyte and reduces the calendar life of the LIB dramatically. As a consequence, LiFePO_4 has been replacing these cathodes. Lately, $\text{LiMn}_{1.5}\text{Ni}_{0.5}\text{O}_4$ (LMN) has attracted interest because it provides the Ni(IV)-Ni(II) formal valences at about 4.7 V vs Li^+/Li .^{31, 32} However, some surface reactions at the cathode/electrolyte interface cause degradation in the electrochemical performance.³³

Table 1.1-1 Characteristics of cathode materials.

Cathode	Voltage / V	Capacity / W h kg ⁻¹	Cycle life	Applications
LiCoO_2	3.60	150 – 200	500 – 1000	Mobile phones, tablets, laptops, cameras
LiMn_2O_4	3.70	100 – 150	300 – 700	Power tools, medical devices, electric powertrains
$\text{Li}(\text{Ni}/\text{Mn}/\text{Co})\text{O}_2$	3.60	150 – 220	1000 – 2000	E-bikes, medical devices, EVs, industrial
LiFePO_4	3.40	90 – 120	1000 – 2000	Portable and stationary needing high load currents and endurance

In recent years research has focused on the improvement of these cathodes. For instance, in $\text{LiNi}_{1/3}\text{Mn}_{1/3}\text{Co}_{1/3}\text{O}_2$ the concentration of antisite defects has been decreased considerably and therefore studies are being performed to improve the disorder of the surface layers. For LiFePO_4 , which can be found already in HEVs and EVs, the research is focus on the reduction of the cost of the synthesis of the material by new routes.³⁴ For LiMnPO_4 and $\text{LiMn}_{1.5}\text{Ni}_{0.5}\text{O}_4$, research is focusing on the improvement of the cathode-electrolyte surface. The formation of a thick SEI layer in contact with commercial electrolytes hinders its stable operation at >4.5 V and

>40 °C. These detrimental surface reactions are accompanied by capacity fade, degradation in the rate capability, and safety problems such as thermal runaway.³⁵ To alleviate the unwanted reaction with electrolyte and the consequent performance degradation, surface-modification approaches with inert oxides^{36, 37} (e.g., Al₂O₃ and AlPO₄) have been pursued.

1.2 Electrolytes

1.2.1 Background

1.2.1.1 Small - scale lithium ion batteries

Small - scale portable electronic devices are well established since they have been used for the last 25 years. For instance, graphite is the most common anode and the use of graphite is enhanced by the addition of ethylene carbonate (EC). This organic material creates a SEI³⁸ with the electrode (graphite) when reductively decomposed at the graphite surface.³⁹⁻⁴³ EC forms a SEI which is stable and electronically insulating but ionically conducting (permeable to Li⁺ cations). The formation of a SEI prevents continuous electrolyte decomposition at the graphite surface at low potentials. The formation of a SEI also inhibits co-insertion during cycling, otherwise it would lead to graphite exfoliation. EC possesses a high dielectric constant which ensures high salt dissociation and prevents ion-pair formation between EC and LiPF₆. Dimethyl and/or diethyl carbonate (DMC and DEC) are added to EC to obtain low viscosities which contribute to a suitable electrolyte solvent mixture and enhance ionic conductivity.³⁹⁻⁴¹ Finally, a lithium salt has to be dissolved in the organic solvent, the carbonates coordinate to the Li⁺ cation strongly, improving the ion transport properties of electrolyte (*i.e.* LiPF₆). The electrolyte properties (*i.e.* flammability or SEI formation) can be modified by using additives, which will be explained in section 1.2.2.1.

1.2.1.2 Large - scale lithium ion batteries

LIBs have become really important in electronic devices (mobile phones, laptops, tablets, etc.) but some improvements are still needed to enhance energy and power densities. However, when these batteries are used for large-scale applications, other aspects such as safety, must be considered. LIBs are electrochemical devices that offer high energy densities and substantial heat

generation when exposed to harsh conditions (mechanical, electrical, and thermal) can occur. Once heat is generated, the electrodes and electrolytes can undergo side reactions which can ultimately lead to fire or explosion of the cell. Therefore, to produce a high performance LIB it is necessary not only to achieve good ionic conductivity, electrochemical inertness towards the cell components and suitable interfacial properties but also electrochemical stability (Figure 1.2-1).

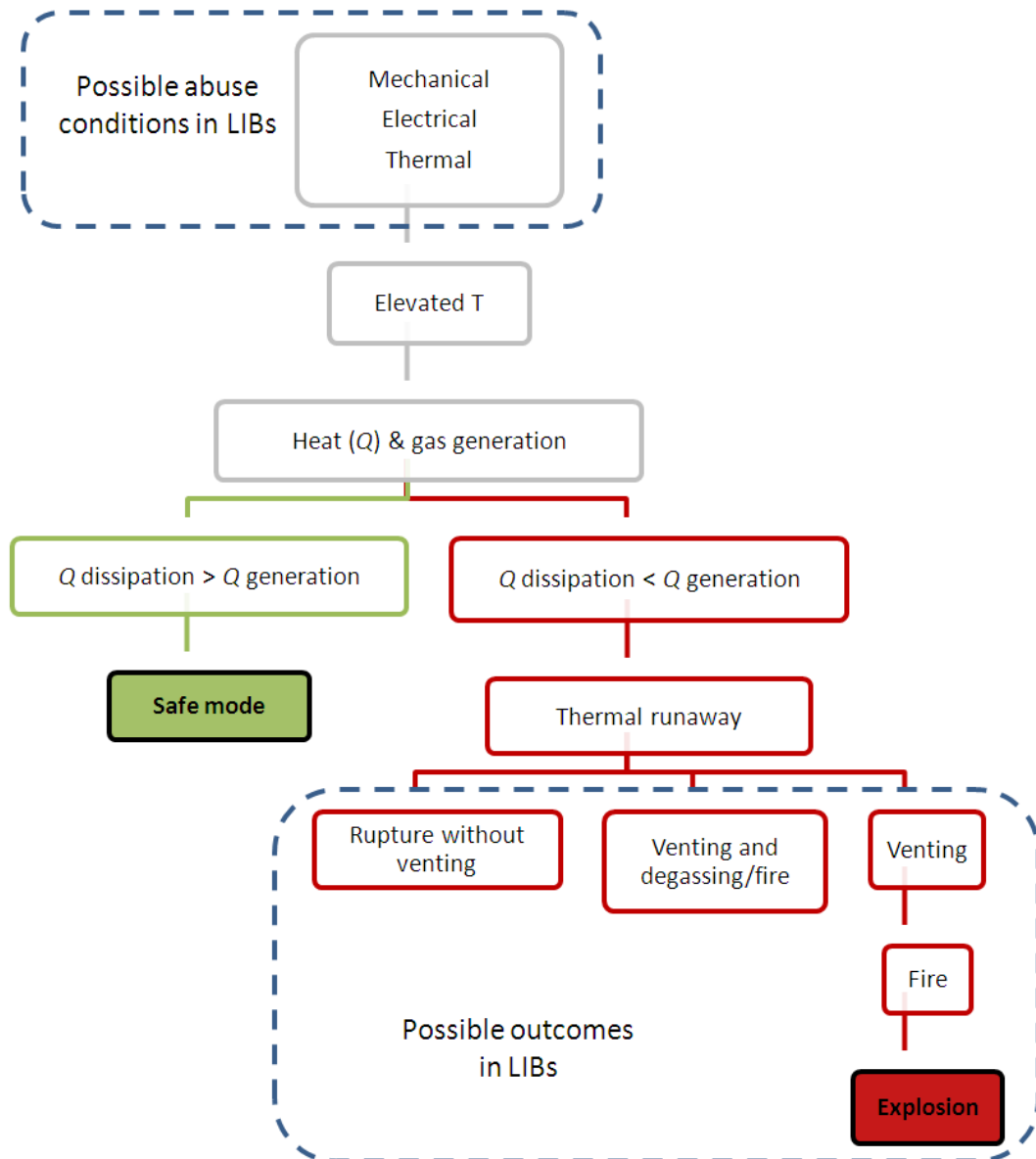


Figure 1.2-1 Schematic overview of possible abuse conditions for LIBs, the resulting behaviour of the cell, and possible outcomes (Figure adapted from Kalhoff *et al.*).⁴⁴

The great demand for batteries with high power and energy densities promotes the need for advanced lithium-ion battery technologies. Solid electrolytes offer the possibility to replace organic liquid electrolytes and thereby improve the safety of next-generation high-energy batteries. Although the advantages of non-flammable solid electrolytes are widely acknowledged, their low ionic conductivities and low chemical and electrochemical stabilities prevent them being used in practical applications.

In an effort to overcome these problems, there has been an ongoing search over the past few decades for new materials for solid electrolytes. This search has considered crystalline, glassy, polymer and composite systems which will be explained in detail in the following section.

1.2.2 Drawbacks for large - scale lithium ion batteries

1.2.2.1 Organic liquid electrolytes

EC is the most common organic solvent used in LIBs, and there is still some room for improvement of its chemical properties. EC is used in solution mixing it with 1 M LiPF₆. The final mixture has high viscosity and results in a relatively low ionic conductivity. Alternatively, other cyclic carbonates have been investigated such as propylene carbonate (PC), however it is not used in high quantities since it does not form a stable SEI. Linear organic carbonates have been suggested as an alternative, these organic compounds show low viscosities which contribute to a suitable ionic conductivity by lowering the overall viscosity of the mixture. However linear organic carbonates show lower dielectric constant which promote the ion-pair formation instead of high salt dissociation, apart from lower boiling points, lower flash points and more volatile than cyclic carbonates.⁴⁵ The SEI formed between the organic solvent and the anode is less stable leading to the continuous decomposition of the electrode at the anode surface and intercalation of the lithium-ion solvation shell.⁴⁶ Xu *et al.* found that mixtures of different organic solvents with linear and cyclic structures had better performance;³⁹ on one hand, by using cyclic organic materials such as EC the ionic conductivity is improved (EC has a high dielectric constant) whereas on the other hand, linear carbonates have low viscosity. Incorporating cyclic with linear carbonates enhanced the reduction in release of toxic gaseous such as CO,

CH₄, or CH₂O, because the decomposition kinetics are decreased comparing to EC itself. Mixing cyclic and linear carbonates also means that SEI formation is also possible and stable. However there are still some concerns such as flammability and thermal stability, since the mixtures of these carbonates still possess low flash points.

Lithium Salts

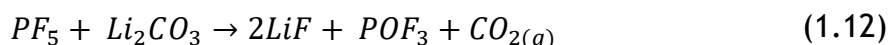
LiPF₆ is the most common lithium salt used in commercial LIBs due to its exceptional properties. It shows high ionic conductivity,^{47, 48} chemical inertness, a wide electrochemical stability window (ESW),⁴⁸ and an ability to passivate the aluminium current collector.⁴⁹ Aluminium is commonly employed as the cathodic current collector because of its low cost and weight. 1 M LiPF₆ can also dissolve EC, whereas EC on its own is solid; the combination of cyclic and linear carbonates (EC and DMC) with LiPF₆ increases the decomposition temperatures⁵⁰ of the mixture. But despite all the benefits of LiPF₆ some improvements remain to be made. If the battery overheats, LiPF₆ decomposes into LiF_(s), insoluble in most of the organic solvents used for LIBs, favouring degradation, and PF_{5(g)} (a strong Lewis acid) which induces ring-opening reactions of cyclic carbonates and continuous electrolyte degradation (1.10).⁵¹⁻⁵³



PF₅ can also lead to toxic reactions in contact with ppm of water forming hydrofluoric acid and can react with the organic solvent forming toxic fluoro-organic compounds (1.11).⁵⁴



HF, apart from being a highly toxic gas, can react with other compounds in the battery and therefore degrade some of the parts resulting in the rapid decay of the entire battery.⁵⁵ The other side product, PF₅, can also react with the SEI layer components and form a solid layer of insulating LiF leading to the death of the battery at relatively low temperatures (≈ 363 K), as equation (1.12) shows.



Other lithium salts can be used to replace LiPF_6 : such as tris(pentafluoroethyl)trifluorophosphate (LIFAP), LiBF_4 or LiAsF_6 . LIFAP could be a good candidate as a lithium salt for electrolytes in LIBs, because compared to LiPF_6 its chemical, electrochemical, and thermal stabilities are higher and it demonstrates enhanced resistance towards hydrolysis due to the presence of stabilized phosphorus-fluorine bonds. However its employment in commercial LIBs has not been reported yet. LiBF_4 shows enhanced thermal stability and reduced sensitivity towards moisture. However LiBF_4 possesses a lower ionic conductivity than LiPF_6 and dissociates in carbonate-based solvents. LiAsF_6 could replace LiPF_6 due to its higher ionic conductivity and superior cycling performance and higher thermal stability. However the potential formation of highly toxic AsF_3 excludes this ionic salt in commercial LIBs.

Additives

As was mentioned earlier (section 1.2.1.1) additives can be used to improve the safety of LIBs, for example by improving thermal stability and reducing the risk of fire-induced reactions. These additives have to be less than 10% in weight or volume; otherwise they have to be considered as cosolvents. For instance, tris(pentafluorophenyl) borane (TPFPB)⁵⁶ or vinylene carbonate (VC)⁵⁷ can be used as additives.

Flame-retardant additives

Flame retardant (FR) additives can be added to the organic carbonate electrolyte solvents preventing either the combustion reaction via radical scavenging (chemical interactions), or FRs such as silica form a thermally insulating barrier which prevent the self-propagating fire forming (mechanical/physical mechanism) (Figure 1.2-2).⁴⁴

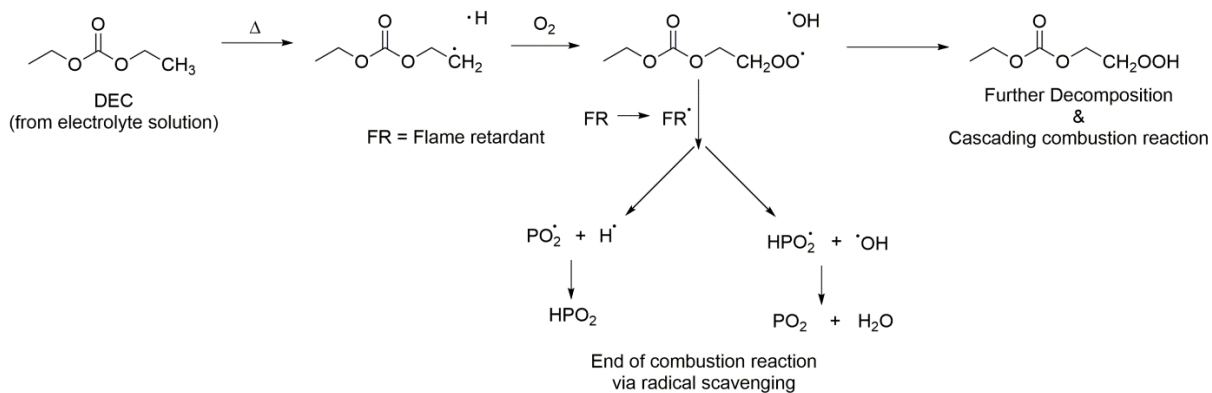


Figure 1.2-2 Schematic illustration of the combustion mechanism of conventional organic carbonate based electrolytes and the effect of FR additives.⁴⁴

The advantages and drawbacks of organic liquid electrolytes (OLEs) have already been discussed in this section. The addition of flame-retardants can improve their safety-performance, however there are still some issues related to thermal stability, flammability, and leakage. This must be taken into consideration if LIBs are to be incorporated in large - scale devices such as vehicles.

1.2.3 Safer electrolytes

New electrolyte systems have been suggested to potentially replace organic liquids electrolytes (OLEs), and these possible electrolytes are shown in Table 1.2-1. In total, seven different systems have been proposed in the literature: ionic liquids (IL), solid - polymer electrolyte (SPE), gel - polymer electrolyte (GPE), solid state electrolytes (SE), and combination between them (OLE-ILs, IL-SPEs, and OLE- IL-SPEs).

Table 1.2-1 Overview of the innovative and optimised electrolyte systems and their potential physicochemical properties, as well as a brief evaluation of their overall safety.⁴⁴

Electrolyte properties	OLEs	ILs	OLE-ILs	SPEs	GPEs	IL-SPEs	OLE-IL-SPEs	SEs
Ionic conductivity	+	o	+	-	+	o*	o*	o
Interfacial properties	+	-	+	-	o*	o*	o*	-
Electrochemical stability	-	+	o*	+	o*	o*	o*	+
Low-temperature performance	o	-	o*	-	o	o*	o*	?
Thermal stability	-	+	+	+	-	o*	o*	+
Overall safety	-	+	o*	+	o	o*	o*	+

+ = high / good; o = medium; - = poor; * = composition and condition dependent. IL = Ionic liquids, SPE = solid – polymer electrolyte, GPE = gel – polymer electrolyte, SE = Solid state electrolyte.

1.2.3.1 Ionic liquids

Ionic liquids (ILs) have been suggested as an alternative to OLEs, as they have negligible vapour pressure and very low (if not negligible) flammability which can make them suitable for large - scale LIBs.⁵⁸⁻⁶⁰ ILs have large, bulky, and asymmetrical cations and anions. The most common IL can be formed by a quaternary ammonium cation (imidazolium, pyridinium, pyrrolidinium, etc.) and an organic or inorganic anion (*i.e.* BF_4^- , $[(\text{CF}_3\text{SO}_2)_2\text{N}]^-$, $[(\text{C}_2\text{F}_5\text{SO}_2)_2\text{N}]^-$, etc.). ILs show low vapour pressure, low flammability, a large liquid phase range (*i.e.* typically from 173 - 673 K, with no evaporation or crystallisation), and a large electrochemical stability window (ESW, up to 5 to 6 V for certain cation-anion combinations). However there are still some concerns about these materials being incompatible with LIBs, due to ILs possessing low ionic conductivity at ambient pressure and bad compatibility with graphite anodes, compared to OELs.⁵⁸⁻⁶⁰

1.2.3.2 Organic liquid – ionic liquid electrolytes

Different groups have suggested combinations of OLEs and ILs as possible electrolytes.⁶¹⁻⁶⁴ Incorporating OLEs lowers the viscosity of the mixture and therefore improves the ionic conductivity. Additionally, stability with graphite electrodes can be achieved because of the formation of a stable SEI. Moreover, ILs increase the safety and stability due to negligible vapour pressure and very low (if not negligible) flammability. For example, electrolyte mixtures of LiPF_6 - $[\text{PP}_{13}][\text{TFSI}]/\text{EC}/\text{DMC}/\text{EMC}$ ⁶³, LiPF_6 - $[\text{EMI}][\text{TFSI}]/\text{EC}/\text{DE}/\text{VC}$,⁶¹ LiTFSI - $[\text{PYR}_{14}][\text{TFSI}]/\text{PC}$,⁶⁴ and LiPF_6 - $[\text{PP}_{13}][\text{TFSI}]/\text{EC}/\text{DMC}/\text{EMC}$ ⁶² have been investigated and provided superior safety (both thermal stability and flammability, considering the current state of art) and did not suppress the ionic conductivity at room temperature.^{61, 63}

1.2.3.3 Solid - polymer electrolytes

Solid polymer electrolytes (SPEs) are attractive as they do not contain flammable liquid organic solvents which also avoids the risk of cell leakage in cases of mechanical abuse.⁶⁵ Moreover, these electrolytes can be incorporated in flexible batteries. Generally, polymers need to show the following properties: (a) electronically insulating; (b) high mechanical strength; (c) thermal, chemical, and electrochemical stability; (d) compatibility with the electrodes and formation of low-resistivity SEI; and (e) low cost.⁶⁶

Two broad types of polymer electrolytes can be considered: (a) high-molecular weight polymers which are called (dry) solid or solvent-free polymers known as Solid-polymer electrolytes (SPEs), the polymer itself acts as an ionic conductor⁶⁷; and (b) gel-polymer electrolyte (GPEs)⁶⁸, ILs (IL-SPEs), or mixtures (OLE-IL-SPEs), where the polymer does not have to act as an ionic conductor.

SPEs are composed of lithium salts dissolved in polymers. The low molecular weight polymers are the most desirable materials because they show better ionic conductivities, but there is a compromise between the molecular weight and the conductivity, since the lighter the polymer is the more dendrites are formed in the anode. High ionic conductivities can be reached up to 10^{-6} and 10^{-5} S cm^{-1} at 298 and 328 K, respectively.⁶⁹⁻⁷²

GPEs combine the advantages of a polymer matrix (*i.e.* mechanical stability, flexibility, reduced leakage) with the high ionic conductivities of liquid organic electrolytes.⁷³ The use of a liquid electrolyte inside a solid host (polymer) enhances cohesive and diffusive properties, as well as contact between the electrode and the electrolyte. Nevertheless, the final compound has to fulfil the same prerequisites and requirements as SPEs and polymer electrolytes.

IL-SPEs show favourable electrochemical and safety properties, but the ionic conductivities remain too low at room temperature and the compatibility with state of the art cathodes is limited.^{74, 75}

1.2.3.4 Ionic liquid – Organic liquid – Solid polymer electrolytes

In order to obtain an optimized electrolyte some researchers have investigated the combination of the three different electrolytes mentioned in this section: known as OLE-IL-SPEs. Combining a lithium-ion conducting polymer, IL(s), organic carbonates, and a lithium salt promises an optimized electrolyte system, potentially providing further improved ionic conductivity, enhanced thermal stability (compared with GPEs), and a stabilised electrode/electrolyte interface, particularly with respect to graphite anodes. However, the use of volatile and flammable organic solvents do not make these compounds safe and thermally stable.⁷⁶

1.2.3.5 Solid state electrolytes

A potential solid state electrolyte (SE) material must meet several requirements. It must have high ionic conductivity (more than 0.1 mS cm^{-1} over the operating temperature range⁴, preferentially 1 mS cm^{-1})⁷⁷ and a negligible electronic conductivity. It must have good chemical stability with the electrodes over the working temperature range of the battery, and good electrochemical stability within the operating potentials of the cell. It should furthermore retain good contact at the interfaces with the electrodes. Ideally it should also have low toxicity, be non-flammable and be inexpensive. Designing suitable solid electrolyte materials for lithium batteries that meet these requirements is a great challenge.⁴

One of the best approaches proposed for a safer LIB would be the incorporation of SEs. These electrolytes have attracted great attention because they can avoid the

use of organic solvents and polymers, which represent the main cause of flammability issues.^{78, 79} Some of the most common SEs are shown in Figure 1.2-3.

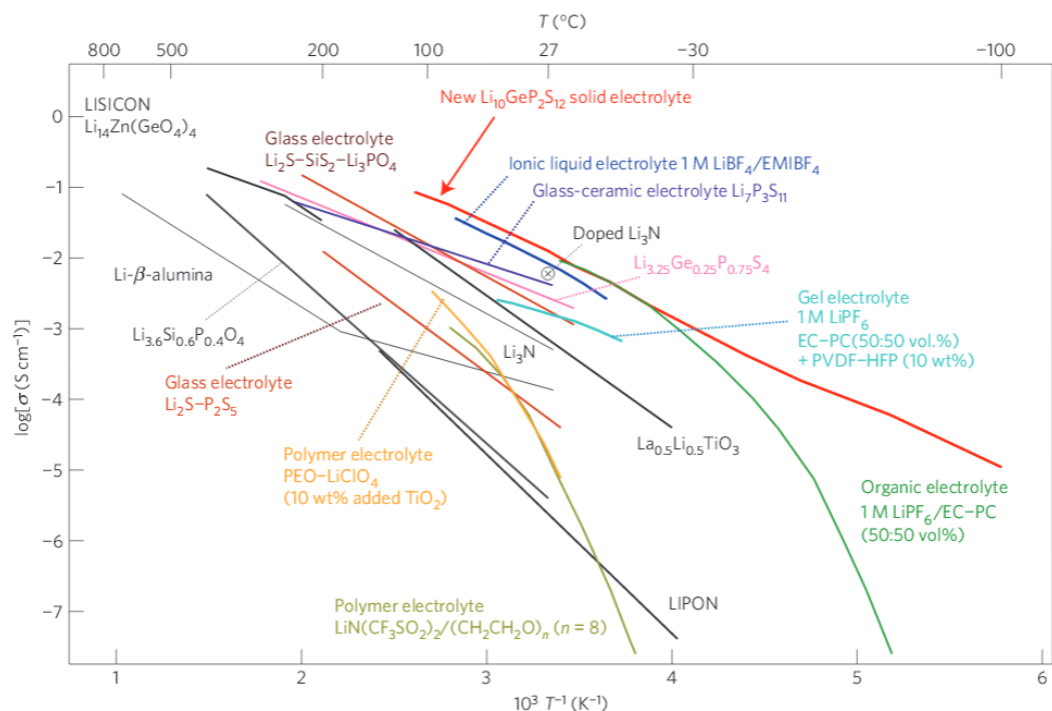


Figure 1.2-3 Ionic conductivity (represented as log) as a function of reciprocal temperature for lithium solid electrolytes, organic liquid electrolytes, polymer electrolytes, ionic liquids and gel electrolytes.⁷⁹⁻⁹⁰

1.2.4 Solid state electrolytes

This section will summarize the most important solid state electrolytes discovered so far. Three different inorganic solid state lithium ion conductors (LICs) can be distinguished: crystalline, composite, and amorphous LICs.

1.2.4.1 Crystalline inorganic Li ion conductors

Firstly, seven different materials families can be considered as examples of crystalline LICs: NASICON-type, LISICON-type, A-site deficient perovskite solid solutions, Thio-LISICON-type, garnet-type, complex hydrides (CHs) and ternary halides.⁹¹

NASICON-type

The first examples of compounds with a structure of the NASICON-type were reported in 1968 and consisted of the phosphates $\text{NaA}^{\text{IV}}(\text{PO}_4)_3$ (where A^{IV} was Ge, Ti and Zr).⁹² After the discovery of this structure, the analogous lithium compounds

were subsequently studied. The A cation site can be shared by different cations, depending on the ionic radii ($\text{LiA}_{2-x}^{\text{IV}}\text{A}'_x^{\text{IV}}(\text{PO}_4)_3$). The NASICON structure is formed by AO_6 octahedra linked by PO_4 tetrahedra to define 3D interconnected channels and two types of interstitial positions (M' and M'') where Li^+ are distributed. The Li^+ cations move from one site to another through “bottlenecks” the size of these is dependent on the nature of the skeleton ions and on the Li occupancy in both types lithium site (M' and M'').^{93, 94}

The higher ionic conductor compounds of the NASICON-type family exist with $A = \text{Ti}^{4+}$ with general formula $\text{Li}_{1+x}\text{Ti}_{2-x}\text{A}_x(\text{PO}_4)_3$ ($A = \text{Al}, \text{Ga}, \text{In}, \text{Sc}$).⁹⁵ In particular, the best performance was obtained with Al^{3+} in $\text{Li}_{1.3}\text{Al}_{0.3}\text{Ti}_{1.7}(\text{PO}_4)_3$ (LATP) (Figure 1.2-4)⁹⁶. Al^{3+} is the smallest cation that can substitute for Ti in these compounds (of Ga, In, and Sc), which reduces the cell parameters and enhances the conductivity by 3 orders of magnitude compared with the other substituent cations ($3 \times 10^{-3} \text{ S cm}^{-1}$ at 298 K, Figure 1.2-6 (u)).⁹⁵ Although $\text{Li}_{1.3}\text{Al}_{0.3}\text{Ti}_{1.7}(\text{PO}_4)_3$ shows high ionic conductivity, it is unstable with Li metal due to the facile reduction of Ti^{4+} to Ti^{3+} .⁹⁷

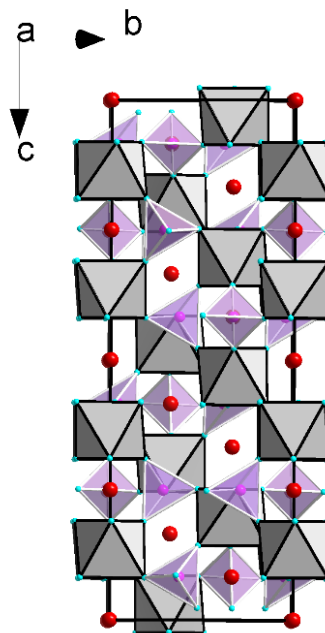


Figure 1.2-4 Crystal structure of $\text{Li}_{1.3}\text{Al}_{0.3}\text{Ti}_{1.7}(\text{PO}_4)_3$. Lithium, oxygen and phosphor are represented as red, light blue and light purple spheres. The octahedra formed by $(\text{Al}/\text{Ti})\text{O}_6$ is represented in light grey. The tetrahedra for PO_4 is represented in light purple.

LISICON

The first LISICON-type material, $\text{Li}_{14}\text{ZnGe}_4\text{O}_{16}$, was reported in 1978, although the ionic conductivity at room temperature is relatively low ($\sim 10^{-7} \text{ S cm}^{-1}$) it has an ionic conductivity of 0.125 S cm^{-1} at 573 K (Figure 1.2-5).^{94, 98-100} In the following years different LISICON phases were synthesised with other compositions (e.g. $\text{Li}_{2+2x}\text{Zn}_{1-x}\text{GeO}_4$ or $\text{Li}_4\text{GeO}_4 - \text{Zn}_2\text{GeO}_4$ solid solution). LISICON can be doped by a range of elements, however the conductivity is not massively improved (e.g. $\gamma\text{-Li}_{14.4}\text{V}_{1.6}\text{Ge}_{2.4}\text{O}_{16}$, $10^{-6} \text{ S cm}^{-1}$ at room temperature). Furthermore, LISICON is highly reactive with lithium metal and the conductivity decreases with time.⁹⁷

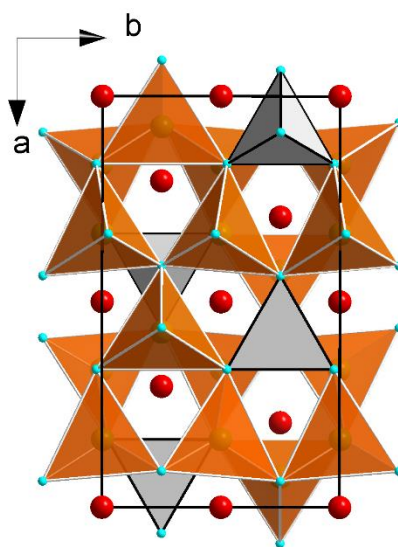


Figure 1.2-5 Crystal structure of $\text{Li}_{14}\text{ZnGe}_4\text{O}_{16}$. Lithium, oxygen and titanium are represented as red, light blue and green spheres. The tetrahedra formed by GeO_4 is represented in light grey. The tetrahedra for $(\text{Li/Zn})\text{O}_4$ is represented in orange.

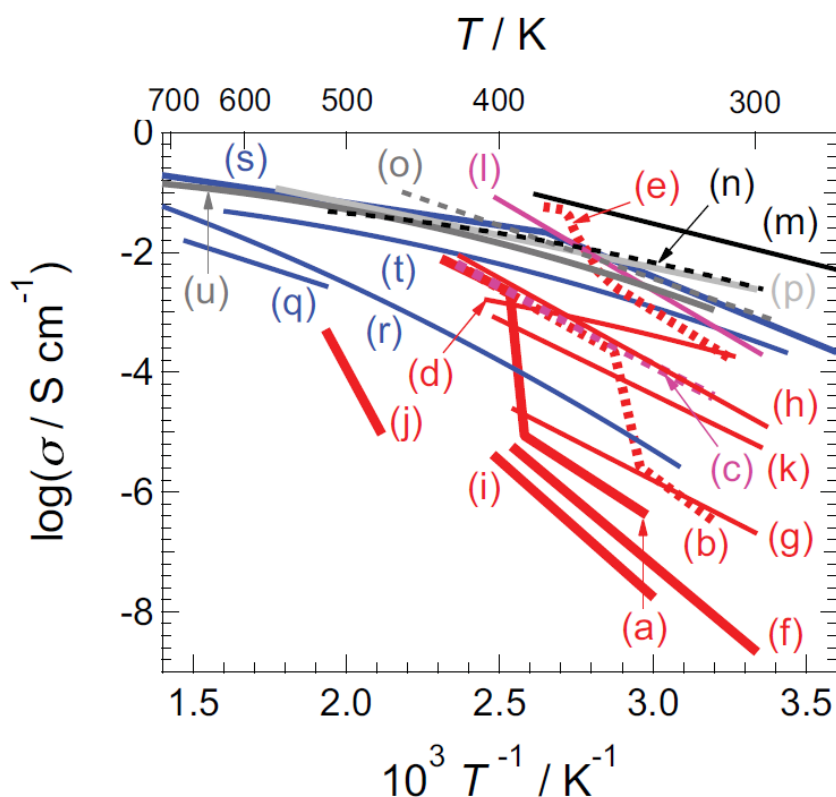


Figure 1.2-6 Total ionic conductivities of Li^+ solid state electrolytes with temperature a) LiBH_4 ,¹⁰¹ b) $\text{Li}(\text{BH}_4)_{0.75}\text{Cl}_{0.25}$,¹⁰² c) $\text{Li}(\text{BH}_4)_{0.75}\text{I}_{0.25}$,¹⁰² d) $\text{Li}_4(\text{BH}_4)(\text{NH}_2)_3$,¹⁰³ e) $\text{Li}_2(\text{BH}_4)(\text{NH}_2)$,¹⁰³ f) LiAlH_4 ,¹⁰⁴ g) Li_3AlH_6 ,¹⁰⁴ h) $\text{Li}(\text{NH}_2)_{0.67}\text{I}_{0.33}$,¹⁰⁵ i) LiNH_2 ,¹⁰⁶ j) $\text{Li}_2\text{Mg}(\text{NH}_2)_2$,¹⁰⁶ k) $\text{Li}_2\text{Ca}(\text{NH}_2)_2$,¹⁰⁶ l) Li_2NH ,^{106, 107} m) $\text{Li}_{10}\text{GeP}_2\text{S}_{12}$,⁷⁹ n) $\text{Li}_7\text{P}_3\text{S}_{11}$ (glass-ceramics),⁸² o) $\text{Li}_2\text{S}-\text{SiS}_2-\text{Li}_3\text{PO}_4$ (glass),^{108, 109} p) $\text{Li}_{3.25}\text{Ge}_{0.25}\text{P}_{0.75}\text{S}_4$ (thio-LISICON),⁸¹ q) Li- β -alumina,^{100, 110} r) $\text{Li}_{14}\text{Zn}(\text{GeO}_4)_4$ (LISICON),¹¹¹ s) $\text{Li}_{0.34}\text{La}_{0.51}\text{TiO}_{2.94}$,^{80, 112} t) $\text{Li}_7\text{La}_3\text{Zr}_2\text{O}_{12}$,^{113, 114} and u) $\text{Li}_{1.3}\text{Al}_{0.3}\text{Ti}_{1.7}(\text{PO}_4)_3$ (LATP).⁹⁶

A-site deficient perovskite solid solutions

The first perovskite (ABO_3)-type lithium lanthanum titanate ionic conductor (LLTO), $\text{Li}_{3x}\text{La}_{(2/3)-x}\text{TiO}_3$ ($0 < x < 0.16$) was discovered in 1987.^{80, 115-117} LLTO consists of a mixture of phases, i.e., a high-temperature phase with cubic $Pm\bar{3}m$ symmetry (α -LLTO) and a lower temperature β -LLTO phase having tetragonal $P4/mmm$ symmetry. The tetragonal LLTO phase can show high ionic conductivities at room temperature because of the large concentration of A-site vacancies, allowing the motion of the Li^+ by a vacancy mechanism and through square planar bottleneck between A sites formed by four O^{2-} ions between two neighbouring A sites.¹¹⁸⁻¹²⁰ The ionic conductivity of this material is proportional to the amount of lithium incorporated into the structure.¹¹⁹ Single crystals show a high ionic conductivity up

to $10^{-3} \text{ S cm}^{-1}$ ($E_a = 0.3\text{-}0.4 \text{ eV}$) at room temperature for $x = 0.11$. However high temperature are required for sintering the mixtures and high Li_2O losses are observed leading to difficulty in controlling Li ion content and ion conductivity. The ionic conductivity of ceramics is much lower than that of the single crystals due to the blocking grain boundaries. However LLTO is unstable against Li metal anode. Lithium can be intercalated into LLTO at a potential below about 1.7-1.8V vs. Li which causes the reduction of Ti^{4+} to Ti^{3+} and induces high electronic conductivity.¹¹⁹

Thio-LISICON-type

Thio-LISICON compounds were reported for the first time in 2000.^{121, 122} Thio-LISICON has the same framework as LISICON but the oxygen site is occupied by the more polarisable sulphide anion, which improves the ionic conductivity due to the decreased interaction between skeleton and Li^+ ions. Additionally, the radius of S^{2-} is larger than that of O^{2-} which therefore enlarges the size of the bottlenecks in the structure compared to regular LISICON compounds.⁹⁴ For the thio-LISICON, $\text{Li}_{4-2x}\text{Zn}_x\text{GeS}_4$, the conductivity remains low at room temperature ($3 \times 10^{-7} \text{ S cm}^{-1}$).¹²¹ Addition of a trivalent or pentavalent cation however can improve the conductivity by *ca.* 3 orders of magnitude; compounds such as $\text{Li}_{4-x}(\text{Ge,Si})_{1-y}\text{M}_y\text{S}_4$. The partial substitution of $\text{Ge}^{4+}/\text{Si}^{4+}$ for $\text{M}^{3+}/\text{M}^{5+}$ may introduce lithium vacancy, and increase the conductivity.¹²³ $\text{Li}_{3.25}\text{Ge}_{0.25}\text{P}_{0.75}\text{S}_4$ reached ionic conductivities of $2.2 \times 10^{-3} \text{ S cm}^{-1}$ at room temperature (Figure 1.2-3 and Figure 1.2-6 (p)).⁸¹ In 2011, a new compound was discovered from this family, $\text{Li}_{10}\text{GeP}_2\text{S}_{12}$ (LGPS), which showed the best ionic conductivity at room temperature compared to any other type of electrolyte, $\sim 10^{-2} \text{ S cm}^{-1}$. The activation energy for Li^+ transport was only 0.24 eV (Figure 1.2-3 and Figure 1.2-6 (m)).^{79, 124} The crystal structure of $\text{Li}_{10}\text{GeP}_2\text{S}_{12}$ is different compared to other Thio-LISICONs, in that it contains three different tetrahedral sites ($(\text{Ge}_{0.5}\text{P}_{0.5})\text{S}_4$, PS_4 , and LiS_4) and one octahedral type (LiS_6).⁹⁴ In 2013, the synthesis of $\text{Li}_{10}\text{SnP}_2\text{S}_{12}$ was reported in which Ge was replaced by Sn. Conductivity measurements showed high ionic conductivities, 0.4 S cm^{-1} at room temperature.¹²⁵ However $\text{Li}_{10}\text{GeP}_2\text{S}_{12}$ and $\text{Li}_{10}\text{SnP}_2\text{S}_{12}$ employment in commercial LIBs has not been reported yet.

Garnet-type

Another family of electrolytes known as garnets which have the general formula $\text{Li}_5\text{La}_3\text{M}_2\text{O}_{12}$ ($M=\text{Ta}, \text{Nb}$) was discovered in 1988. La and M occupy eight- and six-coordinated sites, respectively, while Li^+ occupies a mixture of octahedra and tetrahedra.¹²⁶ The MO_6 octahedra are surrounded by six lithium ions and two Li^+ vacancies. Therefore, the structure facilitates lithium ion conduction.¹²⁷ La^{3+} cations can be substituted by other cations such as Ba^{2+} ,¹²⁸ Sr^{2+} and K^+ .¹²⁹ Ba^{2+} substitution in garnets leads to ionic conductivities of about $4 \times 10^{-5} \text{ S cm}^{-1}$ at 295 K.¹²⁸ The transition metals can be substituted by In^{3+} giving ionic conductivities of $1.8 \times 10^{-4} \text{ S cm}^{-1}$ at 323 K for $\text{Li}_{5.5}\text{La}_3\text{Nb}_{1.75}\text{In}_{0.25}\text{O}_{12}$.¹²⁹ Different substituted garnets with different formulae ($\text{Li}_6\text{ALa}_2\text{M}_2\text{O}_{12}$, $A = \text{Ca}, \text{Sr}, \text{Ba}$) or lanthanide cations ($\text{Li}_5\text{Ln}_3\text{Sb}_2\text{O}_{12}$, $\text{Ln} = \text{La}, \text{Pr}, \text{Nd}, \text{Sm}, \text{Eu}$) were reported, however these compounds showed high activation energies at low temperatures indicative of defect trapping.¹³⁰ In 2007, a new garnet-type, $\text{Li}_7\text{La}_3\text{Zr}_2\text{O}_{12}$ (LLZO) was reported (Figure 1.2-7).¹¹³ LLZO undergoes a phase transition from a cubic to a tetragonal structure at 997 K, space group $Ia\bar{3}d$ and $I4_1/acd$ respectively and yielding ionic conductivities at room temperature of 10^{-4} and $10^{-7} \text{ S cm}^{-1}$, respectively.¹³¹ By heating at 973 K and at 1073 K LLZO it is possible to stabilise the cubic and the tetragonal garnet at room temperature, respectively.¹³¹ In 2012, High ionic conductivities were reported such as $8.7 \times 10^{-4} \text{ S cm}^{-1}$ at room temperature in $\text{Li}_{6.75}\text{La}_3\text{Zr}_{1.75}\text{Ta}_{0.25}\text{O}_{12}$.¹³²

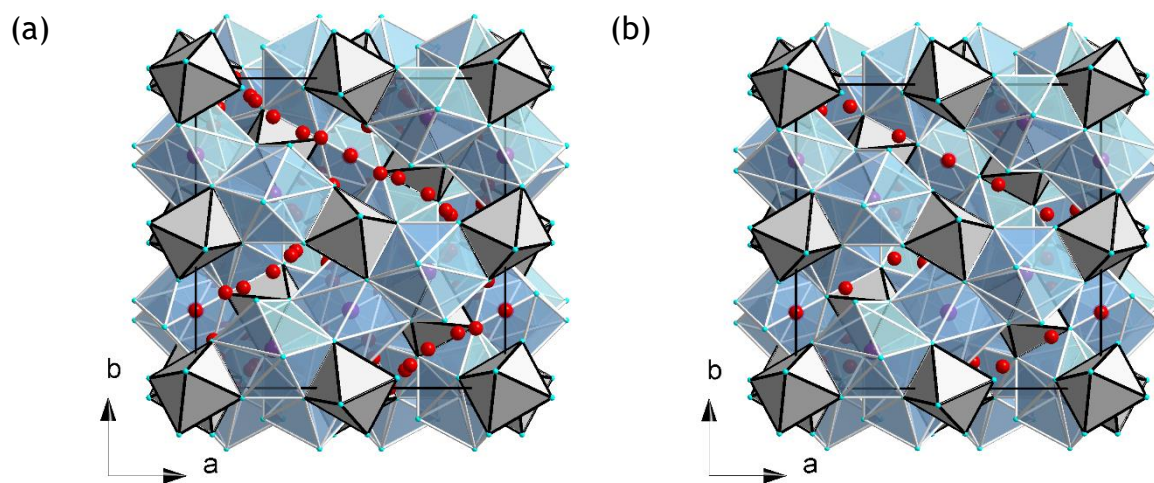


Figure 1.2-7 Crystal structure of (a) cubic ($Ia\bar{3}d$) and (b) tetragonal ($I4_1/acd$) $\text{Li}_7\text{La}_3\text{Zr}_2\text{O}_{12}$. Lithium, oxygen and lanthanum are represented as red, light blue and purple spheres. The ZrO_6 is represented in light grey.

Complex hydrides (CHs)

Complex hydrides (CHs) show different properties from other SEs. For instance, the densities of CHs are much lower than oxides and sulphides which in general would make lighter LIBs.¹³³ CHs can demonstrate high thermal stabilities due to the strong covalency between hydrogen with metals and non-metals in complex anions. The decomposition of these CHs is thus less likely at room temperature.¹³⁴

LT - LiBH₄ (low temperature) was first investigated as a solid state electrolyte in 2007.¹⁰¹ This hydride undergoes a phase transition at 383 K to a hexagonal (high temperature, HT) phase with a lithium ionic conductivity of $2 \times 10^{-3} \text{ S cm}^{-1}$ (Figure 1.2-6 (a)).¹⁰¹ Initial investigations were focused on the stabilisation of the HT phase of LiBH₄.^{135, 136} The stabilisation of the HT phase at room temperature was demonstrated by halide substitution forming Li(BH₄)_{1-x}X'_x (X' = Cl, Br and I)^{102, 137} (Figure 1.2-6, (b) and (c)). Ionic conductivities of $2 \times 10^{-5} \text{ S cm}^{-1}$ were obtained at 300 K in a composition of Li(BH₄)_{0.75}I_{0.25} (Figure 1.2-6 (c)). LiBH₄ and LiI were combined with LiNH₂ in 2009 forming three new electrolytes, Li₂(BH₄)(NH₂), Li₄(BH₄)(NH₂)₃,¹⁰³ and Li₃(NH₂)₂I¹⁰⁵. These materials showed ionic conductivities above $10^{-4} \text{ S cm}^{-1}$ at room temperature (Figure 1.2-6 (d) and (e)). By analogy to the borohydride, in 2010, attention was focused to LiAlH₄ and Li₃AlH₆ as a possible solid state electrolyte.^{104, 138} However, LiAlH₄ and Li₃AlH₆ exhibit ionic conductivities from 2×10^{-9} to $5 \times 10^{-6} \text{ S cm}^{-1}$ and 10^{-7} to $2 \times 10^{-5} \text{ S cm}^{-1}$, respectively, from room temperature to 393K (Figure 1.2-6 (f) and (g)).

In 2012, lithium rare earth (RE) mixed borohydride-halides were reported showing high ionic conductivities at 293 K (1×10^{-4} , 2×10^{-4} , and $1 \times 10^{-4} \text{ S cm}^{-1}$ for RE = Ce¹³⁹, La, and Gd¹⁴⁰, respectively). However synthesis results in byproducts such as RECl₃ and LiCl. It was suggested that high ionic conductivities were observed in these materials because they may possess disordered Li-sites creating continuous conducting paths for Li⁺ in the framework similar to those in Li₁₀GeP₂S₁₂⁷⁹ and Na₂(BH₄)(NH₂)¹⁴¹.

Metal dodecaborates (M_{2/n}B₁₂H₁₂, where *n* is the valence of the metal M), have been considered previously for hydrogen storage.^{142, 143} In 2014, these compounds were suggested as electrolytes for all solid state batteries because of the high

stability of the icosahedral $[B_{12}H_{12}]^{2-}$ anion at high temperatures.¹⁴⁴ $Li_2B_{12}H_{12}$ is also one of the products formed from the dehydrogenation of $LiBH_4$ but can be synthesised and stabilised at room temperature by mixing $LiBH_4$ and $B_{10}H_{14}$, Figure 1.2-8.¹⁴⁵ This lithium dodecaborate shows a total ionic conductivity of $10^{-4} S cm^{-1}$ at room temperature and experiences a phase transition at 615 K.^{146, 147} In 2015, He *et al.*¹⁴⁶ suggested that the formation of a bimetallic dodecaborate could improve the ionic conductivity. Their hypothesis was that the coexistence of bimetallic cations could have a synergic effect on the mobility of each ion. Indeed, they managed to synthesise the bimetallic dodecaborate $LiNaB_{12}H_{12}$ by sintering $LiBH_4$, $NaBH_4$ and $B_{10}H_{14}$ in a molar ratio of 1:1:1. $LiNaB_{12}H_{12}$ reached ionic conductivities of $10^{-5} S cm^{-1}$ and $0.79 S cm^{-1}$ at 550 K, respectively, after a phase transition at 488 K (Figure 1.2-11).^{146, 147}

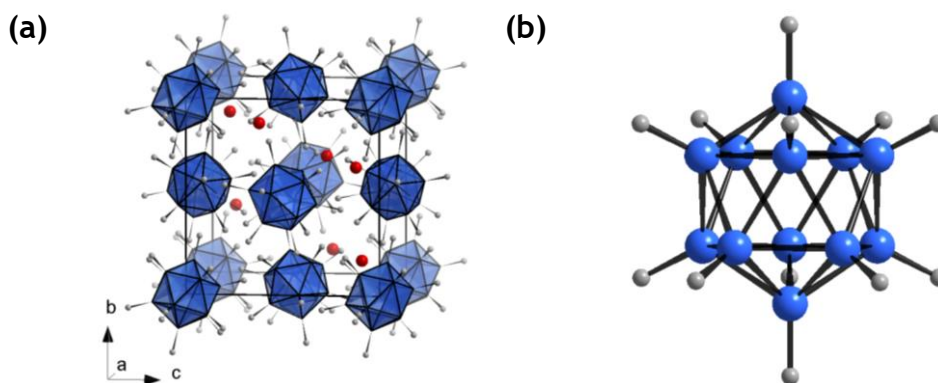


Figure 1.2-8 (a) Structure of $Li_2B_{12}H_{12}$. (b) Relative geometry of the $B_{12}H_{12}^{2-}$ anion with boron and hydrogen atoms denoted by blue and grey spheres, respectively. $Li_2B_{12}H_{12}$ crystallises with a cubic structure (space group $(Pa\bar{3})$ with lattice parameters $a = 9.5771(2) \text{ \AA}$.¹⁴⁵

In 2015, another CH crystal structure, lithium decaborate ($Li_2B_{10}H_{10}$), was reported although no conductivity measurements were published (Figure 1.2-9).¹⁴⁸ Its sodium analogue, $Na_2B_{10}H_{10}$, however displayed one of the highest ionic conductivity values for SEs, $0.01 S cm^{-1}$ at 383 K (Figure 1.2-11).¹⁴⁹

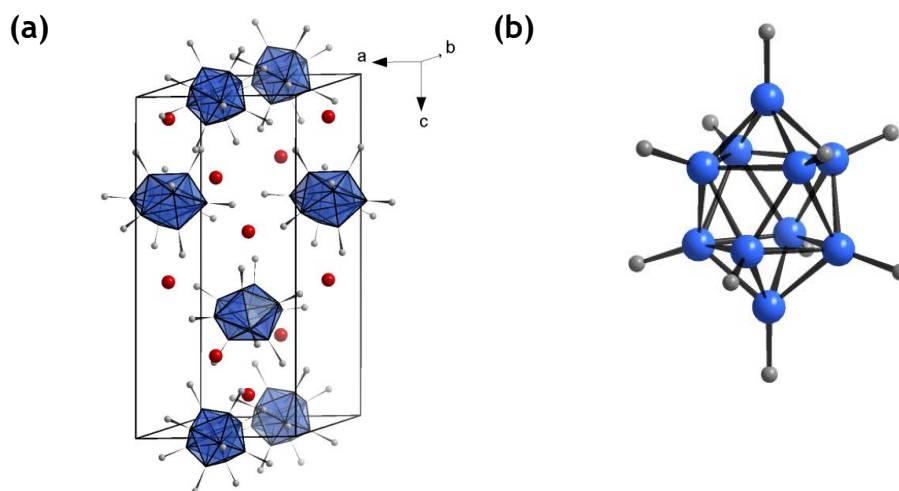


Figure 1.2-9 (a) Structure of $\text{Li}_2\text{B}_{10}\text{H}_{10}$. (b) Relative geometry of the $\text{B}_{10}\text{H}_{10}^{2-}$ anion with boron and hydrogen atoms denoted by blue and grey spheres, respectively. $\text{Li}_2\text{B}_{10}\text{H}_{10}$ crystallises with a hexagonal structure (space group $P6_422$) with lattice parameters $a = 7.042(1)$ and $c = 14.931(2)$ Å.¹⁴⁸

The latest compound reported from these new-generation electrolyte materials was $\text{LiCB}_{11}\text{H}_{12}$ (Figure 1.2-10),¹⁵⁰ which shows a total ionic conductivity of 10^{-6} S cm^{-1} at room temperature and undergoes a phase transition at 400 K reaching conductivities of 0.1 S cm^{-1} (Figure 1.2-11).

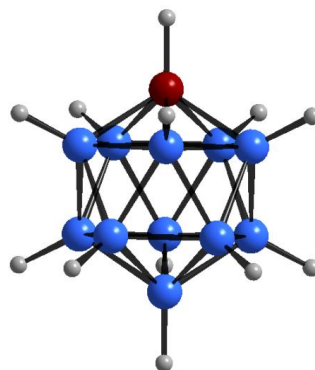


Figure 1.2-10 Relative geometry of the $\text{CB}_{11}\text{H}_{12}^-$ anion with boron, carbon, and hydrogen atoms denoted by blue, brown, and grey spheres, respectively. $\text{LiCB}_{11}\text{H}_{12}$ crystallises in a orthorhombic structure (space group $Pca2_1$) with lattice parameters $a = 9.6668(5)$, $b = 9.4892(5)$ and $c = 9.7273(5)$ Å.¹⁵⁰

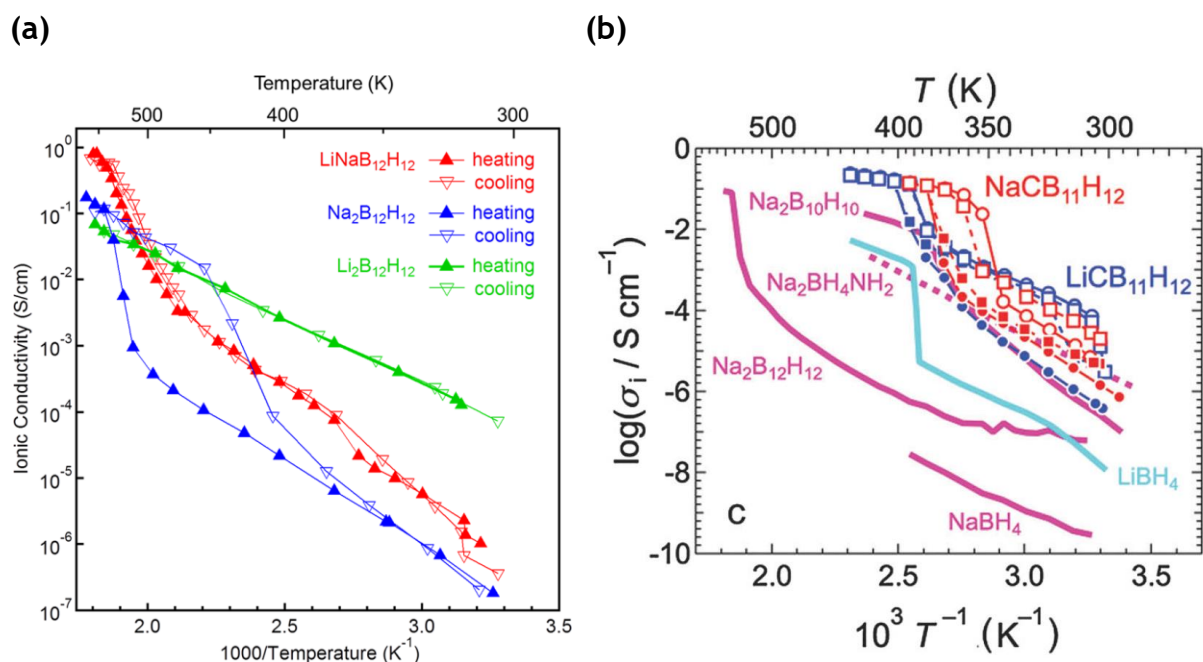


Figure 1.2-11 (a) Ionic conductivity measurements for LiNaB₁₂H₁₂, Na₂B₁₂H₁₂, and Li₂B₁₂H₁₂ and (b) for LiCB₁₁H₁₂ (blue)¹⁵⁰ and NaCB₁₁H₁₂ (red)¹⁵⁰ as a function of temperature (circles and squares denote the conductivities of the respective 1st and 2nd temperature cycles and closed and open symbols denote respective heating and cooling processes). The ionic conductivities are compared to other related materials: Na₂B₁₂H₁₂,¹⁴⁴ Na₂B₁₀H₁₀,¹⁴⁹ Na₂BH₄NH₂,¹⁴¹ NaBH₄¹⁴¹ and LiBH₄¹⁰¹.

Lithium ternary halides

Lithium ternary hydrides and halides are considered as promising candidates in Li ion batteries due to their high ionic conductivity, thermal stability and non-flammable properties. Lithium hydrides from group XIII are not thermally stable apart from LiBH₄ and LiAlH₄ (monoclinic structure, space group *P12₁/c₁*) which decompose at 541 and 373 K, respectively. For instance, LiGaH₄ (monoclinic structure, space group *P12₁/c₁*) and LiInH₄ decompose at 323 K and 273 K, making these materials unsuitable for lithium ion batteries.¹⁵¹

Table 1.2-2 shows some of the halocomplex lithium salts and their conductivities reported to date. Different aluminates and halogenidogallates have been discovered that show low ionic conductivity such as LiAlX₄ (X = Cl, Br)¹⁵²⁻¹⁵⁴ or LiGaBr₄.¹⁵⁵ Also indium halo complexes have been reported such as Li₃InCl₆ and Li₃InBr₆ which undergoes a phase transition at 314 K to become a superionic conductor and LiInI₄.¹⁵⁶⁻¹⁵⁸

Of all the halo complex lithium salts ($M^I M^{III} X_4$, where ($M^I = \text{Li}$, $M^{III} = \text{Al}$, Ga and In, $X = \text{Cl}$, Br and I), LiInBr_4 is perhaps the most interesting material.¹⁵⁷ LiInBr_4 is the only halo complex reported so far which shows a phase transition (similar to LiBH_4). The only report available in the literature on the formation of LiInBr_4 and its ionic conductivity performance was published by Yamada *et al.* in 2006.¹ The compound displays a conductivity of $10^{-3} \text{ S cm}^{-1}$ at 313 K.

Table 1.2-2 Structure of (X = Al, Ga and In) lithium halo complex salts and their conductivities, respectively.

$M^+M^{3+}X_4$	Structure	σ (297 K) / S cm ⁻¹	E_a / eV	Reference
LiAlCl₄	<i>P2₁/c</i> (Monoclinic, #14) $a = 7.007(3)$, $b = 6.504(4)$ and $c = 12.995(10)$ Å, $\beta = 93.32(5)$	1×10^{-6}	0.47	152, 153
LiAlBr₄	---	---	0.44	154
LiAlI₄	---	---	---	*
LiGaCl₄	<i>P2₁/c</i> (Monoclinic, #14) $a = 12.988(13)$, $b = 6.467(5)$ and $c = 7.015(5)$ Å, $\beta = 93.36(7)$	1.13×10^{-2} (LiGaCl ₄ – SOCl ₂ mixture)	---	159, 160
LiGaBr₄	<i>P2₁/a</i> (Monoclinic, #14) $a = 13.696$, $b = 6.854(7)$ and $c = 7.416(7)$ Å, $\beta = 93.14(8)$	7×10^{-6}	0.54	155
LiGaI₄	<i>P2₁/a</i> (Monoclinic, #14) $a = 14.863(5)$, $b = 7.415(1)$ and $c = 8.081(3)$ Å, $\beta = 92.91(2)$	---	---	159
LiInCl₄	---	---	---	*
LT - LiInBr₄	<i>Fd3m</i> (Cubic, #227) $a = 10.974$ Å	5×10^{-7}	0.31(1)	157
	None phase transition reported	5×10^{-9}	0.79	161
LT – HT LiInBr₄ (transition)	Trigonal* $a = 7.625$ Å	5×10^{-2}	0.23(1)	157, 162
HT - LiInBr₄ (post 316 K)	<i>R-3m</i> (Rhombohedral, #166) $a = 6.725(1)$ Å $\alpha = 33.65(1)^\circ$	---	---	157, 162
	None phase transition reported	3×10^{-6} (417 K)	0.79	161
NaInBr₄	<i>P2₁2₁2₁</i> (Orthorhombic, #19) $a = 11.081(1)$, $b = 10.507(1)$ and $c = 6.761(1)$ Å	2×10^{-6}	0.68	163
KInBr₄	<i>Pnna</i> (Orthorhombic, #52) $a = 7.891(12)$, $b = 10.390(5)$ and $c = 10.390(5)$ Å	---	---	164
LiInI₄	<i>P₁2₁/c₁</i> (Monoclinic, #14) $a = 8.398(4)$, $b = 7.512(3)$ and $c = 15.267(8)$ Å, $\beta = 92.67(4)$	5×10^{-9}	---	165, 166

At 297 K unless otherwise indicated. * Salts without reported crystal structures or space group.

1.2.4.2 Composite inorganic Li ion conductors

Composite electrolytes are formed by an insulator (e.g. alumina) and a solid state electrolyte (e.g. LiI) which shows low ionic conductivity (ca. 10^{-5} to 10^{-10} S cm⁻¹). However when a composite is formed between these two materials, the ionic conductivity is enhanced.¹⁶⁷ However the mechanism(s) responsible for this enhancement in the ionic conductivity is still a matter of some debate. A composite containing a significant volume fraction of well dispersed submicron particles will obviously have an extremely large matrix-particle interface area. It has now become widely accepted that the overall effect of forming the composite is to create highly conductive paths along the interfaces between the electrolyte matrix and the dispersed particles. The criterion for identifying a composite as having enhanced ionic conduction is when the conductivity of the composite exceeds the single phase bulk conductivities reported for each of the individual phases found in the composite.

1.2.4.3 Amorphous inorganic Li ion conductors

Glass electrolytes

Glasses can often be considered as electrolytes as they normally show higher ionic conductivity than crystals due to their disordered “open structure”. These materials can show interesting properties such as non-flammability, no grain boundaries, and a wide selection of compositions. Lithium phosphorous oxinitride (LIPON) also forms part of the oxide glass family. Most of the important inorganic Li⁺ conducting glasses come from one of two categories: oxides and sulfides. Oxides are commonly of Li⁺-defective γ -Li₃PO₄ solid solutions, with a typical member composition of Li_{2.88}PO_{3.73}N_{0.14}, which has an ion conductivity of 3.3×10^{-6} S cm⁻¹ at room temperature and an activation energy of 0.54 eV.¹⁶⁸ Among the most notable of sulfide glassy materials are LISON¹⁶⁹ (Li_{0.29}S_{0.28}O_{0.35}N_{0.09}) with ionic conductivities of 2×10^{-5} S cm⁻¹ at room temperature and LIPOS¹⁷⁰ (6LiI-4Li₃PO₄-P₂S₅) with a similar ionic conductivity although unstable in bulk form. These glassy compounds are highly stable in battery operation with minimal evidence of interfacial reactivity.

Sulfide based glassy electrolytes have attracted great interest. As they typically show higher ionic conductivity than oxide glasses. However these glasses are highly hygroscopic which can be an issue for LIBs, generating flammable poisonous and environmentally hazard H₂S gas. Therefore handling of sulfide glasses needs to be done in an inert atmosphere. Partial substitution of oxygen with sulfur can be effective in suppressing H₂S generation, however this can result in a decrease in the conductivity.^{171, 172} Adding lithium salts can enhance the ionic conductivity (Li₂S-SiS₂-P₂S₅-LiI)¹⁷³ because of the increase in migrating ions in the glass. However this strategy tends to facilitate the crystallisation of the glass.

Glass-Ceramic electrolytes

Glass-ceramic electrolytes are produced by the crystallisation of a precursor glass. The precipitation of a superionic conductor crystal from a precursor glass can enhance ionic conductivity. The grain boundaries of the crystal domains are surrounded by an amorphous phase. Therefore, glass-ceramic electrolyte have lower grain boundary resistances than polycrystalline systems.¹⁷⁴

For oxides, the most studied system is the NASICON-type such as Li₂O-Al₂O₃-TiO₂-P₂O₅ (LATP)¹⁷⁵⁻¹⁷⁷ and Li₂O-Al₂O₃-GeO₂-P₂O₅ (LAGP)¹⁷⁸⁻¹⁸⁰ showing high ionic conductivities at room temperature, 10⁻³ ~ 10⁻⁴ S cm⁻¹. However, sulfide glass-ceramic electrolytes show higher ionic conductivities because of the greater ionic radius and higher polarizability of sulfur ions than oxide. For example Li₂S-P₂S₅ glass-ceramics show conductivities values of 10⁻³ S cm⁻¹ at room temperature.¹⁸¹ Recently, a new synthetic route was reported for Li₂S-P₂S₅ glass-ceramic conductors. This new route gave rise to a very high ionic conductivity, 1.7 x 10⁻² S cm⁻¹ at room temperature, by optimising the heat treatment. Using this method the grain boundary resistance was reduced and the ionic conductivity was increased.¹⁸²

1.2.5 Crystal defects, non-stoichiometry and solid solutions

A perfect crystal can be obtained hypothetically only at absolute zero and at infinite size; all real crystals are imperfect. Atoms can be misplaced in a real crystal. Crystals are invariably defective because the presence of defects up to a certain concentration leads to a reduction of free energy (Figure 1.2-12). A certain amount of energy is required, ΔH , when *i.e.* a vacant cation site is created. A single defect

causes a considerable increase in entropy, ΔS , because of the large number of positions which this defect can occupy. The entropy created by having this choice of positions is called *configurational entropy* and is given by the Boltzmann formula:

$$S = k \ln W \quad (1.13)$$

where the probability, W , is proportional to 10^{23} ; other, smaller, entropy changes are also present due to the disturbance of the crystal structure in the neighbourhood of the defect. Therefore the creation of a single defect is possible because the enthalpy required to form initially is more than offset by the gain in the entropy of the crystal. Consequently the free energy is given by the following formula:

$$\Delta G = \Delta H - T\Delta S \quad (1.14)$$

However, when the amount of defects is large, the enthalpy required to form high defects is less than offset by the gain in the entropy of the crystal and hence such a high defect concentration would not be stable. In between these two extremes lie most real materials. Therefore, the defects created in crystal will be the ones with the smallest ΔH and for which the ΔG minimum is associated with the highest defect concentration.

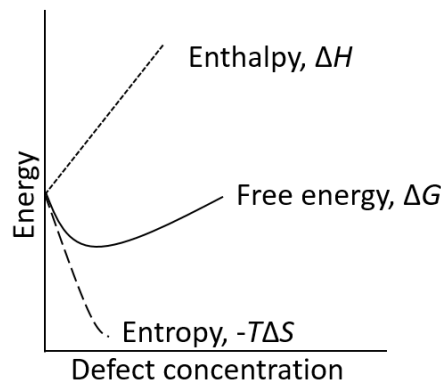


Figure 1.2-12 Energy changes on introducing defects into a perfect crystal at a finite temperature. (Figure adapted from West).¹⁸³

Defects can be divided in two subgroups: *stoichiometric defects* in which the crystal composition is unchanged on introducing the defects, and *non-stoichiometric defects* which are a consequence of a change in crystal compositions. Alternatively, the size and shape are also used to classify the defects: *point defects* which involve

only one atom or site, *e.g.* vacancies or interstitials; *line defects, i.e. dislocations; plane defects*, where a whole plane is missing.

The most common point defects are *Schottky* and *Frenkel*. The *Schottky defect* is a stoichiometric defect in ionic crystals and is defined as a pair of vacant sites, an anion vacancy and a cation vacancy. There are the proportional number of cations and anions, depending on the stoichiometry (eg. in CaCl_2 , Cl^- would have double of vacant sites than Ca^{2+}), to preserve local electroneutrality in the whole crystal and in order to dissociate the pairs, energy equivalent to the enthalpy of association must be provided.

The *Frenkel defect* is also a stoichiometric defect and involves an atom displaced off its lattice site into an interstitial site that is normally empty.

This defects are known as stoichiometric defects which are present in pure crystals and do not involve any change in overall composition. However non-stoichiometric systems can be prepared *i.e.* by doping crystals with *aliovalent impurities*.

In certain materials it can be found that a large number of atoms are interchanged, and especially if it increases with temperature, this gives rise to the formation of *order-disorder phenomena*. When sufficient pairs have swapped places and they no longer show any preference for particular sites the structure is then *disordered*. This *phenomena* occurs in certain ionic structures that contain two or more types of cations or anions. Such structures are therefore examples of substitutional solid solutions (chapter 3, section 3.3.5). For a given system, it is not possible to predict to what extend the solid solution will be formed. Instead, this has to be determined experimentally. Substitution by higher valence cations can give rise to the formation of cation vacancies or interstitial anions. Whereas substitution by lower valence cations gives rise to the formation of anion vacancies or interstitial cations. Double substitution can also be performed when two cations from the same structure are simultaneously substituted.

The study of solid solutions can be performed using X-ray powder diffraction, thermal stability and DTA. Using powder diffraction, information about the

composition of the solid solution can be obtained (the unit cell could undergo a small contraction or expansion as the composition varies across a solid solution). The materials can also show changes in structure on heating which can be studied by DTA.¹⁸³

1.2.6 Requirements for high ionic conductivity

In order to form an ionic conductor certain structural conditions must be satisfied. A large number of the ions of one species should be mobile. A large number of empty sites should be available for the mobile ions to jump into. The empty and occupied sites should have similar potential energies with low activation energy barrier for jumping between neighbouring sites. The structure should have open channels through which mobile ions can migrate. The anion framework should be highly polarizable.¹⁸³

Migration of ions does not occur in most ionic and covalent solids. Rather, the atoms tend to be essentially fixed on their lattice sites and can move only *via* crystal defects. Therefore defect concentrations have to be created so the mobile ions can migrate through vacancies or interstitial sites, typically created by heating the crystal or by addition of aliovalent impurities.¹⁸³

1.3 Scope of this work

The core of this research is the study of LiBH_4 and LiInBr_4 and related compounds, with the aim to explain the good ionic conductivities of their low and high temperature phases and to improve their performance, such that the materials might be considered as future components in all solid state lithium ion batteries. These materials were to be synthesised using conventional or energy-efficient synthetic methods, such as thermal treatment or ball milling, respectively.

Firstly, the results of the stabilisation of the fast ionic, high temperature (HT) phase of LiBH_4 by Br^- substitution are shown. The effect of different synthesis methods in lithium borohydride bromide compounds, $\text{Li}(\text{BH}_4)_{1-x}\text{Br}_x$, were studied and conductivity performances were compared. Structural characterisation of the HT phase of LiBH_4 was conducted using diffraction and spectroscopy techniques. In section 3.3.8 experimental results are presented which show the complex rotational motion of the (BH_4^-) anions.

Secondly, the stabilisation of the high pressure phase of LiBH_4 (HP - LiBH_4) with Na^+ at ambient conditions will be described for the first time. Three different methods will be proposed to stabilise the HP phase: **Method 1** (LiBH_4 - NaBH_4), **Method 2** (LiBH_4 - NaBr) and **Method 3** (LiBH_4 - LiX - NaBH_4 , where $X = \text{Br}^-$ and I^-). The synthesis, structure, and phase diagram that emerges from **Method 3** will be discussed in detail. Conductivity measurements are shown of two more examples of mixed alkali metal mixed-anion borohydrides, $\text{Li}_{(1-y)}\text{Na}_y(\text{BH}_4)_{(1-x+xy)}\text{X}'_{x(1-y)}$ ($X' = \text{I}^-$, Br^-).

Thirdly, the synthesis of lithium ammonia borane complex electrolytes will be proposed for the first time. Ammonia borane could be considered as part of a potential electrolyte structure because of its low molecular weight (30.7 g mol^{-1}), good thermal stability and satisfactory air-stability. Ammonia borane is able to form different compounds with lithium-containing materials. So far, different lithium ammonia borane complexes have been identified with layered structures which could be candidates to display 1D, 2D or 3D lithium ion conductivity. Here in this work, we propose reported lithium ammonia borane complexes originally prepared for hydrogen storage as electrolytes for all solid state lithium ion batteries. Also we report two novel lithium iodide ammonia borane complexes which show high ionic conductivity. High quality powder X-ray diffraction data is reported for both new materials and their thermal stability.

Finally, LiInBr_4 is suggested as a candidate for lithium ion batteries. In principle, this material has similarities with LiBH_4 . It has been reported in the literature that its RT phase shows high ionic conductivity and that it undergoes a phase transition to a HT phase in a similar manner to LiBH_4 . As for LiBH_4 , we investigate its high ionic conductivity. This experiment was performed using neutron powder diffraction and ^7Li NMR measurements. Here we report the RT phase structure which was wrongly assigned in past reports. Our data suggest that a formal phase transition in this material does not occur and instead, the redistribution of Li^+ ions at elevated temperatures leads to two different routes for lithium ion motion in LiInBr_4 .

1.4 References

1. O. Edenhofer, R. P. Madruga, Y. Sokona, K. Seyboth, P. Matschoss, S. Kadner, T. Zwickel, P. Eickemeier, G. Hansen, S. Schlomer and C. V. Stechow, 2012, ISBN 978-1-107-60710-1, Renewable energy sources and climate change mitigation: special report of the Intergovernmental Panel on Climate Change, Cambridge University Press, 1-1076.
2. C. B. Field, V. Barros, T. F. Stocker, Q. Dahe, D. J. Dokken, K. L. Ebi, M. D. Mastrandrea, K. J. Mach, G. K. Plattner, S. K. Allen, M. Tignor and P. M. Midgley, 2012, ISBN 978-1-107-60780-4, Managing the risks of extreme events and disasters to advance climate change adaptation. Special report of the Intergovernmental Panel on Climate Change, Cambridge University Press, 1-592.
3. M. M. Thackeray, C. Wolverton and E. D. Isaacs, *Energy Environ. Sci.*, 2012, **5**, 7854-7863.
4. J. B. Goodenough and Y. Kim, *Chem. Mat.*, 2010, **22**, 587-603.
5. B. Diouf and R. Pode, *Renew. Energy*, 2015, **76**, 375-380.
6. B. Dunn, H. Kamath and J. M. Tarascon, *Science*, 2011, **334**, 928-935.
7. P. D. Yang and J. M. Tarascon, *Nat. Mater.*, 2012, **11**, 560-563.
8. R. A. Marsh, S. Vukson, S. Surampudi, B. V. Ratnakumar, M. C. Smart, M. Manzo and P. J. Dalton, *J. Power Sources*, 2001, **97-8**, 25-27.
9. <https://www.db.com>, accessed on 3rd September 2015.
10. R. Marom, S. F. Amalraj, N. Leifer, D. Jacob and D. Aurbach, *J. Mater. Chem.*, 2011, **21**, 9938-9954.
11. J. B. Goodenough and K. S. Park, *J. Am. Chem. Soc.*, 2013, **135**, 1167-1176.
12. K. Zaghbi, A. Mauger, H. Groult, J. B. Goodenough and C. M. Julien, *Materials*, 2013, **6**, 1028-1049.
13. J.-M. Tarascon and M. Armand, *Nature*, 2001, **414**, 359-367.
14. E. Ferg, R. J. Gummow, A. Dekock and M. M. Thackeray, *J. Electrochem. Soc.*, 1994, **141**, L147-L150.
15. T. Ohzuku, A. Ueda and N. Yamamoto, *J. Electrochem. Soc.*, 1995, **142**, 1431-1435.
16. M. M. Thackeray, *J. Electrochem. Soc.*, 1995, **142**, 2558-2563.
17. S. Megahed and W. Ebner, *J. Power Sources*, 1995, **54**, 155-162.
18. R. Castaing, Y. Reynier, N. Dupre, D. Schleich, S. J. S. Larbi, D. Guyomard and P. Moreau, *J. Power Sources*, 2014, **267**, 744-752.
19. T. Nagaura and K. Tozawa, *Prog. Batter. Sol. Cells*, 1990, **9**, 209-211.
20. H. J. Bang, H. Joachin, H. Yang, K. Amine and J. Prakash, *J. Electrochem. Soc.*, 2006, **153**, A731-A737.
21. K. Zaghbi, J. Dube, A. Dallaire, K. Galoustov, A. Guerfi, M. Ramanathan, A. Benmayza, J. Prakash, A. Mauger and C. M. Julien, *J. Power Sources*, 2012, **219**, 36-44.
22. T. Ohzuku and Y. Makimura, *Chem. Lett.*, 2001, **30**, 642-643.
23. N. Yabuuchi and T. Ohzuku, *J. Power Sources*, 2003, **119**, 171-174.
24. A. Mauger, F. Gendron and C. M. Julien, *J. Alloy. Compd.*, 2012, **520**, 42-51.
25. A. K. Padhi, K. S. Nanjundaswamy and J. B. Goodenough, *J. Electrochem. Soc.*, 1997, **144**, 1188-1194.
26. N. Ravet, Y. Chouinard, J. F. Magnan, S. Besner, M. Gauthier and M. Armand, *J. Power Sources*, 2001, **97-8**, 503-507.
27. K. Rissouli, K. Benkhoucha, J. R. Ramos-Barrado and C. Julien, *Mater. Sci. Eng. B-Solid State Mater. Adv. Technol.*, 2003, **98**, 185-189.
28. N. Ravet, M. Gauthier, K. Zaghbi, J. B. Goodenough, A. Mauger, F. Gendron and C. M. Julien, *Chem. Mat.*, 2007, **19**, 2595-2602.
29. M. L. Trudeau, D. Laul, R. Veillette, A. M. Serventi, A. Mauger, C. M. Julien and K. Zaghbi, *J. Power Sources*, 2011, **196**, 7383-7394.
30. J. Yu, J. Hu and J. Li, *Appl. Surf. Sci.*, 2012, **263**, 277-283.

31. K. Amine, H. Tukamoto, H. Yasuda and Y. Fujita, *J. Power Sources*, 1997, **68**, 604-608.
32. Q. M. Zhong, A. Bonakdarpour, M. J. Zhang, Y. Gao and J. R. Dahn, *J. Electrochem. Soc.*, 1997, **144**, 205-213.
33. J. Liu and A. Manthiram, *Chem. Mat.*, 2009, **21**, 1695-1707.
34. K. Zaghib, P. Charest, M. Dontigny, A. Guerfi, M. Lagace, A. Mauger, M. Kopec and C. M. Julien, *J. Power Sources*, 2010, **195**, 8280-8288.
35. H. Duncan, D. Duguay, Y. Abu-Lebdeh and I. J. Davidson, *J. Electrochem. Soc.*, 2011, **158**, A537-A545.
36. J. Liu and A. Manthiram, *Chem. Mat.*, 2009, **21**, 1695-1707.
37. J. Liu and A. Manthiram, *J. Electrochem. Soc.*, 2009, **156**, A833-A838.
38. E. Peled, *J. Electrochem. Soc.*, 1979, **126**, 2047-2051.
39. K. Xu, *Chem. Rev.*, 2004, **104**, 4303-4417.
40. Y. Nishi, *Chem. Rec.*, 2001, **1**, 406-413.
41. Y. Nishi, *J. Power Sources*, 2001, **100**, 101-106.
42. M. Winter, J. O. Besenhard, M. E. Spahr and P. Novak, *Adv. Mater.*, 1998, **10**, 725-763.
43. V. A. Agubra and J. W. Fergus, *J. Power Sources*, 2014, **268**, 153-162.
44. J. Kalhoff, G. G. Eshetu, D. Bresser and S. Passerini, *ChemSusChem*, 2015, **8**, 2154-2175.
45. J. Arai, *J. Electrochem. Soc.*, 2003, **150**, A219-A228.
46. J. W. Jiang and J. R. Dahn, *Electrochim. Acta*, 2004, **49**, 4599-4604.
47. M. Ue and S. Mori, *J. Electrochem. Soc.*, 1995, **142**, 2577-2581.
48. J. M. Tarascon and D. Guyomard, *Solid State Ionics.*, 1994, **69**, 293-305.
49. X. Y. Zhang, B. Winget, M. Doeff, J. W. Evans and T. M. Devine, *J. Electrochem. Soc.*, 2005, **152**, B448-B454.
50. T. Kawamura, A. Kimura, M. Egashira, S. Okada and J. I. Yamaki, *J. Power Sources*, 2002, **104**, 260-264.
51. D. Aurbach, A. Zaban, Y. Ein-Eli, I. Weissman, O. Chusid, B. Markovsky, M. Levi, E. Levi, A. Schechter and E. Granot, *J. Power Sources*, 1997, **68**, 91-98.
52. K. O. Christe, D. A. Dixon, D. McLemore, W. W. Wilson, J. A. Sheehy and J. A. Boatz, *J. Fluorine Chem.*, 2000, **101**, 151-153.
53. S. E. Sloop, J. B. Kerr and K. Kinoshita, *J. Power Sources*, 2003, **119**, 330-337.
54. U. Heider, R. Oesten and M. Jungnitz, *J. Power Sources*, 1999, **81**, 119-122.
55. C. L. Campion, W. T. Li and B. L. Lucht, *J. Electrochem. Soc.*, 2005, **152**, A2327-A2334.
56. Z. H. Chen and K. Amine, *J. Electrochem. Soc.*, 2006, **153**, A1221-A1225.
57. G. G. Eshetu, S. Grugeon, G. Gachot, D. Mathiron, M. Armand and S. Laruelle, *Electrochim. Acta*, 2013, **102**, 133-141.
58. M. A. Navarra, *MRS Bull.*, 2013, **38**, 548-553.
59. D. R. MacFarlane, N. Tachikawa, M. Forsyth, J. M. Pringle, P. C. Howlett, G. D. Elliott, J. H. Davis, M. Watanabe, P. Simon and C. A. Angell, *Energy Environ. Sci.*, 2014, **7**, 232-250.
60. M. Armand, F. Endres, D. R. MacFarlane, H. Ohno and B. Scrosati, *Nat. Mater.*, 2009, **8**, 621-629.
61. A. Guerfi, M. Dontigny, P. Charest, M. Petitclerc, M. Lagace, A. Vijn and K. Zaghib, *J. Power Sources*, 2010, **195**, 845-852.
62. H. Li, J. Pang, Y. Yin, W. Zhuang, H. Wang, C. Zhai and S. Lu, *Rsc Advances*, 2013, **3**, 13907-13914.
63. H. Nakagawa, Y. Fujino, S. Kozono, Y. Katayama, T. Nukuda, H. Sakaebe, H. Matsumoto and K. Tatsumi, *J. Power Sources*, 2007, **174**, 1021-1026.
64. R. S. Kuehnel, N. Boeckenfeld, S. Passerini, M. Winter and A. Balducci, *Electrochim. Acta*, 2011, **56**, 4092-4099.
65. V. Di Noto, S. Lavina, G. A. Giffin, E. Negro and B. Scrosati, *Electrochim. Acta*, 2011, **57**, 4-13.
66. B. Scrosati and C. A. Vincent, *MRS Bull.*, 2000, **25**, 28-30.
67. M. Armand, *Solid State Ionics.*, 1983, **9-10**, 745-754.
68. A. M. Stephan, *Eur. Polym. J.*, 2006, **42**, 21-42.

69. C. Berthier, W. Gorecki, M. Minier, M. B. Armand, J. M. Chabagno and P. Rigaud, *Solid State Ionics.*, 1983, **11**, 91-95.
70. A. Bouridah, F. Dalard, D. Deroo and M. B. Armand, *Solid State Ionics.*, 1986, **18-9**, 287-290.
71. A. Bouridah, F. Dalard, D. Deroo and M. B. Armand, *J. App. Electrochem.*, 1987, **17**, 625-634.
72. L. Porcarelli, A. S. Shaplov, M. Salsamendi, J. R. Nair, Y. S. Vygodskii, D. Mecerreyes and C. Gerbaldi, *ACS Appl. Mater. Interfaces*, 2016, **8**, 10350-10359.
73. G. Feuillade and P. Perche, *J. App. Electrochem.*, 1975, **5**, 63-69.
74. H. Nakajima and H. Ohno, *Polymer*, 2005, **46**, 11499-11504.
75. I. Choi, H. Ahn and M. J. Park, *Macromolecules*, 2011, **44**, 7327-7334.
76. J. Reiter, J. Vondrak, J. Michalek and Z. Micka, *Electrochim. Acta*, 2006, **52**, 1398-1408.
77. M. Park, X. C. Zhang, M. D. Chung, G. B. Less and A. M. Sastry, *J. Power Sources*, 2010, **195**, 7904-7929.
78. C. Masquelier, *Nat. Mater.*, 2011, **10**, 648-650.
79. N. Kamaya, K. Homma, Y. Yamakawa, M. Hirayama, R. Kanno, M. Yonemura, T. Kamiyama, Y. Kato, S. Hama, K. Kawamoto and A. Mitsui, *Nat. Mater.*, 2011, **10**, 682-686.
80. Y. Inaguma, L. Q. Chen, M. Itoh, T. Nakamura, T. Uchida, H. Ikuta and M. Wakihara, *Solid State Commun.*, 1993, **86**, 689-693.
81. R. Kanno and M. Maruyama, *J. Electrochem. Soc.*, 2001, **148**, A742-A746.
82. F. Mizuno, A. Hayashi, K. Tadanaga and M. Tatsumisago, *Adv. Mater.*, 2005, **17**, 918-921.
83. A. Hayashi, K. Minami, F. Mizuno and M. Tatsumisago, *J. Mater. Sci.*, 2008, **43**, 1885-1889.
84. K. Takada, N. Aotani and S. Kondo, *J. Power Sources*, 1993, **43**, 135-141.
85. T. Lapp, S. Skaarup and A. Hooper, *Solid State Ionics.*, 1983, **11**, 97-103.
86. L. Edman, A. Ferry and M. M. Doeff, *J. Mater. Res.*, 2000, **15**, 1950-1954.
87. F. Croce, G. B. Appetecchi, L. Persi and B. Scrosati, *Nature*, 1998, **394**, 456-458.
88. P. E. Stallworth, J. J. Fontanella, M. C. Wintersgill, C. D. Scheidler, J. J. Immel, S. G. Greenbaum and A. S. Gozdz, *J. Power Sources*, 1999, **81**, 739-747.
89. J. Y. Song, Y. Y. Wang and C. C. Wan, *J. Electrochem. Soc.*, 2000, **147**, 3219-3225.
90. A. Boulouf and D. Louer, *J. Appl. Crystallogr.*, 1991, **24**, 987-993.
91. N. Tapia-Ruiz, M. Segales and D. H. Gregory, *Coordin. Chem. Rev.*, 2013, **257**, 1978-2014.
92. L. O. Hagman and Kierkega.P, *Acta Chem. Scand.*, 1968, **22**, 1822-&.
93. M. Cretin and P. Fabry, *J. Eur. Ceram. Soc.*, 1999, **19**, 2931-2940.
94. H. Li, Z. X. Wang, L. Q. Chen and X. J. Huang, *Adv. Mater.*, 2009, **21**, 4593-4607.
95. K. Arbi, J. M. Rojo and J. Sanz, *J. Eur. Ceram. Soc.*, 2007, **27**, 4215-4218.
96. H. Aono, E. Sugimoto, Y. Sadaoka, N. Imanaka and G. Y. Adachi, *J. Electrochem. Soc.*, 1989, **136**, 590-591.
97. P. Knauth, *Solid State Ionics.*, 2009, **180**, 911-916.
98. P. G. Bruce and A. R. West, *J. Electrochem. Soc.*, 1983, **130**, 662-669.
99. A. D. Robertson, A. R. West and A. G. Ritchie, *Solid State Ionics.*, 1997, **104**, 1-11.
100. H. Y. P. Hong, *Mater. Res. Bull.*, 1978, **13**, 117-124.
101. M. Matsuo, Y. Nakamori, S. Orimo, H. Maekawa and H. Takamura, *Appl. Phys. Lett.*, 2007, **91**, 1-3.
102. H. Maekawa, M. Matsuo, H. Takamura, M. Ando, Y. Noda, T. Karahashi and S. I. Orimo, *J. Am. Chem. Soc.*, 2009, **131**, 894-895.
103. M. Matsuo, A. Remhof, P. Martelli, R. Caputo, M. Ernst, Y. Miura, T. Sato, H. Oguchi, H. Maekawa, H. Takamura, A. Borgschulte, A. Züttel and S. Orimo, *J. Am. Chem. Soc.*, 2009, **131**, 16389-16391.
104. H. Oguchi, M. Matsuo, T. Sato, H. Takamura, H. Maekawa, H. Kuwano and S. Orimo, *J. Appl. Phys.*, 2010, **107**, 1-3.
105. M. Matsuo, T. Sato, Y. Miura, H. Oguchi, Y. Zhou, H. Maekawa, H. Takamura and S. Orimo, *Chem. Mat.*, 2010, **22**, 2702-2704.

106. W. Li, G. T. Wu, Z. T. Xiong, Y. P. Feng and P. Chen, *Phys. Chem. Chem. Phys.*, 2012, **14**, 1596-1606.
107. J. B. Yang, X. D. Zhou, Q. Cai, W. J. James and W. B. Yelon, *Appl. Phys. Lett.*, 2006, **88**, 1-3.
108. S. Kondo, K. Takada and Y. Yamamura, *Solid State Ionics.*, 1992, **53**, 1183-1186.
109. M. Tatsumisago, K. Hirai, T. Minami, K. Takada and S. Kondo, *Nippon Seram. Kyo. Gakk.*, 1993, **101**, 1315-1317.
110. J. L. Briant and G. C. Farrington, *J. Electrochem. Soc.*, 1981, **128**, 1830-1834.
111. U. V. Alpen, M. F. Bell, W. Wichelhaus, K. Y. Cheung and G. J. Dudley, *Electrochim. Acta*, 1978, **23**, 1395-1397.
112. J. Ibarra, A. Varez, C. Leon, J. Santamaria, L. M. Torres-Martinez and J. Sanz, *Solid State Ionics.*, 2000, **134**, 219-228.
113. R. Murugan, V. Thangadurai and W. Weppner, *Angew. Chem.-Int. Edit.*, 2007, **46**, 7778-7781.
114. C. A. Geiger, E. Alekseev, B. Lazic, M. Fisch, T. Armbruster, R. Langner, M. Fechtelkord, N. Kim, T. Pettke and W. Weppner, *Inorg. Chem.*, 2011, **50**, 1089-1097.
115. A. G. Belous, G. N. Novitskaya, S. V. Polyanetskaya and Y. I. Gornikov, *Inorg. Mater.*, 1987, **23**, 412-415.
116. Y. Inaguma, L. Q. Chen, M. Itoh and T. Nakamura, *Solid State Ionics.*, 1994, **70**, 196-202.
117. G. Y. Adachi, N. Imanaka and H. Aono, *Adv. Mater.*, 1996, **8**, 127-135.
118. J. A. Alonso, J. Sanz, J. Santamaria, C. Leon, A. Varez and M. T. Fernandez-Diaz, *Angew. Chem.-Int. Edit.*, 2000, **39**, 619-621.
119. S. Stramare, V. Thangadurai and W. Weppner, *Chem. Mat.*, 2003, **15**, 3974-3990.
120. O. Bohnke, *Solid State Ionics.*, 2008, **179**, 9-15.
121. R. Kanno, T. Hata, Y. Kawamoto and M. Irie, *Solid State Ionics.*, 2000, **130**, 97-104.
122. M. Murayama, R. Kanno, M. Irie, S. Ito, T. Hata, N. Sonoyama and Y. Kawamoto, *J. Solid State Chem.*, 2002, **168**, 140-148.
123. T. Kobayashi, T. Inada, N. Sonoyama, A. Yamada and R. Kanno, *Mater. Res. Soc.*, 2005, **835**, 333-345.
124. S. Hori, M. Kato, K. Suzuki, M. Hirayama, Y. Kato and R. Kanno, *J. Am. Ceram. Soc.*, 2015, **98**, 3352-3360.
125. P. Bron, S. Johansson, K. Zick, J. S. auf der Gunne, S. Dehnen and B. Roling, *J. Am. Chem. Soc.*, 2013, **135**, 15694-15697.
126. E. J. Cussen, *Chem. Commun.*, 2006, 412-413.
127. V. Thangadurai and W. Weppner, *J. Am. Ceram. Soc.*, 2005, **88**, 411-418.
128. V. Thangadurai and W. Weppner, *Adv. Funct. Mater.*, 2005, **15**, 107-112.
129. V. Thangadurai and W. Weppner, *J. Solid State Chem.*, 2006, **179**, 974-984.
130. J. Percival, E. Kendrick and P. R. Slater, *Solid State Ionics.*, 2008, **179**, 1666-1669.
131. I. Kokal, M. Somer, P. H. L. Notten and H. T. Hintzen, *Solid State Ionics.*, 2011, **185**, 42-46.
132. J. L. Allen, J. Wolfenstine, E. Rangasamy and J. Sakamoto, *J. Power Sources*, 2012, **206**, 315-319.
133. A. Unemoto, M. Matsuo and S. Orimo, *Adv. Funct. Mater.*, 2014, **24**, 2267-2279.
134. S. I. Orimo, Y. Nakamori, J. R. Eliseo, A. Züttel and C. M. Jensen, *Chem. Rev.*, 2007, **107**, 4111-4132.
135. H. Oguchi, M. Matsuo, J. S. Hummelshoj, T. Vegge, J. K. Nørskov, T. Sato, Y. Miura, H. Takamura, H. Maekawa and S. Orimo, *Appl. Phys. Lett.*, 2009, **94**, 1-4.
136. D. Sveinbjornsson, J. S. G. Myrdal, D. Blanchard, J. J. Bentzen, T. Hirata, M. B. Mogensen, P. Norby, S. I. Orimo and T. Vegge, *J. Phys. Chem. C*, 2013, **117**, 3249-3257.
137. L. H. Rude, O. Zavorotynska, L. M. Arnbjerg, D. B. Ravnsbaek, R. A. Malmkjaer, H. Grove, B. C. Hauback, M. Baricco, Y. Filinchuk, F. Besenbacher and T. R. Jensen, *Int. J. Hydrog. Energy*, 2011, **36**, 15664-15672.
138. T. Sato, K. Ikeda, H. W. Li, H. Yukawa, M. Morinaga and S. Orimo, *Mater. Trans.*, 2009, **50**, 182-186.

139. M. B. Ley, D. B. Ravnsbaek, Y. Filinchuk, Y. S. Lee, R. Janot, Y. W. Cho, J. Skibsted and T. R. Jensen, *Chem. Mat.*, 2012, **24**, 1654-1663.
140. M. B. Ley, S. Boulineau, R. Janot, Y. Filinchuk and T. R. Jensen, *J. Phys. Chem. C*, 2012, **116**, 21267-21276.
141. M. Matsuo, S. Kuromoto, T. Sato, H. Oguchi, H. Takamura and S. Orimo, *Appl. Phys. Lett.*, 2012, **100**, 1-4.
142. H. W. Li, Y. G. Yan, S. Orimo, A. Züttel and C. M. Jensen, *Energies*, 2011, **4**, 185-214.
143. P. Jena, *J. Phys. Chem. Lett.*, 2015, **6**, 1119-1125.
144. T. J. Udovic, M. Matsuo, A. Unemoto, N. Verdál, V. Stavila, A. V. Skripov, J. J. Rush, H. Takamura and S. Orimo, *Chem. Commun.*, 2014, **50**, 3750-3752.
145. J.-H. Her, M. Yousufuddin, W. Zhou, S. S. Jalisatgi, J. G. Kulleck, J. A. Zan, S.-J. Hwang, R. C. Bowman, Jr. and T. J. Udovic, *Inorg. Chem.*, 2008, **47**, 9757-9759.
146. L. He, H.-W. Li, H. Nakajima, N. Tumanov, Y. Filinchuk, S.-J. Hwang, M. Sharma, H. Hagemann and E. Akiba, *Chem. Mat.*, 2015, **27**, 5483-5486.
147. N. Verdál, J. H. Her, V. Stavila, A. V. Soloninin, O. A. Babanova, A. V. Skripov, T. J. Udovic and J. J. Rush, *J. Solid State Chem.*, 2014, **212**, 81-91.
148. H. Wu, W. S. Tang, V. Stavila, W. Zhou, J. J. Rush and T. J. Udovic, *J. Phys. Chem. C*, 2015, **119**, 6481-6487.
149. T. J. Udovic, M. Matsuo, W. S. Tang, H. Wu, V. Stavila, A. V. Soloninin, R. V. Skoryunov, O. A. Babanova, A. V. Skripov, J. J. Rush, A. Unemoto, H. Takamura and S. Orimo, *Adv. Mater.*, 2014, **26**, 7622-7626.
150. W. S. Tang, A. Unemoto, W. Zhou, V. Stavila, M. Matsuo, H. Wu, S. Orimo and T. J. Udovic, *Energy Environ. Sci.*, 2015, **8**, 3637-3645.
151. A. J. Downs, 1993, ISBN 978-0-7514-0103-5, Chemistry of Aluminium, Gallium, Indium and Thallium, Springer Netherlands.
152. G. Mairesse, P. Barbier and J. P. Wignacourt, *Crystal Struct. Commun.*, 1977, **6(1)**, 15-18.
153. W. Weppner and R. A. Huggins, *J. Electrochem. Soc.*, 1977, **124**, 35-38.
154. K. Yamada, M. Kinoshita, K. Hosokawa and T. Okuda, *Bull. Chem. Soc. Jpn.*, 1993, **66**, 1317-1322.
155. Y. Tomita, H. Ohki, K. Yamada and T. Okuda, *Solid State Ionics.*, 2000, **136**, 351-355.
156. K. Yamada, S. Matsuyama, Y. Tomita and Y. Yamane, *Solid State Ionics.*, 2011, **189**, 7-12.
157. K. Yamada, K. Kumano and T. Okuda, *Solid State Ionics.*, 2006, **177**, 1691-1695.
158. M. O. Schmidt, M. S. Wickleder and G. Meyer, *Z. Anorg. Allg. Chem.*, 1999, **625**, 539-540.
159. W. Honle, B. Hettich and A. Simon, *Z. Naturforsch. B*, 1987, **42**, 248-250.
160. N. D. Dey, J. S. Miller and W. L. Browden, 1983, Duracell Inc., USRE31414, E US 06/199, 160.
161. <http://www.cit.nihon-u.ac.jp/kouendata/No.44/pdf/5-30.pdf>, accessed on 23rd October 2015.
162. K. Yamada, 2006, Annual research report, 222.
163. T. Staffel and G. Meyer, *Z. Anorg. Allg. Chem.*, 1989, **574**, 107-113.
164. J. Quadflieg, M. Scholten and R. Dronskowski, *Z. Krist.-New Cryst. Struct.*, 1998, **213**, 231-231.
165. S. Matsuyama, Y. Yamane and K. Yamada, 2009, Annual report, 49-50.
166. R. Burnus and G. Meyer, *Z. Anorg. Allg. Chem.*, 1991, **602**, 31-37.
167. N. J. Dudney, *Annu. Rev. Mater. Sci.*, 1989, **19**, 103-120.
168. X. H. Yu, J. B. Bates, G. E. Jellison and F. X. Hart, *J. Electrochem. Soc.*, 1997, **144**, 524-532.
169. K. H. Joo, H. J. Sohn, P. Vinatier, B. Pecquenard and A. Levasseur, *Electrochem. Solid State Lett.*, 2004, **7**, A256-A258.
170. S. D. Jones, J. R. Akridge and F. K. Shokoohi, *Solid State Ionics.*, 1994, **69**, 357-368.
171. T. Ohtomo, A. Hayashi, M. Tatsumisago and K. Kawamoto, *J. Non-Cryst. Solids*, 2013, **364**, 57-61.
172. A. Hayashi, H. Muramatsu, T. Ohtomo, S. Hama and M. Tatsumisago, *J. Alloy. Compd.*, 2014, **591**, 247-250.
173. J. H. Kennedy and Z. M. Zhang, *Solid State Ionics.*, 1988, **28**, 726-728.
174. M. Tatsumisago, M. Nagao and A. Hayashi, *J. Asian Ceram. Soc.*, 2013, **1**, 17-25.

175. J. Fu, *Solid State Ionics.*, 1997, **96**, 195-200.
176. M. Kotobuki and M. Koishi, *Ceram. Int.*, 2013, **39**, 4645-4649.
177. V. Patil, A. Patil, S.-J. Yoon and J.-W. Choi, *J. Nanosci. Nanotechnol.*, 2013, **13**, 3665-3668.
178. J. Fu, *Solid State Ionics.*, 1997, **104**, 191-194.
179. J. D. Nikolic, S. V. Smiljanjic, S. D. Matijasevic, V. D. Zivanovic, M. B. Tomic, S. R. Grujic and J. N. Stojanovic, *P. App. Ceram.*, 2013, **7**, 147-151.
180. K. He, C. Zu, Y. Wang, B. Han, X. Yin, H. Zhao, Y. Liu and J. Chen, *Solid State Ionics.*, 2014, **254**, 78-81.
181. M. Tatsumisago, S. Hama, A. Hayashi, H. Morimoto and T. Minami, *Solid State Ionics.*, 2002, **154**, 635-640.
182. Y. Seino, T. Ota, K. Takada, A. Hayashi and M. Tatsumisago, *Energy Environ. Sci.*, 2014, **7**, 627-631.
183. A. R. West, 1988, ISBN 0-471-91798-2, Basic solid state chemistry, Jonh Wiley & Sons Ltd.

2. Experimental

The aim of this chapter is to illustrate in detail the synthetic methods and techniques used to prepare and characterise the Li ion solid state electrolyte materials described in this work.

A variety of different techniques have been employed to characterise these materials. Powder X-ray and neutron diffraction (PXD and PND) have been used for structural determination and phase analysis. Different spectroscopy techniques have been required to provide extra information on the structure/properties of these materials. The spectroscopy techniques include Raman and electrochemical impedance spectroscopy (EIS). Scanning electron microscopy (SEM) has been used to analyse the particle size, morphology and crystallographic features of these electrolytes. Finally, simultaneous thermal analysis coupled with mass spectroscopy (STA/MS) has been utilised to determine the thermal stability of the materials analysed, explore phase transitions and study the gases released in relation to temperature during the decomposition of the materials.

2.1 Preparative methods

2.1.1 Air sensitive handling techniques

The Li ion solid state electrolyte materials synthesised in this work are air and moisture-sensitive, therefore all the procedures needed for the synthesis were carried out in a $N_2(g)$ or $Ar(g)$ atmosphere. MBraun LABstar Glove Box has been used to perform this work which includes a stand, large main antechamber, a rotary vane vacuum pump and an atmosphere controller. This glove box includes a single column inert gas purification system that is fully automatic and regenerable. The glove box maintains atmosphere levels of less than 1 ppm oxygen and moisture.

2.2 Synthetic techniques

2.2.1 Ball milling

2.2.1.1 Background

Ball milling can be used to facilitate the reaction of solids, induced by the input of mechanical energy. This method is becoming a really useful technique for two main reasons: Firstly, it can promote reactions between solids quickly and quantitatively, with no added solvent. The dependence of solvents appears increasingly unsustainable since it is wasteful of fossil fuel-derived materials, environmentally problematic, hazardous and energy-demanding with regard to solvent production, purification and recycling. Secondly, it can reduce particle sizes; a mechanical action is applied by hard surfaces on materials, normally to break up the material and to trigger the increase in the contact surface area between reactants. As the particles become smaller and more intimately mixed the reaction can proceed quicker.¹

2.2.1.2 Ball milling equipment

Ball milling was used in this work primarily to reduce the particle size and ensure good dispersion between the two or three starting materials prior to reaction. During the process, sometimes, phase transitions or gas evolution might occur due to pressure build-up within the grinding vessel and/or heating due to particle friction.

For this work a planetary mill has been used. The ball milling system consists of the turn disc and one bowl. The turn disc rotates in one direction while the bowl rotates in the opposite direction. The centrifugal forces, created by the rotation of the bowl around its own axis together with the rotation of the turn disc, are applied to the powder mixture and milling balls in the bowl, known as Coriolis forces. The powder mixture is fractured and cold welded under high impact

There are different types of grinding media (tungsten carbide, zirconium oxide, polyamide plastic, etc.) and each material is used depending on the type of compound being ground. A Restch PM 100 ball mill was used in all instances in this

work, employing with stainless steel jars and 10 mm stainless steel milling balls. The materials were mechanically milled for different times under argon atmosphere at different speeds. Interval breaks with reverse rotation were applied to avoid heating of the sample and the ball-to-powder ratio was either 80:1 or 400:1. All the samples required preparation in a glove box. This technique was employed for the synthesis of the stabilised HT - LiBH₄ - type (chapter 3, sections 3.3.2 and 3.3.3) and HP - LiBH₄ - type materials at room temperature (chapter 4, section 4.2.1), [LiX][NH₃BH₃] (X = H, BH₄, Br and I) (chapter 5, sections 5.2.1, 5.2.2 and 5.2.3) and LiInBr₄ (chapter 6, section 6.2.1).

2.2.2 Thermal treatment

Conventional thermal treatment was employed either to complete the unfinished reaction from ball milling or to improve the crystallinity of the final compounds. The mixtures were placed in a silica vessel sealed with a rubber septum to avoid air exposure. The reaction vessels were removed from the glovebox and placed in a vertical furnace. Syringes connected to plastic pipes are used as a gas inlet and outlet, lowering the risk of leakage.

2.2.2.1 The Bridgman technique

Crystal growth refers to the artificial synthesis of crystals and it can be classified in to three different groups depending on which phase transition is involved in the crystal formation, *i.e.* solid - solid, liquid - solid, gas - solid. The most common method involves using liquid-solid processes and more specifically for solid state reactions growing crystals from the liquid by melting the solid (Figure 2.2-1).²

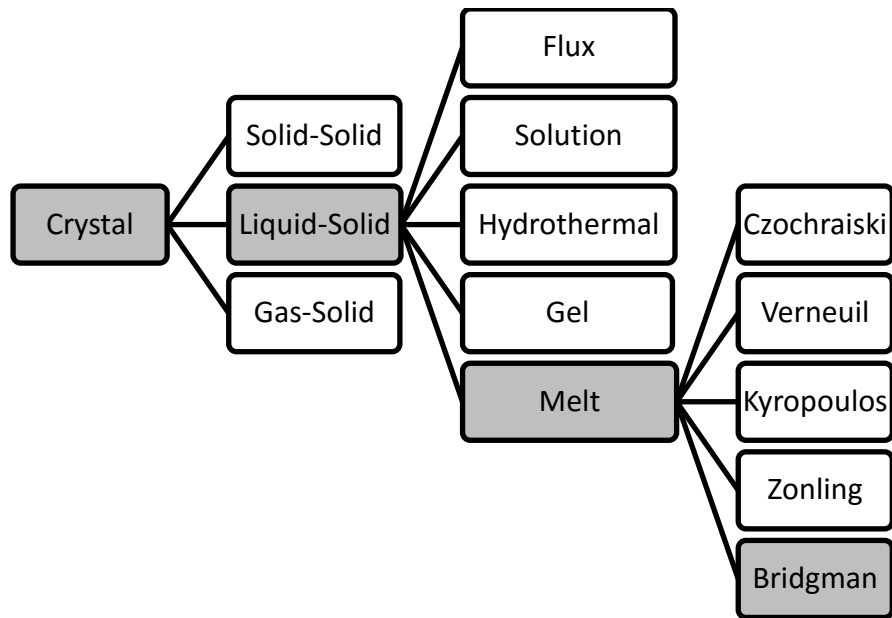


Figure 2.2-1. Classification of crystal growth techniques.³

The Bridgman technique (also known as the Bridgman-Stockbarger technique) was applied in the literature for growing crystals of LiInBr_4 (Chapter 6). This method relies on directional solidification by translating a melt of the material from the hot zone to the cold zone. This technique can be applied in two similar configurations, either vertical or horizontal. The horizontal Bridgman technique was used in the literature because it exhibits higher crystalline quality (Figure 2.2-2). The crystal experiences a lower stress due to the free surface on the top of the melt and it can expand during the entire growth process. The vertical Bridgman techniques allows the growth of crystals in circular shape.

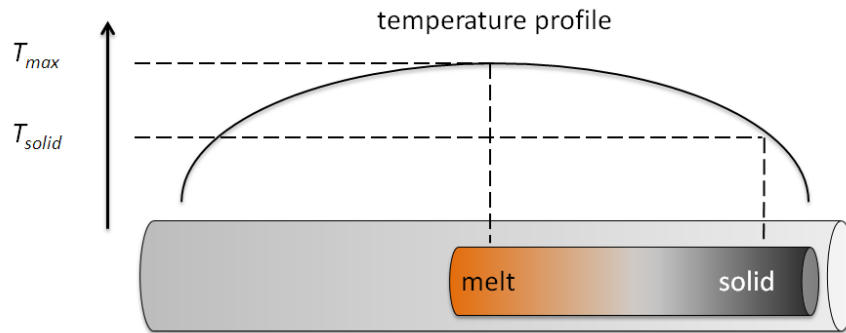


Figure 2.2-2. Horizontal Bridgman technique.

In this work, LiInBr_4 was synthesised via chemical vapor transport technique (CVT). A Carbolite tube furnace was used in all instances in this work. The experiments were performed by pressing approximately 0.5 g of the mixture of the reactants under a load of 2 tonnes to give a 5 mm diameter cylindrical pellet approximately 4-5 mm thick. The pellet was placed in a silica vessel sealed with a rubber septum to avoid air exposure. The reaction vessels were removed from the glovebox, sealed under vacuum and placed in a horizontal furnace. The samples were typically heated at 5 K min^{-1} to 513 K for 12 h and slowly cooled down at 1 K min^{-1} to room temperature. Crystals obtained were transferred to the glovebox and silicon oil was added to isolate them from the atmosphere before the measurements by single crystal X-ray diffraction were taken, however the crystals were highly air and moisture sensitive making challenging the analysis. Therefore, sample preparation for X-ray analysis (technique which will be explained in the following section) was performed inside the glove box. Samples were grounded with an agate mortar and a pestle until fine powder was obtained. The powders were loaded and well packed inside capillaries (0.5 mm thick and 30 mm long). The loaded capillaries were sealed with wax to prevent any oxygen or moisture contamination and once outside the glove box they were sealed using a flame.

2.3 Structural determination and characterisation techniques

2.3.1 Powder X-ray diffraction

2.3.1.1 Background

In 1913, Max von Laue *et al.* first observed the diffraction of X-rays by crystals.⁴

X-ray diffraction is the principal technique used in structural solid state chemistry. X-rays are generated when a beam of high-energy electrons provided by a tungsten filament is accelerated towards a metal target, *i.e.* copper (anode), and a spectrum of X-rays is emitted, called “white radiation”ⁱⁱ. The maximum energy

ⁱⁱ White radiation is the production of a continuous spectrum of X-rays caused by the loss of energy of the electrons by collision with atoms.

lost, $E_{(\max)}$, determines the shortest wavelength, $\lambda_{(\min)}$, that can be obtained according to the equation

$$E = eV = hc/\lambda \quad (2.1)$$

where e is the charge on the electron, V is the accelerating voltage, h is Planck's constant, and c is the speed of light. A more practical form of this equation is given by

$$\lambda = 12.398 / V \quad (2.2)$$

where V is in kilovolts and λ is in Ångstroms ($1 \text{ Å} = 0.1 \text{ nm}$). For a Cu anode and 40 kV, $\lambda_{(\min)}$ is equal to 0.31 Å . The maximum in the intensity of the white radiation occurs at a wavelength that is roughly $1.5 \times \lambda_{(\min)}$. Longer wavelengths are obtained by multiple-collision processes.⁵

The beam of electrons has sufficient energy to cause emission of some of the copper 1s (K shell) electrons. The electrons from outer orbital ($2p$ or $3p$) can jump into the vacant K shell releasing X-radiation. The transition energies have specific values and so a spectrum of characteristic X-rays results. For copper, the $2p \rightarrow 1s$ transition, denoted $K\alpha$, has a wavelength of 1.5418 Å . X-rays are electromagnetic radiation of wavelength 1 Å , comparable to that of the inter-atomic distances within a crystal ($\sim 0.8 - 3 \text{ Å}$). Crystalline phases have characteristic powder patterns which can be used as for identification purposes.⁶

The Bragg approach to diffraction is to regard crystals as built up of layers or planes. Some of the X-rays are diffracted off a plane with the angle of reflection equal to the angle of incidence, but the rest are transmitted to be subsequently reflected by succeeding planes. The derivation of Bragg's law is shown in (Figure 2.3-1).⁷ Two incident X-ray beams strike in different planes of regular arrays of atoms, lattice planes, which are described with Miller indices, hkl . Beam BB' has to travel an extra distance xyz as compared to beam AA' , and for A' and B' to be in phase, distance xyz must be equal to a whole number of wavelengths, $n\lambda$. The perpendicular distance, the d -spacing, d_{hkl} , and the angle of incidence, or Bragg angle, θ , are related to the distance xy by

$$xy = yz = d_{hkl} \sin \theta \quad (2.3)$$

$$xyz = 2d_{hkl} \sin \theta \quad (2.4)$$

$$xyz = n\lambda \quad (2.5)$$

When Bragg's law is satisfied (integral number of wavelength, $n\lambda$), the diffracted beams are in phase and interfere constructively.

$$2d_{hkl} \sin \theta = n\lambda \quad (2.6)$$

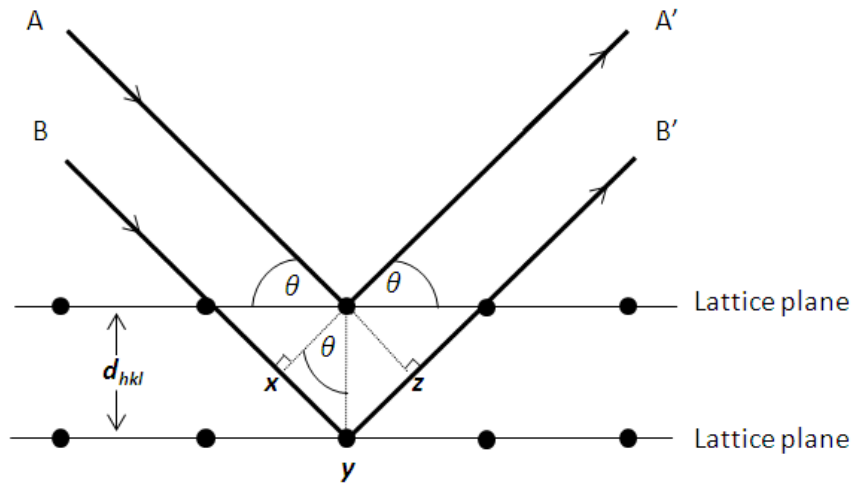


Figure 2.3-1 Schematic used for the derivation of Bragg's law for X-ray diffraction. A and B represent the incident X-ray beams striking with atoms with an angle θ . A' and B' are the scattered X-rays. The lattice spacing is denoted by d_{hkl} . Bragg's law is satisfied when a constructive interference occurs (the angle of incidence has to be equal to the angle of scattering and the distance xyz must be equal to a whole number of wavelengths, $n\lambda$).

Crystals are formed by the arrangement of different atoms in three dimensions. They are defined by their *unit cell* which is the smallest repeating unit which shows the full symmetry of the crystal structure. The unit cell is defined by three distances a , b , c and three angles α , β , γ (Figure 2.3-2).

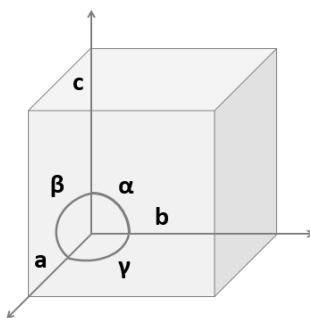


Figure 2.3-2 Representation of a 3D unit cell.

In total there are seven independent unit cell shapes that are possible in three-dimensional crystals structures, which are known as the *seven crystal systems* listed in Table 2.3-1. Each system has a unique volume formula and each is shown in Table 2.3-2. Each crystal is governed by the presence or absence of symmetry in the structure and the essential symmetry is given in the third column (Table 2.3-1).

Lattice points are the coordinates in a crystal lattice where atoms or ions can be placed. The three-dimensional unit cell includes four different types of shapes: the primitive unit cell, P, has a lattice point at each corner; the body-centred unit cell, I, has a lattice point at each corner and one at the centre of the cell; the face-centred unit cell, F, has a lattice point at each corner and one in the centre of each face; the face-centred unit cell, A, B, or C, has a lattice point at each corner, and one in the centres of one pair of opposite faces (*e.g.* an A-centred cell has lattice points in the centred of the *bc* faces). The combination of the seven crystal systems and the four lattice types give the 14 possible *Bravais lattices* describing crystal structures. Combining point groups with planes of symmetry and centres of symmetry, means that in total 32 point groups can describe all the possible non-translational symmetries. By the combination of these 32 point groups with the 14 Bravais lattices, when additional translational symmetry elements are applied, 230 three-dimensional space groups can be found that crystal structures can adopt.⁸ These values can be found in the International Tables for Crystallography.⁹

For each crystal system, with their specific unit cell dimensions, the spacing of the reflecting planes is given by the formulae represented in Table 2.3-3.¹⁰ However lattice centring, screw axes and glide planes need to be considered because

they can lead to destructive interference for some reflections and these extra missing reflections are known as a systematic absences which can be found in Table 3.3-4. For instance, for a primitive cell all reflections will be present but for a face-centred lattice only all odd or all even values for $h k l$ will be present.

Table 2.3-1 Shape and symmetry representing the seven crystal systems.

Crystal system	Unit cell shape	Essential symmetry	Allowed lattices
Cubic	$a = b = c$ $\alpha = \beta = \gamma = 90^\circ$	Four threefold axes	P, F, I
Tetragonal	$a = b \neq c$ $\alpha = \beta = \gamma = 90^\circ$	One fourfold axes	P, I
Orthorhombic	$a \neq b \neq c$ $\alpha = \beta = 90^\circ, \gamma = 120^\circ$	Three twofold axes or mirror planes	P, F, I, A, (B or C)
Hexagonal	$a = b \neq c$ $\alpha = \beta = 90^\circ, \gamma = 120^\circ$	One sixfold axis	P
Trigonal	(a) $a = b \neq c$ $\alpha = \beta = 90^\circ, \gamma = 120^\circ$	One threefold axis	P
	(b) $a = b = c$ $\alpha = \beta = \gamma \neq 90^\circ$	One threefold axis	R
Monoclinic	$a \neq b \neq c$ $\alpha = \gamma = 90^\circ, \beta \neq 90^\circ$	One twofold axis or mirror plane	P, C
Triclinic	$a \neq b \neq c$ $\alpha \neq \beta \neq \gamma \neq 90^\circ$	None	P

Primitive (P), Face centred (F), side centred (C) body centred (I) lattices.

Table 2.3-2 Volume of the unit cell.

Unit Cell	Volume
Cubic	$V = a^3$
Tetragonal	$V = a^2c$
Orthorhombic	$V = abc$
Hexagonal	$V = \frac{\sqrt{3}a^2c}{2} = 0.866a^2c$
Monoclinic	$V = abc \sin \beta$
Triclinic	$V = abc(1 - \cos^2 \alpha - \cos^2 \beta - \cos^2 \gamma + 2 \cos \alpha \cos \beta \cos \gamma)^{1/2}$

Table 2.3-3 Relation of the lattice spacing d_{hkl} to cell parameters in the different crystal systems.

Crystal system	d_{hkl} as a function of the Miller indices and lattice parameters
Cubic	$\frac{1}{d_{hkl}^2} = \frac{h^2 + k^2 + l^2}{a^2}$
Tetragonal	$\frac{1}{d_{hkl}^2} = \frac{h^2 + k^2 + l^2}{a^2} + \frac{l^2}{c^2}$
Orthorhombic	$\frac{1}{d_{hkl}^2} = \frac{h^2}{a^2} + \frac{k^2}{b^2} + \frac{l^2}{c^2}$
Hexagonal	$\frac{1}{d_{hkl}^2} = \frac{4}{3} \left(\frac{h^2 + hk + k^2}{a^2} \right) + \frac{l^2}{c^2}$
Monoclinic	$\frac{1}{d_{hkl}^2} = \frac{1}{\sin^2 \beta} \left(\frac{h^2}{a^2} + \frac{k^2 + \sin^2 \beta}{b^2} + \frac{l^2}{c^2} - \frac{2hl \cos \beta}{ac} \right)$
Triclinic	$\frac{1}{d_{hkl}^2} = \frac{1}{V^2} [h^2b^2c^2 \sin^2 \alpha + k^2a^2c^2 \sin^2 \beta + l^2a^2b^2 \sin^2 \gamma + 2hkabc^2(\cos \alpha \cos \beta - \cos \gamma) + 2kla^2bc(\cos \beta \cos \gamma - \cos \alpha) + 2hlab^2c(\cos \alpha \cos \gamma - \cos \beta)]$

Table 2.3-4 Systematic absences due to lattice type

Lattice type	Rule for reflection to be observed
Primitive, P	None
Body centred, I	$hkl; h + k + l = 2n$
Face centred, F	$hkl; h, k, l$ either all odd or all even
Side centred, e.g. C	$hkl; h + k = 2n$
Rhombohedral, R	$hkl; -h + k + l = 3n$ or $(h - k + l = 3n)$

From X-ray diffraction experiments, a huge amount of information can be obtained, for instance, by measuring the Bragg angles of the reflections and successfully indexing them, information on the size of the unit cell and also on the symmetry can be obtained. The factors which control the intensity of X-ray reflections are the intensity scattered from the large number of atoms that are arranged periodically in the crystal. Atoms diffract or scatter X-rays due to an incident X-ray beam (electromagnetic wave with an oscillating electric field) sets each electron of an atom into a vibration. The electron emits radiation which is in phase or coherent with the incident X-ray beam, acting as a secondary point sources of X-rays (the wave is deflected by the electron without loss of energy and, therefore, without change of the wavelength). The intensity of the radiation scattered coherently by “point source” is given by the Thomson equation (2.7):

$$I_p \propto \frac{1}{2} (1 + \cos^2 2\theta) \quad (2.7)$$

where I_p is the scattered intensity at any point, P, and 2θ , is the angle between the directions of the incident beam and the diffracted beam that passes through P. The scattered beams are most intense when parallel or antiparallel to the incident beam and are weakest when 90° to the incident beam (2.7). The Thomson equation is also known as the polarization factor (standard angular correction factors that must be applied during processing intensity data for use in structure determination).

When an incident beam 1 or 2 interacts with an electron, a phase difference corresponding to the distance XY exists between beams 1'' and 2'' (Figure 2.3-3). This phase difference is rather less than one wavelength (*i.e.* $XY < 1.5418 \text{ \AA}$ for Cu $K\alpha$ X-rays) because distances between electrons within atom are short. Therefore, only partial destructive interference occurs between 1'' and 2''. The overall effect of interference between beams scattered by all the electrons in the atom is to cause a gradual decrease in scattered intensity with increasing angle, 2θ (partial destructive interferences). The scattering factor or form factor (f) is the ratio between the amplitude scattered by the atoms and the electron density of charge. The scattering factor represents a number of electrons that scatter in phase in that direction, so that $\theta = 0$ and $f(0) = Z$. The form factors of atoms are tabulated against $(\sin\theta/\lambda)$ to include the effect of both angle and X-ray wavelength; they can be found in the International Tables for Crystallography.⁹

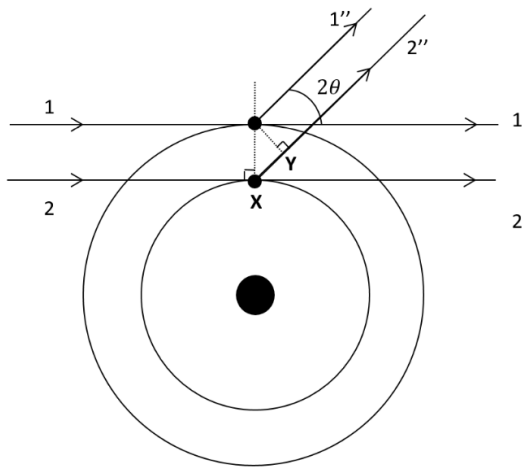


Figure 2.3-3 Interaction of X-ray beam (1 and 2) electrons in an atom. Beam 1' and 2' represent the scattered X-rays, Figure adapted from West.¹¹

The form factors gives rise to two different consequences. First, the powder patterns of most materials contain only weak lines at high angles (above ~ 60 to 70° 2θ). Second, in crystal structures using X-rays, it is difficult to locate light atoms because their diffracted radiation is so weak. Thus hydrogen atoms cannot usually be located unless all the other elements present are also extremely light (Figure 2.3-4).

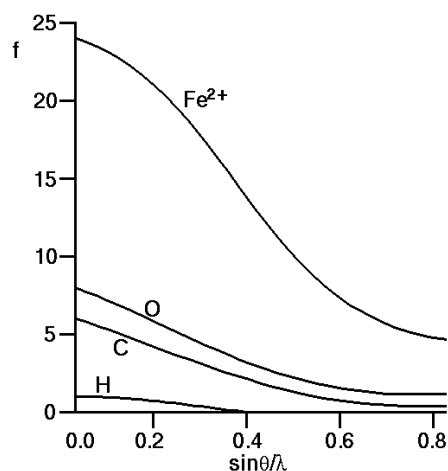


Figure 2.3-4 Form factors of Fe²⁺, O, C and H.¹²

2.3.1.2 Sample preparation for X-ray diffraction

Sample preparation for X-ray analysis was performed inside the glove box because all the materials were air and moisture sensitive. Samples were ground with an agate mortar and pestle until a fine powder was obtained. The powders were loaded and well packed inside capillaries (0.5 mm thick and 30 mm long). The loaded capillaries were sealed with wax to prevent any oxygen or moisture contamination and once outside the glove box they were sealed using a flame.

2.3.1.3 Data collection

Powder X-ray diffraction experiments were conducted with a Bruker d8 Advance powder diffractometer in transmission geometry with spinning sealed capillaries (operating with Cu *K*_α radiation in Debye-Scherrer geometry).⁸ X-rays are generated when a beam of high-energy electrons provided by a tungsten filament are accelerated towards an anode by a potential difference of 40 kV with a current of 40 mA.

The chamber where X-rays are generated is called the X-ray tube. The X-rays will leave the tube through windows made of beryllium. A monochromatic beam of X-rays is needed *i.e.* for copper, *K*_α radiation (1.54184 Å) is desired because it is the most intense line, and therefore a filter (Si (111)) will be used to avoid *K*_β radiation (1.39222 Å). The monochromatic beam of X-rays impact with a sample loaded in a capillary. The diffracted beam is conducted through a standard detector (VÅNTEC

PSD 1 detector) that generates the powder pattern based on the Debye-Scherrer method.

Diffraction data for phase identification were typically collected over $5^\circ \leq 2\theta \leq 85^\circ$ with a 0.017° step size and scan times of 1 h with longer scans used as necessary to improve counting statistics.

2.3.1.4 Data analysis

Data were collected from Bruker d8 powder diffractometer. In order to identify the phases, crystallographic data from the Inorganic Crystal Structure Database, ICSD, were used.¹³ The CELREF software package was used for indexing the lattice parameters using a least squares fitting routine. The data were analysed using Rietveld refinement as implemented in the GSAS software package¹⁴ via the EXPGUI interface¹⁵.

2.3.2 I11 at Diamond

I11 is used widely because it produces high resolution X-ray powder diffraction data not achievable using conventional sources.¹⁶ The Synchrotron X-ray powder diffraction beamline (I11) at the Diamond Light Source was used for the structural analysis of $[\text{Li}][\text{NH}_3\text{BH}_3]$ compounds in chapter (chapter 5, section 5.4.3.5). Synchrotron light is the electromagnetic radiation emitted when electrons, moving at velocities close to the speed of light, are forced to change direction under the action of a magnetic field.

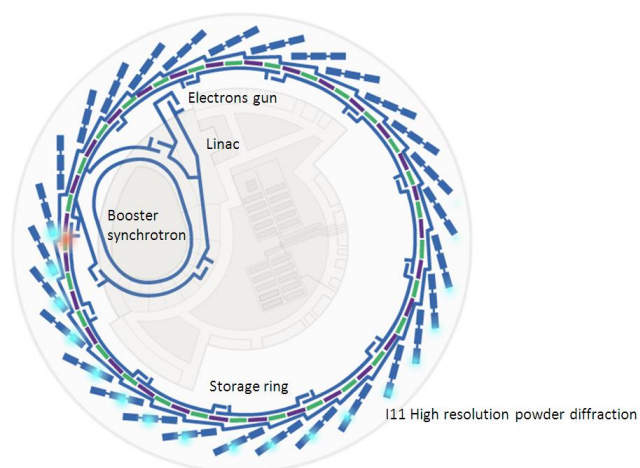


Figure 2.3-5 Schematic of Diamond Light Source in Oxfordshire¹⁶ showing the electron gun and the particle accelerators where the electrons are accelerated afterwards (Linac and Booster synchrotron) and then send into the storage ring where electrons circle until reach almost the speed of light generating a beamline which is directed into separate experimental stations (only shown one, I11).

At the Diamond light source, the electrons are generated and accelerated into the booster synchrotron where the electrons are accelerated further before entering the storage ring at an energy of 3 GeV corresponding to a speed of 99.9% (fraction of speed of light). As the electrons travel round the ring, they are diverted by magnets and in the process produce X-rays. The X-ray beams emitted by the electrons are directed toward beamlines that surround the storage ring in the experimental hall (Figure 2.3-5).

I11 uses 45 detectors to enable data collection in a few seconds. The highest flux is obtained at medium energies (11-20 keV), decaying quickly beyond 20 keV. The experiments carried out in this project were performed with a wavelength of 0.826281(10) Å using a standard silicon sample (Figure 2.3-6).¹⁷

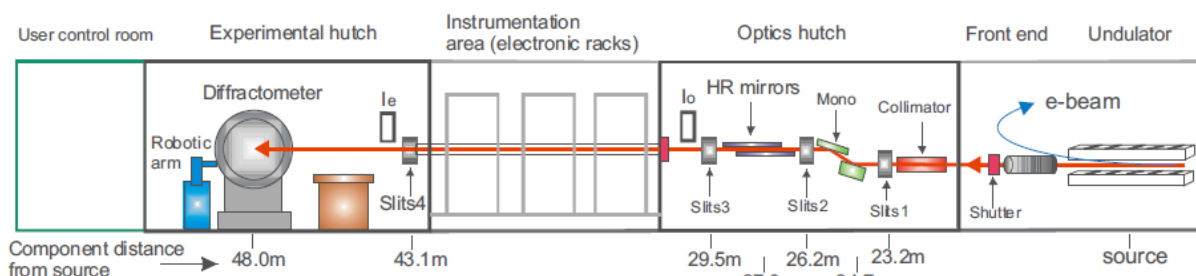


Figure 2.3-6 Schematic representation of Beamline I11 showing the main components and their approximate distances from the IVU (X-ray source).¹⁷

2.4 Powder neutron diffraction

2.4.1 Background

Neutrons interact directly with the nucleus of the atom, and the contribution to the diffracted intensity is different for each isotope. The use of powder neutron diffraction can be vital in identifying the position of light atoms that cannot be reliably detected using X-ray scattering. However, neutron diffraction is expensive and neutron sources are located only in a few places across the world.¹⁸

The materials synthesised in this work were analysed at the ISIS facility, Rutherford laboratory in the United Kingdom (Figure 2.4-1).¹⁹ The neutrons are produced in a spallation process by bombarding tantalum targets with high-energy protons produced using a 800 MeV proton accelerator. On striking the target each proton produces 25-30 fast neutrons.

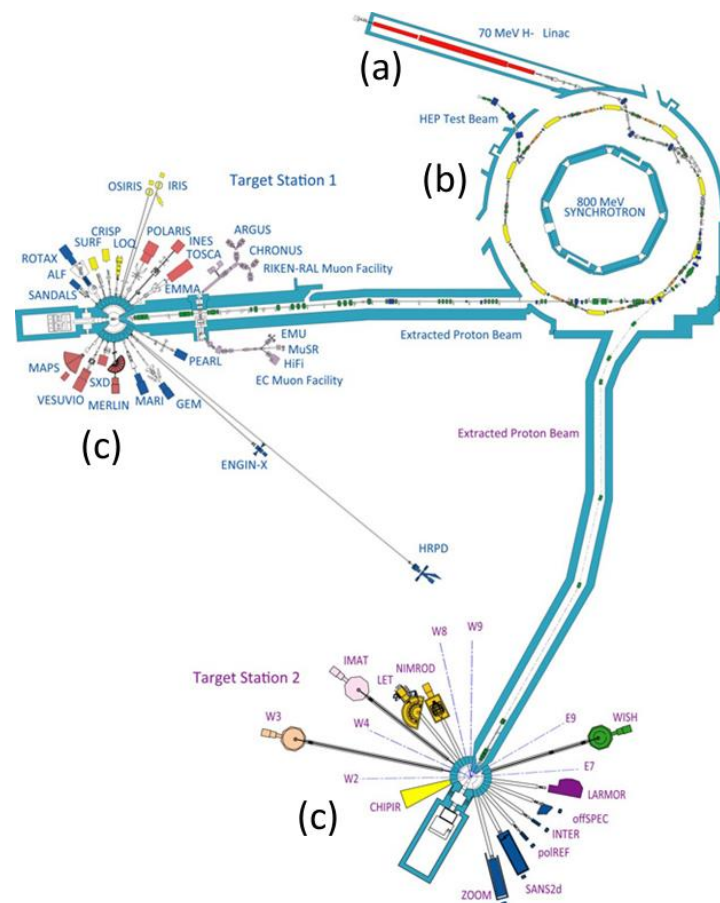


Figure 2.4-1 Rutherford Appleton Laboratory in Oxfordshire. (a) Production of H⁻ ions by a proton accelerator (b) Synchrotron ring where H⁻ ions are fired producing a H⁺ beam (c) Generation of pulses of high energy H⁺ which bombard the tungsten target, producing an extremely intense neutron pulse. The pulse is directed into separate experimental stations (Target Station 1 and 2).

The accelerator produces H^- ions using an electric discharge. The H^- ions are accelerated and separated by a radio frequency quadrupole accelerator. These H^- ions will be further accelerated until they reach a speed that is 37% of the speed of light at the end of the linear accelerator, linac (Figure 2.4-1, a). After acceleration, the H^- ions are fired through a gold foil, which strips off both electrons thus producing a medium-energy proton beam, which is then further accelerated in the main ring to higher energies. The accelerator is formed by an injector and a synchrotron (Figure 2.4-1, b). Once the H^+ are in the synchrotron they will be accelerated by radiofrequency electric fields. Once enough H^+ have been collected they will be liberated with at 84% of the speed of light. These pulses of high energy protons will travel on and bombard the target atoms, tantalum, giving an extremely intense neutron pulse. This neutron pulse is then slowed by interaction with a hydrogenous moderator to give a pulse with an optimal energy distribution for the particular instrument. (Figure 2.4-1, c). ISIS possesses two different target stations. Materials from chapters 3 and 6 (sections 3.3.8, 3.3.9 and 6.2.5) were analysed using GEM which is situated in Target Station 1 (Figure 2.4-1) and will be explained in detail in section 2.4.2.1.

2.4.2 Time of flight Powder Neutron Diffraction

The resultant pulsed beam of neutrons has a wide range of velocities, which can be correlated to wavelengths (λ) by De Broglie law (2.8):

$$\lambda = \frac{h}{p} \quad (2.8)$$

where λ is the wavelength, p is the momentum of the particles ($p = mv$, where m is the mass of the neutron, 1.675×10^{-27} kg and v is the velocity), and h is Planck's constant. A typical velocity of a thermal neutron is 2200 m s^{-1} , which correspond to a wavelength of 1.8 \AA . This value is similar to the atomic interspacing in crystals and thus, it is possible for crystalline materials to diffract neutrons. The distance travelled by the neutrons from the moderator to the sample and finally on to the detector is also known (L). This detector is placed at a fixed 2θ angle and the time of arrival of the neutrons is recorded. The wavelength of the neutrons is directly proportional to the time of flight (t_f), given by:

$$t_f = \frac{\lambda L m}{h} \quad (2.9)$$

where t_f is the time of flight, λ is the wavelength, L is the distance from the moderator to the detector, m is the mass of the neutron and h is Planck's constant.

The non-monochromated wavelengths of the different neutrons can be further used in the Bragg equation (2.6) to determine the d -spacing of the specimen analysed. As the angle is fixed, complete diffraction patterns can be obtained by a single detector although in practice, a number of detectors arranged into fixed banks are used to reduce counting times.

There are several important differences between X-ray and neutron diffraction techniques, X-rays interact with the electronic cloud of an atom whereas neutrons interact with the nucleus. The X-ray interaction (quantified by the scattering factor) is proportional to the atomic number, Z . However for neutrons the neutron scattering factor is more complicated and cannot be easily predicted. Values have to be determined experimentally and they vary for each atom and for each isotope (Figure 2.4-2).

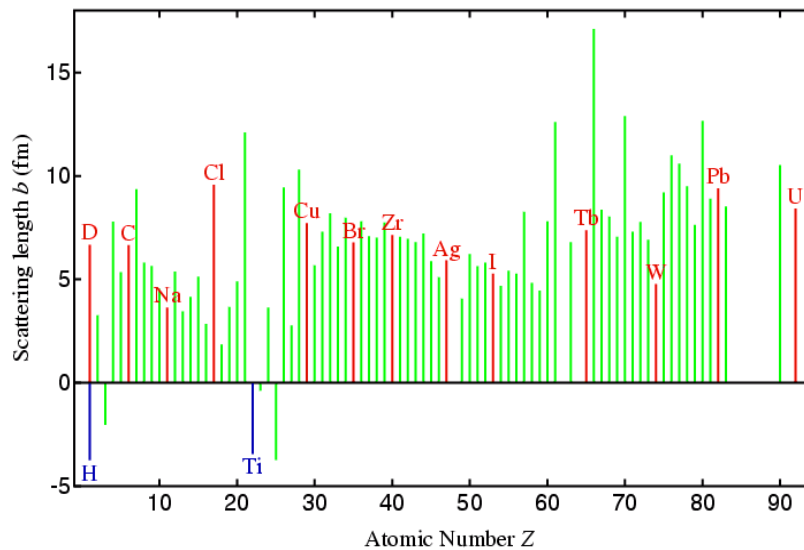


Figure 2.4-2. Neutron scattering factors as a fraction of atomic number, Z^{20}

Table 2.4-1 Scattering length for a selection of elements.²⁰

Element	H	D	Li	⁷ Li	B	¹¹ B	N	V	Br
Scattering length, <i>b</i> (fm)	-3.74	6.67	-1.90	-2.22	5.30	6.65	9.36	-0.405	6.795

Distinction between different isotopes is possible due to the different scattering length of the nuclei. This allows the technique of isotopic substitution to be used to yield structural and dynamic details of the specimen analysed. One of the most useful isotopic substitutions in solid-state chemistry is that of deuterium, D, for H. This replacement can be explained by 1) the higher coherent scattering factor that deuterium possesses when compared to hydrogen (Table 2.4-1); 2) a high incoherent scattering for hydrogen, which leads to a large background from non-Bragg scattering.

2.4.2.1 Data collection

The ToF powder neutron diffraction experiments described in chapters 3 and 6 (sections 3.3.8, 3.3.9 and 6.2.5) were carried out on GEM (GEneral Materials Diffractometer, Figure 2.4-3) at the Rutherford Appleton laboratory. Data were collected with the assistance of Prof D. Keen.

GEM is one of the most advanced neutron diffractometers in the world. Its detector array has a very large area, 7.270 m², and a very wide range in scattering angles, from 1.2 ° to 171.4 °. GEM receives neutrons through a beam port, using liquid methane as a moderator, ensuring that the temperature of the beam stays between 100 and 110 K. The flight path length from the moderator to the sample is 17 m. This relatively long distance gives a high resolution and it leads to a good separation of the Bragg peaks in a powder diffraction pattern. In total eight different detectors can be found for GEM which are ZnS/⁶Li scintillator. The sample has to be contained within an evacuated sample tank.²¹

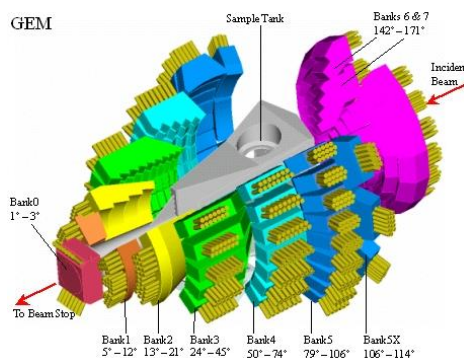


Figure 2.4-3. A schematic layout of the detector banks of the GEM detector array.²²

2.4.2.2 Sample preparation

The sample was loaded into a 6 mm diameter can of vanadium, as the scattering from vanadium is almost entirely incoherent.²² For samples measured at room temperature, an indium wire was used to seal the cans. The samples that were measured at high temperatures were sealed with a copper ring. The materials studied in this project needed to be loaded at the glove box because they were air and moisture sensitive (O_2 and $H_2O > 0.5$ ppm, respectively). The size of sample required for neutron diffraction experiment is larger than for X-rays, about 1 or 2 grams is needed, because of the weaker interaction of the neutron beams leads to a lower probability of Bragg scattering.

2.4.3 Constant Wavelength Powder Neutron Diffraction

All the constant wavelength powder neutron diffraction (CW PND) data presented in this work were obtained from the D20 powder diffractometer at the Institute Laue-Langevin (ILL) in Grenoble (Samples from chapter 5, section 5.4.3.5). Specifications of this instrument will be further detailed in the next section.

The High-Flux Reactor (ILL HFR) is used to create and deliver neutrons. It produces an intense continuous flux of $1.5 \cdot 10^{15}$ neutrons per second per cm^2 , with a thermal power of 58.3 MW. The neutron source is produced by a nuclear fission reaction. The CW PND technique is then based on the same principle as other diffraction methods that use incident monochromatic radiation such as laboratory or synchrotron X-rays. The white beam that exits the moderator hits a monochromator that uses Bragg's law to select a narrow range of wavelengths to strike the sample. The scattered neutrons will be finally measured as a function of the scattering angle

by a position sensitive detector (PSD) that can be scanned to cover a 153.6 ° range of scattering angles.

2.4.3.1 Data collection

Constant wavelength *in-situ* data were collected from the D20 experiment with the assistance of Dr T. Hansen.

D20 is a high intensity powder diffractometer with a high count rate able to perform real-time experiments and kinetic studies on very small samples. D20 is equipped with an ³He gas detector (position sensitive detector, PSD) that covers an angular range of 153.6 °. For the *in-situ* D20 experiment, 0.5 g of ⁷Li(¹¹BD₄)_{0.67}Br_{0.33}) was loaded in a vanadium canister (8 mm *id.*), sealed with indium wire. The preparation was carried out in a MBraun LabSTAR argon filled glovebox in the Gregory laboratory. Data collection was performed at an intermediate resolution using a germanium (113) monochromator to select a wavelength of 1.54 Å (118 ° take off angle). The sample was cooled under vacuum from room temperature to 2 K.

2.4.4 Data analysis: Rietveld refinement

Rietveld refinement is a technique for use in the characterisation of crystalline materials from powder diffraction data using either X-rays or/and neutrons by analysing the whole profile including background. Rietveld developed a method which assigns a Gaussian shape for each peak and then allows the Gaussians to overlap so that an overall line profile can be calculated. Firstly, a trial structure is used which can be modified by changing the atomic positions. The structure can be refined until a best-fit is obtained when the calculated and the observed data have to be almost identical. The data in this project were analysed using Rietveld refinement as implemented in the GSAS software package¹⁴ *via* the EXPGUI interface¹⁵ against multiple data sets.^{23, 24}

The Rietveld refinement method uses a least square approach to refine the calculated profile until it matches with the observed profile, where S_y is the weighted difference between the observed (y_i) and calculated (y_{calc}) diffraction patterns (2.10).

$$S_y = \sum_i w_i [y_i - y_{calc}]^2 \quad (2.10)$$

The calculated intensities (2.11) are determined from the structures factors (F_k), obtained from the crystallographic model by a summation of the calculated contributions from neighbouring Bragg K_{hkl} reflections, plus a background (b_i):

$$y_{calc} = s \sum_K L_K |F_K|^2 \Phi(2\theta_i - 2\theta_k) P_k A + y_{bi} \quad (2.11)$$

where s is a scale factor, which depends on the quantity of irradiated sample present, the intensity of the radiation and instrumental parameters; K represents a Bragg reflection with Miller indices hkl ; L_K contains Lorentz factors, polarization and other multiplicity factors; φ is the reflection profile function, which can be Gaussian, Lorentzian or a combination of both (pseudo-Voigt); $2\theta_i$ and $2\theta_k$ are the experimental and calculated Bragg angles respectively; P_k is preferred orientation function; A is an absorption factor; and y_{bi} is the background intensity at the point i .

The structure factor, F_k , is given by (2.12):

$$F_K = \sum_{j=1}^N N_j f_j \exp[2\pi(hx_j + ky_j + lz_j)] \exp[-M_j] \quad (2.12)$$

where h, k, l are the indices for the K^{th} Bragg reflections; x_j, y_j, z_j are the coordinates for the “ j ” atom; and N_j refers to the multiplicity in the atom occupation. For X-ray data, the form factor, f_j , relates to the number of the electrons when $\sin\theta/\lambda = 0$. In neutron diffraction however, f_j is replaced by b_j , the scattering length. The variation between the scattering factors for X-rays and neutrons has been previously described in 2.4.2 section. Furthermore, M_j from equation can be expressed as (2.13) shows:

$$M_j = 8\pi^2 \overline{u_s^2} \sin^2 \theta / \lambda^2 \quad (2.13)$$

where $\overline{u_s^2}$ is the root-mean-square thermal displacement of the j^{th} atom parallel to the diffraction vector.

The background intensity, y_{bi} , can be modelled as a polynomial function in 2θ , (2.14):

$$y_{bi} = \sum_{n=0}^{N_b} a_n (2\theta_i)^n \quad (2.14)$$

where N_b is the polynomial degree and a_n the polynomial coefficient.

The reflection profile (φ) function in equation (2.11) is strongly determined by the instrument used. The most widely used profile functions for peak shape fitting that can be used are Gaussian (G) (2.15), Lorentzian (L) (2.16) and pseudo-Voigt (pV) (2.17) functions:

$$G = \frac{(4 \ln 2)^{\frac{1}{2}}}{H_k \sqrt{\pi}} \exp(-4 \ln 2 (2\theta_i - 2\theta_k)^2 / H_k^2) \quad (2.15)$$

$$L = \frac{2}{\pi H_k} / \left[1 + 4 \frac{(2\theta_i - 2\theta_k)^2}{H_k^2} \right] \quad (2.16)$$

$$pV = \eta L + (1 - \eta)G \quad (2.17)$$

In equation (2.17) G and L refer to the respective contributions to the peak shape; η is the mixing parameter, which can be refined as a linear function of 2θ ; and N_a and N_b are refinable parameters (2.18):

$$\eta = N_A + N_B(2\theta) \quad (2.18)$$

The Gaussian function represents best the contributions from the experimental factors. The Lorentzian function describes the broadening of the diffraction peaks attributed to grain sizes in the crystallites. The peak shape of diffraction peaks can be adjusted to a pseudo-Voigt function which is a compromise between the Gaussian and Lorentzian equations. For the Gaussian and Lorentzian functions $2\theta_i$ and $2\theta_k$ are the observable and calculated positions for the K^{th} Bragg peak; H_k is the full-width-at-half-maximum (FWHM) of the K^{th} Bragg reflection. The H_k of a Gaussian peak, described by the Cagliotti function, has been shown to vary with the scattering angle $2\theta_k$ modelled as (2.19):

$$H_k^2 = U \tan^2 \theta + V \tan \theta + W \quad (2.19)$$

where U , V and W are refinable parameters and are both instrument and sample dependent.

The crystallites can show a tendency to be aligned, causing a variation in the intensity of the diffraction peaks. In order to correct these intensities the preferred orientation function is used (2.20):

$$P_k = [G_2 + (1 - G_2) \exp(-G_1 a_k^2)] \quad (2.20)$$

where G_1 and G_2 are refinable parameters; and a_k is the angle between the presumed cylindrical symmetry axis and the preferred orientation axis direction.

In order to guide the Rietveld refinement, the difference profile plot can be followed (the fit of the calculated pattern compared with the observed data). The quality of the refinement can also be followed numerically. This is done in terms of the agreement indices or R values. These are: the R -weighted profile value (R_{wp} , (2.21)), R -expected (R_e , (2.22)), R -profile (R_p , (2.23)), R -intensity (R_i , (2.24)), and R -Bragg (R_B , (2.25)):

$$R_{wp} = \left\{ \frac{\sum_i w_i [y_i - y_{calc}]^2}{\sum_i w_i (y_i)^2} \right\}^{1/2} \quad (2.21)$$

$$R_e = \left\{ \frac{(N - P + C)}{\sum w_i (y_i)^2} \right\}^{1/2} \quad (2.22)$$

$$R_p = \frac{\sum |y_i - y_{calc}|}{\sum y_i} \quad (2.23)$$

$$R_i = \frac{\sum |I_{Ki}^2 - I_{Kcalc}^2|}{\sum I_{Ki}^2} \quad (2.24)$$

$$R_B = \frac{\sum I_{Ki} - I_{Kcalc}}{\sum I_{Ki}} \quad (2.25)$$

where I_{Ki} and I_{calc} are the observed and calculated Bragg intensities of the reflection K : and N , P and C represent the number of observations, refined parameters and constraints, respectively. From a mathematical point of view, R_{wp} is perhaps the function that best represents the refinement process since the numerator of the residual corresponds to the least squares function that is minimized in the refinement process (2.10).

Ideally, the final R_{wp} should approach the statistically determined R_e . Thus, the ratio between the two (goodness-of-fit) should approach 1 (2.26). A value of $1.0 \leq \chi^2 \leq 1.5$ is considered as satisfactory. If low values of χ^2 are obtained then the background signal will be significant.

$$\chi^2 = \left(\frac{R_{wp}}{R_e}\right)^2 \quad (2.26)$$

In order to fit the peaks obtained from the time-of-flight data, two different sets of information are required. (1) The diffractometer constants are used to calculate the time-of-flight positions of the Bragg reflections (space group information can be determined); (2) the profile parameters which are used to calculate the width of each of the Bragg reflections.

There are three different parameters in GSAS that can be refined for the diffractometer constants: DIFC, DIFA and ZERO. These three parameters are related to the time of flight, t , of a reflection to its d -spacing, d (2.27):

$$t = DIFCd + DIFAd^2 + ZERO \quad (2.27)$$

DIFC relates the theoretical time-of-flight of a measured Bragg diffraction to its d -spacing. The equation for DIFC can be obtained (2.28) by knowing the total flight path, L , the scattering angle, 2θ , of a detector and using Bragg's law (2.6) and De Broglie relationship ((2.7) - (2.9))

$$DIFC = t/d = \left(\frac{2m}{h}\right)L \sin \theta \quad (2.28)$$

where h is the Plank's constant; m is the neutron mass; t is the time of flight; L is the total flight path from moderator to sample to detector; d is the interplanar distance; and θ is half of the Bragg scattering angle (2θ). By applying the value of the mass of a neutron and Plank's constant, the following can be obtained (2.29), where t is in μs , L is in m and d is in \AA :

$$t = 505.56L \sin \theta d \quad \text{or} \quad d = \frac{1.977 \times 10^{-3}}{L \sin \theta} t \quad (2.29)$$

Assuming that DIFA and ZERO are equal to 0 in (2.27), DIFC is given by equal to the following formula (2.30):

$$DIFC = 505.56L \sin \theta \quad (2.30)$$

This parameter depends on each detector of each bank and therefore normally this value remains fixed.

The neutron absorption cross-section of an atom is wavelength dependent, which means that in a time-of-flight diffraction measurement the short wavelength (low ToF) neutrons will experience less absorption than the larger wavelength (higher ToF) neutrons. The average penetration into the sample, the apparent total flight path and the scattering angle, vary with the neutron wavelength. The observed time-of-flight of the reflections can be different from the one obtained from DIFC, especially at longer *d-spacing* (which are measured with longer wavelengths, where the absorption is greater). DIFA introduces small corrections to the expected time-of-flight of a reflection to allow for peak shifts due to the absorption in the sample. Initially DIFA can be kept at 0.0 but after few cycles this parameter can be refined.

The parameter ZERO accounts for small differences between the various timing signals in the ISIS accelerator and the instrument data acquisition system, and also allows for the finite response times in the detector electronics. It is instrument dependent and must remain fixed.

The profile parameters are used to calculate the widths of each of these Bragg reflections and need to be refined. The peak shape is more complex than constant wavelength experiments and must incorporate a description of the pulse wavelength distribution. The pulse is modeled by back to back exponential functions to reproduce the rapid rise in neutron counts as the fastest neutrons arrive followed by a slower decay as the remainder of the pulse is detected. This back-to-back exponential function must be convoluted with the Gaussian and Lorentzian terms arising from the sample and instrument. The pseudo-Voigt function models the effects of instrument design and detector geometry on the width of reflections, and also any broadening due to the sample such as strain and particle size. The pseudo-Voigt function is the linear combination of the Gaussian and Lorentzian function, whose full widths at half maximum are parameterised in GSAS as follows.

Gaussian width, σ (2.31):

$$\sigma^2 = \sigma_0^2 + \sigma_1^2 d^2 + \sigma_2^2 d^4 \quad (2.31)$$

In GSAS these coefficient parameters are called *sig-0*, *sig-1* and *sig-2* respectively and *d* in equation (2.31).

Lorentzian width, γ (2.32):

$$\gamma^2 = \gamma_0 + \gamma_1 d + \gamma_2 d^2 \text{ (+ other terms associated with strain broadening)} \quad (2.32)$$

In GSAS these first three terms are called *gam-0*, *gam-1* and *gam-2*.

Partial differentiation of the equation above (2.29) relating time-of-flight to d-spacing shows that for a fixed detector the resolution is approximate closely to $\Delta d/d = \text{constant}$. The width of a reflection is proportional to its d-spacing, *i.e.* $\Delta d/kd$. Comparing this expression with the above parameterisations of the Gaussian (2.31) and Lorentzian (2.32) widths it can be seen that the terms σ_1 and γ_1 both describe linear relationships between peak width, Δd , and d-spacing ((2.33) and (2.34)).

$$\Delta d^2 = \sigma^2 = \sigma_1^2 d^2 \text{ } (\sigma_0 \text{ and } \sigma_2 = 0), \text{ therefore } \Delta d/d = \sigma_1 \quad (2.33)$$

$$\Delta d = \gamma = \gamma_1 d \text{ } (\gamma_0 \text{ and } \gamma_2 = 0), \text{ therefore } \Delta d/d = \gamma_1 \quad (2.34)$$

In a structure refinement *sig-1* and *gam-1* could be refined.

However, in most samples there is likely to be some degree of particle size or strain broadening. Particle size broadening has a d^2 dependence and thus is fitted by the *gam-2* parameter, whereas strain broadening has a linear dependence on d and may be fitted by the *gam-1* or *sig-1* parameters.

The rise and decay coefficients for the two exponential functions are described by the parameters *alp*, *bet-0* and *bet-1*. During instrument calibration, these parameters can be refined with care. During structure refinement they must be kept constant.²⁵

Another crystallographic software package used was Jana2006.²⁶ This software focuses on the solution, refinement and interpretation of difficult modulated structures. However structure solution can also be performed using the built-in charge flipping algorithm or by using an external direct methods program.

GSAS was used for the structure refinement of ${}^7\text{Li}(\text{}^{11}\text{BD}_4)_{0.67}\text{Br}_{0.33}$ (chapter 3, sections 3.3.8, 3.3.9 and 3.3.10), HP LiBH_4 type materials (chapter 4, section 4.3.3.3), $[\text{Li}][\text{NH}_3\text{BH}_3]$ and $[\text{Li}][\text{NH}_3\text{BH}_3]_2$ (chapter 5, section 5.4.3.5), and LiInBr_4

(chapter 6, section 6.2.5). Jana2006 was used for the structure solution of $[\text{LiI}][\text{NH}_3\text{BH}_3]$ and $[\text{LiI}][\text{NH}_3\text{BH}_3]_2$ (chapter 5, section 5.4.3.4).

2.5 Spectroscopy techniques

2.5.1 Vibrational spectroscopies: IR and Raman techniques

Infrared and Raman spectroscopies are both concerned with the study of molecular vibrations. Both techniques yield similar but complementary information on the vibrational modes of a molecule. A vibrational mode is Raman active if the polarizability of the molecule changes during the vibration, whereas a vibrational mode is IR active if there is a change in the molecular dipole moment upon vibration (Figure 2.5-1). The mechanism used for each technique is shown in Figure 2.5-2. IR could have been used to analyse the synthesised samples however it was not possible because the IR spectrometer was not equipped for air and moisture sensitive samples. For more detailed accounts of the IR effect other references can be consulted.^{27, 28}

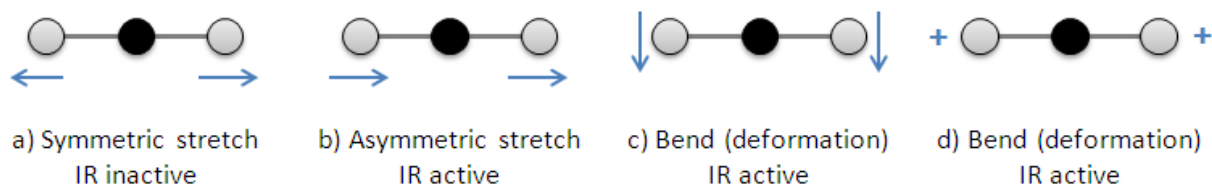


Figure 2.5-1. The vibrational modes of a linear molecule: Vibrations a) and b) are stretching modes. Bending mode c) occurs in the plane of the paper, while d) occurs in a plane perpendicular to that of the paper. The two modes require the same amount of energy and are therefore degenerate.

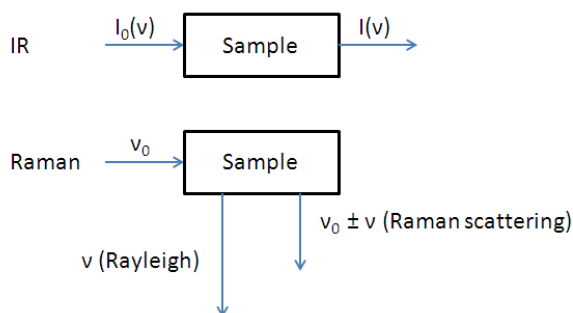


Figure 2.5-2 Mechanism of IR absorption and Raman scattering. In the IR technique, the frequency of the incident radiation is varied and the quantity of radiation absorbed or transmitted by the sample is obtained. In the Raman technique, the sample is illuminated with monochromatic light, usually generated by a laser. Two types of scattered light are produced by the sample. Rayleigh scatter emerges with exactly the same energy and wavelength as the incident light. Raman scatter which is usually less intense than Rayleigh scatter, emerges at either longer or shorter wavelength than the incident light.

2.5.1.1 Raman spectroscopy

When radiation of a particular frequency, ν , falls on a molecule some radiation is scattered (Figure 2.5-2). The scattered radiation is of two types: (1) Rayleigh scattering where the radiation frequency, ν_0 , is equal to that of the incident radiation and (2) Raman scattering involves radiation of frequencies $\nu_0 \pm \nu$ (Figure 2.5-3).

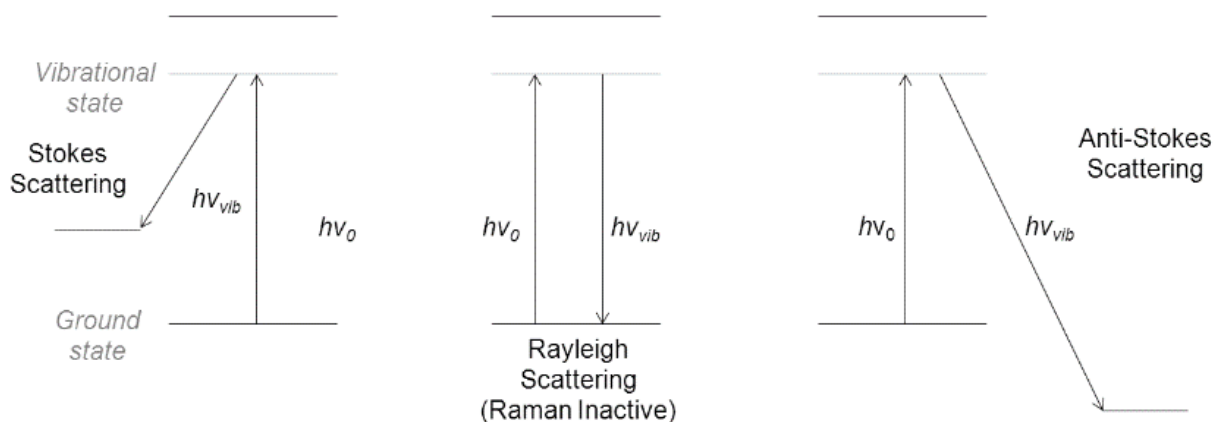


Figure 2.5-3. Energy level diagram illustrating energy changes of different types of Raman scattering.

$$h\nu + E_i = h\nu' + E_f \quad (2.35)$$

$$h(\nu' - \nu) = E_i - E_f = h\Delta\nu_R = hc\Delta\tilde{\nu}_R \quad (2.36)$$

where the shift in frequency is labelled $\Delta\nu_R$ and the shift in wavenumber is labelled $\Delta\tilde{\nu}_R$. Notice that Raman spectroscopy is different from absorption or emission spectroscopy in that the incident light does not need to coincide with a quantized energy difference in the molecule, therefore any frequency of light can be used. Since many final states, of both higher and lower energy than the initial state are possible, many Raman spectral lines can be observed.²⁸

The frequency shifts seen in Raman experiments correspond to vibrational or rotational energy differences, so this kind of spectroscopy gives us information on the vibrational and rotational states of molecules. The Raman effect arises from the induced polarization of scattering molecules that is caused by the electric vector of the electromagnetic radiation. A dipole moment μ is induced in the molecule by an electric field E (2.37):

$$\mu = \alpha E \quad (2.37)$$

where a is the polarizability. The polarizability has the units of dipole moment divided by electric field strength, that is, $\text{C m/V m}^{-1} = \text{C}^2 \text{ m}^2/\text{J}$.

The wavenumber ($\tilde{\nu}_R$) is proportional to the frequency (ν) and inversely proportional to the wavelength (λ):

$$\tilde{\nu}_R = \nu/c = 1/\lambda \quad (2.38)$$

where c is the speed of light in vacuum. The Raman lines will appear at a certain wavenumber ($\tilde{\nu}_R$), which is the result of the difference between the frequency of the active vibration mode (ν) and the laser used (ν_0), normalised with respect to c .

$$\tilde{\nu}_R = (\nu - \nu_0)/c \quad (2.39)$$

At the same time, the frequency of a certain vibration mode (ν) depends on the mass of the two atoms (m_1 and m_2) involved in the active mode, and the force constant of the bond (k) between those atoms. This relationship is expressed as follows:

$$\nu \approx \sqrt{\frac{k}{m}} \quad (2.40)$$

Whereby m is the reduced mass, calculated as:

$$m = \frac{m_1 m_2}{(m_1 + m_2)} \quad (2.41)$$

According to the Maxwell-Boltzman distribution, at room temperature most atoms will reside in the lowest vibrational state; thus, the possibility that Stokes scattering occurs is greater than that for anti-Stokes scattering. This translates to Stokes intensities being increased by a factor of 100 with respect to the anti-Stokes radiation and appears on the positive part of the abscissa.

Raman spectra were collected at room temperature using a Horiba-Jobin-Yvon LabRam HR confocal microscope using a 532 nm laser and equipped with a 50 x objective lens and a Synapse CCD detector. Typically, hole apertures of 50 and 100 μm and 10-100 % of laser intensity were used.

For the measurement, samples were placed in capillaries due to their air-sensitive behaviour. Prior to each measurement, the instrument was calibrated and a spectrum was collected over a period of several minutes from an average of multiple scans at a range of 500 - 4000 cm^{-1} .

2.5.2 Raman spectroscopy of borohydride ions

Vibrational spectroscopy probes the degrees of vibrational freedom ((2.42) and (2.43)). Using Cartesian axes a molecule has $3N$ degrees of freedom which describe the translational, vibrational and rotational motion of each molecule. In general a non linear molecule with N atoms has $3N - 6$ normal modes of vibration (2.42), whereas a linear molecule has $3N - 5$ normal modes of vibration (2.43), because rotation about its molecular axis cannot be observed.

$$\text{non linear molecule} = 3N - 6 \quad (2.42)$$

$$\text{linear molecule} = 3N - 5 \quad (2.43)$$

A tetrahedral molecule such as a free borohydride ion has a total of $3N - 6 = 9$ vibrational modes. They are the ν_1 symmetric stretch (singly degenerate symmetry mode denoted A), ν_2 symmetric bend (doubly degenerate symmetry mode, E), ν_3 asymmetric stretch (triply degenerate symmetry mode, T_2) and ν_4 asymmetric bend (triply degenerate symmetry mode, T_2). These vibrational modes are shown in Figure 2.5-4. Within crystal structures, the symmetry of the borohydride ion is dependent on the symmetry elements of the site. The site symmetry of the borohydride ion will determine the specific symmetry of each bond vibration.^{29, 30}

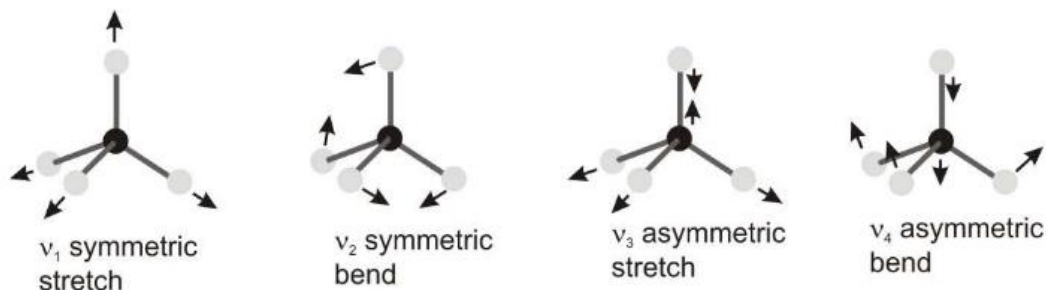


Figure 2.5-4 The vibrational modes of a tetrahedral molecule.^{29, 30}

In LT - LiBH_4 , the borohydride ions are located on a mirror plane and hence have the point group C_s . Then the reducible representation, Γ_{3N} ($\Gamma_{3N} = 15E + 3\sigma_h$, for LT - LiBH_4), is obtained (representation of the total translational, rotational and vibrational modes for the ion). The irreducible representation of Γ_{3N} is calculated from the character table ($\Gamma_{3N} = 9A' + 6A''$ for LT - LiBH_4), and so the translational, rotational and vibrational modes are obtained. The allocation of quadratic terms such as x^2 , y^2 , z^2 , xy , yz , xz in the point group character tables indicates that the modes will be Raman active. The symmetries of the vibrational modes of a borohydride ion with point group C_s are $\nu_1 = A'$, $\nu_2 = A' + A''$, $\nu_3 = 2A' + A''$, $\nu_4 = 2A' + A''$.³⁰

2.6 Electron microscopy

Electron microscopy is used to study the structure, morphology, and crystallite size, to examine defects and to determine the distribution of elements. Scanning electron microscope was used for the characterisation of samples in this project.

2.6.1 Scanning electron microscopy

In this technique, an electron beam is produced by heating a tungsten filament, which causes ionisation to occur. The released electrons are focused by magnetic fields into a single beam in a high vacuum (the vacuum prevents interaction of the beam with any extraneous particles in the atmosphere). The very short wavelength of the electrons allows resolution and magnification down to 3.5 nm (50x - 500x). Once the beam hits the sample, electrons and X-rays are ejected from the sample. Detectors collect these X-rays, backscattered electrons, and secondary electrons and convert them into a signal that is sent to a screen similar to a television screen. This produces the final image.⁶

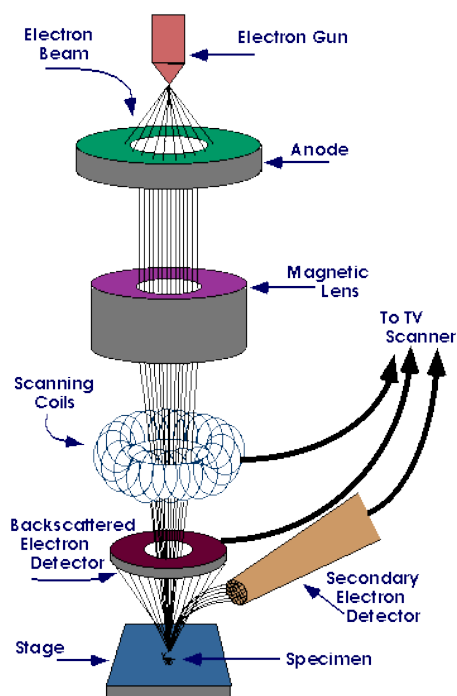


Figure 2.6-1 Schematic of a typical SEM instrument.

Sometimes it is necessary for the samples to be coated with gold or graphite in order to prevent charge building up on the surface which however in this work was not necessary for LiBH_4 samples. For this project the sample morphology as studied using a Philips XL 30 ESEM operating with an accelerating voltage of 25 kV. An Oxford Instruments X-act spectrometer was coupled to this microscope for energy dispersive X-ray (EDX) analysis which provides elemental identification and quantitative compositional information. The instrument is calibrated using the INCA EDX analysis software (Cu was used for all calibration measurements) and the software also allowed selection of regions for analysis and definition of measurement parameters.

The samples were ground with a mortar and pestle until a fine powder was obtained. The powder was then dispersed on an adhesive carbon tab mounted onto an aluminium stub in a glovebox. During loading of the carbon tab samples into the SEM instrument, the samples are unavoidably exposed to air and hence rapid manipulation is required. These results can be found in chapter 3 (section 3.3.4).

2.7 ⁷Li solid state nuclear magnetic resonance

⁷Li solid state NMR experiments were performed by Dr David C. Apperley in the Department of Chemistry at the University of Durham. The measurements were carried out using a Bruker Advance III HD spectrometer operating at 155.52 MHz for ⁷Li. Spectra were obtained as a function of temperature using a quadrupolar echo pulse sequence with a 60 s relaxation delay (unless otherwise stated), 1.3 μs pulses (45° tip angle calibrated on a solution sample) with a delay of 20 μs between them. Spectral referencing is with respect to a 1M aqueous solution of LiCl. Spin-lattice relaxation time measurements were performed using a saturation-recovery method.

2.8 Thermal analysis

Thermal analysis methods investigate the physical properties of solids as a function of a change in temperature. They are useful for investigating phase transitions, thermal stability, loss of mass, and for constructing phase diagrams.

Thermogravimetric analysis (TGA) is a technique which measures the change in mass of a solid as a function of temperature and under a controlled atmosphere. By comparing the heating rate of the sample to an inert standard under the same thermal conditions differential thermal analysis (DTA) can give information on heat capacities and latent heats of phase transitions.

A mass spectrometer (Hiden ANALYTICAL HPR20) is coupled to the Simultaneous Thermal Analysis (STA) for evolved gas analysis (EGA). The mass spectrometer ionises the evolved gases in a high vacuum and then accelerates these ionised species towards a quadrupole analyser, which conducts these ions with a particular mass to charge ratio (m/z) to the detector by altering the magnetic and electric field. The spectrometer can either scan over a range of 0 - 300 amu or monitor individual ions with specific m/z values of interest. This technique can be useful to follow reactions where a weight loss is produced with an evolution of a certain gas or mixtures of gases. In this project this technique was used to study the thermal stability of the synthesised materials.

Thermogravimetric-differential thermal analysis-mass spectrometry (TG-DTA-MS) experiments were conducted under flowing argon (99.998 %, BOC) in a Netzsch 409 PC STA instrument coupled to a Hiden Analytical HPR 20 mass spectrometer. In a typical experiment, between 5 and 10 mg of sample was loaded onto an alumina pan, which was then heated from room temperature to 200 - 300 °C at 5 °C min⁻¹. The instrument was located inside a glove box with a controlled atmosphere (MBraun, UNILAB and O₂ and H₂O < 0.1 ppm). For EGA, any gas released during the reaction was simultaneously monitored (e.g. N₂, NH₃, H₂, B₂H₆ and B₃H₆N₃).^{31, 32}

2.9 Electrochemical impedance spectroscopy

The electrical resistance of a circuit element is the element's ability to resist the flow of electrical current defined by Ohm's law (2.44):

$$R = \frac{V}{I} \quad (2.44)$$

where R is the resistance (in Ohms), V is the voltage (in Volts) and I is the current (in Amperes). An ideal resistor will follow Ohm's law at all current and voltage levels. Voltage across and current through a resistor are in phase with each other when an AC potential is applied. However resistance cannot be used for ionic conductivity because the quantity is independent of frequency and therefore is independent of time, and consequently impedance has to be used which depends on time. Like resistance, impedance (Z) is the ability to resist the flow of electrical current and is measured in Ohms. To measure the impedance of a system a sinusoidal AC potential excitation is applied. The response to this potential is a sinusoid at the same frequency but shifted in phase (Figure 2.9-1, (2.45)).

$$V_t = V_o \sin(\omega t) \quad (2.45)$$

V_t is the potential at time t , V_o is the amplitude of the signal, and ω is the radial frequency.

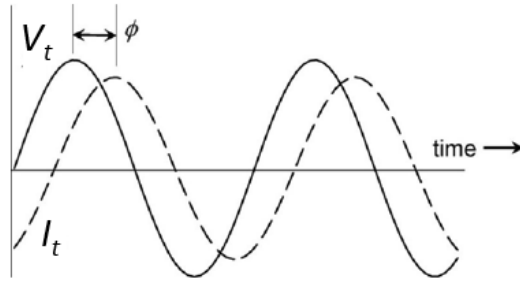


Figure 2.9-1 Alternative current (AC) is a sinusoidal wave shape and has a frequency; therefore both potential (E_t) and current (I_t) oscillate shifted in phase, ϕ .³³

The radial frequency, ω (rad), is defined as in (2.46):

$$\omega = 2\pi f \quad (2.46)$$

where f is frequency (Hz).

In a linear system, the intensity of the responsive wave I_t (A) is shifted in phase and has a different amplitude, I_o (2.47):

$$I_t = I_o \sin(\omega t + \varphi) \quad (2.47)$$

Therefore the impedance can be defined as follows (2.48):

$$Z = \frac{V_t}{I_t} = \frac{V_o \sin(\omega t)}{I_o \sin(\omega t + \varphi)} = Z_0 \frac{\sin(\omega t)}{\sin(\omega t + \varphi)} \quad (2.48)$$

In order to represent the relative magnitude (V_o and I_o) and phase (φ) of the output (voltage) and input (current) signals complex numbers are used (from (2.49) to (2.52)) where j used to represent $(-1)^{1/2}$:

$$z = x + jy \text{ (where } j = \sqrt{-1}\text{)} \quad (2.49)$$

$$\exp(j\varphi) = \cos\varphi + j\sin\varphi \quad (2.50)$$

$$V_t = V_o \exp(j\omega t) \quad (2.51)$$

$$I_t = I_o \sin(j\omega t + \varphi) = I_o \exp(j\varphi) \exp(j\omega t) \quad (2.52)$$

The impedance can be represented as a complex number (from (2.53) to (2.55)):

$$Z(\omega) = \frac{V_t}{I_t} = \frac{V_o \exp(j\omega t)}{I_o \exp(j\varphi) \exp(j\omega t)} = \frac{V_o}{I_o} \exp(-j\varphi) \quad (2.53)$$

$$Z = |Z| \cos(\varphi) + j|Z| \sin(\varphi) \quad (2.54)$$

$$Z = \text{Real}(Z) + \text{Imaginary}(Z) \quad (2.55)$$

In basic linear circuits the following formulae are applied (from (2.56), to (2.60)):

Resistor: $V(t) = RI(t)$ (2.56)

Capacitor: $Q(t) = CV(t)$ (2.57)

$$\int I(t) dt = CV(t) \quad (2.58)$$

$$I(t) = C \frac{dV(t)}{dt} \quad (2.59)$$

Inductors: $V(t) = L \frac{dI(t)}{dt}$ (2.60)

where R is resistance (Ohms), I is current (A), Q is the charge (A s), V is the voltage (V), I is the inductance (H), and L is the length of the system (m).

If voltage and current are in phase there is no imaginary component and therefore (2.61):

$$Z = R \quad (2.61)$$

To calculate the impedance of a capacitor (from (2.62) to (2.65)):

$$I(t) = C \frac{dV(t)}{dt} \quad (2.62)$$

$$V_t = V_o \exp(j\omega t) \quad (2.63)$$

$$\frac{dV(t)}{dt} = V_o j\omega \exp(j\omega t) \quad (2.64)$$

$$I(t) = CV_o j\omega \exp(j\omega t) \quad (2.65)$$

Therefore:

$$Z_c = \frac{V}{I} = \frac{1}{j\omega C} = -\frac{j}{\omega C} \quad (2.66)$$

Then a capacitor will be always frequency dependent (2.66).

The admittance, Y , is the ability to allow the current to flow through the circuit and is measured in Siemens. For a RC circuit Y is defined as follows (2.67):

$$Y = \frac{1}{Z} = G + jB \quad (2.67)$$

where G is the conductance and B is the susceptance both in Siemens. In order to avoid any complex component in the denominator of the fraction, the numerator and the denominator are multiplied by the complex conjugate (from (2.68) to (2.72)):

$$Y = \frac{1}{Z} = \frac{1}{R} - \frac{\omega C}{-j} \left(\frac{j}{j} \right) = \frac{1}{R} + j\omega C \quad (2.68)$$

$$Z = \frac{R}{(1 + j\omega RC)} \quad (2.69)$$

$$Z = \frac{R(1 - j\omega RC)}{(1 + \omega^2 R^2 C^2)} \quad (2.70)$$

$$\text{Real}(Z) = \frac{R}{(1 + \omega^2 R^2 C^2)} \quad (2.71)$$

$$\text{Imaginary}(Z) = \frac{-\omega R^2 C}{(1 + \omega^2 R^2 C^2)} \quad (2.72)$$

Limiting cases are illustrated in Figure 2.9-2.

At the high frequency limit:

$$\text{Re}(Z) \rightarrow 0 \quad (2.73)$$

$$\text{Imag}(Z) \rightarrow 0 \quad (2.74)$$

At the low frequency limit:

$$\text{Re}(Z) \rightarrow R \quad (2.75)$$

$$\text{Im}(Z) \rightarrow 0 \quad (2.76)$$

This is a special case when

$$\omega = \frac{1}{RC} \quad (2.77)$$

$$\text{giving } Re(Z) = \frac{R}{2} \quad \text{and} \quad Imag(Z) = -\frac{R}{2} \quad (2.78)$$

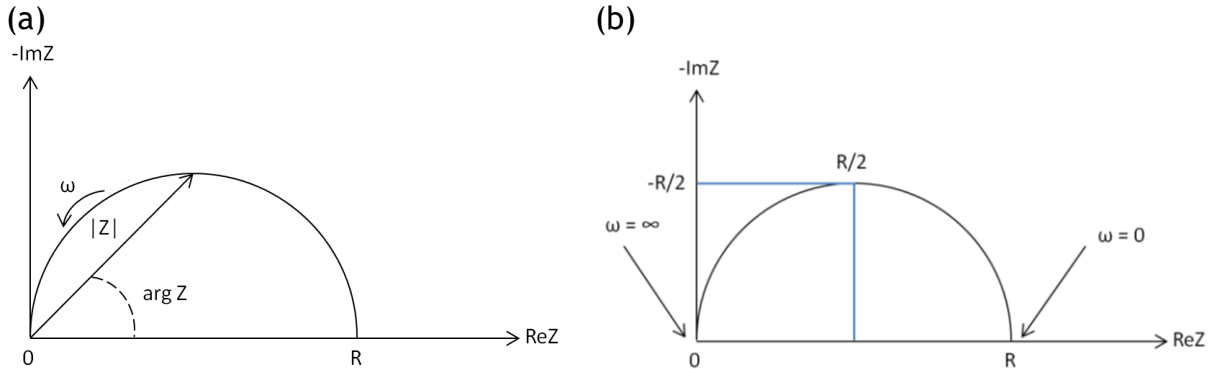


Figure 2.9-2 (a) Nyquist or complex plane plot with the impedance vector indicated (b) Limiting cases for impedance.

In order to understand the conductivity of a material firstly the system to be studied (electrolyte, electrode, etc.) needs to be understood. Possible phenomena in the sample to be measured need to be studied. In a polycrystalline electrolyte system there are three possible components to the resistivity: the interfacial resistance between the electrolyte and the electrodes, the bulk resistance of the electrolyte and the grain boundary resistance.

The bulk resistivity depends solely on the nature of the electrolyte material and the measurement temperature. However, the grain boundary resistivity is related to the grain size and grain boundary structure.

In practice, it is important that the grain boundary resistance should be minimised to obtain the highest conductivity of a polycrystalline electrolyte material. Hence, in order to be able to reduce the grain boundary resistivity, the grain boundary resistance first needs to be identified and then separated from the total resistance of the material. The total resistance of a material can normally be

measured using a DC technique, where a 4-probe arrangement is used to eliminate the contribution of the interfacial resistance between the electrolyte and the electrodes. However, in order to separate the grain boundary resistance from the bulk resistance, the complex impedance technique is necessary.

In an AC field, a resistive material is usually regarded to possess, in addition to a resistance, as an inductance and/or capacitance. It has been found that the resistance and capacitance in parallel can be used to simulate the electrolyte system.³⁴⁻³⁷ For a parallel circuit formed by a simple resistance, R , and capacitance, C , a semicircle is obtained when the imaginary part of the impedance is plotted against the real part of the impedance (complex plane plot, Figure 2.9-2). The diameter of the semicircle is equal to R and the term RC represents the time constant, or relaxation time, of the circuit ((2.77) and (2.78)). Therefore, for an electrolyte system, if the three semicircles which are formed from the three parallel circuits can be separated in a complex plane plot, one can obtain the three individual resistance values corresponding to interfacial, bulk and grain boundary phenomena from the dimensions of the semicircles. However, in order to produce the separate and discrete semicircles in a Nyquist plot, the time constants needs to differ by 3 orders of magnitude. In practice, the three values of the capacitance, C , are also quite different from one another. The highest value is the interface capacitance between the electrolyte and electrode, the second highest is the grain boundary capacitance and bulk capacitance is the lowest.

2.9.1 Analysis data

A simple technique used for lithium ion electrolytes is semicircle fitting from the complex plane plot to determine both the bulk and grain boundary resistances and capacitances of the materials. The software package Zview was used for the fitting of the complex plane plots. The fitting option in Zview is utilised for this purpose, and bulk resistance (R_b) and capacitance (C_b) and grain boundary resistance (R_{gb}) and capacitance (C_{gb}) are calculated using the following information: the high frequency semicircle represents the bulk resistance; The mid-frequency semicircle gives grain boundary resistance; and the low frequency semicircle (if present) indicates the interface resistance between the electrolyte and the electrode.

Similarly the resistance and the capacitance values at different temperatures can be determined. Resistance data are extracted from the semicircles as a function of temperature. Alternatively, a full fit of the data with a suitable equivalent circuit can be attempted. Once the value of the resistance for each circuit is obtained, the value of the conductivity can be extracted using (2.79) and (2.80).

$$R = \frac{\rho L}{A} \quad (2.79)$$

where R is the resistance, ρ is the resistivity, L the length (cm) and A the area of the pellet (cm²).

$$\sigma = \frac{1}{\rho} \quad (2.80)$$

where σ is the conductivity (2.80).

For thermally activated processes such as ionic conduction an activation energy can be derived from the Arrhenius relationship (2.81):

$$\ln \sigma_T = \ln A - \frac{\Delta H_m}{k_B T} \quad (2.81)$$

where σ_T is conductivity in S cm⁻¹, A is the pre-exponential factor, ΔH_m is enthalpy for conduction in J, k_B is the Boltzmann constant, 1.38×10^{-23} J K⁻¹, and T is absolute temperature in K. When plotting $\ln \sigma_T$ versus $1/T$, the slope from (2.81) is defined as $m = \Delta H_m/k_B$ and therefore the activation energy is express as it follows (2.82):

$$E_a(\text{eV}) = \Delta H_m = m \cdot (1.38 \cdot 10^{-23}) \cdot 6.2410^{18}(\text{eV}) \quad (2.82)$$

It is clear from the equation (2.81)), that in the electrolytes, the plot of $\ln \sigma_T$ vs. $1/T$ is linear, and the gradient is equal to the activation energy. Activation energy (E_a) represents the ease of ion hopping and is directly correlated to the crystal structure and openness of the conduction pathways. The majority of ionic solids have densely packed crystal structures with narrow bottlenecks, lacking well-defined conducting pathways. Consequently the activation energies for ion hopping are large (usually 1 eV or greater) and conductivity values are low. In solid electrolytes, by contrast, open conduction pathways exist and activation energies are much lower (as low as 0.03 eV in AgI).¹¹

2.9.2 Sample preparation

The transport properties of complex hydrides were investigated by AC impedance spectroscopy using a Solartron SI 1260 frequency response analyser. The experiments were performed by pressing samples of approximately 0.25 g under a load of 7 tonnes to give a 13 mm diameter cylindrical pellet approximately 2 mm thick. The pellets were attached to two platinum electrodes using platinum paste and heated from room temperature to 413 K and in an atmosphere of dry N₂. The sample was mounted in a spring-loaded sample holder with platinum contacts and data were collected from samples that had been equilibrated for at least 30 minutes. AC impedance data were collected over the range of frequencies $1 \leq f \leq 10^6$ Hz upon heating the sample. Analysis of the data by circle fitting provided estimates for the equivalent capacitance and resistance for the grain boundary and grain interior. Resistance values were then used to determine the conductivities at the grain boundary and in the grain interior and the corresponding activation energies for ionic motion, (~1 eV for both).

2.10 References

1. S. L. James, C. J. Adams, C. Bolm, D. Braga, P. Collier, T. Friscic, F. Grepioni, K. D. M. Harris, G. Hyett, W. Jones, A. Krebs, J. Mack, L. Maini, A. G. Orpen, I. P. Parkin, W. C. Shearouse, J. W. Steed and D. C. Waddell, *Chem. Soc. Rev.*, 2012, **41**, 413-447.
2. C. E. Chang and W. R. Wilcox, *J. Cryst. Growth*, 1974, **21**, 135-140.
3. K. Byrappa and K. Ohachi, 2003, ISBN 0-8155-1453-0, *Crystal growth technology*, Elsevier.
4. W. Friedrich, P. Knipping and M. Laue, *Ann. Phys.-Berlin*, 1913, **41**, 971-988.
5. H. Berger, *X-Ray Spectrom.*, 1986, **15**, 241-243.
6. L. E. Smart and E. A. Moore, 2005, ISBN 0-7487-7516-1, *Solid state chemistry, an introduction*, Chapter 2. Chapman and Hall.
7. C. Hammond, 1997, ISBN 0-19-855966-6, *The basics of crystallography and diffraction*. Oxford University Press Inc.
8. H. P. Myers, 1997, ISBN 0-7484-0660-3, *Introductory solid state physics*. Taylor & Francis. 27-39 and 275-280.
9. T. Hahn, 2006, ISBN 978-0-79236590-4, *International Tables for Crystallography: Volume A Space group symmetry*. Springer-Verlag.
10. M. T. Weller, 2004, ISBN 0-19-855798-1, *Inorganic materials chemistry*. Oxford University Press Inc.
11. A. R. West, 1988, ISBN 0-471-91798-2, *Basic solid state chemistry*, Jonh Wiley & Sons Ltd.
12. G. E. Bacon, 1975, ISBN 0198513534, *Neutron diffraction*. Clarendon Press. 1-649.
13. <http://icsd.cds.rsc.org/search/basic.xhtml>, accessed on 3rd September 2015.
14. A. C. Larson and R. B. Von Dreele, 1994, *General Structure Analysis System (GSAS)*, Los Alamos National Laboratory Report LAUR, 86-748.
15. B. H. Toby, *J. Appl. Crystallogr.*, 2001, **34**, 210-213.

16. D. R. Allan, S. P. Collins, G. Evans, D. Hall, K. McAuley, R. L. Owen, T. Sorensen, C. C. Tang, F. von Delft, A. Wagner and H. Wilhelm, *Eur. Phys. J.*, 2015, **130**, 1-20.
17. S. P. Thompson, J. E. Parker, J. Potter, T. P. Hill, A. Birt, T. M. Cobb, F. Yuan and C. C. Tang, *Rev. Sci. Instrum.*, 2009, **80**, 075107.
18. C. C. Wilson, 2000, ISBN 981-02-3776-6, Single crystal neutron diffraction from molecular materials. World Scientific Publishing Co. Pte. Ltd. 53-81.
19. W. Reimers, A. R. Pyzalla, A. Schreyer and H. Clemens, 2008, ISBN 978-3-527-31533-8, Neutrons and synchrotron radiation in engineering materials science: from fundamentals to material and component characterisation. Wiley-VCH Verlag GmbH & Co. KGAA. 91-97.
20. V. F. Sears, *Neutron news*, 1992, **3**, 29-37.
21. W. G. Williams, R. M. Ibberson, P. Day and J. E. Enderby, *Physica B*, 1997, **241**, 234-236.
22. A. C. Hannon, *Nucl. Instrum. Meth. A.*, 2005, **551**, 88-107.
23. L. B. McCusker, R. B. Von Dreele, D. E. Cox, D. Louer and P. Scardi, *J. Appl. Crystallogr.*, 1999, **32**, 36-50.
24. R. A. Young, 1993, ISBN 0-19-855577-6, The rietveld method. Oxford University Press Inc.
25. P. W. Stephen, *J. Appl. Crystallogr.*, 1999, **32**, 281-289.
26. V. Petricek, M. Dusek and L. Palatinus, *Z. Kristall.*, 2014, **229**, 345-352.
27. C. E. Housecroft and A. G. Sharpe, 2001, ISBN 0-582-31080-6, Inorganic chemistry. Peason Education.
28. M. S. Amer, 2010, ISBN 978-1-84755-240-2, Raman spectroscopy, fullerenes and nanotechnology. The Royal Society of Chemistry. 43-95.
29. S. Gomes, H. Hagemann and K. Yvon, *J. Alloy. Compd.*, 2002, **346**, 206-210.
30. E. A. Nickel, 2010, Structural and thermogravimetric studies of group I and II borohydrides, Thesis submitted to the University of Oxford, 1-344.
31. E. L. Charsley and S. B. Warrington, 1992, ISBN 0-85186-375-2, Thermal analysis, Tehcniques & applications. The Royal Society of Chemistry. 17-31, 84-108.
32. F. W. Fifield and D. Kealey, 2000, ISBN 0-632-05384-4, Principles and Practice of Analytical Chemistry. Blackwell Science Ltd. 428-429.
33. H. D. ErtuğruL and Z. O. Uygun, 2013, ISBN 978-953-51-1004-0, Impedimetric biosensors for label-free and enzymless detection. CCBY3.
34. J. R. Macdonald and R. L. Hurt, *J. Electroanal. Chem.*, 1986, **200**, 69-82.
35. D. P. Almond, G. K. Duncan and A. R. West, *Solid State Ionics.*, 1983, **8**, 159-164.
36. P. G. Bruce, *J. Electroanal. Chem.*, 1984, **181**, 289-294.
37. A. R. West, D. C. Sinclair and N. Hirose, *J. Electroceram.*, 1997, **1**, 65-71.

3. Structural analysis of the fast ionic and high temperature phase of LiBH₄ stabilised by anion substitution

3.1 Introduction

Lithium borohydride is used to a limited extent in organic synthesis as a selective reducing agent for esters.¹ This hydride can be synthesised from the metathesis of sodium borohydride and lithium halides in isopropylamine under reflux (equation (3.1)).²



This material has been suggested as a candidate for hydrogen storage for mobile applications as it has larger gravimetric and volumetric hydrogen density (Table 3.1-1) compared to other alkali metal tetraborohydrides.^{3, 4}

Table 3.1-1 Physical properties for alkali metal tetraborohydrides.

Complex	LiBH ₄	NaBH ₄	KBH ₄
M (g mol ⁻¹)	21.78	37.83	53.94
Density (g cm ⁻³)	0.66	1.07	1.17
Hydrogen density (mass %)	18.36	10.57	7.42
Hydrogen density (kg m ⁻³)	122.5	113.1	87.1
T _m (°C)	268	505	585
ΔH _f ⁰ (kJ mol ⁻¹)	-194	-191	-229

LiBH₄ releases 13.8 mass % of H₂ by decomposition into LiH and B according to the following reaction:



The enthalpy and entropy for equation (3.2) are -103.4 kJ mol⁻¹ and 150 J K⁻¹ mol⁻¹, respectively.⁵

Recently it was discovered that lithium borohydride can also be considered as a solid state electrolyte.⁶ Four LiBH₄ phases are known, two at ambient and two at high pressure (Figure 3.1-1).

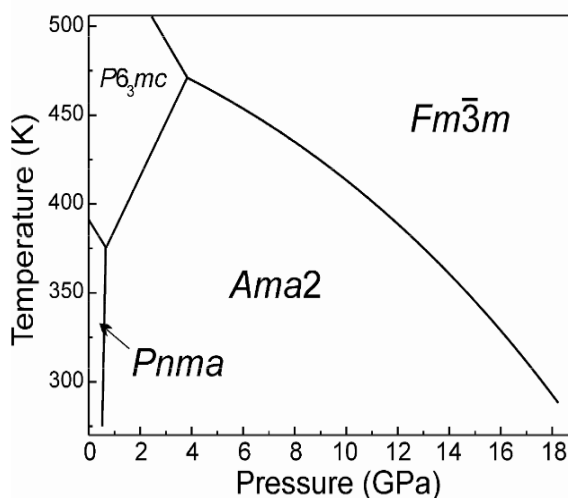


Figure 3.1-1 Pressure-Temperature phase diagram of LiBH₄.⁷

At ambient pressure the hydride can be found with orthorhombic (low temperature phase, LT) and hexagonal (high temperature phase, HT) structures. In the LT orthorhombic structure [space group *Pnma*, $a = 7.17858(4)$, $b = 4.43686(2)$, $c = 6.80321(4)$ Å, $V = 216.685(3)$ Å³, $Z = 4$], each (BH₄⁻) anion is surrounded by four lithium ions and each lithium atom is surrounded by four (BH₄⁻) anions. This arrangement corresponds to distorted wurtzite type structure in which the tetrahedral anions point along two orthogonal directions in an ordered fashion (Figure 3.1-2 (a)).⁸ In comparison, the other alkali metal borohydrides (ABH₄, A = Na, K, Rb, Cs) crystallise with a cubic rock-salt type structure at room temperature where (BH₄⁻) anions are octahedrally surrounded by cations.^{9, 10} LT LiBH₄ does not show high ionic conductivity *ca.* 10⁻⁸ S cm⁻¹ and it has been the focus of recent studies to improve the performance of LiBH₄ for use as an electrolyte Li batteries. At 110 °C the hydride undergoes a phase transition to a hexagonal structure [space group *P6₃mc*, $a = 4.27631(5)$, $c = 6.94844(8)$ Å, $V = 110.041(4)$ Å³, $Z = 2$] (Figure 3.1-1). The Li⁺ ions and BH₄⁻ anions remain tetrahedrally coordinated and the HT phase retains the wurtzite type arrangement of the ions above the phase transition (Figure 3.1-2, (b)). During the phase transition the structure contracts along the orthorhombic *a* direction (hexagonal, *c* direction) and expands in the orthorhombic *bc* plane (hexagonal basal phase).⁸ The HT phase exhibits high ionic conductivity, about five orders of magnitude higher than the LT phase. There are some reports in the literature

regarding the stabilisation of this phase at room temperature. By the addition of lithium halides it has been demonstrated that this material can be stabilised at room temperature and in the process the conductivity can be enhanced.^{11,12,13}

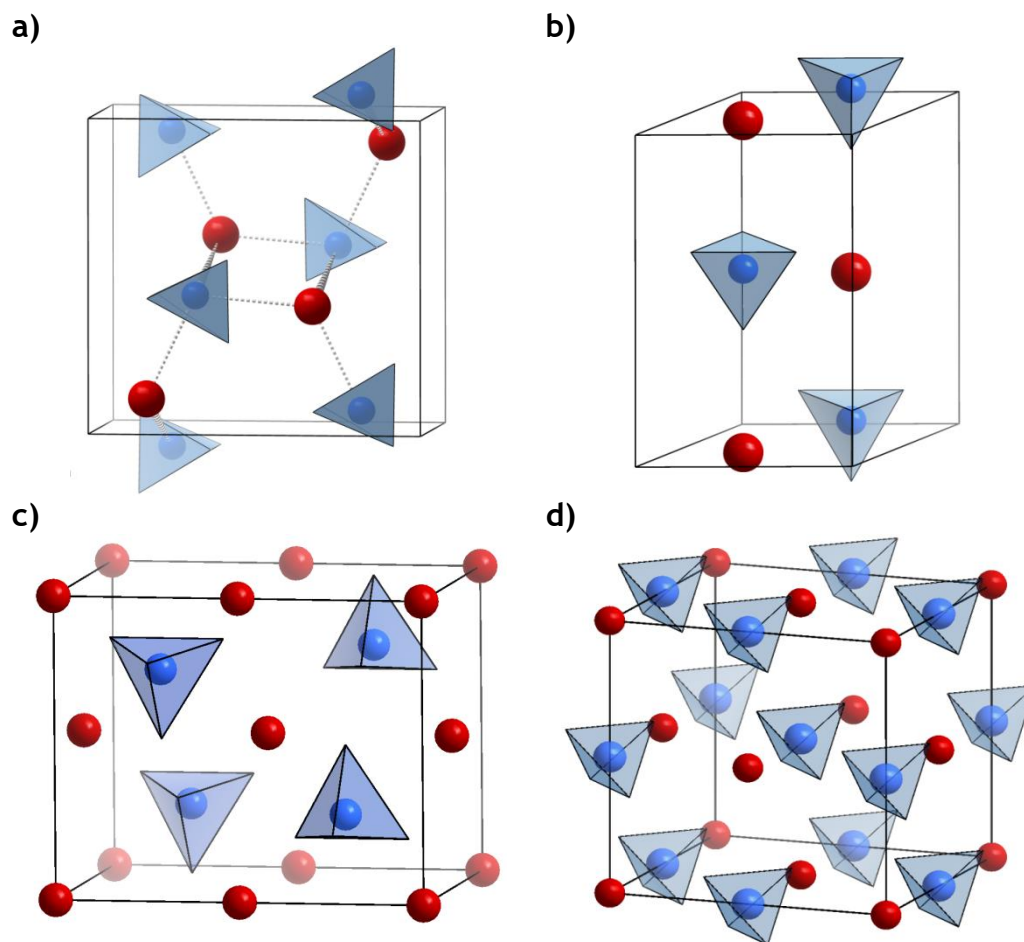


Figure 3.1-2 Crystal structures of a) LT b) HT c) AT - LP and d) HP phases of LiBH_4 , respectively (Li^+ ions are shown in red and BH_4^- in blue tetrahedra).

At room temperature and a pressure of 1.2 GPa (Figure 3.1-1), LiBH_4 undergoes a phase transition and becomes pseudo-tetragonal (space group $Ama2$, ambient temperature - low pressure phase, AT - LP).^{7, 14, 15} It can be considered as an orthorhombically distorted antistructure of PtS, where Li^+ ions are tetrahedrally coordinated by BH_4^- anions and the BH_4^- anions adopt a totally new nearly square-planar coordination to four Li^+ ions (Figure 3.1-2, (c)). This phase has not caused much interest because the increase in ionic conductivity relative to the LT phase, is only one order of magnitude at 6 GPa. Above 10 GPa LiBH_4 undergoes a further phase transition, forming a rock-salt type structure (space group $Fm\bar{3}m$, high temperature

- pressure phase, HP) (Figure 3.1-1). Li^+ ions and BH_4^- anions are octahedrally coordinated (Figure 3.1-2, (d)).⁷ This phase can show high ionic conductivity, about four orders of magnitude higher than the LT phase, $10^{-3} \text{ S cm}^{-1}$ at 4 GPa. This phase has resulted in a great deal of interest and some groups have tried to stabilise it at room temperature (Figure 3.1-3).¹⁶

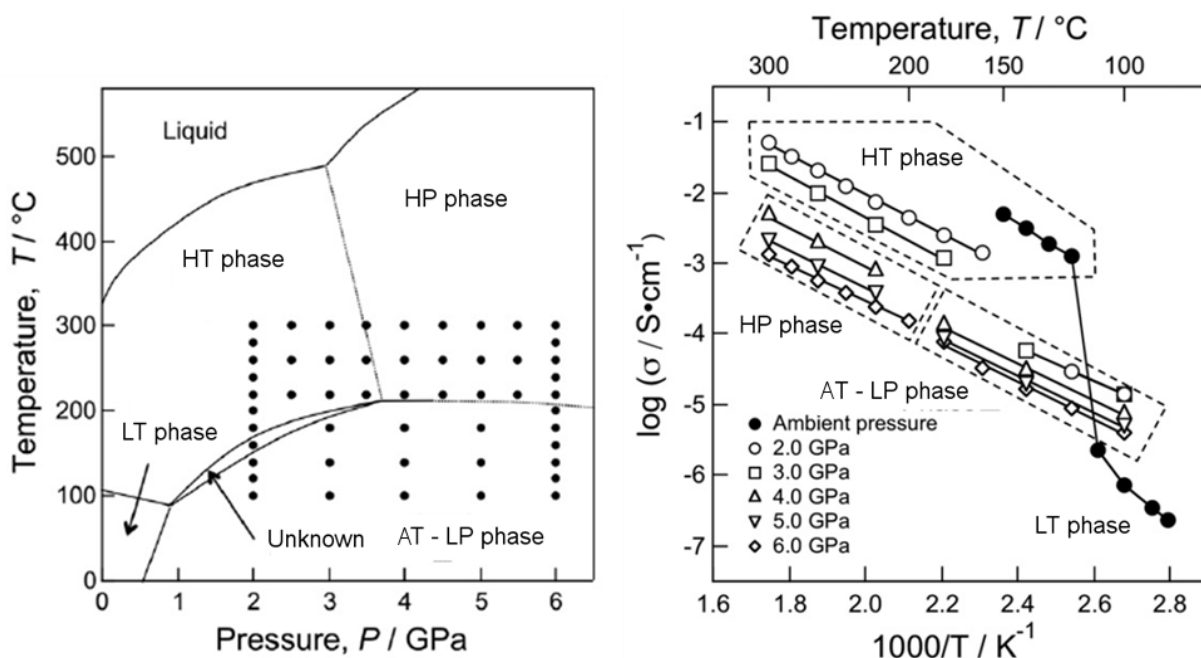


Figure 3.1-3 a) Phase diagram of LiBH_4 depending on the temperature and pressure (dots represent where conductivity measurements were undertaken) and b) Conductivity of LiBH_4 phases.¹⁵

The structure of the HT phase of LiBH_4 contains considerable disorder in the anion orientation and has been the subject of experimental and theoretical studies.^{17,18,19} Several models and interpretations have been proposed to explain the behaviour of the BH_4^- units in the fast Li^+ conducting material. Various degrees of dynamic orientational disorder have been proposed from the 3-fold rotation of BH_4^- about a single B - H bond (possibly combined with occasional exchange between rotationally disordered H atoms and the fixed H atom) to unconstrained, free rotation of all H atoms to give an effectively spherical anion.^{20, 21,22} Attempts have been made to stabilize the hexagonal phase at room temperature using anion substitution. Partial anion replacement, by mechanical and thermal reaction with appropriate halides, leads to the formation of the hexagonal structure analogous to the HT phase of LiBH_4 .^{11,12,13} However, the HT phase substituted by bromide substitution has never been isolated at room temperature as a single phase. This chapter will discuss two

preparative methods that can produce phase pure samples of the fast ion conductive phase with controlled molar ratios $0.29 \leq x \leq 0.50$ in the series $\text{Li}(\text{BH}_4)_{1-x}\text{Br}_x$. These materials have been obtained by either extensively mechanically milling a mixture of LiBH_4 and LiBr or by combining a shortened milling with thermal treatment. These data have been used to compile a phase diagram for the full compositional series $\text{Li}(\text{BH}_4)_{1-x}\text{Br}_x$. The discussion of a detailed structural model of the orientational disorder of the BH_4^- anion in the fast Li^+ conducting hexagonal phase is discussed.

3.2 Experimental

3.2.1 Synthesis

The synthesis of the HT phase of LiBH_4 , stabilised by anion substitution, was performed in a nitrogen atmosphere using a Retsch PM100 ball mill. Anhydrous LiBH_4 (Sigma-Aldrich, $\geq 95\%$) and LiBr (Sigma-Aldrich, $\geq 99\%$) were obtained commercially and used directly without further purification. Approximately 0.5 g LiBH_4 - LiBr mixtures were mechanically milled. The ball milling was performed in periods of 2 min of milling interspersed by 2 min breaks to minimise heating of the samples. The sample to ball ratio was 1:40 and both the vial and 10 mm diameter balls were made from stainless steel. The agitation frequency was 500 rpm. The materials were prepared by two different routes: (a) by mechanochemical milling for 24 h or (b) milling for 4 h followed by heating the milled mixtures to 573 K for 5 - 24 h. The longer annealing times were necessary to give a single phase product for higher bromide concentrations (Table 3.2-1 and Table 3.2-2).

Table 3.2-1 Samples prepared by mechanochemical treatment (1 - 8).

Sample	$\text{LiBH}_4 : \text{LiBr}$	Phases
1	4 : 1	LT – LiBH_4 , HT – LiBH_4 , LiBr
2	3 : 1	LT – LiBH_4 , HT – LiBH_4 , LiBr
3	2 : 1	HT – LiBH_4 , LiBr
4	1 : 1	HT – LiBH_4 , LiBr
5	1 : 2	HT – LiBH_4 , LiBr
6	1 : 3	HT – LiBH_4 , LiBr
7	2 : 1 ($^7\text{Li}(^{11}\text{BD}_4) : \text{LiBr}$)	HT – LiBH_4 , LiBr (Sample for GEM experiment)
8	2 : 1 ($^7\text{Li}(^{11}\text{BD}_4) : \text{LiBr}$)	HT – LiBH_4 , LiBr (Sample for D20 experiment)

Table 3.2-2 Sample composition and preparation technique (9 - 17).

Sample	LiBH ₄ : LiBr	Phases	Nominal Composition	Preparation
9	3 : 1	LT – LiBH ₄ , HT – LiBH ₄	Li(BH ₄) _{3/4} Br _{1/4}	MT ^a , TT ^b
10	2.5 : 1	HT – LiBH ₄	Li(BH ₄) _{5/7} Br _{2/7}	MT ^a , TT ^b
11	2 : 1	HT – LiBH ₄	Li(BH ₄) _{2/3} Br _{1/3}	MT ^a , TT ^c
12	1.5 : 1	HT – LiBH ₄	Li(BH ₄) _{3/5} Br _{2/5}	MT ^a , TT ^d
13	1 : 1	HT – LiBH ₄ , LiBr	Li(BH ₄) _{1/2} Br _{1/2}	MT ^a , TT ^e
14	1 : 2	HT – LiBH ₄ , LiBr	Li(BH ₄) _{1/3} Br _{2/3}	MT ^a , TT ^e
15	1 : 3	HT – LiBH ₄ , LiBr	Li(BH ₄) _{1/4} Br _{3/4}	MT ^a , TT ^e
16	2 : 1	HT – LiBH ₄	⁷ Li(¹¹ BD ₄) _{2/3} Br _{1/3}	MT ^a , TT ^e (GEM)
17	2 : 1	HT – LiBH ₄	⁷ Li(¹¹ BD ₄) _{2/3} Br _{1/3}	MT ^a , TT ^e (D20)

Conditions for the mechanochemical treatment (MT): a) 4h. Conditions for the thermal treatment (TT): b) 573 K/5h, c) 573 K/10h and d) 573 K/15h, e) 573 K/20h, heating and cooling ramp at 4 K min⁻¹.

3.2.2 Characterisation

Powder X-ray diffraction data were obtained at room temperature with a Bruker D8 Advance (θ -2 θ) diffractometer using Cu K α radiation ($\lambda = 1.54056 \text{ \AA}$) and a scanning step size of $0.017^\circ 2\theta$ over the angular range $5\text{-}85^\circ 2\theta$ for *ca.* 1 h. Phase identification from the diffraction patterns was made by comparing to powder patterns in the Inorganic Crystal Structure Database (ICSD) using PowderCell 2.4.^{23, 24} Crystallographic parameters were obtained using CELREF and CELL software packages based on least squares refinement fitting.

Raman spectra were collected at room temperature in the range. Conditions of the Raman experiments can be found in section 2.5.1.1.

Sample morphology and composition were studied using SEM (XL 30 ESEM, Philips, 25 kV accelerating voltage) (section 2.6.1).

Thermal analysis was carried out using a NETZSCH STA 409PC coupled with a HIDEN HPR20 mass spectrometer to determine the stability of the HT phase of LiBH₄ at high temperatures in an inert atmosphere. Samples were heated in a silica pan from room temperature to 573 K at 5 K min⁻¹.

The sample for the neutron scattering experiment was isotopically enriched with D, ⁷Li and ¹¹B to avoid problems with incoherent neutron scattering and

absorption. Anhydrous ${}^7\text{Li}{}^{11}\text{BD}_4$ (Katchem, >99.8 % ${}^7\text{Li}$, >99.8 % ${}^{11}\text{B}$, >98% D) and LiBr (Sigma-Aldrich, $\geq 99\%$) were obtained commercially and used directly without further purification. Samples (1.0 g) were prepared by ball milling and thermal heating with longer heating times being necessary due to the larger quantity of material being prepared. Since the sample is air-sensitive, it was loaded into a sealed vanadium can in an inert atmosphere glovebox before the experiment.

Time-of-flight powder neutron diffraction data were collected between 293-573 K using the General Materials diffractometer, GEM, at the ISIS neutron source at the Rutherford Appleton Laboratory in Oxfordshire (Table 3.2-3).²⁵ Samples were contained in vanadium cans with a diameter of 6 mm. Using a standard procedure, the data from each of the instrument's detector banks were corrected for absorption, normalized to account for the incident neutron spectrum and detector efficiencies and summed.²⁵ The data were analysed using Rietveld refinement as implemented in the GSAS software package²⁶ via the EXPGUI interface²⁷ against multiple data sets.

Table 3.2-3 Summary of PND data collected from GEM at different temperatures (16a-16b) for sample 16.

Sample	16a	16b
Temperature / K	293	393

Constant wavelength in-situ data were collected from the D20 instrument at the "Institut Laue-Langevin" (ILL) in Grenoble. The sample was contained in a vanadium can (6 mm *id.*), sealed with copper wire. The neutron diffraction sample preparation was carried out in an MBraun argon filled glovebox. Data collection was performed at high resolution ($\lambda = 1.54 \text{ \AA}$, 118° take-off angle and using a Ge (335) monochromator) while the sample was cooled down under vacuum at temperatures ranging from 300 to 2 K (Table 3.3-11).

Electrochemical impedance measurements were performed on cylindrical sample pellets of 13 mm diameter and 1-2 mm thickness that had been formed by pressing at room temperature under a load of 1 tonne for 20 min. A platinum paste was applied to opposite faces of the pellet to make electrical contacts. Data were collected on heating and the temperature of the system was allowed to equilibrate

for at least 1 h before every data collection. Data were collected using a Solartron 1260 impedance analyser and were analysed using equivalent circuit analysis as implemented in the ZView2 software package.

3.3 Results and discussion

3.3.1 Ball milling

3.3.1.1 Powder X-ray diffraction

Combinations of mechanical and thermal treatments were used for the stabilisation of the HT - phase of LiBH_4 at room temperature. Figure 3.3-1 shows the patterns from LiBH_4 - LiBr mixtures milled with different molar ratios. Three different phases are observed at a high content of LiBH_4 (1 and 2), which correspond to LT - LiBH_4 , HT - LiBH_4 and LiBr phases. At higher content of LiBr (3 - 6) the LT - LiBH_4 phase content is reduced and HT - LiBH_4 and LiBr phases predominate. However if the amount of LiBr is increased further the quantity of the HT - LiBH_4 phase is decreased and the formation of a cubic LiBr -type phase is preferred (Table 3.2-1).

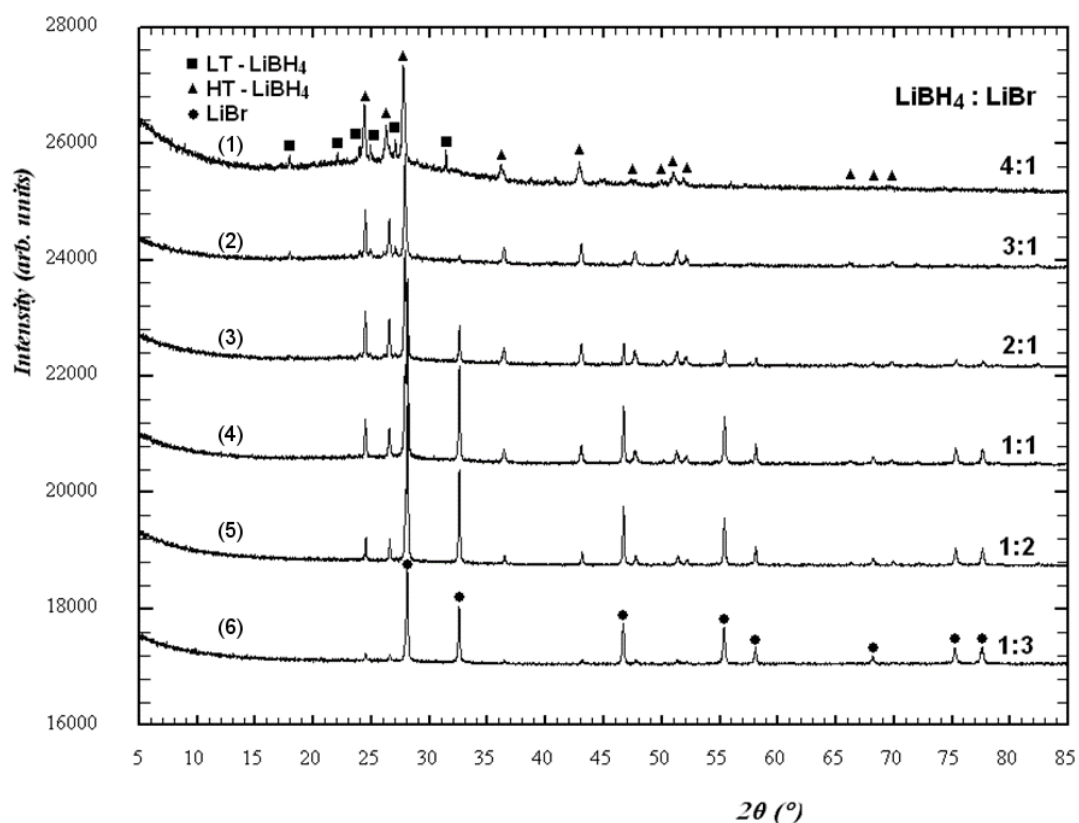


Figure 3.3-1 Powder X-ray diffraction patterns of $\text{Li}(\text{BH}_4)_{1-x}\text{Br}_x$ mixtures after ball-milling. (From top to bottom in terms of LiBH_4 : LiBr ratio: 4:1 (1), 3:1 (2), 2:1 (3), 1:1 (4), 1:2 (5), 1:3 (6)).

Raman spectroscopy was used to follow the transition between the LT and the HT - LiBH_4 phases. Raman spectroscopy is sensitive to the transition of LiBH_4 from orthorhombic to hexagonal *via* the characteristic B - H bending mode splitting at $\nu_2 = 1282 \text{ cm}^{-1}$ and $\nu_2' = 1297 \text{ cm}^{-1}$ in the lower symmetry structure.^{8,28,29,30} Data from the bromide-doped samples show that the intensity of the orthorhombic phase decreases as the Br content increases (Figure 3.3-2 and Figure 3.3-3).

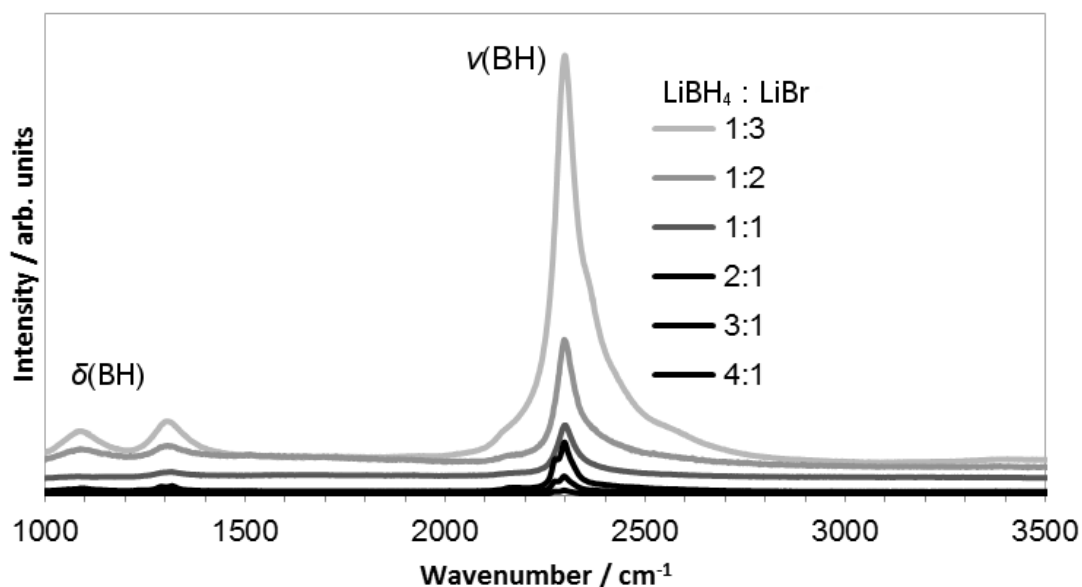


Figure 3.3-2 Raman spectrum of HT - $\text{Li}(\text{BH}_4)_{1-x}\text{Br}_x$ ball milled for 4 h AT 500 rpm. ν = stretching, δ = deformation: bending and torsional modes).

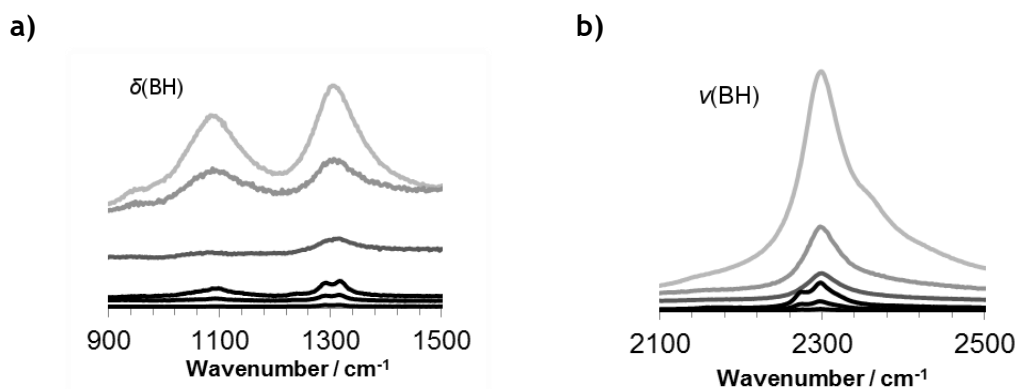


Figure 3.3-3 Raman spectra of HT - $\text{Li}(\text{BH}_4)_{1-x}\text{Br}_x$ a) from 900 – 1500 cm^{-1} b) from 2100 – 2500 cm^{-1} (ν = stretching, δ = deformation: bending and torsional modes).

3.3.2 Ball milling and thermal treatment

The milled mixtures were subsequently heated to 573 K for 5 - 24 h. The longer annealing times were necessary to give a single phase product (HT - LiBH₄ type) for higher bromide concentrations (Table 3.2-2).

PXD was used to characterise the materials prepared. Inspection of the diffraction patterns collected from samples across the compositional series showed that all Bragg peaks could be indexed to one of three phases (Figure 3.3-4). At high content of LiBH₄ (9) LT - LiBH₄ and HT- LiBH₄ type phases can be indexed. The HT - LiBH₄ is isolated with a single phase of composition (10 - 13). At higher Br content (15) the HT - LiBH₄ is no longer observed and the cubic phase of LiBr increases (Figure 3.3-4).

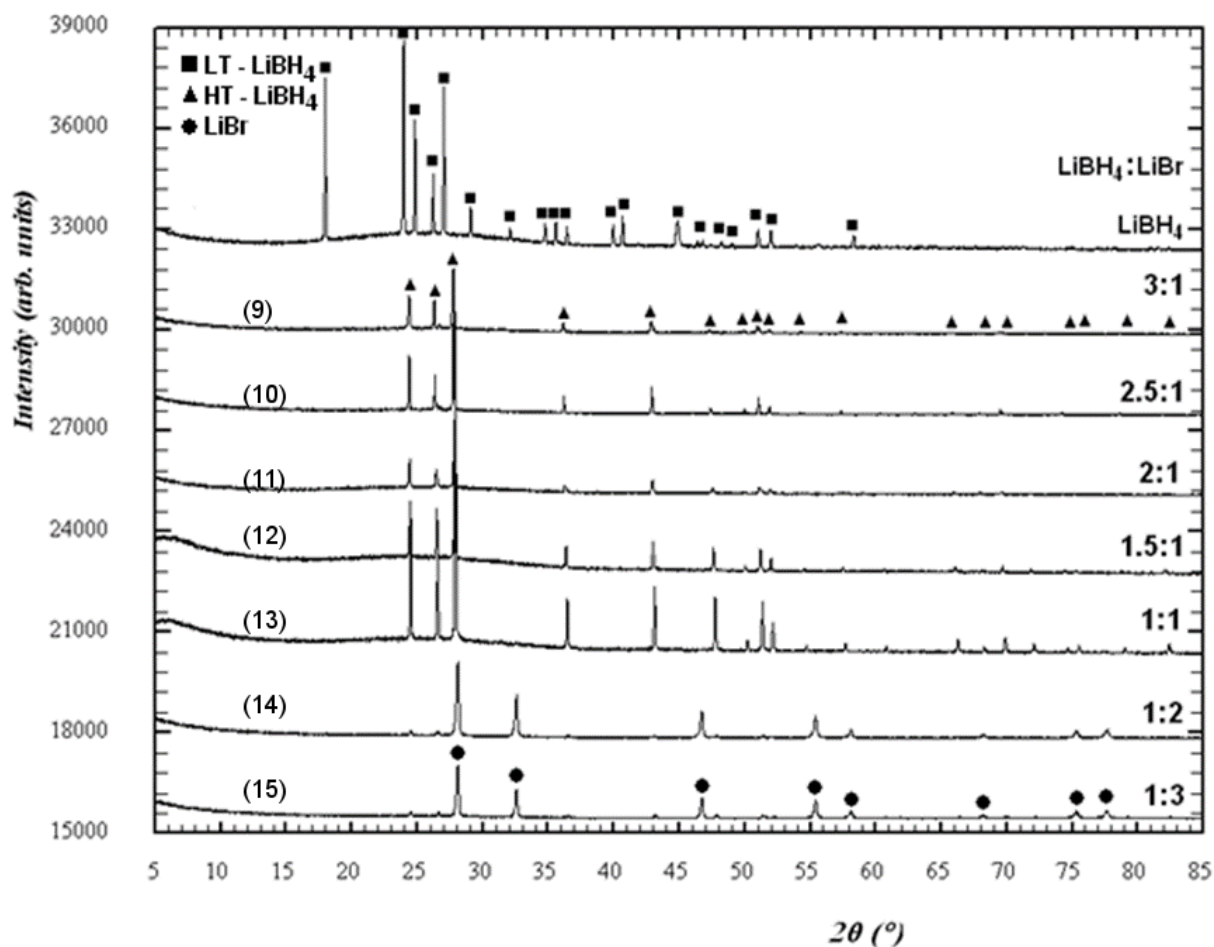


Figure 3.3-4 Powder X-ray diffraction patterns of Li(BH₄)_{1-x}Br_x mixtures after ball-milling and thermal treatment. (From top to bottom in terms of LiBH₄:LiBr ratio: 3:1 (9), 2.5:1 (10), 2:1 (11), 1.5:1 (12), 1:1 (13), 1:2 (14), 1:3 (15)).

Raman spectroscopy was used to identify and confirm the HT - LiBH₄ type phase. In Figure 3.3-5 the Raman spectrum of LT - LiBH₄ is compared with that of HT - LiBH₄.

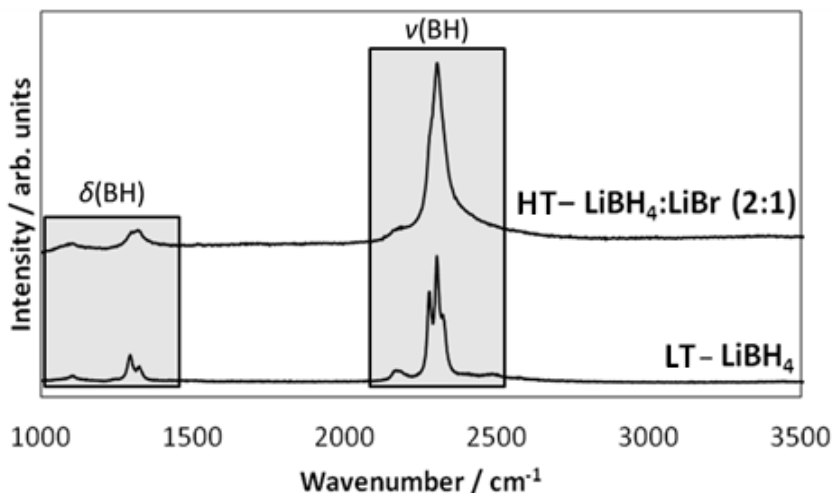


Figure 3.3-5 Raman spectrum of HT - Li(BH₄)_{2/3}Br_{1/3} and a comparison with the corresponding spectrum of LT - LiBH₄ (ν = stretching, δ = deformation: bending and torsional modes).

3.3.3 Ball milling treatment only

Alternatively, the HT LiBH₄ phase can be stabilised at room temperature using only mechanochemical treatment at extended milling times (Table 3.3-1).

Table 3.3-1 Sample Li(BH₄)_{2/3}Br_{1/3} milled for different times (18 - 22).

Sample	Time (h)	Phases
18	4	LT - LiBH ₄ , HT - LiBH ₄ , LiBr
19	8	HT - LiBH ₄ , LiBr
20	12	HT - LiBH ₄ , LiBr
21	16	HT - LiBH ₄ , LiBr
22	24	HT - LiBH ₄

For samples with $x = 0.33$ using a shorter ball milling duration (**18**), LiBH₄ - LiBr mixture yielded three different phases: LT - LiBH₄, HT - LiBH₄ and LiBr. However if the milling time was doubled, an LT - LiBH₄ phase is not formed and an HT - LiBH₄ type phase and LiBr are the products (**19**). In order to obtain a single phase of the HT - LiBH₄ type material, the mechanochemical reaction needs to be performed for at least 3 times longer (**22**) (Figure 3.3-6).

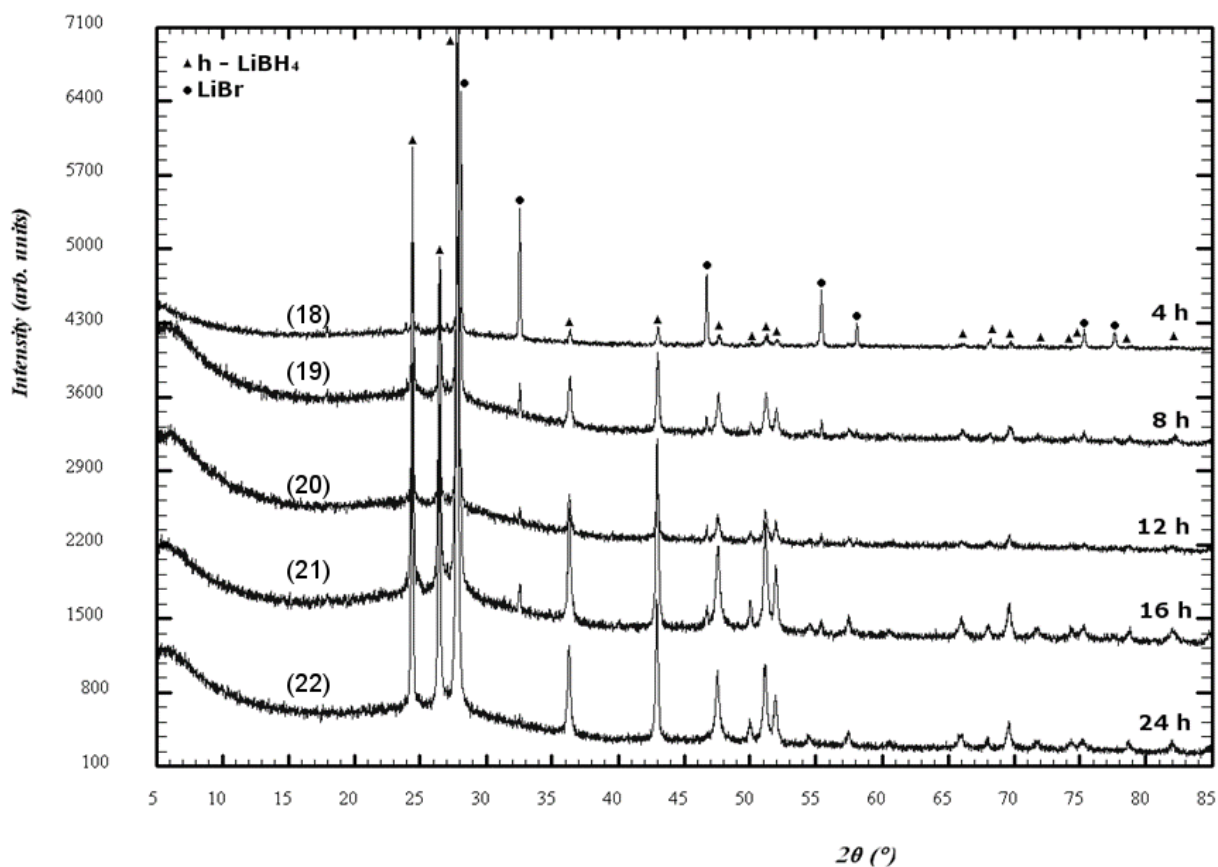


Figure 3.3-6 Powder X-ray diffraction patterns of $\text{Li}(\text{BH}_4)_{2/3}\text{Br}_{1/3}$ mixture ($\text{LiBH}_4:\text{LiBr}$, 2:1) after ball-milling for different periods of time. (From top to bottom in terms of ball milling time: 4 h (18), 8 h (19), 12 h (20), 16 h (21), 24 h (22)).

3.3.4 Scanning electron microscopy

Examination of the samples using scanning electron microscopy reveals particle morphologies that bear little resemblance to those of either of the reagents (LiBH_4 and LiBr), large round microparticles. As noted above, $\text{Li}(\text{BH}_4)_{2/3}\text{Br}_{1/3}$ can be prepared either by extensive milling (22) or by a reduced period of milling followed by thermal treatment (at 573 K) (11). Micrographs from samples prepared *via* these 2 routes revealed that milling only leads to well defined petal-like structures agglomerated into discrete, relatively uniform and almost spherical aggregates. Each sphere is in the region of 50 μm in diameter. The effect of a combined milling and thermal treatment is to give more homogenous, mono-dispersed particles as shown in (Figure 3.3-7).

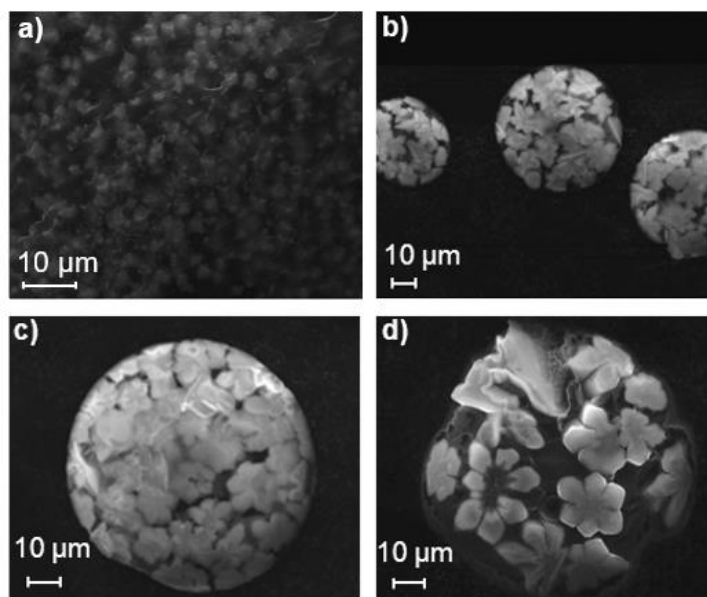


Figure 3.3-7 SEM images from $\text{Li}(\text{BH}_4)_{2/3}\text{Br}_{1/3}$ prepared by: a) milling and thermal treatment; b), c) and d) milling only.

3.3.5 Phase diagram of the $\text{LiBH}_4 - \text{LiBr}$ system

PXD was used to characterize the materials prepared by both the extended milling and milling/heating routes. Inspection of the diffraction patterns collected from samples across the compositional series showed that all Bragg peaks could be indexed to one of three phases (Table 3.3-2). Lattice parameters and the cell volume of each structure over five different regions were obtained.

Table 3.3-2 Structural results from PXRD (23 - 33).

Sample	Nominal composition, x	Phases	Phase fractions	Lattice parameters / Å	Cell Volume, $V / \text{Å}^3$
23	0 (LiBH ₄)	LT-LiBH ₄	100 %	$a = 7.17858(4)$ $b = 4.43686(2)$ $c = 6.80321(4)$	216.685(3)
24	0.09	LT-LiBH ₄	100 %	$a = 7.152(8)$ $b = 4.420(7)$ $c = 6.856(1)$	216.5(5)
25	0.20	LT-LiBH ₄ ,	5.5(6) %	$a = 7.15(1)$ $b = 4.43(1)$ $c = 6.81(1)$	216.0(8)
		HT-LiBH ₄	94.54(7) %	$a = 4.2213(4)$ $c = 6.8041(8)$	105.00(2)
26	0.25	LT-LiBH ₄ ,	5.7(8) %	$a = 7.143(1)$ $b = 4.4216(8)$ $c = 6.8313(8)$	215.76(6)
		HT-LiBH ₄	94.26(6) %	$a = 4.2156(1)$ $c = 6.7763(3)$	104.290(5)
27	0.29	HT-LiBH ₄	100 %	$a = 4.2123(2)$ $c = 6.7613(4)$	103.90(1)
28	0.33	HT-LiBH ₄	100 %	$a = 4.20656(2)$ $c = 6.7321(4)$	103.17(1)
29	0.40	HT-LiBH ₄	100 %	$a = 4.20491(1)$ $c = 6.7244(2)$	102.967(3)
30	0.50	HT-LiBH ₄	100 %	$a = 4.19903(6)$ $c = 6.7244(2)$	102.967(3)
31	0.67	HT-LiBH ₄ ,	24.8(1) %	$a = 4.19550(7)$ $c = 6.7003(1)$	102.139(4)
		LiBr	75.2(3) %	$a = 5.4959(2)$	166.01(2)
32	0.75	HT-LiBH ₄ ,	17.52(5) %	$a = 4.1924(5)$ $c = 6.700(1)$	101.99(2)
		LiBr	82.48(1) %	$a = 5.4959(2)$	166.00(2)
33	1 (LiBr)	LiBr	100 %	$a = 5.4942(9)$	165.858(8)

In composition region I, for the most (BH₄)⁻-rich composition ($0 \leq x < 0.20$, **23** and **24**) only on LT - LiBH₄ type phase is observed. From $x = 0.20$ (region II, **25** and **26**) two different phases are observed (LT - LiBH₄ and HT - LiBH₄ type). Only the cell

volume for the HT - LiBH_4 phase was calculated because the diffraction peaks of LT - LiBH_4 were too weak in intensity to be indexed accurately. However at $0.29 \leq x < 0.50$ (region III, 27 - 30) HT - LiBH_4 type phases can be isolated at room temperature as single phases. If the amount of bromide is increased further, the cubic LiBr co-exist (region IV, 31 and 32), finally in region V (33) LiBr is obtained as a single phase. Although from the compositions discovered in region IV, we believe that LiBr is not a line phase ($\text{Li}(\text{Br},\text{BH}_4)$ exists with the LiBr structure), the precise position of the phase boundary (IV-V) is yet to be determined. For each of the orthorhombic, hexagonal and cubic phases (regions I, III, V) there is a progressive decrease in the cell volume as the Br content is increased.

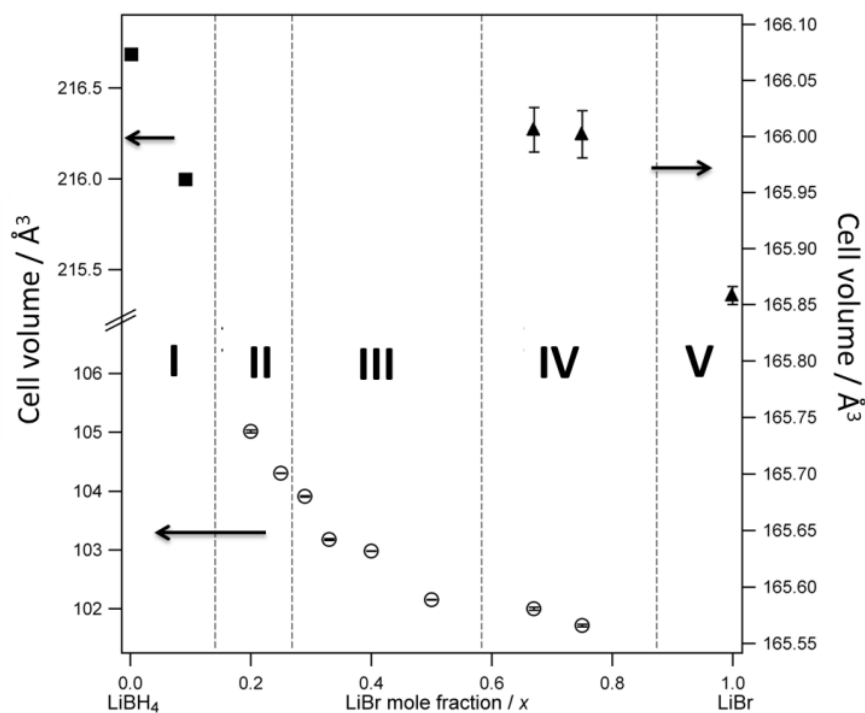


Figure 3.3-8 Structure field map manifested as the respective unit cell volumes as a function of LiBr mole fraction in $\text{Li}(\text{BH}_4)_{1-x}\text{Br}_x$. I-V represent the distinct phase regions within compositional space. Black squares denote the LT orthorhombic LiBH_4 structure (top-left y axis); open circles denote the HT hexagonal LiBH_4 structure (bottom-left y axis); black triangles denote the cubic LiBr (NaCl-type) structure (right y axis).

3.3.6 Thermal stability

The thermal stability of one single composition that was only ball milled was studied, $\text{Li}(\text{BH}_4)_{2/3}\text{Br}_{1/3}$ (**3**). Sample **3** was heated from room temperature to 573 K at 5 K min^{-1} and it was held at this temperature for 2 h. After milling three different phases were observed for **3** which correspond to the LT - LiBH_4 , HT - LiBH_4 and LiBr

type phases. As soon as the sample is heated at 368(1) K an endothermic event occurs. This originates from the transformation of LT - LiBH_4 to HT - LiBH_4 . This material did not show a melting transition or any weight change below 573 K and therefore is stable up to this temperature.

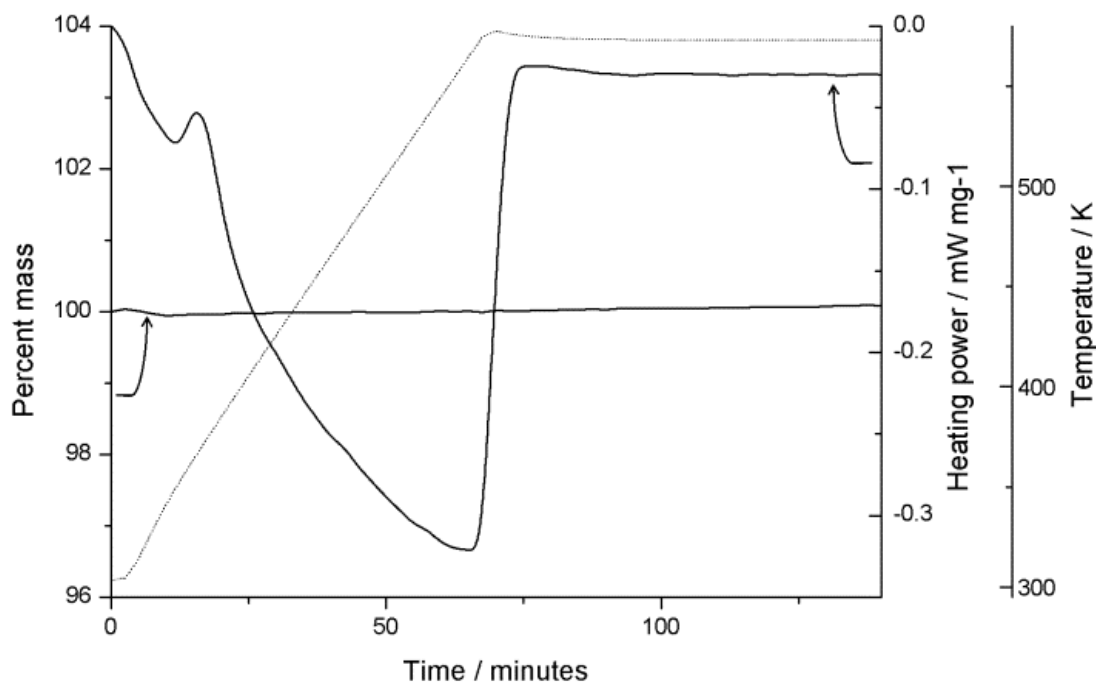


Figure 3.3-9 TG-DTA profile of milled $\text{Li}(\text{BH}_4)_{2/3}\text{Br}_{1/3}$ on heating from room temperature to 573 K. The temperature is indicated by the dotted line.

3.3.7 Electrochemical impedance spectroscopy

Impedance data analysed in the complex plane showed the semicircle at high frequencies and the linear response at low frequencies characteristic of ionic conductivity and ion blocking electrodes. At lower temperatures two semicircles were observed, suggesting intra- and inter-grain transport could be resolved. However, the high frequency semicircle moved out of the measurement range at higher temperatures and so the data were analysed using an equivalent electrical circuit to extract the values for the total resistivity of the material (Figure 3.3-10 and Figure 3.3-11). As shown in Figure 3.3-12, the mixed borohydrides demonstrate conductivities of $\text{ca. } 10^{-6} \text{ S cm}^{-1}$ at 313 K, two orders of magnitude higher than the orthorhombic phase of LiBH_4 .⁶ At 413 K the lithium ionic conductivity is $\text{ca. } 10^{-4} \text{ S cm}^{-1}$. The activation energies for these materials vary in the range of 0.52(2) - 0.64(1) eV (Table 3.3-3). The $x = 1/3$ material was prepared both by extended milling and

milling/thermal routes. The latter method notably led to a higher value of conductivity.

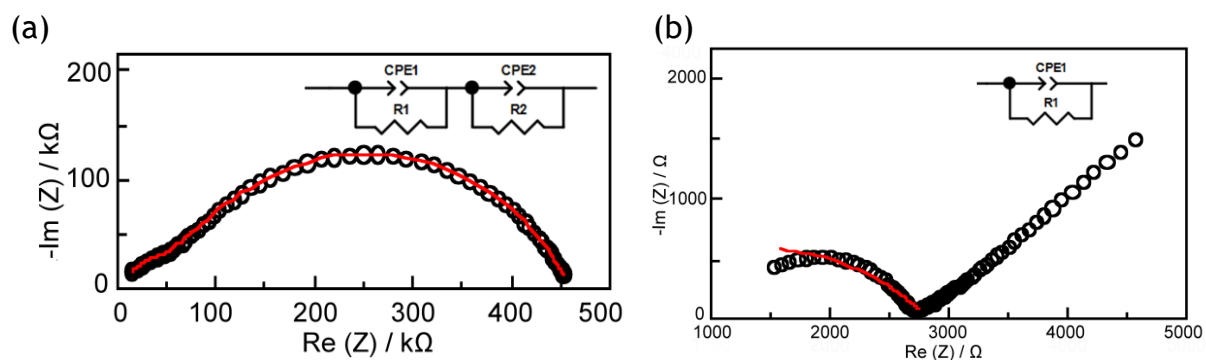


Figure 3.3-10 Impedance data collected from $\text{Li}(\text{BH}_4)_{2/3}\text{Br}_{1/3}$ (MT/TT) (11) (a) at room temperature and (b) at 140 °C (right side). The data can be fitted using equivalent circuits as shown.

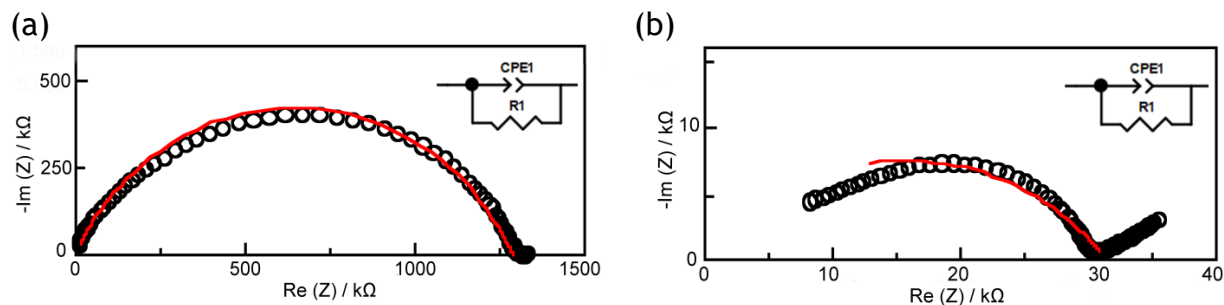


Figure 3.3-11 Impedance data collected from $\text{Li}(\text{BH}_4)_{2/3}\text{Br}_{1/3}$ (MT) (24) (a) at room temperature and (b) at 140 °C (right side). The data can be fitted using equivalent circuits as shown.

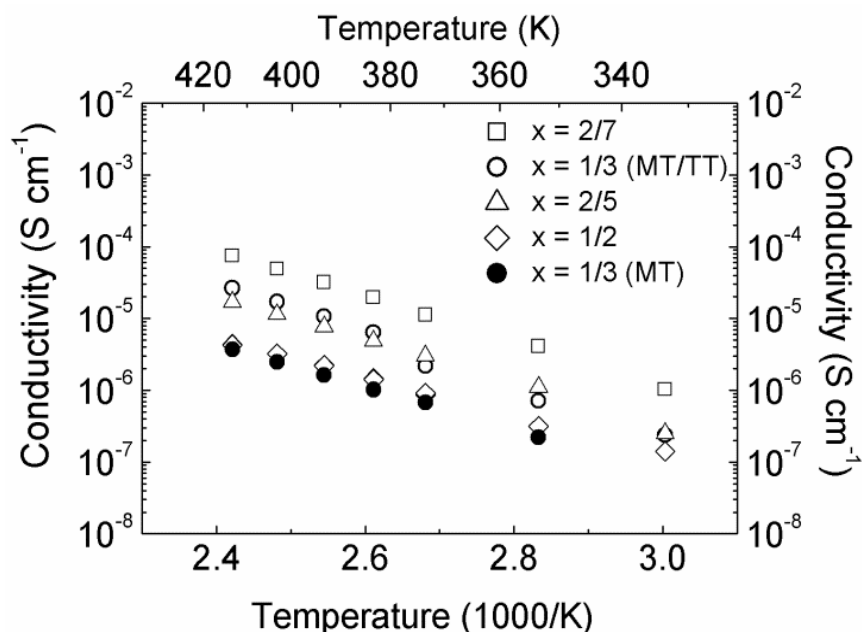


Figure 3.3-12 Plot of conductivity as a function of temperature for $\text{Li}(\text{BH}_4)_{(1-x)}\text{Br}_x$ on heating. Compound $x = 1/3$ was prepared by either mechanochemical and thermal treatment (MT/TT) or by MT.

Table 3.3-3 Electrochemical Impedance measurements.

Nominal composition	$\sigma_{40\text{ }^\circ\text{C}} / \text{S cm}^{-1}$	$\sigma_{140\text{ }^\circ\text{C}} / \text{S cm}^{-1}$	Activation energy / eV
Li(BH₄)_{5/7}Br_{2/7}	3.65 x 10 ⁻⁷	7.41 x 10 ⁻⁵	0.64(1)
Li(BH₄)_{2/3}Br_{1/3}	2.35 x 10 ⁻⁷	4.03 x 10 ⁻⁵	0.61(1)
Li(BH₄)_{3/5}Br_{2/5}	9.42 x 10 ⁻⁸	1.70 x 10 ⁻⁵	0.63(1)
Li(BH₄)_{1/2}Br_{1/2}	6.65 x 10 ⁻⁸	4.33 x 10 ⁻⁶	0.52(2)
Li(BH₄)_{2/3}Br_{1/3} (MT)	5.83 x 10 ⁻⁸	3.70 x 10 ⁻⁶	0.52(1)

3.3.8 Powder neutron diffraction at room temperature

Although it was possible to identify the presence of single-phase samples of hexagonal material from the PXD data, it was not possible to gather substantial insight into the structure of the phases due to the dominance of the X-ray scattering by the relatively heavy bromide ion. We therefore undertook powder neutron diffraction experiments in order to elucidate the structural chemistry that underpins the fast ionic conducting hexagonal phase further. For this purpose a single composition, Li(BH₄)_{2/3}Br_{1/3} was studied in detail as a function of temperature.

High quality PND data were collected from isotopically enriched Li(BH₄)_{2/3}Br_{1/3} at room temperature. One existing structural model of the hexagonal phase of LiBH₄ comprises of a fully-ordered array of (BH₄)⁻ tetrahedral anions and Li⁺ cations.⁸ Our interpretation of the neutron diffraction data from Li(BH₄)_{2/3}Br_{1/3} therefore began by attempting to fit this structural model to our data using a randomly disordered arrangement of bromide and (BH₄)⁻ anions with Br and B occupying the same *2b* site (2/3, 1/3, *z*; where *z* ≈ 0.2) in the lattice. This failed to give a satisfactory fit to the data and a Fourier search of the asymmetric unit showed a second scattering centre close to that occupied by the boron and bromine ions. Attempts to refine occupancies on both the sites simultaneously against neutron diffraction data alone were unsuccessful in producing a stable refinement. Therefore laboratory X-ray diffraction data were incorporated into a multiple histogram refinement (Figure 3.3-13). This exploited the strong scattering of X-rays by the bromide anion to give an unambiguous and robust identification of the bromide position and site occupancy. From this point on, our analysis of structure proceeded simultaneously against neutron and X-ray diffraction data sets.

The deuterium atoms were initially assumed to be located on the vertices of a distorted boron-centred tetrahedron with one crystallographically unique atom and the other three related by a threefold rotation about the z direction.²¹ No constraint was imposed on the ratio of BH_4^- to bromide; the refinement was able to proceed freely to select the anion ratio which best modelled the data. The ratio was fixed once the refinement was stable. With the deuterium atoms thus placed, and their fractional occupancies constrained to be the same as the boron atom, the structure was again refined and a Fourier map used to identify deficiencies in the model. This map showed positive scattering density to be present around the crystallographically unique deuterium atom occupying the $2b$ site, $(2/3, 1/3, z; \text{ with } z \approx 0.4)$, and thus suggested that the deuterium arrangement around the boron anion was heavily positionally-disordered in a manner which can be described as a pseudo-reflection in the xy plane containing the boron atom. The deuterium atoms in the complex anion were distributed around a single boron atom in a manner yielding two distorted tetrahedra; one tetrahedron aligned with an apical B - H bond parallel to the c -axis pointing “up” and conversely one aligned diametrically oppositely (pointing “down”). Attempts to construct a model with two separate boron centres were unsuccessful with the discrete boron atoms converging to one position. The overall fractional occupancy of the deuterium atoms was fixed such that the atoms refined as part of one of the tetrahedral units and the total deuterium content matched the stoichiometry demanded by the $(\text{BH}_4)^-$ anions.

Attempted refinement of anisotropic displacement parameters revealed an exceptionally elongated scattering centre manifested by Li^+ .²⁰ Due to the extreme non-physicality of this distribution we elected to refine the lithium in an isotropic manner. In order to mimic the anisotropic scattering two lithium sites were introduced leading to a stable refinement.^{25,31} The thermal displacement parameters of the boron and bromine atoms were constrained to the same single value, and likewise all the deuterium and lithium atoms were required to take the same U_{iso} value, respectively. We note that the space group $P6_3mc$ is non-centrosymmetric and so it is necessary to define the z coordinate of one of the atoms in the structural model in order to fix the origin for the c -parameter (Figure 3.3-14).

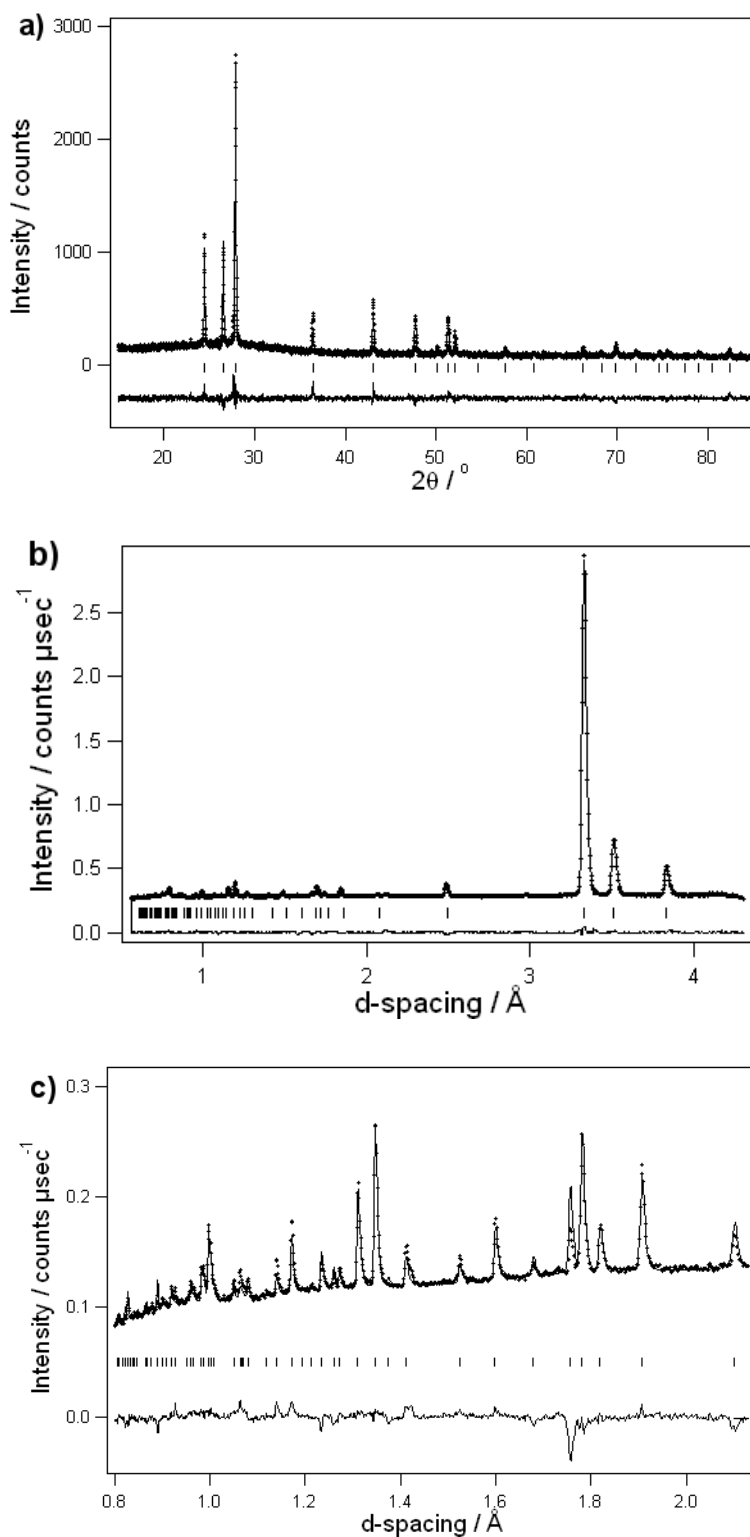


Figure 3.3-13 Rietveld profile fits for (a) PXD data and high-resolution neutron powder diffraction data collected from (b) bank 4 ($50^\circ \leq 2\theta \leq 74^\circ$) and (c) bank 5 ($79^\circ \leq 2\theta \leq 106^\circ$)²⁵ (of the GEM diffractometer for ${}^7\text{Li}({}^{11}\text{BD}_4)_{2/3}\text{Br}_{1/3}$ at 293 K (16a)). Observed data are shown as dots, the calculated pattern as a solid line and the difference profile as a solid line at the bottom of the plot. Vertical bars represent the reflection positions for the phase.

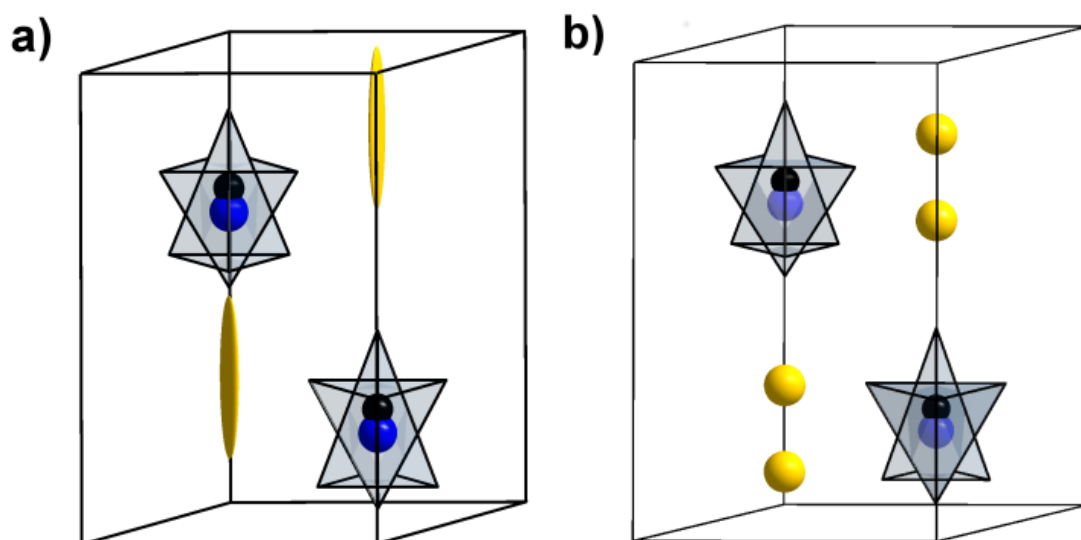


Figure 3.3-14 Crystal structure models of ${}^7\text{Li}({}^{11}\text{BD}_4)_{2/3}\text{Br}_{1/3}$ (16a) with a polyhedral representation of the BD_4^- anion and showing: (a) a single Li site with displacement parameters refined anisotropically; (b) two partially occupied Li positions with isotropic displacement parameters; (D atoms are omitted; Ellipsoids at 50 % probability level). Lithium, boron and bromine are represented as yellow, black and blue spheres. The BD_4 is represented in light blue.

3.3.9 Powder neutron diffraction experiments at 393 - 573 K

Further neutron diffraction datasets were rapidly collected on heating up to 573 K. The count statistics of these data sets were poorer as a consequence of the procedure and so full structural refinement was not attempted. Nevertheless, the same structural model gave good fits to these data and showed a linear evolution in the lattice parameter with temperature (Figure 3.3-15), indicative of a straightforward thermal expansion with no anomalous structural effects. An additional data set was collected at 393 K with the same counting statistics as the room temperature data. Again these data could be fitted in a similar manner, although it is noteworthy that it was not possible to obtain a stable refinement as the positions of all the deuterium atoms were allowed to vary simultaneously. Inspection of the diffraction patterns collected at 393 K show a considerable reduction in the overall Bragg scattering intensities. This would further suggest that at higher temperatures the structure displays an even higher level of disorder, consistent with motion of the complex anions and diffusion of the lithium cations (for example, as manifested in the thermal displacement parameters).

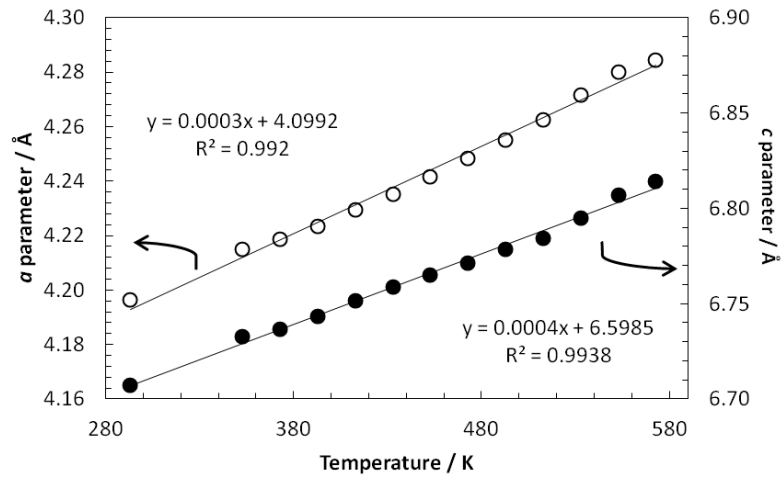


Figure 3.3-15 Cell dimensions of ${}^7\text{Li}({}^{11}\text{BD}_4)_{2/3}\text{Br}_{1/3}$ as a function of temperature (16).

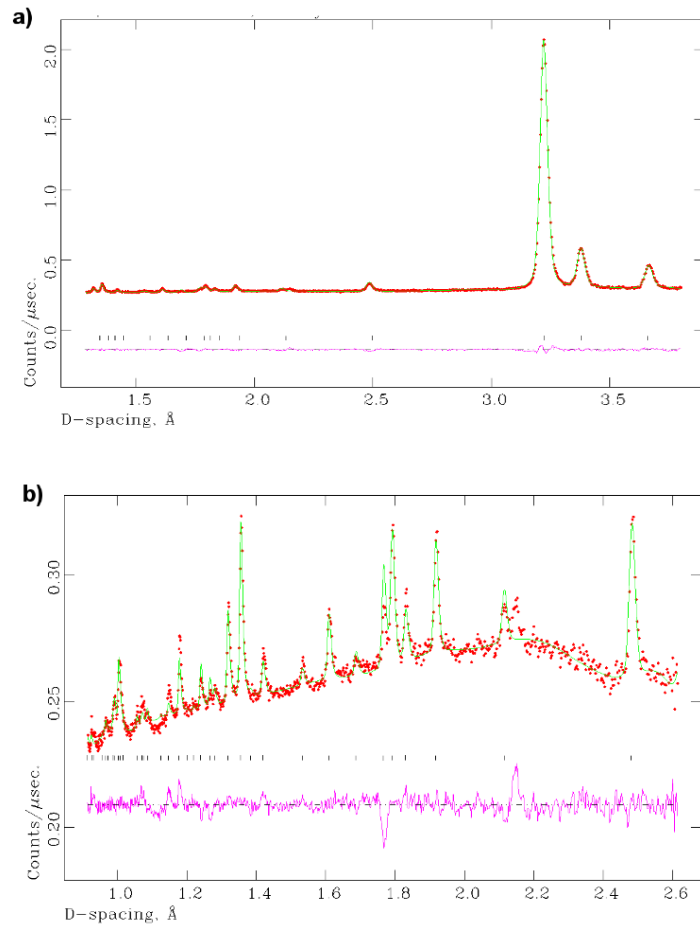


Figure 3.3-16 Rietveld profile fits for (a) GEM detector bank 4 and (b) GEM detector bank 5 for ${}^7\text{Li}({}^{11}\text{BD}_4)_{2/3}\text{Br}_{1/3}$ (16b) using high-resolution neutron powder diffraction data at 393 K. Measured data are shown as dots, the calculated profile is shown by a solid line through the measured data. The difference profile is shown along the bottom of the plot. Vertical bars represent the reflection positions for the phase.

Table 3.3-4 Selected refinement parameters for ${}^7\text{Li}({}^{11}\text{BD}_4)_{2/3}\text{Br}_{1/3}$ (16) from neutron powder diffraction data.

Space group	$P6_3mc$ (no. 186)	$P6_3mc$ (no. 186)
Sample number	16a	16b
Sample temperature / K	293	393
Lattice parameter		
$a / \text{Å}$	4.19622(7)	4.2234(3)
$c / \text{Å}$	6.7070(2)	6.7433(4)
$V / \text{Å}^3$	102.277(4)	104.169(5)
Obs., parameters	6591, 61	1931, 55
R_{wp}	0.0194	0.0123
R_{p}	0.0883	0.0102
χ^2	2.821	1.567

Table 3.3-5 Atomic parameters for ${}^7\text{Li}({}^{11}\text{BD}_4)_{2/3}\text{Br}_{1/3}$ (16a) from neutron powder diffraction data at 293 K.

Atom	Wyck.	x	y	z	Frac. occupation	$U \cdot 100 / \text{Å}^2$
${}^7\text{Li1}$	$2b$	$2/3$	$1/3$	0.626(8)	0.19(1)	4.4(2)
${}^7\text{Li2}$	$2b$	$2/3$	$1/3$	0.801615	0.81(1)	4.4(2)
${}^{11}\text{B}$	$2b$	$2/3$	$1/3$	0.226(2)	0.617	1.58(6)
Br	$2b$	$2/3$	$1/3$	0.180(2)	0.383	1.58(6)
D1	$2b$	$2/3$	$1/3$	0.029(3)	0.481(2)	7.5(2)
D2	$6c$	0.8195(5)	0.1805(6)	0.268(2)	0.481(1)	7.5(2)
D3	$6c$	0.541(2)	0.082(3)	0.088(3)	0.136(2)	7.5(2)
D4	$2b$	$2/3$	$1/3$	0.398(6)	0.136(2)	7.5(2)

Table 3.3-6 Atomic parameters for ${}^7\text{Li}({}^{11}\text{BD}_4)_{2/3}\text{Br}_{1/3}$ (16b) from neutron powder diffraction data at 393 K.

Atom	Wyck.	x	y	z	Frac. occupation	U*100 / Å ²
${}^7\text{Li1}$	2b	2/3	1/3	0.60(1)	0.22(1)	4.2(5)
${}^7\text{Li2}$	2b	2/3	1/3	0.789465	0.78(1)	4.2(5)
${}^{11}\text{B}$	2b	2/3	1/3	0.226(2)	0.617	3.1(2)
Br	2b	2/3	1/3	0.179(2)	0.383	3.1(2)
D1	2b	2/3	1/3	0.02833	0.469(3)	7.4(3)
D2	6c	0.817(1)	0.182(1)	0.262(2)	0.469(3)	7.4(3)
D3	6c	0.548766	0.097535	0.086807	0.147(3)	7.4(3)
D4	2b	2/3	1/3	0.399(8)	0.147(3)	7.4(3)

Table 3.3-7 Selected bond angles for ${}^7\text{Li}({}^{11}\text{BD}_4)_{2/3}\text{Br}_{1/3}$ (16a) from neutron powder diffraction data at 293 K.

Bond angle / °		Bond angle / °	
D1–B–D2	104.4(3)	D2–Li–D3	145.6(17)
D3–B–D4	135.5(4)	D2–Li–D4	95.6(9)
B–Li1–B	113.2(13)	D2–Li–Br	114.4(15)
B–Li1–D2	27.09(24)	D2–Li–Br	30.51(20)
B–Li1–D2	128.9(23)	D3–Li–D3	117.2(14)
B–Li1–D2	86.1(10)	D3–Li–Li2	99.7(26)
B–Li1–D3	121.3(5)	D3–Li–Br	120.82(4)
B–Li1–D3	25.2(11)	D3–Li–D4	80.3(26)
B–Li1–D4	105.5(15)	D4–Li–Li2	180
B–Li1–Br	115.9(10)	D4–Li–Br	98.5(15)
B–Li1–Br	6.95(21)	Li2–Li–Br	180
B–Li–Li2	74.5(15)	Li2–Li–Br	81.5(15)

Table 3.3-8 Selected interatomic distances for ${}^7\text{Li}({}^{11}\text{BD}_4)_{2/3}\text{Br}_{1/3}$ (16a) from neutron powder diffraction data at 293 K.

Bond length / Å		Bond length / Å	
Li1–B	2.68(7)	Li2–B	2.475(3)
Li1–Br	2.45(1)	Li2–Br	2.54(1)
Li1–D1	2.51(2)	Li2–D1	1.53(2)
Li1–D4	2.53(7)	Li2–D4	2.50(1)
Li1–Li2	1.18(6)	B–D2	1.147(5)
B–Br	0.31(1)	B–D3	1.30(1)
B–D1	1.32(1)	B–D4	1.15(3)

Table 3.3-9 Selected bond angles for ${}^7\text{Li}({}^{11}\text{BD}_4)_{2/3}\text{Br}_{1/3}$ (16b) from neutron powder diffraction data at 393 K.

Bond angle / °		Bond angle / °	
D1–B–D2	102.3(6)	Li1–Li2–D2	84.998(0)
D3–B–D4	137.5 (5)	Li1–Li2–Br	180
Br–Li1–Br	101.742(1)	Li1–Li2–Br	73.071(1)
Br–Li1–D3	120.218(0)	Li1–Li2–D3	156.734(1)
Br–Li1–D3	16.001(1)	B–Li2–B	117.104(0)
Br–Li1–D4	107.742(1)	B–Li2–Br	99.926(1)
Br–Li1–Li2	78.253(1)	B–Li2–Br	114.905(1)
D3–Li1–D3	119.454(0)	D2–Li2–D3	74.287(2)
D3–Li1–Li2	94.253(0)	D2–Li2–D3	43.262(1)
D3–Li1–D4	85.741(0)	D2–Li2–D1	95.010(0)
D4–Li1–Li2	180	Br–Li2–D1	106.939(1)
Li1–Li2–B1	80.083(1)	Br–Li2–D3	117.158(0)

Table 3.3-10 Selected interatomic distances for ${}^7\text{Li}({}^{11}\text{BD}_4)_{2/3}\text{Br}_{1/3}$ (16b) from neutron powder diffraction data at 393 K.

Bond length / Å		Bond length / Å	
Li1-B	2.55(1)	Li2-B	2.475(4)
Li1-Br	2.49(2)	Li2-Br	2.549(7)
Li1-D1	2.49(2)	Li2-D1	1.61(2)
Li1-D4	1.4(1)	Li2-D4	2.64(7)
Li1-Li2	1.25(9)	B-D2	1.131(9)
B-Br	0.31(2)	B-D3	1.28(1)
B-D1	1.33(2)	B-D4	1.16(5)

3.3.10 Constant wavelength powder neutron diffraction experiments at low temperature

Data were collected on D20, ILL, Grenoble, between 2-300 K from an isotopically enriched sample of ${}^7\text{Li}({}^{11}\text{BD}_4)_{2/3}\text{Br}_{1/3}$ (17) (Table 3.3-11). Data were analysed by Rietveld refinement with the intention of investigating whether the highly conducting hexagonal polymorph could be stabilised to sub-ambient temperatures or if, like the LiBH_4 parent, it undergoes a structural transition to a fully ordered, lower symmetry polymorph.⁷ It was anticipated that these data would give insight into the behaviour of the borohydride systems, and more generally about the role of ‘paddlewheel’ versus ‘percolation’ mechanisms for Li^+ transport within complex anion lattices.¹¹ Thus, collecting neutron diffraction data below room temperature serves two purposes. First it should be possible to identify any crystallographic transition to a lower symmetry structure driven by the ordering of the BD_4^- units. This would be analogous to the $P63cm$ to $Pnma$ transition observed in LiBH_4 at higher temperature. Second, lower temperatures would decrease the thermal motions of the atoms making it easier to resolve the orientation of the BH_4^- units.

The high counting efficiency of D20 is necessary to achieve meaningful signal-to-noise ratios such that the weak Bragg peaks at a high angle can be resolved and thus should be possible to separate the effects of positional disorder vs those from thermal motions.

Table 3.3-11 Selected refinement parameters for ${}^7\text{Li}({}^{11}\text{BD}_4)_{2/3}\text{Br}_{1/3}$ (17a-17e) from neutron powder diffraction D20 data from ILL.

Space group	$P6_3mc$ (no. 186)				
Sample number	17a	17b	17c	17d	17e
Sample temperature / K	300 (PXD and D20)	150	50	10	2
Lattice parameter					
$a / \text{\AA}$	4.19421(5)	4.1643(2)	4.1574(2)	4.1567(2)	4.1565(2)
$c / \text{\AA}$	6.7067(1)	6.686(1)	6.670(1)	6.6675(9)	6.668(1)
$V / \text{\AA}^3$	102.174(2)	100.41(2)	99.84(2)	99.77(2)	99.76(2)
Obs., parameters	8753, 33	2539, 20	2529, 18	2535, 19	2529, 19
R_{wp}	0.0303	0.0251	0.0267	0.0275	0.0268
R_p	0.0338	0.0157	0.0170	0.0181	0.0172
χ^2	23.57	54.49	61.88	36.11	60.95

3.3.10.1 Results at room temperature

High quality PND data were collected from isotopically enriched $\text{Li}(\text{BH}_4)_{2/3}\text{Br}_{1/3}$ initially at room temperature ($\lambda = 1.54 \text{ \AA}$). Our interpretation of the neutron diffraction data from $\text{Li}(\text{BH}_4)_{2/3}\text{Br}_{1/3}$ therefore began by attempting to fit a structural model to our data using a randomly disordered arrangement of bromide and $(\text{BH}_4)^-$ anions with Br and B occupying different $2b$ site ($2/3, 1/3, z$; where $z \approx 0.2$) in the lattice. Our aim was to obtain an initial model consistent with that derived from GEM and so following the same procedure as for PND data from GEM, Laboratory X-ray diffraction data were incorporated into a multiple histogram refinement with neutron data. Again, this exploited the strong scattering of X-rays by the bromide anion to give an unambiguous and robust identification of the bromide position and site occupancy. These results showed that B and Br atoms were separated $\approx 0.010 \text{ \AA}$ from each other (see Appendix A).

Table 3.3-12 Atomic parameters for ${}^7\text{Li}({}^{11}\text{BD}_4)_{2/3}\text{Br}_{1/3}$ (17a) for neutron powder diffraction data at 300 K.

Atom	Wyck.	x	y	z	Frac. occupation	U*100 / Å ²
${}^7\text{Li1}$	2b	2/3	1/3	0.70(1)	0.3(1)	0.2(1)
${}^7\text{Li2}$	2b	2/3	1/3	0.752(7)	0.7(1)	0.2(1)
${}^{11}\text{B}$	2b	2/3	1/3	0.124(2)	0.562	6.17(7)
Br	2b	2/3	1/3	0.125(3)	0.438	6.17(7)
D1	2b	2/3	1/3	0.9349	0.399(2)	5.8(1)
D2	6c	0.8265(5)	0.1734(5)	0.184(1)	0.399(2)	5.8(1)
D3	6c	0.546(1)	0.092(3)	0.033(2)	0.163(2)	5.8(1)
D4	2b	2/3	1/3	0.3031	0.163(2)	5.8(1)

Table 3.3-13 Complete bond angles ${}^7\text{Li}({}^{11}\text{BD}_4)_{2/3}\text{Br}_{1/3}$ (17a) neutron powder diffraction data at 300 K.

Bond angle / °	
D1–B–D2	109.3(7)
D3–B–D4	124.7(9)

Table 3.3-14 Complete bond lengths ${}^7\text{Li}({}^{11}\text{BD}_4)_{2/3}\text{Br}_{1/3}$ (17a) neutron powder diffraction data at 300 K.

Bond length / Å		Bond length / Å	
Li1–B	2.485(19)	Li2–B	2.49(5)
Li1–Br	2.485(16)	Li2–Br	2.567(13)
Li1–D1	1.53(8)	Li2–D1	1.23(5)
Li1–D4	2.506(21)	Li2–D4	2.445(7)
Li1–Li2	0.31(4)	B–D2	1.231(6)
B–Br	0.010(34)	B–D3	1.068(14)
B–D1	1.266(15)	B–D4	1.203(15)

The same steps followed for the refinement of data collected at GEM were used for D20 data: no constraint was imposed on the ratio of BH_4^- to bromide (the refinement was able to proceed freely to select the anion ratio which best modelled the data) and the ratio was fixed once the refinement was stable. The deuterium atoms in the complex anion were distributed around a single boron atom in a manner

yielding two distorted tetrahedral, and the overall fractional occupancy of the deuterium atoms was fixed such units that the atoms refined as part of one of the tetrahedral units and the total deuterium content matched the stoichiometry demanded by the $(\text{BH}_4)^-$ anions.

The thermal displacement parameters of the boron and bromine atoms were constrained to the same single value, and likewise all the deuterium and lithium atoms were required to take the same U_{iso} value, respectively. It was again necessary to define the z coordinate of one of the atoms in the structural model in order to fix the origin for the c-parameter.

Firstly, the boron and bromide positions and their thermal displacements were refined. Then the deuterium positions were allowed to move with the new B/Br localisation. Afterwards the D fractions were refined. Once the borohydride unit adopted a stable position, Li^+ ion sites and their fractional occupancies were allowed to refine freely. The lithium occupancies were constrained to be the same as the total of amount of boron and bromide (Figure 3.3-17).

The structural data obtained at room temperature from GEM (**16a**) and D20 (**17a**) are shown in Table 3.3-4 and Table 3.3-11, respectively. The samples analysed were synthesised following the same procedure but the final composition was slightly different. Sample **16a** and **17a** contained $\text{Li}(\text{BH}_4)_{0.617}\text{Br}_{0.383}$ and $\text{Li}(\text{BH}_4)_{0.562}\text{Br}_{0.438}$, respectively. The Li1-Li2 distances are 1.25(9) and 0.31(4) Å with a 78 % and 70 % in Li1 site for **16a** and **17a**, respectively. B-Br bond distances are 0.31(2) and 0.010(34) Å for **16a** and **17a**, respectively. These differences in interatomic distances can be due to the slightly difference in BH_4/Br content. This can be reflected in the lattice parameters of both samples, for **16a** are slightly larger than for **17a** ($a = 4.19622(7)$ and $c = 6.7070(2)$ Å; $a = 4.19421(5)$ and $c = 6.7067(1)$ Å, respectively). Apart from these differences, both data agree with the structural model where a randomly disordered arrangement of bromide and $(\text{BH}_4)^-$ is observed facing “up” and “down”. Two lithium sites were introduced in D20 leading to a stable refinement as for GEM data.

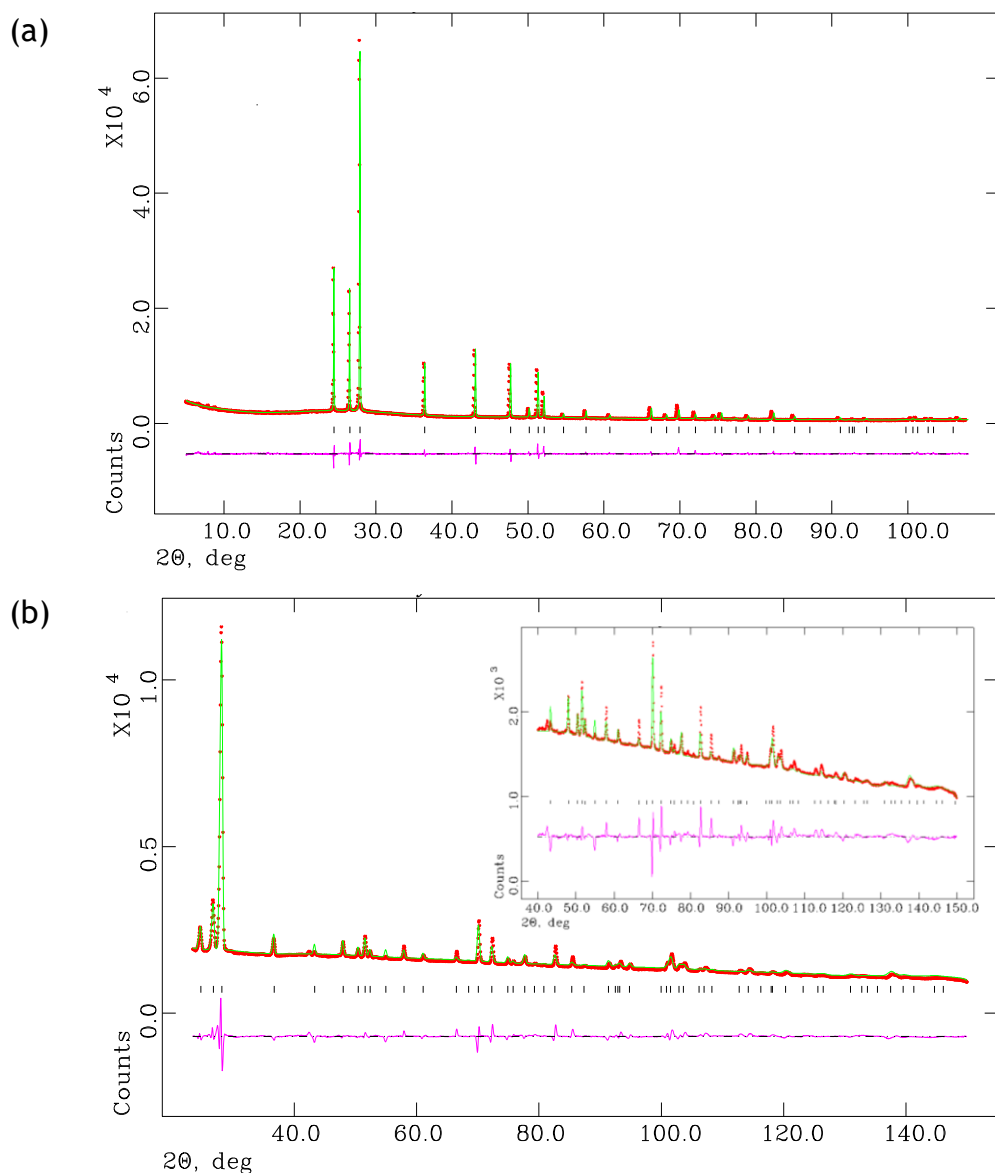


Figure 3.3-17 Rietveld profile fits for (a) PXD data and high-resolution neutron powder diffraction data collected from (b) D20 from ${}^7\text{Li}({}^{11}\text{BD}_4)_{2/3}\text{Br}_{1/3}$ at 300 K (17a). Measured data are shown as dots, the calculated profile is shown by a solid line through the measured data. The difference profile is shown along the bottom of the plot. Vertical bars represent the reflection positions for the phase.

3.3.10.2 Results at low temperature (300 – 2 K)

The same model used at room temperature was initially considered in order to perform the structural analysis of the ${}^7\text{Li}({}^{11}\text{BD}_4)_{0.67}\text{Br}_{0.33}$ at 150 K (Figure 3.3-18, from Table 3.3-15 - Table 3.3-17). At 150 K, Br and B appear to exchange positions (Figure 3.3-19, (a)).

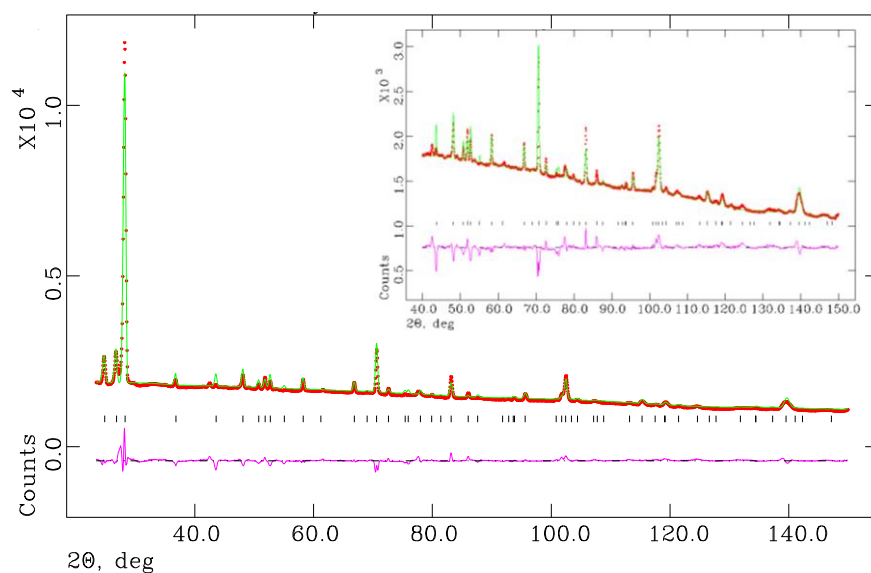


Figure 3.3-18 Rietveld profile fits for high-resolution neutron powder diffraction data collected from D20 from ${}^7\text{Li}({}^{11}\text{BD}_4)_{2/3}\text{Br}_{1/3}$ at 150 K (17b). Measured data are shown as dots, the calculated profile is shown by a solid line through the measured data. The difference profile is shown along the bottom of the plot. Vertical bars represent the reflection positions for the phase.

Table 3.3-15 Atomic parameters for ${}^7\text{Li}({}^{11}\text{BD}_4)_{2/3}\text{Br}_{1/3}$ (17b) from neutron powder diffraction data at 150 K.

Atom	Wyck.	x	y	z	Frac. occupation	U*100 / Å ²
${}^7\text{Li1}$	2b	2/3	1/3	0.502(7)	0.45(2)	0.5(2)
${}^7\text{Li2}$	2b	2/3	1/3	0.620(5)	0.55(2)	0.5(2)
${}^{11}\text{B}$	2b	2/3	1/3	0.082(2)	0.562	2.8(1)
Br	2b	2/3	1/3	0.010(4)	0.438	2.8(1)
D1	2b	2/3	1/3	0.9349	0.387(6)	6.3(2)
D2	6c	0.819(1)	0.181(1)	0.096(4)	0.387(6)	6.3(2)
D3	6c	0.547(3)	0.094(6)	0.920(5)	0.175(6)	6.3(2)
D4	2b	2/3	1/3	0.2831	0.175(6)	6.3(2)

Table 3.3-16 Complete bond angles ${}^7\text{Li}({}^{11}\text{BD}_4)_{2/3}\text{Br}_{1/3}$ (17b) neutron powder diffraction data at 150 K.

	Bond angle / °
D1–B–D2	94.7(7)
D3–B–D4	141.5(10)

Table 3.3-17 Complete bond lengths ${}^7\text{Li}({}^{11}\text{BD}_4)_{2/3}\text{Br}_{1/3}$ (17b) neutron powder diffraction data at 150 K.

	Bond length / Å		Bond length / Å
Li1–B	2.462(9)	Li2–B	2.4177(27)
Li1–Br	3.30(4)	Li2–Br	2.605(27)
Li1–D1	2.446(9)	Li2–D1	2.105(14)
Li1–D4	1.47(5)	Li2–D4	2.253(31)
Li1–Li2	0.786(28)	B–D2	1.101(9)
B–Br	0.484(17)	B–D3	1.387(21)
B–D1	0.983(15)	B–D4	1.345(15)

The same model used at 150 K was considered in order to perform the structural analysis of the sample from 50 - 2 K. At 50 K (from Table 3.3-18 - Table 3.3-26, see Appendix A for OCD plots), the Br and B atoms approximately maintain the same positions as at 150 K (Figure 3.3-19, (a)). Lithium however, now occupies a single site in the cell, close to the Li2 position at 150 K (Figure 3.3-19, (c)) and maintains the single site down to 2 K.

Table 3.3-18 Atomic parameters for ${}^7\text{Li}({}^{11}\text{BD}_4)_{2/3}\text{Br}_{1/3}$ (17c) from neutron powder diffraction data at 50 K.

Atom	Wyck.	x	y	z	Frac. occupation	U*100 / Å ²
${}^7\text{Li1}$	2b	2/3	1/3	0.594(2)	1.000	1.1(2)
${}^{11}\text{B}$	2b	2/3	1/3	0.115(2)	0.562	2.7(1)
Br	2b	2/3	1/3	0.021(3)	0.438	2.7(1)
D1	2b	2/3	1/3	0.9700	0.383(5)	4.8(2)
D2	6c	0.820(1)	0.180(1)	0.120(2)	0.383(5)	4.8(2)
D3	6c	0.546(3)	0.091(5)	0.9546	0.179(5)	4.8(2)
D4	2b	2/3	1/3	0.3014	0.179(5)	4.8(2)

Table 3.3-19 Complete bond angles ${}^7\text{Li}({}^{11}\text{BD}_4)_{2/3}\text{Br}_{1/3}$ (17c) neutron powder diffraction data at 50 K.

Bond angle / °	
D1–B–D2	91.6(6)
D3–B–D4	140.9(8)

Table 3.3-20 Complete bond lengths ${}^7\text{Li}({}^{11}\text{BD}_4)_{2/3}\text{Br}_{1/3}$ (17c) neutron powder diffraction data at 50 K.

Bond length / Å		Bond length / Å	
Li1–B	2.4044(8)	B–D1	0.970(13)
Li1–Br	2.843(17)	B–D2	1.105(8)
Li1–D1	2.540(4)	B–D3	1.383(19)
Li1–D4	1.955(14)	B–D4	1.240(13)
B–Br	0.633(14)		

Table 3.3-21 Atomic parameters for ${}^7\text{Li}({}^{11}\text{BD}_4)_{2/3}\text{Br}_{1/3}$ (17d) from neutron powder diffraction data at 10 K.

Atom	Wyck.	x	y	z	Frac. occupation	U*100 / Å ²
${}^7\text{Li1}$	2b	2/3	1/3	0.597(2)	1.000	1.4(2)
${}^{11}\text{B}$	2b	2/3	1/3	0.111(2)	0.562	1.8(1)
Br	2b	2/3	1/3	0.016(3)	0.438	1.8(1)
D1	2b	2/3	1/3	0.9700	0.385(6)	5.1(2)
D2	6c	0.816(1)	0.184(1)	0.116(3)	0.385(6)	5.1(2)
D3	6c	0.546(3)	0.091(5)	0.950(4)	0.177(6)	5.1(2)
D4	2b	2/3	1/3	0.3014	0.177(6)	5.1(2)

Table 3.3-22 Complete bond angles ${}^7\text{Li}({}^{11}\text{BD}_4)_{2/3}\text{Br}_{1/3}$ (17d) neutron powder diffraction data at 10 K.

Bond angle / °	
D1–B–D2	92.0(7)
D3–B–D4	141.0(8)

Table 3.3-23 Complete bond lengths ${}^7\text{Li}({}^{11}\text{BD}_4)_{2/3}\text{Br}_{1/3}$ (17d) neutron powder diffraction data at 10 K.

Bond length / Å		Bond length / Å	
Li1–B	2.4016(6)	B–D1	0.939(14)
Li1–Br	2.792(17)	B–D2	1.079(8)
Li1–D1	2.546(5)	B–D3	1.384(21)
Li1–D4	1.973(16)	B–D4	1.271(14)
B–Br	0.632(14)		

Table 3.3-24 Atomic parameters for ${}^7\text{Li}({}^{11}\text{BD}_4)_{2/3}\text{Br}_{1/3}$ (17e) from neutron powder diffraction data at 2 K.

Atom	Wyck.	x	y	z	Frac. occupation	U*100 / Å ²
${}^7\text{Li1}$	2b	2/3	1/3	0.600(2)	1.000	1.8(2)
${}^{11}\text{B}$	2b	2/3	1/3	0.110(2)	0.562	1.7(1)
Br	2b	2/3	1/3	0.017(3)	0.438	1.7(1)
D1	2b	2/3	1/3	0.9700	0.384(5)	5.1(2)
D2	6c	0.817(1)	0.183(1)	0.116(3)	0.384(5)	5.1(2)
D3	6c	0.545(3)	0.091(5)	0.946(4)	0.178(5)	5.1(2)
D4	2b	2/3	1/3	0.3014	0.178(5)	5.1(2)

Table 3.3-25 Complete bond angles ${}^7\text{Li}({}^{11}\text{BD}_4)_{2/3}\text{Br}_{1/3}$ (17e) neutron powder diffraction data at 2 K.

Bond angle / °	
D1–B–D2	92.3(6)
D3–B–D4	141.4(8)

Table 3.3-26 Complete bond lengths ${}^7\text{Li}({}^{11}\text{BD}_4)_{2/3}\text{Br}_{1/3}$ (17e) neutron powder diffraction data at 2 K.

Bond length / Å		Bond length / Å	
Li1–B	2.4006(4)	B–D1	0.933(13)
Li1–Br	2.780(16)	B–D2	1.087(8)
Li1–D1	2.552(6)	B–D3	1.398(19)
Li1–D4	1.993(16)	B–D4	1.277(13)
B–Br	0.618(14)		

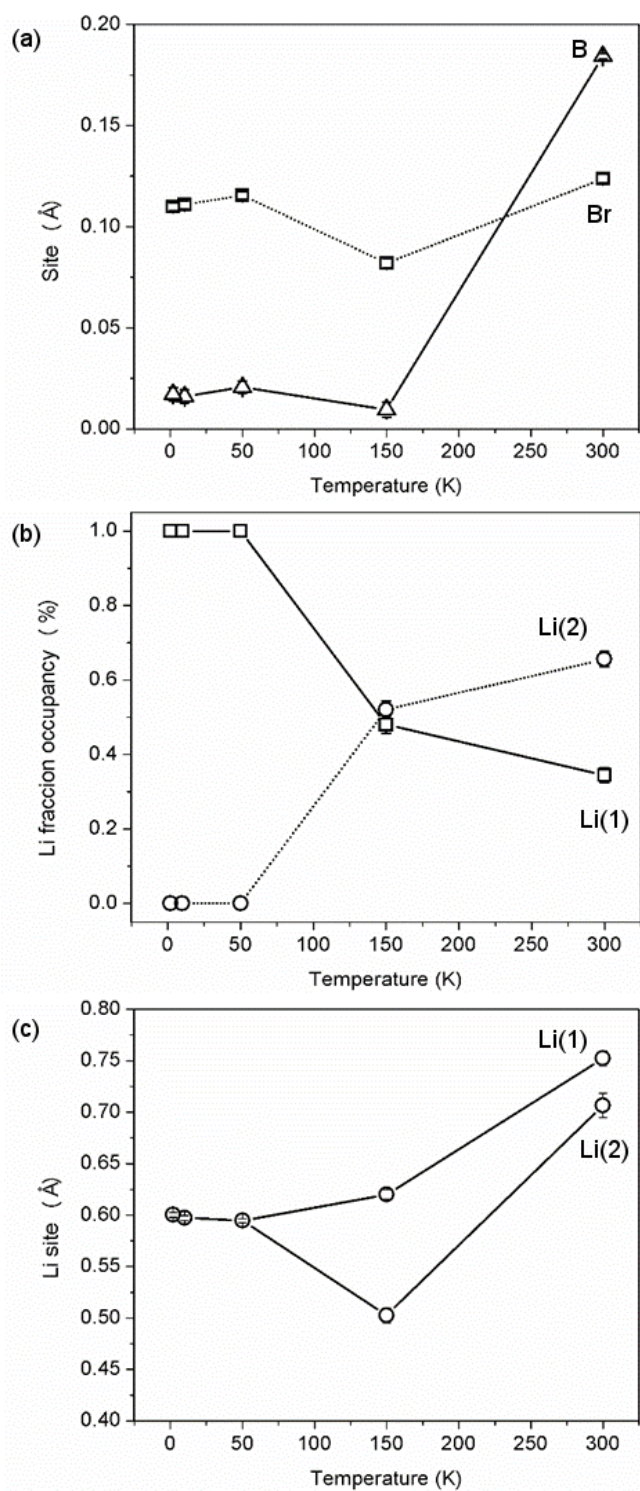


Figure 3.3-19 Variations of (a) atomic parameters from boron and bromide (boron and bromide represented with triangles and squares, respectively), (b) Li fraction occupancy, and (c) atomic parameter from Li on cooling from room temperature to 2 K in ${}^7\text{Li}({}^{11}\text{BD}_4)_{1-x}\text{Br}_x$ (17a - 17e). Error bars are represented in black.

3.3.10.3 Data on cooling from room temperature to 2 K

Figure 3.3-20 shows the data obtained from D20 in ILL.

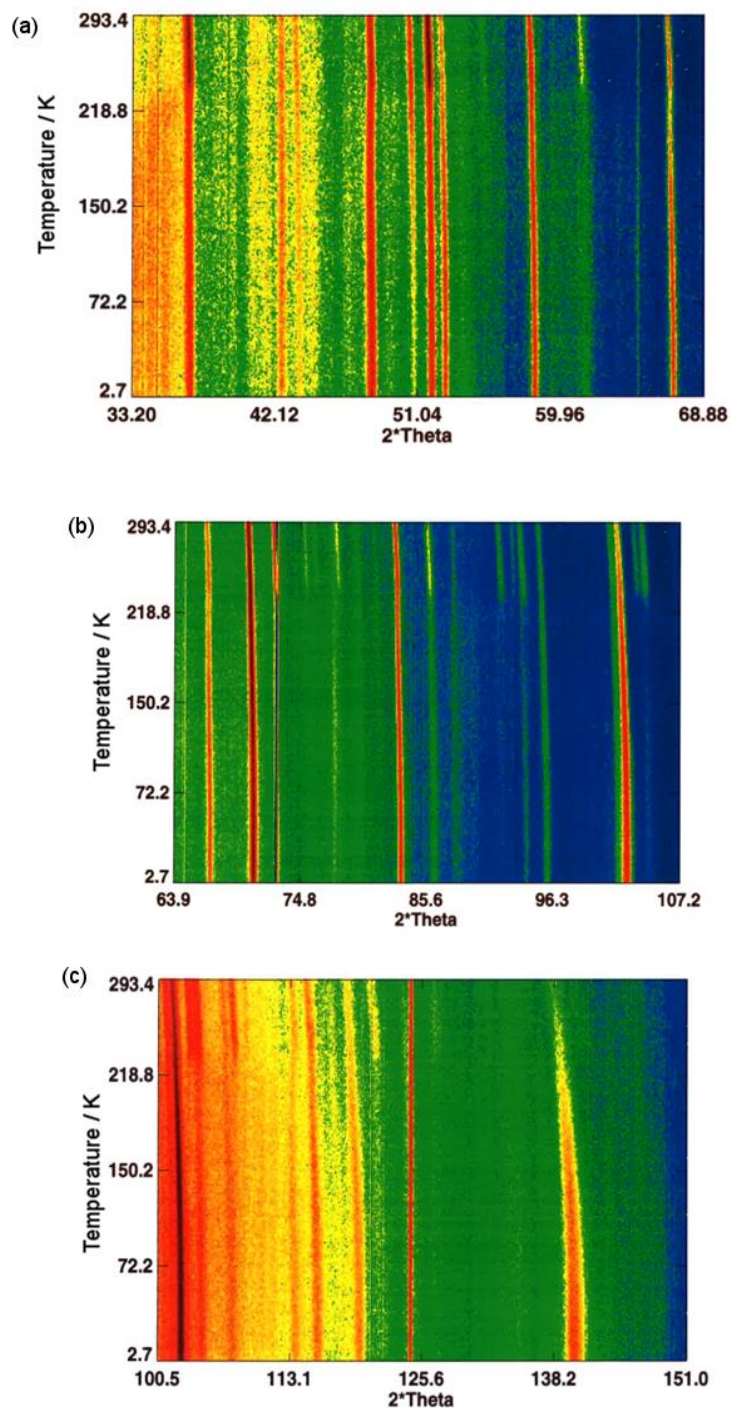
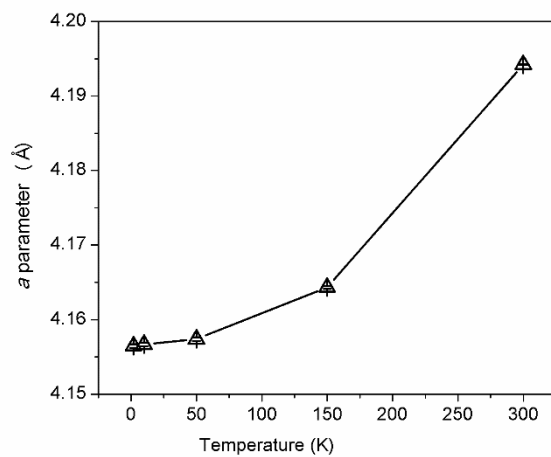
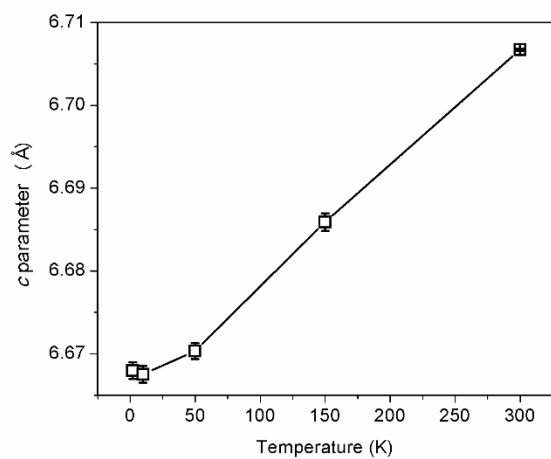


Figure 3.3-20 Powder neutron diffraction patterns for ${}^7\text{Li}({}^{11}\text{BD}_4)_{1-x}\text{Br}_x$ on cooling from room temperature to 2 K as collected on D20 at ILL (17a - 17e) from $2\theta =$ (a) $33.2 - 68.9^\circ$ (b) $63.9 - 107.2^\circ$ and (c) $100.5 - 151.0^\circ$.

(a)



(b)



(c)

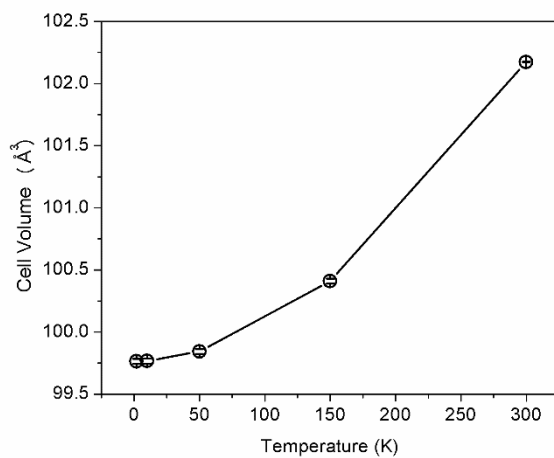


Figure 3.3-21 Variations of unit cell parameters on cooling from room temperature to 2 K in ${}^7\text{Li}({}^{11}\text{BD}_4)_{1-x}\text{Br}_x$ (17a -17e). (a) a parameter, (b) c parameter and (c) cell volume. Error bars are represented in black.

When the sample was cooled from room temperature to 270 K, it was observed that the intensities of some of the reflections increased and diminished respectively (Figure 3.3-20 and Appendix A). This observation was taken into account preparing structural analysis as the observation implied structural changes.

Figure 3.3-21 shows the variation of the unit cell parameters on cooling. It is noticeable that the a parameter decreases much more sharply than c . The c parameter contracts linearly between 300 - 50 K.

3.3.11 Discussion

The reaction between lithium borohydride and lithium bromide can be driven by either mechanically grinding materials together for 24 h, or more readily by a 4 h mechanical treatment followed by heating at 573 K. PXD analysis before and after the TG-DTA examination of the heating stage of the MT/TT synthesis procedure (for example, for $\text{Li}(\text{BH}_4)_{2/3}\text{Br}_{1/3}$ as discussed above) shows that the initial 4h grinding process causes a partial reaction between the LiBr and LiBH_4 . This gives a combination of an almost negligible quantity of the orthorhombic (LT- LiBH_4 -type) phase and predominantly a hexagonal (HT- LiBH_4 -type) and cubic (LiBr-type) phase. The temperature of the endothermic transition from the orthorhombic to hexagonal phase is reduced strongly indicating that bromide has been incorporated into the borohydride structure over 4 h of milling. Both a steady decrease in the proportion of the LiBr-phase and a reduction in the cell parameters of the hexagonal phase can be observed on increasing the milling duration or as a result of subsequent heating. The process can thus be completed to give a single phase material either by further extended milling (24 h) or by subsequent heating to 573 K after initial milling (4 h). Although we used intermittent grinding and rest periods to try and avoid excessive heat generation due to mechanical friction, we note that ball milling is often associated with very significant localized temperatures.³² The degree of heating will of course depend on the heat capacities of the reagents and products involved as well as the coefficients of friction, hardness and toughness, but it should be noted that the relatively modest temperature of 573 K necessary to afford a chemical reaction thermally is significantly lower than what may be achieved by milling. For example, in the case of $\text{La}_7\text{Mo}_7\text{O}_{30}$, ball milling affords a phase which would otherwise only be stabilised by heating at temperatures above 1033 K.³³

Although powder X-ray diffraction results indicate that the materials produced by either mixed mechanochemical/thermal or extended mechanochemical treatments are identical, their morphologies differ very substantially. The mechanochemical/thermal treatment affords regularly shaped particles of broadly cubic symmetry measuring approximately 1 μm across. Extended mechanochemical treatment, however, gives larger particles which appear to be aggregated into spheres around a central point. The observations of these petal-like structures have been made in other chemical systems where the presence of solvent is an essential condition to achieve flower-like growth.³⁴ Although the reaction described herein is between two solids to afford a solid final product, it should be noted that a eutectic mixture could readily form between the reagents. The localised heating during milling may deliver a sufficient quantity of liquid phase to initiate a mechanism of growth analogous to that seen in solution phase chemistry (the melting points of LiBH_4 and LiBr are 541 and 823 K, respectively).³⁵

Syntheses and X-ray diffraction analysis has provided a structure-composition map for the LiBH_4 - LiBr system. The end members of the system are orthorhombic and face-centred cubic respectively, whereas our data demonstrate that intermediate compositions crystallise with the hexagonal structure of the HT phase of LiBH_4 . Two-phase regions have been identified close to the orthorhombic-hexagonal and hexagonal-cubic phase boundaries (*i.e.* regions II and IV). It should be noted that adjustment of the heating conditions and cooling rates may be able to slightly increase the compositional limits of the single phases. Nevertheless our data show a number of interesting points in this compositional system which has hitherto been underappreciated.

Significant incorporation of the bromide anion into the LiBH_4 structure can be achieved within the orthorhombic structure. This substantial solubility means that it is necessary to introduce *ca.* 25% bromide into the structure before the hexagonal polymorph is stabilised at room temperature as a single phase. This hexagonal structure is stable for a wide range of anion compositions; a single phase exists from $0.29 \leq x \leq 0.50$. Interestingly, however, although a threshold value of bromide substitution is required to stabilise the higher Li^+ ion conducting HT phase, beyond this composition point subsequent bromide substitution only serves to reduce the

ionic conductivity. One can assume that this is associated with the concomitant contraction of the hexagonal unit cell and a less open migration pathway for Li⁺ ions to diffuse.

For higher bromide concentrations, the face centred (NaCl-type) cubic structure, familiar from the LiBr phase, is present in growing quantities as *x* increases. The variation in lattice parameters of the cubic phase for different reaction compositions suggests that the cubic material is not present as a line phase of composition LiBr; the incorporation of borohydride into the *fcc* lattice appears to be non-negligible.

Detailed inspection of the lattice parameters shows that significant changes in the unit cell volume occur with an increase in Br⁻ anion content of the overall reaction mixture. Where we have two-phase mixtures it is not possible to assign compositions unambiguously to each of them. Nevertheless, inspection of the unit cell volumes for various reaction mixtures shows smooth evolutions in the lattice parameters implying substantial dissolution of both anions into all three structures. For each of the three structures (orthorhombic, hexagonal and cubic), incorporation of the bromide anion with a radius of 1.96 Å in place of the larger borohydride anion radius of 2.05 Å gives the anticipated reduction in the unit cell volume.³⁶

The high symmetry unit cell of Li(BD₄)_{2/3}Br_{1/3} contains considerable occupational and positional disorder. Similar disorder has been observed in the hexagonal phase of LiBH₄ itself, which is stable above 383 K.^{21, 37, 38} Nonetheless, Rietveld refinement against the neutron data was able to identify a narrow distribution of B-D distances in Li(BD₄)_{2/3}Br_{1/3} (1.147(5) - 1.32(1) Å at 293 K). Our analysis of the mixed anion compound shows that the presence of Br⁻ and BH₄⁻ within the structure leads to lithium bromide distances of 2.45(1) Å and 2.55(1) Å, respectively. Consideration of the BH₄⁻ and Br⁻ species shows that the two anions are displaced up and down the *c*-axis from the normal plane containing the borohydride anions in HT-LiBH₄ to sites which are separated by 0.31(1) Å in the *z*-direction. This displacement is mainly exhibited by the BH₄⁻ units leading to a B...Li separation of only 2.476(3) and 2.68(7) Å (Table 3.3-4 - Table 3.3-10).

The best fits to the diffraction data were obtained when the lithium ions were distributed over two tetrahedral ($2/3, 1/3, z$) sites; the position with $z \approx 0.8$ and that with $z \approx 0.6$. The former position is the one that has been previously identified as occupied in the HT-LiBH₄ structure,^{20, 38, 39} but in the model refined here, this $2b$ site is 80 % occupied.^{40, 41} Interestingly, the location and distribution of the lithium ions is almost identical to that of the cations in another Wurtzite-related compound, β -CuI.^{42, 43} The Cu⁺ ions in β -CuI exhibit a complex diffusion mechanism involving movement of the cations through the edges of the surrounding tetrahedral “cages” formed by I⁻.⁴⁴ The structural similarities suggest that the disorder and diffusion of the Li⁺ and Cu⁺ ions in the respective borohydride and iodide fast ion conducting phases have a very similar origin and alludes to analogous diffusion pathways with a basis that may be essentially anion-independent. Nevertheless, the presence of complex ions in (HT-)Li(BH₄)_{1-x}Br_x necessitates anion orientations that facilitate the anticipated Li⁺ diffusion process, given the observed high values of conductivity.

The orientation of the tetrahedral BH₄⁻ units is of crucial interest in understanding the lithium ion mobility through the structure. Considerable effort has been expended on examining the ionic transport behaviour of undoped LiBH₄, although due to the presence of disorder and the challenges of identifying hydrogen atom positions there remains a considerable degree of uncertainty in this.^{20, 21, 22} Our data could only be satisfactorily modelled by incorporating a distribution of deuterium atoms such that the tetrahedra were composed of two units centred on the same boron atom but with an inverted deuterium distribution. Although there is significant scatter in the B-D distances the observation of this inversion is robust and can be usefully compared with models of disorder that have been proposed from other techniques and calculations.^{18, 19, 31} It should be noted that the understanding of the behaviour of this anion is complicated considerably by the conflict between the trigonal symmetry of the crystallographic site and the tetrahedral symmetry expected for BH₄⁻.

Various analyses have suggested that the dynamic disorder associated with the BH₄⁻ anion arises from rotation about the three-fold molecular axis, or by complete spherical motion of the atoms around the boron centre.^{2, 22, 21, 221} Our data show that

neither of these descriptors provides a complete picture. Whilst there is disorder around the trigonal axis, the data clearly identified well-localised atoms, and attempts to delocalize them to other positions give a halo of scattering density which degraded the quality of fit and refinements failed to stabilise. Likewise, it was necessary to introduce an inverted distribution of deuterium atoms, but again these refined to specific positions and did not exhibit the instability that would be expected if the atoms occupying the unconstrained x , y , z coordinates of the $6c$ general position were free to move around points on a spherical scattering surface. A previous detailed study of the Raman spectra of HT - LiBH_4 suggested two thermally activated reorientations of the BH_4^- unit, with both rotation about the trigonal axis and a higher energy exchange being accessible.⁸ Any assignment must remain tentative, but our structural data are most compatible with such a model. It is important to point out that no restraints were placed on the anion symmetry during refinement (nor for example, were rigid body constraints applied).

Diffraction data collected on heating of the material showed that the key features of the crystalline structure are retained up to at least 573 K. Due to the diminishing Bragg scattering (and increase in diffuse scattering) from the sample at elevated temperatures it was necessary to introduce additional constraints to the structural refinement and so it was not possible to assign the disorder with complete confidence to either thermal motion or the static effects introduced by occupational disorder in the Br^- and BH_4^- sublattice.⁴⁵ The interplay of static and dynamic disorder should become clearer with a detailed study of structure as a function of both temperature and composition within each of the phase regions in the LiBH_4 - LiBr system.

Diffraction data collected on cooling the material showed that the key features of the crystalline structure are retained down to at least 220 K. At 150 K, B and Br atoms appear to exchange positions. At < 150 K, the positional disorder of the lithium atoms is removed and therefore lithium only occupies one site in the structure. No crystallographic transition to a lower symmetry structure was observed on cooling to 2 K. Consequently $[\text{BD}_4]^-$ units do not exhibit any disordering at low and high temperature up to 393 K.

3.4 Conclusions

The hexagonal phase of LiBH_4 has been stabilised and isolated at room temperature by anion substitution over a compositional range $\text{Li}(\text{BH}_4)_{1-x}\text{Br}_x$ ($0.29 \leq x \leq 0.50$). Fast lithium ion conductivity is retained in these phases, although the value of the total conductivity is reduced as the bromide content increases above $x = 2/7$. There is considerable disorder in both the position and orientation of the anions in this structure leading to highly anisotropic thermal motion for lithium. The Br^- and BH_4^- anions are displaced by a distance of 0.31 \AA from each other in the crystallographic model with the latter exhibiting orientational disorder which can only be satisfactorily modelled using an inversion of the deuterium atoms. This implies substantial rotation of the BH_4^- units although not the free spherical rotation which has been observed in other complex anion fast ion conductors. Analysis of the Bragg scattering up to 573 K shows that the material retains the hexagonal structure, although the reduced intensity of the Bragg reflections does suggest increasing disorder (loss of long range order) in the material with heating. Data collected at low temperatures (from $300 - 2 \text{ K}$) revealed that the HT - LiBH_4 type phase for $\text{Li}(\text{BH}_4)_{2/3}\text{Br}_{1/3}$ is stable down to 2 K . The borohydride unit was found to preserve the two borohydride units facing “up” and “down” at low temperatures. At 150 K B and Br interchange sites. When the temperature is decreased to below 150 K the lithium atoms are no longer disordered.

3.5 References

1. A. Giannis and K. Sandhoff, *Angew. Chem. Int. Ed. Engl.*, 1989, **28**, 218-220.
2. H. C. Brown, Y. M. Choi and S. Narasimhan, *Inorg. Chem.*, 1982, **21**, 3657-3661.
3. A. Züttel, A. Borgschulte and S. I. Orimo, *Scr. Mater.*, 2007, **56**, 823-828.
4. H. W. Li, Y. G. Yan, S. Orimo, A. Züttel and C. M. Jensen, *Energies*, 2011, **4**, 185-214.
5. A. Züttel, P. Wenger, S. Rentsch, P. Sudan, P. Mauron and C. Emmenegger, *J. Power Sources*, 2003, **118**, 1-7.
6. M. Matsuo, Y. Nakamori, S. Orimo, H. Maekawa and H. Takamura, *Appl. Phys. Lett.*, 2007, **91**, 1-3.
7. V. Dmitriev, Y. Filinchuk, D. Chernyshov, A. V. Talyzin, A. Dzwilevski, O. Andersson and B. Sundqvist, *Phys. Rev. B*, 2008, **77**, 11.
8. J. P. Soulie, G. Renaudin, R. Cerny and K. Yvon, *J. Alloy. Compd.*, 2002, **346**, 200-205.
9. A. M. Soldate, *J. Am. Chem. Soc.*, 1947, **69**, 987-988.
10. S. C. Abrahams and J. Kalnajs, *J. Chem. Phys.*, 1954, **22**, 434-436.
11. P. Martelli, A. Remhof, A. Borgschulte, R. Ackermann, T. Strassle, J. P. Embs, M. Ernst, M. Matsuo, S. I. Orimo and A. Züttel, *J. Phys. Chem. A*, 2011, **115**, 5329-5334.
12. L. H. Rude, E. Groppo, L. M. Arnbjerg, D. B. Ravnsbaek, R. A. Malmkjaer, Y. Filinchuk, M. Baricco, F. Besenbacher and T. R. Jensen, *J. Alloy. Compd.*, 2011, **509**, 8299-8305.

13. L. H. Rude, T. K. Nielsen, D. B. Ravensbaek, U. Bosenberg, M. B. Ley, B. Richter, L. M. Arnbjerg, M. Dornheim, Y. Filinchuk, F. Besenbacher and T. R. Jensen, *Phys. Status Solidi A-Appl. Mat.*, 2011, **208**, 1754-1773.
14. H. Yamawaki, H. Fujihisa, Y. Gotoh and S. Nakano, *J. Phys. Chem. Solids*, 2015, **76**, 40-44.
15. M. Matsuo and S. Orimo, *Adv. Energy Mater.*, 2011, **1**, 161-172.
16. R. Miyazaki, H. Maekawa and H. Takamura, *Appl. Mater.*, 2014, **2**, 1-6.
17. Y. Filinchuk, D. Chernyshov and R. Cerny, *J. Phys. Chem. C*, 2008, **112**, 10579-10584.
18. R. Hempelmann, 2000, ISBN 0198517432, Quasielastic neutron scattering and solid state diffusion. Oxford University Press Inc.
19. M. Bée, 1988, ISBN 9780852743713, Quasielastic neutron scattering. Adam Hilger.
20. T. Ikeshoji, E. Tsuchida, K. Ikeda, M. Matsuo, H. W. Li, Y. Kawazoe and S. Orimo, *Appl. Phys. Lett.*, 2009, **95**, 221901-221903.
21. N. Verdal, T. J. Udovic and J. J. Rush, *J. Phys. Chem. C*, 2012, **116**, 5276-5276.
22. T. Ikeshoji, E. Tsuchida, T. Morishita, K. Ikeda, M. Matsuo, Y. Kawazoe and S. Orimo, *Phys. Rev. B*, 2011, **83**, 144301-144305.
23. <http://icsd.cds.rsc.org/search/basic.xhtml>, accessed on 3rd September 2015.
24. W. Kraus and G. Nolze, *Powder Diffraction*, 1998, **13**, 256-259.
25. A. C. Hannon, *Nucl. Instrum. Meth. A.*, 2005, **551**, 88-107.
26. A. C. Larson and R. B. Von Dreele, 1994, General Structure Analysis System (GSAS), Los Alamos National Laboratory Report LAUR, 86-748.
27. B. H. Toby, *J. Appl. Crystallogr.*, 2001, **34**, 210-213.
28. M. R. Hartman, J. J. Rush, T. J. Udovic, R. C. Bowman and S. J. Hwang, *J. Solid State Chem.*, 2007, **180**, 1298-1305.
29. S. Orimo, Y. Nakamori and A. Züttel, *Mat. Sci. Eng. B-Solid*, 2004, **108**, 51-53.
30. S. Gomes, H. Hagemann and K. Yvon, *J. Alloy. Compd.*, 2002, **346**, 206-210.
31. G. Renaudin, S. Gomes, H. Hagemann, L. Keller and K. Yvon, *J. Alloy. Compd.*, 2004, **375**, 98-106.
32. S. L. James, C. J. Adams, C. Bolm, D. Braga, P. Collier, T. Friscic, F. Grepioni, K. D. M. Harris, G. Hyett, W. Jones, A. Krebs, J. Mack, L. Maini, A. G. Orpen, I. P. Parkin, W. C. Shearouse, J. W. Steed and D. C. Waddell, *Chem. Soc. Rev.*, 2012, **41**, 413-447.
33. F. Goutenoire, R. Retoux, E. Suard and P. Lacorre, *J. Solid State Chem.*, 1999, **142**, 228-235.
34. E. Benjacob and P. Garik, *Nature*, 1990, **343**, 523-530.
35. W. M. Haynes and T. J. Bruno, 2014-2015, ISBN 9781482208672, Handbook of Chemistry and Physics, 95th Edition. CRC Press.
36. C. E. Housecroft and A. G. Sharpe, 2001, ISBN 0-582-31080-6, Inorganic chemistry. Peason Education.
37. F. Buchter, Z. Lodziana, P. Mauron, A. Remhof, O. Friedrichs, A. Borgschulte, A. Züttel, D. Sheptyakov, T. Strassle and A. J. Ramirez-Cuesta, *Phys. Rev. B*, 2008, **78**, 094302-094310.
38. A. Remhof, Z. Lodziana, P. Martelli, O. Friedrichs, A. Züttel, A. V. Skripov, J. P. Embs and T. Strassle, *Phys. Rev. B*, 2010, **81**, 214304-214313.
39. A. Remhof, Y. G. Yan, J. P. Embs, V. G. Sakai, A. Nale, P. de Jongh, Z. Lodziana and A. Züttel, *QENS/WINS 2014*, 2015, **83**, 02014-02020.
40. P. C. Aeberhard, K. Refson and W. I. F. David, *Phys. Chem. Chem. Phys.*, 2013, **15**, 8081-8087.
41. P. C. Aeberhard, S. R. Williams, D. J. Evans, K. Refson and W. I. F. David, *Phys. Rev. Lett.*, 2012, **108**, 095901-095906.
42. S. Hull and D. A. Keen, *Phys. Rev. B*, 1994, **50**, 5868-5885.
43. D. A. Keen and S. Hull, *J. Phys. Conden. Matter*, 1994, **6**, 1637-1644.
44. J. X. M. ZhengJohansson and R. L. McGreevy, *Solid State Ionics.*, 1996, **83**, 35-48.
45. S. R. Elliott, 1990, ISBN 0470215798, Physics of Amorphous Materials, 2nd ed. Longman.

4. Stabilisation of the fast ionic and high pressure phase (HP) of LiBH_4 stabilised by mixed cation – anion substitution

4.1 Introduction

During the last decades discussion has been focused on the identification of the high pressure phases of LiBH_4 at room temperature and ambient pressure.¹⁻⁴ Due to experimental limitations incorrect assignments were proposed for high pressure LiBH_4 phases.¹⁻⁴ In 2002, synchrotron radiation studies confirmed that only two different high pressure structures of LiBH_4 existed, the ambient temperature - low pressure and the high pressure phases (AT - LP and HP, respectively) (Figure 4.1-1, (b) and (c)). By only applying pressure, the low temperature (LT) LiBH_4 ($Pnma$, at ambient pressure and temperature, Figure 4.1-1 (a)) undergoes a phase transition at 1.2 GPa⁵ and becomes the AT - LP LiBH_4 phase (crystal system $Ama2$, Figure 4.1-1 (b)). The second phase transformation occurs at 10 GPa to form HP - LiBH_4 (crystal system $Fm\bar{3}m$, Figure 4.1-1 (c)).⁶ However the AT - LP and HP phases coexist at the same pressures up to at least 18 GPa (Figure 4.1-2). The complete transition to the HP - LiBH_4 can be rapidly achieved by heating to 500 K at about 10 GPa.⁷ In contrast to HP phase, the AT - LP phase can be quenched to ambient pressure, although this phase is unstable above 190 K.⁸ HP - LiBH_4 has a cubic structure with a disordered arrangement of BH_4 anions ($\alpha\text{-NaBH}_4$ -type)^{9, 10}, with $a = 5.109(2)$ Å at 18.1 GPa.⁷

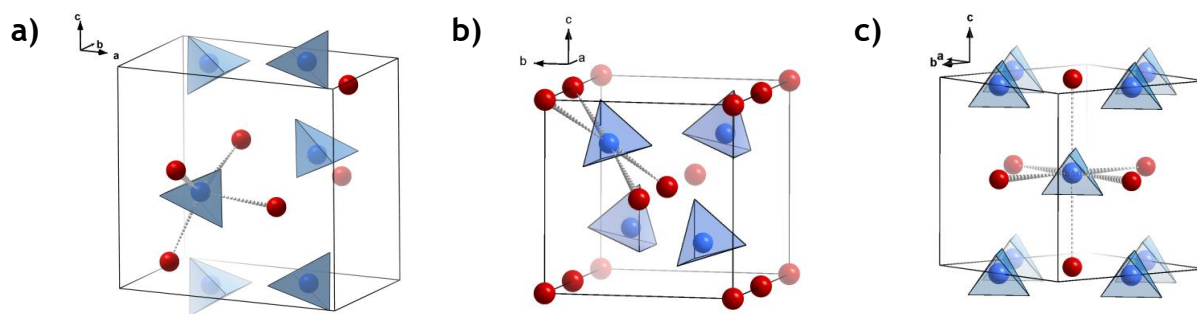


Figure 4.1-1 Crystal structures of the LiBH_4 phases observed at 0–18 GPa at ambient temperature.⁷ Coordination environment of the BH_4 tetrahedra by Li atoms is highlighted. a) Tetrahedral coordination in the LT – phase. b) Square-planar coordination in the AT – LP phase. c) Octahedral coordination in the HP – phase.

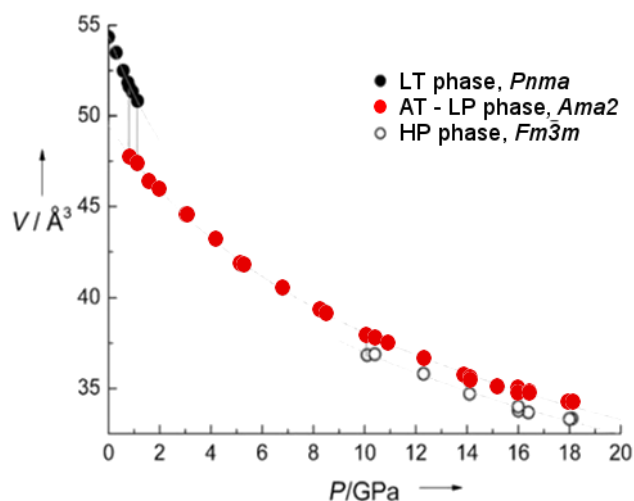


Figure 4.1-2 Variation of the volume of the LiBH_4 formula unit in the three phases at ambient temperature. The circles represent experimental data. Vertical lines represent phase transitions.⁷

After these polymorphs were discovered, there was significant interest in their ionic conductivity.¹¹⁻¹⁴ In 2011, Takamura *et al.* measured the ionic conductivity of these phases. HP - LiBH_4 , with the rock-salt structure, was expected to be ionically conductive due to the fact that it possesses an identical crystal structure to that of $\alpha\text{-LiI}$, which showed high ionic conductivity.¹¹ Indeed, conductivity measurements showed that the AT - LP and HP - LiBH_4 had a total ionic conductivity of 1.3×10^{-4} and $7.6 \times 10^{-4} \text{ S cm}^{-1}$ at 453 and 493 K (under 4 GPa), respectively.¹¹

These conductivity measurements are encouraging, however high temperatures and pressures need to be applied. Ideally, as it was mentioned in the introduction, the perfect solid state electrolyte should show ionic conductivities in the range of $1 - 10^{-3} \text{ S cm}^{-1}$ at ambient conditions. Therefore, some strategies are required to stabilise the high pressure phases of LiBH_4 at room temperature and ambient pressure.

In this chapter three different strategies were attempted to obtain HT - LiBH_4 which are shown in Table 4.1-1. These three different methods will be explained below.

Table 4.1-1 Three different strategies used in this chapter.

Strategy	Reactions
Method 1	$\text{LiBH}_4 + \text{NaBH}_4$
Method 2	$\text{LiBH}_4 + \text{NaBr}$
Method 3	<p>3 - a Synthesis of the precursor, HT – LiBH_4:</p> $(1-x)\text{LiBH}_4 + x\text{LiX}' \rightarrow \text{Li}(\text{BH}_4)_{1-x}\text{X}'_x \quad (\text{X}' = \text{Br} \text{ or } \text{I})$ <p>3 - b Synthesis of the HP – LiBH_4:</p> $(1-y)\text{Li}(\text{BH}_4)_{1-x}\text{X}'_x + y\text{NaBH}_4 \rightarrow \text{Li}_{(1-y)}\text{Na}_y(\text{BH}_4)_{1-x+xy}\text{X}'_{x(1-y)}$

As was mentioned in chapter 3 anion substitution in LT - LiBH_4 can improve conductivity by 3 orders of magnitude. The best performance was obtained by replacing $[\text{BH}_4]^-$ with the larger anion, I^- .¹⁵ In the literature, it has been suggested that larger cations than Li^+ could also improve the conductivity forming borohydrides such as $\text{Li}_{1-x}\text{A}_x\text{BH}_4$, where $\text{A} = \text{Na}^+$ or K^+ . These results proposed better performance with K^+ than Na^+ , as it was observed that as with halides, the bigger the dopant ion the better the conductivity acquired.¹⁶⁻²² S. Orimo *et al.* discovered that anion substitution triggers the stabilisation of the high temperature phase (HT - LiBH_4).^{15, 23, 24} Bernstein *et al.* also suggested that NaBH_4 or KBH_4 would stabilise the HT - LiBH_4 .¹⁸ In this chapter this strategy will be applied (**Method 1**). NaBH_4 would be mixed with LiBH_4 . Our hypothesis is that NaBH_4 would behave as a host for Li^+ , Li^+ would occupy some of the Na^+ sites because Li^+ possesses a smaller ionic radii. (Figure 4.1-3). NaBH_4 at ambient conditions presents the same structure as the HP - LiBH_4 at 18 GPa. Following **Method 1**, a mixed cation (Li-Na) borohydride would be obtained but we predict that this material will crystallise with the high pressure phase of LiBH_4 at ambient conditions and not with the HT - LiBH_4 structure, as Bernstein *et al.* predicted (Figure 4.1-3).¹⁸ In fact, in 2014, Takamura *et al.* demonstrated that the stabilization of HP - LiBH_4 could be performed by cation and anion substitution in borohydride. A mixture of KI and LiBH_4 in different molar ratios were synthesised. LiBH_4 was incorporated in the cubic rock-salt type structure of KI to surprisingly form the HP form of LiBH_4 under ambient pressure and achieving lithium ion conductivities of ca. $8 \times 10^{-4} \text{ S cm}^{-1}$ at 423 K for 3KI-LiBH_4 .¹⁴

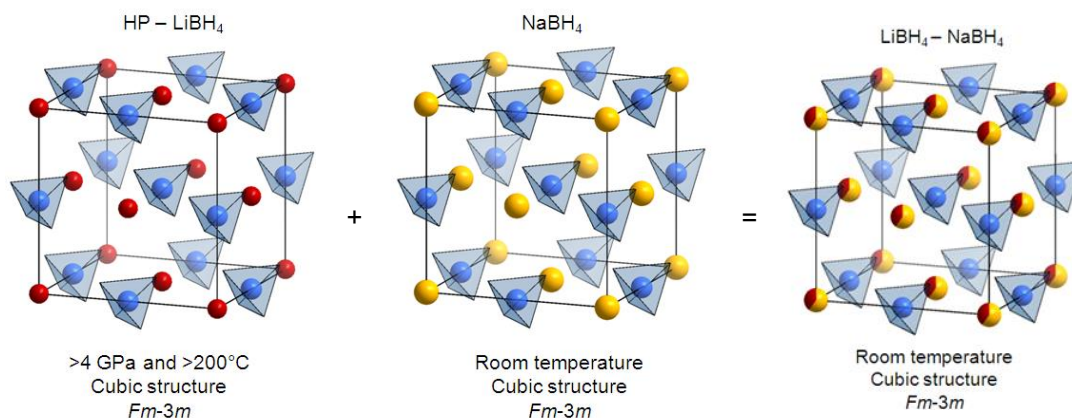


Figure 4.1-3 Proposed mechanism for cation substitution in LiBH₄ using NaBH₄ (Method 1).

Table 4.1-2 Known phases of mixed cation light metal borohydrides and their crystallographic characteristics^{25, 26}

Compound	Space group	<i>a</i> / Å	<i>b</i> / Å	<i>c</i> / Å	β / °	Ref.
LiK(BH ₄) ₂	<i>Pnma</i>	7.91337(5)	4.479067(3)	13.8440(1)		27
NaK(BH ₄) ₂	<i>R3</i>	4.615(2)		22.39(2)		28
LiSc(BH ₄) ₂	<i>P42c</i>	6.07593(6)		12.0338(1)		29
NaSc(BH ₄) ₄	<i>Cmcm</i>	8.170(2)	11.875(3)	9.018(2)		30
KSc(BH ₄) ₄	<i>Pnma</i>	11.856(5)	7.800(3)	10.126(6)		31
LiZn ₂ (BH ₄) ₅	<i>Cmca</i>	8.6244(3)	17.8970(8)	15.4114(8)		32
NaZn ₂ (BH ₄) ₅	<i>P2₁/c</i>	9.397(2)	16.635(3)	9.136(2)	112.66(2)	32
NaZn ₂ (BH ₄) ₃	<i>P2₁/c</i>	8.2714(16)	4.5240(7)	18.757(3)	101.69(1)	32
Al ₃ Li ₄ (BH ₄) ₁₃	<i>P-43n</i>	11.3640(3)				33
Li ₃ MgZn ₅ (BH ₄) ₁₅	<i>P6₃/mcm</i>	15.371(3)		8.586(2)		34
Li ₃ MnZn ₅ (BH ₄) ₁₅	<i>P6₃/mcm</i>	15.391(3)		8.590(2)		34
NaYb(BH ₄) ₄	<i>Cmcm</i>	8.438(4)	12.057(6)	9.057(4)		35
KYb(BH ₄) ₄	<i>Cmcm</i>	8.434(1)	12.445(2)	9.6449(15)		35
KHo(BH ₄) ₄	<i>Cmcm</i>	8.501(2)	12.493(3)	9.643(3)		36

Table 4.1-2 shows the known phases of mixed cation compounds containing at least one alkali metal hydride. However only one stable mixed alkali borohydride has been found; $\text{LiK}(\text{BH}_4)_2$. The results reported from this compound showed that the material cannot be obtained as a single phase, LiBH_4 and KBH_4 are still present in the final compound.²⁷ A metastable mixed alkali hydride $\text{NaK}(\text{BH}_4)_2$ has also been reported²⁸, but after 14 hours this reverted back to the stable starting materials, NaBH_4 and KBH_4 .²⁸ Another possible mixed alkali hydride is $\text{LiNa}(\text{BH}_4)_2$, however nothing has yet been reported about this compound but it has been predicted to be isomorphous with HT - LiBH_4 .^{7, 16-18}

Table 4.1-3 Known phases of mixed cation – anion light metal borohydrides and their crystallographic characteristics.

Compound	Space group	$a / \text{Å}$	$b / \text{Å}$	$c / \text{Å}$	$\beta / ^\circ$	Ref.
$(\text{LiBH}_4)_x(\text{KI})_{1-x}$	$Fm\bar{3}m$	*				14
$\text{LiLa}(\text{BH}_4)_3\text{Cl}$	$I\bar{4}3m$	11.7955(1)				37, 38
$\text{LiCe}(\text{BH}_4)_3\text{Cl}$	$I\bar{4}3m$	11.6243(1)				39
$\text{LiPr}(\text{BH}_4)_3\text{Cl}$	$I\bar{4}3m$	11.5784(1)				40
$\text{LiNd}(\text{BH}_4)_3\text{Cl}$	$I\bar{4}3m$	11.5480(2)				40
$\text{LiGd}(\text{BH}_4)_3\text{Cl}$	$I\bar{4}3m$	11.5627(1)				38
$\text{NaAl}(\text{BH}_4)_x\text{Cl}_{4-x}$	$Pmn2_1$	7.9001(4)	7.0033(3)	6.4888(3)		41
$\text{NaY}(\text{BH}_4)_{1.58}\text{Cl}_{2.42}$ (at 230 °C)	$P2_1/c$	6.6649(4)	8.2058(5)	6.8109(4)	89.959(8)	21
$\text{KZn}(\text{BH}_4)\text{Cl}_2$	$P2_1/m$	7.6948(7)	5.7668(4)	6.8930(6)	98.37(1)	31
$\text{Rb}_2\text{Li}[\text{Y}(\text{BH}_4)_{6-x}\text{Cl}_x]$	$Fm\bar{3}m$	11.1271(9)				42
$\text{Cs}_2\text{Li}[\text{Y}(\text{BH}_4)_{6-x}\text{Cl}_x]$	$Fm\bar{3}m$	11.126(3)				42

*Not reported

Another strategy reported to promote H_2 release and to tune the thermodynamics of the thermal decomposition of solid borohydrides is to substitute both cation and anions in borohydrides. Table 4.1-3 shows all the mixed cation-anion borohydrides reported so far which contain at least one alkali metal. Mixed cation-anion rare earth borohydrides have been the most well-known and studied in the last decade. Apart from Eu, the remainder of rare earth borohydrides (mixed cation,

mixed cation-anion or just the borohydride itself) have been identified.^{36, 40, 43, 44} The ionic conductivity for some of these have been reported ($\text{LiM}(\text{BH}_4)_3\text{Cl}$, where $M = \text{La}, \text{Ce}, \text{Gd}$). Ionic conductivities of 2.3×10^{-4} , 7×10^{-5} and $3.5 \times 10^{-4} \text{ S cm}^{-1}$ were found at 293 K for $\text{LiLa}(\text{BH}_4)_3\text{Cl}$, $\text{LiCe}(\text{BH}_4)_3\text{Cl}$ and $\text{LiGd}(\text{BH}_4)_3\text{Cl}$, respectively.³⁷⁻³⁹

We will use the *fcc* structure of NaBr to try and stabilise the high pressure phase of LiBH_4 at ambient pressure. This is based on the approach of Takamura *et al.*¹⁴ who demonstrated that KI could behave as a host for LiBH_4 (Figure 4.1-4).

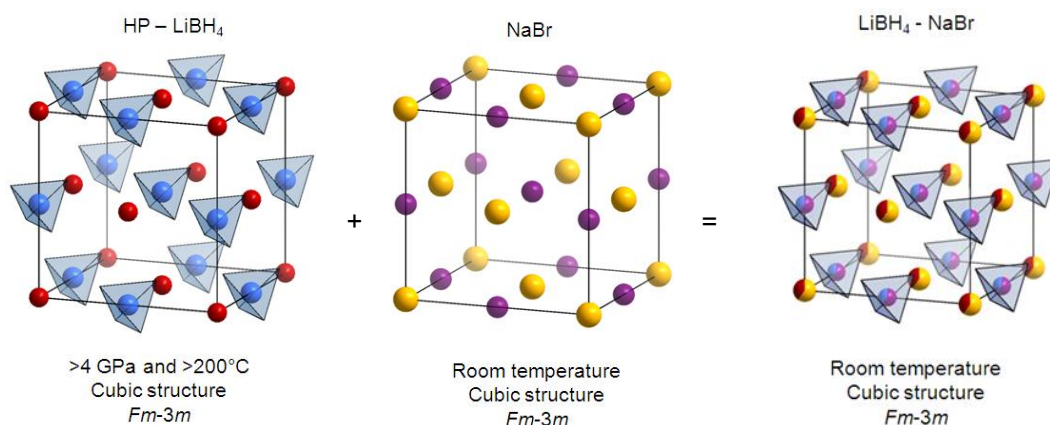


Figure 4.1-4 Proposed mechanism for cation substitution in LiBH_4 using NaBr (Method 2).

On the other hand, another strategy would be to form the mixed anion borohydride ($\text{LiBH}_4\text{-LiBr}$) and then mix it with NaBH_4 to form a mixed cation-anion borohydride ($\text{LiBH}_4\text{X}'\text{-NaBH}_4$, where $\text{X}' = \text{Br}^-$ and I^- , **Method 3**). In this case we will use as a host NaBH_4 for LiBH_4 .

We report the products of these three reaction schemes and show how the structures are related to the ionic transport properties.

4.2 Experimental

4.2.1 Synthesis of substituted HP – LiBH_4 phases

For the synthesis of the substituted HP - LiBH_4 phases, anhydrous LiBH_4 (Sigma-Aldrich, $\geq 95\%$), NaBH_4 (Alfa, 98%), LiI (Sigma-Aldrich, 99.9%, trace metals basis) and LiBr (Sigma-Aldrich, $\geq 99\%$) were used as supplied with no further purification. Synthesis was performed in a nitrogen atmosphere using a Retsch PM100 ball mill.

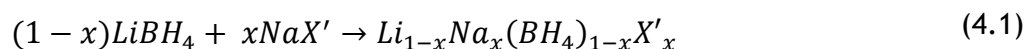
Three different approaches were performed which will be referred to as **Methods 1, 2, and 3**.

4.2.1.1 Method 1 (LiBH₄ – NaBH₄)

Mixtures of LiBH₄ and NaBH₄ were milled for 4 h at 500 rpm (80 : 1, ball-to-powder-ratio). The ball milling was performed in periods of 2 minutes of milling interspersed by 2 min breaks to minimise heating of the samples. The mixtures investigated in this section can be found summarized in Table 4.3-1.

4.2.1.2 Method 2 (LiBH₄ – NaBr)

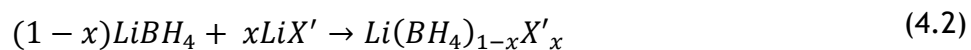
The same milling procedure was applied to LiBH₄ and NaBr. The samples prepared in this section are summarized in Table 4.3-1.



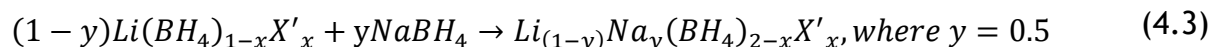
4.2.1.3 Method 3 (LiBH₄ – LiX – NaBH₄, where X = Br and I)

The last approach (**Method 3**) was composed of two steps (**3-a**) and (**3-b**). Firstly, the halide was incorporated in LiBH₄ by milling LiX and LiBH₄, forming the HT phase of LiBH₄ in Li(BH₄)_xX'_(1-x). Different molar ratios of LiBH₄ and LiX were investigated in order to study the effect of halide concentration in the anticipated final HP - LiBH₄ phase. Table 4.3-4, Table 4.3-5, and Table 4.3-6 show the different mixtures studied for X = Br⁻ and X = I⁻ (seven different compositions were studied for I⁻ and just one for Br⁻ to confirm the mechanism). Secondly, once the halide was incorporated in LiBH₄, this product was reacted with NaBH₄ to form the HP - LiBH₄ (Table 4.3-4, Table 4.3-5, and Table 4.3-6). For the second step of the reaction only one molar ratio ([Li(BH₄)_{1-x}X'_x] : NaBH₄, 1:1) was selected in order to maintain a constant 1:1 Li/Na ratio. The halide content of the final material could thus be varied and was studied over the range 8 - 50% for the iodide.

(3-a) Synthesis of the precursor, HT - LiBH₄:

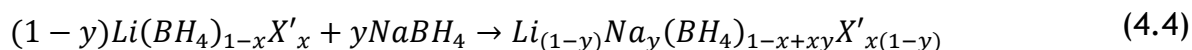


(3-b) Synthesis of HP - LiBH₄:



By fixing the cation ratio we examined the influence of halide content on ionic conductivity. The amount of cation was not modified because in order to perform an experiment where the cation amount has to be different for each sample, the anion amount also would be different for each sample (3-c).

(3-c) Synthesis of HP - LiBH₄:



For the first step of the reaction (3-a), approximately 0.5 g LiBH₄ - LiX' (precursor, where X' = Br, I) mixtures were mechanically milled for 4 and 24 h for I⁻ and Br⁻ samples, respectively. For the second step (3-b), approximately 0.5 g Li(BH₄)_{1-x}X'_x and NaBH₄ (1:1) were mechanically milled for 10 h for both halides. The same conditions for the ball milling process from section 4.2.1.1 were used for this step. The final mixture was heated to 598 K for 20 h for the bromide sample. Samples which contained iodide were heated to 473 K for 2 h after milling.

4.2.2 Characterisation

The conditions for the characterisation, powder neutron diffraction and Raman spectroscopy, can be found in sections 2.3.1.2, 2.3.1.3 and 2.5.1.1.

4.3 Results and discussion

4.3.1 Mixed cation borohydride

4.3.1.1 Method 1 (LiBH₄ – NaBH₄ system)

Different mixtures of LiBH₄ and NaBH₄ were studied in order to form mixed alkali borohydrides as a single phase for the first time. Two different regions were observed in the phase diagram of LiBH₄ - NaBH₄ system (Li_{1-x}Na_xBH₄) (Figure 4.3-1). In region I ($x \leq 0.5$, samples 34 - 36) the peaks observed belonged to both reactants (LT - LiBH₄ and NaBH₄), indicating no reaction between them. In region II (37), the patterns can be fully indexed using a face centred unit cell that show a constant volume with significant variation with Li composition, as shown in Table 4.3-1 and Figure 4.3-1.

Table 4.3-1 Lattice parameters of samples from Method 1 (LiBH₄ – NaBH₄ mixtures, 34 - 37)

Sample	Na content, <i>x</i>	Final compound	<i>a</i> / Å	<i>b</i> / Å	<i>c</i> / Å	<i>V</i> / Å ³
---	LT – LiBH ₄	LT – LiBH ₄	7.17858(4)	4.43686(2)	6.80321(4)	216.685(3) ⁵
34	0.09	LT – LiBH ₄	7.159(9)	4.416(3)	6.843(3)	216.4(3)
		NaBH ₄	6.1(1)	---	---	230(4)
35	0.25	LT – LiBH ₄	7.12(1)	4.435(4)	6.86(1)	216.4(5)
		NaBH ₄	6.155(6)	---	---	233.2(2)
36	0.50	LT – LiBH ₄	*	*	*	*
		NaBH ₄	6.165(3)	---	---	234.3(1)
37	0.91	LT – LiBH ₄	---	---	---	---
		NaBH ₄	6.1641(7)	---	---	234.21(3)
---	NaBH ₄	NaBH ₄	6.1635(5)	---	---	234.14 ⁹

*Not enough reflections for structural analysis and because of dominant Na scattering.

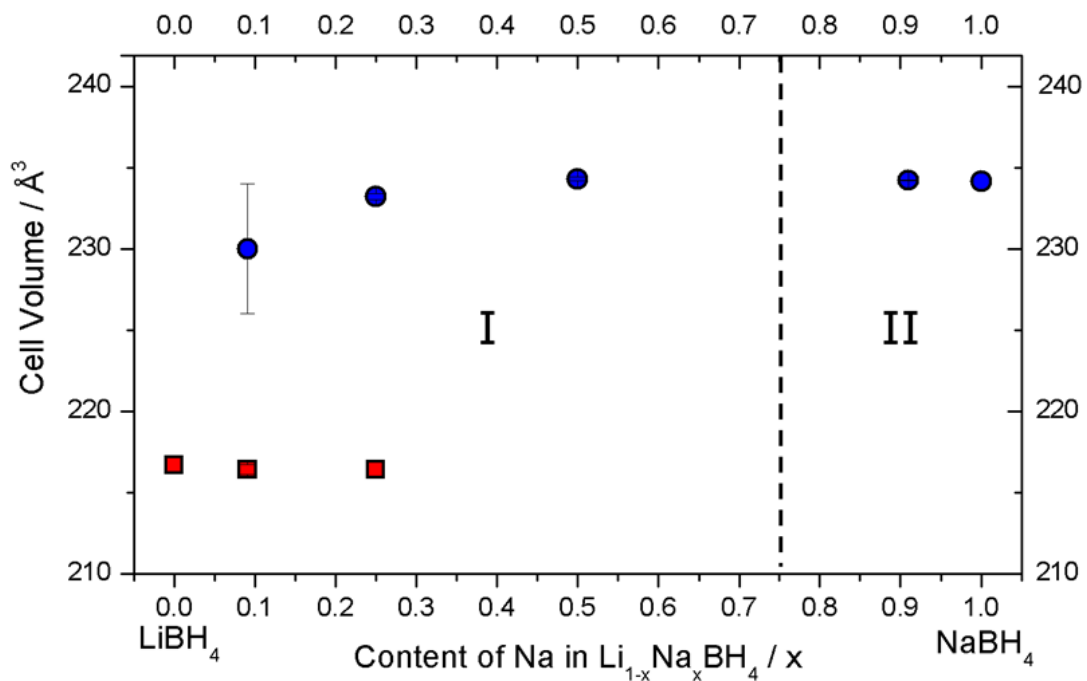


Figure 4.3-1 Na content in Li_{1-x}Na_xBH₄ (Method 1), where LT – LiBH₄ is represented with red squares and NaBH₄ with blue circles. Error bars are shown for each sample.

We conclude that the reaction between these reactants is not possible under these conditions because any the reactant phases remain after the treatment.

4.3.2 Mixed cation – anion borohydrides

4.3.2.1 Method 2 (LiBH_4 – NaBr system)

4.3.2.1.1 Bromide substitution

Method 2: The LiBH_4 - NaBr system was studied for the nine different compositions shown in Table 4.3-2 and Figure 4.3-2. In total, eight different regions were observed in the phase diagram of the LiBH_4 -NaBr system (4.1). Only peaks from the LT phase from LiBH_4 were observed when $x \leq 0.09$ (sample **38**, region I). In region II ($x = 0.16$, **39**) two different phases were present, the LT phase of LiBH_4 and an additional phase that was indexed as a new cubic unit cell. In region III ($x = 0.20$, **40**) the LT - LiBH_4 phase and the new cubic phase were still present, however peaks from the HT - LiBH_4 phase also emerged. When the content of NaBr was increased from 0.25 to 0.30 (region IV, sample **41** and **42**) only the HT - LiBH_4 phase and the new cubic structure were observed. In region V ($x = 0.50$, **43**), three different phases were present which belonged to the new cubic structure, HT - LiBH_4 and NaBr. Only peaks that belonged to three rock salt-type structures were observed (region VI, sample **44**) when the content of NaBr in the solid solution was $0.70 = x$ (NaBr, LiBr and the new cubic structure). However this new structure was absent if the content of Na^+ was increased to $0.70 \leq x$ (region VII, sample **45**), and only NaBr and LiBr were observed. At higher content of NaBr, only peaks from the NaBr phase were observed (region VIII, $0.83 \leq x \leq 1.00$, **46**).

Table 4.3-2 Lattice parameters of samples from Method 2 (LiBH₄ – NaBr mixtures, 38 - 46)

Sample	LiBH ₄ : NaBr	Li content / x	Na content / x	Final compound	a / Å	b / Å	c / Å	V / Å ³
---	LT – LiBH ₄	1.00	0.00	LT – LiBH ₄	7.17858(4)	4.43686(2)	6.80321(4)	216.685(3) ⁵
38	10 : 1	0.91	0.09	LT – LiBH ₄ – type	7.14(6)	4.45(4)	6.76(2)	214(3)
39	5 : 1	0.84	0.16	LT – LiBH ₄ – type	7.32(4)	4.70(2)	6.76(2)	217(2)
				HP – LiBH ₄ – type (Li _{1-x} Na _x (BH ₄) _{1-x} Br _x)	6.08(2)	---	---	225.0(8)
40	4 : 1	0.80	0.20	LT – LiBH ₄ – type	7.20(3)	4.41(4)	6.83(3)	216(3)
				HT – LiBH ₄ – type	4.218(3)	---	6.767(2)	104.27(9)
				HP – LiBH ₄ – type	6.08(2)	---	---	225.0(8)
41	3 : 1	0.75	0.25	HT – LiBH ₄ – type	4.210(8)	---	6.737(2)	103.4(2)
				HP – LiBH ₄ – type	6.06(2)	---	---	223.0(8)
42	2 : 1	0.67	0.33	HT – LiBH ₄ – type	4.209(8)	---	6.749(5)	103.5(2)
				HP – LiBH ₄ – type	6.056(5)	---	---	222.1(2)
43	1 : 1	0.50	0.50	HT – LiBH ₄ – type	4.206(3)	---	6.7277(8)	103.08(6)
				HP – LiBH ₄ – type	6.03(1)	---	---	220.2(4)
				NaBr – type	5.973(5)	---	---	213.1(2)
44	1 : 2.33	0.30	0.70	HT – LiBH ₄ – type	*	*	*	*
				HP – LiBH ₄ – type	6.011(7)	---	---	216.9(3)
				NaBr – type	9.973(3)	---	---	213.09(9)
				LiBr – type	5.510(6)	---	---	167.3(2)
45	1 : 5	0.16	0.84	NaBr – type	5.974(5)	---	---	213.2(2)
				LiBr – type	5.511(4)	---	---	167.4(1)
46	1 : 10	0.09	0.91	NaBr – type	5.966(2)	---	---	212.70(6)
---	NaBr	0.00	1.00	NaBr	5.9738(7)	---	---	213.18 ⁴⁵

*Not enough reflections for structural analysis

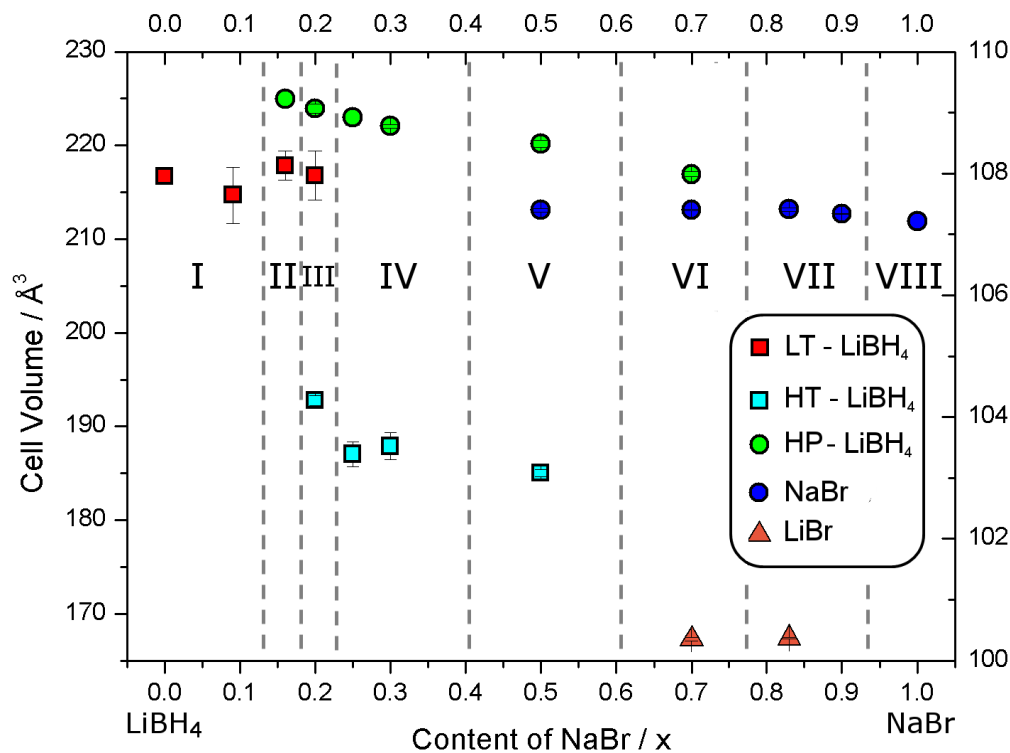


Figure 4.3-2 Phase diagram of LiBH₄ – NaBr system by mechanochemical treatment. Five different phases were identified: LT – LiBH₄ in red squares; HT – LiBH₄ in light blue squares; HP – LiBH₄ (Li_{1-x}Na_x(BH₄)_{1-x}Br_x) in green circles; NaBr in blue circles; and LiBr in orange circles. The left axes is for all the compounds apart from the HT – LiBH₄ that is represented in the right axes (Method 2). Error bars are shown for each sample.

The observation of a new $Fm\bar{3}m$ rock salt type structure in regions III-V suggests the formation of a Li_(1-x)Na_x(BH₄)_{1-x}Br_x solid solution with a similar structure to HP-LiBH₄. This suggests that some Li⁺ can be incorporated into NaBr if the structure is stabilised by [BH₄]⁻. In this case, the ionic radius of BH₄⁻ (2.05 Å)⁴⁶ is slightly larger than Br⁻ (1.96 Å)⁴⁶ and the resulting mixed cation - mixed anion compound cannot be formed as a single phase. Therefore another approach was suggested.

4.3.2.2 Method 3

4.3.2.2.1 Bromide substitution

For bromide system one single composition was prepared using this two-step synthesis (Table 4.3-3). Figure 4.3-3 shows the XRD pattern of the precursor (Method 3-a, 47a) once it was synthesised by ball milling LiBH₄ and LiBr for 24 h.

Table 4.3-3 Composition of samples from Method 3-a (LiBH₄ – LiBr mixtures, 47a)

Sample	LiBH ₄ :LiBr	Final compound
47a	2:1	Li(BH ₄) _{0.67} Br _{0.33}

Table 4.3-4 Lattice parameters of sample from Method 3-b (LiBH₄ – LiBr – NaBH₄ mixture, 47b - 47c).

Sample	NaBH ₄	47b	47c	
[LiBH ₄ :LiBr] : NaBH ₄	---	[2:1] : 1	[2:1] : 1	
Bromide content	0.16	0.16	0.16	
Final compound	---	LT – LiBH ₄ – type	HP – LiBH ₄ – type	Li _{0.5} Na _{0.5} (BH ₄) _{0.84} Br _{0.16}
<i>a</i> / Å	6.1635(5)	7.1659(4)	6.109(5)	6.1021(1)
<i>b</i> / Å		4.4171(4)		
<i>c</i> / Å		6.833(1)		
<i>V</i> / Å ³	234.14 ⁹	216.27(5)	228.0(2)	227.22(1)

Treatment: **47b** (MT) and **47c** (MT/TT) (MT: Mechanochemical treatment, TT: thermal treatment).

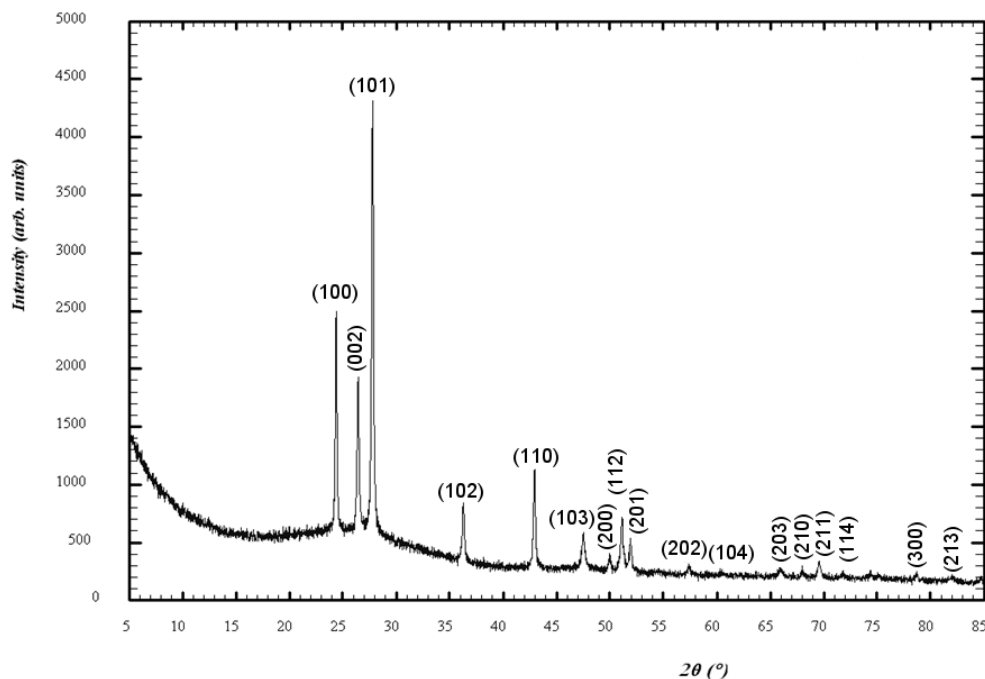


Figure 4.3-3 XRD pattern of sample 47a. Synthesis of the precursor (LiBH₄ : LiBr, 2:1) by mechanochemical treatment, for 24 h at 500 rpm (Method 3-a, HT phase). The peaks are indexed using the *P6₃mc* space group of the high temperature polymorph of LiBH₄ structure.

The Br-substituted HT - LiBH₄ was milled with NaBH₄ in a 1 : 1 molar ratio for 10 h (3-b, 47b) to give the XRD pattern shown in Figure 4.3-4 (Table 4.3-4). Two different phases were identified. HP - LiBH₄ - type (Li, Na) (BH₄, Br) was formed, but another phase was present which could be identified as LT - LiBH₄ - type. These results suggested that the reaction was not completed after ball milling for 10 h. Therefore thermal treatment was applied for 20 h at 598 K. As Figure 4.3-5 shows, a single phase was obtained after the thermal treatment. This phase was assigned to a rock-salt type structure which was composed of mixed cation (50% of Li⁺/Na⁺) and anion (84% of BH₄⁻ and 16% of Br⁻) borohydride. Sample 47c was indexed with a cubic structure, space group *Fm* $\bar{3}$ *m* (#227), *a* = 6.1021(1) Å and *V* = 227.22(1) Å³ (Table 4.3-4).

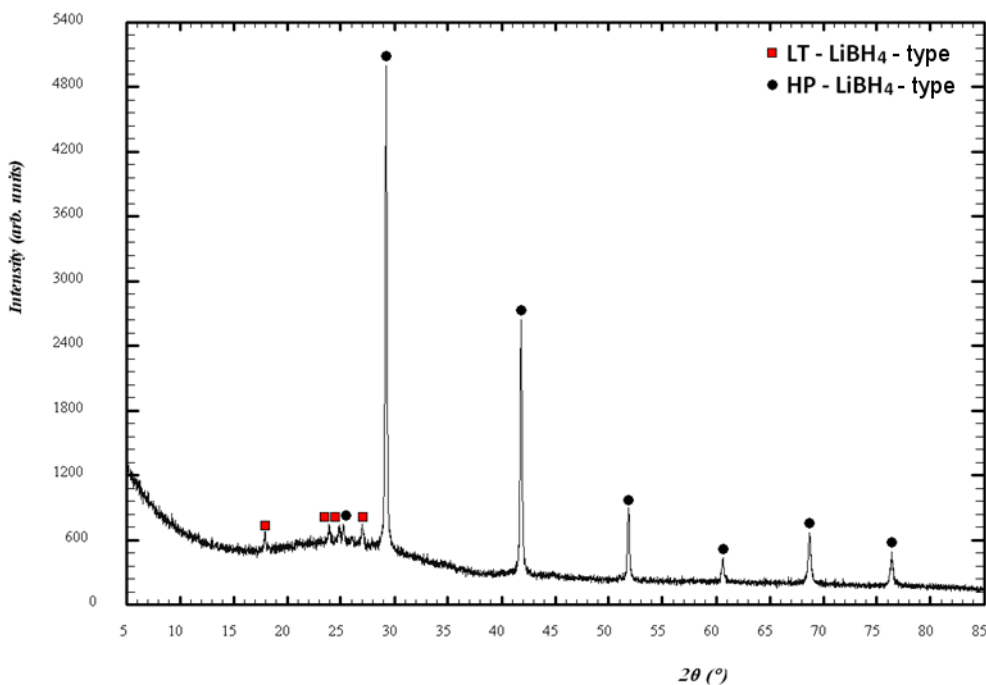


Figure 4.3-4 XRD pattern of sample 47b only by mechanochemical treatment for 10 h at 500 rpm (Method 3-b).

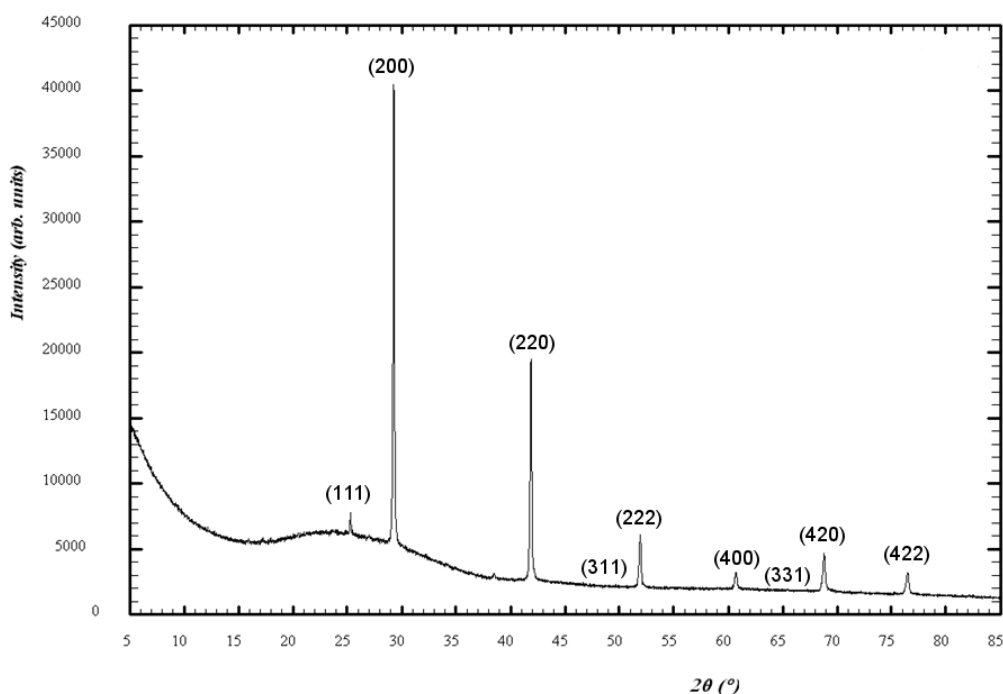


Figure 4.3-5 XRD pattern of sample 47c post mechanochemical (10 h at 500 rpm) and thermal treatment (5 K min⁻¹, 20 h at 598K, Method 3-b, HP phase).

4.3.2.2.2 Iodide substitution

The synthesis of different mixed cation-anion borohydrides, using **Method 3-a** and **3-b** with iodide as halide, was motivated by the results obtained from the analogous bromide sample **47c**. As it was mentioned earlier and in the literature, better ionic conductivity is expected for iodide samples because of its lower migration energy of lithium ions halides with rock salt type structure.⁶¹ Therefore the same study was performed for iodide but more extensively. Firstly, samples of $\text{Li}(\text{BH}_4)_{1-x}\text{I}_x$ with the HT - LiBH_4 structure were synthesised by mechanochemical treatment of LiBH_4 and LiI following method **3-a** (Table 4.3-5). These mixtures were used as precursors for the synthesis of $(\text{Li}, \text{Na})(\text{BH}_4, \text{I})$ with NaBH_4 in a 1 : 1 molar ratio to form materials with 1 : 1 Li and Na in the final compounds but containing variable amounts of halide which ranged from 8 - 50% BH_4^- content (Table 4.3-6).

Figure 4.3-6 shows the XRD patterns from each precursor formed with different compositions of LiBH_4 and LiI (**3-a**). All the peaks corresponded to the HT structure of LiBH_4 . As observed in the Br containing sample, iodide stabilises the HT phase of LiBH_4 .⁴⁷ As the content of I⁻ increased, so the cell volume of the HT - LiBH_4 expanded

because the ionic radius of I⁻ (2.20 Å)⁴⁶ is slightly larger than that of BH₄⁻ (2.05 Å)⁴⁶. Therefore the peaks were displaced to lower 2θ because of the increase in cell volume, as indicated with a red dotted line in Figure 4.3-6.

Figure 4.3-7 shows the patterns of the second step of the reaction (3-b). Only peaks from a rock salt type structure were found in each composition. The cell volume increased as the amount of halide increased in the precursor; therefore all the peaks displaced to lower 2θ as is indicated in Figure 4.3-7 by the red dotted line. Samples 54 - 60 were indexed with a cubic structure, space group $Fm\bar{3}m$ (#227). The lattice parameters and cell volume for each sample can be found in Table 4.3-6.

Table 4.3-5 Composition of samples from Method 3-a (LiBH₄ – Lil mixtures, 48 - 53)

Sample	LiBH ₄ :Lil	Final compound
48	5:1	Li(BH ₄) _{0.83} I _{0.17}
49	4:1	Li(BH ₄) _{0.80} I _{0.20}
50	3:1	Li(BH ₄) _{0.75} I _{0.25}
51	2:1	Li(BH ₄) _{0.67} I _{0.33}
52	1:1	Li(BH ₄) _{0.50} I _{0.50}
53	1:2	Li(BH ₄) _{0.33} I _{0.67}

Table 4.3-6 Lattice parameters of sample from Method 3-b (LiBH₄ – Lil – NaBH₄ mixture, 54 - 60)

Sample	[LiBH ₄ :Lil] : NaBH ₄	Iodide content	Final compound	a / Å	V / Å ³
NaBH ₄	---	0	---	6.1635(5)	234.14 ⁹
54	[5:1] : 1	0.08	Li _{0.5} Na _{0.5} (BH ₄) _{0.92} I _{0.08}	6.216(6)	240.2(2)
55	[4:1] : 1	0.10	Li _{0.5} Na _{0.5} (BH ₄) _{0.90} I _{0.10}	6.227(2)	241.19(8)
56	[3:1] : 1	0.13	Li _{0.5} Na _{0.5} (BH ₄) _{0.87} I _{0.13}	6.241(9)	243.1(4)
57	[2:1] : 1	0.16	Li _{0.5} Na _{0.5} (BH ₄) _{0.84} I _{0.16}	6.264(6)	245.8(2)
58	[1:1] : 1	0.25	Li _{0.5} Na _{0.5} (BH ₄) _{0.75} I _{0.25}	6.324(5)	253.0(2)
59	[1:2] : 1	0.33	Li _{0.5} Na _{0.5} (BH ₄) _{0.67} I _{0.33}	6.371(6)	258.5(2)
60	NaBH ₄ : Lil	0.50	Li _{0.5} Na _{0.5} (BH ₄) _{0.50} I _{0.50}	6.437(6)	266.7(3)

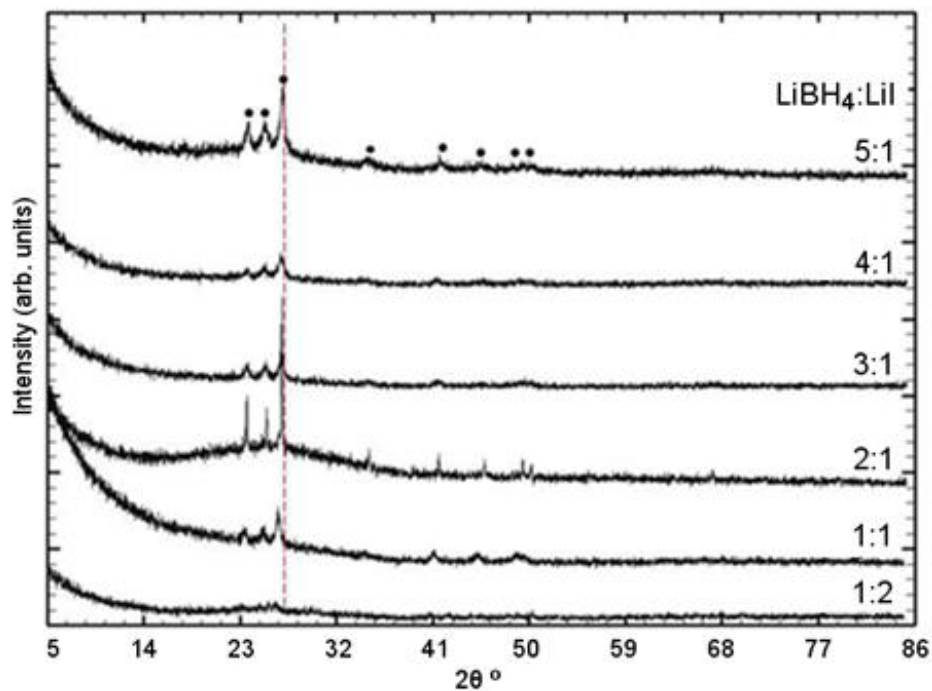


Figure 4.3-6 XRD patterns of the precursors (LiBH_4 : LiI mixtures, HT phase, 48 - 53) (Method 3-a).

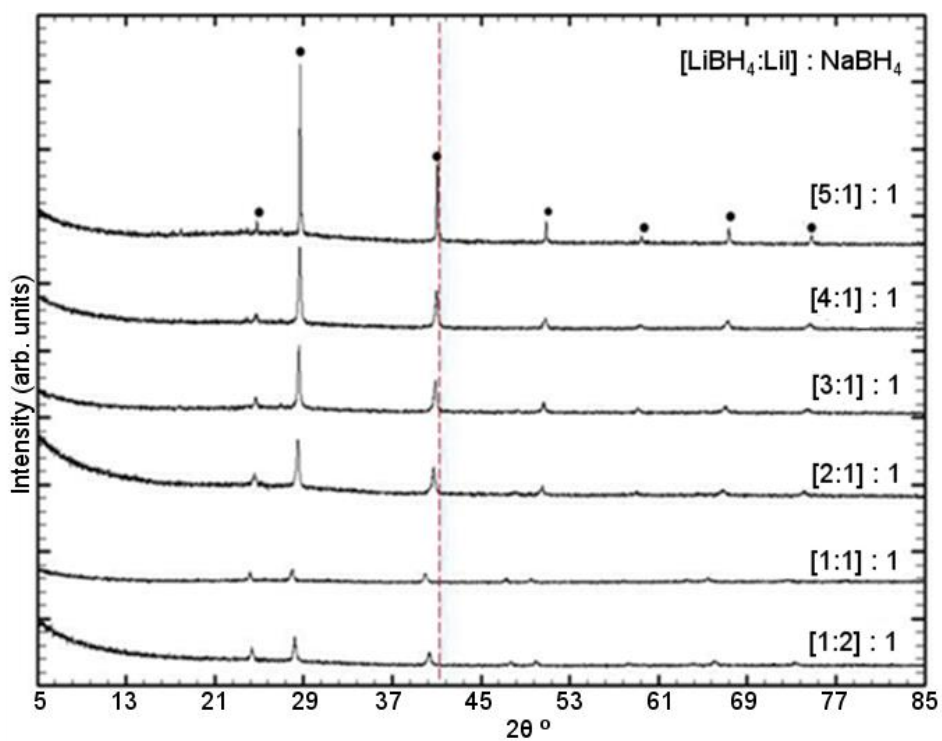


Figure 4.3-7 XRD pattern of $[\text{LiBH}_4 : \text{LiI}] : \text{NaBH}_4$ mixtures (54 - 60, Method 3-b) which could be identified as pure HP - LiBH_4 type phases.

Figure 4.3-8 demonstrates that the cell volume increases linearly with the iodide content across the range of compositions synthesised. In total, seven different composition of HP - LiBH₄ were successfully synthesised.

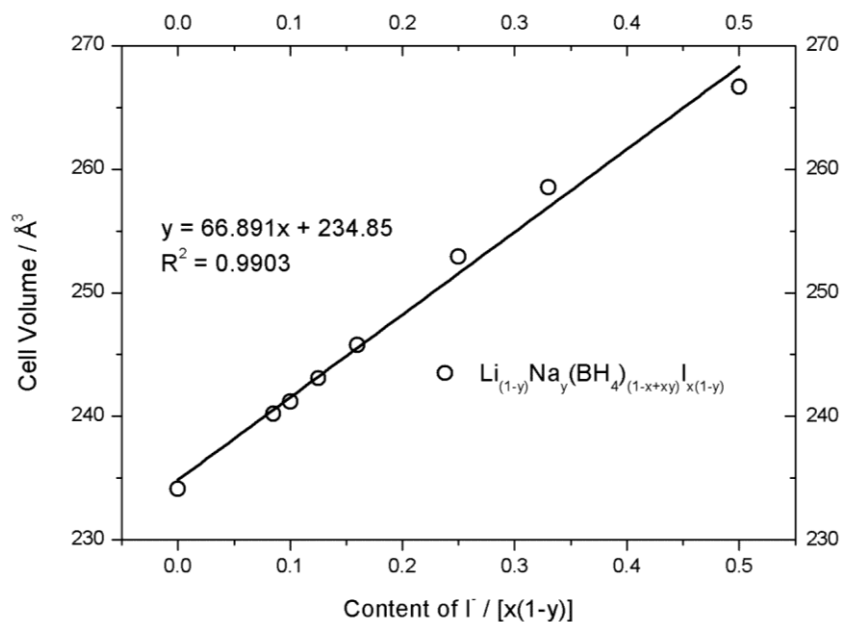


Figure 4.3-8 Cell dimensions of 54 - 60 as a content of iodide. (Method 3-b, HP phase).

4.3.3 Method 3: Characterisation of the HP - LiBH₄ type phases

4.3.3.1 Raman spectroscopy

HP - LiBH₄ type samples synthesised using **Method 3** were investigated using Raman spectroscopy. The Raman spectra of samples 47c, 57, LT - LiBH₄, HT - LiBH₄, and NaBH₄ are shown in Figure 4.3-9. The LT - LiBH₄ phase showed the splitting of the bending modes (ν_2 and ν_2'), due to the anisotropy of the B - H atomistic vibrations in the orthorhombic structure, as was reported by Orimo *et al.*⁴⁸ However, if the LT - LiBH₄ phase is heated the splitting diminishes.^{5, 49} When the HT phase of LiBH₄ is stabilised at room temperature by anion substitution with halides, the same phenomenon is observed (Figure 4.3-9). One sample with the HP - LiBH₄ structure from each of the halides were selected for Raman measurements. The samples selected containing Br⁻ and I⁻ were 47c and 57 respectively. Both samples contained 16% of halide and 50% of Li⁺/Na⁺. These samples were selected because they showed the best performance in ionic conductivity which will be discussed in section 4.3.3.2.

Both HP - LiBH₄ type samples synthesised (**47c** and **57**) showed similar Raman shifts compared to isostructural NaBH₄, as on the one hand, the Raman shift of the B - H stretching mode was slightly higher for both samples than for NaBH₄ ($\nu_1 = 2325 \text{ cm}^{-1}$). On the other hand, the B - H bending modes decreased in wavenumber in the order of NaBH₄ ($\nu_2 = 1274 \text{ cm}^{-1}$) > **47c** ($\nu_2 = 1270 \text{ cm}^{-1}$) > **57** ($\nu_2 = 1260 \text{ cm}^{-1}$).

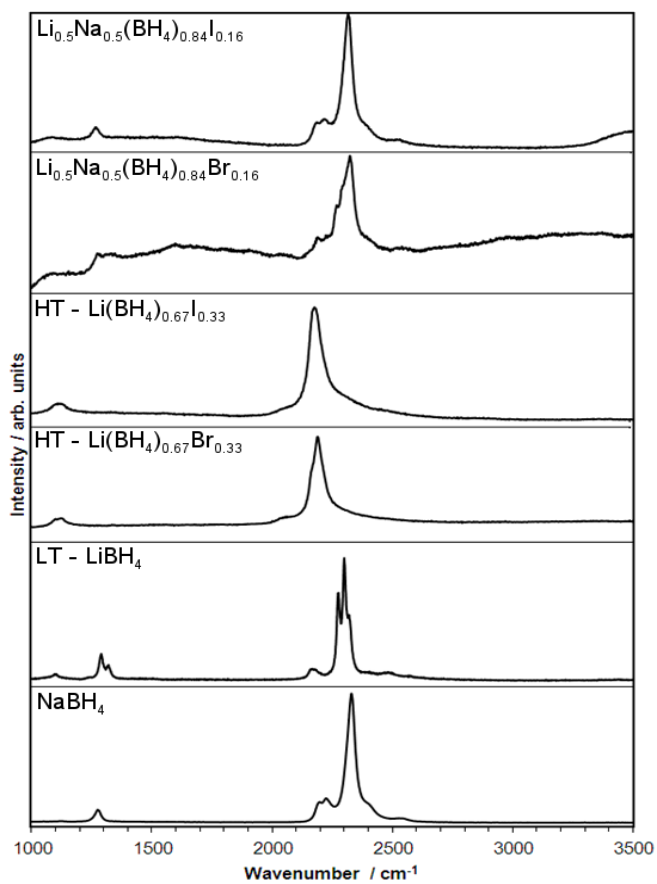


Figure 4.3-9 Raman spectra of **47c** ($\text{Li}_{0.5}\text{Na}_{0.5}(\text{BH}_4)_{0.84}\text{Br}_{0.16}$) and **57** ($\text{Li}_{0.5}\text{Na}_{0.5}(\text{BH}_4)_{0.84}\text{I}_{0.16}$) and a comparison with the corresponding modes of HT - $\text{Li}(\text{BH}_4)_{0.67}\text{Br}_{0.33}$, HT - $\text{Li}(\text{BH}_4)_{0.67}\text{I}_{0.33}$, LT - LiBH₄ and NaBH₄.

4.3.3.2 Electrochemical impedance spectroscopy

4.3.3.2.1 HP - LiBH₄ stabilised with 16 % halide ($\text{Li}_{0.5}\text{Na}_{0.5}(\text{BH}_4)_{0.84}\text{X}_{0.16}$, X = Br⁻ and I⁻)

Conductivity measurements were performed for the bromide and iodide HP - LiBH₄ type samples (**47c** and **57**, respectively). Impedance data analysed in the complex plane showed a semicircle at high frequencies and a linear response in the lower frequency range caused by the electrode contribution (Figure 4.3-10). Due to the observation of a single semicircle it is not possible to extract values for intra-and

inter-grain resistance. The data were analysed using an equivalent electrical circuit to extract the values for the total resistivity of the material. Especially at high temperatures and low frequencies, the spectra were governed by electrode polarization due to the usage of ion-blocking electrodes. An estimate of the total conductivity was made from the combination of a resistor and a constant phase element in parallel. Figure 4.3-10 shows the Nyquist plot from **47c** and **57** which have similar composition, 16% halide and 50% Li⁺/Na⁺ content. Sample **57** demonstrated conductivities of ca. 10⁻⁶ S cm⁻¹ at 313 K with activation energies in the range 0.56 - 0.60 eV, whereas **47c** showed a total ionic conductivity of ca. 10⁻⁷ S cm⁻¹ at the same temperature with higher values of activation energy, 0.62 - 0.66 eV (Figure 4.3-11 and Table 4.3-7). At 413 K, **47c** and **57** exhibited total ionic conductivities of 9.0 × 10⁻⁵ and 6.1 × 10⁻⁴ S cm⁻¹, respectively. *i.e.* ca. 3 and 4 orders of magnitude higher than NaBH₄ at an equivalent temperature (ca. 10⁻⁸ S cm⁻¹, see Table 4.3-7).

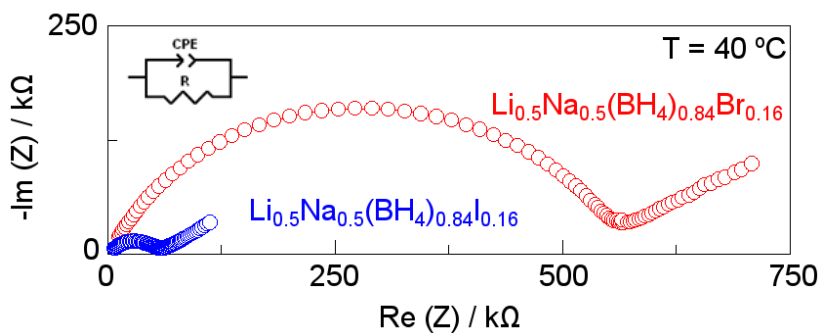


Figure 4.3-10 Nyquist plot of **47c** and **57** at 313 K.

Table 4.3-7 Ionic conductivities (σ) at 313 K and the activation energies (E_a) for conduction in Li_{0.5}Na_{0.5}(BH₄)_{0.84}Br_{0.16} (**47c**, HP – LiBH₄), Li_{0.5}Na_{0.5}(BH₄)_{0.84}I_{0.16} (**57**, HP – LiBH₄), LT – LiBH₄, HP – LiBH₄, LiI and NaBH₄.

Complex hydride	Ionic conductivity at 313 K (S cm ⁻¹)	Activation energy (eV)
Li _{0.5} Na _{0.5} (BH ₄) _{0.84} Br _{0.16} , 47c	4.0 × 10 ⁻⁷	0.64(2)
Li _{0.5} Na _{0.5} (BH ₄) _{0.84} I _{0.16} , 57	3.6 × 10 ⁻⁶	0.58(2)
LT – LiBH ₄	2 × 10 ⁻⁸	0.69 ²⁴
HP – LiBH ₄	7.6 × 10 ⁻⁴ (493 K and under 4 GPa)	0.56 ¹¹
LiI	10 ⁻⁸	0.43 ¹⁵
NaBH ₄	5 × 10 ⁻⁹	0.61 ²⁰

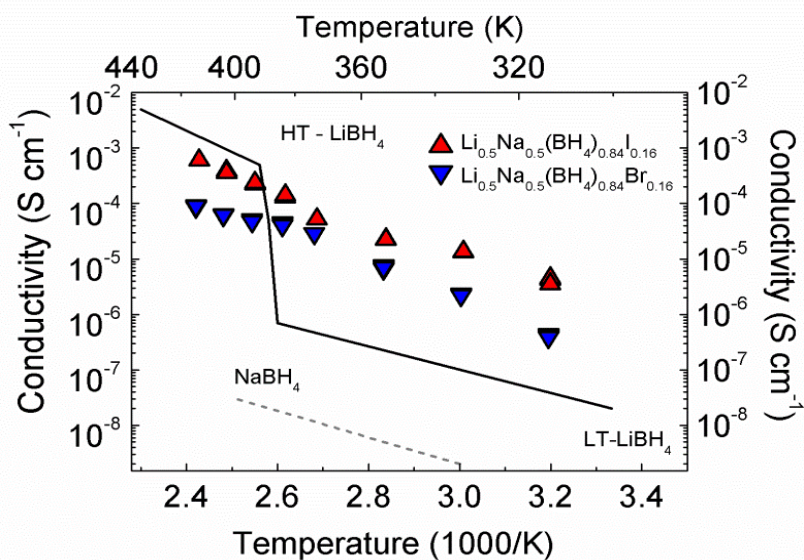


Figure 4.3-11 Plot of conductivity as a function of temperature for LiBH_4 ²⁴, NaBH_4 ²⁰, and $\text{Li}_{(1-y)}\text{Na}_y(\text{BH}_4)_{(1-x+xy)}\text{X}'_{x(1-y)}$ or HP - LiBH_4 ($\text{X}' = \text{Br}^-$ (47c) and I^- (57) on heating.

Overall, Table 4.3-7 shows that ionic conductivities are higher for the HP - LiBH_4 samples (47c and 57) at 313 K than the reactants at the same temperature (LT - LiBH_4 , LiI and NaBH_4) and the HP phase - LiBH_4 at 493 K and under 4 GPa. The E_a were slightly larger than HP - LiBH_4 , LiI and NaBH_4 . This fact will be discussed in section 4.3.3.4.

4.3.3.2.2 Lithium sodium borohydride iodides with the HP - LiBH_4 structure

Conductivity measurements were carried out for the iodide substituted HP - LiBH_4 - type (54 - 59). Impedance data analysed in the complex plane showed a semicircle at high frequencies and a linear response at low frequencies characteristic of ionic conductivity and ion blocking electrodes. The data were analysed using an equivalent electrical circuit to extract the values for the total resistivity of the material. Figure 4.3-12 shows the results from one of the samples measured at 313 and at 413 K (57), as an example. The data from the other samples (54 - 56, 58 and 59) can be found in Appendix B.

The results of the measurements were collected in to two categories, those with either low or high content of anion substitution as shown in Figure 4.3-13 and Figure 4.3-14, respectively. The best performance in terms of ionic conductivity was obtained in materials with a halide content of 16% (57). Samples with lower content

of halide (**54**, **55**, and **56**) showed ionic conductivities similar to LT - LiBH_4 . A similar phenomenon was observed for samples with more than 16% of halide (**58** and **59**).

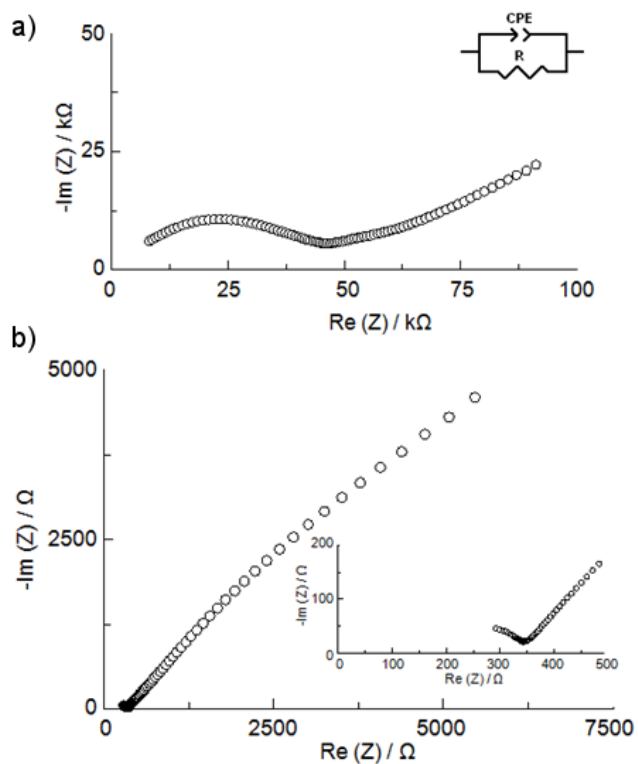


Figure 4.3-12 Nyquist plots of **57** (frequency range 1MHz to 1Hz at 1mV). Measurements performed at a) 313 K and b) 413 K.

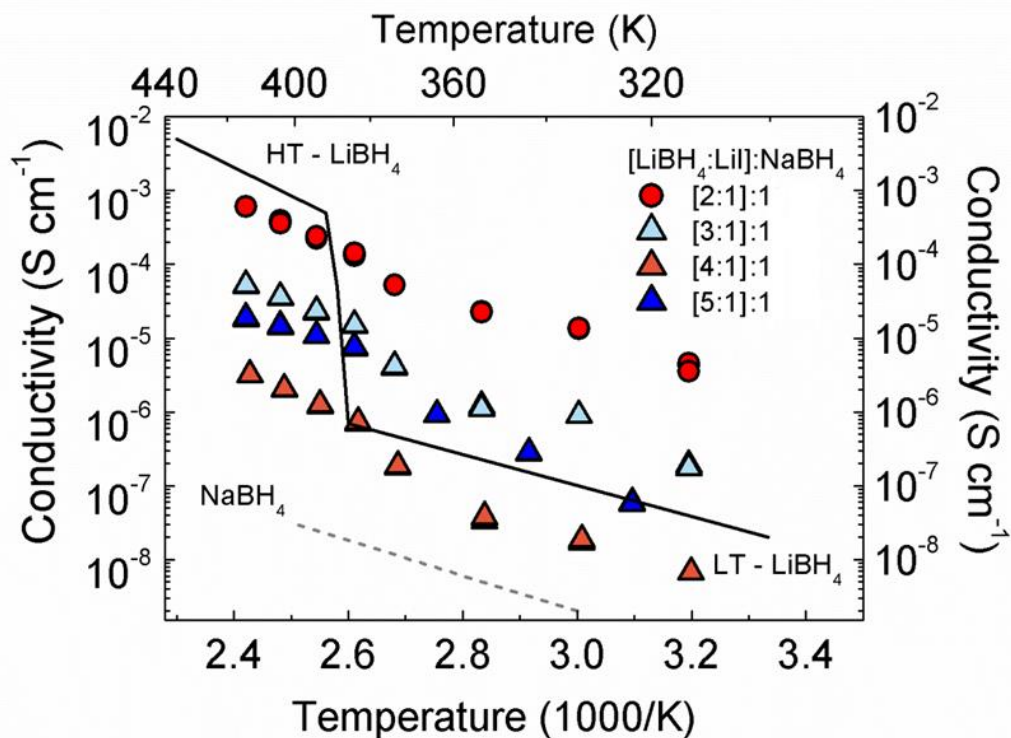


Figure 4.3-13 Conductivity measurements for (Li,Na) (BH₄,I) with low iodide content. Samples from bottom to top: 54, 55, 56 and 57.

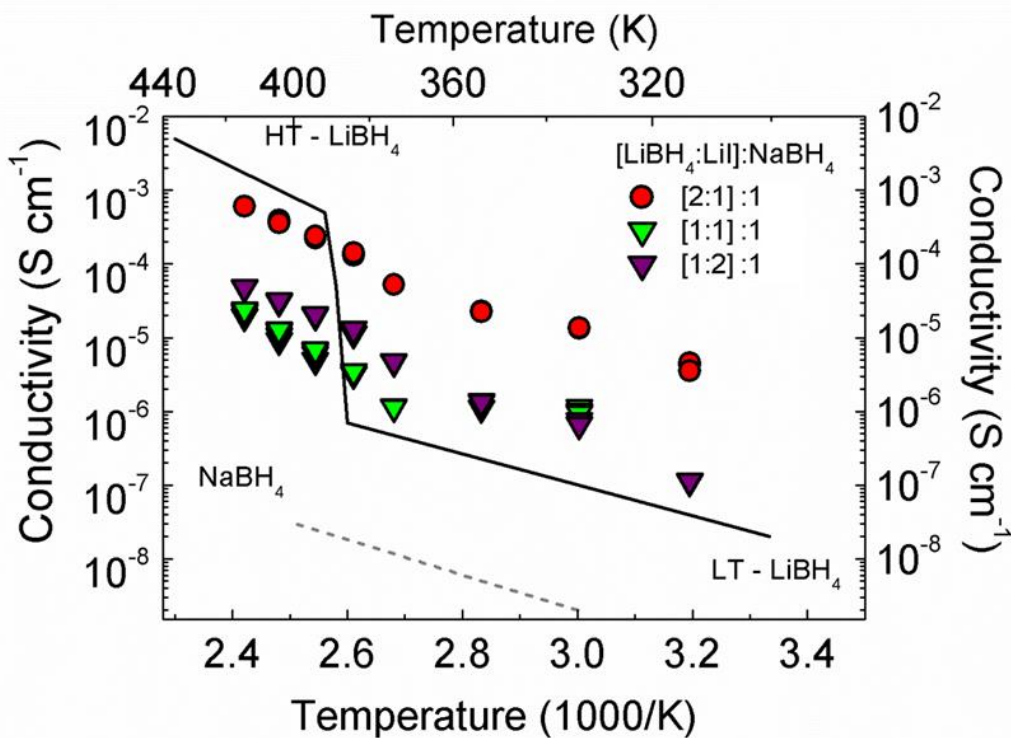


Figure 4.3-14 Conductivity measurements for (Li,Na) (BH₄,I) with higher levels of iodide substitution. Samples from top to bottom: 57, 58 and 59.

4.3.3.3 Powder X-ray diffraction experiments

Fully structural characterisation was performed for the samples which demonstrated the highest ionic conductivity at room temperature (samples **47c** and **57**). Laboratory X-ray powder diffraction data collected showed that a single cubic phase was formed [$Fm\bar{3}m$: $a = 6.1021(1)$ Å and $6.263(3)$ Å for Br^- (**47c**) and I^- (**57**), respectively] and hence that NaCl-type NaBH_4 structures containing Li^+ (50 %) can be stabilized at room temperature by substitution with 16 % halide (Figure 4.3-15). Hence the bromide and iodide structures contract and expand respectively compared to NaBH_4 [ionic radii of I^- (2.20 Å) > BH_4^- (2.05 Å) > Br^- (1.96 Å) respectively].⁴⁶

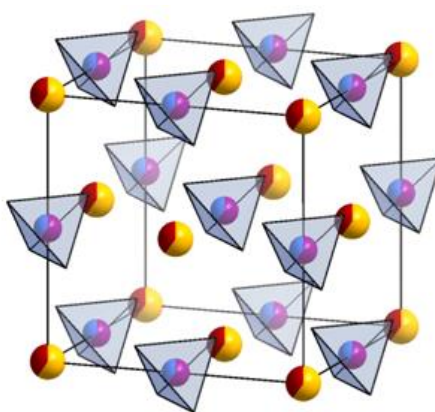
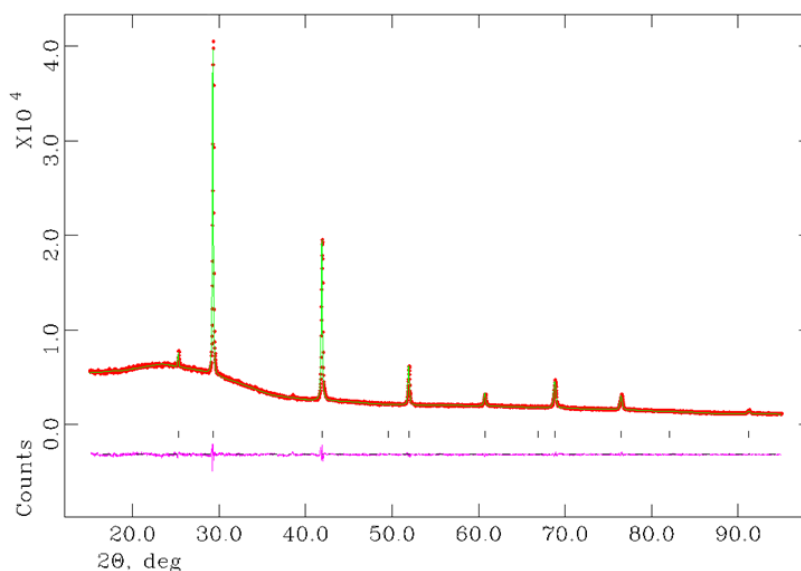


Figure 4.3-15 Crystal structure of cubic $\text{Li}_{(1-y)}\text{Na}_y(\text{BH}_4)_{(1-x+xy)}\text{X}'_{x(1-y)}$ (HP – LiBH_4 - type). Borohydride anions are shown as B - centred polyhedra (blue) and halides are represented by purple spheres, whilst the cations are represented by spheres, Li^+ as red spheres and Na^+ as yellow spheres.

Following initial phase identification and indexing from the PXD data collected for the white powder products, the final structures for each of the borohydride halides were refined (Figure 4.3-16, Table 4.3-8, Table 4.3-9 and Appendix B). The background was successfully modelled using linear interpolation. This was followed by the refinement of the cell parameters, atomic positions, profile parameters and temperature factors. The peak shape was modelled using a pseudo-Voigt function. The site occupancies were refined with the constraint that both the anion and cation sites remain fully occupied. The two compounds crystallise with the same space group ($Fm\bar{3}m$). Sample **47c** ($a = 6.1021(1)$ Å) and **57** ($a = 6.2670(1)$ Å) show different lattice parameters comparing with NaBH_4 ($Fm\bar{3}m$, $a = 6.1635(5)$ Å)⁹ due to a 50% in content of Li^+ and a 16% in content of I(Br). The rock-salt structures contain both cations and anions that are statically disordered; the $4b$ position is occupied by both

BH_4^- and Br(I)^- and the Li^+ ions partly (50%) occupy the octahedral sodium positions (4a sites) (Figure 4.3-15). The anions and cations occupy the octahedral sites with Li(Na)-B(Br/I) distances of 3.05106(5) and 3.1348(6) Å, respectively, whereas for NaBH_4 the value is 3.0818 Å, for NaBr it is 2.9810 Å and for NaI it is 3.3000 Å.⁹ The Li(Na)-B(Br/I) distances shows that these compounds can be ordered in size as follows $\text{NaBr} < 47\text{c} < \text{NaBH}_4 < 57 < \text{NaI}$ because 47c and 57 have both 16% of Br and I, respectively.

a)



b)

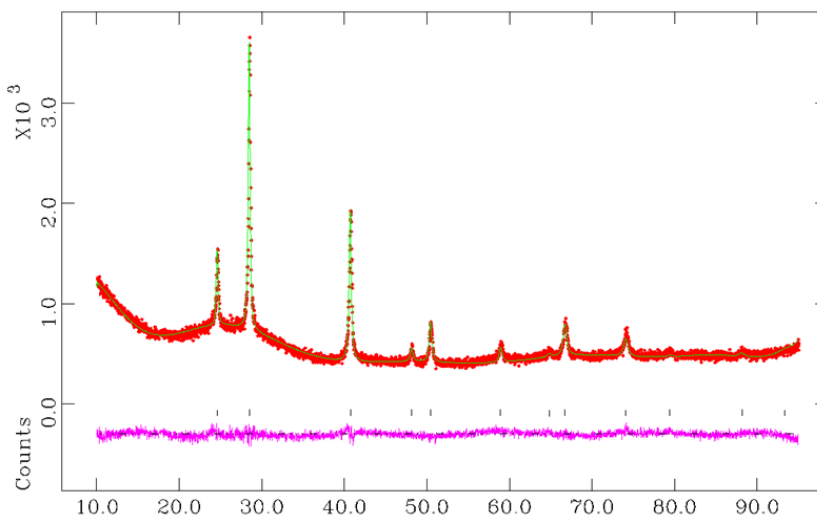


Figure 4.3-16 Profile plot from the Rietveld refinement against X-ray powder diffraction data for (a) $\text{Li}_{0.52(6)}\text{Na}_{0.48(6)}(\text{BH}_4)_{0.83(3)}\text{Br}_{0.17(3)}$ (47c) (b) $\text{Li}_{0.6(1)}\text{Na}_{0.4(1)}(\text{BH}_4)_{0.84(4)}\text{I}_{0.16(4)}$ (57) (Red crosses: experimental profile; green line: calculated profile; pink line: difference profile; tick marks: Bragg reflections for the NaCl-type borohydride halide phase).

Table 4.3-8. Atom positions and isotropic temperature factors obtained from Rietveld refinement against PXD data of the $\text{Li}_{0.5}\text{Na}_{0.5}(\text{BH}_4)_{0.84}\text{Br}_{0.16}$ compounds at room temperature (47c).

Atom	Li	Na	B	Br
Site	4a	4a	4b	4b
x	0	0	1/2	1/2
y	0	0	0	0
z	0	0	0	0
100 x U_{iso} / Å	2.2(2)	2.2(2)	7.6(3)	7.6(3)
Occupancy	0.52(6)	0.48(6)	0.83(3)	0.17(3)

Table 4.3-9. Atom positions and isotropic temperature factors obtained from Rietveld refinement against PXD data of the $\text{Li}_{0.5}\text{Na}_{0.5}(\text{BH}_4)_{0.84}\text{I}_{0.16}$ compounds at room temperature (57).

Atom	Li	Na	B	I
Site	4a	4a	4b	4b
x	0	0	1/2	1/2
y	0	0	0	0
z	0	0	0	10
100 x U_{iso} / Å	2.5(3)	2.5(3)	3.9(3)	3.9(3)
Occupancy	0.6(1)	0.4(1)	0.84(4)	0.16(4)

4.3.3.4 Li^+ ion migration in HP – LiBH_4 – type materials

In order to understand the origin of the activation energy for migration in the above samples (Table 4.3-7), one needs to consider the possible paths that may be taken by a Li^+ ion in jumping from its lattice site into an adjacent vacancy. Some studies have suggested possible Li ion diffusion in the rock-salt type LiX phases ($X = \text{F}, \text{Cl}, \text{Br}$ and I) by the same kinds of diffusion paths as NaCl , *i.e.*, “direct” and “indirect” jumps.⁶⁰ Sections of the cubic structure are shown in Figure 4.3-17. A simple cube with the cations and anions at alternate corners can be considered, which corresponds to one-eighth of the unit cell of substituted NaBH_4 .

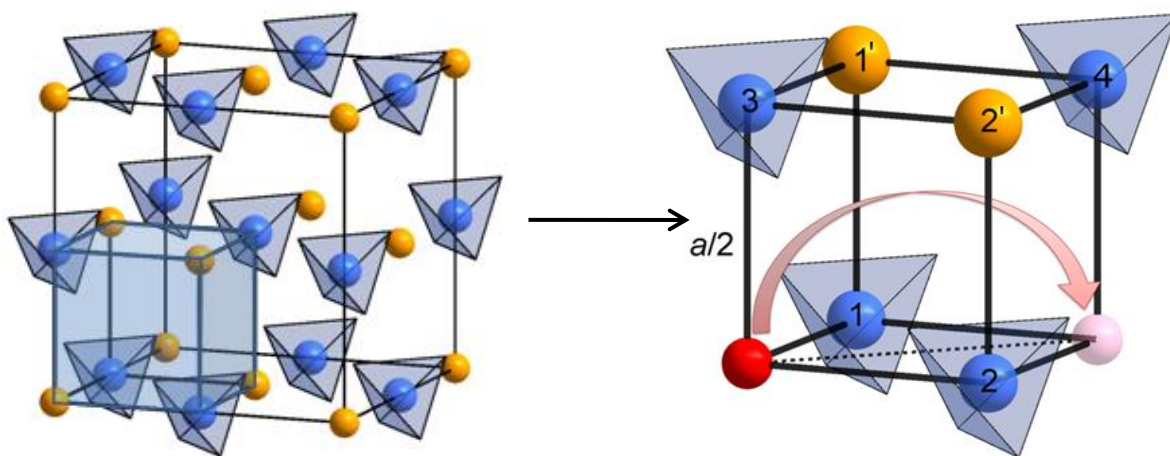


Figure 4.3-17 pathway for Li^+ migration in $\text{Li}_{0.5}\text{Na}_{0.5}(\text{BH}_4)_{(1-x+xy)}\text{X}'_x(1-y)$ (HP - LiBH_4 - type). Borohydride anions are shown as $\text{B}(\text{X}')$ - centred polyhedra (blue), whilst the cations are represented by spheres, Li^+ as red spheres and Na^+ as yellow spheres. One corner Li^+ site is shown as “empty” (just as in NaCl , $(\text{Li}, \text{Na})(\text{BH}_4/\text{X}')$ would be expected to include a small number of intrinsic cation and anion vacancies) and a Li^+ ion from opposite corner moves to occupy it. The direct and indirect jump are represented as dotted line and curved arrow, respectively.

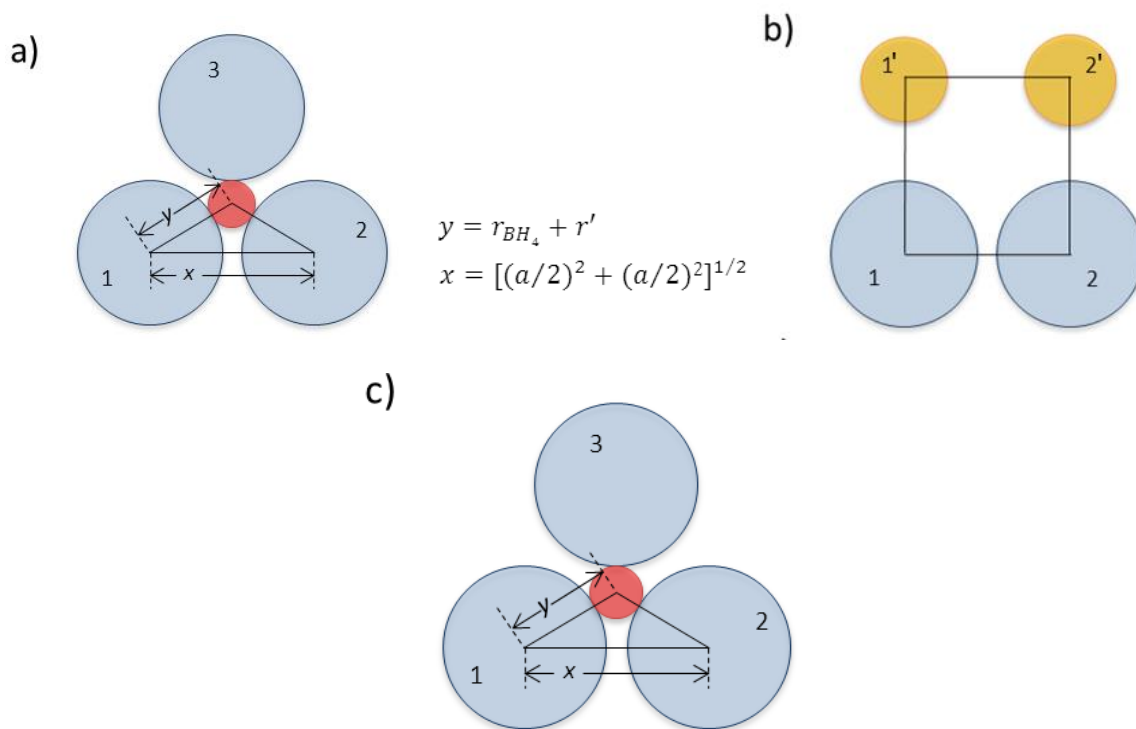


Figure 4.3-18 a) and c) represent the triangular channel of radius r' through which a moving Li^+ ion must pass in the borohydride compound. Blue circles 1, 2 and 3 are anions, either BH_4^- or X^- (where $\text{X} = \text{Br}$ or I). Yellow circles are cations (Li^+ or Na^+ , 50% probability). Note that this figure is adapted from West.⁶⁰

The direct jump of Li^+ across the sub-cube face is very unlikely because BH_4^- / $(\text{I}, \text{Br})^-$ anion 1 and 2 are very close (blue atoms) and it could be physically unfavourable for a Li^+ ion to occupy the space between them. Instead Li^+ must take

an indirect route that passes through the middle of the sub-cube. At the cube centre is an interstitial site that is equidistant from the eight corners. Four of the corners are occupied by $(\text{BH}_4)^-/\text{X}^-$ ions which are arranged tetrahedrally about the site. Before the Li^+ ion arrives at this central interstitial site, it has to pass through a triangular window formed by anions 1, 2 and 3. The time that the cation (Li^+) spends in this site must be short because of the proximity of the other cations (Li^+/Na^+ represented by yellow spheres), 1' and 2'.

Treating $(\text{BH}_4)^-$ as a sphere, the radius r' of the 'triangular' window formed by the BH_4^- ions is given by ((4.5)-(4.9)) (Figure 4.3-18):

$$y = (0.84r_{\text{BH}_4^-} + 0.16r_{\text{I}^-}) + r' \quad (4.5)$$

$$x = \left[\left(\frac{a}{2} \right)^2 + \left(\frac{a}{2} \right)^2 \right]^{\frac{1}{2}} \quad (4.6)$$

$$\cos 30^\circ = \frac{x/2}{y} \quad (4.7)$$

$$\cos 30^\circ = \frac{\left[\left(\frac{a}{2} \right)^2 + \left(\frac{a}{2} \right)^2 \right]^{\frac{1}{2}} / 2}{((0.84r_{\text{BH}_4^-} + 0.16r_{\text{I}^-}) + r')} \quad (4.8)$$

$$\text{then } r' = 0.48\text{\AA} \quad (4.9)$$

The Li^+ ion then leaves the tetrahedral hole by passing through another triangular gap formed by anions 1, 2 and 4 to occupy the vacant octahedral site on the other sub-cube corner.

The radius r'' of the tetrahedral interstitial site at the cube centre is given by:

$$y = (0.84r_{\text{BH}_4^-} + 0.16r_{\text{I}^-}) + r' \quad (4.10)$$

$$2(0.84r_{\text{BH}_4^-} + 0.16r_{\text{I}^-}) + 2r'' = \left[\left(\frac{a}{2} \right)^2 + \left(\frac{a}{2} \right)^2 + \left(\frac{a}{2} \right)^2 \right]^{\frac{1}{2}} \quad (4.11)$$

$$\text{then } r'' = 0.64\text{\AA} \quad (4.12)$$

Table 4.3-10 shows the space available for cation interstitial in NaCl, **47c**, and **57**. It might be argued that in our materials the conductivity could be enhanced because the migrating ion, Li^+ which is smaller than Na^+ , would have larger space to move through the voids and the space into which it can migrate is larger than in NaCl.

Table 4.3-10 Indirect jump mechanism

Sample	Compound	Migrating ion	Ionic radii (Å)	r' (Å)	r'' (Å)
---	NaCl	Na^+	1.02	0.45	0.59
47c	$\text{Li}_{0.5}\text{Na}_{0.5}(\text{BH}_4)_{0.84}\text{Br}_{0.16}$	Li^+	0.76	0.46	0.60
57	$\text{Li}_{0.5}\text{Na}_{0.5}(\text{BH}_4)_{0.84}\text{I}_{0.16}$	Li^+	0.76	0.48	0.64

r' : radius of the ‘triangular’ window formed by anions $(\text{BH}_4)^-$ and I^-/Br^- . r'' : radius of the interstitial site at the cube centre.

Certainly, the space available for Li^+ to migrate is slightly larger for **57** than for **47c**, which could tend to the superior results in the conductivity. This mechanism is inevitably somewhat idealized since relaxation or distortion of the structure must occur in the vicinity of the defects, thereby modifying the distances involved. They do nevertheless show that the migration of Li^+ ions could be possible, but would be associated with a considerable activation energy barrier.⁵⁰

Calculations of migration energies of Li^+ ion in LiX ($X = \text{F}, \text{Cl}, \text{Br}, \text{and I}$) showed a tendency to decrease the migration energy with the increase in the periodic number of the halide in the Periodic table (Table 4.3-11).⁵¹ Table 4.3-7 shows the activation energies for each of the samples. As was predicted in the literature, experimentally LiI shows the lowest activation energy (0.43 eV)¹⁵ because it has a larger open channel for Li^+ . HP - LiBH_4 with a rock-salt type structure has a larger activation energy (0.56 eV)¹¹ than LiI because the ionic radius of BH_4^- (2.05 Å) is slightly smaller than I^- (2.20 Å). The same phenomenon was observed in compounds **47c** and **57** where the activation energy was higher for **47c** (0.64(2) eV) than **57** (0.58(2) eV) because Br^- (1.96 Å) has a smaller radius than I^- (2.20 Å) leaving less space for the Li^+ ions to jump through the indirect path. However the activation energies for **47c** and **57** are slightly larger than HP - LiBH_4 , when they should be similar, since they have almost the same content of anion (100% for HP - LiBH_4 and 84% for **47c** and **57** of BH_4^-). However **47c** and **57** have also the Na^+ contribution, as this can be noticed in the activation

energies of **47c** (0.64(2) eV) and **57** (0.58(2) eV) which are similar to NaBH₄ (0.61 eV) which also has a rock-salt type structure (Table 4.3-7).

Table 4.3-11 Migration energies of Li⁺ ion through the two kinds of diffusion path in rock-salt type LiX (X = F, Cl, Br and I).⁵¹

Compound	Migration energy, $E_{Li^+}^M$ / eV	
	Direct path	Indirect path
LiF	0.80	0.82
LiCl	0.70	0.58
LiBr	0.65	0.50
LiI	0.65	0.42

4.4 Conclusions

In this chapter different solid solutions were investigated to stabilise the HP - LiBH₄ - type phase at room temperature and ambient pressure. In total three different approaches were proposed to stabilise this phase which otherwise is only available under extreme conditions (**Method 1**, **2** and **3**). Firstly, by **Method 1**, mixed alkali borohydrides were studied using LiBH₄ and NaBH₄. NaBH₄ was used because it has the same structure as the HP - LiBH₄ phase, a rock salt type structure. In this way this compound could serve as a “host” for the Li cations. The formation of Li_{1-x}Na_x(BH₄) was suggested in other reports.^{7, 16-18} However different mixtures with different molar ratios of LiBH₄ and NaBH₄ prepared by mechanochemical treatment showed no evidence of mixed cation borohydrides. These results suggest that the direct substitution of Li⁺ in NaBH₄ is not favourable. All the patterns showed peaks that belonged to both reactants and the cell parameters of each of them were not modified (**34 - 37**, Table 4.3-1).

Secondly, in **Method 2** the formation of mixed alkali metal - mixed anion borohydrides was suggested as an alternative route. Mixtures with different molar ratios of LiBH₄ and NaBr were studied (**38 - 46**, Table 4.3-2). NaBr was used because it has the same structure as HP - LiBH₄ again, a rock salt type structure. The phase diagram of this system was investigated in detail. The presence of new phases were observed in LiBH₄ - NaBr system, which could be indexed to a cubic rock-salt type

structure. This showed the possible stabilisation of HP - LiBH₄ by substitution of both cations and anions at ambient conditions. The cubic phase was observed with a content of 0.20 > NaBr > 0.70, coexisting with other phases (LT - LiBH₄ - type, HT - LiBH₄ - type, HP - LiBH₄ - type, NaBr - type and LiBr - type). This approach indicated that the stabilisation of the HP - LiBH₄ phase could be possible. Since Li⁺ is smaller than Na⁺, the substitution of a halide is necessary to fulfil the space left by the cation.

Finally, **Method 3** relied on the use of HT - LiBH₄ phases as precursors in mixtures with NaBH₄. In this way the halide to be substituted is already incorporated in the precursor. As in **Method 1**, NaBH₄ was used as a “host” for the Li cations. This is an example of “chemical pressure”, whereby substitution of smaller ions mimics the action of high pressure by condensing a phase further. These materials were studied with two different halides, Br⁻ and I⁻. For Br⁻, a single composition was studied (**47c**) and it showed higher ionic conductivity than NaBH₄ itself by *ca.* 3 orders of magnitude at 413 K. For I⁻, seven different compositions were studied (**54 - 60**, Table 4.3-6). Conductivity measurements were performed for each of the samples and the optimum composition obtained contains 16% of iodide (**57**). This showed ionic conductivity *ca.* 4 orders of magnitude higher than NaBH₄ at 413 K. In comparison with the parent borohydrides, Table 4.3-7, the halides showed higher activation energies and higher conductivities. Higher activation energies could be due to partial occupation of isovalent elements in the same sites. As predicted in the literature for lithium compounds with the rock-salt type structure (LiX where X = F, Cl, Br, and I, Table 4.3-11)⁵¹, the migration energies show a tendency to decrease with the increase in the periodic number of the halide in the Periodic table (**47c** (0.64(2) eV) > **57** (0.58(2) eV) > HP - LiBH₄ (0.56 eV)¹¹ > LiI (0.43 eV)¹⁵, Table 4.3-7). Larger anions in a rock salt structure allow Li⁺ ions to jump through the middle of the cell because of their larger open channels.

In conclusion, it was shown that two groups of halide-substituted borohydrides could be synthesised with the HP structure of LiBH₄ and stabilised at ambient conditions (**47c** and **54 - 60** for bromide and iodide, respectively).

4.5 References

1. P. C. W., *Z. Phys. Chem. Neue. Fol.*, 1974, **88**, 253-263.
2. P. Vajeeston, P. Ravindran, A. Kjekshus and H. Fjellvag, *J. Alloy. Compd.*, 2005, **387**, 97-104.
3. T. J. Frankcombe, G. J. Kroes and A. Züttel, *Chemical Physics Letters*, 2005, **405**, 73-78.
4. Z. Lodziana and T. Vegge, *Phys. Rev. Lett.*, 2004, **93**, 4.
5. J. P. Soulie, G. Renaudin, R. Cerny and K. Yvon, *J. Alloy. Compd.*, 2002, **346**, 200-205.
6. H. Yamawaki, H. Fujihisa, Y. Gotoh and S. Nakano, *J. Phys. Chem. Solids*, 2015, **76**, 40-44.
7. Y. Filinchuk, D. Chernyshov, A. Nevidomskyy and V. Dmitriev, *Angew. Chem.-Int. Edit.*, 2008, **47**, 529-532.
8. A. V. Talyzin, O. Andersson, B. Sundqvist, A. Kurnosov and L. Dubrovinsky, *J. Solid State Chem.*, 2007, **180**, 510-517.
9. S. C. Abrahams and J. Kalnajs, *J. Chem. Phys.*, 1954, **22**, 434-436.
10. P. Fischer and A. Züttel, *European Powder Diffraction Epdic 8*, 2004, **443-4**, 287-290.
11. H. Takamura, Y. Kuronuma, H. Maekawa, M. Matsuo and S. Orimo, *Solid State Ionics.*, 2011, **192**, 118-121.
12. B. Sundqvist, M. G. Yao and O. Andersson, *High Pressure Res.*, 2013, **33**, 141-151.
13. B. Sundqvist and O. Andersson, *Int. J. Thermophys.*, 2009, **30**, 1118-1129.
14. R. Miyazaki, H. Maekawa and H. Takamura, *Appl. Mater.*, 2014, **2**, 1-6.
15. H. Maekawa, M. Matsuo, H. Takamura, M. Ando, Y. Noda, T. Karahashi and S. I. Orimo, *J. Am. Chem. Soc.*, 2009, **131**, 894-895.
16. N. Bernstein, M. D. Johannes and K. Hoang, *Phys. Rev. B*, 2013, **88**, 5.
17. J. S. G. Myrdal, D. Sveinbjornsson and T. Vegge, ECS Meeting Abstracts, MA2011-2002 Sec. B2019, abstract No. 2756.
18. N. Bernstein, M. D. Johannes and K. Hoang, *Phys. Rev. B*, 2013, **88**.
19. M. Matsuo, A. Remhof, P. Martelli, R. Caputo, M. Ernst, Y. Miura, T. Sato, H. Oguchi, H. Maekawa, H. Takamura, A. Borgschulte, A. Züttel and S. Orimo, *J. Am. Chem. Soc.*, 2009, **131**, 16389-16391.
20. M. Matsuo, H. Oguchi, T. Sato, H. Takamura, E. Tsuchida, T. Ikeshoji and S. Orimo, *J. Alloy. Compd.*, 2013, **580**, S98-S101.
21. D. B. Ravnsbaek, M. B. Ley, Y. S. Lee, H. Hagemann, V. D'Anna, Y. W. Cho, Y. Filinchuk and T. R. Jensen, *Int. J. Hydrog. Energy*, 2012, **37**, 8428-8438.
22. M. B. Ley, D. B. Ravnsbaek, Y. Filinchuk, Y. S. Lee, R. Janot, Y. W. Cho, J. Skibsted and T. R. Jensen, *Chem. Mat.*, 2012, **24**, 1654-1663.
23. L. H. Rude, O. Zavorotynska, L. M. Arnbjerg, D. B. Ravnsbaek, R. A. Malmkjaer, H. Grove, B. C. Hauback, M. Baricco, Y. Filinchuk, F. Besenbacher and T. R. Jensen, *Int. J. Hydrog. Energy*, 2011, **36**, 15664-15672.
24. M. Matsuo, Y. Nakamori, S. Orimo, H. Maekawa and H. Takamura, *Appl. Phys. Lett.*, 2007, **91**, 1-3.
25. Y. Filinchuk, D. Chernyshov and V. Dmitriev, *Z. Kristall.*, 2008, **223**, 649-659.
26. M. Paskevicius, M. B. Ley, D. A. Sheppard, T. R. Jensen and C. E. Buckley, *Phys. Chem. Chem. Phys.*, 2013, **15**, 19774-19789.
27. E. A. Nickels, M. O. Jones, W. I. F. David, S. R. Johnson, R. L. Lowton, M. Sommariva and P. P. Edwards, *Angew. Chem.-Int. Edit.*, 2008, **47**, 2817-2819.
28. L. Seballos, J. Z. Zhang, E. Roennebro, J. L. Herberg and E. H. Majzoub, *J. Alloy. Compd.*, 2009, **476**, 446-450.
29. C. Kim, S. J. Hwang, R. C. Bowman, J. W. Reiter, J. A. Zan, J. G. Kulleck, H. Kabbour, E. H. Majzoub and V. Ozolins, *J. Phys. Chem. C*, 2009, **113**, 9956-9968.
30. R. Ccaronernyacute, G. Severa, D. B. Ravnsbaek, Y. Filinchuk, V. D'Anna, H. Hagemann, D. Haase, C. M. Jensen and T. R. Jensen, *J. Phys. Chem. C*, 2010, **114**, 1357-1364.

31. R. Cerny, D. B. Ravnsbaek, G. Severa, Y. Filinchuk, V. D' Anna, H. Hagemann, D. Haase, J. Skibsted, C. M. Jensen and T. R. Jensen, *J. Phys. Chem. C*, 2010, **114**, 19540-19549.
32. R. Cerny, K. C. Kim, N. Penin, V. D'Anna, H. Hagemann and D. S. Sholl, *J. Phys. Chem. C*, 2010, **114**, 19127-19133.
33. I. Lindemann, R. Domenech-Ferrer, L. Dunsch, Y. Filinchuk, R. Cerny, H. Hagemann, V. D'Anna, L. M. L. Daku, L. Schultz and O. Gutfleisch, *Chem.-Eur. J.*, 2010, **16**, 8707-8712.
34. R. Cerny, P. Schouwink, Y. Sadikin, K. Stare, L. Smrcok, B. Richter and T. R. Jensen, *Inorg. Chem.*, 2013, **52**, 9941-9947.
35. W. Wegner, T. Jaron and W. Grochala, *Acta Crystallogr. Sect. C-Cryst. Struct. Commun.*, 2013, **69**, 1289-1291.
36. W. Wegner, T. Jaron and W. Grochala, *Int. J. Hydrog. Energy*, 2014, **39**, 20024-20030.
37. A. V. Skripov, A. V. Soloninin, M. B. Ley, T. R. Jensen and Y. Filinchuk, *J. Phys. Chem. C*, 2013, **117**, 14965-14972.
38. M. B. Ley, S. Boulineau, R. Janot, Y. Filinchuk and T. R. Jensen, *J. Phys. Chem. C*, 2012, **116**, 21267-21276.
39. M. B. Ley, D. B. Ravnsbaek, Y. Filinchuk, Y. S. Lee, R. Janot, Y. W. Cho, J. Skibsted and T. R. Jensen, *Chem. Mat.*, 2012, **24**, 1654-1663.
40. J. E. Olsen, C. Frommen, T. R. Jensen, M. D. Riktor, M. H. Sorby and B. C. Hauback, *Rsc Advances*, 2014, **4**, 1570-1582.
41. I. Lindemann, R. D. Ferrer, L. Dunsch, R. Cerny, H. Hagemann, V. D'Anna, Y. Filinchuk, L. Schultz and O. Gutfleisch, *Faraday Discuss.*, 2011, **151**, 231-242.
42. T. Jaron, W. Wegner and W. Grochala, *Dalton Trans.*, 2013, **42**, 6886-6893.
43. T. Sato, K. Miwa, Y. Nakamori, K. Ohoyama, H. Li, T. Noritake, M. Aoki, S. Towata and S. Orimo, *Phys. Rev. B*, 2008, **77**.
44. H. Hagemann, M. Longhini, J. W. Kaminski, T. A. Wesolowski, R. Cerny, N. Penin, M. H. Sorby, B. C. Hauback, G. Severa and C. M. Jensen, *J. Phys. Chem. A*, 2008, **112**, 7551-7555.
45. J. E. Nickels, M. A. Fineman and W. E. Wallace, *J. Phys. Colloid. Chem.*, 1949, **53**, 625-628.
46. C. E. Housecroft and A. G. Sharpe, 2001, ISBN 0-582-31080-6, Inorganic chemistry. Peason Education.
47. L. H. Rude, E. Groppo, L. M. Arnbjerg, D. B. Ravnsbaek, R. A. Malmkjaer, Y. Filinchuk, M. Baricco, F. Besenbacher and T. R. Jensen, *J. Alloy. Compd.*, 2011, **509**, 8299-8305.
48. S. Orimo, Y. Nakamori and A. Züttel, *Mat. Sci. Eng. B-Solid*, 2004, **108**, 51-53.
49. S. Gomes, H. Hagemann and K. Yvon, *J. Alloy. Compd.*, 2002, **346**, 206-210.
50. A. R. West, 1988, ISBN 0-471-91798-2, Basic solid state chemistry. John Wiley & Sons Ltd.
51. Y. Koyama, Y. Yamada, I. Tanaka, S. R. Nishitani, H. Adachi, M. Murayama and R. Kanno, *Mater. Trans.*, 2002, **43**, 1460-1463.

5. Lithium aminoboranes as candidates for solid state electrolytes

5.1 Introduction

One of the most promising materials suggested as a hydrogen storage material for a future sustainable hydrogen economy is ammonia borane (NH_3BH_3) which contains 19.6 wt % of hydrogen, is solid at room temperature and pressure and is neither flammable nor explosive. Ammonia borane is a crystalline solid first synthesised in 1955. It adopts a tetragonal structure with space group $I\bar{4}mm$ and lattice parameters of $a = 5.240$ and $c = 5.028$ Å at room temperature.¹ The bond lengths were determined by Bowden *et al.* using single-crystal X-ray data finding N-B distances of $1.597(3)$ Å at room temperature (Figure 5.1-1).²

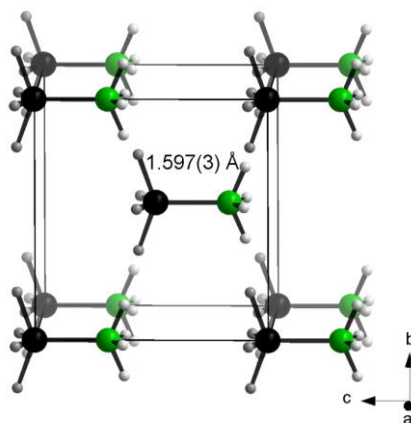
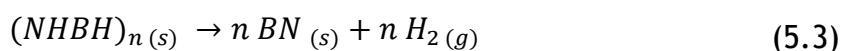
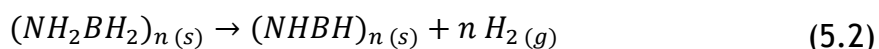
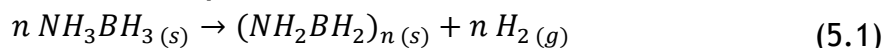


Figure 5.1-1 Crystal structure of NH_3BH_3 .³ Boron and nitrogen atoms are represented in black and green, respectively.

NH_3BH_3 melts at 114 °C. The molten NH_3BH_3 evolves H_2 following reaction (4.5) and forming polyaminoborane $(\text{NH}_2\text{BH}_2)_n$ at 125 °C. $(\text{NH}_2\text{BH}_2)_n$ decomposes at 155 °C giving off hydrogen and polyiminoborane $(\text{NHBH})_n$ and a small fraction of borazine, $(\text{B}_3\text{H}_6\text{N}_3)$ and other products which have not been characterised ((5.2), (5.3) and Scheme 5.1-1)⁴. At 500 °C $(\text{NHBH})_n$ further decomposes into BN but the temperature of this process is not considered practical for hydrogen storage. These results were obtained with a heating rate of 2 °C min^{-1} .⁵ It has been observed from the thermogravimetric and differential scanning curves that the exact temperature at which each decomposition step occurs is very much dependent on the heating rate.⁶

Scheme 5.1-1 Generalised thermal decomposition of ammonia borane.⁴

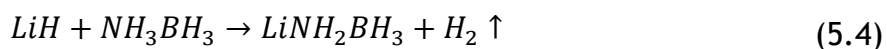
$[\text{NHBH}]_x$ = polyiminoborane, borazine, polyborazine, cross-linked materials, mostly poorly defined and characterised.

This material combined with charge carriers could be considered as a potential electrolyte because of its low molecular weight (30.7 g mol⁻¹), thermal stability and satisfactory air-stability. Several lithium amino boranes have been reported for hydrogen storage materials, but these compounds have never been studied as electrolytes. Some of them show particular structures where the ammonia borane is found in pseudo-layers which could provide different pathways for ions to move through the structure.⁷⁻⁹ It is important to study these materials as electrolytes since they could exhibit 1D, 2D or 3D lithium ion conductivity. For instance the combination between LiH and NH₃BH₃ in different molar ratios gives the formation of diverse compounds such as α - and β - LiNH₂BH₃, LiNH₂BH₃·(NH₃BH₃) and Li[BH₃NH₂BH₂NH₂BH₃] (Table 5.1-1).

Table 5.1-1 Reported lithium ammonia borane compounds.

Compound	Structure	Reaction	Molar ratio	T _d (°C)	Ref.
α - LiNH ₂ BH ₃	Orthorhombic	LiH + NH ₃ BH ₃	1:1	114	3-6, 10, 11
β - LiNH ₂ BH ₃	Orthorhombic	LiH + NH ₃ BH ₃	1:1	---	12
LiNH ₂ BH ₃ ·NH ₃ BH ₃	Tetragonal	LiH + NH ₃ BH ₃	1:2	---	13, 14
Li[BH ₃ NH ₂ BH ₂ NH ₂ BH ₃]	Tetragonal	LiH + NH ₃ BH ₃	1:3	140	9
Li ₂ [BH ₄][NH ₂ BH ₃]	Orthorhombic	LiNH ₂ BH ₃ + LiBH ₄	1:1	---	15
Li ₂ [BH ₄] ₂ [NH ₃ BH ₃]	Orthorhombic	LiBH ₄ + NH ₃ BH ₃	2:1	105	7, 8

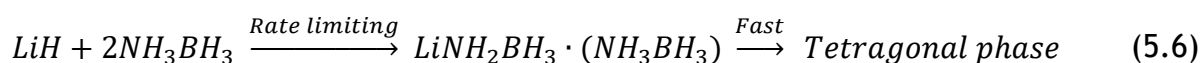
The first alkali-metal amidoborane complexes were reported by Edwards *et al.* in 2008.³ Lithium and sodium amidoboranes are formed by ball milling the alkali-metal hydrides (LiH and NaH) with ammonia borane in 1 : 1 molar ratio. It is suggested that the driving force for the formation of LiNH₂BH₃ is the production of the gas as reaction (5.4) shows.^{11, 12}



For lithium, two different phases are reported, α - and β - LiNH_2BH_3 .³ α - LiNH_2BH_3 crystallises in the orthorhombic space group $Pbca$, with $a = 7.11274(6)$, $b = 13.94877(14)$, $c = 5.15018(6)$ Å, and $V = 510.970(15)$ Å³.¹⁰ Only two years later the second polymorph of LiNH_2BH_3 was reported, β - LiNH_2BH_3 .¹² This compound crystallises in the same space group as α - LiNH_2BH_3 , $Pbca$, but with different lattice constants: $a = 15.146(6)$, $b = 7.721(3)$ and $c = 9.268(4)$ Å, and $V = 1083.7(8)$ Å³. However β - LiNH_2BH_3 can only be observed by ball milling and transforms to α - LiNH_2BH_3 upon extended milling.¹² Another structure was reported from the mixture of LiH and NH_3BH_3 in a 1 : 2 molar ratio by Wu *et al.* shown in reaction (5.5).



$\text{LiNH}_2\text{BH}_3 \cdot (\text{NH}_3\text{BH}_3)$ crystallises in a $Cmc2_1$ orthorhombic structure ($a = 9.100(2)$, $b = 4.371(1)$, $c = 6.441(2)$ Å, and $\beta = 93.19^\circ$).^{13, 14} In 2011, it was pointed out that a new unidentified structure could be obtained from LiH and NH_3BH_3 in a 1 : 2 molar ratio. It was wrongly assigned to a tetragonal structure with space group $P4_2mc$ formed from the decomposition of $\text{LiNH}_2\text{BH}_3 \cdot (\text{NH}_3\text{BH}_3)$ ($a = 4.0288(2)$ Å, $c = 16.958(2)$ Å, $V = 275.26(5)$ Å³). However the stoichiometry of the product obtained was not clarified (5.6).¹⁶



In 2014, this was clarified by Grochala *et al.* who showed that the structure was that of $\text{Li}[\text{BH}_3\text{NH}_2\text{BH}_2\text{NH}_2\text{BH}_3]$ which has a tetragonal structure with space group $P\bar{4}2c$ ($a = 4.02(1)$ Å, $c = 16.95(5)$ Å, $V = 273.9(12)$ Å³). LiNH_2BH_3 undergoes decomposition leading to the formation of LiNHBH_2 releasing H_2 or $\text{Li}[\text{BH}_3\text{NH}_2\text{BH}_2\text{NH}_2\text{BH}_3]$ releasing NH_3 , which is stable at room temperature (Figure 5.1-2).

³ Whenever in this report LiNH_2BH_3 is mentioned without specification of α - or β phase, we would always refer to the first reported structure of LiNH_2BH_3 , α .

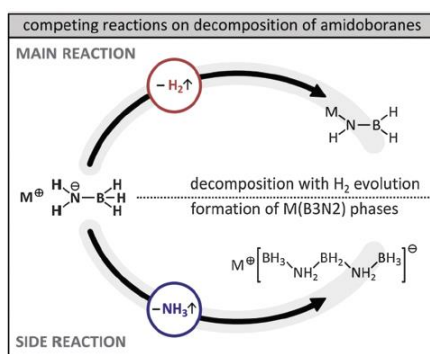


Figure 5.1-2 The simplified mechanism of two competing reactions during the thermal decomposition of alkali metal amidoboranes: direct evolution of H₂ (top) and formation of M[BH₃NH₂BH₂NH₂BH₃] phases with the evolution of NH₃ (bottom).⁹

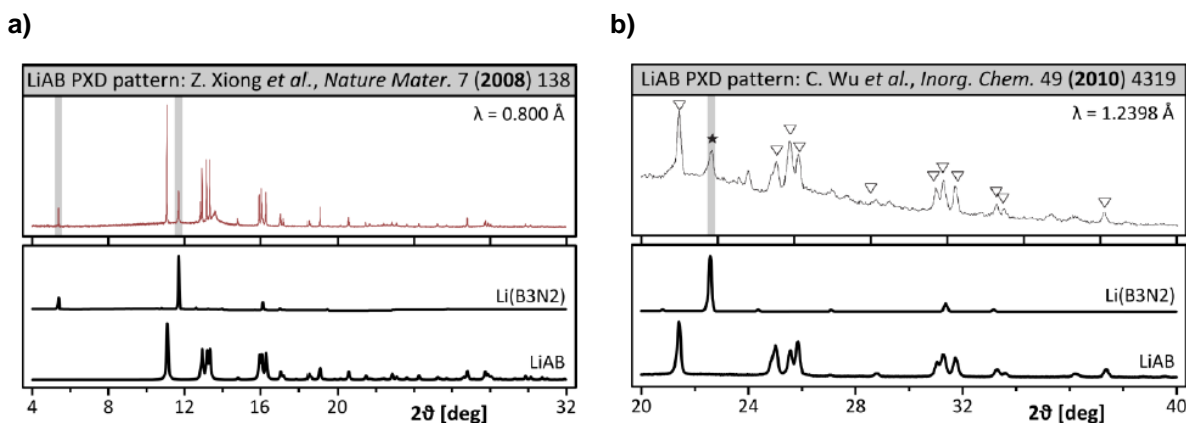


Figure 5.1-3 a) PXD powder pattern of LiNH₂BH₃ presented by Z. Xiong *et al.* in 2008 (top).³ Signals representing Li[BH₃NH₂BH₂NH₂BH₃] are marked with grey stripes (top). For comparison PXD patterns of LiNH₂BH₃ and Li[BH₃NH₂BH₂NH₂BH₃] are shown (bottom). b) PXD powder pattern of LiNH₂BH₃ by C. Wu *et al.* in 2010 (top).^{12, 14} Signals representing Li[BH₃NH₂BH₂NH₂BH₃] are marked with grey stripes (top). For comparison PXD pattern of LiNH₂BH₃ and Li[BH₃NH₂BH₂NH₂BH₃] are shown (bottom).⁹

Grochala *et al.* confirmed that over some period of time some reflections of Li[BH₃NH₂BH₂NH₂BH₃] can be detected in LiNH₂BH₃ (Figure 5.1-3).⁹ The data reported by Xiong *et al.* showed two peaks in LiNH₂BH₃ pattern which belonged to Li[BH₃NH₂BH₂NH₂BH₃]. However they claimed that only a single phase was observed, LiNH₂BH₃.³ C. Wu *et al.* showed partial decomposition to a new phase that they were unable to identify.¹² Subsequently, Li[BH₃NH₂BH₂NH₂BH₃] was identified as this decomposition product.⁹

Li[BH₃NH₂BH₂NH₂BH₃] can be synthesised following a two-step reaction where LiH and NH₃BH₃ are mixed by ball milling in a 1 : 3 molar ratio followed by thermal desorption of excess NH₃ (equations (5.7) and (5.8)):

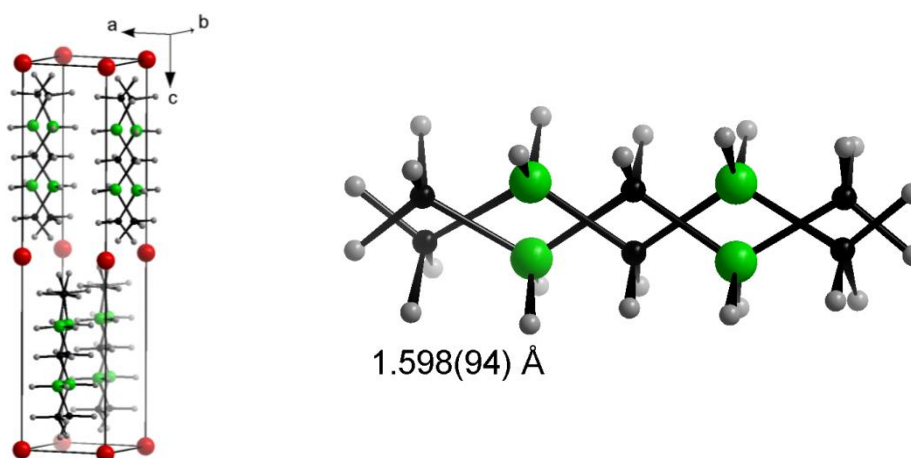
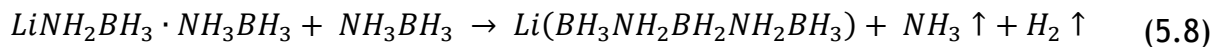
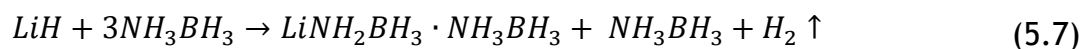


Figure 5.1-4 Crystal structure of Li[BH₃NH₂BH₂NH₂BH₃].

The crystal structure of Li[BH₃NH₂BH₂NH₂BH₃] consists of Li⁺ layers which are linked *via* five member chain [BH₃NH₂BH₂NH₂BH₃]⁻ anions which coordinate lithium cations using the hydrogen atoms of terminal [BH₃] groups only (Figure 5.1-4). Lithium cations are found in tetrahedral coordination of four hydrogen atoms, resembling those found for the orthorhombic form of LiBH₄.¹⁷ The shortest Li-H distance is 2.0(2) Å (as compared with the corresponding distance of 1.98(1) Å in *Pbca* LiNH₂BH₃ and 1.98(1) Å in *Pnma* LiBH₄).^{3, 17} The average B-N bond length of the [BH₃NH₂BH₂NH₂BH₃]⁻ anion is *ca.* 1.59(6) Å (as compared with 1.55 Å for LiNH₂BH₃),³ whereas the average angles between the B-N bonds (115 °) are close to the tetrahedral angle. The crystal structure contains disordered [BH₃NH₂BH₂NH₂BH₃]⁻ anions lying along the z axis of the unit cell.⁹

Continuous efforts were made to modify NH₃BH₃ to improve its hydrogen storage performance.⁶ One avenue for modifying ammonia borane in this regard has been to form metal borohydride ammonia boranes *via* mixing borohydrides such as LiBH₄, Mg(BH₄)₂ and Ca(BH₄)₂ with NH₃BH₃. This has led to crystalline borohydrides such as Mg[BH₄]₂[NH₃BH₃]₂^{18, 19} and layered compounds such as [LiBH₄]₂[NH₃BH₃]⁷ and Ca[BH₄]₂[NH₃BH₃]⁷ (Figure 5.1-5).

$\text{Li}_2[\text{BH}_4]_2[\text{NH}_3\text{BH}_3]$ is composed of alternating “layers” of borohydride and ammonia borane and is formed by mixing LiBH_4 and NH_3BH_3 in a 2 : 1 molar ratio by ball milling (5.9). It could be extremely useful in the application of Li^+ ion batteries since it can be obtained as a single phase and is stable up to 105°C . It crystallises in an orthorhombic structure with space group $Pnma$ ($a = 8.3118(8)$, $b = 12.428(1)$, $c = 6.5944(7)$ Å, and $V = 681.20(11)$ Å³)⁷ and is composed of alternate layers of LiBH_4 and NH_3BH_3 (Figure 5.1-5 (a)).

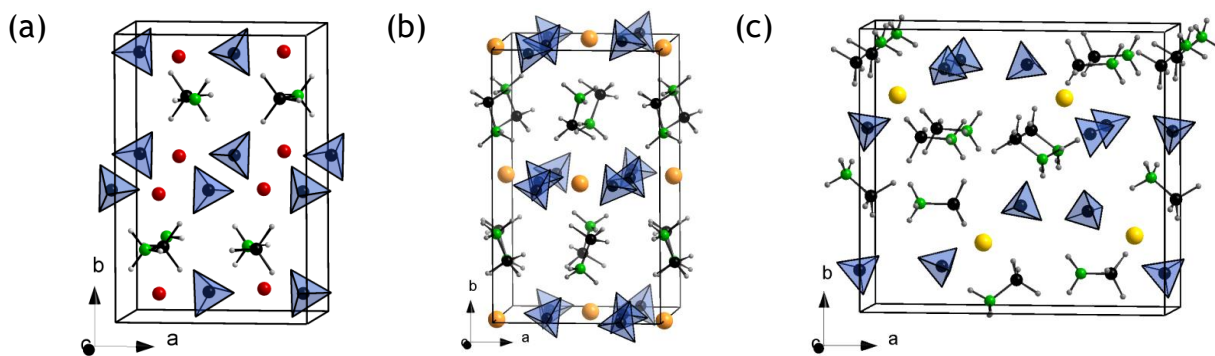


Figure 5.1-5 Crystal structures of a) $[\text{LiBH}_4]_2[\text{NH}_3\text{BH}_3]$, b) $\text{Ca}[\text{BH}_4]_2[\text{NH}_3\text{BH}_3]$ and c) $\text{Mg}[\text{BH}_4]_2[\text{NH}_3\text{BH}_3]_2$.



Recently another “layered” compound $\text{Li}_2[\text{BH}_4][\text{NH}_2\text{BH}_3]$ was discovered.¹⁵ This material was synthesised by mixing different ratios of LiNH_2BH_3 and LiBH_4 . One single composition was obtained using a 2 : 1 molar ratio ($\text{LiBH}_4 : \text{LiNH}_2\text{BH}_3$), however the stoichiometry of the product obtained was $\text{Li}_2[\text{BH}_4][\text{NH}_2\text{BH}_3]$ which would correspond to a 1 : 1 molar ratio of the starting materials. This could indicate the formation of an amorphous phase of the remaining LiBH_4 which does not react. If this material shows the presence of different phases, it could not be considered as a potential electrolyte since this could cause interferences in the total ionic conductivity and reduce it. The new $\text{Li}_2[\text{BH}_4][\text{NH}_2\text{BH}_3]$ phase was reported with an orthorhombic structure (space group $Pbca$, $a = 7.05$ Å, $b = 14.81$ Å, $c = 5.13$ Å, $\beta = 97.5^\circ$, $V = 531.6$ Å³) (equation (5.10)).¹⁵



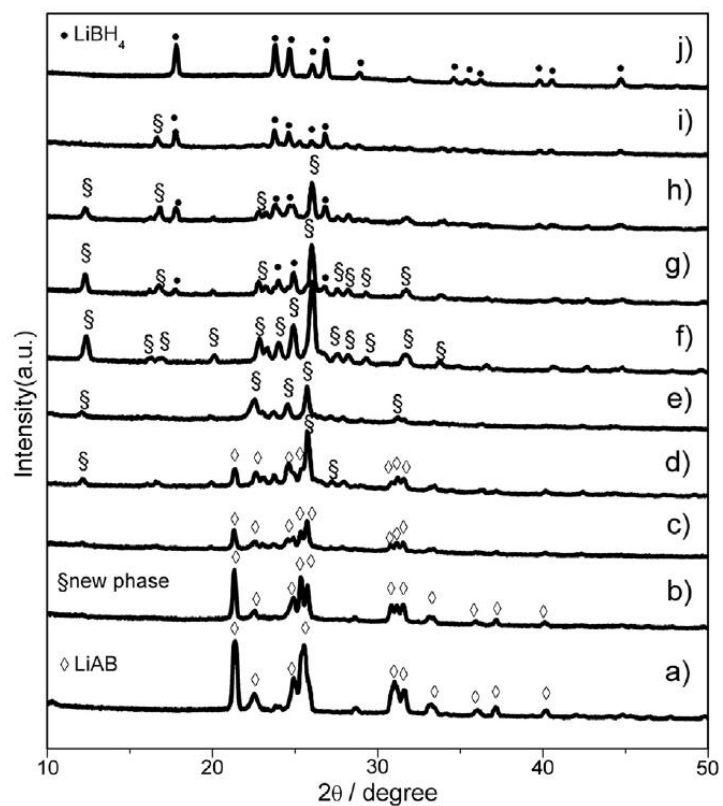


Figure 5.1-6. XRD patterns of the LiNH_2BH_3 (LiAB) – $x\text{LiBH}_4$ mixtures with (b) $x = 0.1$, (c) $x = 0.2$, (d) $x = 0.25$, (e) $x = 0.33$, (f) $x = 0.5$, (g) $x = 1$, (h) $x = 2$, (i) $x = 10$, respectively. XRD patterns of (a) as prepared LiNH_2BH_3 and (j) commercial LiBH_4 are shown for comparison.¹⁵

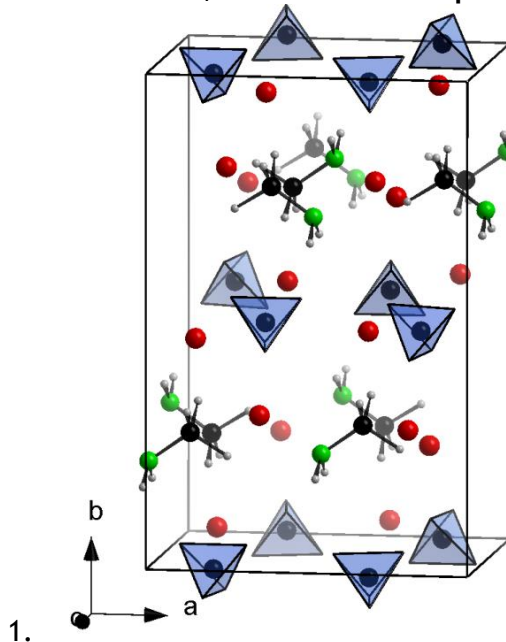


Figure 5.1-7 Crystal structure of $\text{Li}_2[\text{BH}_4][\text{NH}_2\text{BH}_3]$.

The aim of the work described in this chapter was to synthesise lithium ammonia borane hydrides, earlier considered as candidates for hydrogen storage, and study their properties as electrolytes. Being motivated by the synthesis of these materials other possible combinations were studied as well. We proposed the synthesis of novel electrolytes using the combination of NH_3BH_3 with other materials containing lithium such as lithium halides which have shown an improvement in conductivity when substituted in other materials such as LiBH_4 .²⁰ Our purpose was to synthesise novel materials with open structures to provoke ionic conductivity via either 1D, 2D or 3D pathways.

5.2 Experimental

5.2.1 LiH – $[\text{NH}_3\text{BH}_3]$ system

5.2.1.1 Synthesis of LiNH_2BH_3 (α – LiNH_2BH_3 and β – LiNH_2BH_3)

For the synthesis of α - LiNH_2BH_3 and β - LiNH_2BH_3 , LiH (Sigma Aldrich, 99%) and NH_3BH_3 (Sigma Aldrich, 98%) mixtures in a 1 : 1 molar ratio were prepared in an Argon filled recirculating glovebox (Table 5.2-1). The compounds were synthesised using a Retsch PM100 ball mill, as detailed in section 2.2.1. A total of ca. 0.1 or 0.5 g (ball : powder ratio 400 : 1 and 80 : 1, respectively) of the powder mixture was loaded into a hardened steel jar (50 ml) together with 10 hardened steel balls of 10 mm in diameter. The resultant products, white in colour, were collected in the glovebox for characterisation.

Table 5.2-1 Summary of reactions (61 - 65), including experimental parameters used and powder X – ray products.

Sample	Ball milling time / h	Ball : powder ratio	Time resting min / min	Speed / rpm	Expected compound	X – ray product
61	16	80 : 1	2 / 2	200	α – LiNH_2BH_3	$\text{Li}[\text{BH}_3\text{NH}_2\text{BH}_2\text{NH}_2\text{BH}_3]$, NH_3BH_3 , α – LiNH_2BH_3 , $\text{LiNH}_2\text{BH}_3 \cdot \text{NH}_3\text{BH}_3$ and an unknown phase
62	16	400 : 1	2 / 2	200	α – LiNH_2BH_3	α – LiNH_2BH_3 (after hours decomposes into $\text{LiNH}_2\text{BH}_3 \cdot \text{NH}_3\text{BH}_3$).
63	2	400 : 1	5 / 25	200	α – LiNH_2BH_3	$\text{Li}[\text{BH}_3\text{NH}_2\text{BH}_2\text{NH}_2\text{BH}_3]$, NH_3BH_3
64	5	80 : 1	2 / 2	200	β – LiNH_2BH_3	$\text{Li}[\text{BH}_3\text{NH}_2\text{BH}_2\text{NH}_2\text{BH}_3]$, NH_3BH_3 , α – LiNH_2BH_3
65	5	400 : 1	2 / 2	200	β – LiNH_2BH_3	$\text{Li}[\text{BH}_3\text{NH}_2\text{BH}_2\text{NH}_2\text{BH}_3]$, NH_3BH_3 , α – LiNH_2BH_3 , $\text{LiNH}_2\text{BH}_3 \cdot \text{NH}_3\text{BH}_3$, β – LiNH_2BH_3

5.2.1.2 Synthesis of $\text{LiNH}_2\text{BH}_3 \cdot \text{NH}_3\text{BH}_3$

The synthesis of $\text{LiNH}_2\text{BH}_3 \cdot \text{NH}_3\text{BH}_3$ was performed using LiH (Sigma Aldrich, 99%) and NH_3BH_3 (Sigma Aldrich, 98%) mixtures in a 1 : 2 molar ratio prepared in an Argon filled recirculating glovebox (Table 5.2-2). A total of ca. 0.1 g of the powder mixture was loaded into a hardened steel jar (50 ml) together with 10 hardened steel balls of 10 mm in diameter. The resultant product, white in colour, was collected in the glovebox for characterisation.

Table 5.2-2 Experimental conditions for synthesis of 66 including powder X – ray products.

Sample	Ball milling time / h	Ball : powder ratio	Time resting min / min	Speed / rpm	X – ray product
66	2	400 : 1	5 / 25	200	$\text{LiNH}_2\text{BH}_3 \cdot \text{NH}_3\text{BH}_3$, $\text{Li}[\text{BH}_3\text{NH}_2\text{BH}_2\text{NH}_2\text{BH}_3]$ and NH_3BH_3

5.2.1.3 Synthesis of $\text{Li}[\text{BH}_3\text{NH}_2\text{BH}_2\text{NH}_2\text{BH}_3]$

The synthesis of $\text{Li}[\text{BH}_3\text{NH}_2\text{BH}_2\text{NH}_2\text{BH}_3]$ was performed by reacting approximately 0.13 g of a mixture of LiH (Sigma Aldrich, 99%) and NH_3BH_3 (Sigma Aldrich, 98%) in a 1 : 3 molar ratio (Table 5.2-3). The powder was loaded into a steel jar with steel balls (same conditions as samples from section 5.2.1.1). The final mixture was heated to complete the reaction using conditions from Table 5.2-4.

Table 5.2-3 Experimental conditions for synthesis of 67 including powder X – ray products.

Sample	Ball milling time / h	Ball : powder ratio	Time resting min / min	Speed / rpm	X – ray product
67	2	400 : 1	5 / 25	200	$\text{LiNH}_2\text{BH}_3 \cdot \text{NH}_3\text{BH}_3$, NH_3BH_3

Table 5.2-4 Experimental conditions for synthesis of 67a including powder X – ray product.

Sample	Time / h	Temperature / °C	Ramp / °C min ⁻¹	X – ray product
67a	12	75	5	$\text{Li}[\text{BH}_3\text{NH}_2\text{BH}_2\text{NH}_2\text{BH}_3]$

5.2.1.4 Synthesis of $\text{Li}[\text{BH}_3\text{NH}_2\text{BH}_2\text{NH}_2\text{BH}_2\text{NH}_2\text{BH}_3]$

The synthesis of $\text{Li}[\text{BH}_3\text{NH}_2\text{BH}_2\text{NH}_2\text{BH}_2\text{NH}_2\text{BH}_3]$ electrolyte was attempted by reacting approximately 0.17 g of a mixture of LiH (Sigma Aldrich, 99%) and NH_3BH_3 (Sigma Aldrich, 98%) with 1 : 4 molar ratio ((5.11) and (5.12)). The powder was loaded into a steel jar with steel balls (same conditions as samples from section 5.2.1.1, Table 5.2-5, to form $\text{LiNH}_2\text{BH}_3 \cdot \text{NH}_3\text{BH}_3$ and NH_3BH_3 releasing H_2 (equation (5.11)). The final mixture was heated to complete the reaction using conditions from Table 5.2-6 to form $\text{Li}[\text{BH}_3\text{NH}_2\text{BH}_2\text{NH}_2\text{BH}_2\text{NH}_2\text{BH}_3]$ releasing NH_3 and H_2 (equation (5.12)).

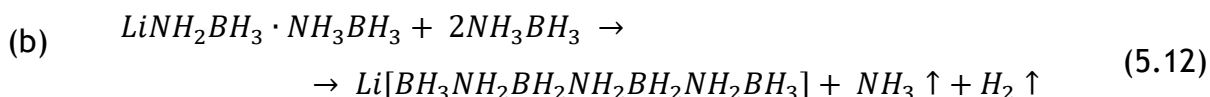


Table 5.2-5 Experimental conditions for synthesis of 68 including powder X – ray product.

Sample	Ball milling time / h	Ball : powder ratio	Time resting min / min	Speed / rpm	X – ray product
68	2	400 : 1	5 / 25	200	$\text{Li}[\text{BH}_3\text{NH}_2\text{BH}_2\text{NH}_2\text{BH}_3]$, NH_3BH_3

Table 5.2-6 Experimental conditions for synthesis of 68a including powder X – ray product.

Sample	Time / h	Temperature / °C	Ramp / °C min ⁻¹	X – ray product
68a	12	75	5	Formation of gel

5.2.1.5 Synthesis of $Li[BH_4]_{1-x}[NH_2BH_3]_x$

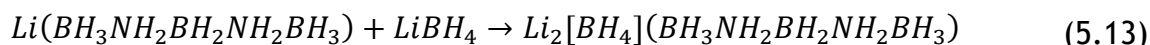
The synthesis of $Li[BH_4]_{1-x}[NH_2BH_3]_x$ was attempted by mixing powders of α - $LiNH_2BH_3$, previously synthesised, and $LiBH_4$ (Sigma-Aldrich, ≥ 95). Approximately 0.1 g of mixture was milled for 2 h at 200 rpm (400 : 1, ball-to-powder-ratio). The ball milling was performed in periods of 2 minutes of milling interspersed by 2 min breaks to minimise heating of the samples (Table 5.2-7).

Table 5.2-7 Summary of reactions (69 - 70), including experimental parameters used and powder X – ray product.

Sample	Molar ratio	X – ray product
	$LiNH_2BH_3$ (62): $LiBH_4$	
69	1 : 1	$Li_2[BH_4][NH_2BH_3]$, $LiBH_4$
70	2 : 1	$Li_2[BH_4][NH_2BH_3]$

5.2.1.6 Synthesis of $Li_2[BH_4][BH_3NH_2BH_2NH_2BH_3]$

The synthesis of $Li_2[BH_4][BH_3NH_2BH_2NH_2BH_3]$ was attempted by mixing powders of previously synthesised $Li[BH_3NH_2BH_2NH_2BH_3]$ (Table 5.2-3 and Table 5.2-4), and $LiBH_4$ (Sigma-Aldrich, ≥ 95 %) (Table 5.2-8 and equation (5.13)). Approximately 0.1 g of mixture was milled for 2 h at 250 rpm (400 : 1, ball-to-powder-ratio). The ball milling was performed in periods of 2 min of milling interspersed by 2 min breaks to minimise heating of the samples.

**Table 5.2-8 Summary of reaction (71), including experimental parameters used and powder X – ray product.**

Sample	Molar ratio	X – ray product
	$Li[BH_3NH_2BH_2NH_2BH_3]$: $LiBH_4$	
71	1 : 1	$Li[BH_3NH_2BH_2NH_2BH_3]$, $LiBH_4$

5.2.2 LiBH₄ – [NH₃BH₃] system

For the synthesis of LiBH₄ - NH₃BH₃ materials, LiBH₄ (Sigma-Aldrich, ≥ 95 %) and NH₃BH₃ (Sigma Aldrich, 98%) mixtures with different molar ratios were prepared in an Argon filled recirculating glovebox (Table 5.2-9). A total of *ca.* 0.1 g of the powder mixture was loaded in a steel jar together with steel balls and milled for 2 h at 250 rpm (400 : 1, ball-to-powder-ratio). The ball milling was performed in periods of 2 min of milling interspersed by 2 min breaks to minimise heating of the samples. The resultant products, white in colour, were collected in the glovebox for characterisation.

Table 5.2-9 Summary of reactions (72 - 77), including experimental parameters used and powder X – ray product.

Sample	Molar ratio LiBH ₄ : NH ₃ BH ₃	X – ray product
72	1 : 1	LiBH ₄ ·NH ₃ BH ₃ , [LiBH ₄] ₂ NH ₃ BH ₃ , LiBH ₄
73	2 : 1	[LiBH ₄] ₂ NH ₃ BH ₃
74	3 : 1	[LiBH ₄] ₂ NH ₃ BH ₃ , LiBH ₄
75	4 : 1	[LiBH ₄] ₂ NH ₃ BH ₃ , LiBH ₄
76	5 : 1	[LiBH ₄] ₂ NH ₃ BH ₃ , LiBH ₄
77	6 : 1	[LiBH ₄] ₂ NH ₃ BH ₃ , LiBH ₄

5.2.3 LiX' – [NH₃BH₃] (X' = Br, I)

For the synthesis of LiX' - NH₃BH₃, where X' = Br and I, different mixtures were prepared using LiBr (Sigma-Aldrich, ≥99%) or Lil (Sigma Aldrich, beads, 99%) and NH₃BH₃ (Sigma Aldrich, 98%) inside the glovebox (Table 5.2-10 and Table 5.2-11). The mixture was loaded into a steel jar with steel balls and ball milled using a Retsch PM100 ball mill. A total of *ca.* 0.2 g of the powder mixture was loaded into a hardened steel jar (50 ml) together with 10 hardened steel balls of 10 mm in diameter. The mixture was milled for 2 h at 250 rpm (400 : 1, ball-to-powder-ratio). The ball milling was performed in periods of 2 min of milling interspersed by 2 min breaks to minimise heating of the samples. The resultant product, white in colour, was collected in the glovebox for characterisation.

Table 5.2-10 Summary of reactions (78 - 82), including experimental parameters used and powder X – ray product.

Sample	Molar ratio LiBr : NH ₃ BH ₃	X – ray product
78	2 : 1	LiBr, NH ₃ BH ₃
79	1 : 1	LiBr, NH ₃ BH ₃
80	1 : 2	LiBr, NH ₃ BH ₃
81	1 : 3	LiBr, NH ₃ BH ₃
82	1 : 4	LiBr, NH ₃ BH ₃

Table 5.2-11 Summary of reactions (83 - 86), including experimental parameters used and powder X – ray product.

Sample	Molar ratio LiI : NH ₃ BH ₃	X – ray product
83	2 : 1	LiI, [LiI][NH ₃ BH ₃]
84	1 : 1	[LiI][NH ₃ BH ₃]
85	2 : 3	[LiI][NH ₃ BH ₃], [LiI][NH ₃ BH ₃] ₂
86	1 : 2	[LiI][NH ₃ BH ₃] ₂

5.3 Characterisation

Powder X - ray diffraction (PXD) data of samples **64 - 86** were obtained at room temperature with a Bruker D8 Advance (θ -2 θ) diffractometer, using Cu K α radiation with a scanning step size of 0.017 ° 2 θ over an angular range 5 - 85 ° 2 θ for ca. 1 h (From Table 5.2-1 to Table 5.2-11). Experimental diffraction data were compared to powder patterns generated from data in the Inorganic Crystal Structure Database (ICSD)²¹ using Powdercell 2.4.²² All data were indexed and refined by least squares fitting when possible using the CELREF package.²³ Jana2006 was used for the identification of the unknown compounds using a test of the best cell candidate.²⁴ The background was fitted using the shifted Chebyshev polynomial and the unit cell parameters were then refined, followed by the peak profile parameters, atomic positions and isotropic displacement parameters. High resolution data were collected from the I11 instrument at the Diamond Light Source, synchrotron facility located at the Harwell Science and Innovation Campus in Oxfordshire, to obtain complete

models derived from our original lab PXD structure refinements with new crystal structures. The far superior intensity of synchrotron radiation was used to confirm our proposed structures and map any occupational or positional disorder in the structures. The data were analysed using Rietveld refinement as implemented in the GSAS software package²⁵ via the EXPGUI interface²⁶ against multiple data sets. Data collected were fitted using a starting model obtained from previous lab PXD results. The background was fitted using the shifted Chebyshev polynomial and the unit cell parameters were then refined, followed by the peak profile parameters, atomic positions and isotropic displacement parameters. Modelling of the peak shape was carried out using GSAS function 2 (pseudo-Voigt combination and an asymmetrical peak shape).^{25, 26} The refinements were considered finished when they converged, all the variables were stable and the R-values minimised.

Raman spectra were collected in the range 500 - 4000 cm^{-1} at room temperature using a Horiba LabRAM HT confocal microscope system with a 532 nm laser, a hole aperture of 100 μm and a 200 gr mm^{-1} grating.

Thermal analysis was carried out using a NETZSCH STA 4090C coupled with a HIDEN HPR20 mass spectrometer to determine the stability of the lithium aminoborane compounds at high temperatures in an inert atmosphere. Samples were heated in a silica pan from room temperature to 200 $^{\circ}\text{C}$ at 5 $^{\circ}\text{C min}^{-1}$ under an Ar flow. Mass spectra were collected simultaneously. Gases monitored were H_2 , NH_3 , diborane (B_2H_6), borazine ($\text{B}_3\text{H}_6\text{N}_3$), H_2O and Ar. Masses of 26, 27 and 28 g mol^{-1} were used to monitor of diborane (mass 27.67 g mol^{-1}).

5.4 Results and discussion

5.4.1 [LiH][NH_3BH_3] system

5.4.1.1 Synthesis of LiNH_2BH_3 (α - LiNH_2BH_3 and β - LiNH_2BH_3)

The synthesis of α - LiNH_2BH_3 was attempted using a route already proposed in the literature where LiH and NH_3BH_3 were milled in a 1 : 1 molar ratio.³ In the literature the ball to powder ratio was not mentioned. Initial reaction with a ratio of 80 : 1 (sample 61) led to the formation of multiple phases: $\text{Li}[\text{BH}_3\text{NH}_2\text{BH}_2\text{NH}_2\text{BH}_3]$, NH_3BH_3 , α - LiNH_2BH_3 , $\text{LiNH}_2\text{BH}_3 \cdot \text{NH}_3\text{BH}_3$ and an unknown phase. The reaction was

performed again using a ball to powder ratio increased by five times, from 80 : 1 to 400 : 1. Powder X-ray Diffraction (PXD) data of the product after milling (sample 62) are shown in Figure 5.4-1. Powder X-ray data revealed the presence of α - LiNH_2BH_3 , which was indexed in orthorhombic space group $Pbca$. This crystal structure agrees with that previously reported by Xiong *et al.*³

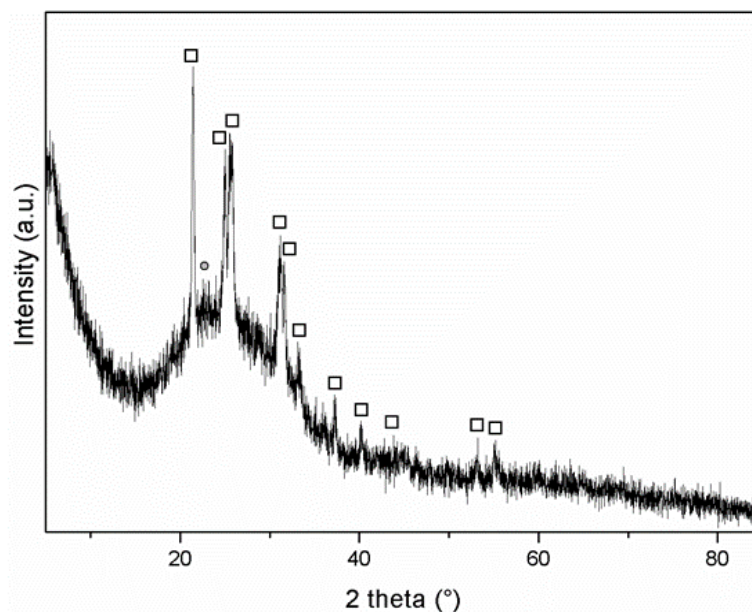


Figure 5.4-1 PXD pattern of the reaction product (62) after ball milling $\text{LiH} : \text{NH}_3\text{BH}_3$ (1:1), ball milling for 16 h, 1 : 400. White squares represent α - LiNH_2BH_3 and grey circles represent $\text{Li}[\text{BH}_3\text{NH}_2\text{BH}_2\text{NH}_2\text{BH}_3]$.

However as Fijalkowski *et al.*⁹ demonstrated, this phase is unstable. A PXD measurement performed, days after the synthesis, confirmed that α - LiNH_2BH_3 decomposes into $\text{Li}[\text{BH}_3\text{NH}_2\text{BH}_2\text{NH}_2\text{BH}_3]$ and $\text{LiNH}_2\text{BH}_3 \cdot \text{NH}_3\text{BH}_3$ as Figure 5.4-2 shows.

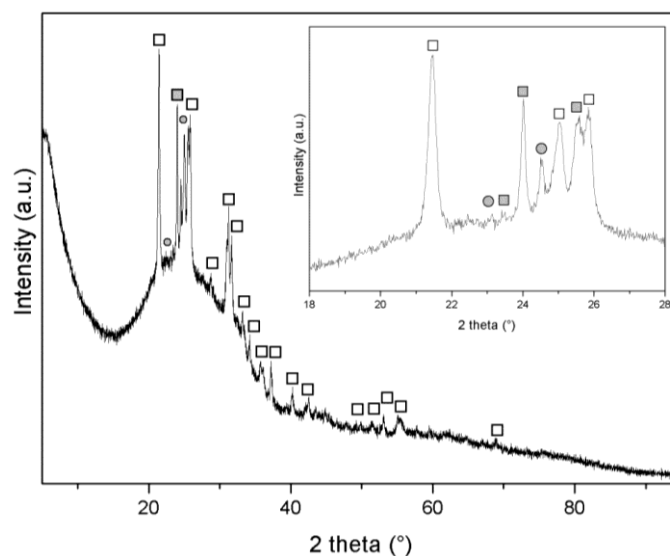


Figure 5.4-2 PXD pattern of the reaction product (62) measured 2 days after being synthesised. White squares represent α - LiNH_2BH_3 ; grey squares represent $\text{LiNH}_2\text{BH}_3 \cdot \text{NH}_3\text{BH}_3$; and grey circles represent $\text{Li}[\text{BH}_3\text{NH}_2\text{BH}_2\text{NH}_2\text{BH}_3]$.

Another route was used in order to stabilise the α - phase, following the conditions reported by Weng *et al.*¹¹ The PXD pattern of sample 63 indicated the presence of the three phases found in sample 62, α - LiNH_2BH_3 , $\text{Li}[\text{BH}_3\text{NH}_2\text{BH}_2\text{NH}_2\text{BH}_3]$ and $\text{LiNH}_2\text{BH}_3 \cdot \text{NH}_3\text{BH}_3$ (Figure 5.4-3).

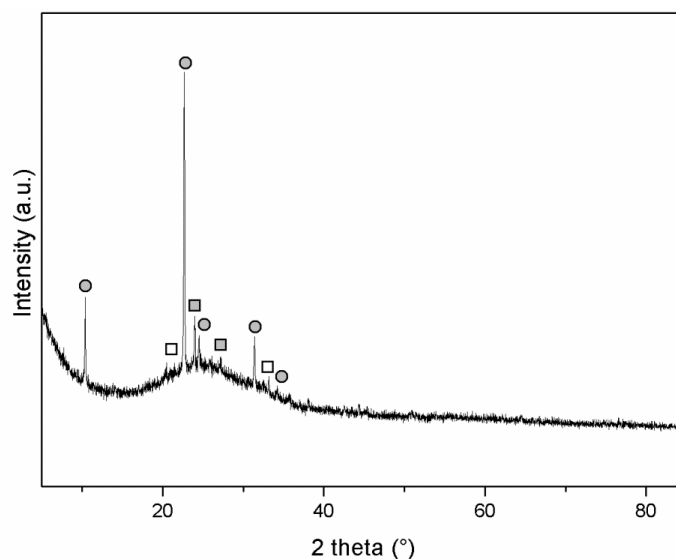


Figure 5.4-3 PXD pattern of the reaction product (63) after ball milling $\text{LiH} : \text{NH}_3\text{BH}_3$ (1:1), for 16 h (1 : 400, ball : powder ratio). White squares represent α - LiNH_2BH_3 , grey squares represent $\text{LiNH}_2\text{BH}_3 \cdot \text{NH}_3\text{BH}_3$ and grey circles represent $\text{Li}[\text{BH}_3\text{NH}_2\text{BH}_2\text{NH}_2\text{BH}_3]$.

The synthesis of the polymorph of LiNH_2BH_3 , the β phase, was performed following the conditions reported by Wu *et al.*¹². β - LiNH_2BH_3 was obtained by ball milling LiH and NH_3BH_3 using shorter ball milling times than those for preparation of α - LiNH_2BH_3 (Table 5.2-1).¹² Two different ball to powder ratio conditions were used (80 : 1 and 400 : 1) due to the unreported conditions in the literature. The PXD pattern from the mixture of LiH and NH_3BH_3 (1:1) ball milled with a low ball to powder ratio (sample **64**) did not indicate the presence of β phase, only reflections from α - LiNH_2BH_3 , $\text{Li}[\text{BH}_3\text{NH}_2\text{BH}_2\text{NH}_2\text{BH}_3]$ and $\text{LiNH}_2\text{BH}_3 \cdot \text{NH}_3\text{BH}_3$. However if the ball to powder ratio is increased (sample **65**) four different phases are observed: α - LiNH_2BH_3 , $\text{LiNH}_2\text{BH}_3 \cdot \text{NH}_3\text{BH}_3$, $\text{Li}[\text{BH}_3\text{NH}_2\text{BH}_2\text{NH}_2\text{BH}_3]$ and a new phase. This phase has been assigned in the literature to the polymorph of LiNH_2BH_3 (Figure 5.4-4). No further experiments were performed because the β - phase is metastable and eventually transforms to the α - phase. As was mentioned earlier in this section the α - phase decomposes into $\text{Li}[\text{BH}_3\text{NH}_2\text{BH}_2\text{NH}_2\text{BH}_3]$ over some period of time, therefore we decided that both phases were not applicable for application as electrolytes given their low thermal stability.

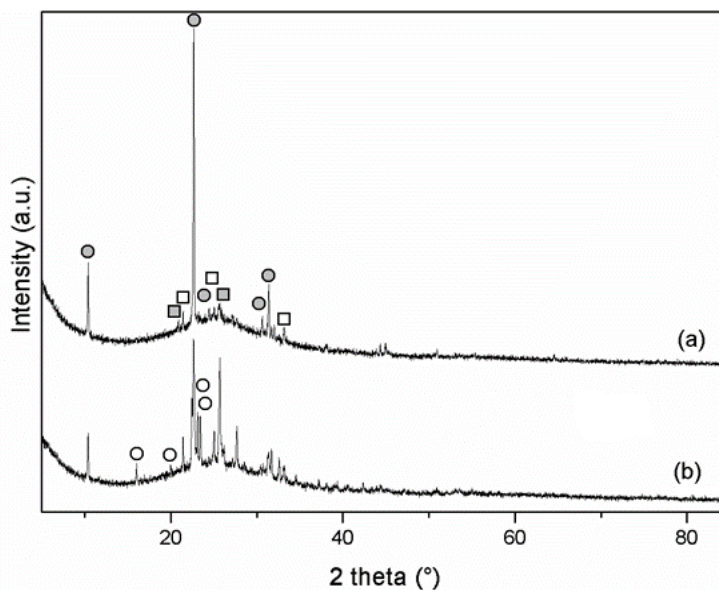


Figure 5.4-4 PXD pattern of the reaction products after ball milling $\text{LiH} : \text{NH}_3\text{BH}_3$ (1:1), for 5 h with ball : powder ratio of: (a) 1 : 80 (**64**) and (b) 1 : 400 (**65**). White squares represent α - LiNH_2BH_3 , grey squares represent $\text{LiNH}_2\text{BH}_3 \cdot \text{NH}_3\text{BH}_3$, grey circles represent $\text{Li}[\text{BH}_3\text{NH}_2\text{BH}_2\text{NH}_2\text{BH}_3]$ and white circles represent β - LiNH_2BH_3 .

5.4.1.2 Synthesis of $\text{LiNH}_2\text{BH}_3 \cdot \text{NH}_3\text{BH}_3$

Synthesis of $\text{LiNH}_2\text{BH}_3 \cdot \text{NH}_3\text{BH}_3$ was attempted following the conditions in the experimental section (Table 5.2-2).¹⁴ LiH and NH_3BH_3 were ball milled in a 1 : 2 molar ratio. As Fijalkowski *et al.*⁹ showed for LiNH_2BH_3 , $\text{LiNH}_2\text{BH}_3 \cdot \text{NH}_3\text{BH}_3$ also eventually transforms into $\text{Li}[\text{BH}_3\text{NH}_2\text{BH}_2\text{NH}_2\text{BH}_3]$ (Figure 5.4-5). Therefore this material was not considered suitable for investigation as an electrolyte.

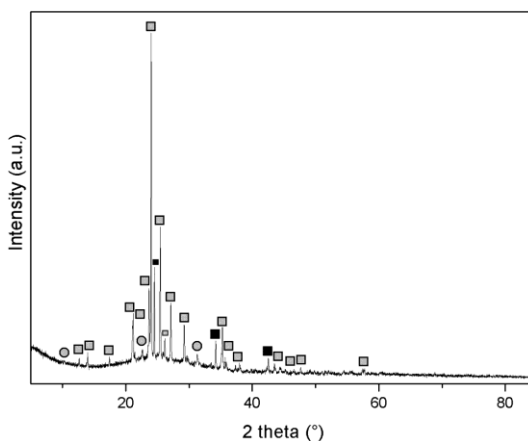


Figure 5.4-5 PXD pattern of the reaction product (66) after ball milling $\text{LiH} : \text{NH}_3\text{BH}_3$ (1:2), ball milling for 2 h (1 : 400 ball : powder ratio). Grey squares represent $\text{LiNH}_2\text{BH}_3 \cdot \text{NH}_3\text{BH}_3$, grey circles represent $\text{Li}[\text{BH}_3\text{NH}_2\text{BH}_2\text{NH}_2\text{BH}_3]$ and black squares represent NH_3BH_3 .

5.4.1.3 Synthesis of $\text{Li}[\text{BH}_3\text{NH}_2\text{BH}_2\text{NH}_2\text{BH}_3]$

The synthesis of $\text{Li}[\text{BH}_3\text{NH}_2\text{BH}_2\text{NH}_2\text{BH}_3]$ consists of two stages: milling at room temperature and further heating at 75°C . In the first stage hydrogen is evolved following reaction (equation (5.7)). The PXD pattern in Figure 5.4-6 shows three different phases which correspond to NH_3BH_3 , $\text{LiNH}_2\text{BH}_3 \cdot \text{NH}_3\text{BH}_3$ and $\text{Li}[\text{BH}_3\text{NH}_2\text{BH}_2\text{NH}_2\text{BH}_3]$. The presence of the $\text{Li}[\text{BH}_3\text{NH}_2\text{BH}_2\text{NH}_2\text{BH}_3]$ phase at this stage means that the second part of the reaction (equation (5.7)) could occur during milling before heating and therefore partial release of $\text{NH}_{3(g)}$ may occur.

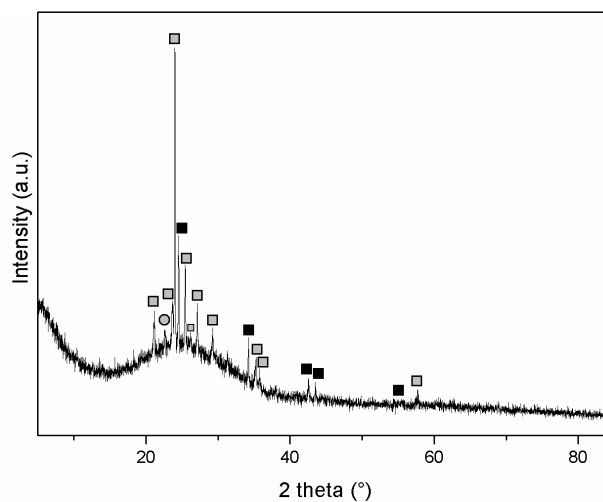


Figure 5.4-6 PXD pattern of the reaction product (67) post ball milling LiH : NH₃BH₃ (1:3), for 2 h, (1 : 400, ball : powder ratio). Grey squares represent LiNH₂BH₃·NH₃BH₃, grey circles represent Li[BH₃NH₂BH₂NH₂BH₃] and black squares represent NH₃BH₃.

Upon heating to 75 °C ammonia is evolved along with formation of Li[BH₃NH₂BH₂NH₂BH₃], as reaction (5.8) shows (Figure 5.4-7). The reflections can be assigned to the tetragonal phase reported by Fijalkowski *et al.* (space group $P\bar{4}2c$, $a = 4.02(1)$ and $c = 16.95(5)$ Å, $V = 273.9(12)$ Å³)⁹.

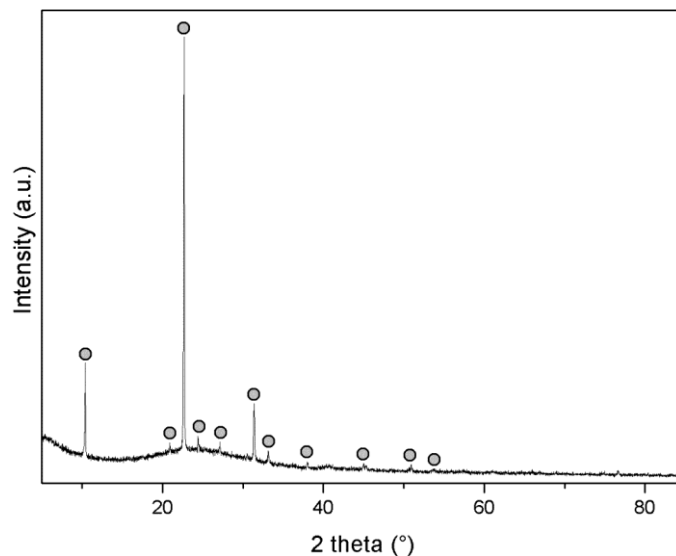


Figure 5.4-7 PXD pattern of the reaction product (67a) of LiH : NH₃BH₃ (1:3) post ball milling and thermal treatment at 75 °C. Grey circles represent Li[BH₃NH₂BH₂NH₂BH₃].

The alkali metal $\text{Li}[\text{BH}_3\text{NH}_2\text{BH}_2\text{NH}_2\text{BH}_3]$ phase was characterised by Raman spectroscopy and is easily distinguishable from the spectra of ammonia-borane and LiNH_2BH_3 (Figure 5.4-8 and Table 5.4-1).⁹ For instance, the symmetric N - H stretching mode for $\text{Li}[\text{BH}_3\text{NH}_2\text{BH}_2\text{NH}_2\text{BH}_3]$ appears at lower numbers (3314 cm^{-1}) than LiNH_2BH_3 (3361 cm^{-1}). Whereas the most intense B - H stretching bands from $\text{Li}[\text{BH}_3\text{NH}_2\text{BH}_2\text{NH}_2\text{BH}_3]$ are at higher wavenumbers (2320 cm^{-1}), compared to LiNH_2BH_3 (2191 cm^{-1}). In the literature this effect has been related to the fact that N - H bonds could be weaker in $\text{Li}[\text{BH}_3\text{NH}_2\text{BH}_2\text{NH}_2\text{BH}_3]$ than in LiNH_2BH_3 , and it could be the opposite for B - H bonds being stronger.⁹ The stiffening of the B - H bonds was predicted from DFT calculations for the isolated $(\text{NH}_2\text{BH}_3)^-$ and $[\text{BH}_3\text{NH}_2\text{BH}_2\text{NH}_2\text{BH}_3]^-$ anions in the gas phase. However the softening of the N - H bonds observed in the Raman spectra was in disagreement with the calculated trend. This might be due to solid state effects (differences of packing, interactions of anions with cations, or secondary interactions, such as possible dihydrogen bonding in the molecule) (Table 5.4-1).⁹

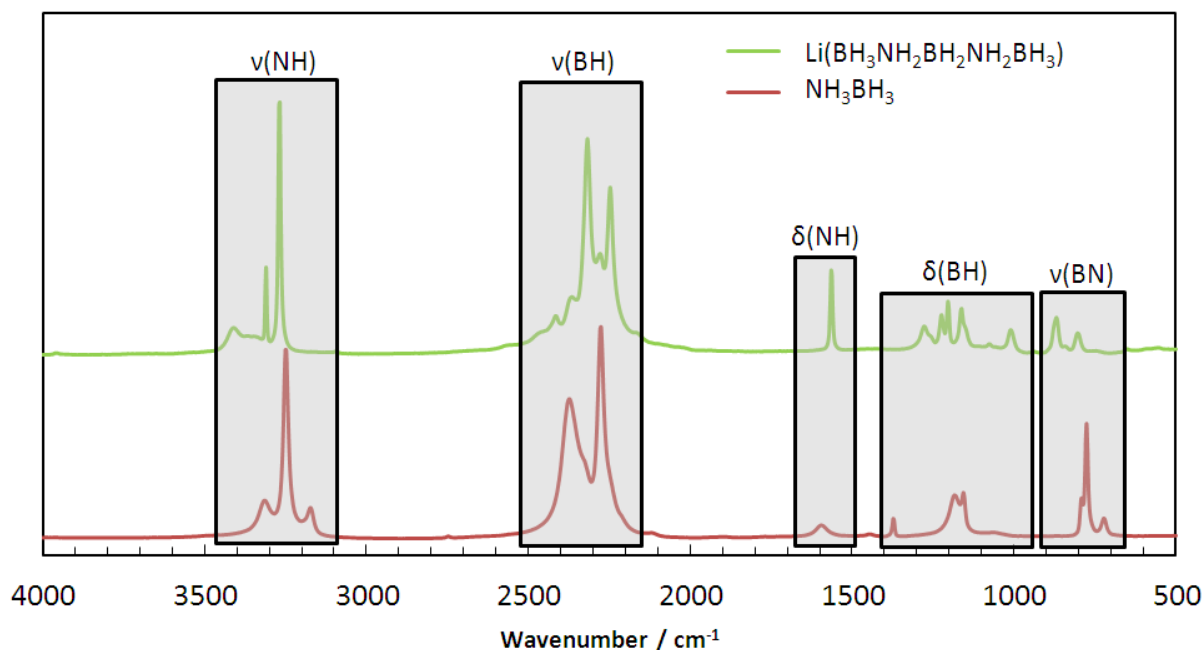


Figure 5.4-8 Raman spectra in the range $500 - 4000\text{ cm}^{-1}$ using a 532 nm laser of commercial NH_3BH_3 and $\text{Li}[\text{BH}_3\text{NH}_2\text{BH}_2\text{NH}_2\text{BH}_3]$ (sample 67a) (ν = stretching, δ = deformation: bending and torsional modes).

Table 5.4-1 Assignment of Raman spectra (wavenumber [cm⁻¹]) of Li[BH₃NH₂BH₂NH₂BH₃] and LiNH₂BH₃ at room temperature. Absorption bands of fresh ammonia borane (AB) at RT are shown for comparison. (ν = stretching, δ = deformation: bending and torsional modes) (Abbreviations: sh, shoulder, s, strong; m, medium; w, weak).⁹

Band	NH₃BH₃	LiNH₂BH₃	Li[BH₃NH₂BH₂NH₂BH₃]
ν (NH)		3361 s	
	3314 m	3303 vs	3314 m
	3253 vs		3272 s
	3177 m		
ν (BH)			2418 vw
	2378 vs	2368 w	2370 w
		2327 sh	2320 vs
		2317 sh	
			2282 m
	2284 vs		2250 s
		2191 s	
	2153 s	2166vw	
δ (NH)		1650 vw	
	1598 m	1613 vw	1567 m
	1583 m		
		1524 vw	
δ (BH)			1281 w
			1259 vw
			1226 w
			1206 m
	1190 sh		
	1168 m	1152 m	1166 w
		1122 vw	
1069 vw			
	1021 vw	1010w	
ν (BN)		919 m	
		901 s	895 vw
			873 w
	800 w	818 m	806 w
	785 m		
	729 w		
		603 w	
	584 w		

5.4.1.3.1 Thermal analysis

The thermal stability of $\text{Li}[\text{BH}_3\text{NH}_2\text{BH}_2\text{NH}_2\text{BH}_3]$ was studied under inert argon atmosphere (from room temperature and on heating to 200 °C, Figure 5.4-9). $\text{Li}[\text{BH}_3\text{NH}_2\text{BH}_2\text{NH}_2\text{BH}_3]$ decomposed exothermally at *ca.* 140 °C. LiBH_4 was identified in the solid residue after the dehydrogenation of the respective $\text{Li}[\text{BH}_3\text{NH}_2\text{BH}_2\text{NH}_2\text{BH}_3]$ phase in the literature, suggesting the following mechanism for the thermal decomposition (Table 5.4-2):

Table 5.4-2 Decomposition pathway suggested in the literature for $\text{Li}[\text{BH}_3\text{NH}_2\text{BH}_2\text{NH}_2\text{BH}_3]$. ^{9, 27}

Decomposition pathway	Gas evolved (wt. %)	Ref.
(a) $\text{Li}[\text{BH}_3\text{NH}_2\text{BH}_2\text{NH}_2\text{BH}_3]_{(s)} \rightarrow \text{LiBH}_4_{(s)} + 2(\text{NHBH})_n_{(s)} + 2\text{H}_2_{(g)}$	5.0 (H_2) (140 °C) ^{9, 27}	(5.14)
$\text{LiBH}_4_{(s)} + 2(\text{NHBH})_n_{(s)} \rightarrow \text{LiBH}_4_{(s)} + 2\text{BN}_{(s)} + 2\text{H}_2_{(g)}$	10.0 (H_2) (200 °C) ^{9, 27}	(5.15)

The expected mass loss according to equation (5.14) is 5 %. According to Owarzany *et al.*^{9, 27}, some mass loss is observed at temperatures up to 200 °C due to $(\text{NHBH})_n$ decomposing into BN, releasing H_2 following reaction (5.15). $\text{Li}[\text{BH}_3\text{NH}_2\text{BH}_2\text{NH}_2\text{BH}_3]$ is reported to release only H_2 gas which is free from ammonia or any other N-B-H impurities.^{9, 27}

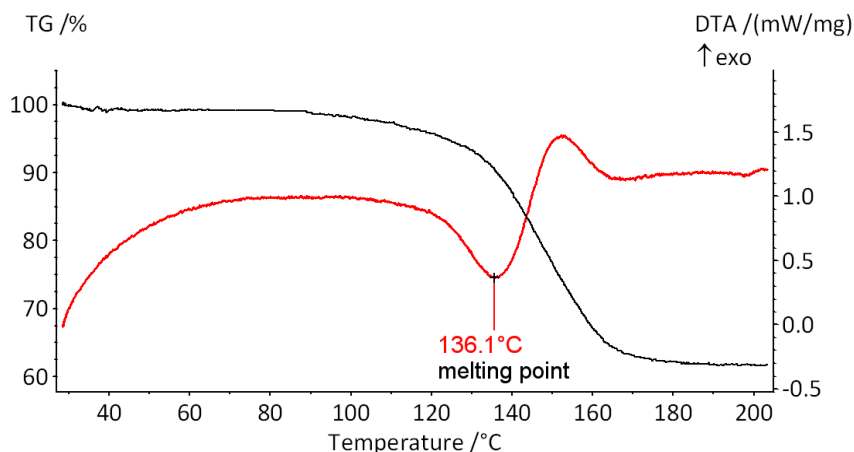


Figure 5.4-9 Typical TG-DTA plot of sample 67a. STA analysis was carried out in an Ar atmosphere, heating the sample at 5 °C min⁻¹ from ambient temperature to 200 °C. Black line represents TG curve and red line represents DTA curve.

NH₃BH₃ shows two desorption steps at 125 and 155 °C and **67a** decomposes at 129.7 (onset temperature) and 150.1 °C which suggests a similarity to the first and second decomposition steps of NH₃BH₃ (Table 5.4-3 and Figure 5.4-9).²⁸

Table 5.4-3 Summary of thermal stability analysis including data from TGA/MS, XRD data and Raman analysis.

Sample	Li[BH ₃ NH ₂ BH ₂ NH ₂ BH ₃] (67a)	Li[BH ₃ NH ₂ BH ₂ NH ₂ BH ₃] ⁹
Formula mass	81.38	81.38
Onset before change in the DTA T / °C	129.7	140
Melting point	136.1	140
Total weight loss / %	34.02	9
Gases evolved	H ₂ , B ₂ H ₆ N ₃ , B ₂ H ₆ , NH ₃	H ₂
XRD pattern post decomposition	amorphous	LiBH ₄
Raman spectra	(NH ₂ BH ₂) _n and (NHBH) _n	---

Li[BH₃NH₂BH₂NH₂BH₃] loses 34.02 % of mass during heating; STA results show that this mass loss is due to H₂, B₃H₆N₃, B₂H₆ and NH₃ being released (Figure 5.4-10).

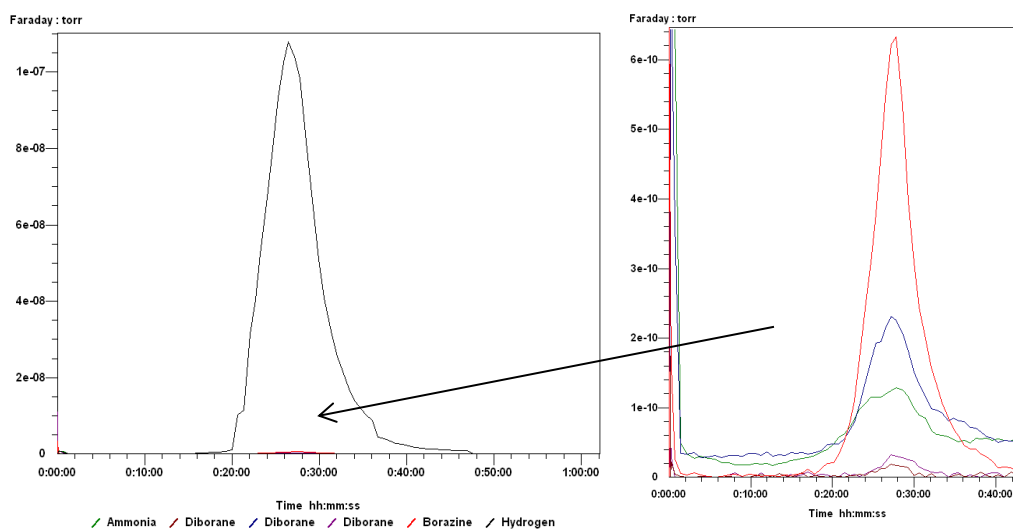


Figure 5.4-10 Typical mass spectrum recorded of Li[BH₃NH₂BH₂NH₂BH₃] (67a) during thermal treatment. Gases monitored were: NH₃ (green); B₂H₆ (brown, blue and purple); B₃H₆N₃ (red); H₂ (black).

Figure 5.4-11 shows an amorphous pattern obtained after the thermal treatment.

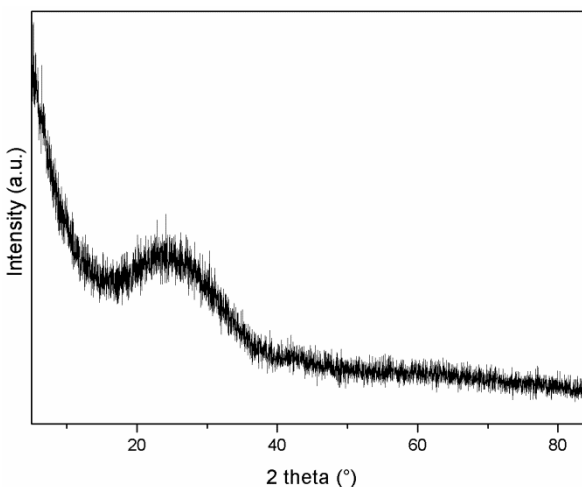


Figure 5.4-11 Post-TGA product after heating sample 7a under an Argon flow from room temperature to 200 °C at 5 °C min⁻¹.

As was mentioned in the introduction of this chapter, ammonia borane goes through two different decomposition steps (4.5) and (5.2). During the decomposition process it first forms polyaminoborane $(\text{NH}_2\text{BH}_2)_n$ (4.5) and subsequently polyiminoborane $(\text{NHBH})_n$ (5.2). In Raman spectroscopy ammonia borane shows $\nu_s(\text{NH}_3)$ and $\nu_{as}(\text{NH}_3)$ at *ca.* 3250 and 3300 cm^{-1} , respectively, and $\nu_s(\text{BH}_3)$ and $\nu_{as}(\text{BH}_3)$ at *ca.* 2280 and 2400 cm^{-1} , respectively. At 125 °C, ammonia borane starts to decompose and forms $(\text{NH}_2\text{BH}_2)_n$ and a new peak is observed at 3250 cm^{-1} which belongs to the $\nu_s(\text{NH}_2)$. At 155 °C, $(\text{NH}_2\text{BH}_2)_n$ starts to decompose into $(\text{NHBH})_n$, indicated by a signal at 3434 cm^{-1} which belongs to $\nu(\text{NH})$ mode. As it has been mentioned before, after the decomposition of $\text{Li}[\text{BH}_3\text{NH}_2\text{BH}_2\text{NH}_2\text{BH}_3]$, it was not possible to assign any compound due to the amorphous PXD pattern (Table 4.3-8). Therefore Raman analysis was performed to characterise the final compounds after the thermal decomposition of $\text{Li}[\text{BH}_3\text{NH}_2\text{BH}_2\text{NH}_2\text{BH}_3]$. Figure 5.4-12 shows the Raman spectrum of **67a** after STA measurement. LiBH_4 and $(\text{NHBH})_n$ are expected as final products after the decomposition according to equation (5.14).^{9, 27} The absence of LiBH_4 peaks in the powder XRD pattern may have been due to the material not being able to crystallise under the reaction conditions. It has been commented on in other studies that LiBH_4 is unable to crystallise under dehydrogenation conditions and so is

often not observed in powder XRD patterns despite it being an expected decomposition product.²⁹ From Raman spectra $(\text{NH}_2\text{BH}_2)_n$ and $(\text{NHBH})_n$ are identified by observing peaks that belong to $\nu(\text{NH}_2)$ and $\nu(\text{NH})$, showing that the complete decomposition of ammonia borane did not occur.²⁸ A peak is observed at 2296 cm^{-1} , which could also correspond to the $\nu_1 (A_1)$ mode from LiBH_4 .

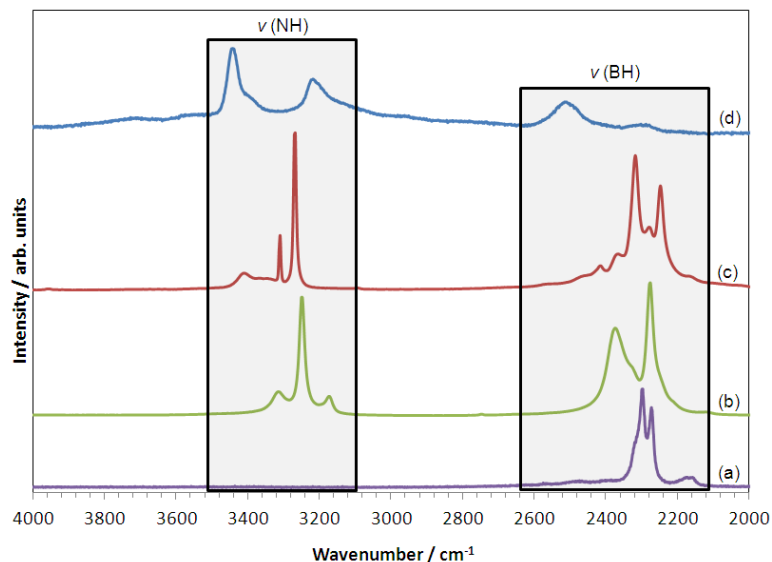


Figure 5.4-12 Raman spectra in the range $2000 - 4000\text{ cm}^{-1}$ using a 532 nm laser of (a) commercial LT - LiBH_4 , (b) commercial NH_3BH_3 , (c) $\text{Li}[\text{BH}_3\text{NH}_2\text{BH}_2\text{NH}_2\text{BH}_3]$ (67a), and (d) post-TGA product after heating $\text{Li}[\text{BH}_3\text{NH}_2\text{BH}_2\text{NH}_2\text{BH}_3]$ (67a) under an Argon flow from room temperature to $200\text{ }^\circ\text{C}$ at $5\text{ }^\circ\text{C min}^{-1}$.

Therefore, we suggest that the decomposition pathway for $\text{Li}[\text{BH}_3\text{NH}_2\text{BH}_2\text{NH}_3\text{BH}_3]$ could involve the release of H_2 according to equations (5.17) and (5.18). However our data suggest that reaction (5.17) does not go to completion due to the presence of $(\text{NH}_2\text{BH}_2)_n$ in Raman spectra. We suggest that reactions (1.19) and (5.20) are likely to happen since the release of $\text{B}_3\text{H}_6\text{N}_3$, NH_3 and B_2H_6 is observed in the mass spectrum (Figure 5.4-10).

Table 5.4-4 Possible decomposition pathways for Li[BH₃NH₂BH₂NH₃BH₃] (7a), according to this work. (b) and (c) are theoretical proposed reactions and calculated weight losses.

Decomposition pathway	Gas evolved (wt. %)	Ref.
(a) Li[BH ₃ NH ₂ BH ₂ NH ₃ BH ₃] (s) → LiBH ₄ (s) + 2(NH ₂ BH ₂) _n (s)	-	(5.16)
LiBH ₄ (s) + 2(NH ₂ BH ₂) _n (s) → LiBH ₄ (s) + 2(NHBH) _n (s) + 2H ₂ (g)	5.0 (H ₂) (140 °C) ^{9, 27}	(5.17)
LiBH ₄ (s) + 2(NHBH) _n (s) → LiBH ₄ (s) + 2BN (s) + 2H ₂ (g)	10.0 (H ₂) (200 °C) ^{9, 27}	(5.18)
(b) Li[BH ₃ NH ₂ BH ₂ NH ₂ BH ₃] (s) → LiBH ₄ (s) + H ₂ (g) + 1/2B ₂ H ₆ (g) + NH ₃ (g) + BN (s)	41 (this work)	(5.19)
(c) Li[BH ₃ NH ₂ BH ₂ NH ₂ BH ₃] (s) → LiBH ₄ (s) + 2/3B ₃ H ₆ N ₃ (g) + 2H ₂ (g)	73 (this work)	(5.20)

5.4.1.4 Synthesis of Li[BH₃NH₂BH₂NH₂BH₂NH₂BH₃]

In this section some experiments were performed with the aim of elongating the chain of the ammonia borane derived anion, motivated in part by the encouraging results obtained from Li[BH₃NH₂BH₂NH₂BH₃] using LiH and NH₃BH₃ in a 1 : 3 molar ratio. The amount of ammonia borane was increased in order to increase the length of the chain, a 1 : 4 LiH : NH₃BH₃ ratio was used. The same conditions used for the synthesis of samples **67** and **67a** were used for samples **68** and **68a**. The synthesis of Li[BH₃NH₂BH₂NH₂BH₂NH₂BH₃] consists of two stages: milling at room temperature and further heating at 75 °C. In the first stage hydrogen is expected to be evolved following reaction (5.11), while in the second stage, upon heating to 75 °C, ammonia would be desorbed along with formation of Li[BH₃NH₂BH₂NH₂BH₂NH₂BH₃], as reaction (5.12) shows.

The PXD pattern in Figure 5.4-13 shows the presence of two phases: NH₃BH₃ and Li[BH₃NH₂BH₂NH₂BH₃]. Increasing the amount of ammonia borane facilitates reaction (5.21) as opposed to the formation of the desired longer chain compound (5.12).



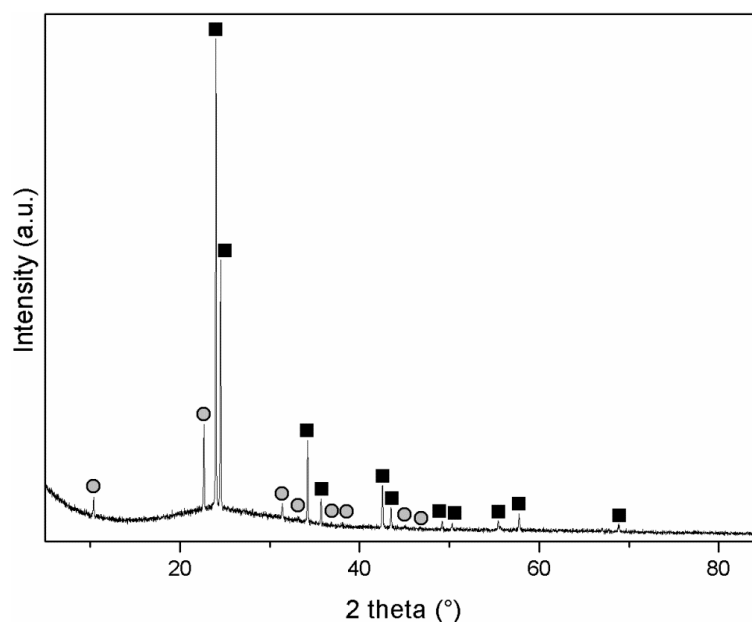


Figure 5.4-13 PXD pattern of the reaction product (68) of LiH : NH₃BH₃ (1:4) post ball milling. Grey circles represent Li[BH₃NH₂BH₂NH₂BH₃] and black squares represent NH₃BH₃.

The thermal treatment at 75 °C was attempted, however the resultant material had a gel consistency and PXD measurements were not able to be performed.

5.4.1.5 Synthesis of Li₂[BH₄]_{1-x}[NH₂BH₃]_x

Li₂[BH₄][NH₂BH₃] was successfully obtained by milling LiNH₂BH₃ and LiBH₄ following reaction (5.10) using a 1 : 2 molar ratio (Table 5.2-7). The synthesised ammonia borane compound was characterised by PXD. As shown in the PXD pattern (Figure 5.4-14) the Li₂[BH₄][NH₂BH₃] phase was synthesised with no trace of the starting material suggesting the formation of a possible amorphous component

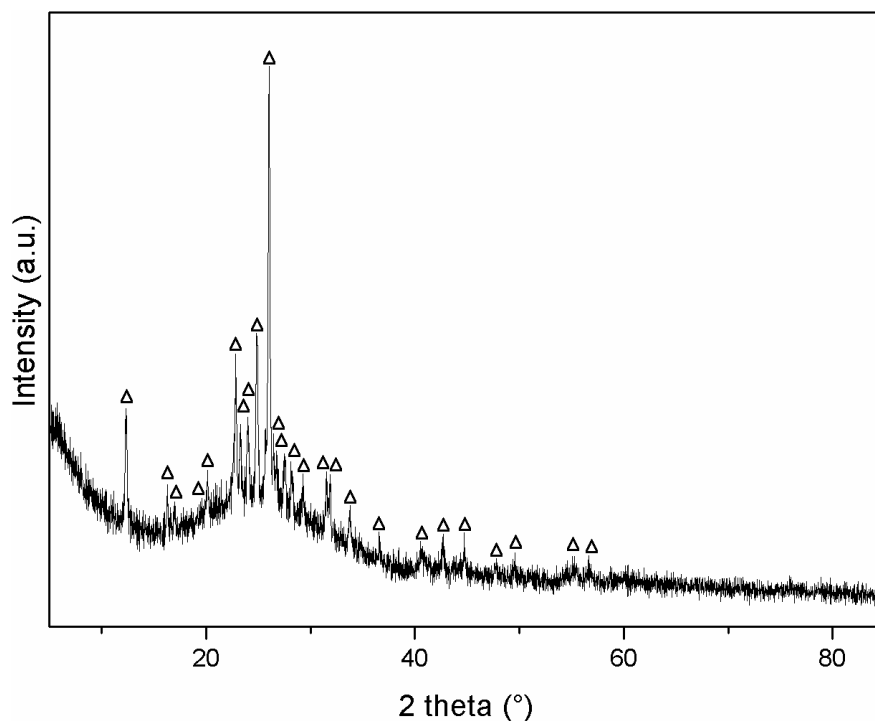


Figure 5.4-14 PXD pattern of the reaction product (70) of LiBH_4 : LiNH_2BH_3 (1:2), ball milling 2 h. White triangles represent $\text{Li}_2[\text{BH}_4][\text{NH}_2\text{BH}_3]$.

The same conditions were used for the correct reaction stoichiometry according to equation (5.10). LiBH_4 and LiNH_2BH_3 were ball milled in a 1 : 1 molar ratio in order to obtain the desired compound, $\text{Li}_2[\text{BH}_4][\text{NH}_2\text{BH}_3]$. However two different phases were observed (Figure 5.4-15). The two phases can be assigned to $\text{Li}_2[\text{BH}_4][\text{NH}_2\text{BH}_3]$ and LiBH_4 . These results confirm the possible formation of amorphous phases that cannot be characterised by PXD. Even though a single phase was obtained according to PXD as Figure 5.4-14 shows, this sample was decided not to be used for impedance measurements as it could not be confirmed which phase would be responsible for the conductivity.

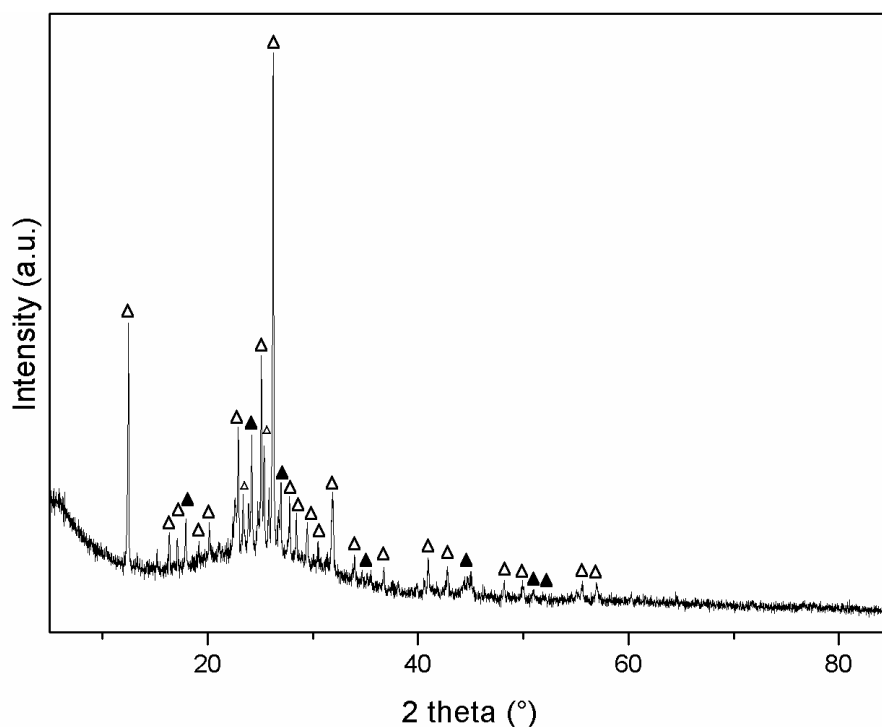


Figure 5.4-15 PXD pattern of the reaction product (69) of LiBH_4 : LiNH_2BH_3 (1:1) after ball milling for 2 h. White triangles represent $\text{Li}_2[\text{BH}_4][\text{NH}_2\text{BH}_3]$; and black triangles represent LT – LiBH_4 .

5.4.1.6 Synthesis of $\text{Li}_2[\text{BH}_4][\text{BH}_3\text{NH}_2\text{BH}_2\text{NH}_2\text{BH}_3]$

Initial attempts focused on synthesising a compound containing a combination of long chain ammonia borane derived complex anions and borohydride anions. This was done by mixing $\text{Li}[\text{BH}_3\text{NH}_2\text{BH}_2\text{NH}_2\text{BH}_3]$ (sample 67a) and LiBH_4 in a 1 : 1 molar ratio by ball milling (5.13). As shown in Figure 5.4-16, the PXD pattern of the post-milled product indicated peaks from $\text{Li}[\text{BH}_3\text{NH}_2\text{BH}_2\text{NH}_2\text{BH}_3]$ and the formation of a possible amorphous phase which cannot be characterised with PXD measurements. Future work could be performed modifying the speed, the duration, the stoichiometry of the reaction or applying heat.

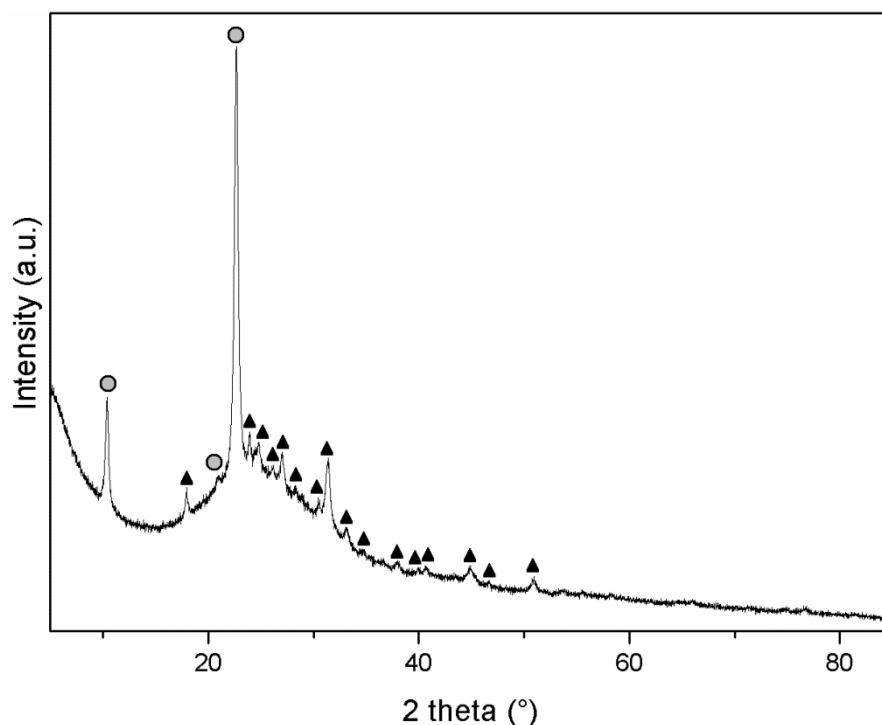


Figure 5.4-16 PXD pattern of the reaction product (71) of $\text{Li}[\text{BH}_3\text{NH}_2\text{BH}_2\text{NH}_2\text{BH}_3]: \text{LiBH}_4$ (1:1), after ball milling for 2 h. Grey spheres represent $[\text{BH}_3\text{NH}_2\text{BH}_2\text{NH}_2\text{BH}_3]$ and black triangles represent $\text{LT} - \text{LiBH}_4$.

5.4.2 $[\text{LiBH}_4][\text{NH}_3\text{BH}_3]$ system

5.4.2.1 Powder X-ray diffraction experiments

Synthesis of compositions in the $[\text{LiBH}_4][\text{NH}_3\text{BH}_3]$ system was studied using different stoichiometries of LiBH_4 and NH_3BH_3 . Table 5.2-9 shows the different mixtures investigated in this section. Sample **72** with a molar ratio of 1 : 1 (LiBH_4 : NH_3BH_3) contains three different phases (Figure 5.4-17 (c)). Two of the phases observed have already been reported in the literature. The first corresponds to a monoclinic unit cell, space group $P2_1$ (No. 4), with lattice parameters of $a = 14.3131(11) \text{ \AA}$, $b = 4.3634(5) \text{ \AA}$ and $c = 15.3500(13) \text{ \AA}$, and $\beta = 90.325(11)^\circ$. This phase was assigned to a crystal structure $\text{LiBH}_4 \cdot \text{NH}_3\text{BH}_3$ (Figure 5.4-17 (c)).⁸ In the literature it was mentioned that it was possible to isolate this phase, however it decomposes at low temperatures, 54°C and therefore it was not considered suitable as a potential electrolyte material.⁸

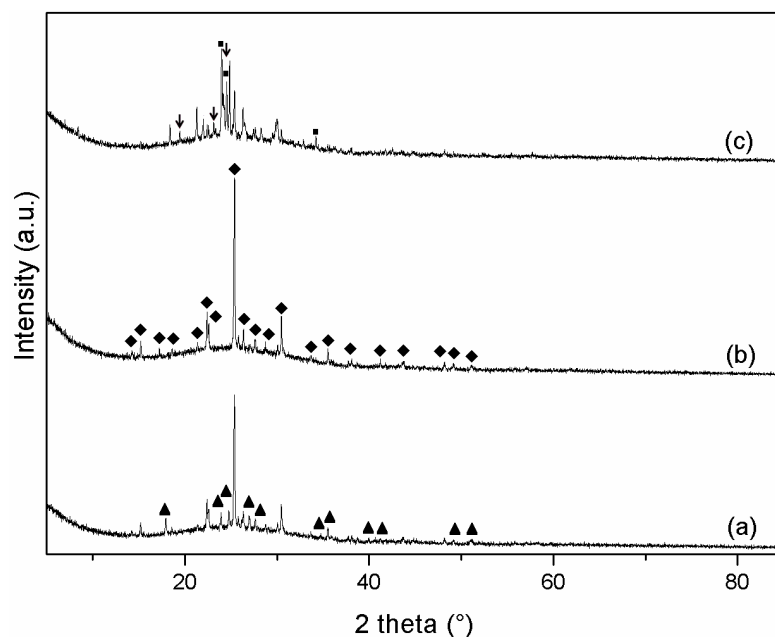


Figure 5.4-17 PXD pattern of the reaction products of $\text{LiBH}_4 : \text{NH}_3\text{BH}_3$ mixtures (a) 3:1 (74) (b) 2:1 (73) (c) 1:1 (72). Arrows represent $\text{LiBH}_4 \cdot \text{NH}_3\text{BH}_3$; black squares represent NH_3BH_3 ; black diamonds represent $\text{Li}_2[\text{BH}_4]_2[\text{NH}_3\text{BH}_3]$; and black triangles represent $\text{LT} - \text{LiBH}_4$.

More interestingly sample **73** with a 2 : 1 molar ratio ($\text{LiBH}_4 : \text{NH}_3\text{BH}_3$) formed $[\text{LiBH}_4]_2[\text{NH}_3\text{BH}_3]$ as a single phase. The PXD pattern of sample **73** is shown in Figure 5.4-18. This phase is orthorhombic and can be indexed with the space group $Pnma$ (No. 62) with $a = 8.3118(8) \text{ \AA}$, $b = 12.428(1) \text{ \AA}$ and $c = 6.5944(7) \text{ \AA}$.⁷

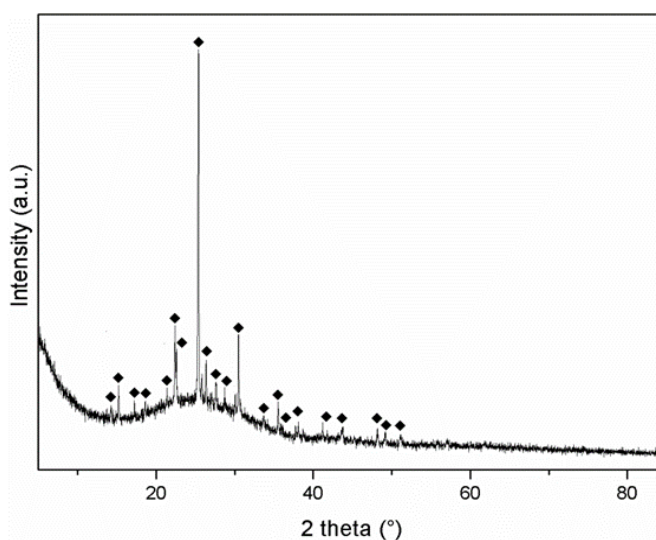


Figure 5.4-18. PXD pattern of the reaction product (73) of $\text{LiBH}_4 : \text{NH}_3\text{BH}_3$ (2:1). Black diamonds represent $\text{Li}_2[\text{BH}_4]_2[\text{NH}_3\text{BH}_3]$.

5.4.2.2 Raman spectroscopy

Raman spectroscopy is an excellent probe for the study of ammonia borane materials. Changes in the position and appearance of new modes in the Raman spectrum can, for example, indicate the presence of the NH_3BH_3 in the new compound and the formation of a new material.

Raman spectroscopic analysis was performed on sample **73** ($[\text{LiBH}_4]_2[\text{NH}_3\text{BH}_3]$) and was compared with LT - LiBH_4 and NH_3BH_3 . Typical Raman spectra of the commercial LT - LiBH_4 show various modes at *ca.* 1250 and 2300 cm^{-1} . Commercial ammonia borane shows various modes at *ca.* 800, 1250, 1600, 2300 and 3250 cm^{-1} (Table 5.4-1). Using this technique, the modes corresponding to N - H, B - H and N - B can be studied. As Figure 5.4-19 shows, the stretching bands from N - H, B - H and B - N bonds are still present in sample **73** ($[\text{LiBH}_4]_2[\text{NH}_3\text{BH}_3]$), indicated by the bending modes from N - H and B - H. This confirms that ammonia borane is still present in the crystal structure and that no decomposition has occurred during the ball milling process.

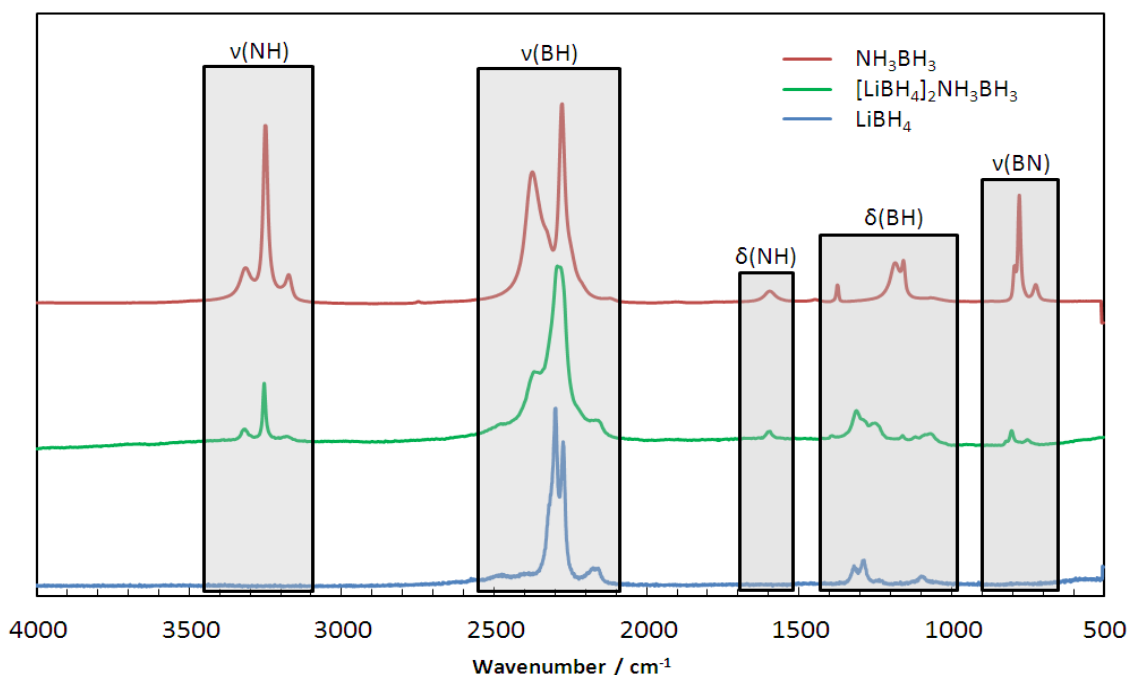


Figure 5.4-19. Raman spectra in the range 500 – 4000 cm^{-1} using a 532 nm laser of NH_3BH_3 , $[\text{LiBH}_4]_2\text{NH}_3\text{BH}_3$ (sample 73) and LiBH_4 , (ν = stretching, δ = deformation: bending and torsional modes).

5.4.2.3 Thermal analysis

The thermal stability of $[\text{LiBH}_4]_2[\text{NH}_3\text{BH}_3]$ (**73**) was measured. A summary of the thermal data are shown in Table 5.4-5.

Table 5.4-5 Summary of thermal stability analysis including data from TGA/MS analysis.

Sample	$[\text{LiBH}_4]_2[\text{NH}_3\text{BH}_3]$ (73)	$[\text{LiBH}_4]_2[\text{NH}_3\text{BH}_3]^7$
Ball milling time / h	2	2
Onset before mass loss T / °C	110	105 – 135
Phase transition LT to HT LiBH_4	111.2	*
Total weight loss / %	27.4	27
**Theor. weight loss / %	5.4	5.4
Gases evolved	$\text{H}_2, \text{NH}_3, \text{B}_3\text{H}_6\text{N}_3, \text{B}_2\text{H}_6$	$\text{H}_2, \text{NH}_3, \text{B}_3\text{H}_6\text{N}_3, \text{B}_2\text{H}_6$

* Not reported ** Assuming loss of H_2

Figure 5.4-20 shows the TG-DTA profiles for the decomposition of as-synthesised $[\text{LiBH}_4]_2[\text{NH}_3\text{BH}_3]$ (**73**). In the STA plot the weight loss is shown as a black line. The weight loss of the sample was measured under an Ar flow from room temperature to 200 °C at 5 °C min⁻¹. The thermal stability tests was carried out with a ramp heating of 5 °C min⁻¹ due to instrumental limitations. Only one report is available with the same heating rate, 5 °C min⁻¹. However the TGA and DTA experiments were performed with different heating rates (5 and 10 °C min⁻¹, respectively)⁴ which means that the decomposition events would not have occurred at the same temperatures.⁶ In the same report it was pointed out that ammonia borane forms a visible foaming caused by the formation of volatiles, presenting a general problem in the thermal decomposition of ammonia borane.⁴ Therefore, we decided to compare our results with Hu *et al.* where a simpler decomposition pathway of ammonia borane was shown such as Scheme 5.1-1.⁵

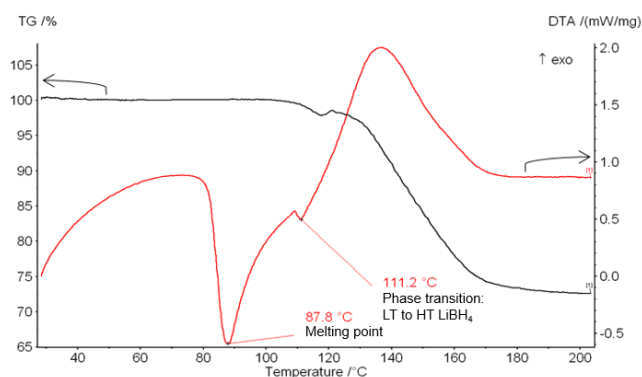


Figure 5.4-20 Typical TG-DTA plot of sample **73**. STA analysis was carried out in an Ar atmosphere, heating the sample at $5\text{ }^{\circ}\text{C min}^{-1}$ from ambient temperature to $200\text{ }^{\circ}\text{C}$. The black line represents the TG curve and the red line represents the DTA curve.

The melting point of the compound occurs at $87.8\text{ }^{\circ}\text{C}$. When the sample was heated to $111.2\text{ }^{\circ}\text{C}$, an endothermic event occurred. This was probably due to the LT HT - LiBH_4 phase transition, which is at a similar temperature to that reported for LiBH_4 itself ($110\text{ }^{\circ}\text{C}$).¹⁷ A weight loss occurred just after the phase transition which occurs within two events, at *ca.* 118 and $139\text{ }^{\circ}\text{C}$ leading to the formation of $(\text{NH}_2\text{BH}_2)_n$ and $(\text{NHBH})_n$. XRD pattern from post TG-DTA showed the formation of LT - LiBH_4 (Figure 5.4-21), suggesting that the mass loss was mainly caused by NH_3BH_3 (5.22)⁷ (Table 5.4-6). No presence of HT - LiBH_4 was observed in the PXD pattern collected for **73** after being heated to $200\text{ }^{\circ}\text{C}$ this is not unexpected since the HT LiBH_4 phase is not stable at ambient temperature, as was mentioned chapter 3.¹⁷

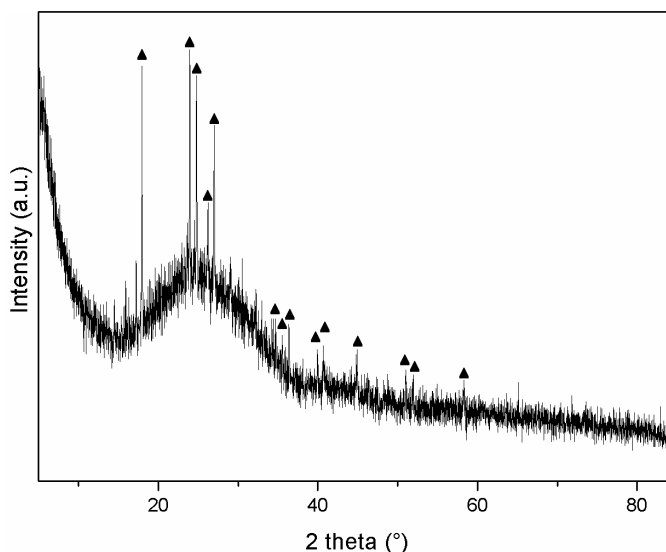


Figure 5.4-21 Post TG-DTA product after heating sample **73** under an Argon flow from room temperature to $200\text{ }^{\circ}\text{C}$ at $5\text{ }^{\circ}\text{C min}^{-1}$. Black triangles represent LT - LiBH_4 .

According to the literature, NH_3BH_3 undergoes two desorption steps at 125 °C and 155 °C and 73 decomposes apparently in two steps at 120 °C and at 133 °C.²⁸

Table 5.4-6 Decomposition pathway suggested in the literature for $[\text{LiBH}_4]_2[\text{NH}_3\text{BH}_3]$.^{9, 27}

Decomposition pathway (up to 200 °C)	Gas evolved (wt. %)	Ref.
$[\text{LiBH}_4]_2[\text{NH}_3\text{BH}_3] \text{ (s)} \rightarrow 2\text{LiBH}_4 \text{ (s)} + (\text{NH}_3\text{BH}_3) \text{ (s)}$	---	(5.22) ⁷
$\rightarrow 2\text{LiBH}_4 \text{ (s)} + (\text{NH}_2\text{BH}_2)_n \text{ (s)} + \text{H}_2 \text{ (g)}$	2.7	(5.23) ⁷
$\rightarrow 2\text{LiBH}_4 \text{ (s)} + (\text{NHBH})_n \text{ (s)} + 2\text{H}_2 \text{ (g)}$	5.4	(5.24) ⁷
or $2\text{LiBH}_4 \text{ (s)} + 1/3\text{B}_3\text{H}_6\text{N}_3 \text{ (g)} + 2\text{H}_2 \text{ (g)}$	42.7	(5.25) ⁷

$[\text{LiBH}_4]_2[\text{NH}_3\text{BH}_3]$ loses 27.4 % of mass on heating to 200 °C; MS results show that this mass loss is due to release of H_2 , $\text{B}_3\text{H}_6\text{N}_3$ and B_2H_6 and maybe also some NH_3 gas. The small weight loss at 112 °C was observed in the literature which could be due to ammonia borane decomposing into $(\text{NH}_2\text{BH}_2)_n$. All the endothermic events cannot be compared because DTA data were not reported in the literature for $[\text{LiBH}_4]_2[\text{NH}_3\text{BH}_3]$.⁷ Therefore the melting point and the phase transition temperatures cannot be compared.

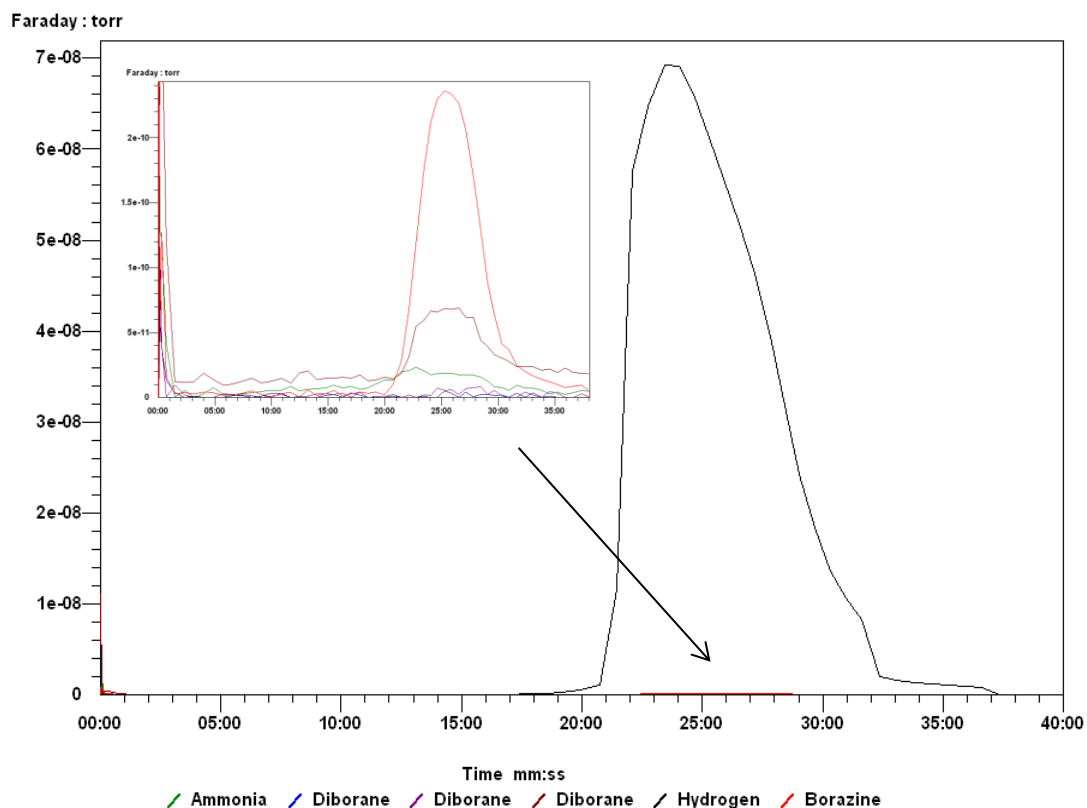


Figure 5.4-22 Typical mass spectra recorded of $[\text{LiBH}_4]_2[\text{NH}_3\text{BH}_3]$ (73) during thermal treatment. Gases monitored were: NH_3 (green); B_2H_6 (brown, blue and purple); $\text{B}_3\text{H}_6\text{N}_3$ (red); H_2 (black).

Raman spectroscopy was performed on sample **73** after the decomposition step (Figure 5.4-23). Ammonia borane decomposes into polyaminoborane $(\text{NH}_2\text{BH}_2)_n$ and polyiminoborane $(\text{NHBH})_n$, however only polyiminoborane was detected from its characteristic peak at 3434 cm^{-1} corresponding to the $\nu(\text{NH})$ mode. No peak from the $\nu(\text{NH}_2)$ mode at 3250 cm^{-1} from polyaminoborane was present.²⁸ Therefore it can be considered that the decomposition of $[\text{LiBH}_4]_2[\text{NH}_3\text{BH}_3]$ forms LT - LiBH_4 and $(\text{NHBH})_n$ releasing H_2 , NH_3 , B_2H_6 , and $\text{B}_3\text{H}_6\text{N}_3$.

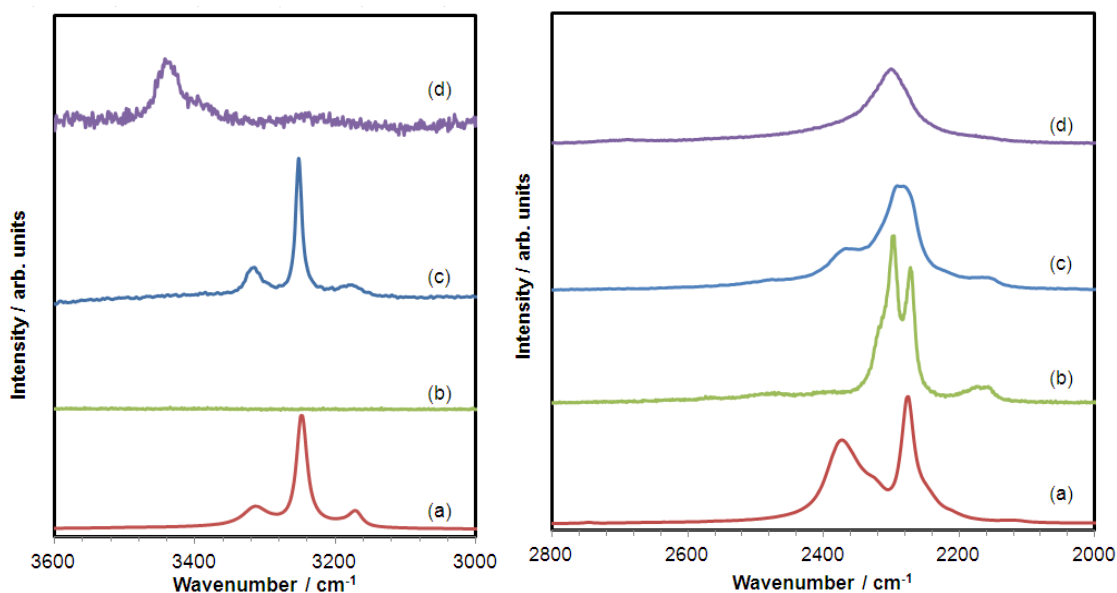


Figure 5.4-23 Raman spectra in the range of 3000 - 3600 cm^{-1} and 2000 - 2800 cm^{-1} (on the left and on the right, respectively) using a 532 nm laser of (a) NH_3BH_3 , (b) LiBH_4 , (c) $[\text{LiBH}_4]_2[\text{NH}_3\text{BH}_3]$ (sample 73), and (d) post-TGA product after heating sample 73 under an Argon flow from room temperature to 200 $^\circ\text{C}$ at 5 $^\circ\text{C min}^{-1}$.

5.4.3 $\text{LiX}' - [\text{NH}_3\text{BH}_3]$

Ammonia borane can be integrated into structures to form layered materials which could be beneficial for the ionic conductivity of lithium electrolytes. For instance, three different lithium complexes have been reported which involve the use of ammonia borane in the synthesis and crystallise with layered structures: $[\text{LiBH}_4]_2[\text{NH}_3\text{BH}_3]$ (**73**)⁸, $\text{Li}_2[\text{BH}_4][\text{NH}_2\text{BH}_3]$ ¹⁵ and $\text{Li}[\text{BH}_3\text{NH}_2\text{BH}_2\text{NH}_2\text{BH}_3]$ (**67a**)⁹. In this section two new systems will be discussed motivated by the successful synthesis of samples **67a** and **73**. Substitution of halides has been shown to improve the lithium ionic conductivity of other complex anion materials (chapter 3), therefore LiBr and LiI were chosen as halide components.

5.4.3.1 $\text{LiBr} - [\text{NH}_3\text{BH}_3]$ system

Compounds in the $\text{LiBr} - \text{NH}_3\text{BH}_3$ system were synthesised by ball milling. Different mixtures of LiBr and NH_3BH_3 were used in different molar ratios (Table 5.2-10). The PXD patterns of the post-milled mixtures show peaks that belong to two different phases, LiBr and NH_3BH_3 . No formation of other new phases was observed, indicating that reaction between LiBr and NH_3BH_3 is not favourable under these conditions (Figure 5.4-24).

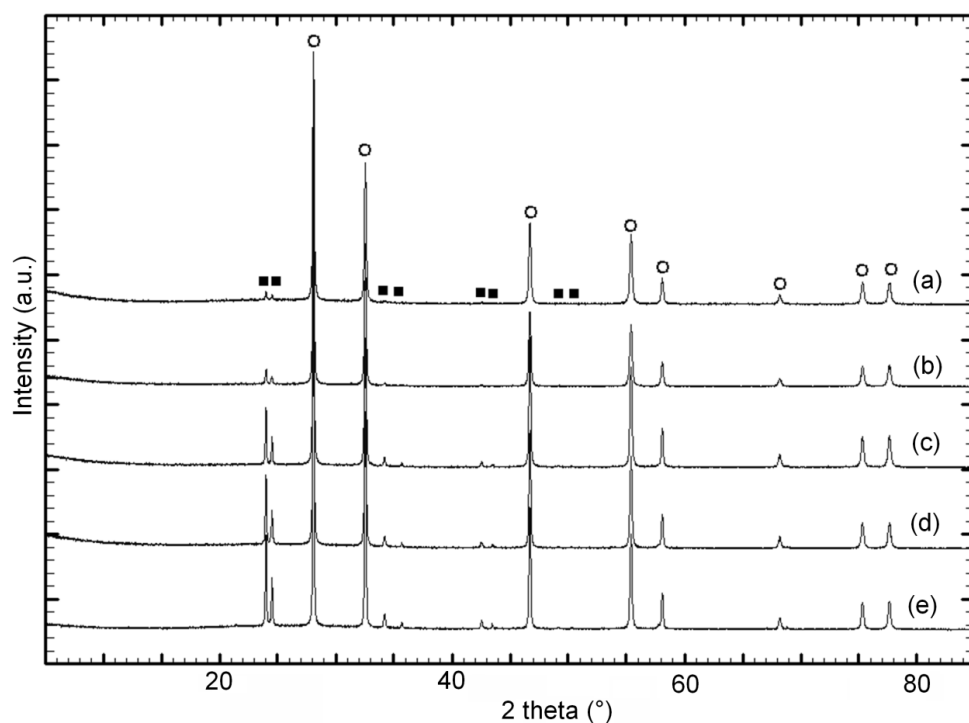


Figure 5.4-24 PXD patterns of the reaction products of LiBr : NH_3BH_3 mixtures of: (a) 2:1 (78); (b) 1:1 (79); (c) 1:2 (80); (d) 1:3 (81); and (e) 1:4 (82) ratios respectively. Black squares represent NH_3BH_3 and white circles represent LiBr.

5.4.3.2 *Lil* – [NH_3BH_3] system

5.4.3.2.1 PXRD results

The *Lil* - NH_3BH_3 system was studied as previous results had indicated that iodide substitution can drastically improve the ionic conductivity in other complex anion systems.^{30, 31} A study of the series of *Lil*- NH_3BH_3 samples found that different lithium halide ammonia borane compounds might be formed upon changing the molar ratio of the component phases (Table 5.2-11). As shown in Figure 5.4-25, mechanical milling of the mixture in 1 : 1 (sample) and 1 : 2 (sample **86**) (*Lil* : NH_3BH_3 molar ratio) produces two new different crystalline phases. To gain insight into the formation of the new phases, the phase evolution was examined as a function of reaction stoichiometry. If the molar ratio is increased to 2 : 1 (sample **83**) a cubic *Lil* phase appears. At a molar ratio of 2 : 3 (sample **85**) both the above mentioned new compounds coexist.

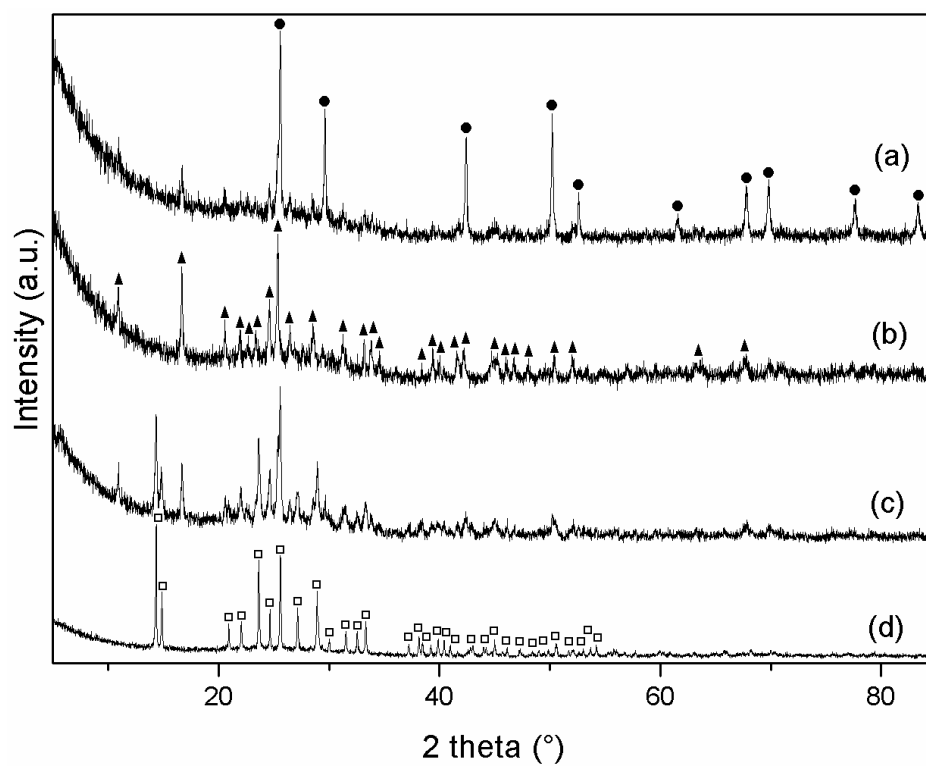


Figure 5.4-25 XRD patterns of the reaction products of LiI : NH₃BH₃ mixtures: (a) 2:1 (83); (b) 1:1 (84); (c) 2:3 (85) and (d) 1:2 (86). Black circles represent LiI; black triangles represent “[LiI][NH₃BH₃]”; and white squares represent “[LiI][NH₃BH₃]₂”.

5.4.3.2.2 Raman spectroscopy

The two samples which produced PXD patterns containing only new sets of reflections, **84** and **86**, were studied using Raman spectroscopy.

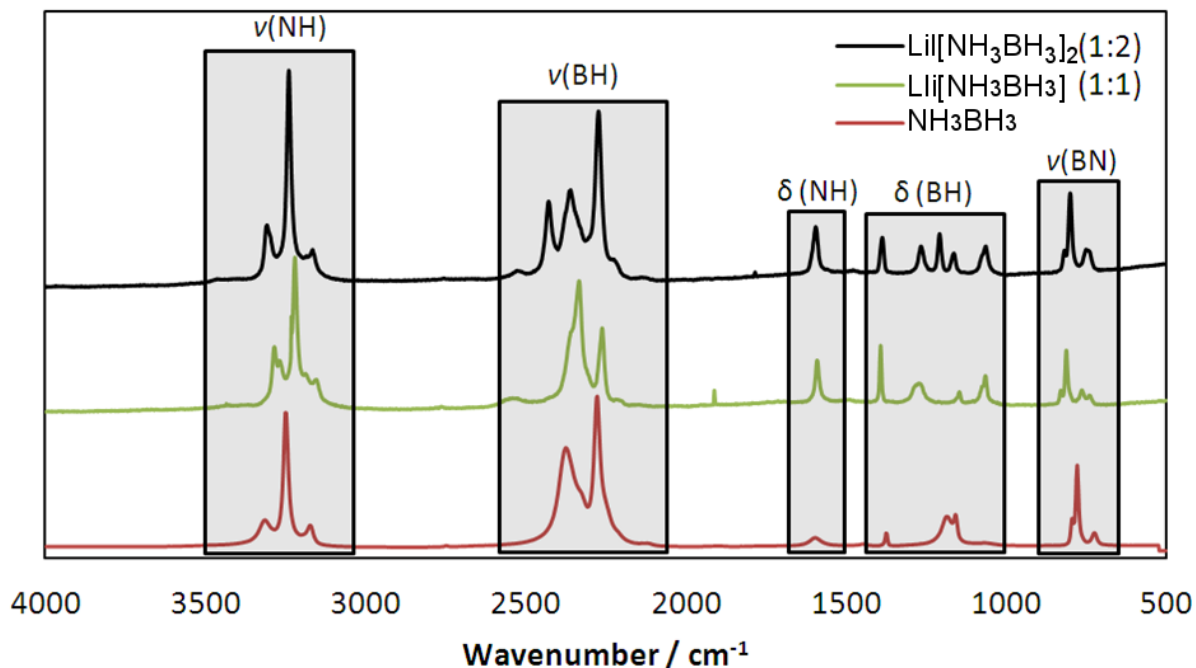


Figure 5.4-26 Raman spectra of NH_3BH_3 , $[\text{Li}][\text{NH}_3\text{BH}_3]$ (sample **84**) and $[\text{Li}][\text{NH}_3\text{BH}_3]_2$ (sample **86**) (ν = stretching, δ = deformation: bending and torsional modes).

Figure 5.4-26 shows Raman spectra of the two new compounds (**84** and **86**) compared with ammonia borane. In both samples the characteristic stretching, ν , and deformation, δ , are present. This fact confirms that ammonia borane has not undergone decomposition during the milling process. Structural analysis of both compositions will be discussed in the following sections, 5.4.3.4 and 5.4.3.5.

5.4.3.3 Thermal analysis

The thermal stability of both compositions was studied prior to possible ionic conductivity experiments. Material **84** melts at 119.5 °C and material **86** is stable up to 114.2 °C and both decompose just above their melting points (Figure 5.4-27 and Table 5.4-7).

Table 5.4-7 Summary of thermal stability analysis including data from TGA/MS analysis, XRD data and Raman spectroscopy.

Sample	[LiI][NH ₃ BH ₃] (84)	[LiI][NH ₃ BH ₃] ₂ (86)
Ball milling time / h	2	2
Formula mass	164.81	195.46
Onset before change in the DTA T / °C	115.3	108.0
Melting point	119.5	114.2
Total weight loss / %	11.92	16.40
Gases evolved	H ₂ , B ₃ H ₆ N ₃ , NH ₃ , B ₂ H ₆	H ₂ , B ₃ H ₆ N ₃ , NH ₃ , B ₂ H ₆
XRD pattern post decomposition	LiI	LiI
Raman spectra	(NH ₂ BH ₂) _n and (NHBH) _n	(NHBH) _n

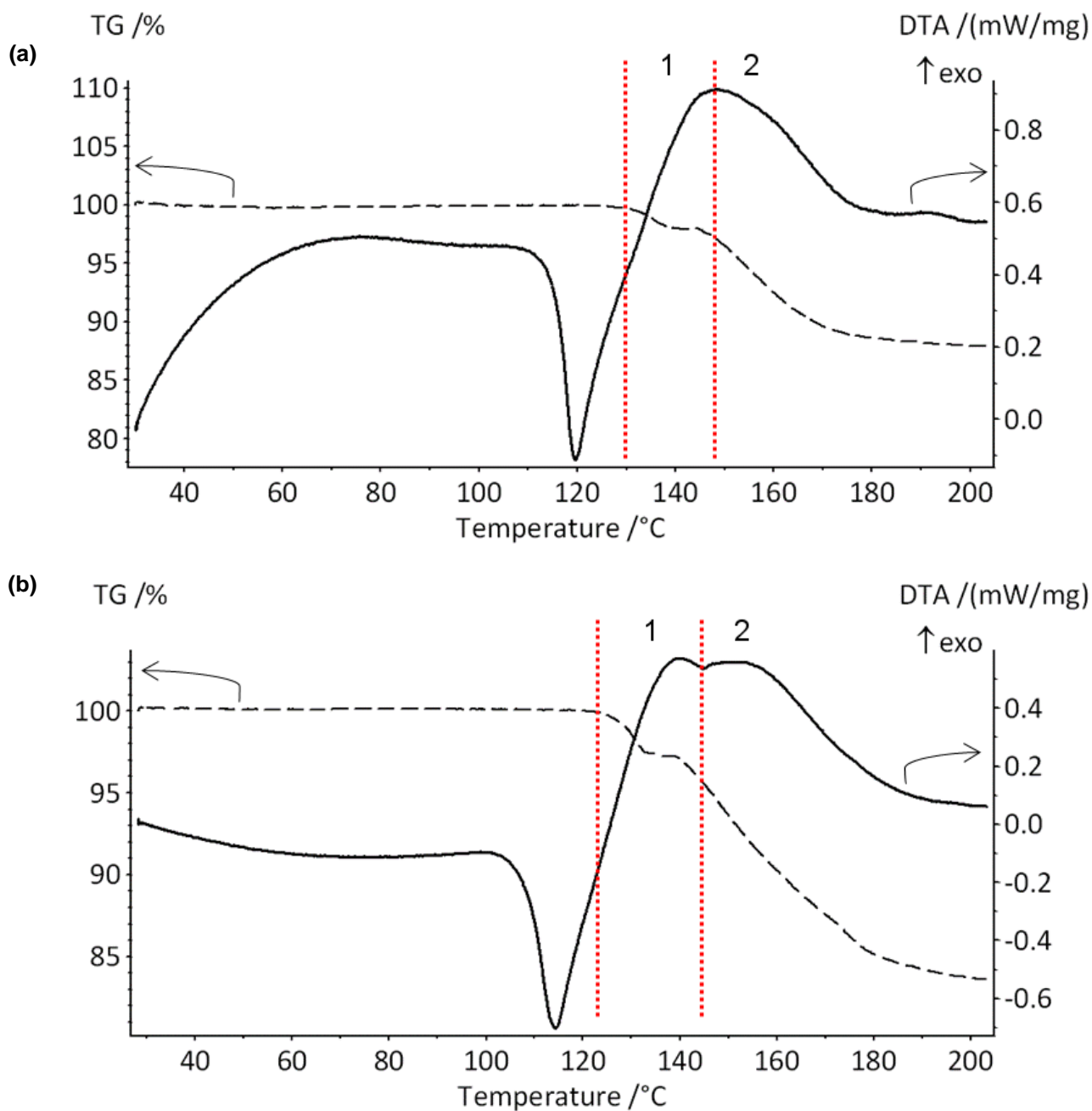


Figure 5.4-27 Typical TG-DTA profiles of samples (a) 84 and (b) 86. STA analysis was carried out in an Ar atmosphere, heating the sample at $5\text{ }^{\circ}\text{C min}^{-1}$ from ambient temperature to $200\text{ }^{\circ}\text{C}$. Straight lines represent STA curve and discontinuous lines represents TG curve.

The PXD pattern collected for **84** after the two desorption steps shows the formation of Lil (Figure 5.4-28), suggesting that both desorption steps were mainly caused by NH_3BH_3 .

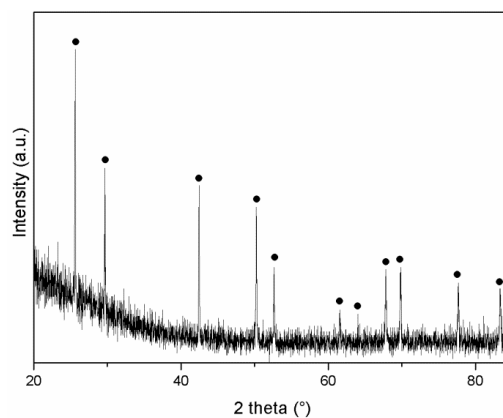


Figure 5.4-28 Post-TGA product after heating sample 84 under an Argon flow from room temperature to 200 °C at 5 °C min⁻¹. Black circles represent LiI.

NH₃BH₃ shows two desorption steps at 125 and 155 °C and **84** decomposes at 130 °C and at 148 °C which indicates the decomposition of NH₃BH₃ into (NH₂BH₂)_n and (NHBH)_n.²⁸ [LiI][NH₃BH₃] loses 11.9 wt. % upon heating to 200 °C; STA results show that this mass loss is due to the evolution of H₂, NH₃, B₃H₆N₃, and B₂H₆ (Figure 5.4-29).

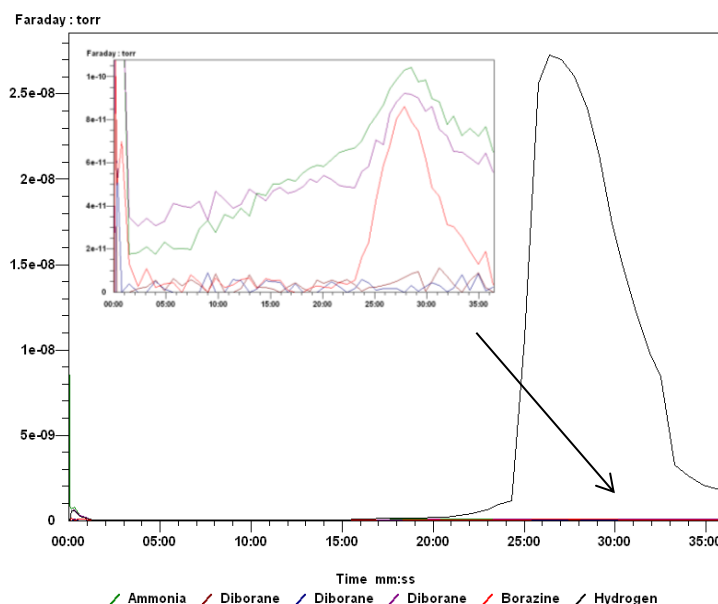


Figure 5.4-29 Typical mass spectrum recorded for [LiI][NH₃BH₃] (84**) during thermal treatment. Gases monitored were: NH₃ (green); B₂H₆ (brown, blue and purple); B₃H₆N₃ (red); H₂ (black).**

Raman spectroscopy was performed for sample **84** after the decomposition step (Figure 5.4-30). Ammonia borane decomposes into polyaminoborane (NH₂BH₂)_n and polyiminoborane (NHBH)_n and both bands corresponding to (NH₂BH₂)_n and (NHBH)_n

3434 cm^{-1} for the $\nu(\text{NH})$ mode and 3250 cm^{-1} for the $\nu(\text{NH}_2)$ mode were observed.²⁸ Therefore the decomposition of $[\text{Li}][\text{NH}_3\text{BH}_3]$ probably results in LiI , $(\text{NH}_2\text{BH}_2)_n$ and $(\text{NHBH})_n$ releasing H_2 , NH_3 , $\text{B}_3\text{H}_6\text{N}_3$, and B_2H_6 .

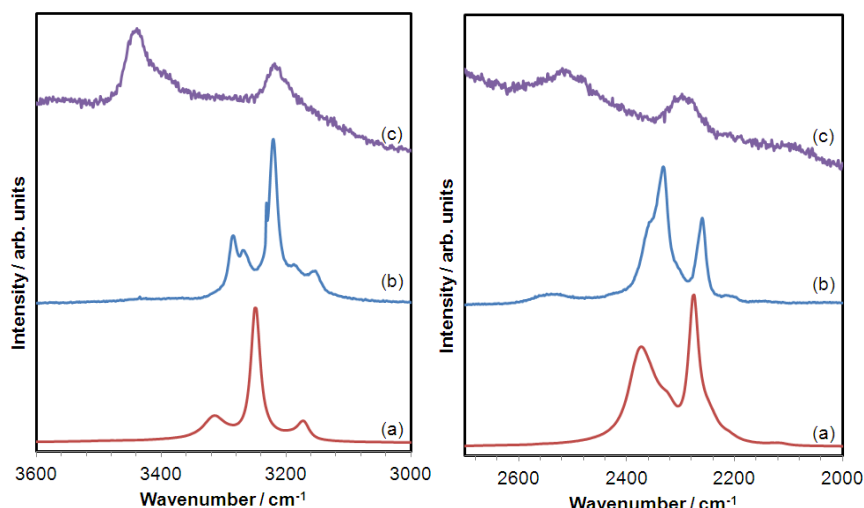


Figure 5.4-30 Raman spectra in the range of 3000 - 3600 cm^{-1} and 2000 - 2800 cm^{-1} (on the left and on the right, respectively) of (a) NH_3BH_3 , (b) $[\text{Li}][\text{NH}_3\text{BH}_3]$ (sample 84) and (c) post-TGA product after heating sample 84 under an Argon flow from room temperature to 200 $^{\circ}\text{C}$ at 5 $^{\circ}\text{C min}^{-1}$.

The PXD pattern of sample **86** indicated LiI as the only crystalline decomposition product after being heated at 200 $^{\circ}\text{C min}^{-1}$ (Figure 5.4-31).

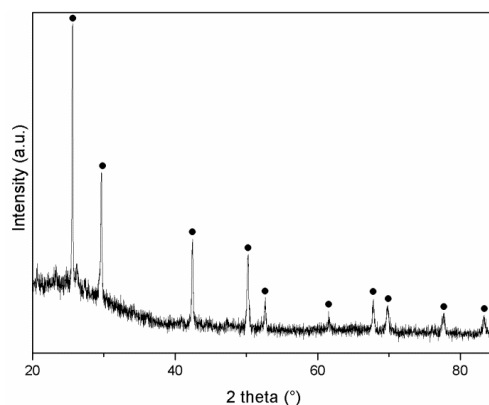


Figure 5.4-31 Post-TGA product after heating sample 86 under an Argon flow from room temperature to 200 $^{\circ}\text{C}$ at 5 $^{\circ}\text{C min}^{-1}$. Black circles represent LiI .

NH_3BH_3 shows two desorption steps at 125 and 155 $^{\circ}\text{C}$ and **86** loses mass at 108 $^{\circ}\text{C}$ which could suggest the first step of the decomposition of ammonia borane. At 143 $^{\circ}\text{C}$ another endothermic peak is observed in conjunction with a major weight loss

which could be due to the second step of the decomposition of ammonia borane.²⁸ $[\text{LiI}][\text{NH}_3\text{BH}_3]_2$ loses 16.52 % of mass on heating to 200 °C; STA results show that this mass loss is due to H_2 , $\text{B}_3\text{H}_6\text{N}_3$, B_2H_6 and NH_3 (Figure 5.4-32).

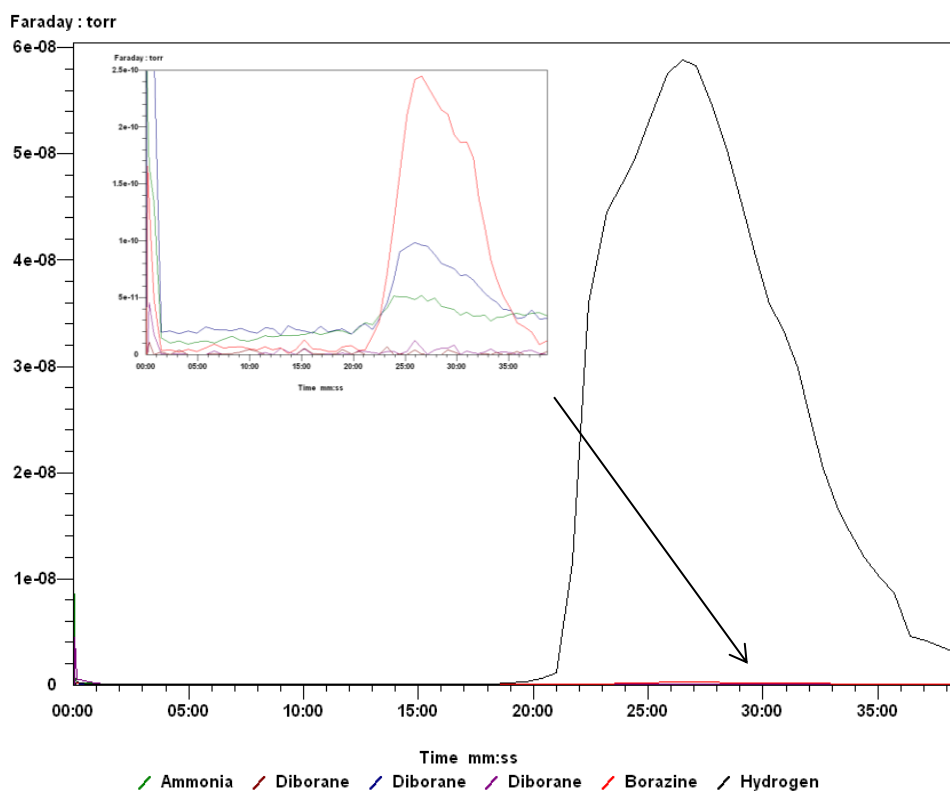


Figure 5.4-32 Typical mass spectra recorded of $[\text{LiI}][\text{NH}_3\text{BH}_3]_2$ (86) during thermal treatment. Gases monitored were: NH_3 (green); B_2H_6 (brown, blue and purple); $\text{B}_3\text{H}_6\text{N}_3$ (red); H_2 (black).

Raman spectroscopy was performed on sample **86** after the decomposition step (Figure 5.4-33). Only bands corresponding to $(\text{NHBH})_n$ were detected with its characteristic peaks at 3434 cm^{-1} from the $\nu(\text{NH})$ mode.²⁸ Therefore the likely decomposition of $[\text{LiI}][\text{NH}_3\text{BH}_3]_2$ results in LiI and $(\text{NHBH})_n$ releasing H_2 , NH_3 , $\text{B}_3\text{H}_6\text{N}_3$, and B_2H_6 .

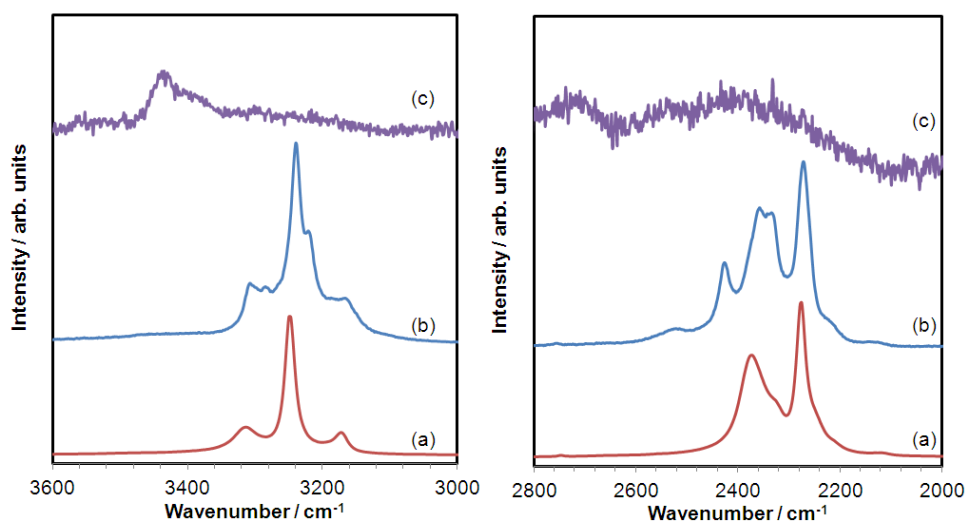


Figure 5.4-33 Raman spectra in the range of 3000 - 3600 cm^{-1} and 2000 - 2800 cm^{-1} (on the left and on the right, respectively) (a) NH_3BH_3 , (b) $[\text{LiI}][\text{NH}_3\text{BH}_3]_2$ (sample 86) and (c) post-TGA product after heating sample 86 under an Argon flow from room temperature to 200 $^\circ\text{C}$ at 5 $^\circ\text{C min}^{-1}$.

The decomposition pathway for **84**, “[LiI][NH_3BH_3]”, (Table 5.4-8 and Table 5.4-9) involves the release of H_2 probably following equations (5.30) and (5.31) however equation (5.30) is not totally completed due to the presence of $(\text{NH}_2\text{BH}_2)_n$ in the Raman spectra. Reaction (5.32) is more likely to occur than (5.33) since the observed release of NH_3 and B_2H_6 is greater than that of $\text{B}_3\text{H}_6\text{N}_3$.

The decomposition pathway for **86**, “[LiI][NH_3BH_3] $_2$ ”, (Table 5.4-8 and Table 5.4-10) appears to follow equations (5.34) and (5.35) with release of H_2 . Due to the absence of $(\text{NH}_2\text{BH}_2)_n$ in Raman spectra, reaction (5.35) could totally be finished forming $(\text{NHBH})_n$. Reaction (5.37) is more likely to happen than (5.36) since the observed as release of $\text{B}_3\text{H}_6\text{N}_3$ appears to be greater than NH_3 and B_2H_6 .

The mass loss of sample **86** “[LiI][NH_3BH_3] $_2$ ” more substantial than that for **84** (“[LiI][NH_3BH_3]”) due to the apparent total decomposition of NH_3BH_3 into H_2 and the higher amount of ammonia borane in the compound. Decomposition of NH_3BH_3 into either $\text{B}_3\text{H}_6\text{N}_3$ or NH_3 and B_2H_6 cannot be distinguished from the mass loss because both reaction pathways provide the same wt. % (equations (5.28) and (5.29)). A deeper study could potentially be carried out to determine the wt. % evolved of each gas, however the principal purpose of this study was to determine the thermal stability of both materials (**84** and **86**) and to assess their suitability for the measurement of the ionic conductivity at high temperature.

Table 5.4-8 Possible decomposition pathways for NH₃BH₃.

Decomposition pathway	Gas evolved (wt. %)	Equation number
(a) NH ₃ BH ₃ (s) → 1/2(NH ₂ BH ₂) _n (s) + H ₂ (g)	6.4 (H ₂)	(5.26)
(NH ₂ BH ₂) _n (s) → (NHBH) _n (s) + H ₂ (g)	13 (H ₂)	(5.27)
(b) NH ₃ BH ₃ (s) → 1/2B ₂ H ₆ (g) + NH ₃ (g)	100	(5.28)
(c) NH ₃ BH ₃ (s) → 1/3B ₃ H ₆ N ₃ (g) + 2H ₂ (g)	100	(5.29)

Table 5.4-9 Possible decomposition pathways for [LiI][NH₃BH₃] (84).

Decomposition pathway	Gas evolved (wt. %)	Equation number
(a) [LiI][NH ₃ BH ₃] (s) → LiI _(s) + 1/2(NH ₂ BH ₂) _n (s) + H ₂ (g)	1.2 (H ₂)	(5.30)
LiI _(s) + (NH ₂ BH ₂) _n (s) → (NHBH) _n (s) + H ₂ (g)	4.2 (H ₂)	(5.31)
(b) [LiI][NH ₃ BH ₃] (s) → LiI (s) + 1/2B ₂ H ₆ (g) + NH ₃ (g)	18.7	(5.32)
(c) [LiI][NH ₃ BH ₃] (s) → LiI (s) + 1/3B ₃ H ₆ N ₃ (g) + 2H ₂ (g)	18.7	(5.33)

Table 5.4-10 Possible decomposition pathways for [LiI][NH₃BH₃]₂ (86).

Decomposition pathway	Gas evolved (wt. %)	Equation number
(a) [LiI][NH ₃ BH ₃] ₂ (s) → LiI (s) + 2(NH ₂ BH ₂) _n (s) + 2H ₂ (g)	2.0 (H ₂)	(5.34)
LiI _(s) + 2(NH ₂ BH ₂) _n (s) → LiI (s) + 2(NHBH) _n (s) + 2H ₂ (g)	4.1 (H ₂)	(5.35)
(b) [LiI][NH ₃ BH ₃] ₂ (s) → LiI (s) + B ₂ H ₆ (g) + 2NH ₃ (g)	37.4	(5.36)
(c) [LiI][NH ₃ BH ₃] ₂ (s) → LiI (s) + 2/3B ₃ H ₆ N ₃ (g) + 4H ₂ (g)	37.4	(5.37)

5.4.3.4 Structural Analysis

5.4.3.4.1 [LiI][NH₃BH₃]

The structural analysis for [LiI][NH₃BH₃]₂ was performed using Jana2006.²⁴ 50 peaks were used to find the right structure. Powder X-ray diffraction characterisation of [LiI][NH₃BH₃] (**84**) (synthesised *via* mechanochemical reaction of a mixture of LiI and NH₃BH₃ in stoichiometric quantities) suggests the formation of a monoclinic phase at room temperature (space group *P2*₁/*c*1, #14). This space group has a total of four

symmetry operators: a two-fold screw axis parallel to the monoclinic b -axis through the point $(0, 0, \frac{1}{4})$, an inversion centre in the origin, and a c -glide with translation vector $[0\ 0\ \frac{1}{2}]$ parallel to the x - z plane through the point with coordinates $(0, \frac{1}{4}, 0)$. Unit cell parameters are $a = 4.3897(1)$, $b = 16.1663(2)$, $c = 7.1536(1)$ Å and $\beta = 101.52(1)^\circ$. Selected Rietveld refinement data of $[\text{LiI}][\text{NH}_3\text{BH}_3]$ (**84**) are displayed in Table 5.4-11 and Table 4.3-8 and the observed, calculated and difference (OCD) plots for refinement is illustrated in Figure 5.4-34. As observed in the OCD plot, the experimental data fit well to the theoretical model.

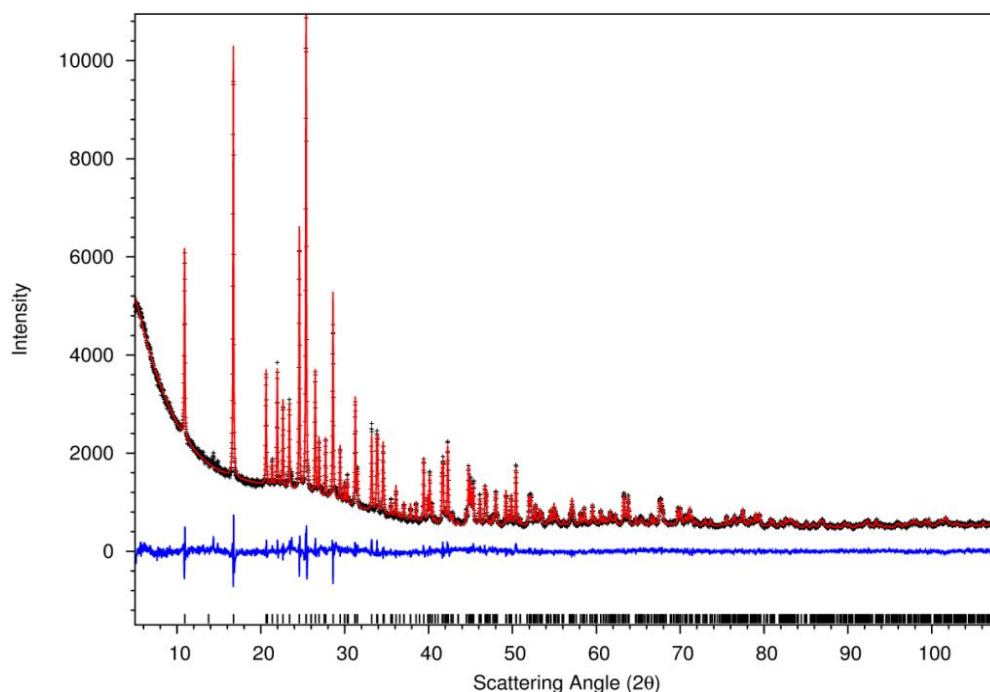


Figure 5.4-34 Profile plot from the Rietveld Refinement against X-ray powder diffraction data for (a) (black crosses: experimental profile; red line: calculated profile; blue line: difference profile; tick marks: Bragg reflections for the $[\text{LiI}][\text{NH}_3\text{BH}_3]$).

In our model the structure of compound **84** consists of single pseudo-layers of NH_3BH_3 and LiI (Figure 5.4-35). Firstly, the iodide ions were localised in the structure using the data from the observed Fourier map. Iodide ions have a high scattering factor because of the large size of the electron cloud making facile to locate the ions. Compound **84** has well defined N and B positions determined by Fourier maps. The refined B - N bond distances for **84** was $1.598(1)$ Å. This value correlates well with the bond lengths in NH_3BH_3 itself (with B - N distances of $1.5974(3)$ Å),³ however the X-ray scattering is inevitably dominated by the relatively heavy iodine anions.

Thermal factors from hydrogens bonded to nitrogen and boron needed to be fixed. Given the presence of multiple light scatterers: lithium, boron and nitrogen (and hydrogen), the location of lithium and a definitive crystal structure could not be determined accurately using lab X-ray data. The far superior intensity of synchrotron radiation however should allow us to confirm our proposed structures and map any occupational or positional disorder in the ammonia borane complex. Therefore, experiments on I11 at Diamond for the collection of high resolution data were performed to obtain more reliable models derived from PXD structure refinements (section 5.4.3.5.1).

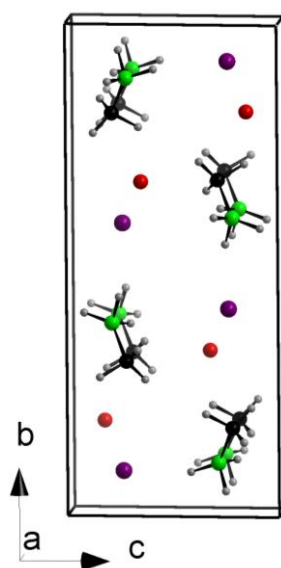


Figure 5.4-35 Crystal structure of [LiI][NH₃BH₃] (84). Lithium, iodide, nitrogen, boron and hydrogens are represented as red, purple, green, black and grey spheres, respectively.

Table 5.4-11 Selected Rietveld refinement data from PXD data of the [Li][NH₃BH₃] (84) compound at 292 K.

Sample number	84
Empirical formula	[Li][NH ₃ BH ₃]
Collection temperature / K	292
Crystal system	Monoclinic
Space group	<i>P</i> 2 ₁ / <i>c</i> 1
Z	4
Unit cell formula weight, <i>M_w</i>	658.8
Calculated density, ρ / g cm⁻³	2.199
Unit cell dimensions:	
<i>a</i> / Å	4.3897(1)
<i>b</i> / Å	16.1663(2)
<i>c</i> / Å	7.1536(1)
β / °	101.52(1)
<i>V</i> / Å³	497.43(12)
Observations, parameters	6059, 82
R_{wp}	4.17
R_p	3.11
χ²	1.35

Table 5.4-12. Atom positions and isotropic temperature factors obtained from Rietveld refinement against PXD data of the [LiI][NH₃BH₃] compound at 292 K (84).

Atom	Site	x	y	z	100 x <i>U</i> _{iso} / Å
Li	4e	0.874(8)	0.316(2)	0.607(5)	1.4(13)
I	4e	0.40954(8)	0.41233(8)	0.7515(2)	0.93(5)
N	4e	0.070(3)	0.3886(8)	0.219(3)	2.4(5)
B	4e	0.857(5)	0.317(1)	0.280(3)	1.1(7)
H1B	4e	0.7505	0.2866	0.1642	1.33
H2B	4e	0.9892	0.2783	0.3700	1.33
H3B	4e	0.6971	0.3427	0.3448	1.33
H1N	4e	0.2529	0.3872	0.2936	2.94
H2N	4e	0.0884	0.3810	0.1018	2.94
H3N	4e	0.9841	0.4366	0.2296	2.94

5.4.3.4.2 [LiI][NH₃BH₃]₂

The structural analysis for [LiI][NH₃BH₃]₂ was performed using Jana2006.²⁴ Different possible structures were obtained from the cell candidates (Table 5.4-13). 66 peaks were used to find the right structure. No. 2 was selected because it is the double of parameter *c* in No. 1, since No. 1 considers two unit cells instead of the primitive one. Refining the structure with Jana2006 gave two different options for the correct symmetry, either trigonal or monoclinic. A monoclinic structure was selected as the option of higher symmetry. The possible space groups were *C2/m*, *Cm* or *C2* (Figure 5.4-36).

Table 5.4-13 Cell candidates for [LiI][NH₃BH₃]₂ (86).

No.	<i>a</i> / Å	<i>b</i> / Å	<i>c</i> / Å	β / °	<i>V</i> / Å ³	Indexing method	FOM
1	12.3812	7.2125	8.8296	106.17	757.29	Treor	16.0
2	11.9293	7.2114	4.4137	94.60	378.48	lto	209.7
3	11.9296	7.2114	4.4138	94.60	378.47	lto	100.8
4	11.9309	7.2115	4.4139	94.59	378.55	lto	94.8
5	11.9310	7.2115	4.4136	94.59	378.56	lto	94.7

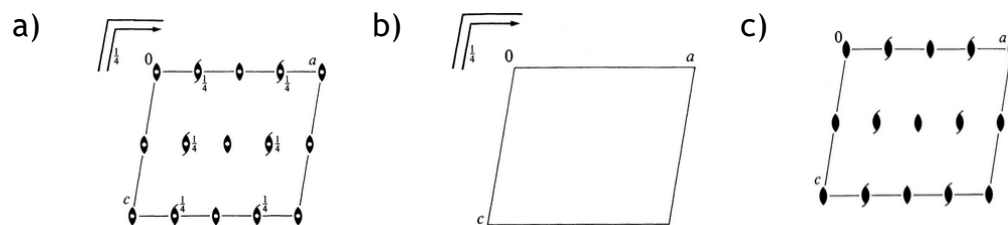


Figure 5.4-36 Possible space groups for $[\text{LiI}][\text{NH}_3\text{BH}_3]_2$ a) $C2/m$, b) Cm and c) $C2$.³²

If $C2/m$ was the correct space group it would produce a mirror plane in the plane (020) (Figure 5.4-37). Residual electron density in the difference Fourier map could suggest three atoms located in the mirror plane. However if iodine atoms are located on $(0, 0, \frac{1}{2})$ sites (purple spheres), then ammonia borane molecules should be located in the centre meaning that $C2/m$ could not be the correct space group (Figure 5.4-38).

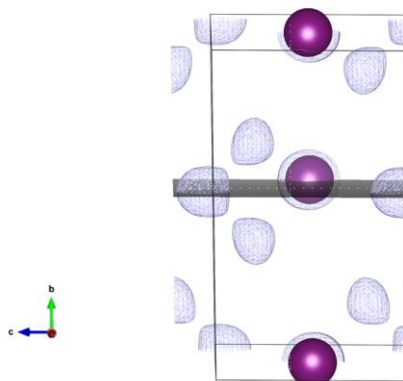


Figure 5.4-37. $C2/m$, only half of the cell is represented with a mirror plane at (020), iodine atoms are shown in purple and residual electron density is in light blue.

When the atoms are located in their correct sites, it is possible to observe that the mirror plane cannot exist, as the ammonia borane is not symmetric, confirming that $C2$ symmetry is a better choice than $C2/m$. From the high U_{iso} values observed for N and B, positive and negative respectively, the atom positions were exchanged to produce a better fit.

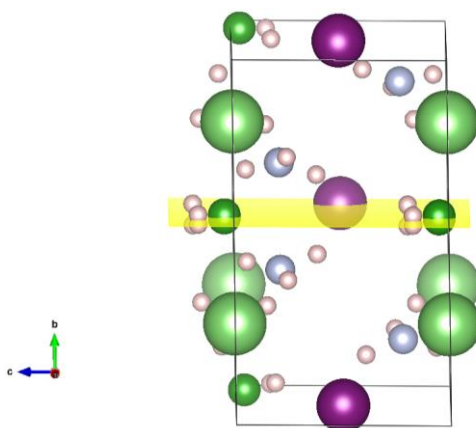


Figure 5.4-38. Hypothetical $C2/m$ symmetry model with the mirror plane represented in yellow. Lithium, iodide, nitrogen, boron and hydrogens are represented as green (large spheres), purple, dark green (small spheres), and light blue and white spheres, respectively.

N and B atoms were located where the light purple and the green spheres are indicated in Figure 5.4-38, respectively. Finally $C2$ was chosen as the correct symmetry. Afterwards H atoms were located in the appropriate geometries around the B and N atoms. The final structure was refined. As shown in Figure 5.4-39, there is no mirror plane in (020).

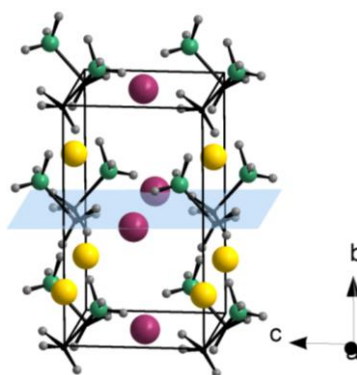


Figure 5.4-39. Crystal structure of $[LiI][NH_3BH_3]_2$ (**86**) as refined in space group $C2$. Lithium, iodide, nitrogen, boron and hydrogens are represented as yellow, purple, green, black and grey spheres, respectively.

The lattice parameters of the monoclinic unit cell are $a = 12.3850(2)$, $b = 7.2113(3)$, $c = 4.4134(1)$ Å and $\beta = 106.22(0)^\circ$. Selected Rietveld refinement data of $[LiI][NH_3BH_3]_2$ (**86**) are displayed in Table 5.4-14 and Table 5.4-15, and the observed, calculated, and difference (OCD) plot for the refinement is illustrated in Figure 5.4-40.

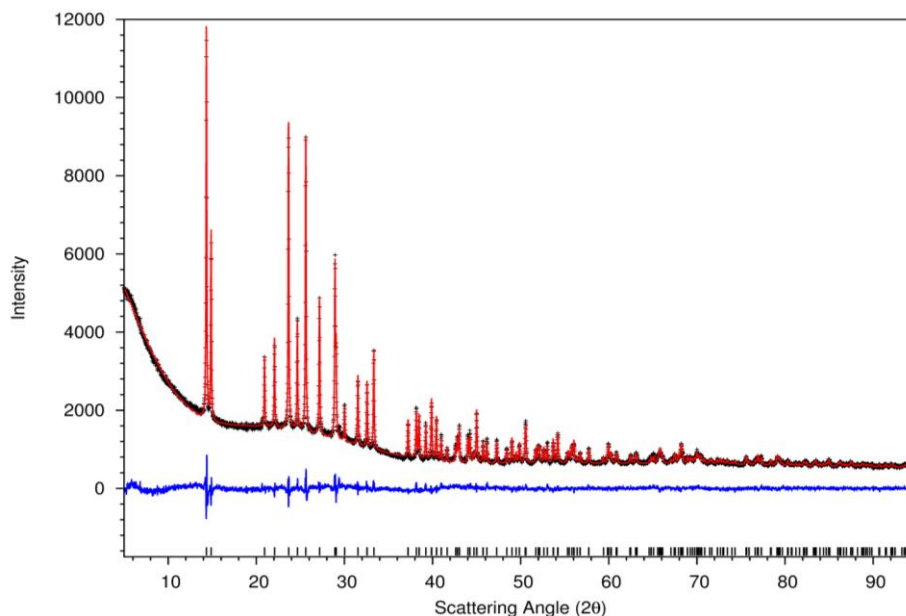


Figure 5.4-40 Profile plot from the Rietveld refinement against X-ray powder diffraction data for $[\text{LiI}][\text{NH}_3\text{BH}_3]_2$ (**86**) (black crosses: experimental profile; red line: calculated profile; blue line: difference profile; tick marks: Bragg reflections for the $[\text{LiI}][\text{NH}_3\text{BH}_3]_2$).

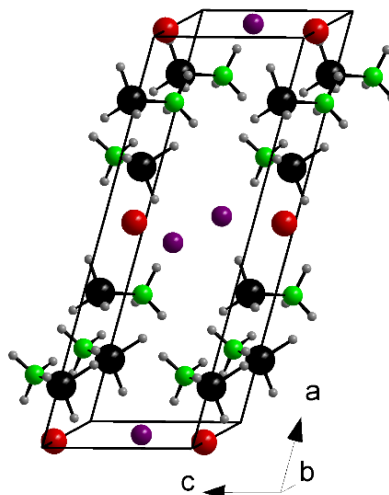


Figure 5.4-41 Crystal structure of $[\text{LiI}][\text{NH}_3\text{BH}_3]_2$ (**86**). Lithium, iodide, nitrogen, boron and hydrogens are represented as red, purple, green, black and grey spheres, respectively.

In our model, the structure of compound $[\text{LiI}][\text{NH}_3\text{BH}_3]_2$ (**86**) comprises single LiI layers separated by double layers of NH_3BH_3 (Figure 5.4-41). Compound **86** has well defined N and B positions determined by Fourier maps. B - N bonding distance for **86** was 1.596(4) Å, which correlates well with the value in NH_3BH_3 itself (with B - N distances of 1.5974(3) Å).³ However the X-ray scattering is inevitably dominated by the relatively heavy iodine anions. Given again the presence of multiple light

scatterers: lithium, boron and nitrogen (and hydrogen), the location of lithium and a definitive crystal structure cannot be determined accurately using lab X-ray data. Thermal factors from hydrogens bonded to nitrogen and boron needed to be fixed. High resolution data experiments on I11 were performed in order to obtain complete models derived from PXD structure refinements (section 5.4.3.5.2).

Table 5.4-14 Selected Rietveld refinement data from PXD data of the [Li][NH₃BH₃]₂ (86) compound at 292 K.

Sample number	86
Empirical formula	[Li][NH ₃ BH ₃] ₂
Collection temperature / K	292
Crystal system	Monoclinic
Space group	C2
Z	2
Unit cell formula weight, <i>M_w</i>	391.2
Calculated density, ρ / g cm⁻³	1.7152
Unit cell dimensions:	
<i>a</i> / Å	12.3850(2)
<i>b</i> / Å	7.2113(2)
<i>c</i> / Å	4.4134(1)
β / °	106.22(0)
<i>V</i> / Å ³	378.11(14)
Observations, parameters	5295, 38
R_{wp}	3.72
R_p	2.86
χ²	1.31

Table 5.4-15. Atom positions and isotropic temperature factors obtained from Rietveld refinement against PXD data for [LiI][NH₃BH₃]₂ compound at 292 K (86).

Atom	Site	x	y	z	100 x U_{iso} / Å ²
Li	2a	0	0.277(5)	0	2.6(15)
I	2b	0.5	0.0	0.5	1.56(7)
N	4c	0.169(1)	0.1469(8)	0.216(2)	2.4(4)
B	4c	0.846(1)	0.996(2)	0.042(3)	3.2(5)
H1B	4c	0.799813	0.028923	0.187551	3.88
H2B	4c	0.819800	0.873439	0.939763	3.88
H3B	4c	0.926701	0.986627	0.163799	3.88
H1N	4c	0.193632	0.248242	0.152403	2.82
H2N	4c	0.104152	0.168496	0.251013	2.82
H3N	4c	0.216451	0.108844	0.389197	2.82

5.4.3.5 High-resolution synchrotron diffraction at 292 K

5.4.3.5.1 [LiI][NH₃BH₃]

The high-resolution synchrotron diffraction data from compound **84** indicates that the powder was well crystallised, however two other phases were observed, NH₄I and [LiI][NH₃BH₃]₂ (Figure 5.4-42), which were not observed in the laboratory XRD data. This could be due to the fact that the compound partially decomposed under the beam.

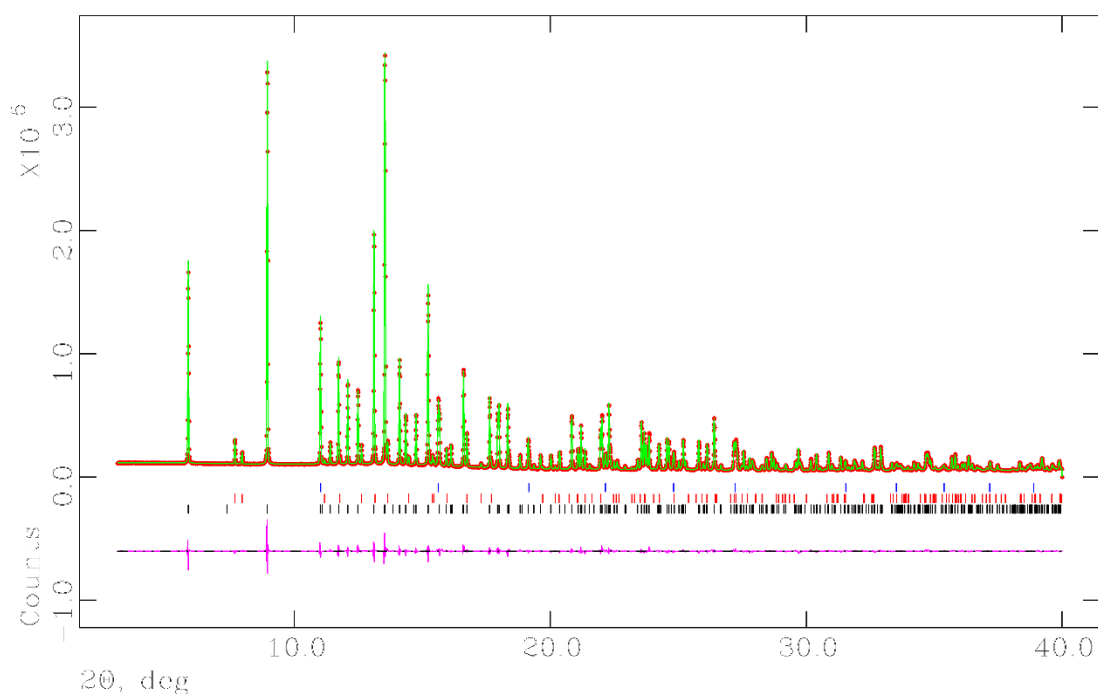


Figure 5.4-42 Plot for 24 from the Rietveld refinement against high-resolution synchrotron diffraction data (red dots: experimental profile; green line: calculated profile; pink line: difference profile; tick marks: Bragg reflections for the NH_4I (top), $[\text{LiI}][\text{NH}_3\text{BH}_3]_2$ (middle) and $[\text{LiI}][\text{NH}_3\text{BH}_3]$ (bottom)).

The structural model was fully refined against the synchrotron data starting from the structural model obtained from laboratory X-ray powder diffraction, in the space group $P12_1/c1$ and the respective data are presented in Table 5.4-16 - Table 5.4-19. Firstly, the iodide ions were localised and confirmed with Fourier observed map calculations. Then B and N were allocated in their respective sites and the positions were refined. Lastly, the position of Li ions was refined. At this stage isotropic temperature factors were used for all the atoms apart from hydrogen. Given the low scattering factor of light atoms such as hydrogen, the thermal factors were maintained constant. The final model is shown in Figure 5.4-43. The χ^2 obtained was unexpectedly large (Table 5.4-16). The structure contains one Li one I, B and N bonded to three H atoms, respectively, all on general positions $4e$. The average of the B-N distances is $1.574(6)$ Å, and the average of the H-B-N and H-N-B angles in the tetrahedron are 109.2° and 109.1° , respectively (Table 5.4-19). The synchrotron powder diffraction data obtained on I11 were of high quality. If there is a slight difference between the observed and the calculated data this gives high χ^2 values.

However if the patterns obtained have worse quality and more noise, lower χ^2 values can be expected. The same issue was experienced with sample **84**.

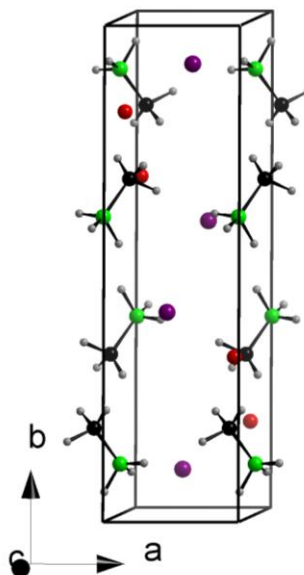


Figure 5.4-43 Crystal structure of $[\text{LiI}][\text{NH}_3\text{BH}_3]$ (**84**). Lithium, iodide, nitrogen, boron and hydrogens are represented as red, purple, green, black and grey spheres, respectively.

Table 5.4-16 Selected Rietveld refinement data from synchrotron powder diffraction data of the compound [LiI][NH₃BH₃] at 292 K (84).

Sample number	84
Empirical formula	[LiI][NH ₃ BH ₃]
Collection temperature / K	292
Crystal system	Monoclinic
Space group	<i>P</i> 12 ₁ / <i>c</i> 1
Z	4
Unit cell formula weight, <i>M_w</i>	658.84
Calculated density, ρ / g cm⁻³	2.197
Phase fractions / %	
[LiI][NH₃BH₃]	73.8
[LiI][NH₃BH₃]₂	7.0
NH₄I	19.2
Unit cell dimensions:	
<i>a</i> / Å	4.39139(1)
<i>b</i> / Å	16.17289(5)
<i>c</i> / Å	7.15684(2)
β / °	101.524(0)
<i>V</i> / Å³	498.043(3)
Observations, parameters	450, 82
R_{wp}	0.0343
R_p	0.0238
χ²	14.39

Table 5.4-17. Atom positions and isotropic temperature factors obtained from Rietveld refinement against synchrotron powder diffraction data for the [LiI][NH₃BH₃] compound at 292 K (84).

Atom	Site	x	y	z	100 x <i>U</i> _{iso} / Å ²
Li	4e	0.883(2)	0.3231(6)	0.649(1)	2.6(3)
I	4e	0.40882(9)	0.41515(2)	0.75230(6)	3.29(2)
N	4e	0.0568(9)	0.3935(2)	0.2132(7)	2.7(2)
B	4e	0.880(2)	0.3171(3)	0.285(1)	2.6(4)
H1B	4e	0.7505	0.2866	0.1642	1.33
H2B	4e	0.9892	0.2783	0.3700	1.33
H3B	4e	0.6971	0.3427	0.3448	1.33
H1N	4e	0.9500	0.3872	0.2935	2.94
H2N	4e	0.1083	0.4110	0.0800	2.94
H3N	4e	0.9500	0.4466	0.2496	2.94

Table 5.4-18 Selected bond lengths [LiI][NH₃BH₃] (84) from high-resolution synchrotron diffraction data at 292 K.

Bond length / Å		Bond length / Å	
B – N	1.574(6) x 1	B – Li	2.454(10) x 1
B – H1B	1.060(7) x 1	N – H1N	0.939(4) x 1
B – H2B	0.933(7) x 1	N – H2N	1.067(4) x 1
B – H3B	1.067(6) x 1	N – H3N	1.065(4) x 1
B – Li	2.602(12) x 1		

Table 5.4-19 Selected angles [Li][NH₃BH₃] (84) from high-resolution synchrotron diffraction data at 292 K.

	Bond angle / °		Bond angle / °
H1B – B – H2B	109.9(5)	H1N – N – H2N	103.80(34)
H1B – B – H3B	100.4(6)	H1N – N – H3N	107.6(6)
H2B – B – H3B	109.4(7)	H2N – N – H3N	98.91(30)
H1B – B – N	107.7(5)	H1N – N – B	101.0(4)
H2B – B – N	120.4(6)	H2N – N – B	136.6(4)
H3B – B – N	107.4(1)	H3N – N – B	106.7(4)

5.4.3.5.2 [Li][NH₃BH₃]₂

The high-resolution synchrotron diffraction data from compound **86** indicates that the powder was pure and well crystallised (Figure 5.4-44). Only one phase was observed.

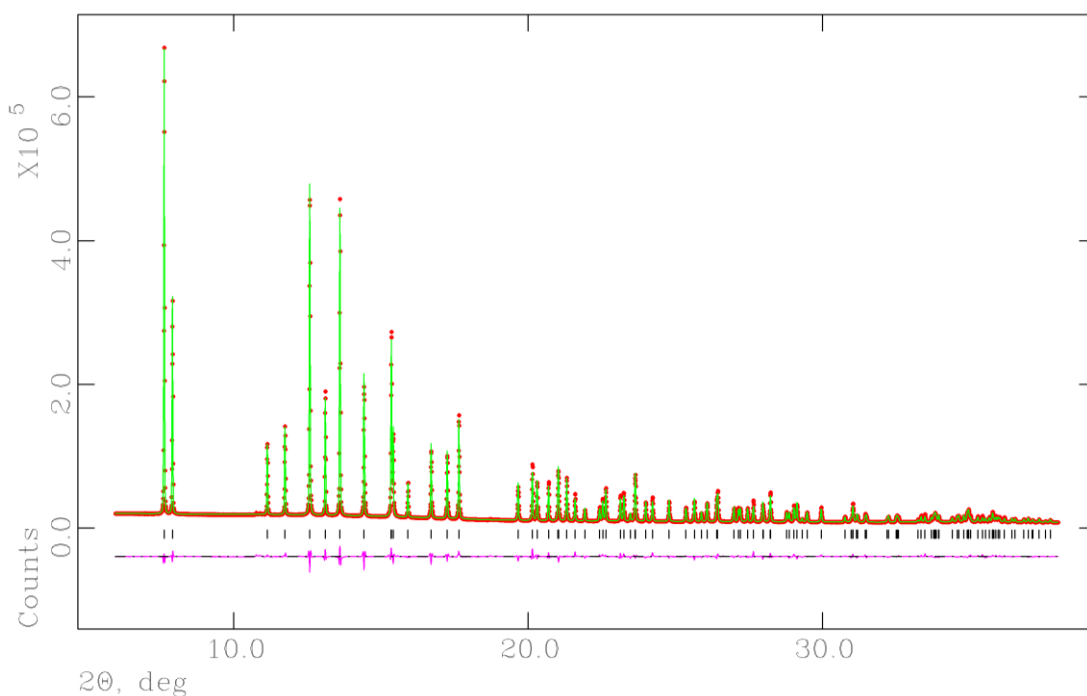


Figure 5.4-44 Profile plot from the Rietveld refinement against high-resolution synchrotron diffraction data for **86** (red dots: experimental profile; green line: calculated profile; pink line: difference profile; tick marks: Bragg reflections for [Li][NH₃BH₃]₂).

The refinement was performed starting from the structural model obtained from lab X-ray powder diffraction, in the space group $C2$ and all the relevant data are shown in Table 5.4-20 - Table 5.4-23. The synchrotron powder diffraction Rietveld refinement proceeded normally, and profile and atomic parameters were added to the model as variables as the refinement progressed. The refinements converged to satisfactory residuals, but the χ^2 value was slightly large. As was commented above, due to the high quality data, any small difference between the observed and calculated data can lead to slightly high values of χ^2 (Table 5.4-20). The precision of the refined light-atom parameters such as hydrogen need to be obtained from neutron refinement. Therefore the thermal factors from hydrogen atoms were maintained constant. This structure type consists of pseudo ammonia borane layers. Lithium cations and iodide anions provide interlayer charge balancing. B-N distances were 1.559 (14) Å (Table 5.4-22). The average H-B-N and H-N-B angles were 108.9 ° and 109.4 °, respectively (Table 5.4-23). The crystal structure of $[\text{LiI}][\text{NH}_3\text{BH}_3]_2$ is illustrated in Figure 5.4-45.

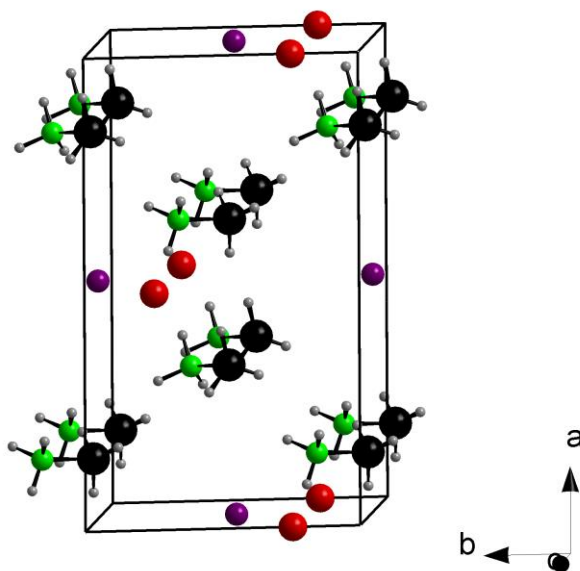


Figure 5.4-45 Crystal structure of $[\text{LiI}][\text{NH}_3\text{BH}_3]_2$ (86). Lithium, iodide, nitrogen, boron and hydrogens are represented as red, purple, green, black and grey spheres, respectively.

Table 5.4-20 Selected Rietveld refinement data from synchrotron powder diffraction data of [Li][NH₃BH₃]₂ (86) compound at 292 K.

Sample number	86
Empirical formula	[Li][NH ₃ BH ₃] ₂
Collection temperature / K	292
Crystal system	Monoclinic
Space group	C2
Z	2
Unit cell formula weight, <i>M_w</i>	391.15
Calculated density, ρ / g cm⁻³	1.708
Unit cell dimensions:	
<i>a</i> / Å	12.40673(5)
<i>b</i> / Å	7.22089(3)
<i>c</i> / Å	4.42016(1)
β / °	106.211(0)
<i>V</i> / Å ³	380.247(3)
Observations, parameters	719, 38
R_{wp}	0.0404
R_p	0.0265
χ²	29.46

Table 5.4-21. Atom positions and isotropic temperature factors obtained from Rietveld refinement against synchrotron powder diffraction data of the [LiI][NH₃BH₃]₂ compound (86) at 292 K.

Atom	Site	x	y	z	100 x <i>U</i>_{iso} / Å²
Li	2a	0	0.242(2)	0	5.7(6)
I	2b	0.5	0	0.5	3.82(2)
N	4c	0.1679(3)	0.1367(5)	0.2156(8)	3.3(2)
B	4c	0.8482(4)	0.029(3)	0.027(1)	7.7(4)
H1B	4c	0.7998	0.0289	0.1876	1.33
H2B	4c	0.8198	0.8734	0.9398	1.33
H3B	4c	0.9267	0.9866	0.1638	1.33
H1N	4c	0.1936	0.2482	0.1524	2.94
H2N	4c	0.1042	0.1685	0.2510	2.94
H3N	4c	0.2165	0.1088	0.3892	2.94

Table 5.4-22 Selected bond lengths [LiI][NH₃BH₃]₂ (86) from high-resolution synchrotron data at 292 K.

	Bond length / Å		Bond length / Å
B – N	1.559(14) x 1	B – Li	2.759(18) x 1
B – H1B	1.126(9) x 1	N – H1N	0.951(4) x 1
B – H2B	0.833(16) x 1	N – H2N	0.881(4) x 1
B – H3B	1.015(6) x 1	N – H3N	0.849(4) x 1

Table 5.4-23 Selected bond angles [LiI][NH₃BH₃]₂ (86) from high-resolution synchrotron data at 292 K.

	Bond angle / °		Bond angle / °
H1B – B – H2B	112.3(9)	H1N – N – H2N	101.84(35)
H1B – B – H3B	99.5(7)	H1N – N – H3N	104.3(4)
H2B – B – H3B	124.2(16)	H2N – N – H3N	110.7(4)
H1B – B – N	100.5(12)	H1N – N – B	115.4(6)
H2B – B – N	112.6(5)	H2N – N – B	112.5(5)
H3B – B – N	104.6(11)	H3N – N – B	111.5(6)

The final isotropic temperature factor of B is large compared with N. This fact could indicate that N and B were wrongly assigned. B and N allocated in the site 4c, in case the ammonia borane rotated in its position. However attempts to place N at $x = 0.1679(3)$, $y = 0.1367(5)$, and $z = 0.2156(8)$ and B at $x = 0.8482(4)$, $y = 0.029(3)$, and $z = 0.027(1)$ resulted in occupancy factors ≤ 0 .

5.4.3.6 Electrochemical impedance spectroscopy

The lithium-ion conductivity was studied for the four successful synthesised lithium ammonia borane complexes: Li[BH₃NH₂BH₂NH₂BH₃] (**67a**), [LiBH₄]₂[NH₃BH₃] (**73**), [LiI][NH₃BH₃] (**84**) and [LiI][NH₃BH₃]₂ (**86**). The ionic conductivity was performed by the AC measurements in temperature ranges between room temperature and the respective melting points (Figure 5.4-46 and Figure 5.4-47). Impedance data analysed in the complex plane showed the semicircle at high frequencies and the linear

response at low frequencies characteristic of ionic conductivity and ion blocking electrodes. At lower temperatures two semicircles were observed, suggesting intra- and inter-grain transport could be resolved. However, the high frequency semicircle moved out of the measurement range at higher temperatures and so the data were analysed using an equivalent electrical circuit to extract the values for the total resistivity of the material. As shown in Figure 5.4-48, the temperature dependencies of the conductivities of **73**, **84** and **86** follow Arrhenius behaviour between room temperature and their melting points. The room temperature conductivity of **67a** was significantly lower (10^{-10} S cm $^{-1}$) but exhibited Arrhenius behaviour from 70 to 130 °C. The conductivity of **67a** increased sharply and almost linearly from 8.2×10^{-9} to 6.7×10^{-7} S cm $^{-1}$ (from 70 to 130 °C). From room temperature to the melting points, the remainders of the compounds showed conductivities from 1.3×10^{-6} - 2.8×10^{-5} S cm $^{-1}$ (mp. at 87 °C) for **73** from 3.4×10^{-8} - 7.5×10^{-6} S cm $^{-1}$ (mp. at 119 °C) for **84**; and from 1.2×10^{-6} - 2.0×10^{-4} S cm $^{-1}$ (mp. at 114 °C) for **86**.

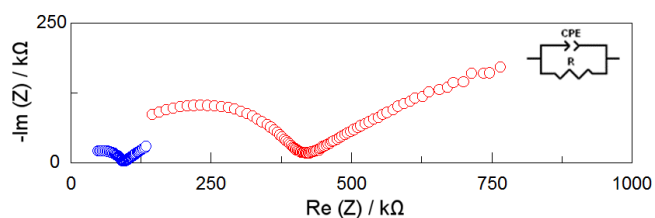


Figure 5.4-46 Nyquist plot for $[\text{LiBH}_4]_2[\text{NH}_3\text{BH}_3]$ (**73**) and $[\text{Li}][\text{NH}_3\text{BH}_3]_2$ (**86**) at 292 K represented in red and blue, respectively.

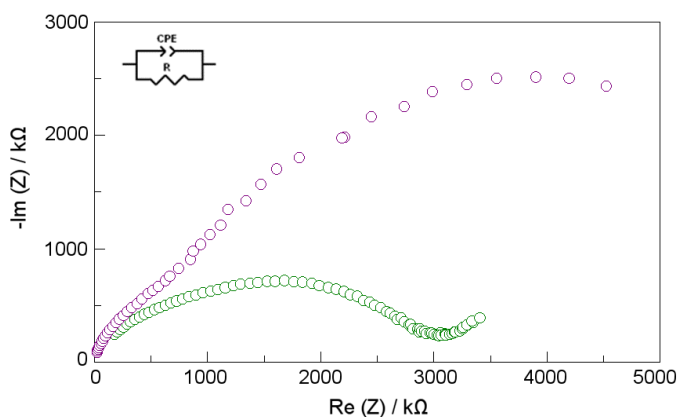


Figure 5.4-47 Nyquist plot for $\text{Li}[\text{BH}_3\text{NH}_2\text{BH}_2\text{NH}_2\text{BH}_3]$ (**67a**) (at 353 K) and $[\text{Li}][\text{NH}_3\text{BH}_3]$ (**84**) (at 292 K) represented in purple and green, respectively.

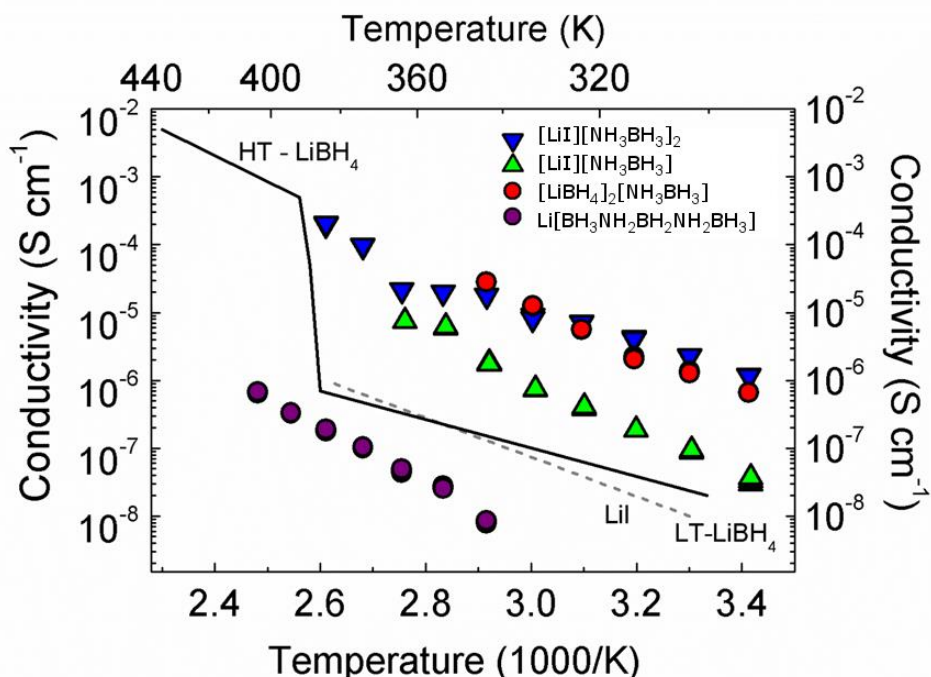


Figure 5.4-48 Plot of conductivity for $\text{Li}[\text{BH}_3\text{NH}_2\text{BH}_2\text{NH}_2\text{BH}_3]$ (67a), $[\text{LiBH}_4]_2[\text{NH}_3\text{BH}_3]$ (73), $[\text{LiI}][\text{NH}_3\text{BH}_3]$ (84) and $[\text{LiI}][\text{NH}_3\text{BH}_3]_2$ (86) as a function of temperature on heating. LT – LiBH_4 ³³ and LiI are plotted for comparison.

From the ionic conductivity measurements it is possible to conclude that materials with less favourable space in conductivity pathways lead to lower ionic conductivity, even at high temperatures, *i.e.* sample 67a ($\text{Li}[\text{BH}_3\text{NH}_2\text{BH}_2\text{NH}_2\text{BH}_3]$) contains channels of 1.8 Å in *ab* planes which may not be enough to allow the Li carriers to smoothly pass. Layered materials showed better ionic conductivity (such as 73, 84 and 86) even at room temperature. Sample 86 contains less lithium, less carriers, in comparison with 84, however it shows better total ionic conductivity. Material 86 contains pseudo-ammonia borane layers facilitating the migration of the lithium ions through the crystal structure in the *bc* plane (Figure 5.4-49).

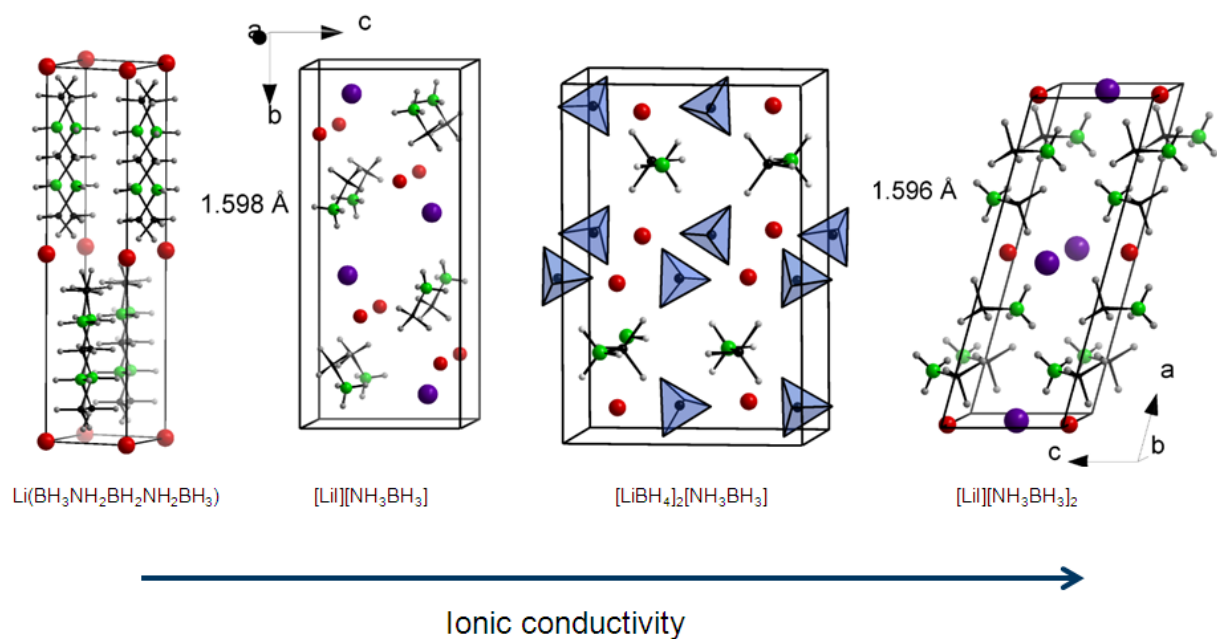


Figure 5.4-49 Comparison of the ionic conductivity between the four different lithium ammonia borane complexes synthesised (67a, 73, 84 and 86).

For all the systems the addition of alkali halide improved their ionic conductivity. Table 5.4-24 shows in summary of some of the complex hydrides that have been studied with iodide addition in order to improve their ionic conductivities.

Table 5.4-24 Ionic conductivities (σ) at 343 K and the activation energies (E_a) for conduction in Li[BH₃NH₂BH₂NH₂BH₃] (67a), [LiBH₄]₂[NH₃BH₃] (73), [LiI][NH₃BH₃] (84), [LiI][NH₃BH₃]₂ (86), LiBH₄ and LiI compared with some lithium complex hydrides.

Complex hydride	σ at 343 K (S cm ⁻¹)	E_a (eV)	Ref.
Li[BH ₃ NH ₂ BH ₂ NH ₂ BH ₃] (67a)	4.11 x 10 ⁻⁹	0.864(1)	Our work
[LiBH ₄] ₂ [NH ₃ BH ₃] (73)	2.83 x 10 ⁻⁵	0.730(2)	Our work
[LiI][NH ₃ BH ₃] (84)	1.80 x 10 ⁻⁶	0.694(1)	Our work
[LiI][NH ₃ BH ₃] ₂ (86)	1.79 x 10 ⁻⁵	0.479(1)	Our work
Li ₄ (BH ₄) ₃ I	8 x 10 ⁻³	0.53	20, 34
LT – LiBH ₄	7 x 10 ⁻⁶	0.69(LT) / 0.53(HT)	33, 35
LiI	1 x 10 ⁻⁷	0.43	20
Li ₃ (NH ₂) ₂ I	8 x 10 ⁻³	0.58	36
LiNH ₂	4 x 10 ⁻¹⁰	1.05	35, 37
Li ₃ AlH ₆ + 0.33LiI	9 x 10 ⁻³	0.48	31
LiAlH ₄	1 x 10 ⁻⁷	0.74	31
Li ₃ AlH ₆	1 x 10 ⁻⁶	0.61	31
Na ₄ (BH ₄) ₃ I	1 x 10 ⁻⁸	---	38
NaBH ₄	9 x 10 ⁻⁸	0.61	38, 39
NaI	9 x 10 ⁻⁸	---	38
Na ₂ (NH ₂)I	1 x 10 ⁻⁷	---	38
NaNH ₂	8 x 10 ⁻⁸	1.40	38, 39
Na ₃ AlH ₆ + 0.33NaI	9 x 10 ⁻⁴	---	31
NaAlH ₄	2 x 10 ⁻⁸	0.79	30
Na ₃ AlH ₆	1 x 10 ⁻⁵	0.62	30

In 2007, Matsuo et al. discovered that LiBH₄ goes through a phase transition at high temperature and becomes a fast ionic conductor (more than 1 x 10⁻³ S cm⁻¹ above 110 °C).³³ The high temperature phase was stabilised by the substitution of I⁻ for BH₄⁻ making an increase in the ionic conductivity of five orders of magnitude at room temperature.^{20, 34} Then the effect of the addition of lithium iodide was studied on the conductivity of other materials such as LiNH₂³⁶ and Li₃AlH₆ (Table 5.4-24).³¹ The most surprising system was Li₃AlH₆ + 0.33LiI which showed the largest increase in

conductivity, about three orders of magnitude than that of Li_3AlH_6 . Li_3AlH_6 crystallises in a trigonal structure with space group $R\bar{3}$. The structure can be described as a distorted *bcc* structure of AlH_6^{3-} units with all tetrahedral sites filled with Li. This large increase in the ionic conductivity was related to the addition of lithium iodide, with the authors claiming there was an increase in carrier concentration caused by dispersion of residual LiI, which was found by X-ray powder diffraction. The other possible origin was the formation of lithium vacancies caused by a dissolution of LiI into Li_3AlH_6 , which has been observed in LiBH_4 , and consequential substitution of $(\text{AlH}_6)^{3-}$ by I^- . Therefore a slightly contraction of the cell was observed.³¹

$\text{Li}_3(\text{NH}_2)_2\text{I}$ was found to crystallise in an hexagonal structure with space group $P6_3mc$. The Li atoms are located in two different crystallographic positions. Both Li atoms are tetrahedrally coordinated by three N atoms and one I atom. The clusters are composed of tetrahedra sharing edges with each other. It possesses a pseudo-double layered structure. The lithium fast-ion conduction of $\text{Li}_3(\text{NH}_2)_2\text{I}$ is believed to be due to the intrinsic vacancies at the centre of each cluster composed of six tetrahedral and between the clusters. It is possible that Li^+ ions move through these vacancies.³⁶ ^7Li and ^1H NMR studies suggested that Li^+ high mobility cannot be ascribed to the effects of NH_2 reorientations; it seemed more probable that it is related to the structural features of the Li-site sublattice, such as short Li-Li distances and abundant interstitial sites of large volume.⁴⁰ $\text{Li}_3(\text{NH}_2)_2\text{I}$ shows an ionic conductivity of $1.7 \times 10^{-5} \text{ S cm}^{-1}$ at 300 K, which is four and three orders of magnitude higher than that of the host materials $\text{Li}(\text{NH}_2)$ and LiI.³⁶

Considering the similar chemical formulas of lithium and sodium complex hydrides, the same approach was performed using NaI in sodium materials. Therefore the effect of the addition of sodium iodide has been studied on the conductivity of other materials such as NaBH_4 ,³⁸ NaNH_2 ,³⁸ and Na_3AlH_6 .³⁰

The crystal structure of $\text{Na}_2(\text{NH}_2)\text{I}$ is the AgN_3 -type orthorhombic structure (space group *Ibam*) which shows a low ionic conductivity on the order of $10^{-9} \text{ S cm}^{-1}$. $\text{Na}_2(\text{NH}_2)\text{I}$ is composed of pseudo-amine layers and sodium cations and iodide anions provide interlayer charge balancing.

The formation of a pseudo-layer can improve the ionic conductivity such as for $\text{Li}_3(\text{NH}_2)_2\text{I}$ and $\text{Na}_2(\text{NH}_2)\text{I}$ which also occurs in $[\text{LiBH}_4]_2\text{NH}_3\text{BH}_3$ and $\text{LiI}[\text{NH}_3\text{BH}_3]_2$. The presence of abundant interstitial sites of large volume is important to enhance the ionic conductivity in materials such as $\text{Li}_3(\text{NH}_2)_2\text{I}$, $[\text{LiBH}_4]_2\text{NH}_3\text{BH}_3$ and $\text{LiI}[\text{NH}_3\text{BH}_3]_2$. However materials with interstitial sites of small volume show much lower ionic conductivity such as $\text{Li}(\text{BH}_3\text{NH}_2\text{BH}_2\text{NH}_2\text{BH}_3)$ and $\text{LiI}[\text{NH}_3\text{BH}_3]$ causing detrimental consequences such as in $\text{Na}_2(\text{NH}_2)\text{I}$ which shows much lower ionic conductivity because of the bigger size of the cation carrier. The presence of higher number of carriers improves the ionic conductivity as it has been observed in Li_3AlH_6 . However $\text{LiI}[\text{NH}_3\text{BH}_3]_2$ with less carriers than $\text{LiI}[\text{NH}_3\text{BH}_3]$ shows better ionic conductivity implying that for these materials the pseudo-layer structure makes more impact in the total ionic conductivity than the Li amount.

Structural analysis of the new materials synthesised, $\text{LiI}[\text{NH}_3\text{BH}_3]$ and $\text{LiI}[\text{NH}_3\text{BH}_3]_2$, showed no exchange in the N and B positions in the ammonia borane. This could indicate that N and B are fairly static and there is no NH_3BH_3 reorientation. As mentioned above, the same phenomenon was observed for $\text{Li}_3(\text{NH}_2)_2\text{I}$. Therefore, Li motion in these materials could possibly be due to the structural features of Li-site sublattice, such as short Li-Li distances and abundant interstitial sites of large volume.

5.5 Conclusions

Firstly, the synthesis of four lithium ammonia borane derived hydride materials were reported as possible candidates for solid state electrolytes for lithium ion batteries ($[\text{LiBH}_4]_2[\text{NH}_3\text{BH}_3]$, $\text{Li}[\text{BH}_3\text{NH}_2\text{BH}_2\text{NH}_2\text{BH}_3]$, $[\text{LiI}][\text{NH}_3\text{BH}_3]$ and $[\text{LiI}][\text{NH}_3\text{BH}_3]_2$).

Secondly, the thermal stability for each compound was studied as a precursor to measuring ionic conductivity. $[\text{LiI}][\text{NH}_3\text{BH}_3]_2$ and $[\text{LiI}][\text{NH}_3\text{BH}_3]$ showed the highest thermal stability. Raman spectroscopy was used to determine the presence of the NH_3BH_3 in the final compound, where appropriate.

Thirdly, two new compounds were reported, $[\text{LiI}][\text{NH}_3\text{BH}_3]$ and $[\text{LiI}][\text{NH}_3\text{BH}_3]_2$. Full structural characterisation was performed for both compositions using high-resolution synchrotron diffraction at room temperature to confirm proposed models from previous lab PXD data.

Finally, ionic conductivity measurements were performed for the four samples. Pseudo-layered ammonia borane compounds ($[\text{LiBH}_4]_2[\text{NH}_3\text{BH}_3]$ and $[\text{Li}][\text{NH}_3\text{BH}_3]_2$) showed better performance than ($\text{Li}[\text{BH}_3\text{NH}_2\text{BH}_2\text{NH}_2\text{BH}_3]$ and $[\text{Li}][\text{NH}_3\text{BH}_3]$) which do not form structures in which the molecular and ionic compounds are well positioned.

Overall, a number of novel compounds have been discussed in this chapter which show high ionic conductivity and high thermal stability making them potentially suitable for electrolytes and further development.

5.6 References

1. S. G. Shore and R. W. Parry, *J. Am. Chem. Soc.*, 1955, **77**, 6084-6085.
2. M. E. Bowden, G. J. Gainsford and W. T. Robinson, *Aust. J. Chem.*, 2007, **60**, 149-153.
3. Z. T. Xiong, C. K. Yong, G. T. Wu, P. Chen, W. Shaw, A. Karkamkar, T. Autrey, M. O. Jones, S. R. Johnson, P. P. Edwards and W. I. F. David, *Nat. Mater.*, 2008, **7**, 138-141.
4. M. G. Hu, R. A. Geanangel and W. W. Wendlandt, *Thermochim. Acta*, 1978, **23**, 249-255.
5. R. A. Geanangel and W. W. Wendlandt, *Thermochim. Acta*, 1987, **113**, 379-382.
6. A. Staubitz, A. P. Robertson and I. Manners, *Chem. Rev.*, 2010, **110**, 4079-4124.
7. H. Wu, W. Zhou, F. E. Pinkerton, M. S. Meyer, G. Srinivas, T. Yildirim, T. J. Udovic and J. J. Rush, *Journal of Materials Chemistry*, 2010, **20**, 6550-6556.
8. J. Luo, H. Wu, W. Zhou, X. Kang, Z. Fang and P. Wang, *Int. J. Hydrog. Energy*, 2012, **37**, 10750-10757.
9. K. J. Fijalkowski, T. Jaron, P. J. Leszczynski, E. Magos-Palasyuk, T. Palasyuk, M. K. Cyranski and W. Grochala, *Phys. Chem. Chem. Phys.*, 2014, **16**, 23340-23346.
10. M. Ramzan, F. Silvearv, A. Blomqvist, R. H. Scheicher, S. Lebegue and R. Ahuja, *Phys. Rev. B*, 2009, **79**, 1-4.
11. B. Weng, Z. Wu, Z. Li and H. Yang, *Int. J. Hydrog. Energy*, 2012, **37**, 5152-5160.
12. C. Wu, G. Wu, Z. Xiong, W. I. F. David, K. R. Ryan, M. O. Jones, P. P. Edwards, H. Chu and P. Chen, *Inorg. Chem.*, 2010, **49**, 4319-4323.
13. H. Wu, W. Zhou and T. Yildirim, *J. Am. Chem. Soc.*, 2008, **130**, 14834-14839.
14. C. Z. Wu, G. T. Wu, Z. T. Xiong, X. W. Han, H. L. Chu, T. He and P. Chen, *Chem. Mat.*, 2010, **22**, 3-5.
15. J. Chen, T. He, G. T. Wu, Z. T. Xiong and P. Chen, *Int. J. Hydrog. Energy*, 2013, **38**, 10944-10949.
16. I. C. Evans, 2011, PhD dissertation, University of Birmingham.
17. J. P. Soulie, G. Renaudin, R. Cerny and K. Yvon, *J. Alloy. Compd.*, 2002, **346**, 200-205.
18. L. H. Jepsen, V. Ban, K. T. Moller, Y. S. Lee, Y. W. Cho, F. Besenbacher, Y. Filinchuk, J. Skibsted and T. R. Jensen, *J. Phys. Chem. C*, 2014, **118**, 12141-12153.
19. X. W. Chen, F. Yuan, Q. F. Gu and X. B. Yu, *Dalton Trans.*, 2013, **42**, 14365-14368.
20. H. Maekawa, M. Matsuo, H. Takamura, M. Ando, Y. Noda, T. Karahashi and S. I. Orimo, *J. Am. Chem. Soc.*, 2009, **131**, 894-895.
21. <http://icsd.cds.rsc.org/search/basic.xhtml>, accessed on 3rd September 2015.
22. W. Kraus and G. Nolze, *Powder Diffraction*, 1998, **13**, 256-259.
23. J. Laugier and B. Bochu, LMGP-Suite suite of programs for the interpretation of X-ray experiments. .
24. V. Petricek, M. Dusek and L. Palatinus, *Z. Kristall.*, 2014, **229**, 345-352.

25. A. C. Larson and R. B. Von Dreele, 1994, General Structure Analysis System (GSAS), Los Alamos National Laboratory Report LAUR, 86-748.
26. B. H. Toby, *J. Appl. Crystallogr.*, 2001, **34**, 210-213.
27. R. Owarzany, K. J. Fijalkowski, T. Jaroń, P. J. Leszczyński, Ł. Dobrzycki, M. K. Cyrański and W. Grochala, *Inorg. Chem.*, 2015, **215**, 324-332.
28. R. S. Chellappa, T. Autrey, M. Somayazulu, V. V. Struzhkin and R. J. Hemley, *Chemphyschem*, 2010, **11**, 93-96.
29. H. Chu, G. Wu, Z. Xiong, J. Guo, T. He and P. Chen, *Chem. Mat.*, 2010, **22**, 6021-6028.
30. H. Oguchi, M. Matsuo, S. Kuronoto, H. Kuwano and S. Orimo, *J. Appl. Phys.*, 2012, **111**, 036102.
31. H. Oguchi, M. Matsuo, T. Sato, H. Takamura, H. Maekawa, H. Kuwano and S. Orimo, *J. Appl. Phys.*, 2010, **107**, 1-3.
32. T. Hahn, 2006, ISBN 978-0-79236590-4, International Tables for Crystallography: Volume A Space group symmetry. Springer-Verlag.
33. M. Matsuo, Y. Nakamori, S. Orimo, H. Maekawa and H. Takamura, *Appl. Phys. Lett.*, 2007, **91**, 1-3.
34. L. H. Rude, E. Groppo, L. M. Arnbjerg, D. B. Ravnsbaek, R. A. Malmkjaer, Y. Filinchuk, M. Baricco, F. Besenbacher and T. R. Jensen, *J. Alloy. Compd.*, 2011, **509**, 8299-8305.
35. W. Li, G. T. Wu, Z. T. Xiong, Y. P. Feng and P. Chen, *Phys. Chem. Chem. Phys.*, 2012, **14**, 1596-1606.
36. M. Matsuo, T. Sato, Y. Miura, H. Oguchi, Y. Zhou, H. Maekawa, H. Takamura and S. Orimo, *Chem. Mat.*, 2010, **22**, 2702-2704.
37. M. Matsuo, A. Remhof, P. Martelli, R. Caputo, M. Ernst, Y. Miura, T. Sato, H. Oguchi, H. Maekawa, H. Takamura, A. Borgschulte, A. Züttel and S. Orimo, *J. Am. Chem. Soc.*, 2009, **131**, 16389-16391.
38. M. Matsuo, S. Kuromoto, T. Sato, H. Oguchi, H. Takamura and S. Orimo, *Appl. Phys. Lett.*, 2012, **100**, 1-4.
39. M. Matsuo, H. Oguchi, T. Sato, H. Takamura, E. Tsuchida, T. Ikeshoji and S. Orimo, *J. Alloy. Compd.*, 2013, **580**, S98-S101.
40. A. V. Skripov, R. V. Skoryunov, A. V. Soloninin, O. A. Babanova, M. Matsuo and S. Orimo, *The Journal of Physical Chemistry C*, 2015, **119**, 13459-13464.

6. Structural analysis of LiInBr₄

In this chapter, lithium indium bromide has been explored as a possible solid state electrolyte and the results of its structural characterisation are presented herein. Section 6.1 reports the synthesis of LiInBr₄ via mechanochemical milling and subsequent crystal growth via the adapted Bridgman-Stockbarger technique. Section 6.2 discusses the structure of LiInBr₄ at room temperature and at 353 K using powder neutron diffraction (*ca.* below and above the proposed phase transition at 314 K, according to Yamada *et al.*¹ and as discussed below).

6.1 Introduction

Ternary lithium hydrides and halides are considered as promising candidates as an electrolytes in Li ion batteries due to their high ionic conductivity and thermal stability. Ternary lithium halides typically show high ionic conductivities at high temperatures.¹ As mentioned in the introduction some complex lithium non-oxide compounds such as LiBH₄ have been reported that show high ionic conductivities above a phase transition in the case of LiBH₄ this transition occurs at 383 K and hexagonal (HT phase LiBH₄) shows lithium ionic conductivity of $2 \times 10^{-3} \text{ S cm}^{-1}$.²⁻⁴ By comparison LiAlH₄ and Li₃AlH₆ exhibit ionic conductivities from $2 \times 10^{-9} - 5 \times 10^{-6} \text{ S cm}^{-1}$ and $10^{-7} - 2 \times 10^{-5} \text{ S cm}^{-1}$, respectively, from room temperature to 393 K.^{5, 6}

Motivated by the results obtained with LiBH₄, we investigated other compounds with the same empirical formulae from group XIII ($M^I M^{III} X_4$, where $M^I = \text{Li}$, $M^{III} = \text{B, Al, Ga and In}$, and $X = \text{H, F, Cl, Br and I}$). The hydrides from group XIII (Figure 6.1-1) are not thermally stable apart from LiBH₄ and LiAlH₄ which decompose at 541 and 373 K, respectively. For instance, LiGaH₄ and LiInH₄ decompose at 323 K and 273 K respectively, making these materials unsuitable for lithium ion batteries.⁷ Therefore we decided to investigate lithium ternary halides from group XIII which might show similar physical properties to LiBH₄.

XIII	XIV	XV	XVI	XVII
5 B	6 C	7 N	8 O	9 F
13 Al	14 Si	15 P	16 S	17 Cl
31 Ga	32 Ge	33 As	34 Se	35 Br
49 In	50 Sn	51 Sb	52 Te	53 I

Figure 6.1-1 p block metals are represented in light orange; Metalloids are represented in green; Non-metals are represented in purple. Halogens are represented in light blue.

From all of the halocomplex lithium salts ($M^I M^{III} X_4$, where $M^I = \text{Li}$, $M^{III} = \text{Al}$, Ga and In, $X = \text{Cl}$, Br and I), we found LiInBr_4 to be the most interesting material. LiInBr_4 is the only halocomplex reported so far which shows a relatively low temperature phase transition similar to LiBH_4 . The only report available in the literature on the formation of LiInBr_4 and its ionic conductivity performance was published by Yamada *et al.* in 2006.¹ The compound displays a conductivity of $10^{-3} \text{ S cm}^{-1}$ at 313 K and was synthesised *via* the Bridgman-Stockbarger technique from a mixture of LiBr and InBr_3 . At room temperature (RT), LiInBr_4 was reported as crystallising in a cubic spinel structure, which undergoes a phase transition upon heating above 316 K (Figure 6.1-2 and Figure 6.1-5). However, the high temperature (HT) LiInBr_4 phase was not characterised. The proposed cubic spinel structure of LiInBr_4 (space group $Fd\bar{3}m$) contains bromide ions which occupy the $32e$ position and In^{3+} which populate half of the $16d$ sites randomly. Hence, the structure was represented as $(\text{Li})[\text{In}\square]\text{Br}_4$ or $(\square)[\text{LiIn}]\text{Br}_4$, where () and [] represent a tetrahedral ($8b$) and octahedral ($16d$) site, respectively.¹ However, as discussed in the following sections our structural investigations using powder X-ray diffraction and Powder Neutron diffraction indicate that the previously proposed cubic crystal structure was wrongly assigned (Figure 6.1-3).

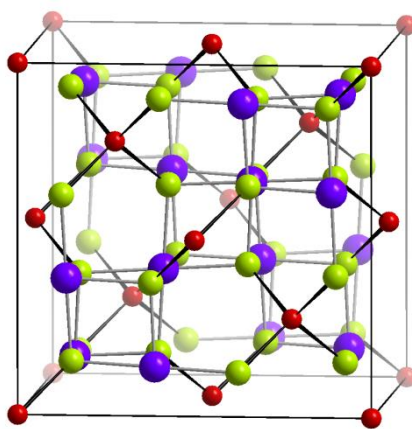


Figure 6.1-2 Proposed cubic spinel structure by Yamada *et al.*¹ Lithium, indium and bromide ions are represented as red, purple, and green spheres, respectively.

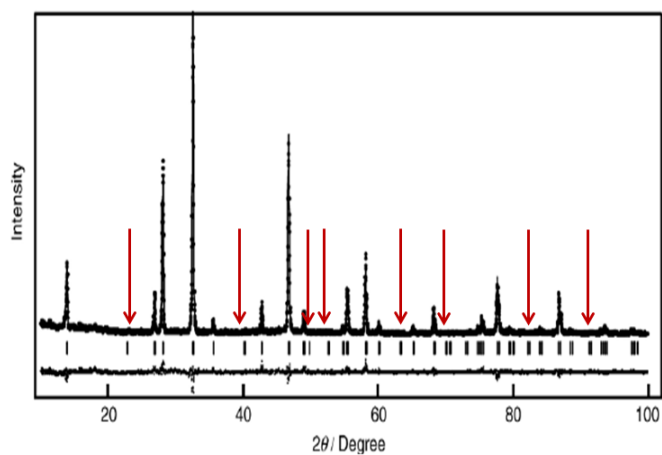


Figure 6.1-3 Profile plot from the Rietveld Refinement against X-ray powder diffraction data for LiInBr_4 conducted by Yamada *et al.*¹ Black dots: experimental profile; black line: calculated profile lower; black line (apparently): difference profile; tick marks: Bragg reflections for the cubic LiInBr_4 phase. Red arrows indicate missing reflections.¹

Another ternary lithium halide known is Li_3InBr_6 which crystallises in a monoclinic structure at 350 K with space group $C2/m$ (#12) and is isomorph with Li_3InCl_6 .¹ In^{3+} occupies the octahedral sites and Li^+ is located between In layers (Figure 6.1-4). However the room temperature structure of Li_3InBr_6 is unknown. Li_3InBr_6 undergoes a phase transition upon heating above 314 K (Figure 6.1-5) with an activation energy of 0.31(1) eV.

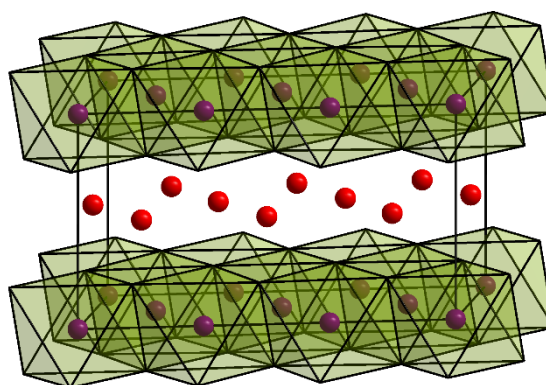


Figure 6.1-4 Proposed monoclinic spinel structure by Yamada et al.¹ Lithium, indium and bromide ions are represented as red, purple, and black spheres, respectively.

Figure 6.1-5 shows the conductivity plot from both materials, LiInBr_4 and Li_3InBr_6 . Both compounds demonstrate similar phase transition temperatures and Arrhenius plots and therefore similar activation energies below and above the phase transition. This fact could indicate that both ternary lithium halides have similarities in their conductivity pathway and structure such as layers form by bromide, indium occupying the octahedral sites and lithium ions located in between the layers (Figure 6.1-4).

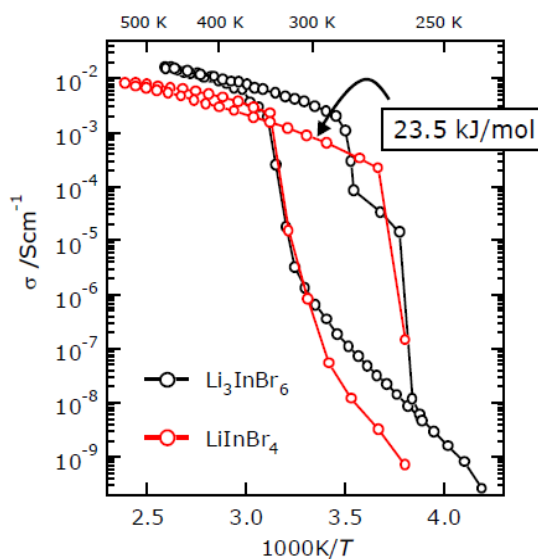


Figure 6.1-5 Plot of conductivity as a function of temperature for LiInBr_4 and Li_3InBr_6 on heating.¹

In this work, structural characterisation of LiInBr_4 at room temperature and high temperature is described using powder X-ray diffraction, Raman spectroscopy, thermal analysis, powder neutron diffraction, conductivity measurements and ^7Li

solid state NMR spectroscopy (above and below the proposed phase transition at 314 K)¹. The existence of a phase transition and/or increased in defect concentration will be discussed on the basis of these results.

6.1.1 Experimental

6.1.1.1 Synthesis of LiInBr_4

For the synthesis of LiInBr_4 , anhydrous LiBr (Sigma-Aldrich, $\geq 99\%$) and InBr_3 (Sigma-Aldrich, 99%) were obtained commercially and used directly without further purification. Mixtures of LiBr and InBr_3 powders with molar ratio of 1 : 1 were prepared in an N_2 -filled recirculating glovebox (Table 6.1-1 and Table 6.1-2). The composites were synthesised using a Retsch PM100 ball mill. A total of ca. of 0.5 g of the powder mixture was loaded into a hardened steel jar (50 ml) together with 10 hardened steel balls of 10 mm in diameter (ball to powder ratio 80 : 1). Ball milling was conducted at 500 rpm for 4 h. After each 2 min milling period, the milling was paused for 2 min followed by inverse rotation. A cylindrical sample pellet was formed from the resultant powder and was heated *via* conventional thermal treatment (section 2.2.2 and Figure 6.1-6). The resultant product, grey in colour, was collected in the glovebox for characterisation.

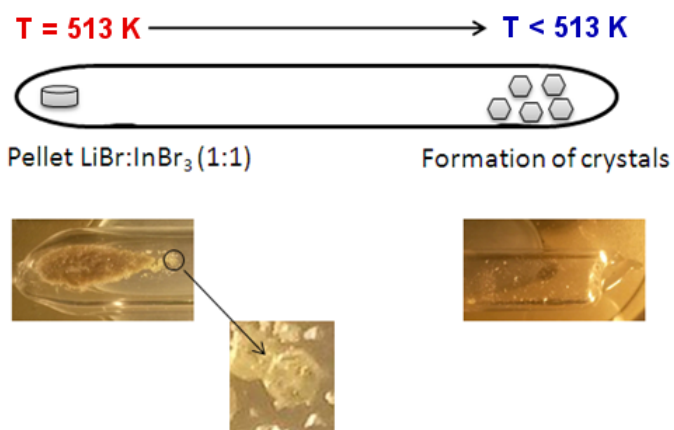


Figure 6.1-6. LiInBr_4 formation using CVT using a sealed silica tube.

6.1.1.2 Characterisation

Powder X-ray diffraction data of sample **87** obtained at room temperature with a Bruker D8 Advance (θ - 2θ) diffractometer, using Cu $K\alpha$ radiation with a scanning step size of $0.017^\circ 2\theta$ over an angular range 5 - $95^\circ 2\theta$ for ca. 12 h. All data were

indexed and refined by least squares fitting when possible using the CELREF software package.

Table 6.1-1 Summary of LiBr-InBr₃ reactions (87 and 88). For experimental details, see text.

Sample	LiBr:InBr ₃	Treatment
87	1 : 1	Milling (4 h) and heating
88	1 : 1	As 1, but quenched to 77 K (N ₂ (l))

In situ Raman spectra were collected for sample **87** in the range 30-250 cm⁻¹ at room temperature and on heating (292-353 K, holding at a set temperature for 1 h). A Horiba LabRAM HR confocal microscope system was used with a 532 nm laser, a hole aperture of 250 μm and a 600 gr mm⁻¹ grating.

Time-of-flight powder neutron diffraction data were collected at set temperatures between 292-353 K (**87a** - **87d**, Table 6.1-2). The General Materials diffractometer (GEM) was used at the ISIS neutron source at the Rutherford Appleton Laboratory in Oxfordshire.⁸ The sample was contained in vanadium cans with a diameter of 6 mm. Using standard procedure, the data from each of the instrument's detector banks were corrected for absorption, normalized to account for the incident neutron spectrum and detector efficiencies and summed.⁸ The data were analysed using Rietveld refinement as implemented in the GSAS software package⁹ via the EXPGUI interface¹⁰ against multiple data sets.

Table 6.1-2 Summary of PND data collected from GEM at different temperatures (87a-87d) for sample 87.

Sample	87a	87b	87c	87d
Temperature / K	292	308	333	353

Data collected were fitted using the 2 different models proposed by Yamada *et al.*,¹ the cubic $Fd\bar{3}m$ (#227 and $a = 10.974 \text{ \AA}$)¹ and the rhombohedral $R\bar{3}m$ (#166, $a = 6.725(1) \text{ \AA}$ and $\alpha = 33.65(1)^\circ$)^{1, 11} space groups (Table 6.2-1), however neither model converged to a solution. Data collected were fitted using an appropriate starting model (detailed in subsequent sections) obtained from the online ICSD database.¹² The background was fitted using the shifted Chebyshev polynomial

function and the unit cell parameters were then refined, followed by the peak profile parameters, atomic positions and isotropic displacement parameters. Modelling of the peak shape was performed using GSAS function 2 (pseudo-Voigt combination and an asymmetric peak shape).^{9, 10} Lastly, occupancies were refined for Li sites in the case of the HT LiInBr₄ phase at 353 K. Constraints were applied to the thermal parameters of the cations in RT and HT LiInBr₄. The refinements were considered finished when they converged, all the variables were stable and the R-values minimised.

⁷Li solid state NMR experiments were performed by Dr D. Carty in the Department of Chemistry at the University of Durham. ⁷Li solid state NMR measurements were performed using a Bruker Avance III HD spectrometer operating at 155.52 MHz for ⁷Li. Spectra were obtained as a function of temperature using a quadrupolar echo pulse sequence with a 60 s relaxation delay (unless otherwise stated), 1.3 μs pulses (45° tip angle calibrated on a solution sample) with a delay of 20 μs between them. Spectral referencing is with respect to a 1M aqueous solution of LiCl. Spin-lattice relaxation time measurements were performed using a saturation-recovery method.

Simultaneous thermal analyses (thermogravimetric and differential thermal analysis) were performed using a NETZSCH STA 409PC instrument coupled with a HIDEN HPR20 mass spectrometer. Samples were placed in an alumina pan and heated from room temperature to 533 K at 5 K min⁻¹, and in some cases held at this temperature for 20 min.

6.2 Results and discussion

6.2.1 Synthesis

Table 6.2-1 shows the cell parameters calculated for LiInBr_4 (**87** and **88**) as compared with those reported by Yamada *et al.*¹

Table 6.2-1 Lattice parameters of LiInBr_4 samples (LiBr-InBr₃ mixtures, **87 and **88**)**

Sample	LiBr:InBr ₃	Compound, space group	$a / \text{Å}$	$c / \text{Å}$	$V / \text{Å}^3$
87	1 : 1	LiInBr_4 , $R\bar{3}m$ (#166)	3.8830(4)	19.0255(2)	248.43(3)
88	1 : 1	LiInBr_4 , $R\bar{3}m$ (#166)	3.8825(4)	19.0213(5)	248.31(3)
Yamada <i>et al.</i> ¹	1 : 1	LiInBr_4 , $Fd\bar{3}m$ (#227)	10.974		1321.58

Powder X-ray diffraction (PXRD) data of the as-formed product (**87**) after mechanochemical milling for 4 h is shown in Figure 6.2-1. Powder X-ray data revealed the presence of a single phase, the RT phase of LiInBr_4 ¹, which was indexed in a rhombohedral space group $R\bar{3}m$ with $a = 3.885(2)$, $c = 19.0250(1)$ Å and $V = 248.7(1)$ Å³. This crystal structure differs with the spinel and trigonal structures reported by Yamada *et al.*^{1, 11}

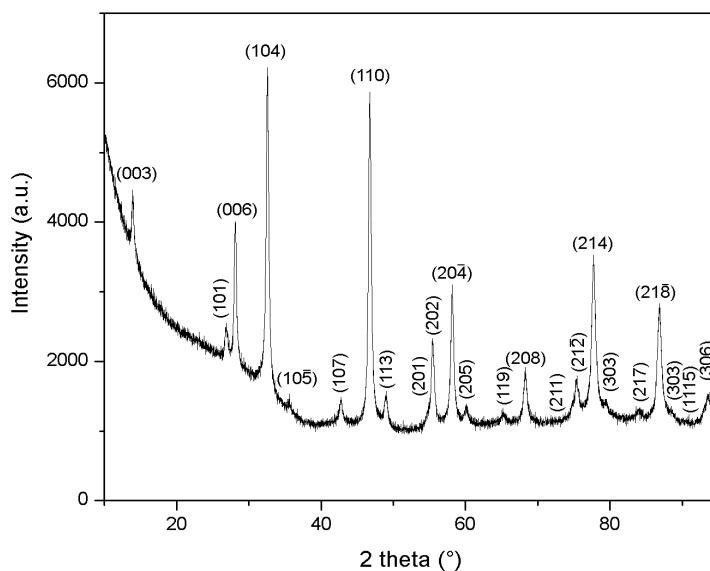


Figure 6.2-1 PXRD pattern of the reaction product after mechanochemical milling for 4 h (**87**). Miller indices for the rhombohedral LiInBr_4 phase are indicated.

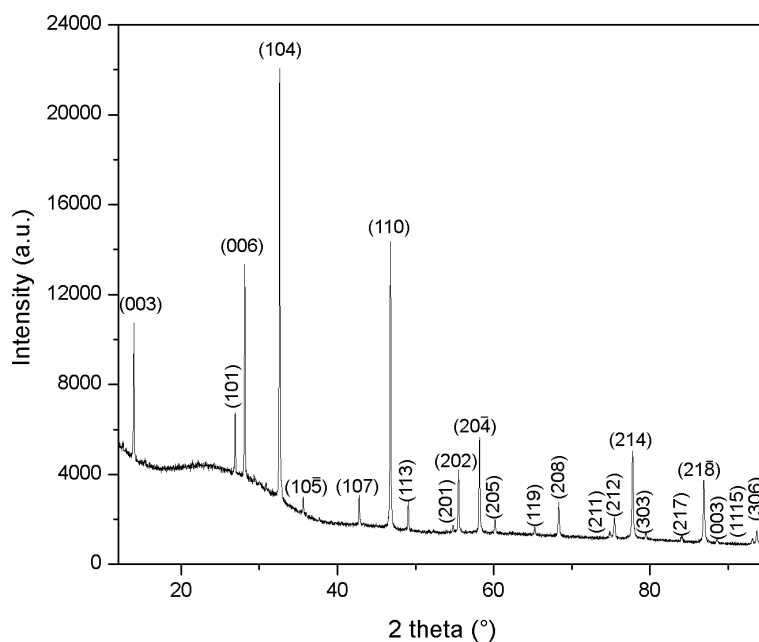


Figure 6.2-2 PXD pattern of the reaction product after mechanochemical milling for 4 h and adapted Bridgman-Stockbarger methods for 12 h at 513 K (**87**). Miller indices for the rhombohedral LiInBr_4 phase are indicated.

After application of adapted Bridgman-Stockbarger methods, a single phase product (**87**) consisting of LiInBr_4 ($R\bar{3}m$; $a = 3.8830(4)$, $c = 19.0255(2)$ Å, and $V = 248.43(3)$ Å³) was formed (Figure 6.2-2).

Typically, LiInBr_4 has been synthesised from lithium bromide and indium bromide (III) using adapted Bridgman-Stockbarger techniques, but the authors did not report the synthesis temperature.^{1,8} Accordingly, the product of previous synthesis was reported to be the cubic “RT LiInBr_4 ” phase (space group $Fd\bar{3}m$). To the best of our knowledge, there are no other reports regarding the synthesis of LiInBr_4 . Sample **87** could be indexed in space group $Fd\bar{3}m$ but Rietveld refinement in this space group $Fd\bar{3}m$ did not converge. While exploring a possible route to stabilise the “HT LiInBr_4 ” phase, we found that RT LiInBr_4 phase was wrongly assigned. Our studies suggest that the RT LiInBr_4 phase could be modelled more effectively in space group $R\bar{3}m$.

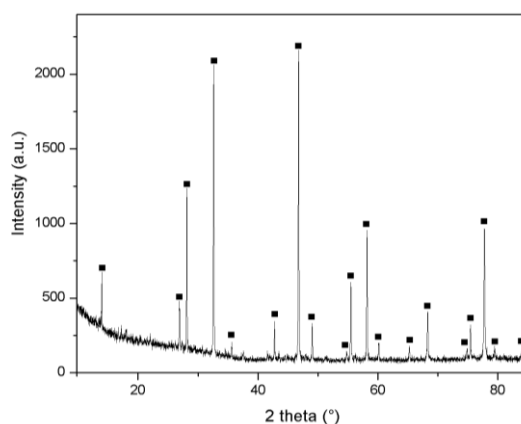


Figure 6.2-3 PXD pattern of the reaction product after quenching with liquid N₂ (**88**). Black squares represent RT LiInBr₄ phase.

According to with Yamada *et al.*,^{1, 9, 13, 14} the HT LiInBr₄ is formed from the RT phase above 314 K. Synthesis of HT LiInBr₄ was attempted by quenching the reaction mixture from 523 K with liquid N₂ (77 K, sample **88**).

Figure 6.1-4 shows the comparison between **87** and **88** (Table 6.1-1 and Table 6.2-1). No difference in the peak position was observed. However some of the intensities of the peaks were modified. A local distortion could have happened, such as movement of the lithium ions. But these results do not suggest the presence of a new structure. New reflections with low intensities were observed after quenching (Figure 6.2-3 and Figure 6.2-4) which could be due to the formation of oxides because of a cracking in the sealed tube during the quenching process.

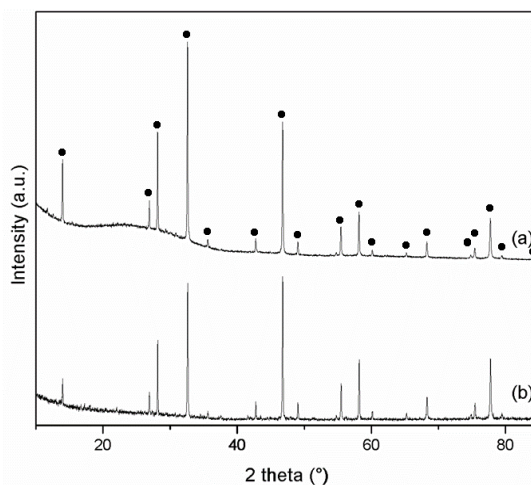


Figure 6.2-4 PXD of the reaction product after (a) mechanochemical milling for 4 h and adapted Bridgman-Stockbarger methods for 12 h at 513 K (**87**) and (b) quenching with liquid N₂ (**88**). Black circles represent RT LiInBr₄ phase.

6.2.2 Raman spectroscopy

Raman spectra for LiInBr_4 (**87**) were collected and the results are discussed in this section. Spectra at room temperature and on heating from room temperature to 343 K while scanning over the range 30 - 250 cm^{-1} are shown in Table 6.2-2 and Figure 6.2-5.

Table 6.2-2 Vibrational spectra of crystalline LiInBr_4 (w: weak, m: medium, s: strong).¹⁵

Compound	Band ν (In-Br) / cm^{-1}			
	ν_1'	ν_1	ν_2	ν_5
LiInBr_4 (at room temperature)	189s	161m	77w	55w
LiInBr_4 (at 328 K)	190m	164s	106w	54w

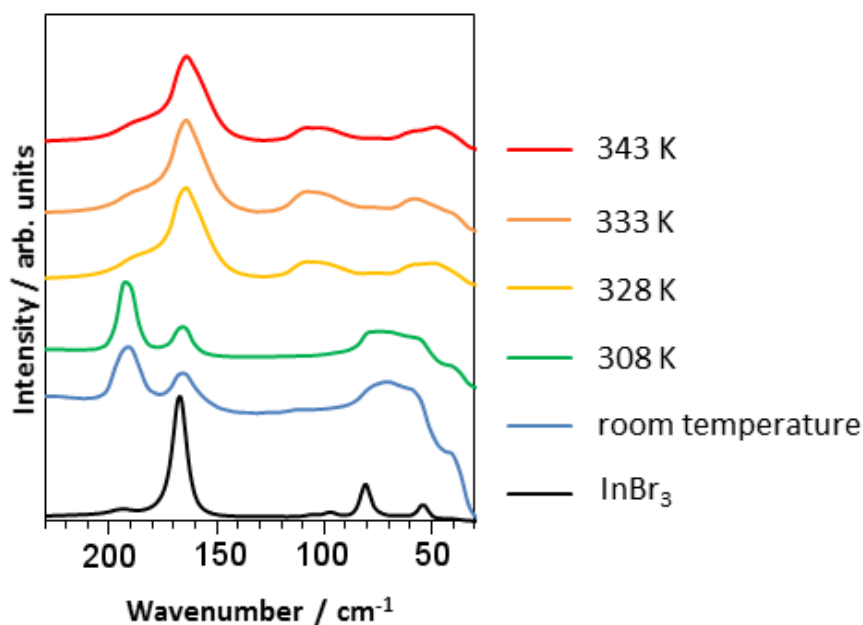


Figure 6.2-5 Variable temperature Raman spectra from 30 – 250 cm^{-1} for LiInBr_4 (**87**).

Several bands were observed below 100 cm^{-1} . However these bands were not studied since they cannot be unambiguously assigned due to the presence of lattice modes.¹⁶ InBr_3 is isostructural with InCl_3 ($C2/m$ (#12)), and has very similar Raman and IR spectra (Table 6.2-3).¹⁵ Indium is in a 6-co-ordinate environment and explains why it exhibits lowest metal-halogen stretching frequencies as compared to InI_3 where indium is only 4-co-ordinated.¹⁵

Table 6.2-3 Vibrational spectra of crystalline indium trichloride and tribromide.¹⁵

Compound	$\nu_1(\text{R})$	$\nu_2(\text{R})$	$\nu_3(\text{IR})$	$\nu_4(\text{IR})$	$\nu_5(\text{R}) / \text{cm}^{-1}$
InCl_3	279	127	255	119	87
InBr_3	171	84	180	82	54

Figure 6.2-6 shows the six normal modes of vibration of an octahedral ML_6 molecule. Stretching and bending modes are shown separately ((a) - (c) and (d) - (f), respectively).

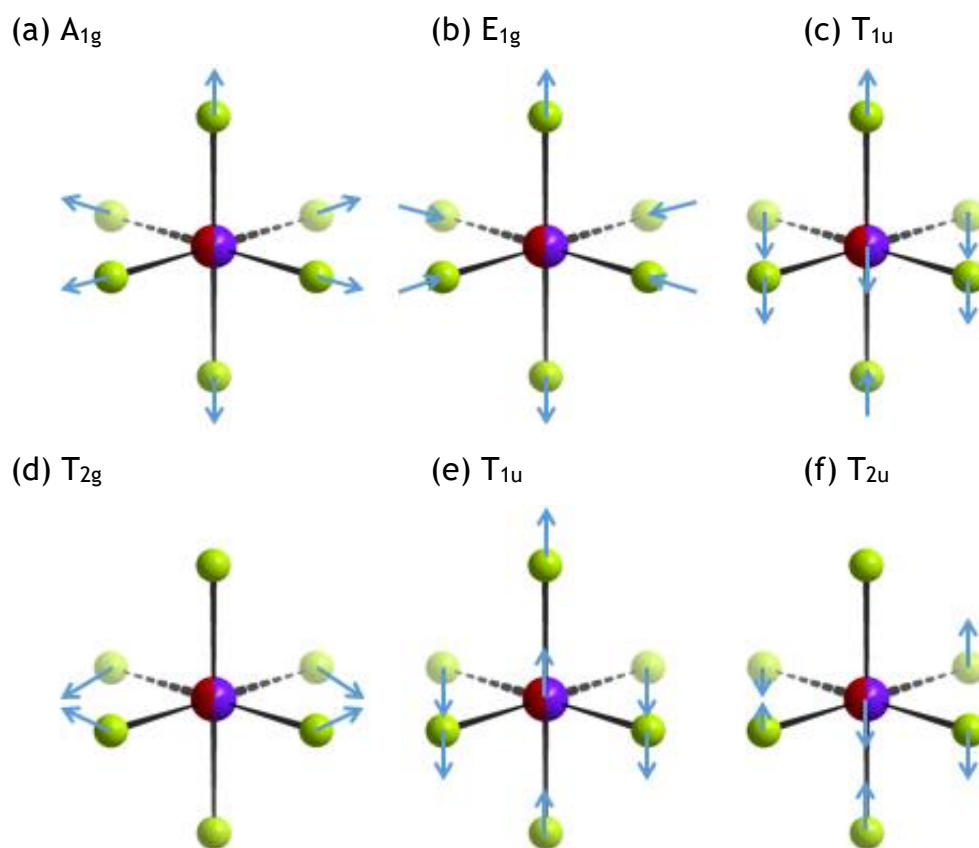


Figure 6.2-6 Normal modes of vibration of an octahedral ML_6 molecule belonging to the O_h point group. Stretching modes: (a), (b), and (c) and bending modes: (d), (e), and (f) are shown. Li/In cations are represented by red and purple spheres and Br anion by green spheres (Figure adapted from Reddy).¹⁷

Group theory indicates that a molecule of this symmetry has three Raman-active modes [$\nu_1(A_{1g})$, $\nu_2(E_g)$, $\nu_5(T_{2g})$] and two infrared-active modes [$\nu_3(T_{1u})$ and $\nu_4(T_{1u})$]. In an octahedral molecule with a centre of symmetry, all the modes which

are “g” type are Raman active and those with “u” symmetry are infrared active. The T_{2u} mode is inactive in both spectra. ¹⁵

At room temperature, bands observed in the spectrum of LiInBr_4 can be assigned to the In - Br stretching bands at 189 and 161 cm^{-1} ($\nu_1(A_{1g})$ and to $\nu_2(E_g)$, respectively) and the bending mode at 77 cm^{-1} ($\nu_5(T_{2g})$).^{16, 18-20} Above 328 K , the Raman spectra barely change in the region from 130 to 230 cm^{-1} , where the stretching bands are observed. However the relative intensities of these bands are modified (Figure 6.2-5 and Table 6.2-2). These results are in agreement with thermal analysis and ionic conductivity measurements in that they indicate a structural change in LiInBr_4 above 326 K , whereas PND did not show any major changes in the diffraction patterns (sections 6.2.3, 6.2.4 and 6.2.5).

6.2.3 Thermal analysis

The thermal stability of the RT LiInBr_4 phase was studied using thermogravimetric analysis and differential thermal analysis under flowing argon. Figure 6.2-7 shows the behaviour of the as-prepared product (**87**) when heating to 533 K at 5 K min^{-1} . These results showed that a negligible weight loss occurred under these conditions. The peak at 326 K in the DTA plot might suggest a phase transition occurring in LiInBr_4 (RT \rightarrow HT phase). Yamada *et al.* reported a phase transition at 316 K on the basis of thermal analysis and conductivity measurements.¹ The peak at 516 K in the DTA plot corresponds to LiInBr_4 melting point, in close agreement to the melting point of 520 K , reported by Yamada *et al.*¹¹

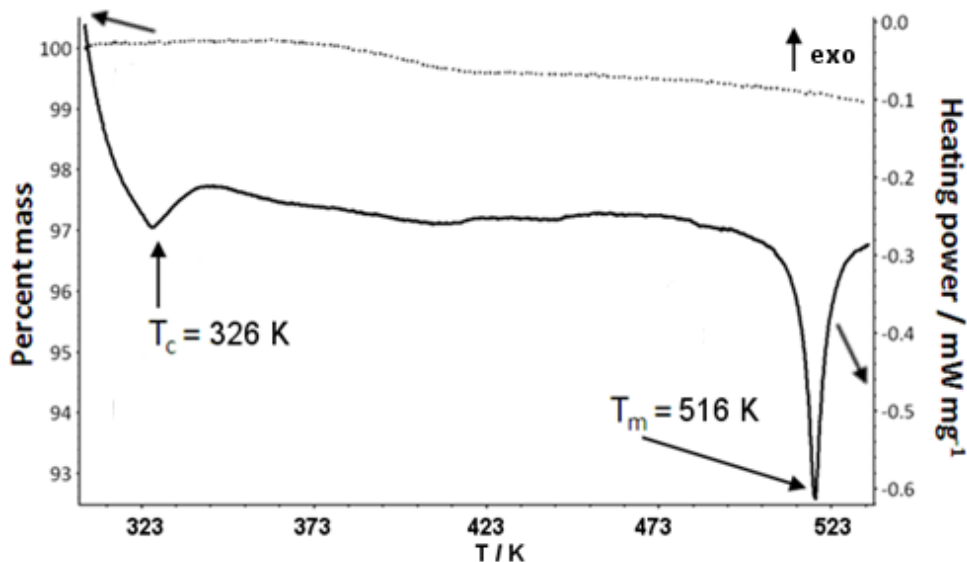


Figure 6.2-7 Typical TG-DTA plot of LiInBr_4 . STA analysis was carried out in an Ar atmosphere, heating the sample at 5 K min^{-1} from ambient temperature to 533 K. The black dotted line represents the TG curve and the solid black line represents the DTA curve.

Mass spectrometry run in combination with the thermal treatment showed that no gases were evolved during the heating process, thus corroborating the thermal stability of the sample analysed in this temperature range.

The final product was characterised using PXD. The pattern of the final compound showed that following heating (and cooling) RT - LiInBr_4 appears to retain its initial structure. However, the RT LiInBr_4 phase appears to exhibit hysteresis on heating and low cooling. Figure 6.2-8 shows the TG and DTA curves of the as-prepared product (**87**) when it was heated to 373 K at 5 K min^{-1} , and held at and holding this temperature for 20 min and subsequently cooled at 1 K min^{-1} to 306 K. These results suggested that the sample did not return from the HT to the RT LiInBr_4 phase. Due to instrumental limitations the TGA could only measure down to 305 K, and the HT \rightarrow RT transition was not detected above this temperature as the sample was cooled. Yamada *et al.* reported that the hysteresis effect was large and that the phase transition occurred at 260 K on cooling, which proved to be consistent with their conductivity measurements.¹

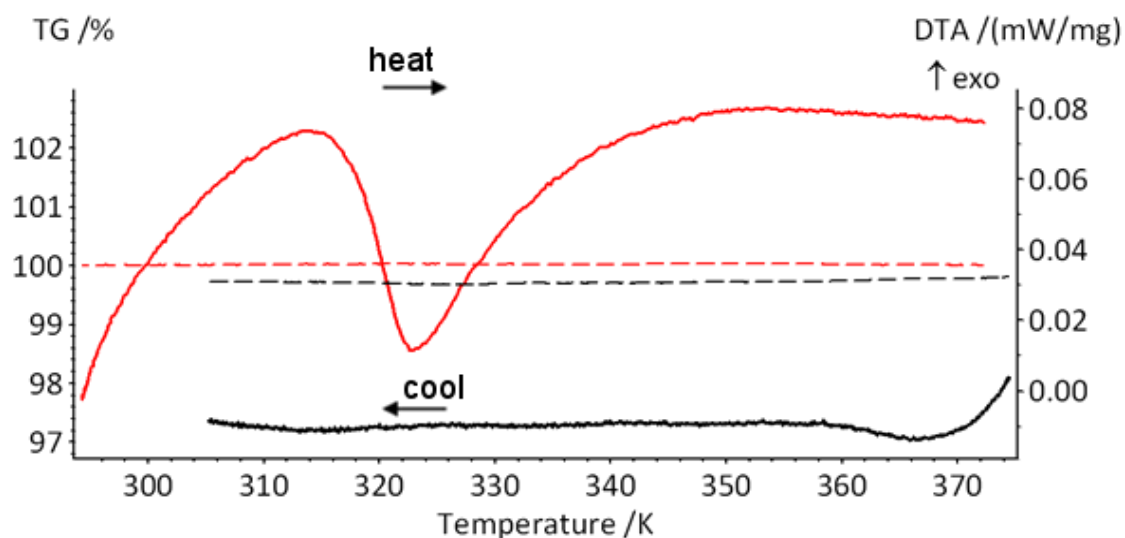


Figure 6.2-8 TG-DTA plot of LiInBr_4 on heating and cooling. STA analysis was carried out in an Ar atmosphere, heating the sample at 5 K min^{-1} from ambient temperature to 373 K, holding the temperature for 20 min (not shown) and cooled down to 305 K at 5 K min^{-1} . Red dotted line represents the TG curve and the solid red line represents the DTA curve, for heating. The black dotted line represents the TG curve and the black solid line represents the DTA curve, for cooling.

6.2.4 Electrochemical impedance spectroscopy

Conductivity measurements were performed for **87**. Impedance data analysed in the complex plane showed a semicircle at high frequencies (derived from bulk resistance, without any grain boundary contribution) and a linear response in the lower frequency range caused by the electrode contribution. The data were analysed using an equivalent electrical circuit to extract the values for the total resistivity of the material. The spectra were dominated by electrode polarization especially at high temperatures and low frequencies due to the usage of ion-blocking electrodes. An estimate of the total conductivity was made from the combination of a resistor and a constant phase element in parallel. Figure 6.2-9 shows the Nyquist plot from LiInBr_4 (**87**) at room temperature and at 353 K. Figure 6.2-10 shows the ionic conductivity of LiInBr_4 which yielded conductivities of $ca. 10^{-7} \text{ S cm}^{-1}$ at 295 K with an activation energy of 0.577(1) eV, whereas above 326 K LiInBr_4 showed a total lithium ionic conductivity of $ca. 10^{-5} \text{ S cm}^{-1}$ with a lower value of the activation energy; 0.227(1) eV where Yamada *et al.* reported 0.24 eV¹, indicating a change in the ionic conductivity mechanism (Figure 6.2-10). However higher conductivities were reported for LiInBr_4 above 326 K, $10^{-3} \text{ S cm}^{-1}$.¹

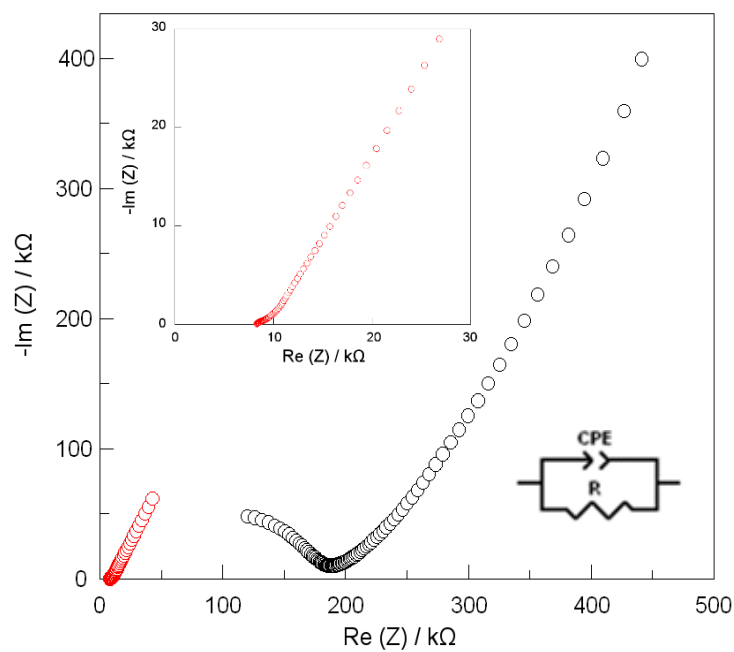


Figure 6.2-9 Nyquist plot of LiInBr_4 , 87, at room temperature (black open circles) and at 353 K (red open circles). Inset: Zoom the Nyquist plot of LiInBr_4 at 353 K.

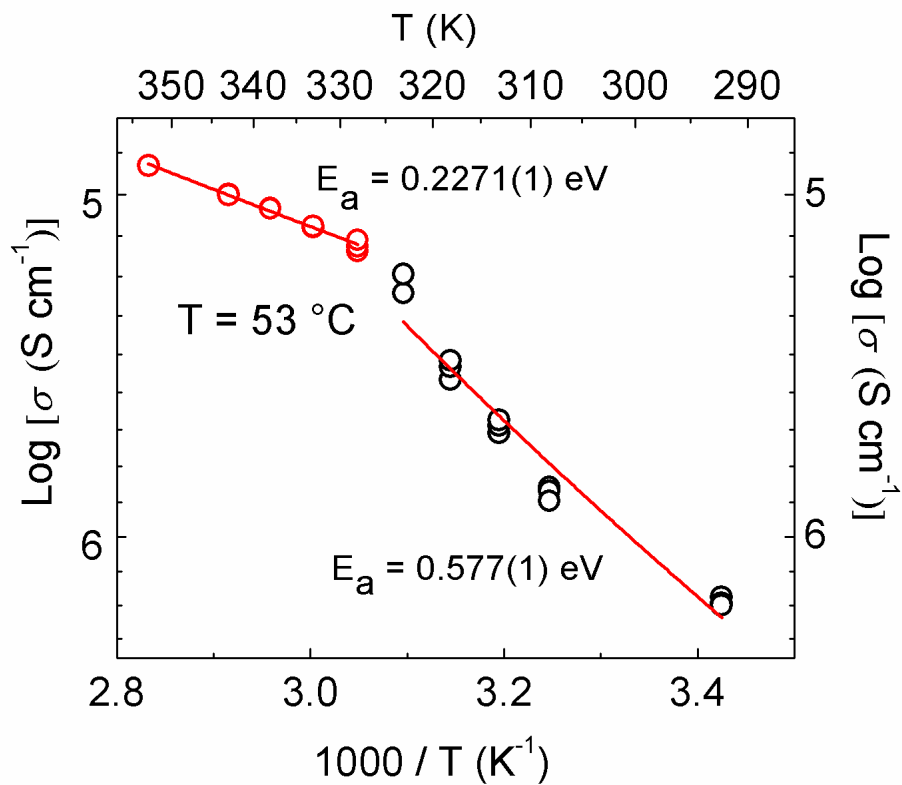


Figure 6.2-10 Plot of log conductivity as a function of temperature for LiInBr_4 on heating.

6.2.5 Powder neutron diffraction experiments

PND investigation described in this work involved in-situ characterisation of **87** following milling and heating (GEM, RAL; section 2.4). It was anticipated that PND data could provide accurate structural models for LiInBr_4 , allowing precise positions of Li and site occupancies to be determined.

6.2.5.1 Powder neutron diffraction at room temperature

Selected Rietveld refinement data for **87**, are displayed in Table 6.2-4 and the observed, calculated, and difference (OCD) plots for the data obtained are illustrated in Figure 6.2-11.

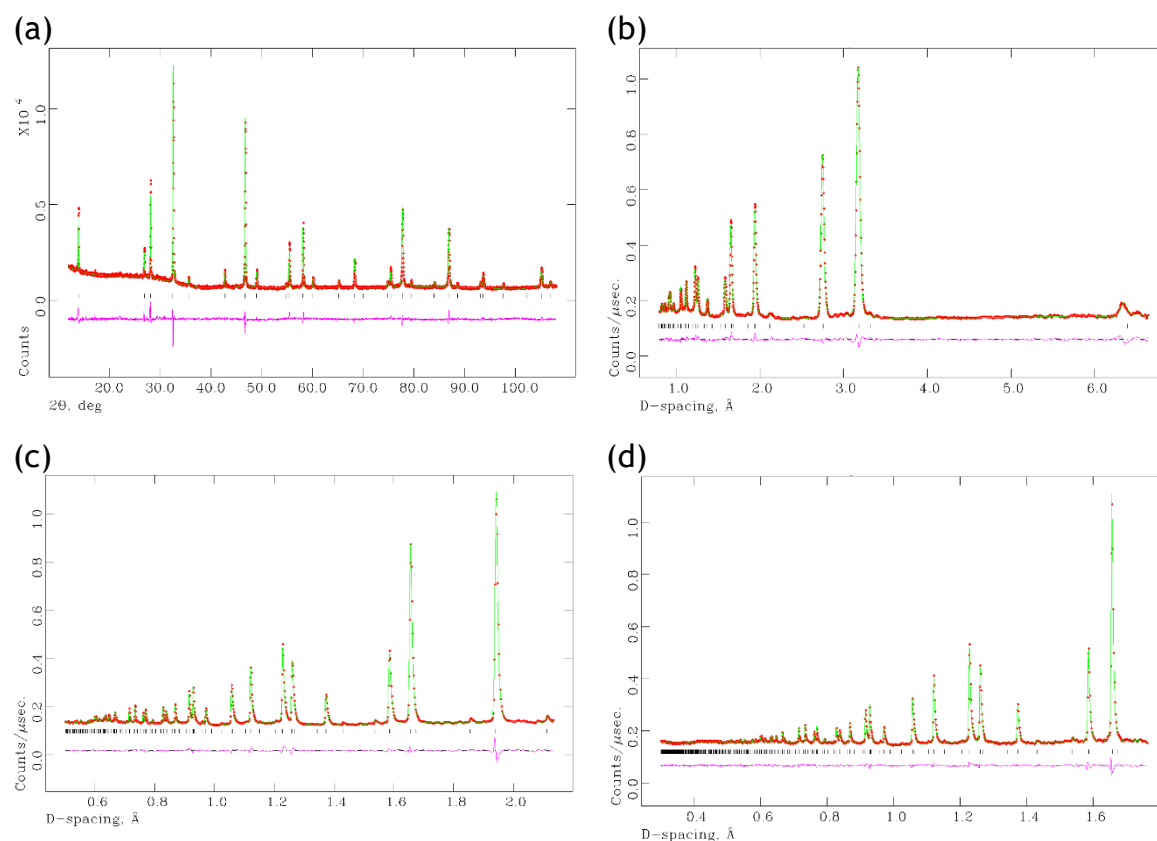


Figure 6.2-11 Profile plot from the Rietveld refinement against (a) lab powder X-ray data and (b-d) GEM ToF powder neutron diffraction data; (b) bank 3, (c) bank 5, and (d) bank 6 at room temperature (red dots: experimental profile; green line: calculated profile; pink line: difference profile; tick marks: Bragg reflections for LiInBr_4 (**87**)).

Rietveld refinement showed the presence of a single phase which we associated with RT - LiInBr_4 with a rhombohedral structure ($R\bar{3}m$). As observed in the OCD plot, the experimental data can be fitted well to the theoretical model.

Refinements were also attempted using the previously reported cubic and trigonal cells but the refinements did not converge in either case.

Table 6.2-4 Selected Rietveld refinement data from powder neutron diffraction data of the LiInBr_4 compound at room temperature (87).

Sample number	87
Empirical formula	$\text{Li}_{0.494(1)}\text{In}_{0.506(1)}\text{Br}_2$
Collection temperature / K	292
Crystal system	Trigonal
Space group	$R\bar{3}m$ (#166)
Z	3
Formula weight, M_w	221.356
Calculated density, ρ / g cm⁻³	4.447
Unit cell dimensions:	
a / Å	3.88077(8)
c / Å	19.0135(9)
V / Å³	247.986(6)
Observations, parameters	10.699, 80
R_{wp}	0.0253
R_p	0.0418
χ^2	3.274

Atomic positions and isotropic temperature factors are presented in Table 6.2-5 and selected interatomic distances and bond angles are shown in Table 6.2-6 and Table 6.2-7, respectively.

Table 6.2-5. Atom positions and isotropic temperature factors obtained from Rietveld refinement against neutron diffraction data of the LiInBr_4 compounds at room temperature (87).

Atom	Li	In	Br
Site	3b	3b	6c
<i>x</i>	1/3	1/3	2/3
<i>y</i>	2/3	2/3	1/3
<i>z</i>	1/6	1/6	0.08660(4)
100 x U_{iso} / Å	1.78(5)	1.78(5)	1.75(1)
Occupancy	0.494(1)	0.506(1)	1

Table 6.2-6 Interatomic distances in LiInBr_4 (87) from powder neutron diffraction data at room temperature.

	Bond length / Å		Bond length / Å
Li(In) – Br	2.7088(5) x 6	Br – Br	3.7802(1) x 3
Li(In) – Br	4.7326(0) x 6	Br – Br	3.8808(0) x 6
Li(In) – Br	4.8154(2) x 2	Br – Br	3.9831(9) x 3
Li(In) – Li(In)	3.8808(1) x 6		

Table 6.2-7 Bond angles in LiInBr_4 (87) from powder neutron diffraction data at room temperature.

	Bond angle / °
Br – Li(In) – Br	91.502(20)
Br – Li(In) – Br	88.497(20)
Br – Li(In) – Br	180

The RT - LiInBr_4 phase has a rhombohedral structure with $a = 3.88077(8)$ and $c = 19.0135(9)$ Å. Li atoms essentially half occupy (site occupancy of 0.494(1)) the 3b site with In (site occupancy of 0.506(1)) with the metal cations octahedrally coordinated to Br. Bromide atoms fully occupy the 6c site and are coordinated to Li/In atoms trigonally with Br-Li(In) distances of 2.7088(5) Å. The refined formula for the RT - LiInBr_4 phase (87) was $\text{Li}_{0.494(1)}\text{In}_{0.506(1)}\text{Br}_2$.

Figure 6.2-12 shows the crystal structure of the LT - LiInBr_4 phase obtained from the Rietveld Refinement.

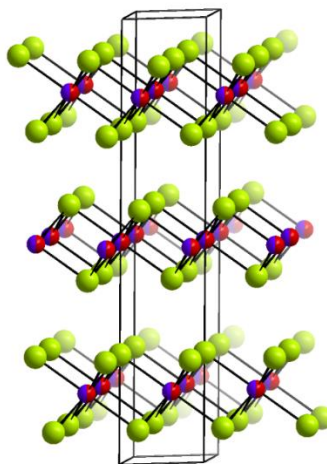


Figure 6.2-12 Proposed crystal structure for the RT – LiInBr_4 . Bromide anions are represented as green spheres. Lithium and indium cations are represented as red/purple spheres, sharing the same site.

Another ternary lithium indium bromide known is Li_3InBr_6 but only the crystal structure was reported, $C2/m$. However Li_3InCl_6 is isomorph to Li_3InBr_6 .²¹ Li_3InCl_6 possesses Cl-Cl distances from 3.52 - 3.84 Å and LiInBr_4 has Br-Br bond distances from 3.78 - 3.98 Å. Regarding Li-Li and In-In distances, for Li_3InCl_6 the values vary from 3.68 - 3.73 and 3.69 - 3.71 Å, respectively and is 3.8808(1) Å for LiInBr_4 , being the same value for Li-Li and In-In since Li and In share the same site. In-Cl and Li-Cl distances for Li_3InCl_6 fluctuate from 2.51 - 4.61 Å and 2.63 - 4.59 Å, respectively, whereas Li(In)-Br in LiInBr_4 are slightly larger, from 2.70 - 4.82 Å. No other previous article of lithium and indium bromide are reported so far. LiGaBr_4 shows Br-Br from 3.71-4.15 Å, within the range of LiInBr_4 , from 3.78 - 3.98 Å. Ga-Ga, Li-Li and Li - Ga are 4.85 Å, 4.19 Å and 3.42 - 4.47 Å, respectively, much larger than in LiInBr_4 , 3.8808(1) Å. For Br-Ga and Br-Li vary from 2.31 - 4.90 and 2.61 - 4.95 Å, respectively, Li(In)-Br in LiInBr_4 are found in the same range, 2.70 - 4.82 Å.²² Comparing LiBr with LiInBr_4 , it shows that Br-Br distances in LiBr are 3.88 Å which would be in the range of LiInBr_4 , 3.78 - 3.98 Å. Br-Li bonds vary from 2.75 - 4.76 Å, similar to LiInBr_4 that shows bond distances from 2.71 - 4.82 Å. Li-Li distances in LiBr are 3.89 Å, which are really similar for Li(In)-Li(In) in LiInBr_4 , 3.8808(1) Å (Table 6.2-6).

6.2.5.2 Powder neutron diffraction from room temperature to 353 K

Neutron diffraction patterns were recorded at various temperatures (from room temperature to 353 K, **87** and **87a-87d**) in order to follow the thermal behaviour of LiInBr_4 . Thermal evolution of the unit cell parameters and the bromide position are given in Figure 6.2-13. As expected, we observed an increase in the cell volume. The a parameter increases continuously in the whole temperature range investigated. However, the c parameter increases sharply between 292-308 K but varies less significantly above 308 K. exhibit a discontinuity over the same temperature range the bromide position also appears to, as shown in Figure 6.2-13 (d).

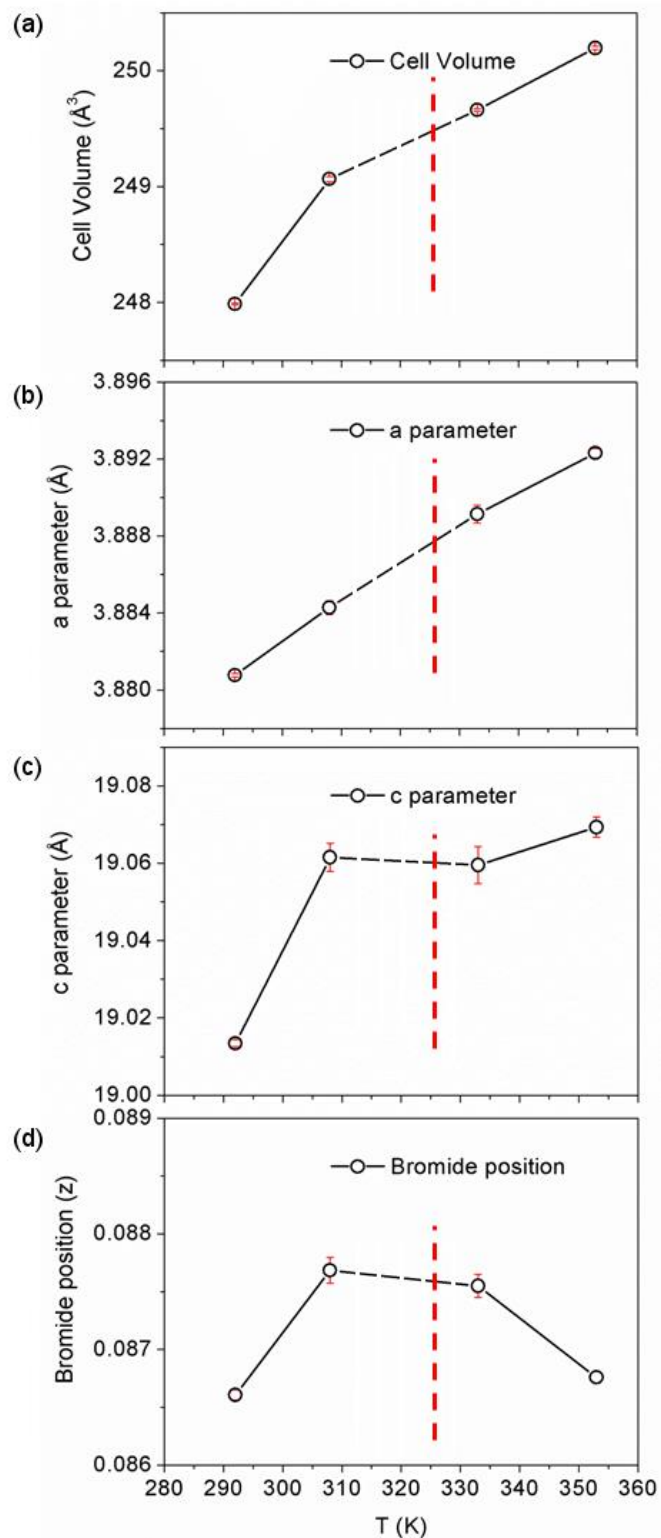


Figure 6.2-13 Variations of the unit cell parameters and the Br z coordinate on heating (87) from 292-353 K: (a) Cell Volume (b) a parameter (c) c parameter (d) bromide position. Error bars are represented in red.

At 292 K, the calculated observed Fourier Map reveals only the position of Li atoms (with an intensity of $0.728 \times 10^{-6} \text{ \AA}^{-2}$), sharing the site with In (Figure 6.2-14). At 353 K, in the calculated Fourier-difference map two new peaks emerge, located at (0, 0, 0.3196) (**Model 1**) and (1/2, 0, 1/2) (second model, Figure 6.2-16) (with intensities of -0.079 and $-0.075 \times 10^{-6} \text{ \AA}^{-2}$, respectively). These negative peaks are found above 308 K and could correspond to a new lithium site, Li2, located in between the bromide layers (Figure 6.2-15). In **Model 1**, introduction of the new Li2 site between the (Li,In)Br₆ octahedral layers (6c) allowed the stable refinement of its position and thermal factor, ($x = 1/3$, $y = 2/3$, and $z = 0.277$). The fractional occupancies of Li across the Li(In)1 and Li2 sites were refined resulting in 6 % of Li on the Li2 site.

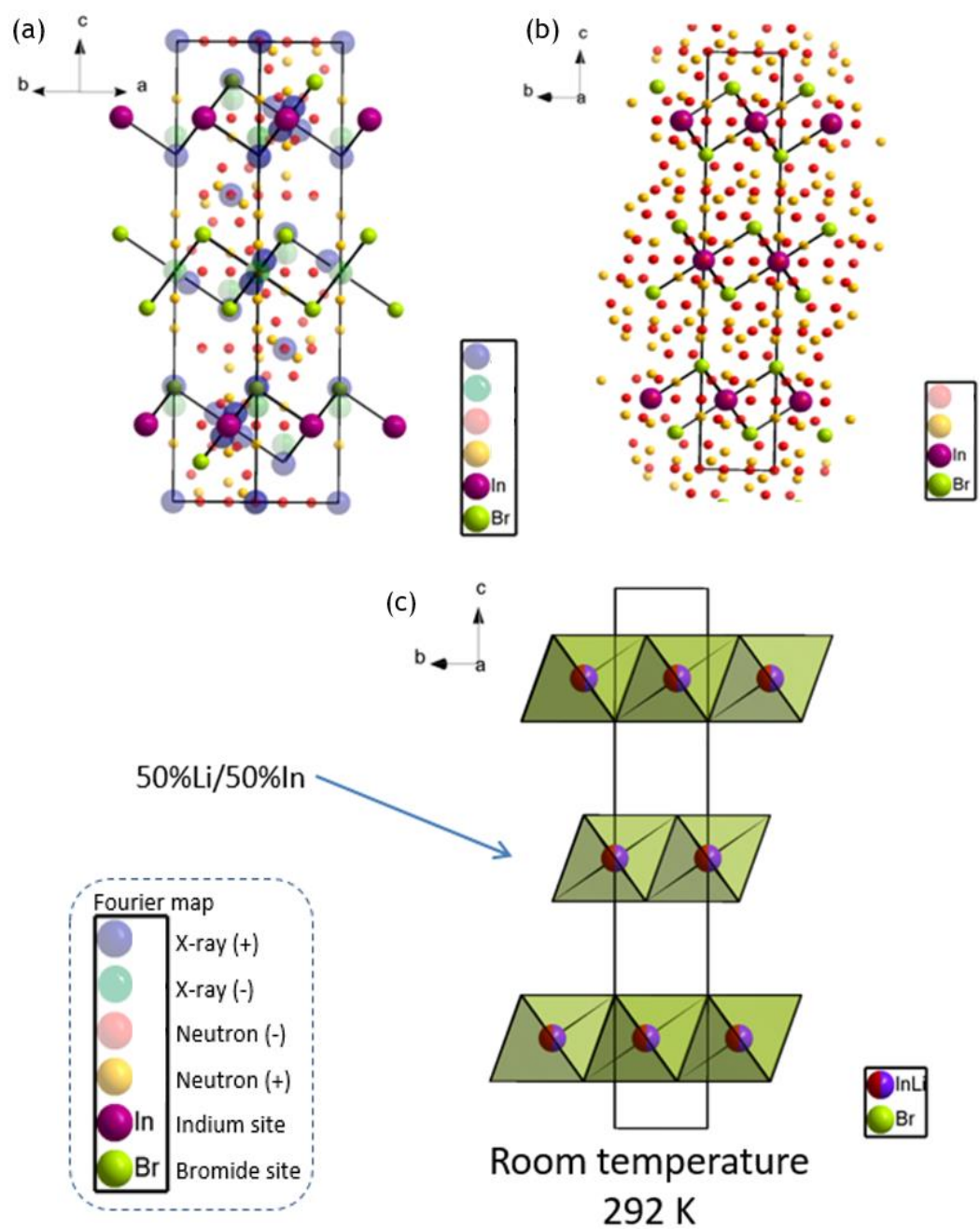


Figure 6.2-14 Fourier-observed calculation at room temperature: (a) powder X-ray data combined with powder neutron diffraction data and (b) powder neutron diffraction data. (c) Crystal structure of LiInBr_4 at room temperature.

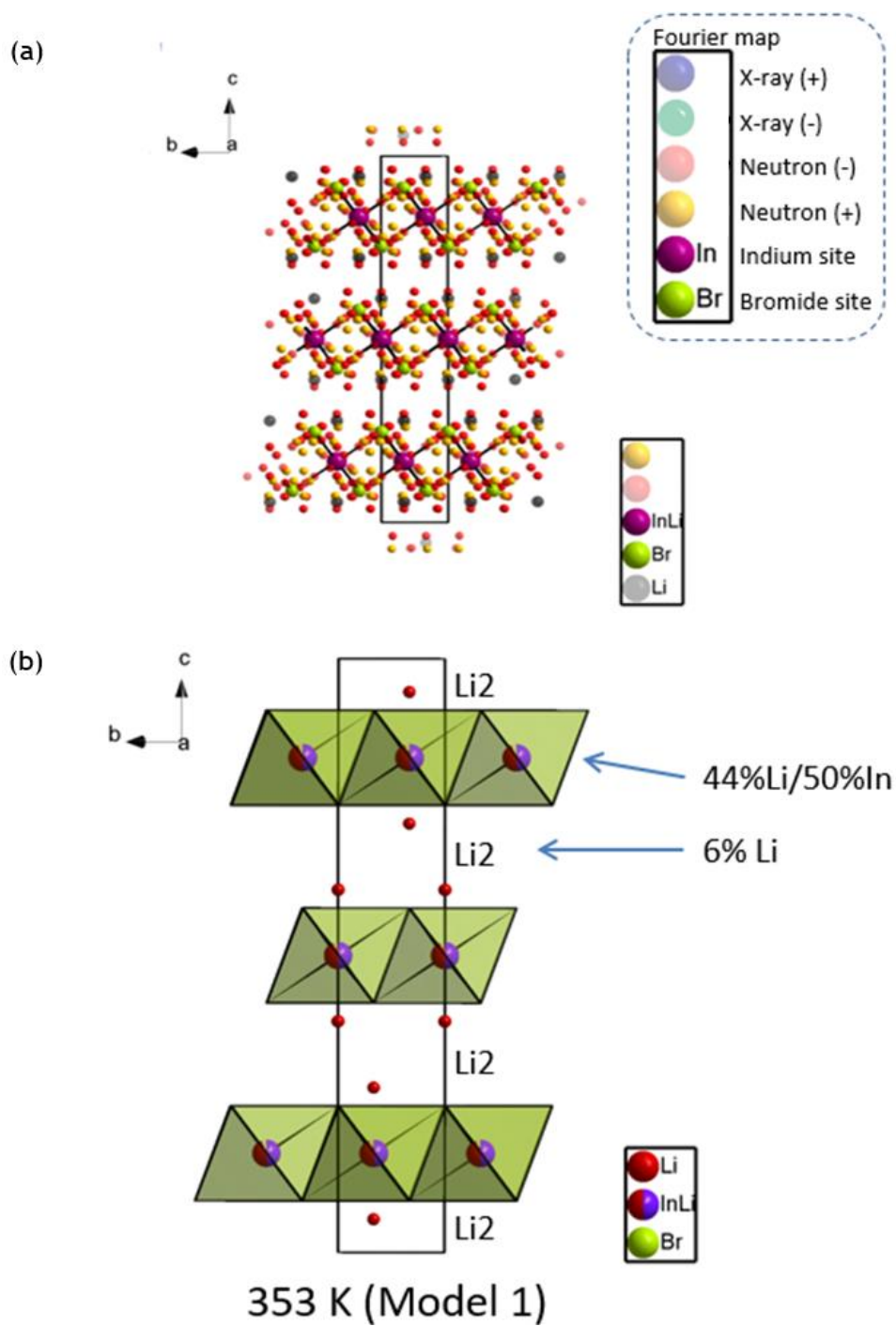


Figure 6.2-15 Fourier-observed calculation at 353 K for Model 1: (a) powder neutron diffraction data. (b) Model 1 of LiInBr_4 at 353 K.

For the second model, introduction of the new Li2 site within the (Li/In)Br₆ octahedral layers (9d site) was attempted, but the refinement was unstable and did not converge (Figure 6.2-16).

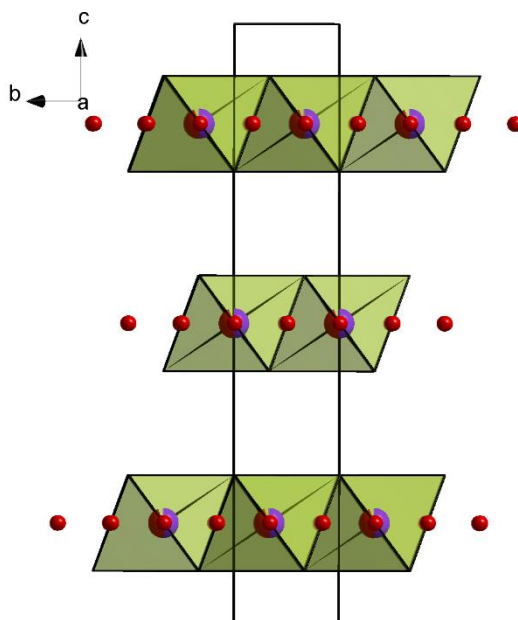


Figure 6.2-16 Second model proposed for LiInBr₄ at 353 K. Lithium and indium ions are represented as red and purple spheres. Octahedra formed by (Li/In) and bromide are presented in light green.

6.2.5.3 Powder neutron diffraction at high temperature (353 K)

Final results at 353 K are given in Table 6.2-8 and illustrated in Figure 6.2-17 showing the experimental data can be fitted well by the theoretical model. Interatomic distances and bond angles are shown in Table 6.2-10 and Table 6.2-11, respectively. For completeness, as previously, the cubic and trigonal cells from the literature were also considered as models, but the refinements did not converge in either case.^{1, 11}

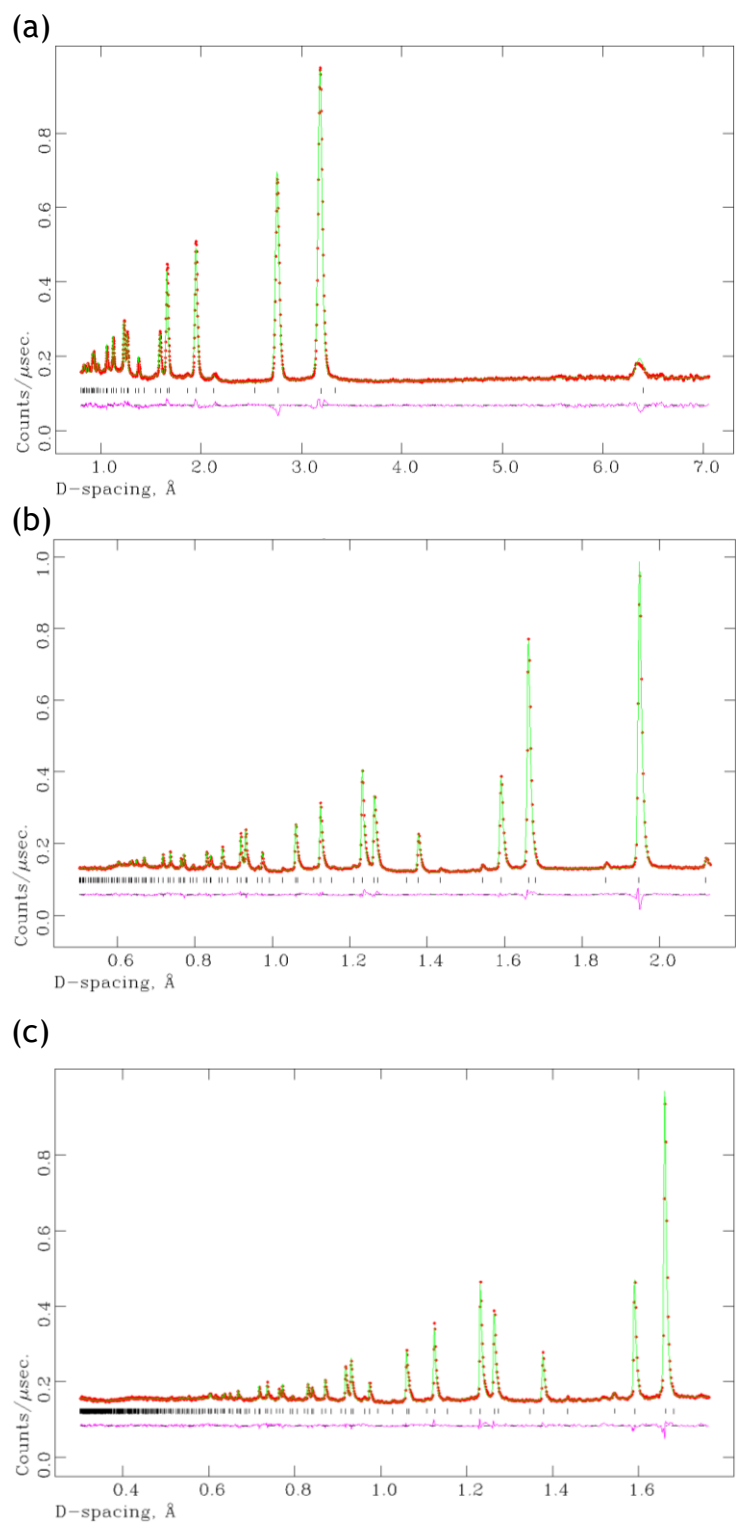


Figure 6.2-17 Profile plot for sample 87 from the Rietveld refinement against GEM ToF powder neutron diffraction data from (a) detector bank 3, (b) detector bank 5, and (c) detector bank 6 (red dots: experimental profile; green line: calculated profile; pink line: difference profile; tick marks: Bragg reflections for the LiInBr_4).

Table 6.2-8 Selected Rietveld refinement data for LiInBr₄ at 353 K (87d).

Sample number	87d
Empirical formula	[Li _{0.067}][Li _{0.433} In _{0.5} Br ₂]
Collection temperature / °C	353
Crystal system	Trigonal
Space group	$R\bar{3}m$ (#166)
Z	3
Formula weight, M_w	662.071
Calculated density, ρ / g cm⁻³	4.394
Unit cell dimensions:	
a / Å	3.8923(3)
c / Å	19.070(6)
V / Å³	250.20(2)
Observations, parameters	4901, 75
R_{wp}	0.0169
R_p	0.0135
χ^2	2.445

Table 6.2-9. Atom positions and isotropic temperature factors obtained from Rietveld refinement against powder neutron diffraction data for LiInBr₄ at 353 K (87d).

Atom	Li	Li2	In	Br
Site	3b	6c	3b	6c
x	1/3	1/3	1/3	2/3
y	2/3	2/3	2/3	1/3
z	1/6	0.273(3)	1/6	0.08666(5)
100 x U_{iso} / Å	2.04(6)	2.04(6)	2.04(6)	2.17(1)
Occupancy	0.432	0.034	0.5	1

Table 6.2-10 Interatomic distances for LiInBr₄ at 353 K (87d).

	Bond length / Å		Bond length / Å
Li(In) – Br	2.7163(6) x 6	Li2 – Li2	3.8923(1) x 6
Li(In) – Br	4.7463(3) x 6	Br – Br	3.7899(11) x 3
Li(In) – Br	4.8308(12) x 2	Br – Br	3.8923(1) x 6
Li(In) – Li(In)	3.8923(3) x 6	Br – Br	3.9965(2) x 3
Li2 – Br	2.80(5) x 1	Li(In) – Li2	2.03(5) x 2
Li2 – Li2	3.21(7) x 3	Li2 – Br	2.304(11) x 3

A slight change in the remaining space between the layers (Br-Br) was observed with heating (Table 6.2-6 and Table 6.2-10). Br-Br distances vary from 3.7802(1) - 3.9831(9) Å to 3.7899(11) - 3.9965(2) Å from 292 - 353 K, respectively. However LiInBr₄ shows a larger increment in Li(In)-Br from 292 - 353 K, from 2.7088(5) - 4.8154(2) Å to 2.7163(6) - 4.8308(12) Å. This increase in Li(In)-Br distance bonds would imply more possible voids in Li(In)Br₆ octahedra for Li⁺ mobility towards the layers (Li2). This new Li⁺ distribution in the layers could explain why an increase in the conductivity above 326 K. A decrease in the activation energy is observed when heating which could indicate that the Li⁺ motion is easier in between the layers (Li2).

Table 6.2-11 Bond angles for LiInBr₄ at 353 K (87d).

	Bond angle / °		Bond angle / °
Br – Li(In) – Br	91.526(26)	Li2 – Br – Li2	115.3(9)
Br – Li(In) – Br	88.473(26)	Li2 – Br – Li2	77.3(12)
Br – Li(In) – Br	180	Li(In) – Br – Li2	46.9(12)
Br – Li(In) – Li2	124.178(19)	Li(In) – Li2 – Br	180
Br – Li(In) – Li2	55.822(19)	Li(In) – Li2 – Br	77.3(12)
Li2 – Li(In) – Li2	180	Br – Li2 - Br	102.7(12)

6.2.6 ^7Li NMR

Figure 6.2-18 shows the ^7Li solid state NMR spectrum as a function of temperature. At 25 °C (uncalibrated probe temperature) the line is broad with no clear narrow component. By 55 °C the line shape has changed with a narrow component superimposed on a broader one. From 60-100 °C there is a slight further change of the line shape. On cooling, the multicomponent nature of the bandshape is retained to 0 °C.

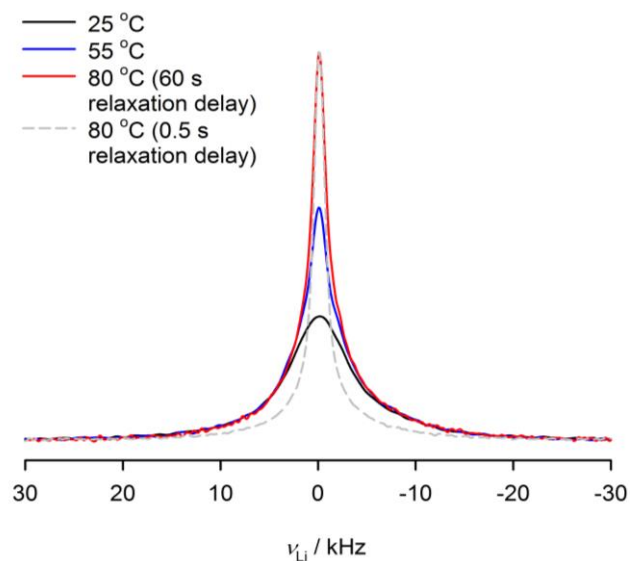


Figure 6.2-18 Linewidth as a function of temperature.

Figure 6.2-19 gives the half-height linewidth over the experimental temperature range and illustrates the changing nature of the spectrum. On heating the half-height linewidth decreases linearly with temperature. Above 50 °C, the half-height linewidth decreases drastically and then keeps constant from 60-100 °C and also when cooling to 0 °C, exhibiting hysteresis on heating and low cooling. These results are in agreement with thermal analysis. At 80 °C a second spectrum was recorded with much shorter relaxation delay of 0.5s (Figure 6.2-18). This shows a loss of a broad component in the spectrum. In this “high-temperature” regime, there are at least two types of lithium environment present. This is deduced from the number of superimposed component peaks with the same or similar half-height linewidth.

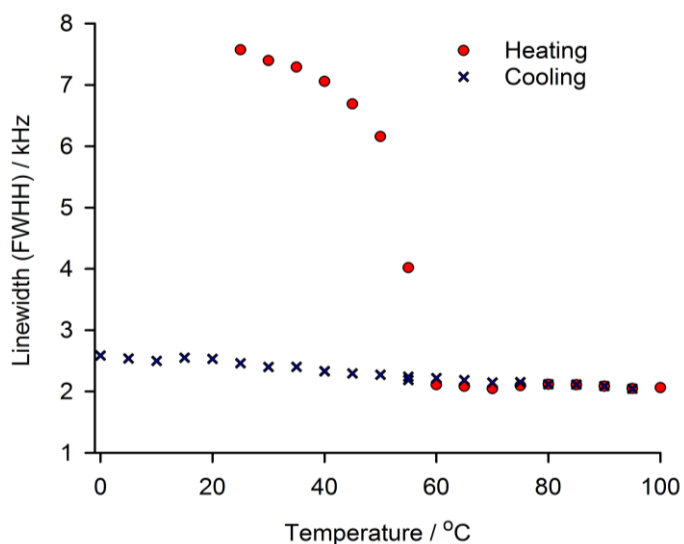


Figure 6.2-19 Half-height linewidth as a function of temperature.

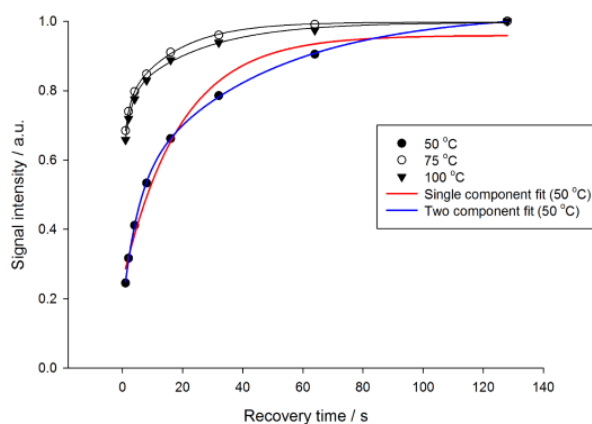


Figure 6.2-20 Fitting of the recovery curve with one and two components.

Spin-lattice relaxation time (T_1) measurements over the same temperature range provided additional insight into the nature of the sample. As indicated in Figure 6.2-20, by the spectra obtained at 50 °C, the relaxation behaviour requires at least two components in order to be able to model it with accuracy. However, at 80 °C, the recovery curve is best represented by three components as Figure 6.2-21 illustrates.

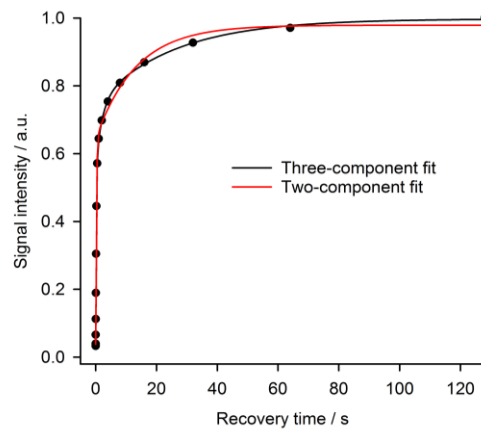


Figure 6.2-21 Two vs three component fit at 80 °C.

The change in the T_1 value is accompanied by a change in the relative populations of the three components (equation (6.1)).

$$\frac{1}{T_1} = \frac{P(1)}{T_1(1)} + \frac{P(2)}{T_1(2)} + \frac{P(3)}{T_1(3)} \quad (6.1)$$

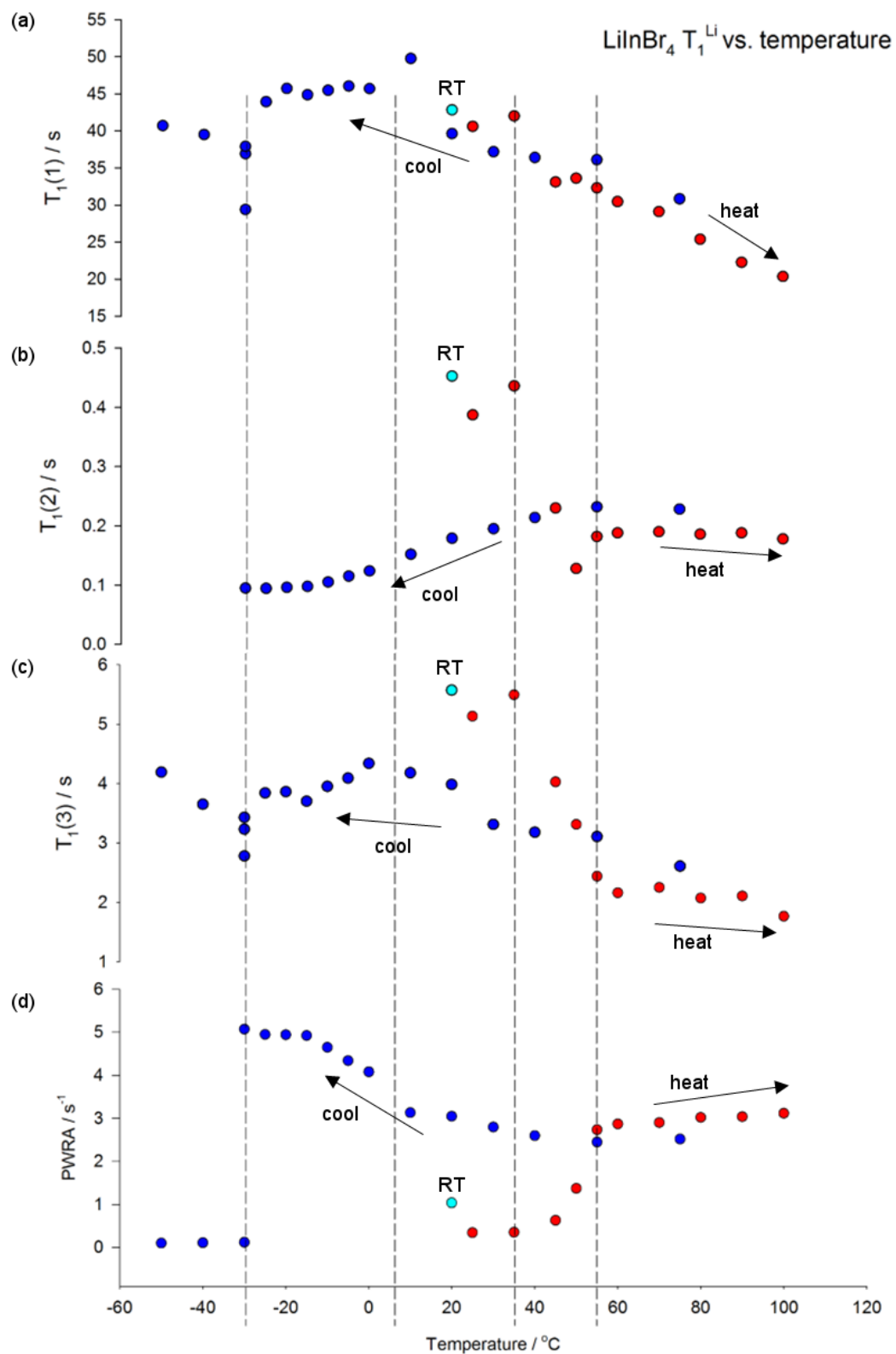


Figure 6.2-22 T₁ (spin-lattice relaxation time) measurements, divided into three components ((a) T₁(1), (b) T₁(2) and (c) T₁(3) which correspond to long, short and intermediate relaxing components) and (d) PWRA for these three components. Measurements taken at heating, cooling and at RT after the measurement was performed and are indicated in red, dark blue and cyan. Vertical lines show when there is a change in the tendency of the measurement.

Figure 6.2-22d shows the population weighted relaxation rate average (PWRA) for these three components as a function of temperature. The step change in behaviour between 40 and 60 °C on heating is clear as is the relative insensitivity to changing temperature above 60 °C. There is only a slight change in the PWRA on cooling from 100 to 10 °C. On further cooling to -15 °C, however, there appears to be a steeper rate of change in the relaxation behaviour (largely associated with a loss of the fastest relaxing component ($T_1(2)$), Figure 6.2-22b). These facts would be due to the large hysteresis effect. These results would be in agreement with Yamada *et al.* report where the thermal analysis showed an exothermic peak around -13 °C in the cooling process. The conductivity results also showed a decrease in the ionic conductivity at the same temperature.¹ At -30 °C the fast relaxing (lowest linewidth, $T_1(2)$) component is no longer detectable and the relaxation recovery curve is fitted to two components only and the bandshape returns to its original form.

The long $T_1(1)$ component appears to behave in an approximately linear fashion over the temperature range from 25 - 100 °C (Figure 6.2-22a). Producing an Arrhenius plot for these points gives an approximate straight line which can be fitted to give a gradient proportional to the activation energy for the process driving this relaxation (Figure 6.2-23). For the slowest relaxing component ($T_1(1)$) it was possible to extract an activation energy of 0.09 ± 0.007 eV over the temperature range 25 to 100 °C (Figure 6.2-23). E_a obtained from conductivity measurements were slightly bigger, 0.55 and 0.22 eV below and above the phase transition, respectively. When analysing diffusion ^7Li NMR rate peaks, we expect activation energies being much smaller than those probed by conductivity. This is due to the fact that NMR is in general sensitive to the local jump process rather than to long-range ion transport.²³

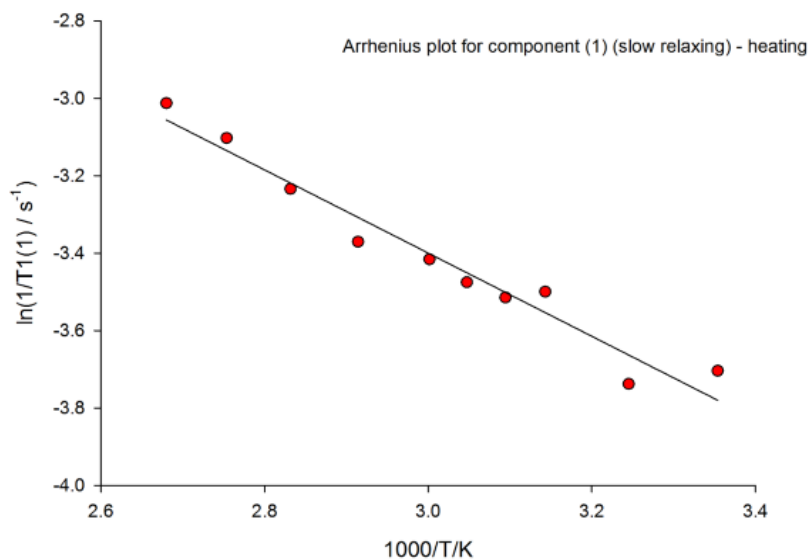


Figure 6.2-23 Arrhenius plot for component T₁(1) (slow relaxing) – heating.

From our results alone we are confident that there are (at least) two Li environments above 50 °C. The slowly relaxing, broader lined one (that is present at all temperatures) is consistent with lithium in the layers sharing the sites with indium. The faster relaxing, narrower lined (more mobile species) one above 50 °C is consistent with the interlayer lithium environment that occurs above the RT → HT phase transition.

6.3 Conclusions

A rhombohedral phase of LiInBr₄ has been isolated and characterised at room temperature. The Br layers are displaced by a distance of 3.9831(9) Å from each other at room temperature. This implies that there is substantial space remaining in the structure which lithium could occupy. However no lithium was observed between the layers at room temperature. Analysis of the Bragg scattering up to 353 K shows that the material retains a rhombohedral structure, although thermal analysis, Raman spectroscopy and ionic conductivity measurements suggest significant structural perturbations in the material upon heating. An in-depth study into bond distances shows that Br-Br do not significantly change when heating, Br-Br distances vary from 3.7802(1) - 3.9831(9) Å to 3.7899(11) - 3.9965(2) Å from 292 - 353 K, respectively. However Li(In)-Br undergo a larger increase, from 2.7088(5) - 4.8154(2) Å to 2.7163(6)

- 4.8308(12) Å. This increase in Li(In)-Br distance bonds shows more possible voids in Li(In)Br₆ octahedra for Li⁺ mobility towards the layers (Li2). This new Li⁺ distribution in the layers could explain the increase in the conductivity above 326 K. A decrease in the activation energy is observed when heating, which could indicate that the Li⁺ motion is easier in between the layers (Li2), in the space that exists between the layers.⁷Li NMR measurements were undertaken and revealed the possibility of (at least) two different sites for the lithium atoms at high temperature (above 326 K).

Overall, the structure of LiInBr₄ has been resolved at room and high temperature. Considering all the results, it is possible to confirm that LiInBr₄ shows enhanced conductivity at high temperature due to local structural perturbations which facilitate easier pathways for lithium motion. The final structural characterisation would not have been possible without using all the various techniques. In this specific case all of them complement each other. Raman spectra of LiInBr₄ shows a slightly change in Li(In)-Br vibrations on heating, indicating these local perturbations when RT → HT. The same phenomenon could be observed with thermal analysis, conductivity measurements and ⁷Li NMR.

6.4 References

1. K. Yamada, K. Kumano and T. Okuda, *Solid State Ionics.*, 2006, **177**, 1691-1695.
2. M. Matsuo, Y. Nakamori, S. Orimo, H. Maekawa and H. Takamura, *Appl. Phys. Lett.*, 2007, **91**, 1-3.
3. H. Oguchi, M. Matsuo, J. S. Hummelshoj, T. Vegge, J. K. Nørskov, T. Sato, Y. Miura, H. Takamura, H. Maekawa and S. Orimo, *Appl. Phys. Lett.*, 2009, **94**, 1-4.
4. D. Sveinbjornsson, J. S. G. Myrdal, D. Blanchard, J. J. Bentzen, T. Hirata, M. B. Mogensen, P. Norby, S. I. Orimo and T. Vegge, *J. Phys. Chem. C*, 2013, **117**, 3249-3257.
5. T. Sato, K. Ikeda, H. W. Li, H. Yukawa, M. Morinaga and S. Orimo, *Mater. Trans.*, 2009, **50**, 182-186.
6. H. Oguchi, M. Matsuo, T. Sato, H. Takamura, H. Maekawa, H. Kuwano and S. Orimo, *J. Appl. Phys.*, 2010, **107**, 1-3.
7. A. J. Downs, 1993, ISBN 978-0-7514-0103-5, Chemistry of Aluminium, Gallium, Indium and Thallium, Springer Netherlands.
8. A. C. Hannon, *Nucl. Instrum. Meth. A.*, 2005, **551**, 88-107.
9. A. C. Larson and R. B. Von Dreele, 1994, General Structure Analysis System (GSAS), Los Alamos National Laboratory Report LAUR, 86-748.
10. B. H. Toby, *J. Appl. Crystallogr.*, 2001, **34**, 210-213.
11. K. Yamada, 2006, Annual research report, 222.
12. <http://icsd.cds.rsc.org/search/basic.xhtml>, accessed on 3rd September 2015.
13. A. R. West, 1988, ISBN 0-471-91798-2, Basic solid state chemistry. Jonh Wiley & Sons Ltd.
14. S. Matsuyama, Y. Yamane and K. Yamada, 2009, Annual report, 49-50.
15. N. N. Greenwood, D. J. Prince and B. P. Straughan, *J. Chem. Soc. A*, 1968, 1694-1696.

16. L. G. Waterwor and I. J. Worrall, *Inorg. Nucl. Chem. Lett.*, 1972, **8**, 123-125.
17. K. V. Reddy, 2005, ISBN 812241142, *Symmetry and spectroscopy of molecules*, New Age International, Chapter 78.
18. J. E. Davies, L. G. Waterwor and I. J. Worrall, *J. Inorg. Nucl. Chem.*, 1974, **36**, 805-807.
19. J. M. Winfield and M. G. H. Wallbridge, *Annu. Rep. Prog. Chem., Sect. A. Inorg. and Phys. Chem.*, 1973, **70**, 279-315.
20. W. Bues, Z. Akhras and G. Okon, *Z. Anorg. Allg. Chem.*, 1976, **425**, 193-199.
21. M. O. Schmidt, M. S. Wickleder and G. Meyer, *Z. Anorg. Allg. Chem.*, 1999, **625**, 539-540.
22. Y. Tomita, H. Ohki, K. Yamada and T. Okuda, *Solid State Ionics.*, 2000, **136**, 351-355.
23. A. Dunst, V. Epp, I. Hanzu, S. A. Freunberger and M. Wilkening, *Energy Environ. Sci.*, 2014, **7**, 2739-2752.

7. Conclusions

The work described in this thesis covers investigations into the synthesis and characterisation on LiBH_4 - based compounds, complex phases based on lithium ammonia borane and LiInBr_4 materials aid their use as potential solid state electrolytes.

Firstly, the hexagonal phase of LiBH_4 has been stabilised and isolated at room temperature by halide substitution over a compositional range $\text{Li}(\text{BH}_4)_{1-x}\text{Br}_x$ ($0.29 \leq x \leq 0.50$). Fast lithium ion conductivity is retained in these phases, although the value of the total conductivity is reduced as the bromide content increases above $x = 2/7$. There is considerable disorder in both the position and orientation of the anions in this structure leading to highly anisotropic distribution of lithium scattering. The Br^- and BH_4^- anions are displaced by a distance of 0.31 \AA from each other in the crystallographic model with the latter exhibiting orientational disorder which can only be satisfactorily modelled using an inversion of the deuterium atoms. This implies substantial rotation of the BH_4^- units although not the free spherical rotation which has been observed in other complex anion fast ion conductors. Analysis of the Bragg scattering up to 573 K shows that the material retains this structure, although the reduced intensity of the Bragg reflections does suggest increasing disorder (loss of long range order) in the material with heating. Diffraction data collected on cooling the material showed that the key features of the crystalline structure are retained down to at least 220 K . By 150 K B and Br atoms appear to exchange positions. At $< 150 \text{ K}$, the positional disorder of the lithium atoms is removed and therefore lithium only occupies one site in the structure. No crystallographic transition to a lower symmetry structure was observed on cooling to 2 K . Consequently $[\text{BD}_4]^-$ units do not exhibit any disordering at low and high temperature up to 393 K . Overall, the high temperature phase LiBH_4 has been stabilised at room temperature and has been studied in a wide range (from $2\text{-}393 \text{ K}$). It was anticipated that these data would give insight about the role of ‘paddlewheel’ versus ‘percolation’ mechanisms for Li^+ transport within complex anion lattices. For instance, materials such as Li_2SO_4 or Li_3PO_4 are not only cation conductors, but also plastic crystals, since the anions exhibit dynamic rotational disorder. Part of the motivation for the study of these compounds, has arisen from a dispute about a

possible cation mobility enhancement by dynamic coupling of cation migration and anion reorientation. Proponents of this coupling model have coined the term paddle-wheel mechanism. However the percolation theory is related to effects of variable range interactions in disordered systems. In this project, we suggest the percolation instead of the paddle wheel mechanism for Li^+ transport within the hexagonal structure of LiBH_4 . A randomly disordered arrangement of bromide and $(\text{BH}_4)^-$ was observed facing “up” and “down”. The Fourier map calculations, from neutron powder diffraction studies, showed defined deuterium positions in the studied range (2-393 K). Therefore we conclude that BD_4^- units have a disordered arrangement with fixed deuterium positions.

Secondly, the stabilization of the HP phase of LiBH_4 at ambient pressure is a challenge. Herein we report the synthesis of the HP phase of LiBH_4 that has been stabilised with Na^+ at room temperature and ambient pressure and achieves high ionic conductivity. In this chapter the results from the three different approaches used to stabilise the HP - LiBH_4 were discussed (**Methods 1, 2, and 3**). **Method 3** relied on the use of HT - LiBH_4 phases as precursors in mixtures with NaBH_4 . In this way the halide to be substituted is already incorporated in the precursor. As in **Method 1**, NaBH_4 was used as a “host” for the Li cations. This is an example of “chemical pressure”, whereby substitution of smaller ions mimics the action of high pressure by condensing a phase further. These materials were studied with two different halides, Br^- and I^- . For Br^- , a single composition was studied and it showed higher ionic conductivity than (the commercial) NaBH_4 itself by *ca.* 3 orders of magnitude at 413 K. For I^- , seven different compositions were studied. Conductivity measurements were performed for each of the samples and the optimum composition was obtained contains 16% of iodide. This showed ionic conductivity *ca.* 4 orders of magnitude higher than NaBH_4 at 413 K. In comparison with the parent borohydrides, the halides showed higher activation energies and higher conductivities. Higher activation energies could be due to partial occupation of isovalent elements in the same sites. As predicted in the literature for lithium compounds with the rock-salt type structure (LiX where $X = \text{F}, \text{Cl}, \text{Br}, \text{and I}$), the migration energies show a tendency to decrease with the increase in the periodic number of the halide in the Periodic table. In

conclusion, larger anions in a rock salt structure allow Li^+ ions to jump through the middle of the cell because of their larger open channels.

Thirdly, lithium ammonia borane solid solutions were proposed for the first time as solid state electrolytes. Different lithium ammonia borane complexes were discussed as possible candidates for solid state electrolytes for lithium ion batteries. This study showed that ($[\text{LiBH}_4]_2[\text{NH}_3\text{BH}_3]$, $\text{Li}(\text{BH}_3\text{NH}_2\text{BH}_2\text{NH}_2\text{BH}_3)$, $[\text{LiI}][\text{NH}_3\text{BH}_3]$, and $[\text{LiI}][\text{NH}_3\text{BH}_3]_2$) possessed the highest thermal stability. Ionic conductivity measurements were performed for the four materials. Pseudo-Layered ammonia borane compounds ($[\text{LiBH}_4]_2[\text{NH}_3\text{BH}_3]$ and $[\text{LiI}][\text{NH}_3\text{BH}_3]_2$) showed better performance than $\text{Li}(\text{BH}_3\text{NH}_2\text{BH}_2\text{NH}_2\text{BH}_3)$ and $[\text{LiI}][\text{NH}_3\text{BH}_3]$ which did not show the ammonia borane hydrides as layers. The formation of a pseudo-layer can improve the ionic conductivity such as for $[\text{LiBH}_4]_2\text{NH}_3\text{BH}_3$ and $\text{LiI}[\text{NH}_3\text{BH}_3]_2$. However it is also important the presence of abundant interstitial sites of large volume enhancing the ionic conductivity. However materials with interstitial sites of small volume show much lower ionic conductivity such as $\text{Li}(\text{BH}_3\text{NH}_2\text{BH}_2\text{NH}_2\text{BH}_3)$ and $\text{LiI}[\text{NH}_3\text{BH}_3]$. $\text{LiI}[\text{NH}_3\text{BH}_3]_2$ with less carriers than $\text{LiI}[\text{NH}_3\text{BH}_3]$ shows better ionic conductivity implying that for these materials the pseudo-layer structure makes more impact in the total ionic conductivity than the relative Li amount.

Structural analysis of the new materials synthesised, $\text{LiI}[\text{NH}_3\text{BH}_3]$ and $\text{LiI}[\text{NH}_3\text{BH}_3]_2$, showed no exchange in the N and B positions in the ammonia borane. This could indicate that N and B are fairly static and there is no NH_3BH_3 reorientation. In conclusion, Li motion in these materials could possibly be due to the structural features of Li-site sublattice, such as short Li-Li distances and abundant interstitial sites of large volume.

Fourthly, from all of the halocomplex lithium salts ($M^I M^{III} X_4$, where ($M^I = \text{Li}$, $M^{III} = \text{Al}$, Ga and In , $X = \text{Cl}$, Br and I), LiInBr_4 was the most interesting material. LiInBr_4 is the only halocomplex reported so far which shows a readily accessible phase transition and high ionic conductivity in similarity to LiBH_4 . In this section we discussed the nature of the phase transition and the distribution of defects using different techniques. Neutron powder diffraction suggested a rhombohedral cell with the space group $R\bar{3}m$. The LiInBr_4 structure consists of $(\text{Li}, \text{In})\text{Br}_6$ octahedral layers,

with a distance of 3.9831(9) Å from each other at room temperature. However none of the lithium was observed in the in-between layers, at room temperature. This model was confirmed with solid state ^7Li NMR studies. At higher temperatures, “above the phase transition temperature”, neutron powder diffraction data and ^7Li NMR studies showed that a proportion of Li^+ moved into the in-between $(\text{Li}/\text{In})\text{Br}_6$ octahedral layers explaining the increase in ionic conductivity. Overall, the structure of LiInBr_4 has been resolved at room and high temperature. Considering all the results, it is possible to confirm that LiInBr_4 shows enhanced conductivity at high temperature due to local structural perturbations which facilitate easier pathways for lithium motion. The final structural characterisation would not have been possible without using all the various techniques. In this specific case all of them complement each other. Raman spectra of LiInBr_4 shows a slightly change in $\text{Li}(\text{In})\text{-Br}$ vibrations on heating, indicating these local perturbations when $\text{RT} \rightarrow \text{HT}$. The same phenomenon could be observed with thermal analysis, conductivity measurements and ^7Li NMR.

Overall, the syntheses of novel lithium ion conductors with potential for development as solid state electrolytes have been performed, introducing new species such as ammonia borane, never considered as possible components before. Different routes have been proposed for the stabilisation of high symmetry, potentially high conductivity phases at room temperature. Moreover, the structural analysis of different materials has been performed in order to study in detail the lithium migration pathways in solid state electrolytes.

8. Appendices

8.1 Appendix A: Tables and Figures for Chapter 3

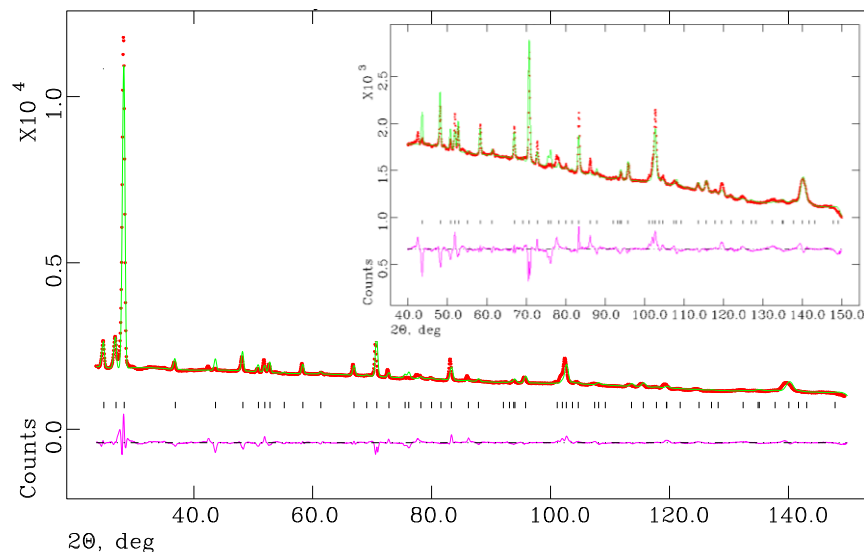


Figure 8.1-1 Rietveld profile fits for high-resolution neutron powder diffraction data collected from D20 from ${}^7\text{Li}({}^{11}\text{BD}_4)_{2/3}\text{Br}_{1/3}$ at 50 K (17c). Measured data are shown as dots, the calculated profile is shown by a solid line through the measured data. The difference profile is shown along the bottom of the plot. Vertical bars represent the reflection positions for the phase.

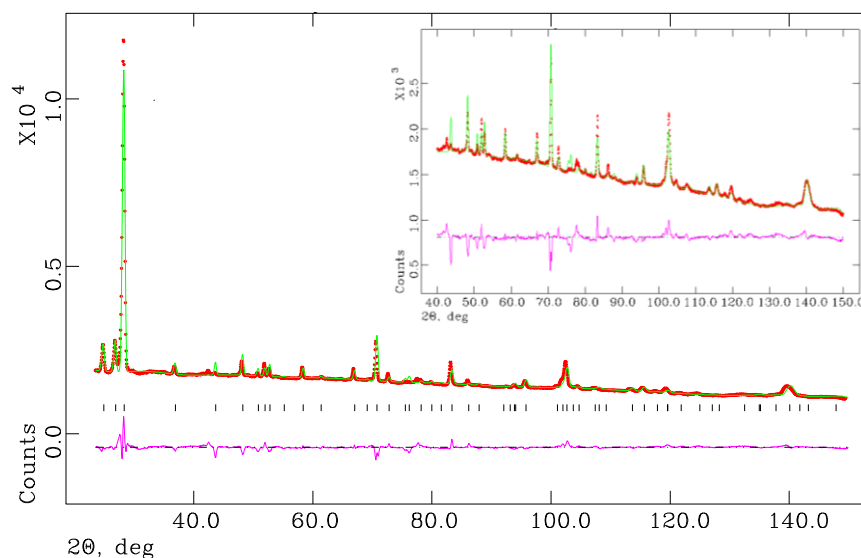


Figure 8.1-2 Rietveld profile fits for high-resolution neutron powder diffraction data collected from D20 from ${}^7\text{Li}({}^{11}\text{BD}_4)_{2/3}\text{Br}_{1/3}$ at 10 K (17d). Measured data are shown as dots, the calculated profile is shown by a solid line through the measured data. The difference profile is shown along the bottom of the plot. Vertical bars represent the reflection positions for the phase.

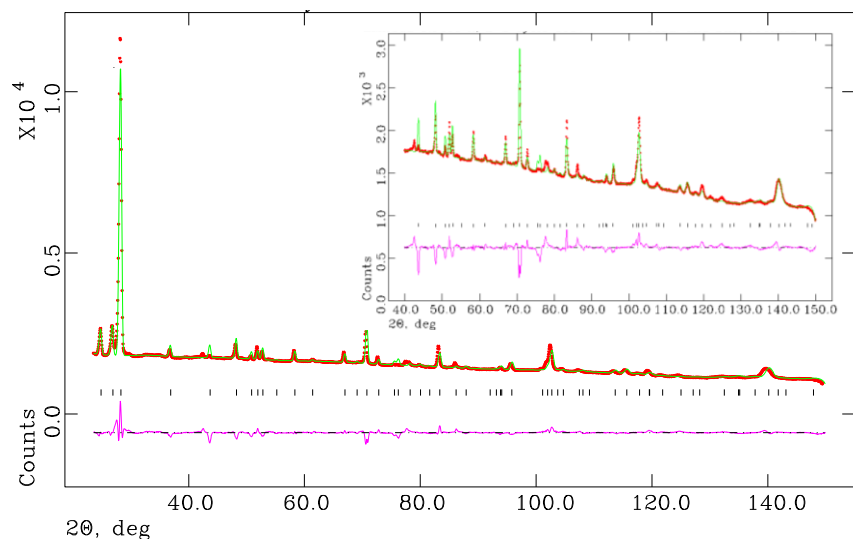


Figure 8.1-3 Rietveld profile fits for high-resolution neutron powder diffraction data collected from D20 from ${}^7\text{Li}({}^{11}\text{BD}_4)_{2/3}\text{Br}_{1/3}$ at 2 K (17e). Measured data are shown as dots, the calculated profile is shown by a solid line through the measured data. The difference profile is shown along the bottom of the plot. Vertical bars represent the reflection positions for the phase.

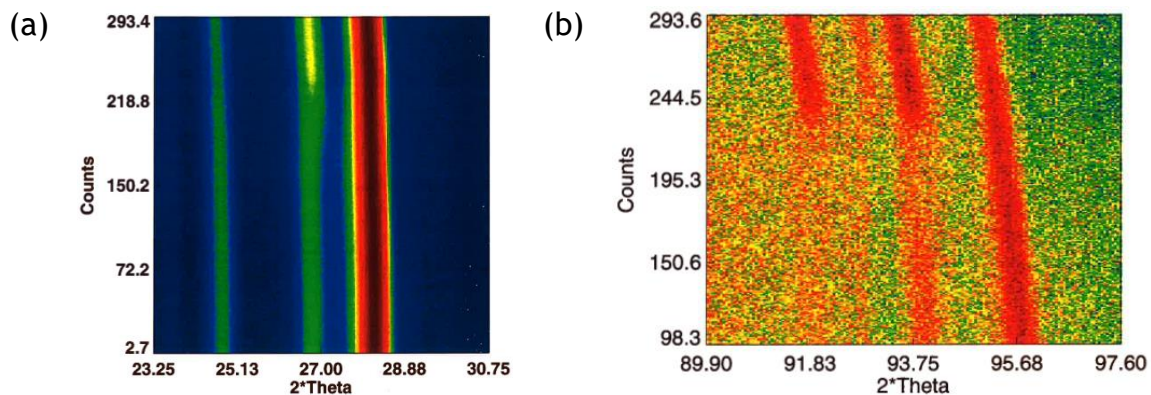


Figure 8.1-4 Diffraction pattern on cooling from ${}^7\text{Li}({}^{11}\text{BD}_4)_{1-x}\text{Br}_x$ from room temperature to 2 K. Data collected at ILL (17).

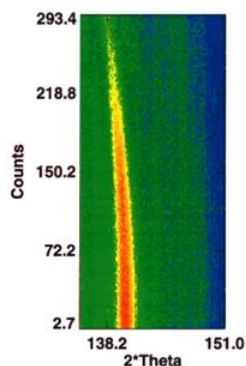


Figure 8.1-5 Diffraction pattern on cooling from room temperature to 2 K. Data collected at ILL (17).

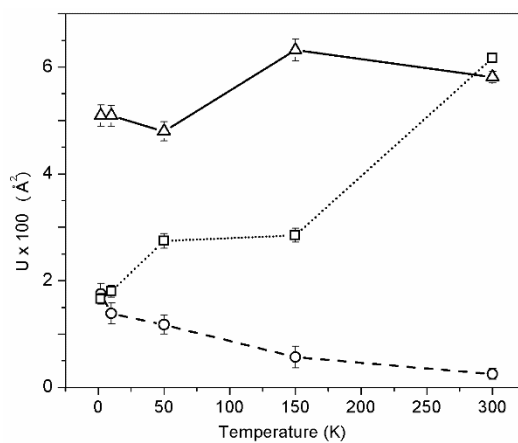


Figure 8.1-6 Thermal factors of deuterium, boron/bromide and lithium atoms represented with triangles, squares, and circles, respectively (17). Error bars are represented.

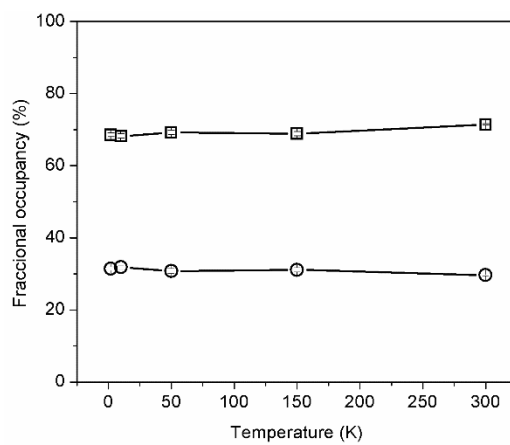


Figure 8.1-7 Fractional occupancy of the two tetrahedra units (BH₄⁻) (17).

8.2 Appendix B: Tables and Figures for Chapter 4

Table 8.2-1 Selected Rietveld refinement data from PXD data of the $\text{Li}_{0.5}\text{Na}_{0.5}(\text{BH}_4)_{0.84}\text{Br}_{0.16}$ (47c) compound at room temperature.

Sample number	47c
Empirical formula	$\text{Li}_{0.5}\text{Na}_{0.5}(\text{BH}_4)_{0.84}\text{Br}_{0.16}$
Collection temperature / °C	20
Crystal system	Cubic
Space group	$Fm\bar{3}m$
Z	4
Unit cell formula weight, M_w	1.083
Calculated density, ρ / g cm ⁻³	148.125
Unit cell dimensions:	
a / Å	6.1021(1)
V / Å ³	227.22(1)
Observations, parameters	4847, 32
R_{wp}	0.0239
R_p	0.0183
χ^2	1.688

Table 8.2-2 Complete bond lengths $\text{Li}_{0.5}\text{Na}_{0.5}(\text{BH}_4)_{0.84}\text{Br}_{0.16}$ (47c) powder diffraction data at room temperature.

Bond length / Å	
Li(Na)–B(Br)	3.05106(5)

Table 8.2-3 Complete bond angles $\text{Li}_{0.5}\text{Na}_{0.5}(\text{BH}_4)_{0.84}\text{Br}_{0.16}$ (47c) powder diffraction data at room temperature.

Bond angle / °	
B(Br)–Li(Na)–B(Br)	180
B(Br)–Li(Na)–B(Br)	90

Table 8.2-4 Selected Rietveld refinement data from PXD data of the $\text{Li}_{0.5}\text{Na}_{0.5}(\text{BH}_4)_{0.84}\text{I}_{0.16}$ (57) compound at room temperature

Sample number	57
Empirical formula	$\text{Li}_{0.5}\text{Na}_{0.5}(\text{BH}_4)_{0.84}\text{I}_{0.16}$
Collection temperature / °C	20
Crystal system	Cubic
Space group	$\text{Fm}\bar{3}\text{m}$
Z	4
Unit cell formula weight, M_w	166.634
Calculated density, ρ / g cm^{-3}	1.124
Unit cell dimensions:	
a / Å	6.2670(1)
V / Å ³	246.1(1)
Observations, parameters	5133, 30
R_{wp}	0.0511
R_p	0.0402
χ^2	1.510

Table 8.2-5 Complete bond lengths $\text{Li}_{0.5}\text{Na}_{0.5}(\text{BH}_4)_{0.84}\text{I}_{0.16}$ (57) powder diffraction data at room temperature.

Bond length / Å	
Li(Na)–B(I)	3.1348(6)

Table 8.2-6 Complete bond angles $\text{Li}_{0.5}\text{Na}_{0.5}(\text{BH}_4)_{0.84}\text{I}_{0.16}$ (57) powder diffraction data at room temperature.

Bond angle / °	
B(I)–Li(Na)–B(I)	180
B(I)–Li(Na)–B(I)	90

8.3 Appendix C: Tables and Figures for Chapter 5

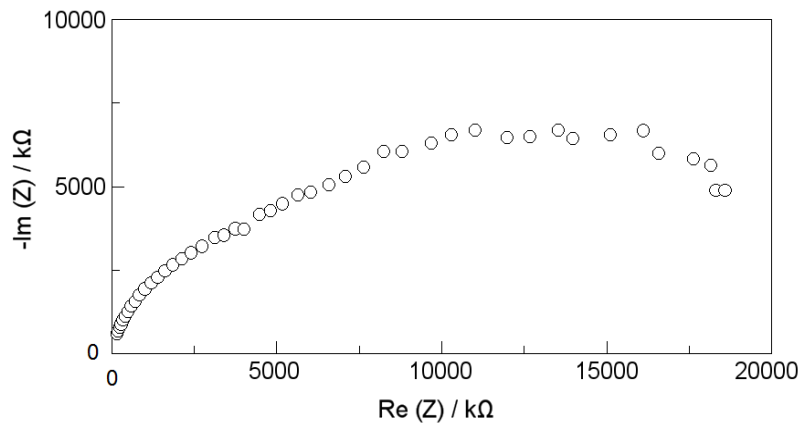


Figure 8.3-1 Nyquist plot of 55 at 313 K.

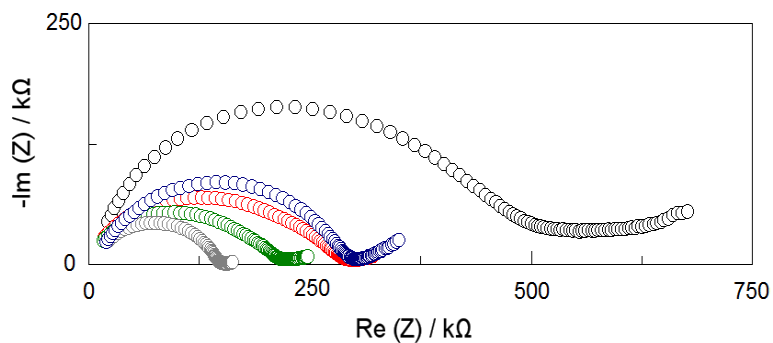


Figure 8.3-2 Nyquist plot of 54 (black), 56 (red), 58 (green), 59 (grey) and 60 (blue) at 298 K.

